



ARISTOTLE UNIVERSITY OF THESSALONIKI
SCHOOL OF GEOLOGY
DEPARTMENT OF GEOPHYSICS



CHARIKLEIA G. GKARLAOUNI
M.Sc. Geologist

STUDY OF SEISMICITY PROPERTIES BASED ON THE INTERACTION AND
EVOLUTION OF ACTIVE FAULT SYSTEMS IN THE AEGEAN AND ITS
SURROUNDINGS

Ph.D. THESIS

THESSALONIKI 2020



ΧΑΡΙΚΛΕΙΑ Γ. ΓΚΑΡΛΑΟΥΝΗ
Πτυχιούχος M.Sc. Γεωλόγος

ΜΕΛΕΤΗ ΤΩΝ ΙΔΙΟΤΗΤΩΝ ΤΗΣ ΣΕΙΣΜΙΚΟΤΗΤΑΣ ΜΕ ΒΑΣΗ ΤΗΝ
ΑΛΛΗΛΕΠΙΔΡΑΣΗ ΚΑΙ ΑΝΑΠΤΥΞΗ ΣΥΣΤΗΜΑΤΩΝ ΣΕΙΣΜΟΓΟΝΩΝ
ΡΗΓΜΑΤΩΝ ΣΤΟΝ ΕΥΡΥΤΕΡΟ ΧΩΡΟ ΤΟΥ ΑΙΓΑΙΟΥ

ΔΙΔΑΚΤΟΡΙΚΗ ΔΙΑΤΡΙΒΗ

Υποβλήθηκε στο Τμήμα Γεωλογίας
Τομέας Γεωφυσικής
Ημερομηνία Προφορικής Εξέτασης: 28 Απριλίου 2020

Τριμελής Συμβουλευτική Επιτροπή

Καθηγήτρια Παπαδημητρίου Ελευθερία, Επιβλέπουσα
Καθηγητής Stanisław Lasocki, Μέλος Τριμελούς Συμβουλευτικής Επιτροπής
Καθηγητής Κίλιας Αδαμάντιος, Μέλος Τριμελούς Συμβουλευτικής Επιτροπής

Επταμελής Εξεταστική Επιτροπή

Καθηγήτρια Παπαδημητρίου Ελευθερία, Επιβλέπουσα
Καθηγητής Stanisław Lasocki, Σύμβουλος
Καθηγητής Κίλιας Αδαμάντιος, Σύμβουλος
Καθηγητής Καρακώστας Βασίλειος, Εξεταστής
Καθηγητής Τσακλίδης Γεώργιος, Εξεταστής
Καθηγήτρια Beata Orłowska-Sikora, Εξετάστρια
Καθηγητής Καρακαϊσής Γεώργιος, Εξεταστής



© Χαρίκλεια Γεωργίου Γκαρλαούνη, 2020

© ΑΠΘ

Με επιφύλαξη παντός δικαιώματος.

Μελέτη των ιδιοτήτων της σεισμικότητας με βάση την αλληλεπίδραση και ανάπτυξη συστημάτων σεισμογόνων ρηγμάτων στον ευρύτερο χώρο του Αιγαίου

ISBN

Η έγκριση της παρούσης Διδακτορικής Διατριβής από το Τμήμα Γεωλογίας του Αριστοτελείου Πανεπιστημίου Θεσσαλονίκης δεν υποδηλώνει αποδοχή των γνώμων του συγγραφέως (Ν. 5343/1932, άρθρο 202, παρ. 2)

Η παρούσα διδακτορική διατριβή έχει συγχρηματοδοτηθεί από την Ευρωπαϊκή Ένωση (Ευρωπαϊκό Κοινωνικό Ταμείο – ΕΚΤ) και από εθνικούς πόρους μέσω του Επιχειρησιακού Προγράμματος «Εκπαίδευση και Δια Βίου Μάθηση» του Εθνικού Στρατηγικού Πλαισίου Αναφοράς (ΕΣΠΑ) – Ερευνητικό Χρηματοδοτούμενο Έργο: Ηράκλειτος ΙΙ. Επένδυση στην κοινωνία της γνώσης μέσω του Ευρωπαϊκού Κοινωνικού Ταμείου.





CHARIKLEIA G. GKARLAOUNI

M.Sc. Geologist

STUDY OF SEISMICITY PROPERTIES BASED ON THE INTERACTION AND
EVOLUTION OF ACTIVE FAULT SYSTEMS IN THE AEGEAN AND ITS
SURROUNDINGS

Ph.D. THESIS

Submitted to the School of Geology

Department of Geophysics

Defense Date: April 28th 2020

Advisory Committee

Professor Papadimitriou Eleftheria, Supervisor

Professor Stanisław Lasocki, Member of the Advisory Committee

Professor Kiliadis Adamantios, Member of the Advisory Committee

Examining Committee

Professor Papadimitriou Eleftheria, Supervisor

Professor Stanisław Lasocki, Advisor

Professor Kiliadis Adamantios, Advisor

Professor Karakostas Vasileios, Examiner

Professor Tsaklidis Georgios, Examiner

Professor Beata Orłowska-Sikora, Examiner

Professor Karakaisis Georgios, Examiner



© Charikleia Georgios Gkarlaouni, 2020

© AUTH

All rights reserved.

Study of seismicity properties based on the interaction and evolution of active fault systems in the Aegean and its surroundings

ISBN

The approval of this Ph.D. Thesis by the school of Geology of the Aristotle University of Thessaloniki does not imply acceptance of the opinions of the author (L. 5343/1932, Article 202, par. 2)

This Ph.D. Thesis has been co-financed by the European Union (European Social Fund–ESF) and Greek national funds through the Operational Program "Education and Lifelong Learning" of the National Strategic Reference Framework (NSRF) – Research Funding Program: Heracleitus II Investing in knowledge society through the European Social Fund.





Dedicated to my family and especially to my father,
who inspired me to science and knowledge

"So all a man could win in the conflict between plague and life was knowledge and memory" Albert Camus (1913-1960)



Acknowledgements

I would like to express my gratitude towards the people who supported me and contributed to the completion of the dissertation. My gratitude is sincerely expressed to my supervisor Professor Papadimitriou Eleftheria for entrusting me with this thesis. I appreciate her guidance and encouragement from the beginning of my studies until the completion of this thesis. I appreciate her strong prompt for visiting other institutions and for participating in scientific conferences and I thank her for encouraging me to collaborate with other members of the international scientific community. I would like to deeply thank Professor Stanislaw Lasocki from the Institute of Geophysics, Polish Academy of Sciences, for inspiring me to explore stochastic analysis and for his constructive comments. I would like to express my sincere gratitude to Professor Adamantios Kiliias for his encouragement and especially for the scientific discussions we had and his seismotectonic remarks. I am also grateful to Professor Karakostas Vasileios for his valuable contribution and collaboration regarding earthquake relocation procedures as well as the seismotectonic analysis. I also owe many thanks to Professor Tsaklidis George for his scientific guidance and his instructions on statistical issues. I deeply appreciate Professor Georgios Karakaisis for the attentive reading of the thesis and meaningful comments and Professor Beata Orlecka-Sikora for her remarks.

I would also like to express my thanks to Dr. Grzegorz Lizurek from the Institute of Geophysics, Polish Academy of Sciences, for his scientific assistance on my first steps in statistical seismology and the fruitful discussions we had. A special thanks is devoted to my friends and colleagues Dr. Leptokaropoulos Kostas, Dr. Pennos Christos and Dr. Paparadisopoulou Popi for being real partners all these years and for sharing with them all these efforts and thoughts and feelings. I would also like to thank Dimitris Chorozoglou for spending our happy office time together and for his precious Matlab tips and Kony Kementzetidou for her assistance in searching the seismological station bulletin. I respect the opportunity that the Geophysics Department has given to me during the thesis to gain scientific experience on seismology and on real-time analysis, which has proved to be valuable. I would also like to thank Nikolas Kortimanitsis for his support and assistance and Anna Messini for the long hospitality that she offered to me.

Words are not enough to express my deep feelings towards my parents Giorgos and Maria and my lovely sister Titi for their substantial and continuous support and patience over the years... a huge heartfelt thank you!

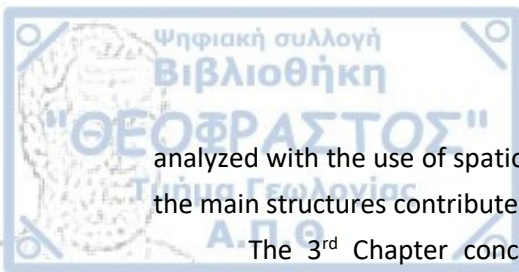
The stress/strain tensors were calculated using the DIS3D code of S. Dunbar, which was later improved by Erikson (1986) and the expressions of G. Converse. The majority of the figures are made with the use of the QGIS Geographic Information System, Open Source Geospatial Foundation Project (<http://qgis.osgeo.org>) version QGIS 3.8.2. Cross sections are plotted with the use of the Generic Mapping Tools – GMT 4.5.3 (www.soest.hawaii.edu/gmt, Wessel and Smith 1998).

Seismogenic rifts and basins are often the most popular places on earth in need of protection from potential seismic hazard, because they are densely populated and enclose significant developed infrastructure. For this reason, basins regard a fundamental scientific research object in the view of seismotectonic, seismological and hazard assessment studies. This thesis is directed towards the Aegean area where the crust undergoes significant horizontal stretching due to extensional forces and leads to the formation of basins with active fault populations, hazardous seismogenic faults and intense seismicity and occasional devastating earthquakes. The approximation of the location or the recurrence time or the magnitude of an impending earthquake in these specified areas, is hardly explained by a periodic seismic cycle on a fault isolated from the adjacent faults. On the opposite the recurrence time, location and size of the earthquakes are associated with the ability of faults to interact and earthquakes to trigger subsequent ones. In this study, an attempt was made to identify earthquake interrelations in the seismicity process in two extensional fault populations in Greece. The investigation is eventually developed toward three separate scientific objects which contribute from their aspect to hazard assessment and the justification of the deformational stage for the two study areas. The thesis was conducted in order to respond to the questions below:

- Which are the seismicity characteristics in the two extensional areas and how they are expressed?
- Is there a characteristic trend of the current seismicity to allow us extract information on future earthquakes?
- What is the impact of strain on the earthquake process?
- Does the seismic process reveal information on the evolution of the fault populations?

In the 1st Chapter, there is an introduction to the selected study areas which fulfill the requirements for intense seismicity and a satisfactory archive for strong historical earthquakes. A description is given about the seismotectonic properties of the fault network and its features, as well as the seismic activity with emphasis on the strong historical earthquakes. Both study areas, Mygdonia graben and Corinth Rift have been in the focus of the scientific interest due to their intense earthquake activity, thus there is a bulk amount of information provided from geological, seismotectonic, geodetic or geomorphological studies. The integration of all scientific approaches is important for the comparative interpretation of the analysis results.

The content of the 2nd Chapter includes the earthquake relocation process of recent seismicity (2008-2014) a procedure aiming to provide an earthquake catalog with improved focal coordinates. The relocation methodology and the adopted criteria are described individually for the two study areas. The spatial and temporal properties of seismicity are



analyzed with the use of spatiotemporal diagrams and tools. Cross sections perpendicular to the main structures contribute to the understanding of the fault geometry at depth.

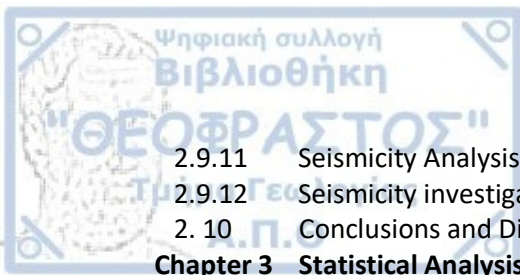
The 3rd Chapter concerns the stochastic analysis of the seismicity for different earthquake catalogs depending on the completeness threshold and the study period. Complete seismicity catalogs for strong earthquakes, moderate earthquakes, recent seismicity and declustered recent seismicity are studied with the help of stochastic tools. In this chapter there is a description of the stochastic methodologies and techniques which were developed or adopted for the aim of the study. The main concern is to quantify interrelations through memory and clustering of earthquakes for interevent time, interevent distance and magnitude.

In Chapter 4, the stress impact of strong earthquakes in terms of the static coseismic Coulomb stress changes along with the constant slip rates along faults are considered. The potential triggering between strong earthquakes, and the interaction of faults for promoting or hindering strong earthquakes is examined. The successive stages of the evolutionary stress field is reconstructed from 1677 in Mygdonia and 1700 in the Corinth Rift and extrapolated in the future. The correlation between the spatial distribution of moderate and recent seismicity with the strong earthquake occurrence is additionally investigated.

In the last chapter, there is a synthesis of the conclusions that were drawn, from the application of the individual methodologies. The two study areas are compared and seismicity is explained under the framework of the localization of deformation in the two seismotectonic regimes. The appendix provides information about the station time delays which were calculated during the Wadati relocation process, the time series and information about the calculated seismic moment tensors and seismic strain tensors.

Table of Contents

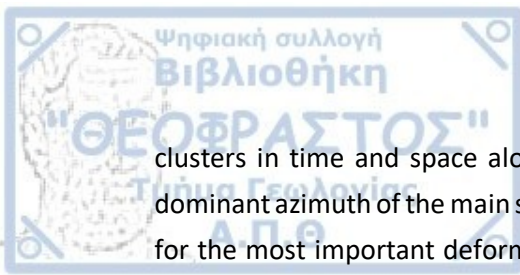
English Abstract	12
Ελληνική Περίληψη	15
Publications	18
Chapter 1 Introduction	20
1. 1 Introduction	21
1. 2 Aim of the Study - Research Objectives.....	22
1. 3 Seismotectonic Setting	25
1.3.1 Seismotectonic Setting of the Aegean Sea	25
1.3.2 Seismotectonic Setting of Mygdonia Graben.....	27
1.3.3 Seismotectonic Setting of Corinth Rift.....	33
1. 4 Relevant Research in the Study Areas	29
1.4.1 Seismotectonic Investigation in Mygdonia Graben.....	29
1.4.2 Seismotectonic Investigation in Corinth Rift.....	32
1.4.3 Stochastic Investigation of the seismic process in Greece	35
1.4.4 Coulomb Stress Investigation in Greece	37
Chapter 2 Seismotectonic Analysis	40
2. 1 Introduction	41
2. 2 Data	42
2.2.1 Seismological Network	42
2.2.2 Seismic Wave Phases.....	42
2. 3 Relocation Techniques.....	43
2.3.1 Introduction	43
2.3.2 Earthquake Location Algorithms	43
2. 4 Velocity Models.....	44
2. 5 Velocity Ratio, V_P/V_S	45
2. 6 Station Time Corrections	46
2. 7 Magnitude Corrections.....	46
2. 8 Relocation Results for Mygdonia Graben	48
2.8.1 Introduction	48
2.8.2 Data	48
2.8.3 Velocity Model	50
2.8.4 Wadati Plots	51
2.8.5 Station Time Corrections	52
2.8.6 Relocation process.....	52
2.8.7 Implications for the width of the seismogenic layer	53
2.8.8 Earthquake Magnitude Assignment and Correction	55
2.8.9 Final Seismicity Catalog.....	58
2.8.10 Seismicity Analysis for Mygdonia Graben.....	60
2. 9 Earthquake Relocation Results for Corinth Rift	74
2.9.1 Introduction	74
2.9.2 Data	75
2.9.3 Velocity Model	76
2.9.4 Wadati Plots	77
2.9.5 Station Time Corrections	80
2.9.6 Relocation Process and Implications for the width of the seismogenic layer	81
2.9.7 Earthquake Magnitude Assignment and Correction	88
2.9.8 Final Seismicity Catalog.....	89
2.9.9 Seismicity Analysis for Corinth Rift.....	91
2.9.10 Seismicity investigation for Kato Achaia area	107



2.9.11	Seismicity Analysis for the Xylocastro area.....	113
2.9.12	Seismicity investigation for the Alkyonides area.....	120
2. 10	Conclusions and Discussion	128
Chapter 3	Statistical Analysis	135
3. 1	Introduction	136
3.1.1	Statistical analysis of seismicity.....	136
3.1.2	Objective of the study	137
3. 2	Data Sets and Data Process.....	138
3.2.1	Data Resources	138
3.2.2	Data Process.....	139
3.2.3	Long Term Memory Analysis.....	146
3.2.4	Short Term Memory Analysis - Autocorrelation Coefficient.....	159
3.2.5	Clustering Analysis - Mutsumura Coefficient of Randomness	163
3.1	Synthesis of the results - Discussion.....	167
Chapter 4	Coulomb Stress Analysis	173
4. 1	Introduction	174
4.1.1	Earthquake, fault interaction and tectonic deformation.....	174
4.1.2	Objective of the study	175
4. 2	Coulomb Stress Changes.....	177
4.2.1	Methodology.....	177
4.2.2	Seismic Sources	182
4.2.3	Fault segmentation and long term slip rate constraints.....	187
4.2.4	Coseismic Coulomb stress changes for Mygdonia	194
4.2.5	Coseismic Coulomb stress changes in Corinth rift	206
4.2.6	Evolutionary stress models	228
4.2.7	Correlation between Stress Coulomb and Seismicity.....	241
4. 3	Synthesis of the results and discussion	256
Chapter 5	Concluding Remarks	260
Appendix	265
References	272

The main purpose of this dissertation is the study and the identification of the seismotectonic and stochastic characteristics of two active fault populations which are located in Greece. Emphasis is given on the seismogenic faults which are responsible for strong and minor earthquake occurrence. The investigation of possible interactions between faults and earthquakes along with the quantification of these interrelations is based on the stochastic tools which unveil hidden information on seismic activity and the dependence of earthquakes on the stress distribution in the study areas. The two study areas, namely the Mygdonia basin (N. Greece) and Corinth Rift (central Greece) are parts of the back-arc Aegean Sea and have been selected because they have experienced strong and frequent seismicity. This active geotectonic pattern is attributed to the subduction and the retreat of the Mediterranean oceanic plate under the fast southward moving Aegean, giving rise to the Hellenic Arc and the westward extrusion along the North Anatolian Fault into the North Aegean (North Aegean Trough). The combination of these features impose the fast spread of the Aegean microplate to the southwest, the extension and thinning of the crust which gives rise to the formation of neotectonic basins oriented in an East-West direction according to the active stress field, they are bounded by active faults and related to strong seismicity. A significant number of devastating earthquakes with magnitudes $M \geq 6.0$ have occurred in these areas, both in historical times and during the instrumental period like in 1932 (Ierissos, M7.0) in 1978 (Stivos, M6.5) regarding Mygdonia and in 1981 (Alkyonides, M6.7) in 1995 (Aigio, M6.5) for the eastern and the western Corinth Rift respectively. The scientific interest for these areas is significant and many researchers have put an effort to clarify the seismotectonic properties of these two regions.

The epicentral distribution of earthquakes provides information on the presence of major or subsidiary faults, therefore their study contributes to the identification of the characteristics associated with the evolution and the dominance of the faulting network. For this reason, one of the most important objectives inevitably is the relocation of the earthquake coordinates for the recent seismicity in the two study areas. The data used, correspond to pairs of P- and S- seismic wave phases. Wave arrivals which have been recorded at the seismological stations belonging to the Hellenic Unified Seismological Network (HUSN) are employed for the application of Wadati methodology. The velocity ratio is computed for each region and an important spatial variation is identified in Corinth gulf area which is divided into six sub areas due to the structural complexity. For all areas, time corrections for the seismological stations located in short distance from the epicentral area are estimated. All the above data, along with the best fitted crustal velocity model are further used as an input to the Hypoinverse algorithm for the relocation procedure. In cases of strong spatial clustering between earthquakes, the HypoDD algorithm is further applied. The spatial and temporal investigation of earthquake distribution shows that there is an important indication of earthquakes migration even in the case of minor magnitudes. Microseismicity is found in



clusters in time and space along adjacent fault zones. Cross sections perpendicular to the dominant azimuth of the main seismogenic faults contributes to the identification of geometry for the most important deformation zones. The depth of the seismogenic layer is therefore defined with adequate precision in both areas.

After defining the major seismogenic faults and reaching the striking observation according to which, seismic activity is interacting and migrating along them, the second objective of the study is the quantification of the interaction mechanisms between earthquakes and the ability of seismicity to maintain its characteristic behavior in time and to form clusters. This refers to the fact that earthquakes are triggered from previous ones or they impose an effect on the properties of the successive earthquakes. Therefore, stochastic methodologies are adopted and applied on seismic catalogs owing different features in all magnitude scales. For each data set the completeness magnitude is estimated and catalogs are declustered when needed. Considering that the seismic process is composed of three different parameters in time, in space and in size, the investigation of the properties is of great importance, close related to seismic hazard assessment. In the current work, time-series were created for the interevent time and the interevent distance between consecutive events along with successive magnitudes and were investigated for their complexity, their clustering and the existence of long and short memory in all cases of strong and minor seismicity. The existence of long or short memory content is investigated with the help of the Hurst coefficient and the autocorrelation coefficient (ACF). A spatial and temporal investigation is performed for Hurst coefficient and its relation with seismicity changes is studied. Long memory is proved to be one of the most important characteristics of seismicity, especially for the recent microseismicity of the Corinth gulf. The clustering ability of earthquakes is examined with the use of randomness coefficient indicating strong clustering in time and space. The final objective is the investigation of the interactions among the major faults in each study area, based on the evolution of the stress field. For this reason, the strong earthquakes that occurred in the two study areas since 1700 are considered. Rupture models for the corresponding earthquakes are prepared according to seismotectonic information and scaling relations. Coseismic stress Coulomb changes are computed for the 7 strong events associated with Mygdonia area and the 30 strong events which occurred in the Corinth Rift. The incorporation of the tectonic loading measured by geodetic means is incorporated into the analysis and the evolutionary stress field is reconstructed for the two areas, until present. Finally, after the full exploitation of strong and minor seismicity a synthesis of all results extracted from the analysis is attempted, in combination with the geological and seismotectonic information.

Results show that the different degree of deformation localization into the two study areas is imprinted on seismicity. The stronger localization of strain in the Corinth Rift is responsible for the strong indications of clustering and long memory content for interevent time and distance, meaning that seismicity mostly occurs along the main fault zones. On the other hand, a relatively more distributed deformation pattern in Mygdonia graben, compared



to Corinth Rift, where subsidiary small faults, are brought into failure due to the occurrence of strong earthquakes account for earthquake occurrence and exhibit a weaker degree of spatiotemporal memory and clustering.

Στόχος της διατριβής είναι η μελέτη και ανάδειξη των δυναμικών και στοχαστικών χαρακτηριστικών δύο πληθυσμών σεισμογόνων ρηγμάτων του Ελλαδικού χώρου, δηλαδή η μελέτη των ενεργών εκείνων ρηγμάτων τα οποία συνδέονται με τη γένεση ισχυρών σεισμών και μικροσεισμικότητας. Η διερεύνηση της αλληλεξάρτησης και η ποσοτικοποίηση του βαθμού αλληλεπίδρασης μεταξύ των ρηγμάτων, η οποία πραγματοποιείται λόγω της κατανομής των τάσεων, αποτυπώνεται στις ιδιότητες της σεισμικής διαδικασίας. Οι δύο περιοχές μελέτης αποτελούν τμήματα της οπισθότοξης περιοχής του Αιγαίου. Ο χώρος αυτός παρουσιάζει έντονη και ισχυρή σεισμικότητα. Αυτό οφείλεται στην κατάδυση της ωκεάνιας Μεσογειακής πλάκας κάτω από το Αιγαίο κατά μήκος του Ελληνικού τόξου, καθώς και στην ισχυρή δράση του ρήγματος της Β.Ανατολίας και την προέκταση του στο βόρειο Αιγαίο, σχηματίζοντας την τάφρο του Β.Αιγαίου. Η συνδυαστική αυτή δράση επιβάλλει την προς τα ΝΔ ταχεία κίνηση της μικροπλάκας του Αιγαίου, την έντονη εφελκυστική παραμόρφωση και τη λέπτυνση του φλοιού στην οπισθότοξη περιοχή με αποτέλεσμα την ανάπτυξη εφελκυστικών δομών (λεκανών). Οι λεκάνες περιβάλλονται από ενεργά ρήγματα και εκδηλώνουν ισχυρή σεισμικότητα, όπως οι περιοχές που μελετώνται, η Μυγδονία λεκάνη και η λεκάνη του Κορινθιακού κόλπου. Ισχυροί και καταστροφικοί σεισμοί με μεγέθη $M \geq 6.0$ έχουν γίνει σε αυτές, τόσο στους ιστορικούς χρόνους όσο και κατά την ενόργανη περίοδο όπως το 1932 (Ιερισός, $M7.0$) και το 1978 (Στίβος, $M6.5$) στη Μυγδονία ή το 1981 (Αλκυονίδες, $M6.7$) και το 1995 (Αίγιο, $M6.5$) στον Κορινθιακό κόλπο. Η διατριβή αποτελείται από τρία επιμέρους ερευνητικά αντικείμενα τα οποία εν τέλει συνδυάζονται και συμβάλλουν στην ολοκληρωμένη προσέγγιση του στόχου.

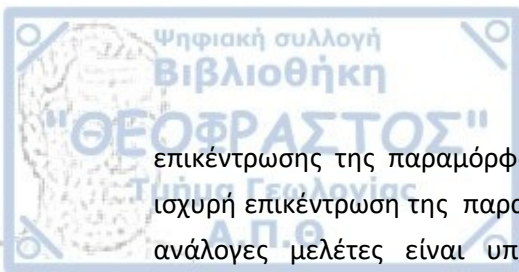
Η κατανομή των σεισμικών εστιών αποκαλύπτει πληροφορίες για την ανάπτυξη και τη γεωμετρία του σεισμοτεκτονικού ιστού. Συνεπώς, είναι απαραίτητη η όσο το δυνατό πιστότερη ακρίβεια των εστιακών παραμέτρων των σεισμών. Για το λόγο αυτό τίθεται και ως πρωταρχικός σκοπός ο επαναπροσδιορισμός των παράμετρων της εστίας για τους πιο πρόσφατους σεισμούς. Για το λόγο αυτό συλλέγονται δεδομένα σεισμικότητας τα οποία αφορούν τις αφίξεις ζευγών εγκαρσίων και επιμήκων σεισμικών κυμάτων. Τα δεδομένα αυτά έχουν καταγραφεί από σταθμούς του Ενοποιημένου Ελληνικού Σεισμολογικού Δικτύου (ΕΕΣΔ) και χρησιμοποιούνται για την εφαρμογή της μεθοδολογίας *Wadati*. Εκτιμάται ο λόγος ταχυτήτων για κάθε περιοχή όπου για τον Κορινθιακό κόλπο παρουσιάζει σημαντική χωρική διαφοροποίηση. Η περιοχή αυτή λόγω της πολύπλοκότητας της δομής της, διαιρείται σε 6 επιμέρους υπο-περιοχές, σε κάθε μία από τις οποίες επαναλαμβάνεται η παραπάνω διαδικασία. Συνεπώς, υπολογίζονται οι χρονικές διορθώσεις των σεισμολογικών σταθμών και μαζί με το μοντέλο ταχυτήτων, εισάγονται στο πρόγραμμα Hygroinverse για τον επαναπροσδιορισμό των εστιακών συντεταγμένων των σεισμών. Στις περιπτώσεις ισχυρής ομαδοποίησης των σεισμών εφαρμόζεται ο αλγόριθμος HygroDD ο οποίος λαμβάνει υπόψη την ισχυρή χωρική συσχέτιση μεταξύ των σεισμών με αποτέλεσμα τη βέλτιστη ακρίβεια στον επαναπροσδιορισμό των εστιακών συντεταγμένων και επομένως στην ανάδειξη της

γεωμετρίας των ρηγμάτων. Η χρονική και χωρική κατανομή της σεισμικότητας δείχνει σημαντική μετανάστευση σεισμών μεταξύ των ρηγμάτων, ακόμη και μεταξύ μικρού μεγέθους σεισμών. Προκύπτει επίσης, ότι η μικρο-σεισμικότητα δημιουργεί ομάδες οι οποίες συσχετίζονται μεταξύ τους και η αλληλεπίδραση αυτή υπερισχύει για τους σεισμούς μεταξύ των κύριων δομών. Η διερεύνηση του σειсмоγόνου όγκου και της γεωμετρίας των ρηγμάτων σε βάθος πραγματοποιείται με την υλοποίηση κατακόρυφων τομών σε διεύθυνση κάθετη στην επικρατούσα διεύθυνση των κύριων ρηγμάτων.

Επόμενο στόχο της εργασίας αποτελεί η ποσοτικοποίηση της αλληλεπίδρασης μεταξύ των σεισμών, δηλαδή η ιδιότητα της σεισμικής διαδικασίας να διατηρεί τα χαρακτηριστικά της και να ομαδοποιείται. Προκειμένου να προσεγγιστεί το παραπάνω πρόβλημα υιοθετούνται στοχαστικές μεθοδολογίες. Απαραίτητη προϋπόθεση είναι η ανεύρεση του μεγέθους πληρότητας και η αποκλασματοποίηση των σεισμικών καταλόγων. Η σεισμική διαδικασία περιγράφεται από επιμέρους παραμέτρους στον χώρο, στο χρόνο και το μέγεθος. Δημιουργούνται χρονοσειρές από τους ενδιαμέσους χρόνους και τις ενδιαμέσες αποστάσεις μεταξύ δύο διαδοχικών σεισμών καθώς και τα διαδοχικά μεγέθη. Εξετάζονται η ύπαρξη πολυπλοκότητας, συσταδοποίησης, μακράς και βραχείας μνήμης-εμμονής της πρόσφατης αλλά και της ισχυρής σεισμικότητας. Η παρουσία μακροπρόθεσμης και βραχυπρόθεσμης μνήμης της σεισμικής διαδικασίας μελετάται με τη βοήθεια του συντελεστή Hurst και του συντελεστή αυτοσυσχέτισης ACF μαζί με τη πιθανή συσχέτιση του Hurst με τη χωρική και χρονική μεταβολή της σεισμικότητας. Η δυναμική παρουσία της μνήμης αποδुकνείεται έντονα, ειδικά για τους ενδιαμέσους χρόνους με τον Κορινθιακό κόλπο να υπερτερεί σημαντικά. Ο βαθμός ομαδοποίησης μελετούνται με τη χρήση του συντελεστή τυχαιότητας, αναδεικνύοντας έναν ισχυρό βαθμό ομαδοποίησης.

Τελικό στόχο της διατριβής αποτελεί η διερεύνηση της αλληλεπίδρασης μεταξύ των σημαντικότερων ρηγμάτων σύμφωνα με την εξέλιξη του πεδίου των τάσεων λόγω της σεισμικής ολίσθησης και της τεκτονικής φόρτισης. Για το σκοπό αυτό λαμβάνονται υπόψιν οι ισχυροί σεισμοί ($M \geq 6.0$) οι οποίοι έχουν γίνει στις δύο περιοχές μελέτης από το 1700 μέχρι σήμερα. Για κάθε σεισμό προσδιορίζεται το αντίστοιχο μοντέλο διάρρηξης, με βάση σεισμοτεκτονικές παρατηρήσεις και υφιστάμενες μαθηματικές σχέσεις. Υπολογίζονται οι μεταβολές της τάσης Coulomb οι οποίες προκαλούνται ύστερα από τη γένεση κάθε σεισμού για τους επτά σημαντικούς ισχυρούς σεισμούς της Μυγδονίας λεκάνης καθώς και για τους 30 ισχυρούς σεισμούς στην περίπτωση του Κορινθιακού κόλπου. Λαμβάνοντας υπόψιν την τεκτονική φόρτιση η οποία προκαλείται από την διαρκή κίνηση των μικροπλακών στην περιοχή του Αιγαίου, ανακατασκευάζεται το διαδοχικό πεδίο των τάσεων πριν και μετά από κάθε σεισμό μέχρι τη σημερινή κατάσταση.

Τελικά, τα αποτελέσματα τα οποία προκύπτουν από τις επιμέρους μεθοδολογίες, αξιολογούνται και συνδυάζονται με τις διαθέσιμες γεωλογικές και σεισμοτεκτονικές πληροφορίες, προσδιορίζονται τα χαρακτηριστικά των πληθυσμών ρηγμάτων και εξάγονται αποτελέσματα σχετικά με τη πιθανότητα μελλοντικής ισχυρής σεισμικότητας σε δύο από τις πιο σημαντικές περιοχές του Ελλαδικού χώρου. Τα αποτελέσματα δείχνουν ότι ο βαθμός



επικέντρωσης της παραμόρφωσης εκδηλώνεται μέσω της σεισμικής συμπεριφοράς. Η ισχυρή επικέντρωση της παραμόρφωσης στον Κορινθιακό κόλπο όπως αποδεικνύεται από ανάλογες μελέτες είναι υπεύθυνη για την ισχυρή παρουσία συσταδοποίησης και μακροπρόθεσμης μνήμης για τους ενδιαμεσους χρόνους και αποστάσεις μεταξύ των σεισμών, οι οποίοι προκαλούνται πάνω σε κυρίαρχες τεκτονικές δομές. Αντίθετα, στην Μυγδονία συγκριτικά με τον Κορινθιακό, πραγματοποιείται μια περισσότερο κατανεμημένη παραμόρφωση στο πληθυσμό ρηγμάτων, όπου μικρά δευτερεύοντα ρήγματα συμμετέχουν ενεργά στην εξέλιξη της σεισμικότητας η οποία εκδηλώνει μια σεισμική συμπεριφορά με πιο ασθενή την διατήρηση μνήμης και την χωροχρονική συσταδοποίηση συγκριτικά με τον Κορινθιακό κόλπο.

Peer Reviewed Papers in Scientific Journals

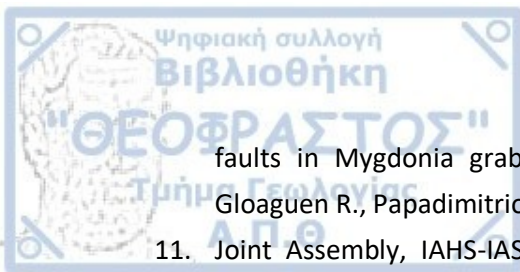
1. Gkarlaouni, C., Lasocki, S., Papadimitriou, E. and Tsaklidis, G. (2017) Hurst analysis of seismicity in Corinth rift and Mygdonia graben (Greece), *Chaos Solitons and Fractals*, 96, 30-42, DOI: 10.1016/j.chaos.2017.01.001.
2. Gkarlaouni, C., Papadimitriou, E., Karakostas, V., Kiliyas, A. and Lasocki, S. (2015) Fault population recognition through microseismicity in Mygdonia region (northern Greece), *Bollettino di Geofisica Teorica ed Applicata*, 56 (3), 367-382, DOI 10.4430/bgta0153.

Peer Reviewed Papers in Conference Proceedings

3. Gkarlaouni, C., Papadimitriou, E. and Kiliyas, A., (2016) On-fault stress along major faults in basin boundaries, *Bul. Geol. Soc. Greece, Proceedings of the 14th International Congress*, L, 1485-1494.
4. Gkarlaouni, C., Lasocki, S., Papadimitriou, E. and Tsaklidis, G., (2015) Investigation of earthquake magnitude and interevent time distribution in Corinth gulf and Mygdonia basin with the use of stochastic tools, *Proceedings of the 28th Panhellenic Statistical Conference*, Athens, 385-399.
5. Gkarlaouni, C., Lasocki, S., Tsaklidis, G. and Karakostas V. (2014) Investigation of the short and long memory of the seismic process, *Proceedings of the 27th Panhellenic Statistical Conference*, Thessaloniki, 53-67 (in Greek).
6. Gkarlaouni, C., Papadimitriou, E., Lasocki, S., Lizurek, G., Karakostas, V. and Kiliyas, A., (2014) Stochastic analysis of earthquake activity in two seismogenic fault systems in Greece, *Bul. Geol. Soc. Greece, Proceedings of the 13th International Congress*, Chania, 1099-1008.

Oral Presentations in International Scientific Conferences

7. 14th International Congress of the Geological Society of Greece, 2016, May 5-8, Thessaloniki, Greece. "On-fault stress along major faults in basin boundaries", Gkarlaouni, C., Papadimitriou, E. and Kiliyas, A.
8. 28th Hellenic Conference in Statistics, 2015, April 15-18, Charokopeio University, Athens. "Investigation of earthquake magnitude and interevent time distribution in Corinth Gulf and Mygdonia basin with the use of stochastic tools", Gkarlaouni, C., Lasocki, S. and Tsaklidis G.
9. 27th Hellenic Conference in Statistics, Big data analysis-business analytics, 2014, April 23-26, Thessaloniki, "Investigation of earthquake interaction in terms of long and short range memory", Gkarlaouni, C., Papadimitriou, E., Lasocki, S., Karakostas, V. and Kiliyas, A.
10. 10th International Congress of the Hellenic Geographical Society, 2014, October 22-24, Thessaloniki. "Seismological and remote-sensed geomorphology analysis along major



faults in Mygdonia graben (N. Greece)", Gkarlaouni, C., Andreani, L., Pennos, C., Gloaguen R., Papadimitriou E., Kiliias A. and Michail M.

11. Joint Assembly, IAHS-IASPO- IASPEI, "Knowledge for the future", 2013, July 22-26, Gothenburg, Sweden. "Application of stochastic tools for the investigation of recent seismicity properties in Corinth Gulf (Central Greece)", Gkarlaouni, C., Papadimitriou, E., Lasocki, S., Lizurek, G., Karakostas, V. and Kiliias, A.
12. 13th International Congress of the Geological Society of Greece, 2013, September 5-8, Chania, Crete, Greece. "Stochastic Analysis of earthquake activity in two seismogenic fault systems in Greece", Gkarlaouni, C., Papadimitriou, E., Lasocki, S., Lizurek, G., Karakostas, V. and Kiliias, A.

Poster Presentations in International Scientific Conferences

13. International Conference 'Science in Technology' SCinTE, 2015, November, 5-7 Athens. "Seismicity Memory Properties in Corinth Gulf", Gkarlaouni, C., Lasocki, S. and Papadimitriou E.
14. 9th International Workshop on Statistical Seismology, 2015, June, 14-19, GFZ, Potsdam, Germany. "Seismicity properties revealed by stochastic means: Application in Corinth Gulf and Mygdonia Basin (Greece) seismic zones" Gkarlaouni Ch., Lasocki S. and Papadimitriou E.
15. European Geosciences Union, General Assembly, 2014, April 29-May 2, Vienna, Austria. "Active tectonics in the Mygdonia basin (northern Greece): a combined seismological and remote-sensed geomorphology approach". Gkarlaouni, C., Andreani, L., Pennos, C., Gloaguen, R., Papadimitriou, E., Kiliias, A. and Michail, M.
16. Joint Assembly, IAHS – IASPO- IASPEI, "Knowledge for the future", 2013, July, 22-26, Gothenburg, Sweden. "Application of stochastic tools for the investigation of recent seismicity properties in Corinth Gulf (Central Greece)", Gkarlaouni, C., Papadimitriou, E., Lasocki, S., Lizurek, G., Karakostas, V. and Kiliias, A.
17. European Seismological Commission, 33rd General Assembly, 2012, August 19-24, Moscow, Russia. "Statistical analysis of the seismicity of fault zones in Mygdonia Basin (Greece)", Lizurek, G., Gkarlaouni, C., Papadimitriou, E., Lasocki, S., Karakostas, V. and Kiliias, A.
18. European Geosciences Union, General Assembly, 2012, April, 22-27, Vienna, Austria. "Seismotectonic properties with implications on faulting identification revealed from recent seismicity in Greece", Gkarlaouni, C., Karakostas, V., Papadimitriou, E., Kiliias, A., Lasocki, S. and Lizurek, G.

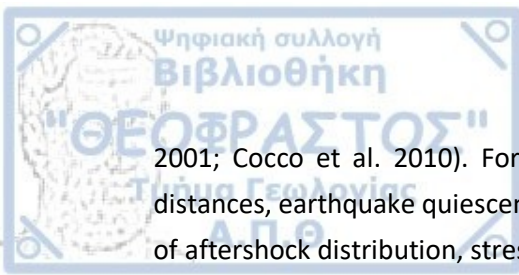


Chapter 1

Introduction

Seismogenesis is a strong indication of active fault properties comprising segmentation, linkage or the fault ability to interact with other faults through their stress field. Seismogenic faults do not appear as isolated structures on earth, but continuously interact mechanically or through their stress field (Scholz, 2002) often generating stronger earthquakes than the ones anticipated, an effect that further complicates the relation between faults and earthquakes. Factors such as rapid or slow strain accumulation on faults or static stress transfer mechanisms control earthquake occurrence since they define the seismogenic and hazardous faults for which slip is either enhanced or inhibited along with their slip rate. Faults form populations, which comprise a synthesis of all isolated, segmented or linked faults, which are developed during one or multiple tectonic episodes and coexist in a region (Peacock et al., 2000; Ben-Zion and Sammis, 2003). Within the fault population, faults grow, interact with the adjacent faults, link, become inactive (Crider and Pollard, 1998) and record the impact of the gradual seismotectonic evolution (Scholz, 2002; Schultz et al., 2009). Seismic processes and features like earthquake triggering along rupture zones, seismicity rate, recurrence times for strong earthquakes, maximum earthquake magnitude potential, indicate that fault populations influence the seismicity stochastic behavior (Das and Scholz, 1981). On the other hand, the properties of faults which participate in this collaborative seismogenic process, can be extracted from spatiotemporal seismicity properties whose knowledge sheds light into the intrinsic behavior of the entire fault network and provides an approximation of the interaction mechanisms. Sornette and Sornette (1990) suggested that the geometric and statistical characteristics of fault populations and earthquakes evolve with the increase of deformation, being self-organizing, in this sense. In seismotectonic environments such as the Aegean Sea, where strain is fast accommodated and is seismically released on frequent and strong earthquakes, cascading and fault synchronization are dominant processes and have been thoroughly discussed so far (Scholz, 2010). Therefore, comprehensive combined seismotectonic investigation and stochastic seismicity analysis is a fundamental key for hazard assessment.

Earthquake interaction has been studied through static or dynamic stress transfer or by time-dependent models. The geometry of the fault network, the poroelastic properties of the seismogenic volume and the stress redistributions are those parameters mostly accounted for seismicity properties and subsequent effects. The significance of earthquake triggering imposed by Coulomb stress changes was first highlighted by Stein et al. (1994) for the 1992 Landers earthquake on the San Andreas Fault. Positive or negative Coulomb stress changes of the order of 0.1-1.0 bars encourage or hinder subsequent earthquakes respectively (Lin and Stein, 2004). Many aspects of seismicity properties are closely related to stress changes induced from a precedent strong event, such as microseismicity spatial and temporal clustering, earthquake cascade or seismic quiescence, while stress redistribution is also dependent on crustal properties, fluid presence and fault friction (Harris 1998; King and Cocco



2001; Cocco et al. 2010). For the investigation of earthquake triggering in small or long distances, earthquake quiescence or fault asperities, changes in seismicity rate or the pattern of aftershock distribution, stress Coulomb changes is proved to be served as a useful tool for studying seismicity and faults.

The principal aim of this study is to decipher possible interaction mechanisms among seismogenic faults and earthquakes, which belong to active fault populations in Greece. A full exploitation of the recorded and relocated by this study seismicity is attempted, in order to extract spatiotemporal and stochastic seismicity characteristics and implement it with findings on the stress and deformational characteristics of their seismogenic volume. Strong, moderate and small magnitude seismicity is considered for this scope and the interrelation characteristics of earthquakes are sought for revealing a trend or a systematic behavior after applying stochastic methodologies on the seismicity process, methods that often contribute to unveiling the hidden features of seismogenesis.

1.2 Aim of the Study - Research Objectives

In this thesis there is an attempt to reveal details of the current seismotectonic state in two extensional regimes under the framework of seismicity properties including both instrumental and historical earthquakes. The study areas are the Mygdonia graben (Northern Greece) and the Corinth Rift (central Greece), which represent two of the most important active grabens in Greece, as it is described in the following paragraphs. The study areas satisfy common criteria in reference to their high seismicity rate, their fault population complexity and the significant amount of the accommodated strain under a unique extensional setting. Briefly, the thesis was directed towards the investigation of three main objectives, schematically shown in Figure 1-1.

- i. The first goal of the study is the identification of the fault population characteristics in the two study areas. The determination of the fault geometrical properties can be achieved by studying the relocated recent seismicity. The investigation is conducted for the improvement of earthquake focal coordinates, which were instrumentally recorded by the permanent seismological network, HUSN. For this purpose, the adopted methodology includes the incorporation of the most suitable velocity model, the application of the Wadati technique and the calculation of seismological stations time delays, for each area. A new seismicity catalog is compiled and checked for magnitude homogeneity. Earthquake spatiotemporal characteristics are analyzed in time and space domains, for defining earthquake bursts and active fault geometry. Available information of past seismicity, fault plane solutions or fault kinematics are employed for this reason and an investigation of the main and secondary seismotectonic features and their contribution to seismic hazard assessment is attempted. The existence of inherited fault geometries and old weakness planes are investigated for better understanding of the spatiotemporal distribution of

earthquakes. The thickness of the brittle crust, its viscosity, fluid presence and friction properties which influence the evolution of the faults at depth play an important role at fault capacity to occasionally generate strong earthquakes.

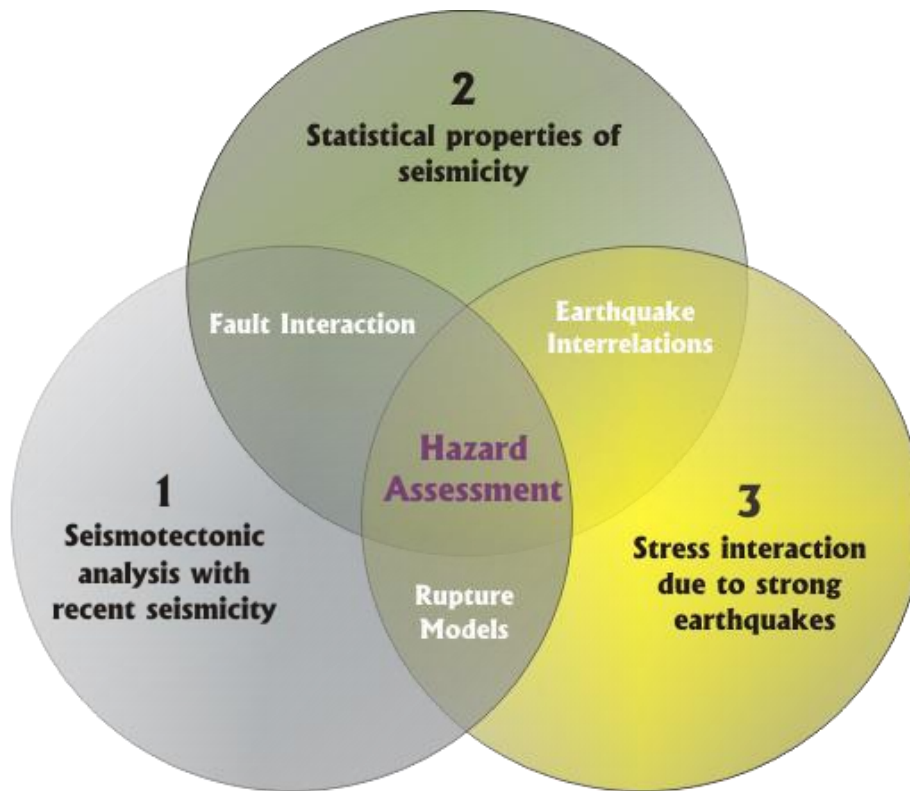


Figure 1-1 Schematic view of the three study principal objectives and the association between the distinctive fields of study.

- ii. The second goal is to unveil possible interrelation characteristics between all ranges of earthquake magnitudes through the seismic stochastic process. Since interaction mechanisms between earthquakes exist, these must be imprinted on the earthquake process. Therefore, in this part seismicity is parameterized and certain stochastic tools chosen for this scope, are applied to all earthquake catalogs in terms of size, interevent time and interevent distance between consecutive events. The adopted stochastic tools were chosen for their ability to indicate properties like short-term and long-term memory possession, as well as clustering or correlation effects between earthquakes, like the Hurst coefficient, the autocorrelation coefficient and the Matsumura coefficient. Magnitude completeness is ascertained and catalog declustering diminish the impact of the strongly dependent fraction of seismicity (i.e. aftershocks). All statistical methodologies are performed on both non-declustered and declustered data. The theoretical statistical distribution of interevent time and magnitude were investigated and the multimodality test was used for investigating the unimodality of the optimal distributions. The investigation was performed on strong, moderate and small magnitude earthquakes, when data are statistically

adequate. The stochastic analysis between the two study areas arises discrepancies, which are mainly attributed to fault behavior and interaction. Correlation effects in terms of strong, moderate and minor earthquakes are studied with emphasis on interevent time which seems to be a promising parameter for the best interpretation of clustering and persistence in seismicity process.

- iii. The third objective is the detection of the triggering ability of strong earthquakes in the last 300 years, in terms of the Coulomb static stress field. Coulomb stress perturbations due to the coseismic slip of an earlier strong event, are assumed to adequately provoke or inhibit the occurrence of a subsequent earthquake and they have a significant effect on the seismicity process. The Coulomb failure criterion which quantifies failure on faults is applied with the computation of coseismic static stress changes for strong ($M \geq 6.0$) earthquakes, seven rupture models in Mygdonia and thirty rupture models in the Corinth Rift. The rupture models are constrained and speculations are made about the friction properties of the brittle crust where strain is accommodated. Constant tectonic loading along rupture zones is added and geometrical, kinematic characteristics of fault segments were assessed for the reconstruction of the stress evolutionary model from 1700 (for Corinth Rift) and 1677 (for Mygdonia Graben) onwards. Stress variations are also calculated across the major rupture zones for identifying the preference for a higher accumulation of coseismic slip across the zone. The model performance is tested upon different values of crustal friction properties, like the friction coefficient and Skempton's coefficient. The stress evolutionary field is extrapolated for the next thirty years, in order to approximate the future stress enhanced locations close to failure. The spatial distribution of recent (2008-2014) and moderate seismicity ($M \geq 4.0$) in association with the localities of the strong earthquakes, along with the frictional properties of the crust are examined and significant discrepancies are identified between the two study areas. Stress transfer contribution to the interpretation of strong earthquake occurrence was highlighted, however the interpretation of moderate and small magnitude seismicity requires further investigation.



1.3 Seismotectonic Setting

1.3.1 Seismotectonic Setting of the Aegean Sea

Eastern Mediterranean is one of the most active and complicated continental regions within the Alpine-Himalayan geotectonic zone. It experiences a high seismicity rate, intense seismic excitations and frequent occurrence of moderate and strong earthquakes. The broader Aegean Sea in particular has been the focus of numerous studies and is indicatively described as a natural laboratory (Fig. 1-2). The first evidence for the seismotectonic complexity of the region was the observation on the spatial distribution of intermediate depth earthquakes of the southern Aegean in an amphitheatric shape, shedding light to the existence of a Wadati-Beniof seismic zone (Papazachos and Comninakis, 1971). Present day seismotectonic activity mainly stems from the convergence, the subduction and the retreat of the oceanic part of the eastern Mediterranean plate under the Aegean microplate, along with the subsequent formation of the Hellenic Arc (Le Pichon and Angelier, 1979; McKenzie, 1978; Papazachos and Papazachou, 2003). Extensive shortening is observed along the subduction front and the Hellenides mountain range, where compression applies between the buoyant Apulian continental platform to the west and the Outer Hellenides to the east. Additionally, a widespread NNW-SSE extension which is orthogonal to the subduction zone is imposed along the Aegean microplate. The second dominant seismotectonic process is attributed to the lateral extrusion of the Anatolian microplate as a result of its collision against the Arabian plate and the westward prolongation of the North Anatolia Fault (NAF) into the Aegean Sea (Jackson and McKenzie, 1988; Taymaz et al., 1991). The westward propagating NAF reached the Aegean Sea and formed the Northern Aegean Trough (NAT) at approximately 5-6Ma ago (McKenzie, 1972). Strike slip faulting along NAT interacted with the preexisted extension and progressively increased the extensional deformation in central Greece (Armijo et al., 1996). Due to differential movements and rheology variations across the Aegean lithosphere, strike slip faulting prevails at the boundaries of the Aegean, the Cephalonia Transform Fault (CTF) with a dextral strike slip motion (Scordilis et al., 1985) to the west and the Rodos Transform Fault (RTF) with a sinistral strike slip motion to the east (Papazachos and Papazachou, 2003).

The Aegean microplate accommodates a southwestward movement relative to the stable Eurasia with a velocity rate of 32-35mm/yr (Le Pichon et al., 1995) imposing a widespread extension in the interior of the plate. The exact timing of the crustal stretching onset is still under debate. According to a number of studies, back-arc extension initiated between 15 and 20Ma (Angelier et al., 1982; Mercier et al., 1989), however geological evidence based on Cenozoic metamorphic core complexes imposed constraints on the age estimation, suggesting a gradual propagation of the extension from the northern Aegean (30-35Ma) to the South (Gautier et al., 1999; Jolivet et al., 2013). 5Ma ago extensional forces within the Aegean were further reinforced due to the propagation of NAF into the Aegean Sea (McKenzie, 1972). Since then the Aegean microplate has been plausibly rotated clockwise for

about 30° around a stable pole in North Adriatic sea, as imprinted on many geomorphological and geological structures as also verified from paleomagnetic measurements (Kissel et al., 1985; Kissel and Laj, 1988). Currently, the extensional axis generally strikes in an almost N-S direction, according to geodetic measurements (Armijo et al., 1996) and fault plane solutions for strong earthquakes (Papazachos et al., 1998).

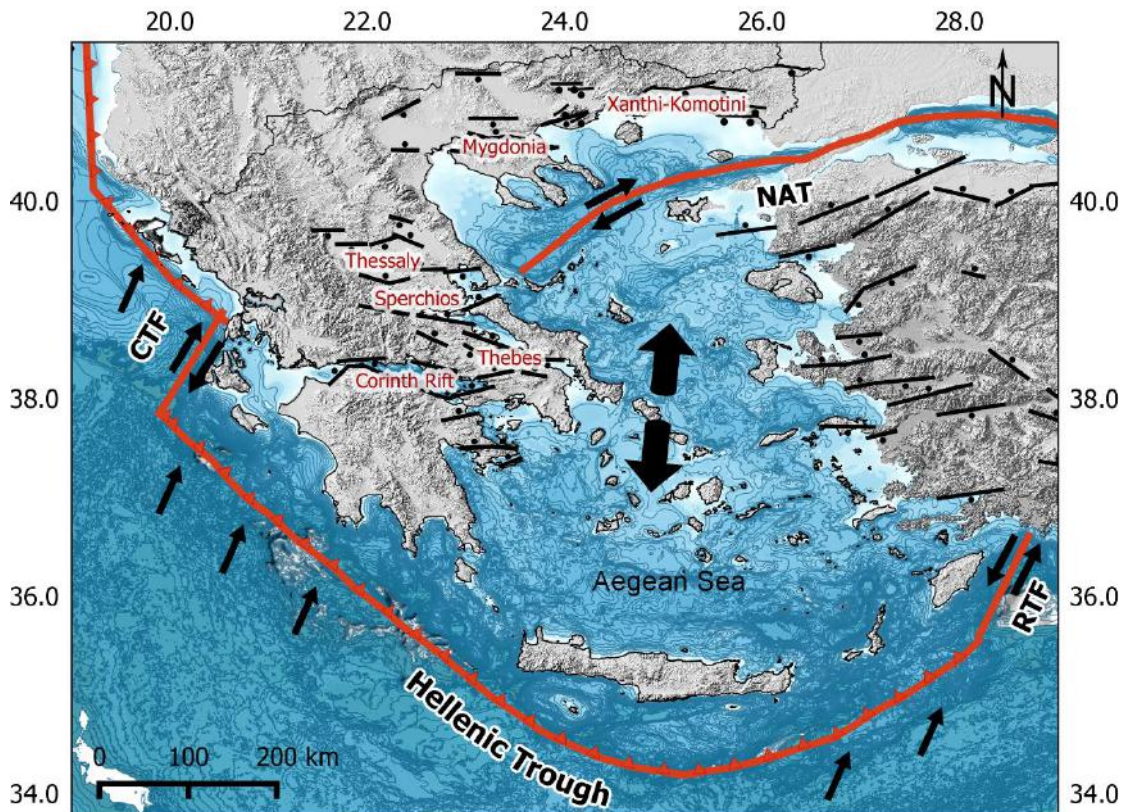
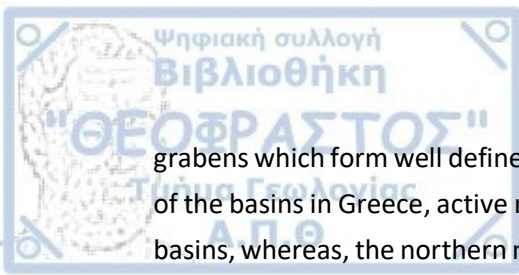


Figure 1-2 Simplified map of the Aegean Sea and the surrounding areas including the dominant seismotectonic features (thick red lines), such as the Hellenic Trench (thick red line with triangles), the North Aegean Trough (NAT), which accommodates the westward prolongation of NAF into the Aegean, the Cephalonia dextral Transform Fault (CTF) and the Rodos sinistral Transform Fault (RTF). Black arrows represent the kinematics along major fault zones as well as the main deformational pattern in the Aegean, characterized by compression along the Hellenic Arc and extension in the back-arc area. The most important normal faults forming the corresponding neotectonic basins in the Aegean are also presented.

Widespread extension and back arc active tectonics along with Tertiary volcanism are the dominant characteristics of the Aegean and have given rise to the formation of several neotectonic basins in the broader area, the Greek hinterland, the Aegean sea, the southern Balkans and the western Asia Minor. These basins mainly exhibit back-arc characteristics and can be compared worldwide with rifts which are related to back-arc tectonics such as the Taupo Rift, the Basin and Range province (North America), the East Rift African system, etc (Bell et al., 2008). The majority of the Aegean basins evolve in an approximately E-W orientation, where major faulting is concentrated (Goldsworthy et al., 2002). Characteristic cases of extension are the Corinth Rift, Thebes, Spercheios, Thessaly basins in central Greece, Mygdonia and Kavala – Xanthi – Komotini basins in Northern Greece (Fig.1-2). Strong earthquakes and localization of seismic activity are associated with the aforementioned



grabens which form well defined seismic zones. According to Goldsworthy et al. (2002) in most of the basins in Greece, active normal faulting mainly controls the southern boundaries of the basins, whereas, the northern margins are composed of older fault structures. It has also been shown that active faults defining block boundaries have changed their behavior through time, exhibiting a characteristic migration into the hanging walls of the existing basins in the last 1Ma (Leeder and Jackson, 1993; Goldsworthy et al. 2002). The study areas chosen for the purposes of this study, are the Mygdonia graben which is located in Macedonia, North Greece and the broader area of the Corinth Gulf rift in central Greece. The reasons for their selection lies to the fact that they share some common seismotectonic characteristics, their extensional origin and the dominance of south bounding faults. They exhibit a good archive of historical earthquakes and they are well monitored. A brief description of the most featured seismotectonic characteristics of the two study areas and the conducted scientific research are given in the following paragraphs.

1.3.2 Seismotectonic Setting of Mygdonia Graben

1.3.2.1 *Development and evolution of Mygdonia graben*

The study area of Mygdonia comprises the main Mygdonian graben and secondary basins surrounded by mountainous volumes (Fig.1-3). It concerns a complicated extensional graben bounded by normal faults with variable orientation which give the basin a characteristic S-like shape development. It is considered a rather high seismicity area, the most active in the northern Greek mainland, with strong and destructive earthquakes that occasionally occurred and affected the metropolitan city of Thessaloniki (Papazachos and Papazachou, 2003). The current seismotectonic pattern is the combined result from successive seismotectonic episodes on the pre-alpine and alpine basement rocks which belong to the Servomacedonian massif and the NNW-SSE Circum Rhodope Belt Thrust System (Mountrakis et al., 1996a, b). The initial breakaway of the basin originates in Late Miocene – Pliocene and continues up to Quaternary times. During the extensional deformation episode of early or mid Miocene, a NW-SE continental basin was formed, the Pre-Mygdonian basin (Pavlidis and Kiliadis, 1987; Tranos et al., 1999). During Pleistocene, smaller NE- SE and E-W rift sub-basins further opened within the existing graben due to spatial strain variations, such as the Mygdonian basin where Lagadas and Volvi Lakes are found, the Marathousa (Mar.bs), the Zagkliveri (Zgl.bs) and the Vromolimnes (Vr.bs) basin all later filled with Neogene and Quaternary sediments (Psilovikos and Sotiriadis, 1983) (Fig. 1-3). These basins are associated with high-angle normal faults, most of which can be easily located due to the topography expression and the steep slopes along faults. South of Lagadas and Volvi Lakes the area is cut by a series of E-W, northdipping faults which form a subparallel array similar to other regions like Corinth rift, northern Evia rift and Anthemountas basin (Anth.bs) (Goldsworthy and Jackson, 2000; 2002). Central Chalkidiki peninsula which is enclosed in the study, is a mountainous land also cut by a number of faults with a varying strike, since they follow the

kinematics of former tectonic discontinuities which were lately re-activated. There is a morphology of elongated basins and ridges in a NW-SE strike cross cut by numerous E-W faults. The extensional deformation that dominates in northern Greece was oriented with the least principal stress axis (σ_3) in a NE-SW direction in Late Miocene-Pliocene which has subsequently been rotated in N-S direction since Quaternary times (Pavlidis and Kiliyas, 1987; Mercier et al., 1989; Tranos et al., 1999).

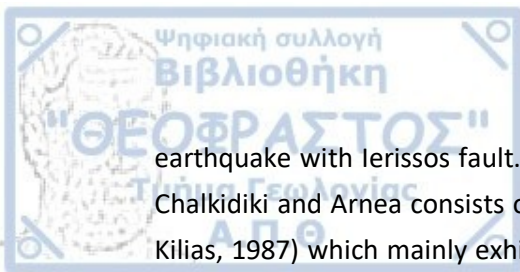
1.3.2.2 *Fault population characteristics*

The fault population of the Mygdonia graben incorporates faults with NW-SE, NNE-SSW, NE-SW and E-W strike variations, some of which are inherited structures, being active at least since Miocene (Pavlidis and Kiliyas, 1987; Pavlidis et al., 1990; Mountrakis et al., 1996a, b; Tranos and Mountrakis, 1988). Mygdonia fault population mainly consists of E-W trending faults, which accommodate the active deformation and have played a fundamental role in the formation of the basin until present (Tranos and Mountrakis, 1998; Chatzipetros, 1998). Field data and stress field estimations reveal that the E-W trending faults are associated with the current seismic activity, have a verified Quaternary activity and reveal either a left or a dextral lateral component (Pavlidis and Kiliyas, 1987; Mountrakis et al., 1983, 1996a,b; Tranos et al., 2003; Vamvakaris et al. 2006; Paradisopoulou et al., 2004). NW-SE striking faults follow the direction of the Circum-Rhodope ridge (Mercier et al., 1983; Pavlidis and Kiliyas 1987) and they are responsible for developing Thermaikos Gulf (Mountrakis et al., 1993) and the coastlines of the three Chalidikiki peninsulas (Goldsworthy et al., 2002).

The most impressive fault structures met in Mygdonian region are profoundly etched upon the relief as observed in Figure 1-3. The southern boundary of Mygdonia basin is formed by the existence of approximately E-W striking en-echelon faults, dipping with high angles to the North, the Thessaloniki – Gerakarou Fault Zone (TGFZ) with three main fracture lines, the western, the central and the eastern part (Tranos et al., 2003). TGFZ central part starts west from Peristeronas through Stivos village and terminates to the west of Gerakarou village is composed of E-W generally trending normal faults, in places turning to ENE-WSW and NW-SE striking segments, probably expressing reactivated older faults. According to field measurements the fault zone is dipping with high angles to the North (70°-80°). TGFZ is strongly associated with the seismic sequence of 1978 in Thessaloniki, verified by surface ruptures along the fault trace with measurements of maximum throw equal to 0.23m close to Gerakarou village. The central part of the zone consists of WNW-ESE striking faults dipping with high angles to the North. Further to the east of TGFZ the Loutra – Volvi – Nea Apollonia Fault System (LVF – NApF) is located, which initiates from Peristeronas village ending up to Loutra Volvi along which thermal springs are met (Mountrakis et al., 1983). An evidence for surface rupture during the 1978 earthquake is partially associated with this zone. The 10km fault zone of Nea Apollonia – Nea Maditos (NApM FS) is further extended to the east with a WNW- ESE direction (N85°) which dips to the north with a 60°-70° dip.

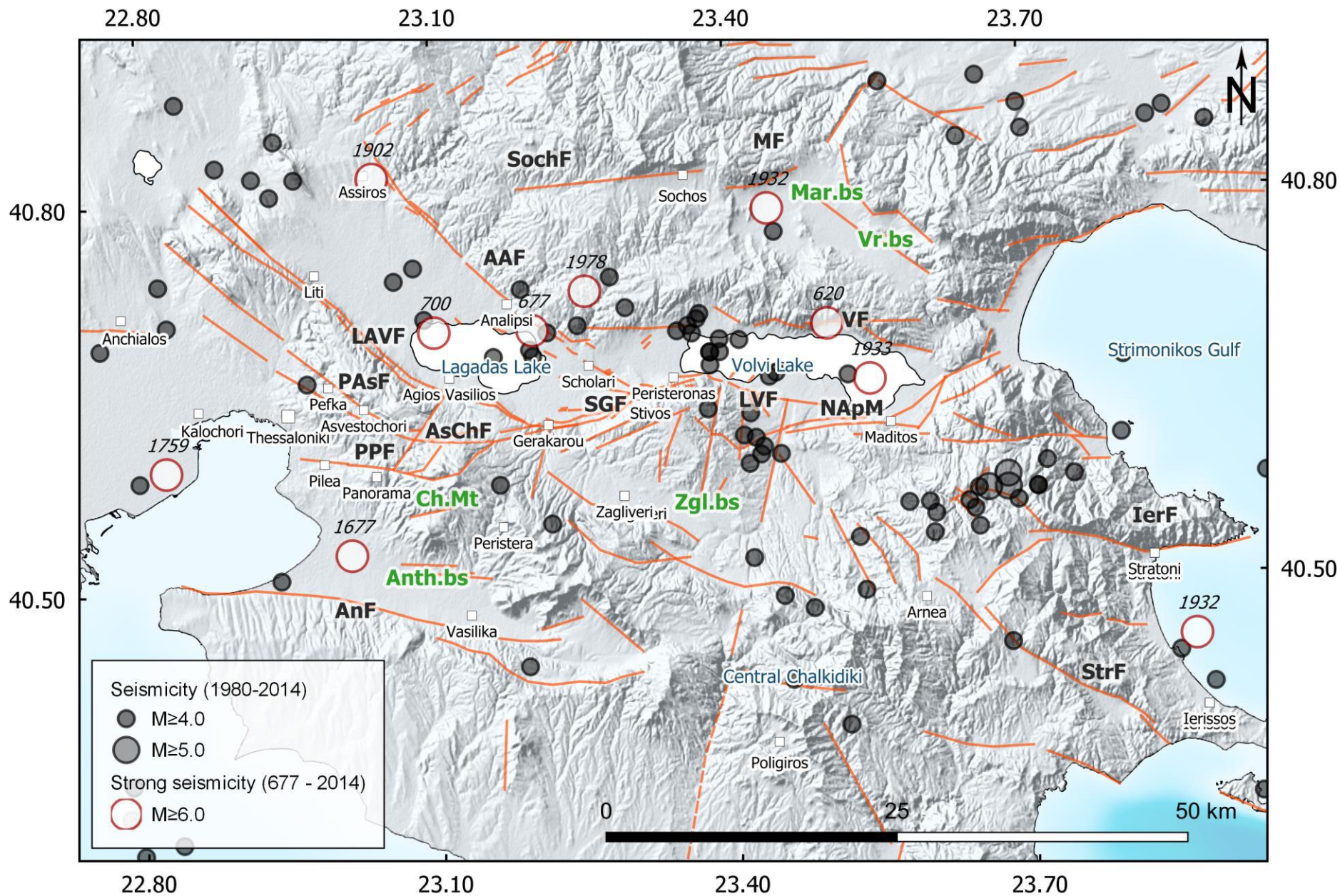
Another pronounced structure which characterizes the western boundary of Lagadas Lake in the south, is the Liti – Agios Vasileios (LAVF) fault segment that consists the extent of Thessaloniki – Gerakarou fault system to the west, in a NW-SE direction. Its length extends more than 20km and reveals a sinistral strike slip component evidenced from slip measurements along the fault scarp (Mercier et al., 1983; Pavlides and Kiliyas, 1987). The probably antithetic fault zone is the Assiros – Analipsis Fault System (AAF) which bounds the Lagadas sub basin to the North, extending from Scholari to Assiros. This 20km long normal fault with a NW-SE azimuth dipping to NW gets significant sinistral component. It is assumed that this segment has been activated during the 1978 earthquake since surface ruptures were found in the broader region. To the south of LAVF the semi parallel zone of Pefka – Asvestochori fault (PAF) has an ESE-WNW direction and dips to the NNE with high angles (55°-80°). It is a 7km normal active fault zone with a left lateral strike slip displacement, penetrating Pleistocene formations. To the east, the segment of PAF extends to the Asvestochori – Chortiatis fault segment (AChF) and the Pilea-Panorama fault zone (PPF). Tranos et al. (2004) suggest the existence of a pattern with small fault (<6km in length) faults in the broader area of Thessaloniki and strikes ranging from SSW-NNE to SSE-NNW and they coalesce in the case of stronger seismicity (>M5.0).

To the north, the study area is bounded by the active south dipping Sochos fault (SochF) and the western Mavrouda (MF) fault segment, which exhibit clear escarpments. Sochos fault is a normal fault extending for 30km in an E-W strike (90°) and dip with high angle to the south, forming a right-stepping geometry between the two fault segments (Mountrakis et al., 1996a). The parallel NW-SE Skepasto (SkF) and Limni (LmF) faults bound the Vromolimnes and Marathousa basin from the east (Goldsworthy et al., 2002). To the south there are some other significant active faults, rather isolated with a sparse contemporary seismicity. Anthemountas (or Angelochori) Fault System (AnF) is located in the southeastern part of Thessaloniki city and is an E-W trending, 30km elongated normal fault zone which bounds Anthemountas basin (Anth.bs) from the south. According to Zervopoulou (2010) it is composed of two fault segments, one NW-SE (100°) segment 17km long and an E-W (90°) segment, 15km long in respect and dips at approximately 70° to the north. A third segment extending into Thermaikos gulf is questioned. It is an active fault with a total fault throw in Quaternary, equal to 200m (Mountrakis et al., 1997). Stratoni (StrF) and Ierissos (IFS) active faults are the ones that dominate at the eastern part of Chalkidiki peninsula. StrF comprises an E-W (90°-110°) striking active normal fault with an observed length of 15-20 km, however, its trace to the east is obscured (Pavlides and Tranos, 1991). Chatzipetros et al. (2005) suggest the existence of at least three segments with NW-SE and E-W strike based on the orientation and the geomorphic expression of the hanging wall. IFS (or Gomati fault) is a 20km normal fault zone with a NN-SSWE strike (130°) which dips 60°-70° to the southwest. Stratoni fault is associated with the disastrous 1932 earthquake, for which the distribution of the maximum macroseismic intensities and surface ruptures are perfectly aligned with the fault strike (Papazachos et al., 1982). Caputo et al. (2012) suggest the association of the 1933 M6.3 strong



earthquake with Ierissos fault. The fault network around the mountainous area of northern Chalkidiki and Arnea consists of cut crossing active faults, with various strikes (Pavlidis and Kiliadis, 1987) which mainly exhibit extensional characteristics, and the NW-SE faults showing sinistral strike slip component. The major E-W northdipping faults like Zagliveri (ZglF) and Geroplatanos (GF) faults probably related to a M5.3 earthquake in 1995 are also found in central Chalkidiki (Goldsworthy et al., 2002).

Figure 1-3 Digital elevation model for Mygdonia basin and the surrounding area. Red lines correspond to important fault zones, such as the East-West "Thessaloniki – Gerakarou" (TGFS) normal fault system which bounds the basin from the south, along with secondary fault segments such as: "Lagina-Ag. Vasileios" (LFS), "Assiros-Analipsi" (AAFS), "Pilaia-Asvestochori" (PAsFS), "Asvestochori-Chortiatis" (AChFS), "Pilaia-Panorama" (PPFS), "Peristera" (PrFS) and "Nea Apollonia" (NAFS) Fault Systems. Other important faults are "Sochos" (SochFS) bounding the area from the North, "Anthemountas" fault (AnFS), "Stratoni" (StrFS) and "Ierissos" (I.FS) Fault Systems. Secondary sub basins Vr.bs: Vromolimnes basin, Marbs: Marathousa basin, Anth.bs: Anthemountas basin, Zgl.bs: Zagliveri basin (fault information gathered by Pavlidis and Kiliadis, 1987; Tranos et al., 2003; Tranos, 2011)



1.3.2.3 Strong seismicity

Recent seismicity in the area of Mygdonia basin includes moderate magnitude events, opposed to the strong earthquakes of the last centuries as inferred by historical archives (Papazachos and Papazachou, 2003) when it was repeatedly struck by destructive events, ($M \geq 6.5$, shown with red circles in Fig.1-3) and this seismic activity classifies the area as the most active seismogenic zone in northern Greek mainland. Although historical records might be incomplete, detailed descriptions are available for the seven more recent destructive ($M \geq 6.0$) earthquakes since 1677, whose temporal distribution is given in Figure 1-4. According to historical sources (Papazachos and Papazachou, 2003; Ambrasseys, 2009) the $M 6.2$ 1677 earthquake (VIII, Vasilika) caused severe damage to Vasilika village, whereas the $M 6.3$ 1759 strong event (IX, Thessaloniki) was disastrous for the city of Thessaloniki, probably related to Anthemountas rupture zone. It is uncertain whether the absence of strong for the next 143 years is a seismicity feature or it is attributed to the lack of historical information. The $M 6.5$ 1902 (IX, Assiros) earthquake caused the collapse of buildings and chimneys in Assiros and Lagadas area, with various interpretations on the causative fault. In 1932, a $M 7.0$ (X, Ierissos) earthquake occurred at the eastern part of the study area, causing damage in the broader Chalkidiki peninsula, possibly associated with the reactivation of the Stratonii Fault.

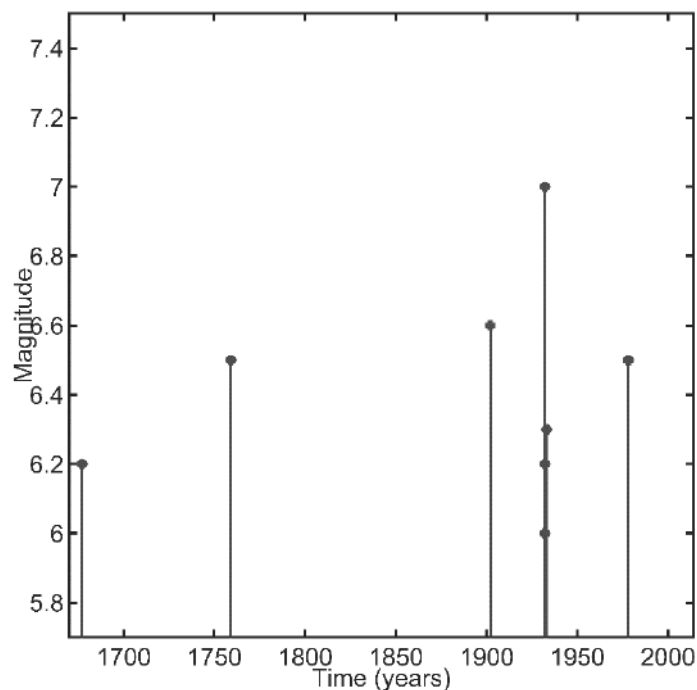


Figure 1-4 Temporal distribution of the known historical and instrumental strong earthquakes ($M \geq 6.0$) in Mygdonia Graben from 1677 until 2014.

The last strong event is the 1978 Stivos earthquake (June 20, $M 6.5$) was preceded by two strong foreshocks (May 23, $M 5.8$ and June 19, $M 5.3$) and followed by the largest aftershock on July 4 ($M 5.0$). Since 1978 the seismicity rate is moderate and is characterized by the absence of strong events with some exceptions which have occurred in the broader area. There are three events in Mygdonia in 1983 ($M 5.0$), in 1993 ($M 5.1$) and the last one on May

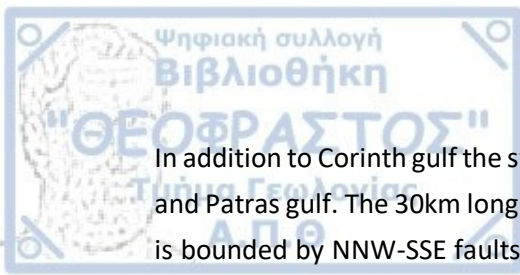


4, 1995 (Arnea, M5.8) all of them having struck the eastern part of Chalkidiki peninsula (Fig.1-3). For the time interval 2000-2014 for which the seismicity data were processed in this study, earthquake magnitudes are smaller than 4.8, with only six events with magnitudes $4.0 \leq M \leq 4.8$. The area is studied and monitored since 1980 by an adequate number of seismological stations, but occasionally transient deployments have also been set to study small earthquake excitations. Due to the overall intense seismic activity and the presence of active faults along with its proximity to Thessaloniki, it is essential to decode the seismicity process characteristics by exploiting all the available earthquake information that this study is aiming to.

1.3.3 Seismotectonic Setting of Corinth Rift

1.3.3.1 *Development and evolution*

The continental Corinth Rift constitutes an elongated rift in central Greece, which divides the external Hellenides expressed by the Pindos mountain range into the Greek mainland and the Peloponnese peninsula (Fig.1-5). The rift extends from the Corinth canal up to the east, up to the Patras gulf to the west. It represents one of the most rapidly extending areas in a worldwide scale and the high extensional rate is confirmed by geological (Bell et al., 2009), geodetic (Briole et al., 2000) and seismological information (Papazachos and Papazachou, 2003; Ambraseys and Jackson, 1990, 1997). The geomorphological expression of the coastal topography and the sharp escarpments is at a first glance a strong indicator of significant tectonic displacements, part of it being associated with the occurrence of devastating earthquakes. The rift development initiated in Pliocene-Pleistocene and after Miocene, NE – SW extensional deformation gave rise to the first formation of the graben (McKenzie, 1978), whereas during Quaternary times the extensional deformation re-activated in a N-S direction (Westaway, 2002) probably due to the propagation of the North Anatolian Fault (Armijo et al., 1999) and presently it absorbs about 12mm/year of opening. All available information, geological, seismological, GPS measurements advocate for an asymmetric graben where the northdipping faults are mainly seismogenic. Uplift rate is evidenced by a number of geological markers and shows considerable variations along the south margin of the gulf. Uplift markers show that the southern margin of the rift operates as a hanging wall with an important degree of uplift, whereas the northern part is mainly subsiding, with some local uplift only around Galaxidi area (Bell et al., 2009). According to Armijo et al. (1996) the Helike and Xylocastro faults in the southern margin were the first to impose an uplift to the gulf. It was first commented that a considerable variation in displacement is found between the southern and the northern boundary of the Corinth Gulf. There is evidence that the opening rates show a more rapid extension in the western in relation to the eastern part, due to the clockwise rotation of central Greece compared to the northern Peloponnese (Goldsworthy et al., 2002; Avallone et al., 2004).



In addition to Corinth gulf the study area encompasses the secondary graben of Trichonis Lake and Patras gulf. The 30km long Patras gulf is located at the western part of the study area and is bounded by NNW-SSE faults which exhibit high rates of subsidence (Doutsos et al., 1988).

The earliest identified fault system in the NW Peloponnese is the N–S to NNW–SSE striking thrusts with secondary sinistral WNW–ESE and dextral WSW–ENE strike-slip faults (Kamberis et al. 2000) active from the late Eocene to the Oligocene (Sotiropoulos et al. 2003; van Hinsbergen and Schmid, 2012). Trichonis basin lays parallel to Corinth gulf, however, it is separated through a mountainous area not highly populated. The seismicity in Lake Trichonis graben is also studied because of its proximity to the Corinth rift and the recent seismicity which is marked by sparse activity interrupted by the occurrence of several strong earthquakes. The graben is semiparallel to Corinth-Patras rift with a WNW-ESE trend, bounded by normal faults (Doutsos et al., 1988) and a recent seismic excitation studied by Kiratzi et al. (2008). The faults responsible for the development of the graben are antithetic ones striking in an east-west direction and to the east they take a NW-SE direction. The north dipping normal faults seem to consist the prevailing seismotectonic agent that controls the area according to Doutsos et al. (1988) and Goldsworthy et al. (2002).

1.3.3.2 *Fault population characteristics*

The architecture of the fault population in the Corinth gulf was investigated by a number of studies, including geophysical surveys and seismic data (Stefatos et al., 2002; Sakellariou et al., 2007; Bell et al., 2008; Nixon et al., 2016) seismotectonic studies (Rigo et al., 1996; Ambrasseys and Jackson, 1997; Bernard et al., 1997; 2006; Hatzfeld et al., 2000; Pacchiani and Lyon-Caen, 2010; Lambotte et al., 2013) and geomorphological studies (Palyvos et al., 2004; Tsodoulos et al., 2008; Bell et al., 2009). The north dipping faults, are considered to be the most active boundaries while the south dipping antithetic faults are of minor importance (Roberts and Jackson, 1991; Armijo et al., 1996). The fault array in the southern margin is developed in an en-echelon arrangement for onshore and offshore fault segments extended approximately in an E-W direction. The seismotectonic setting exhibits discrepancies between the west and east part of the gulf, related also to the uplift or the seismicity rate (Fig. 1-5). Starting from the western termination of the gulf, the Psathopyrgos Fault (PsF) which is 15km-20km long is responsible for a couple of known strong earthquakes (1714, M6.4 and 1806, M6.5) (Console et al., 2013). To its east, the Aigio fault segment (AigF) is 10-16km long associated with the 1748 (M6.6), 1817 (M6.6) and 1888 (M6.3) earthquakes. AigF is responsible for the recent M6.2 1995 earthquake which severely damaged the city of Aigion also evidenced by the existence of surface ruptures along the fault trace (Bernard et al., 1997). Aigion segment is the middle en echelon segment between the onshore segments of Psathopyrgos and Eliki fault (EIF). The EIF is associated with historical earthquakes in 373BC and in 1861, has a length of 22km and is divided into the eastern and western segment. Western Helike presently appears in microseismicity quiescence, consistent with the geological estimates by Pantosti et al. (2004) and Flotté (2005) who proposed that this

segment is no longer active, or has an extremely low slip rate. Thus, the western Helike fault is most probably deactivated, in its western section and is replaced by Kamarai fault, consistent with geological investigations. Akrata (AkrF) and Derveni (DerF) faults are developed to the east of EIF fault with a 8km length (Brooks and Ferentinos, 1984; Higgs, 1988; Stefatos et al., 2002). The eastern boundaries are controlled by the existence of onshore Xylocastro and offshore Xylocastro fault (XFZ). The first one is the eastern extension of Derveni fault to the east and it is supposed to be inactive (Armijo et al., 1996). It has a 20km length and is related with a recent seismic swarm. The displacement rate along Xylocastro fault is inferred to be equal to 11mm/yr, based on geodetic information and marine sedimentation (Armijo et al., 1996). To the east of the offshore XFZ, there is a series of fault segments both offshore and along the coast. The gulf becomes narrower and it forms the Alkyonides and Lechaion gulfs where at first glance it seems that are fully controlled by the normal fault arrays bounding the area from south and north. The termination of the Corinth gulf to the east encompasses major faults, related to the 1981 seismic sequence and to a significant number of devastating earthquakes during historical times and for this reason it has been scrutinized by a number of studies, some of them controversial (Leeder et al., 2005; Bernard et al., 2006). Detailed mapping has shown that the Alkyonides fault (SAIF) is 38km in length with a NW-SE azimuth and dips about 45° to the north.

The South Alkyonides fault trace extends from Vouliagmeni lake to the west, up to Alepochori village. A total displacement of 2.5 – 3km is suggested for the Alkyonides segment from the offset of Mesozoic rocks along its trace, according to the geomorphological throw (Roberts and Koukouvelas, 1996) and a lateral propagation of the western fault tip is suggested by Morewood and Roberts (1999, 2001) with a different throw rate for each tip. On the hanging wall of the basin, the most important antithetic south dipping faults in the vicinity of Alkyonides gulf is the Kaparelli Fault Zone (KpF), which is an E-W trending fault with 200° strike and 60°-70° dip, bounding Parnitha Mountain from the north. According to Jackson et al. (1982) the Kaparelli normal fault is composed of three segments forming left – stepping en echelon geometry. It is associated with the third of the 1981 triplet, after which surface traces appeared. Livadostras fault (LivF) is an active normal fault next to the Kapareli fault segment (KpF). Trizonia fault (TrF) is an antithetic north-dipping (Moretti et al., 2003) offshore fault in the western Corinth gulf. Delfi fault (DelF) is an oblique normal fault in an almost E-W trend, which is located at the foothill of Parnassos mountain and a south dip. The fault system of Eratini (ErF) is composed of two antithetic offshore faults which overlap, developing a horst at the north of the Corinth gulf (McNeil et al., 2005; Bell et al., 2008). In the south part, NW-SE Athikia or Kechries fault segment (AthF) is dipping to the south and is visible from its morphological trace. Athikia Fault Zone (AthF) bounds the eastern part of the Corinth –Nemea basin gulf from the south in a NE-SW strike for approximately 23km. It is a normal fault with a dominant fault-slip direction NW-SE measured by Roberts and Koukouvelas (1996) all along the fault. It is assumed that this fault is related to several strong earthquakes which occurred in the 18th - 19th century. Trichonis sub basin is situated NW of the Corinth rift, where the lake

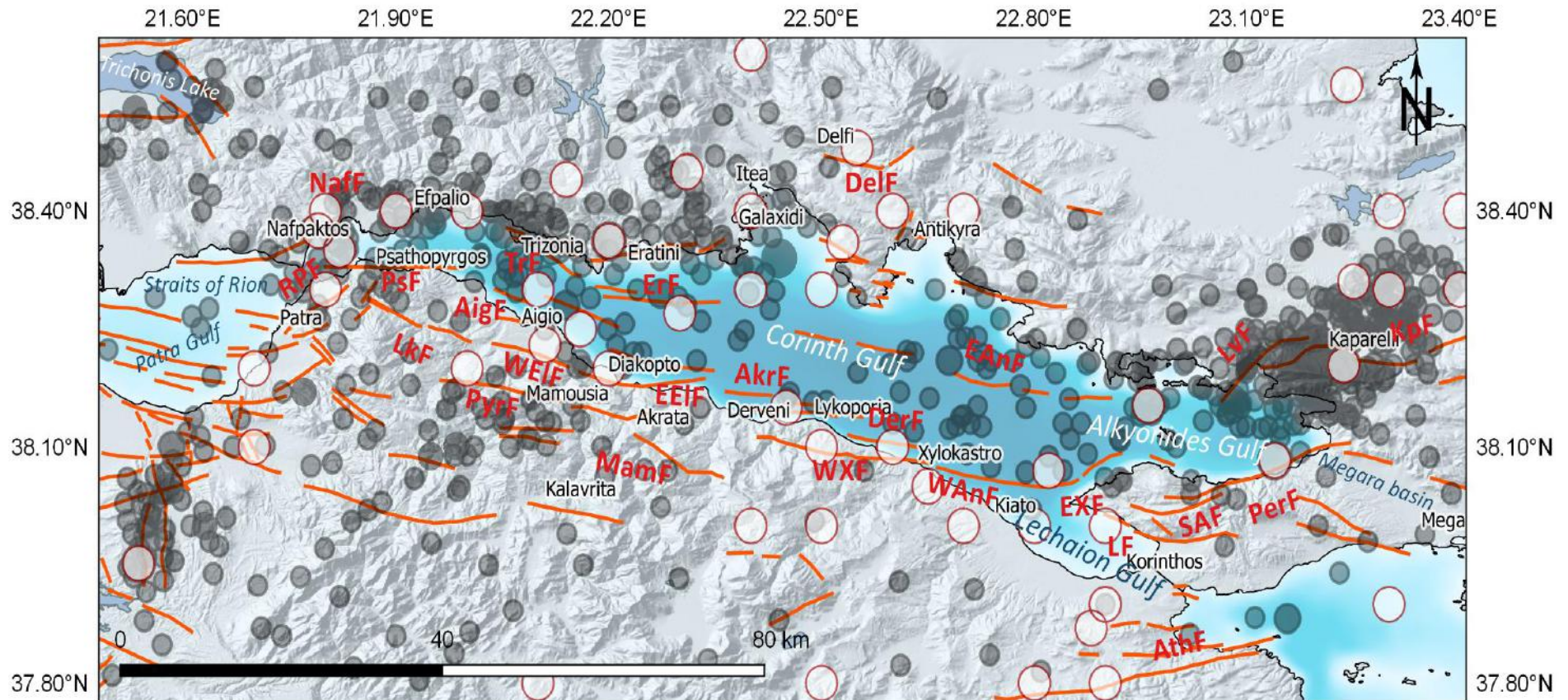


Figure 1-5 Digital elevation model for the Corinth Gulf Rift and the surrounding area. Red lines correspond to important fault zones, such as the "Psathopyrgos" (PsF), the "Aigion" fault (AigF), the "Eliki" (EIF), to the western Corinth Gulf, the "Akrata" (AkrF), the "Derveni" fault (DerF) and the "Xylocastro" fault (XFS) to the central part and the "South Alkyonides" (SAIKFS). Other important faults are the antithetic faults of "Kaparelli" (KpFS) "Livadostras" fault (LivFS), as well as "Delphi" (Delf) and "Eratini" Fault Systems (fault information gathered by Bernard et al., 2006, Armijo et al., 1996; Bell., 2009 and references therein).

Trichonis lies and cuts across a mountainous part of the south Pindos range. Normal faulting in the Gulf of Corinth, Trichonis basin and Gulf of Patras are found in the vicinity of the Kefalonia strike-slip fault (<50km), which forms the northern boundary of the Hellenic subduction system.

1.3.3.3 Strong seismicity

Historical sources and geological evidence reveal that seismicity in Corinth Rift was very intense in the last 2500 years, since historical cities such as ancient Heliki (in 373 BC) that completely disappeared, Delphi (in 348 BC, 279 BC) ancient Corinth (in 543, 580) have been totally destroyed and monuments have collapsed (Ambraseys and Jackson, 1990; Papazachos and Papazachou, 2003). Strong earthquakes are also verified by paleoseismological studies along the main faults where successive seismotectonic episodes in Holocene occurred (Collier et al., 1998; Pantosti et al., 2004; McNeil et al., 2005; Kokkalas et al., 2007). Strong seismicity ($M \geq 6.0$) in the last 300 years is shown in Figure 1-6 (Papazachos and Papazachou, 2003). Console et al. (2010) suggest that the archive for strong seismicity before 1700 is irregular and missing information. The temporal distribution shows a generally constant rate of earthquake occurrence with periods of clustering of events but also some periods of quiescence, such as from 1817 to 1858 and from 1928 to 1965 being the largest gaps. During the study period there are 30 strong earthquakes with maximum magnitude $M 6.8$ which are associated with specific seismogenic faults along the Rift. However there are parts with an absence of frequent strong seismicity like the Trichonis area and Achaia area.

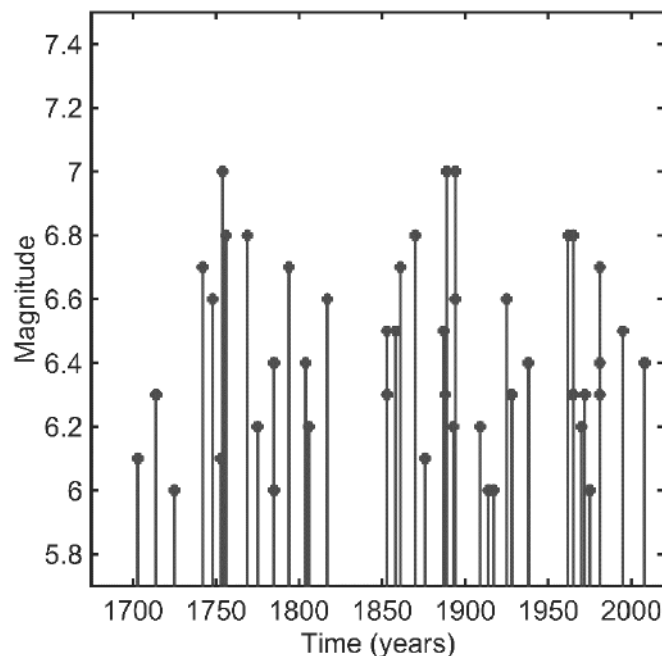


Figure 1-6 Temporal distribution of the known historical and instrumental strong earthquakes ($M \geq 6.0$) in Corinth Rift for 1700 until 2014.

The first strong earthquake happened in 1703 and strong earthquakes continued occurring the western part of the gulf which has been struck by a big number of earthquakes which are mainly attributed to the Psathopyrgos fault (1714, 1804, 1806), Aigio fault (1748, 1817, 1888, 1995) and

Eliki fault (1861). In the eastern part of the gulf the strong earthquakes are attributed to Xylocastro fault (1742, 1753, 1970) and the latest instrumentally recorded 1981 triplet at Skinios, Alepochori and Kaparelli faults. There are also references for a devastating earthquake at the north coasts at Delfi fault (1870) and the segment of Nafpaktos is considered responsible for important earthquakes in 1703, 1725, 1756, 1769, 1917. In the northwest margin of the Corinth rift the 1975 and 2007 earthquakes have to be highlighted since they occurred in a semi parallel sub rift with Patras – Corinth rift (Delibasis and Karydis, 1977; Kiratzi et al., 2008) with the exception of the 1994 earthquake in Patras with magnitude $M < 6.0$ (Karakostas et al., 1994). The most recent seismotectonic setting in the area has been studied especially after the 1995 Aigion earthquake ($M 6.2$) and the 2008 Achaia earthquake ($M 6.4$) which caused extensive damage.

1.4 Relevant Research in the Study Areas

1.4.1 Seismotectonic Investigation in Mygdonia Graben

The cornerstone for the seismological research outburst in Mygdonia basin was the 1978 Stivos earthquake ($M 6.5$) because of the devastating impact on Thessaloniki city. Some of the most characteristic seismological studies up to now are briefly described in the following paragraphs. Papazachos et al. (1979) conducted a field study and identified the earthquake driven surficial co-seismic traces, landslides and liquefaction effects around the $M 6.5$ Stivos epicentral area. The developed fault traces were categorized into three different groups according to their strike, SE-NW direction traces between Stivos – Scholari – Evangelismos villages, E-W traces from Peristeronas to Gerakarou villages and NW-SE striking ones from Stivos towards Lagadas Lake. The fault plane solutions for the mainshock and the strongest foreshock of the seismic sequence were computed, which coincided with the second trace group and suggested that the main nodal plane is a strike slip sinistral fault (strike: 124°) with a small reverse component, dipping with 80° to the North. Papazachos et al. (1980) revised their former calculations on fault plane solutions, suggesting the existence of normal fault structures instead and accounted them for the reported polarity readings of short and long period data. Carver and Bolliger (1981) installed a 20 days portable seismological network on July 3, 1978 across the epicentral area and recorded 116 aftershocks with magnitudes ranging from 2.5 to 4.5. Their analysis showed that the spatial distribution of the aftershocks is diffuse, since their locations were found north of the two lakes in approximately 10km distance from the fault trace as well as at the western part of Lagadas Lake. They suggested that the strain was released gradually from the central part of the fault eastward and further northwest. The aftershock foci ranged from 3 to 12km forming planes dipping at high angles to the north, indicating either normal or sinistral strike slip ruptures. Soufleris and Steward (1981) and Soufleris et al. (1982) defined the source parameters and relocated the focal coordinates of the mainshock and the strongest events by using both teleseismic data and local recordings. Fault plane solutions which exhibited significant similarity agreed with the results of Papazachos et al. (1980) for three almost E-W adjacent fault segments.

Fault plane solution for Stivos earthquake by Soufleris et al. (1982) was employed in this study. Aftershocks recorded from the local network operating from July 20 to August 31, 1978 whose distribution showed the presence of three seismic clusters, one northern than Lagadas Lake, one between the two lakes and a third small cluster below the northern coast of Volvi Lake, probably associated with three distinct segments. The analysis showed that hypocentral depths ranged from 3km to 12km and they defined planes dipping to the north with a variety of focal mechanisms, reflecting a complicated deformational pattern. Mercier et al. (1983) investigated the distribution and kinematics of the co-seismic ruptures after the occurrence of Stivos earthquake and proposed that the tensional axis calculated from the surface cracks is compatible with the one derived from the fault plane solutions obtained from Soufleris and Stewart (1981). They also combined the existing geological data with the aftershock activity and verified the good agreement with the extensional axis for the broader area and among others they concluded that the Asvestochori fault to the west of the epicentral area was probably activated during the seismic sequence. A seismicity analysis of the broader Servomacedonian area which encompasses the graben of Mygdonia was firstly conducted by Scordilis (1985). This study was based on the recordings of the newly established permanent seismological network with seven seismological stations in Northern Greece. Wadati methodology was applied and the velocity ratio was estimated equal to 1.77. Recorded seismicity for the period 1981 to 1984 exhibited clustering with most of the earthquakes to be concentrated around the epicentral area of the 1978 main shock.

Transient local deployments were further installed for the investigation of seismicity and seismogenic faults in the area. Hatzfeld et al. (1986/87) conducted an experiment with the installation of 29 seismological stations and recorded 524 earthquakes (March – April 1984). They proposed that the seismicity forms separate clusters, one close to Thessaloniki, a second one between the two lakes and a third around Arnea, concluding that the earthquakes could not be easily assigned to specific faults. The majority of the fault plane solutions indicated the existence of normal faults trending E-W, some of them normal NW-SE faults with a sinistral strike slip component, some other revealed NNE-SSW dextral strike slip faults. Combining seismotectonic results with geological information they proposed a model based on the inherited fault network and the current extensional field, which accounts for the localization of the deformation on the E-W faults and creates geometric barriers which locally hinder earthquake occurrence and produce the current seismicity pattern. Long term seismicity in the broader area was later studied by Scordilis et al. (1989) who found a b-value equal to 0.92 for the period 1981-1986 for earthquakes with $M_L \geq 2.1$. Hatzidimitriou et al. (1991) operated a portable network in the vicinity of Thessaloniki, aiming to enhance the scientific knowledge on the properties of Asvestochori fault, probably activated during Stivos earthquake. They recorded 282 earthquakes in three weeks with magnitudes ranging from -0.2 to 3.0 distributed over the study area, especially around Thessaloniki. They found that earthquake foci vary from 5-12km and a cluster of events south of Lagadas Lake. The most well located events were related with normal faults in a SW-NE strike and extensional T axis striking 340° . These solutions were not compatible with the Asvestochori Fault

geometry, however, they suggested the existence of other secondary active faults. Karakaisis and Mikumo (1993) modelled the temporal variations of the rupture propagation of the 1978 earthquake and suggested that the fault rupture lasted 7sec and reached 36cm average displacement. Average displacement based on the seismic moment was equal to 64cm according to Mercier et al. (1983). These calculations are taken into account for the rupture model constraints. Static stress drop values between 6.6 and 12 bars was regarded low for intraplate earthquakes (Mercier et al., 1983; Karakaisis and Mikumo, 1993). Papazachos et al. (2000) installed a nine station network due to a minor seismic excitation in the area of Asvestochori. A number of the recordings accounted for quarry blasts operating in the adjacent area and a seismic cluster was identified forming a southdipping fault plane with a NNW-SSE strike. The strongest earthquake (M3.7) was associated with a normal fault plane in accordance with the geological observations. The authors suggested the possible fault continuation towards the city of Thessaloniki. The last spatiotemporal investigation of Mygdonia seismicity was achieved by Paradisopoulou et al. (2006) who established a temporary digital network composed of 12 seismological stations for 19 months. They detected 277 earthquakes with magnitudes ranging between 1.0 and 4.5, mostly located to the west of Lagadas Lake. Hypocentral depths of the well located earthquake reached 18km at some clusters indicating planes steeply dipping. A seismic burst that occurred during the network operation (October 2001, largest event with M4.5) contributed to the identification of a blind continuation of Pilea-Peristera fault to the east. Based on the maximum stress axis variations across the study area, they proposed that the extensional velocity ranges from 0.63mm/yr at the northern part up to 0.21mm/yr at the southern part of their study area. Vamvakaris et al. (2006) computed fault plane solutions for earthquakes with magnitudes $M \geq 3.0$, which occurred between 1989 and 1999, incorporated all the available fault plane solutions from recordings on local deployments and defined the orientation of the local stress axis across the area. They concluded that seismological and seismotectonic data are in agreement and suggested a general N-S extension exhibiting small-scale variations. This fact highlights the importance of unveiling the role of the behavior of the inherited fault network or the existence of blind faults in the area of Mygdonia, an issue that was attempted to be answered in this study. The investigations of Roumelioti et al. (2006) by applying P- and S- waveform inversion for the 1978 earthquake rupture reconstruction, revealed a considerable displacement patch confined between the lakes of Lagadas and Volvi and a second one located in Lagadas Lake, both reaching the surface. They defined the areas of largest surface deformation in between the two lakes and computed peak values for the co-seismic displacement of the order of 2.5 – 3.0m.

The aforementioned seismicity studies on the 1978 earthquake and some short seismic excitations that occurred in the study area are fundamental for the comprehension of the fault population synthesis and its seismotectonic attributes. In addition to these, a long term survey for studying the microseismicity in the recent years was significant, since the seismological network has been considerably enhanced after 1981 with additional stations installed around northern Greece and earthquake detectability has been improved accordingly. The exploitation of the recently recorded seismicity along with all the available seismicity data should contribute

to the identification of the hazardous faults in the study area which is potentially posing a natural disaster threat for the city of Thessaloniki.

1.4.2 Seismotectonic Investigation in Corinth Rift

Contrary to Mygdonia basin where the investigations are mainly limited around the unique recent strong event, Corinth rift has extensively been the center of investigations for a number of scientists due to the high seismicity rate and the frequent strong earthquakes. A brief review on the most characteristic research studies focusing on seismotectonics, earthquake location and the spatiotemporal seismicity analysis in Corinth rift is given in the following paragraphs. After the 1981 Alkyonides earthquake occurred, King et al. (1985) established an array of analog seismographs for five weeks around the eastern termination of Corinth rift. During the experiment 133 earthquakes were recorded and fault plane solutions were determined, indicating normal faulting with a sinistral strike slip component. Active antithetic faulting was revealed from the foci distribution, with hypocenters not greater than 10km at depth. A model was proposed by the authors according to which, the active faults at the eastern part of the gulf rely on the evolution of pre-existing weakness zones with an antithetic character. Melis et al. (1989) monitored the seismicity around Patras gulf by installing a local network from May 1983 to April 1984 and recorded and located 650 events. They suggested that Patras gulf, which is rather aseismic, is linked due to a shallow decollement surface with the Corinth rift to the east and that Patras gulf is displaced to the south due to a NE-SW transfer fault through Rion – Antirion channel (Brooks and Ferendinos, 1984). Hatzfeld et al. (1990) set up a temporary network that operated for some weeks in 1986 located 671 small earthquakes and determined their fault plane solutions. Among their microseismicity findings, they detected one seismic cluster around Rion area exhibiting normal faulting, NE dipping with depths ranging from 5km to 15km, an observation in agreement with Melis et al. (1989) and properties of previous strong earthquakes in the area. Moreover, a cluster around Trichonis Lake was detected in N-S direction, with foci ranging between 5-20km and fault plane solutions inconsistent with the extensional pattern of the basin, alternatively exhibiting strike slip and reverse components.

Rigo et al. (1996) set up a dense network of 51 digital seismological stations in the Western Corinth gulf during July and August 1991 when they obtained 5000 events with accurate locations and well-constrained fault-plane solutions. Among others, they suggested that all the major northdipping faults are downwards connected, forming a detachment zone at around 10km depth, gently dipping (with 15°) to the north, an opinion also expressed by King et al. (1985) for the eastern part of the gulf. They proposed that the microseismicity activity in this area occurs at lower depths in respect to the main shocks due to stress transfer mechanisms from the lower semi-brittle zone to the upper brittle zone, slipping along the detachment zone.

Rietbrock et al. (1996) utilizing the data recorded from Rigo (1994) performed a cluster analysis through waveform coherence and they ascertained the existence of low angle faulting at the southern margin of the gulf exhibiting an average dip 10° to the north. They supported the idea that even considering uncertainties these cannot exceed 15° and the northdipping planes cannot

dip more than 30° , like in a material characterized by low friction coefficient ($\mu \sim 0.1$). Hatzfeld et al. (1996) operated a temporary seismological network composed of 35 stations around the epicentral area of M6.2 Galaxidi earthquake in 1992, five days after the main event. A number of 255 events of minor magnitude shocks were recorded, which showed a rather diffuse distribution and did not contribute to the accurate definition of the causative fault. The aftershock sequence was poor and similar to the 1965 Eratini (M6.4) earthquake, as pointed out by the same authors. This absence of aftershocks set the first profound evidence for discrepancies in seismicity properties between the eastern and the western Corinth rift. The authors interpreted this seismic behavior in terms of the crustal properties, suggesting either the existence of a fault asperity, or a non-uniform spatial distribution of strain accumulation within the seismogenic volume of the rift. The 1995 Aigion (M6.2) earthquake attracted the recent scientific attention to the Corinth gulf. Bernard et al. (1997) installed a seismological and geodetic network, three days after the 1995 mainshock and recorded the aftershock sequence. Their analysis showed that the vast majority of strong events or microearthquakes were concentrated to the western part of the causative fault mainly attributed to the Psathopyrgos and Elike faults.

Hatzfeld et al. (2000) proposed the existence of several prominent variations between the eastern and the western part of the Corinth gulf. The foci distribution of the earthquakes revealed the activation of steeper southdipping and northdipping faults, contrary to the western part, where northdipping faults seemed to prevail. Based on the maximum hypocentral depth to the east they implied the different transition depth between the brittle and the ductile crust to the east. Hatzfeld et al. (2000) attributed these variations to a speculative scenario of rotating faults, introduced by Jackson and McKenzie (1983) according to which, block rotations impose a varying degree of extension on the eastern and the western part of the gulf. In 2000/2001 a permanent seismic network composed of 12 seismological stations was established around Aigion (CRLNET network, Lyon-Caen et al., 2004) and an important number of studies came into light based on these recordings. The first investigation on these recordings was performed by Lyon-Caen et al. (2004) who stated that the seismicity in the gulf during 2000-2001 was not associated with faults exhibiting a surface expression with foci distributed between 6 and 8km. They computed the fault plane solution of the M4.2 event in 2001 Agios Ioannis swarm and pinpointed its association with a SW-NE active fault owing a dextral strike slip component which is in contrast with the stress regime of the Corinth gulf. Bernard et al. (2006) analyzed the two year recordings of the CRLN network mostly located at the western part of the gulf. They concluded that Corinth gulf seismicity was mostly located in a layer with 1.5 ± 0.5 km thick at about 6-8km depth which is the one that accommodates strain. However, they suggested that all active northdipping faults to the west of the gulf, are dipping with large angles 50° - 60° to the North and they root into the predefined seismicity layer with high seismicity. On the other hand, to the east, faults dip at 30° - 35° . They proposed that the Aigion and Helike are active around 3-5km in depth, whereas Psathopyrgos fault is locked at this depth. West Helike fault is inactive since it lacks seismicity and it coincides with the geological observations.

Kiratzi et al. (2008) provided further insight into the seismotectonic properties of Trichonis basin, since they investigated the properties of the earthquake swarm in 2007. According to their study, the earthquakes indicated the existence of an active NNW-SSE rupture zone, bounding the lake to the southeast, contrary to the well – documented E-W faults. They revealed a sinistral strike slip displacement acting as a shear zone linking Trichonis lake and Corinth rift. Pacchiani and Lyon-Caen (2010) investigated the spatiotemporal properties of the 2001 Agios Ioannis seismic activity and revealed the complex geometric structure of Kerinitis fault, a dextral oblique-slip normal fault that strikes 230°N and dips at 40°NW . This geometry was revealed by the fault plane solution of the largest earthquake of the swarm ($M_w 4.3$) and coincides with the regional extensional stress regime. They proposed that this fault is an inherited rupture which was reactivated because of the stress redistribution. Potanina et al. (2011) studied the seismic activity during 2000 and 2005 in terms of statistical analysis, and in particular the temporal variations of seismicity properties in Corinth Gulf, and associated them with seismic swarms. Especially, they figured out two periods of swarm activity in 2001 and in 2003-2004 in the western part of the rift and underlined the existence of different stages through the evolution of the seismic bursts.

Karakostas et al (2012) investigated the spatiotemporal properties of the 2010 Efpalio doublet seismic sequence and the stress transfer effect in the evolution of the activity. The accurate earthquake coordinates revealed the geometry of the two segments probably attributed to Pspathopyrgos fault. Additionally Karakostas et al. (2012) showed that there is significant interaction through stress Coulomb changes between the different clusters of aftershocks during the seismic sequence. Sokos et al. (2012) who also investigated the Efpalio sequence provided an alternative interpretation. They stated that the sequence triggered shallow earthquake occurrence at the northern coast of Corinth gulf along steep southdipping faults. The detailed relocation analysis of Lambotte et al. (2013) was based on the recorded seismicity from the crln network, for 2000-2007 with the use of the HypoDD cross-correlation methodology. They suggested that the northdipping faults of the west Corinth gulf (West Helike, Lakka, Kamarai - Lamprini fault) root into a seismogenic layer constrained at 6-8km depth. Furthermore, they questioned the capacity of the Trizonia and Kalithea southdipping faults to generate strong earthquakes. For the understanding of Corinth gulf seismicity, they suggested an alternative theory for the seismotectonic properties of the western Corinth gulf, in contrast to the model proposed by Rigo et al. (1996). According to their model, the horizontal layer is the stretching result due to the existence of a lower viscous layer attributed to fluid presence. Ganas et al. (2013) studied the 2010 Efpalio sequence and suggested that the first event of the doublet ruptured a blind, north-dipping fault, accommodating north-south extension of the Western Gulf of Corinth. Regarding the second event they suggested that the source properties are rather unclear, with implications on a south dipping plane in the post-22 January 2010 aftershock distribution. They proposed that high-angle faults at 10–15 km depth, were reactivated because of Coulomb stress transfer, to the west and south of Efpalio. Godano et al. (2014) determined fault plane solutions by means of hypocentral multiplet identification on the microseismicity recorded by the CRLN

network, between 2000 and 2007. They extracted 15 multiplets of which they suggested that there is a dip increase with depth towards north. At the central part of the gulf fault dips were obtaining values from 50°-60° degrees at 7km depth, whereas to the north the angles are smaller around 20°-30°. Duverger et al. (2015) investigated the 2003 – 2004 seismic activity in the western Corinth rift and showed that the seismic excitation was related to the activation of the two parallel north dipping faults, the eastern one, Aigion Fault and the western Fassouleika Fault due to the existence of a relay ramp between these two en-echelon faults. They further emphasized on the hydromechanical processes through the fractured crust which cause the migration of seismicity and the implications for high pore fluid pressures.

The 2013 swarm around Heliki has been investigated for the temporal and spatial characteristics (Chouliaras et al., 2015; Kapetanidis et al., 2015 and Mesimeri et al., 2015). The last defined a significant number of earthquakes, with the use of HypoDD algorithm and cross correlation data. According to Kapetanidis et al. (2015) the swarm defined a planar surface dipping at 50° to the N-NW with maximum depths at 9.5km. The occurrence of the swarm accounts for the lowest part of the Pyrgaki fault. The contribution of fluid diffusion and stress transfer has been highlighted for the migration of seismicity along the rupture zone. Chouliaras et al. (2015) suggested that the swarm is distinguished into two parts and that there is a significant variance of the stress field associated with the occurrence of the swarm. In addition, Mesimeri et al. (2015) suggest that the fault zone responsible for the swarm corresponds to a normal north-dipping fault plane at 40°-50° which is also associated with several fault branches and Pyrgaki fault. The most recent research for the 2008 strong Patras earthquake was conducted by Karakostas et al. (2017) (after Konstantinou et al. 2009; Serpetsidaki et al. 2014) who thoroughly investigated the aftershock seismic activity with a large data amount, concluded that the seismic excitation was attributed to a dextral NNE-SSW. The deep foci distribution revealed the same characteristics for the seismogenic layer with the 1993 strong Patras earthquake, that occurred at an adjacent location. Kapetanidis (2017) relocated seismicity in the western Corinth Rift for the period 2000 to 2009 and analyzed specific seismic sequences with waveform cross correlation and double difference relocation techniques.

1.4.3 Stochastic Investigation of the seismic process in Greece

Seismicity in Greece has been analyzed under the framework of stochastic means for the interpretation of its complex process, for the investigation of correlations in time, space and size of the earthquakes. Some of the most recent and relevant procedures and tools that have been applied in seismogenic areas in Greece in terms of clustering and interaction are briefly described in this paragraph. Dimitriu and Papadimitriou (1990) calculated the fractal dimension for several seismicity zones in the Aegean sea for quantifying clustering among shallow earthquakes and classified the zones into three distinct groups of clustering (exhibiting high, intermediate and low fractal dimension). Xu and Burton (1999) studied the spatial clustering properties in central Greece in terms of fractality and hierarchy, searching for correlation between the fractal dimension and the b-value in different areas of Greece. Especially for the western Corinth Gulf

and Patras area they suggested that there is a positive correlation among these two parameters along with the temporal evolution of seismicity. The variations of the fractal dimension which varies between 0.33 and 1.56 in different areas were interpreted on the basis of the different seismotectonic properties and fluid presence. Dimitriu et al. (2000) investigated the evolution of earthquake spatial clustering 14 years before the 1995 M5.3 Arnea earthquake in Northern Greece. According to the temporal fluctuations of the fractal dimension they suggested that there is a preparatory phase during which the fractal dimension obtains a maximum value and then drops before the main event occurs. The minor events were responsible of causing this clustering effect and the entire process according to the authors, was found in agreement with the percolation theory. Telesca et al. (2000) investigated the clustering properties of the Greek seismicity catalog (1964-1996) along the southern Aegean arc for shallow and intermediate earthquakes. They concluded that the intermediate seismicity is adequately described as a Poissonian process and the shallow one exhibits a scaling behavior for specific time lags. However, the more the lower magnitude threshold in seismicity series is increased, the more the correlation decreases. Some years later Telesca et al. (2002) performed a monofractal and a multifractal analysis for the seismicity in Corinth Gulf for the period 1983-2000 revealing the scaling behavior in earthquake time-occurrences and a clustering enhancement when larger events are included in the analysis.

Xu and Burton (2001) showed that there are indications for persistence on the occurrence of moderate and strong earthquakes in the broader Mediterranean area and Xu and Burton (2006) applied the Rescaled Range analysis along with Monte Carlo simulations in Greece and three sub-areas including the Corinth Rift. Their study was accommodated in terms of interevent time, energy release and earthquake frequency and concluded to different memory patterns for the entire area and individual zones. They suggested that for the interval 1901-1999 in Greece, the seismicity process holds an important memory content for earthquakes with magnitude $M > 4.0$ and $M > 5.0$, however, memory properties for the studied parameters are not significant for individual zones, with the exception of earthquake frequency which was persistent in all cases. Their results are further discussed in Chapter 3 and compared with the results of the current study. Regarding magnitude, Lasocki and Papadimitriou (2006) studied the complexity in the magnitude distribution in Greece by using the smoothed bootstrap test for multimodality that is also applied in this study. The methodology was tested in three different seismotectonic settings (N. Aegean fault, Thessaly and the Ionian islands) for earthquakes exceeding $M 4.0$ in different time intervals. Complex magnitude distribution which cannot be described with parametric models was revealed in the two areas. Kotti and Tsaklidis (2012) investigated the seismicity in Northern Aegean for 1970-2011 and earthquakes with magnitude $M \geq 4.0$, showing that the interevent time between the earthquakes can be sufficiently approximated with a fractal process, exhibiting strong clustering in the time domain as well as positive autocorrelation.

Console et al. (2013) modelled the interevent times and the Coulomb static stress transfer for strong earthquakes along the major fault systems in the Corinth gulf. They found that the renewal models are better approximated with the Weibull and less with the Brownian Passage

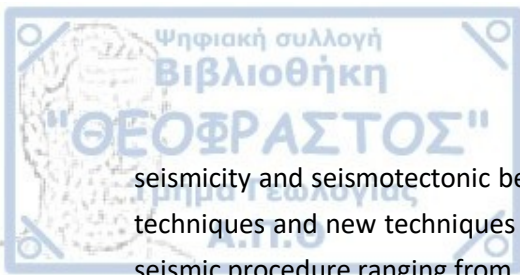
time distribution rather than a Poissonian process. Console et al. (2015) based on synthetic datasets and the characteristic earthquake hypothesis simulated seismic activity in Corinth Rift. Boiselet et al. (2014) computed the probability of occurrence for $M \geq 6$ earthquakes for the Corinth gulf for time dependent models based on the Brownian Passage time and Weibul probability distribution, suggesting that the Psathopyrgos fault possesses the highest probability for a strong earthquake to occur in the following 30 years. Michas et al. (2015) investigated the interevent time properties for earthquakes, for 2008-2013 in the Corinth gulf, in terms of the multifractal detrended fluctuation analysis. They proposed that the multi fractality degree vastly fluctuates in time, showing a decreasing value after the occurrence of the Efpalio doublet in 2010. They assumed that there are characteristic indications for a non-Poissonian behavior for earthquakes. Mesimeri et al. (2019) investigated clustering in the western part of the Corinth gulf, analyzed the cluster properties based on skewness and kurtosis and highlighted the swarm-like clusters.

1.4.4 Coulomb Stress Investigation in Greece

Coulomb stress changes play an important role in the interpretation of strong earthquake occurrence (King et al., 1994) and a massive number of studies has this criterion to quantify faults proximity to failure. Earthquake interaction due to the spatial distribution of positive and negative stress changes has also been widely studied in the broader area of the Aegean Sea and a strong correlation has been ascertained between earthquakes of different orders of magnitudes. The first application of the Coulomb failure criterion in Greece was introduced by Nalbant et al. (1998) who studied the Coulomb changes for 29 earthquakes ($M \geq 6.0$) during 1912-1983 that occurred in NW Turkey and North Aegean Sea. They stated that if 1bar is efficient to bring a fault closer to failure, then 16 events were highly triggered by the stress Coulomb changes induced by earlier events, while the ones found in stress shadow zones where there is a small likelihood for seismogenesis, are explained due to insufficient knowledge on historical earthquakes or omitting stress accumulation along faults. Moreover, they investigated the occurrence of smaller magnitudes and demonstrated the strong correlation between positive stress changes with microseismicity locations. Incorporation of the tectonic loading onto major regional faults was later achieved by Papadimitriou and Sykes (2001) who reconstructed the Coulomb stress state caused by the occurrence of six strong earthquakes ($M \geq 7.0$) that occurred from 1905 to 1999 in the Northern Aegean Sea. The evolution of the stress field was based on the coseismic stress changes induced by the earthquakes along with the tectonic stress build-up during this time along the NAT strike slip deformational zone. They showed that the large earthquakes produced changes more than 0.1 bar, sufficient enough to modify the seismicity pattern in the region and that localized stress enhanced the locations of the following earthquakes, since faults were brought closer to failure. This methodology is also followed in this study and will be further discussed in Chapter 4. Stress Coulomb methodology in Mygdonia was firstly applied by Tranos et al. (2003) who investigated the coseismic stress changes of the 1978 M6.5 strong earthquake along the well-defined causative fault zone. They showed that the stress changes due to the strongest foreshock on 23 May 1978, created a stress bright zone with high positive values along

the target fault responsible for the main shock of the 20th June 1978. In the current study the last 300 years historical information on strong seismicity is used in order to define the zones with increased likelihood of rupture in the future and results are compared with Tranos et al. (2003). A number of studies that followed, highlighted the significant contribution of the Coulomb Stress Changes in the interpretation of strong and minor seismicity occurrence, in Greece. Papadimitriou et al. (2005) reconstructed the evolutionary stress field of the strong seismicity in south Aegean, as well as the stress evolutionary field in other tectonic basins such as the Thessaly basin in central Greece (Papadimitriou and Karakostas, 2003) south Balkan and Northern Greece (Papadimitriou et al., 2006) the Kavala – Thrace basin in Northern Greece (Gkarlaoui et al., 2007), the western part of the Hellenic arc (Messini et al., 2007). Paradisopoulou (2009, 2010a) testified whether the cumulative stress field changes in the broader Greek region provide a reasoning for the spatial distribution of the strongest earthquakes ($M \geq 6.5$) location which have occurred since the beginning of the 20th century, by obtaining constant fault slip rates along major dislocation zones. The obtained result was quantified with the use of the probability estimation and stressing rate for a strong earthquake occurrence in the Aegean domain for a 30 year window and suggested a strong correlation between specific areas and adjacent faults.

Leptokaropoulos et al. (2012) investigated seismicity rate changes in the region of North Aegean, from 1981 December 19 to 2010 August 31. The influence of the Coulomb stress changes due to the coseismic slip of the six stronger events ($M_w \geq 5.8$) that occurred during this time interval was examined in connection with the occurrence rate of small events for the interevent periods. Seismicity was translated into earthquake probabilities for these events and a Rate/State model was applied to associate static stress changes with seismicity rate and compare the observed with the expected seismicity rates for each period. Karakostas et al. (2014) modelled the influence of the geometrical and frictional constraints of the 2013 North Aegean seismic sequence ($M 5.8$) approximating the optimal correlation between the aftershock seismicity and Coulomb stress changes distribution. After testing all possible combinations for the friction parameters they suggested that the distribution of the off-fault seismicity is better explained in the case of high friction (for $\mu=0.5$, $B=0.0$), since more than 70% of the aftershock seismicity is located in stress enhanced areas. Segou et al. (2014) also studied the stress perturbations caused by 2008 Patras earthquake and suggested that stress Coulomb promoted the occurrence of the 2010 Efpalio sequence. Leptokaropoulos et al. (2016) investigated the temporal and spatial evolution of the stress field in the western Corinth gulf since 1975 on the basis of stress rate changes and stress inversion. They suggested that there is a sufficient correlation between the stress-estimating methods, even in the near field. Mangira et al. (2018) investigated the earthquake activity in the Corinth gulf for earthquakes between 1911-2010 by using the linked stress release model on Stress Coulomb and proposed the one way interaction between the eastern and western Corinth gulf so that stress changes occurring in the eastern part of the Corinth gulf are only able to impose seismic excitations in the western part. The above brief description is indicative of the international scientific interest which is expressed on the two study areas and on the tools that have been developed and applied in order to investigate their



seismicity and seismotectonic behavior. In this study an attempt was made based on the above techniques and new techniques were developed and combined for identifying properties of the seismic procedure ranging from microseismicity to strong earthquakes.



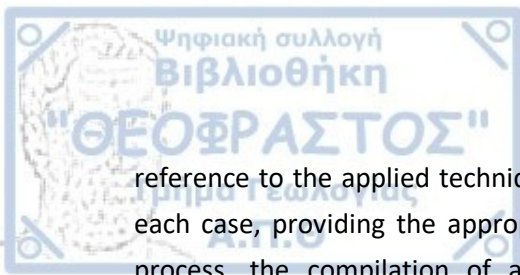
Chapter 2

Seismotectonic Analysis

The distribution of earthquake epicentres, is closely related to the development of the active fault population, since precisely defined earthquake foci can adequately describe the properties of the fault network. Microseismicity unlike strong earthquakes may occur everywhere, as well as onto the major hazardous faults which are often prominent to generate strong earthquakes. The identification of all active structures is then essential in terms of seismotectonic investigation and hazard assessment. The principle target of this study, is to identify the active seismogenic sources through seismicity, by improving focal coordinates beforehand. Even if there is an absence of earthquake sequences, the investigation of minor earthquakes is essential, since it is the only source of information, when seeking for faulting and seismogenesis patterns.

The adopted strategy, is based on a combined use of methodologies which have widely been applied for local seismicity, resulting in precise focal earthquake coordinates. Indicatively, Akyol et al. (2006) calculated average station delays out of earthquake recordings and used them to improve focal earthquake parameters across western Anatolia. In the area of Apennines, Bagh et al. (2007) with a basis on the Wadati methodology calculated velocity ratios for improving the velocity model and subsequently the background seismicity, whereas under the same concept Maggi et al. (2009) and Sgroi et al. (2012) improved the precision of the seismicity catalog for southern Italy and central Sicily, respectively. Small magnitude seismicity was studied with the application of the HYPODD algorithm from Piccinini et al. (2009) for defining seismicity swarms in northern Apennines, whereas Tan et al. (2014) applied it for extracting seismicity properties in western Turkey. In addition to the aforementioned examples in cases of local seismicity, the Wadati methodology was also applied into the analysis of induced seismicity data in mines (Rudziński and Dębski, 2008; Julia et al., 2009) improving earthquake location, despite the facts that earthquake occurrence in mines is described by a totally different physical background and that epicentral distances are very short compared to the ones in nature. Concerning station delays in Greece, Panagiotopoulos et al. (1985) calculated residuals for all permanent seismological stations in the broader southeastern Europe and Turkey, proposing that in western Greece residuals are positive ranging from 1.2 to 1.6 sec, whereas in northern Greece negative values between -1.1 and -0.2 sec prevail. Taymaz (1996) also studied the variations of time delays in the southern Aegean and Crete. In regional scales, time delays were calculated for the improvement of earthquake hypocenters in the long term seismicity of the North Anatolia Fault, as well as in the case of a seismic swarm in central Greece (Karamanos et al., 2007; 2010). The procedure followed in the current thesis has been also used for the most accurate investigation of seismic excitations in the Corinth rift, the north Aegean and Cephalonia island improving considerably earthquake locations, despite the variations in the seismotectonic setting among these areas (Karakostas et al., 2012; 2013; 2015).

The relocation procedure and employed methodologies for improving local earthquake coordinates in Mygdonia graben and Corinth rift are fully described in this chapter. A detailed



reference to the applied techniques is given, along with the data description and treatment in each case, providing the appropriate criteria for their selection. After the completion of the process, the compilation of a new improved earthquake catalog is achieved, after the incorporation of the required magnitude corrections. Following, the spatiotemporal investigation of the seismic activity is performed with the scope to analyze and clarify clustering and triggering properties among earthquakes. A seismotectonic interpretation for each study area is made based on the spatiotemporal distribution of the compiled earthquake catalog and the association of earthquakes with their seismogenic sources. Geometrical properties of faults are inferred from the distribution of earthquake hypocenters. Information on all available published data (structural information and fault plane solutions) is taken into account for an integrated seismotectonic interpretation. The final task of this procedure is to determine the active fault population responsible for the occurrence of recent seismicity in the two areas of interest.

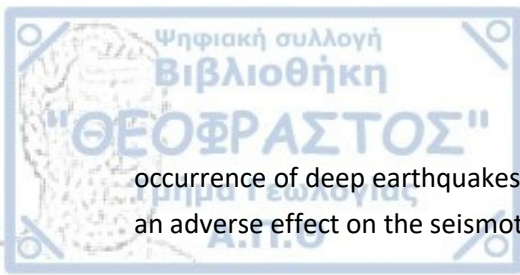
2.2 Data

2.2.1 Seismological Network

Up to 2008, earthquake monitoring in Greece was supported by four distinct permanent seismological networks operated by the Aristotle University of Thessaloniki (AUTH), the National Observatory of Athens (NOA), the Athens University (UOA) and the Patras University (UOP). On the onset of 2008 all the above networks were merged into one permanent network which now operates under the maintenance of the Hellenic Unified Seismic Network (HUSN). HUSN launched its operation with the scope to unify the separate seismological networks and upgrade seismicity catalogs through dense monitoring. This network configuration undoubtedly enhances the detectability of smaller earthquakes in the broader Aegean area. For this reason, the earthquake data used for the relocation procedure in the current thesis, mainly coincide with the incorporation of the AUTH seismological network into the HUSN establishment.

2.2.2 Seismic Wave Phases

The earthquake data exploited for the relocation purposes, refer to pairs of primary, P and secondary, S seismic wave phases for local earthquakes which occurred in the study areas between January 2000 - June 2016 for Mygdonia graben and between August 2008 – June 2014 for the Corinth rift. The seismic phases are collected from the monthly bulletins of the AUTH Seismological Station which include earthquakes recorded in the seismological stations of HUSN and they refer to open-source seismic data, being available at the station's website and stored in GSE2.0 format. In the case of the Mygdonian graben due to the absence of a significant number of earthquake phases since 2008, the study period was expanded for 16 years (2000 – 2016). It should be mentioned that earthquakes with a hypocentral depth ≥ 40 km are excluded from the original data sets, since their source mechanisms depend on deeper crustal properties. The



occurrence of deep earthquakes lies beyond the scope of this study and their existence imposes an adverse effect on the seismotectonic analysis of earthquakes with shallow depths.

2.3 Relocation Techniques

2.3.1 Introduction

Although data provision is lately enhanced and location accuracy is improved, a number of uncertainties which are inevitably involved in the existing earthquake catalogs, necessitates the application of relocation procedures for the most accurate definition of earthquake focal parameters. The determination of focal coordinates is strongly affected by the crustal structure, since geological layers control the propagation of seismic waves through the Earth's interior, always imprinting a geological impact on the recordings. Even in the case of an optimally installed seismological network (in terms of the spatial distribution of the seismological stations) imperfect or restricted information on the velocity model limits our ability for accurate estimation of focal parameters. The key for minimizing crustal interference, is to eliminate errors in the arrival time of the seismic waves which are related to the horizontal azimuthal distribution of the seismological stations and secondly to consider crustal heterogeneities as a function of depth. Under this concept, the relocation process in this study, gradually comprises the following steps:

- seismicity data selection,
- specification of the seismic body-wave velocity model,
- estimation of the velocity ratio (Wadati plot),
- calculation of station time delays for seismological stations,
- assignment of earthquake magnitude corrections,
- earthquake relocation analysis with the incorporation of the above parameters,
- application of earthquake location algorithms,
- spatiotemporal analysis of seismicity in the two study areas.

The above techniques and methodologies have been partially or wholly applied by a number of researchers, who anticipated the necessity to increase the credibility of earthquake focal coordinates in their analysis.

2.3.2 Earthquake Location Algorithms

2.3.2.1 Hypoinverse Relocation Algorithm

Earthquake data processing is initially performed with the application of the Hypoinverse location algorithm (Klein 2000) creating preliminary and final results for earthquake relocations, which are finally compared. The preliminary earthquake locations in both study areas are reached with the adoption of a regional velocity model which is representative for the whole Aegean area. Final earthquake solutions are generated with the incorporation of Wadati results, station time delays and computed velocity ratio, put into the Hypoinverse relocation algorithm. The two data sets are compared to each other in terms of quality parameters, which are given by the

Hypoinverse algorithm. Error histograms are constructed in order to express the errors in origin time (root mean square error, RMSE) in horizontal distance (mean horizontal error, ERH) and in focal depth (mean vertical error, ERZ) for distinct data sets, further explained below. Although the calculated errors bear only a mathematical meaning, error histograms for different data sets are used because they evidence the improvement in the location accuracy for the final results, especially regarding focal depths.

2.3.2.2 HypoDD Relative Relocation Algorithm

Earthquakes which occurred close in time and space, are further used as an input to the HypoDD (Double Difference) earthquake location program (Waldhauser and Ellsworth 2000; Waldhauser 2001). The HypoDD algorithm has been developed to optimally relocate seismic events in the presence of location errors and Earth model uncertainty. This technique avoids the requirements for station corrections or for high accuracy on the predicted travel times. It is based upon a relative relocation equation which combines the residual between the difference in the observed and the predicted phase travel time for earthquake pairs, along with changes in the vector connecting their hypocenters through the partial derivatives of the travel times. This approach is especially useful in regions with a dense distribution of seismicity, where distances between neighboring events are of the order of few kilometers. The improvement in earthquake location is achieved with the performance of repeated calculations by setting a number of constrains in each iteration. Relocation and clustering extraction is affected by parameters such as the damping factor, the maximum separation among neighboring events and the minimum number of observations. Proper phase data weighting and re-weighting on the arrival times improves the correlation between events, the distribution of the remaining earthquakes is far denser and follows more restricted requirements. The number of the examined earthquakes relocated with HypoDD is finally smaller than the one provided with the Hypoinverse algorithm, since uncorrelated events are excluded from the original catalog, as outliers. In this study, the fact that the HypoDD data input has been already relocated with the use of regional crustal parameters contributes to results with even higher location precision.

2.4 Velocity Models

Earthquake location algorithms presuppose the adoption of a crustal velocity model that best approximates the multi-layered properties of the Earth's interior in relation to depth. There is a number of 1-dimensional crustal models proposed for the Aegean area and the most suitable among them were tested, as analyzed in detail in the following paragraphs. The regional velocity model used in the case of the preliminary results is the one proposed by Panagiotopoulos and Papazachos (1985). This model simplifies the structure of the Earth crust under the broader Aegean sea and it is described by the following P wave velocities for their three corresponding layer thickness: i) $v_g = 6.0$ km/sec, $d_1 = 19$ km, for the granitic layer, ii) $v_b = 6.6$ km/sec, $d_2 = 12$ km, for the basaltic layer and iii) $v_n = 7.9$ km/sec, for the mantle half space. Detailed structure

investigations have been further performed in a regional scale over the two study areas. A considerable number of local velocity models have been derived from microseismicity analysis of previous studies in Mygdonia (Hatzfeld et al., 1986/1987; Papazachos et al., 2000; Paradisopoulou et al., 2006) with the most of the cases the earthquake data that were used regarded a short time duration and the epicentral distances were smaller than the ones from the permanent network. The particular seismotectonic pattern of the Corinth rift has also encouraged a significant number of studies for the investigation of the crustal structure and a variety of velocity models have been proposed. Rigo et al. (1996) used the data of a transient local network and determined a multilayered one dimensional P-wave velocity model for the western part of the Corinth rift, which has been widely used in similar studies, up to now. Some years later, methodologies on three-dimensional seismic tomography analysis were performed (Lattore et al., 2004; Gautier et al., 2006; Jansky et al., 2007). Novotny et al. (2008) with an initial basis on Rigo et al (1996) results, defined a more detailed velocity model for the same area, with the inversion of earthquake arrival times. Melis and Tselentis (1998) modelled the velocity pattern for the western part of the Corinth rift and defined relatively low velocity areas. In the western part of the Corinth rift, Haslinger et al. (1999) used local data to compute an one-dimensional velocity model in a tomography experiment at the west termination of the Corinth rift.

2.5 Velocity Ratio, V_P/V_S

Velocity models provide a measurement of the average expected velocity of P and S seismic waves, in association with the crust depth. For an improved earthquake relocation, the ratio of the velocities for the two seismic waves should be as precisely estimated as possible, for this reason the ratio should be defined by the current data. The determination of the velocity ratio is based on the Wadati methodology (Wadati, 1933) according to which, an average velocity ratio is acquired from all available pairs of local earthquake seismic waves. Velocity ratio varies with the geological properties and it is described by a unique value for each region. Despite its sensitivity, the estimation of the velocity ratio is deprived of errors due to crustal properties. According to the method of Chatelain (1978), if a seismic event k is recorded in two seismological stations named i and j , which are situated in x_i and x_j hypocentral distances respectively, then the time delay DT_P for P wave arrivals and DT_S for S wave arrivals between the two stations is respectively given by:

$$DT_P = P_i - P_j = (x_i - x_j)/V_P \quad \text{Eq. 2-1}$$

$$DT_S = S_i - S_j = (x_i - x_j)/V_S \quad \text{Eq. 2-2}$$

Where V_P and V_S correspond to the seismic wave velocities of P and S waves in respect. In the case of local seismological deployments, the hypocentral distances are almost identical, so after dividing Eq. 2-1 against Eq. 2-2, the velocity ratio (V_P/V_S) is given by the ratio:



$$\frac{DT_S}{DT_P} = \frac{V_P}{V_S} \quad \text{Eq. 2-3}$$

Fitting pairs of DT_P versus DT_S linear regression analysis gives a slope equal to the velocity ratio (Wadati diagrams). Considering that the time difference, $T_S - T_P$ at the earthquake hypocenter is zero, a line fitting on the Wadati diagram gives the origin time at the intercept with the P- arrival time axis. Using Wadati graphical technique new origin times for earthquakes can be obtained. Errors in the calculation of occurrence time as well as focal coordinates influence the wave travel time often making it unreliable. The achievement of obtaining new origin times lies to the fact that time is deprived of uncertainties. In our case, velocity ratio values for individual events are calculated and plotted in Wadati diagrams and an average velocity ratio is assumed. The average velocity ratio is calculated in each area and is afterwards incorporated into the Hypoinverse and HypoDD algorithms for the earthquake relocation procedure.

2.6 Station Time Corrections

In addition with the crustal variation at depth, travel times also depend upon the spatial and the azimuthal horizontal distribution of the seismological stations around the earthquake epicenters. In particular, there are horizontal velocity discrepancies which affect the accuracy of earthquake focal properties. For minimizing horizontal errors, time differences between the observed and the theoretical travel times of seismic body waves are estimated, known as station time delays or station time corrections. Positive or negative station time delays are used as time corrections in each station by adding the observed arrival time to the theoretical. The smaller the time delays are, the more the theoretical model we use, approximates real earth crustal conditions. A positive station delay indicates that the observed time is greater than the expected theoretical time, implying that the wave propagation is faster than the time suggested by the theoretical model. On the other hand, a negative time delay signifies a slower propagation and hence a lower value of the body wave velocity. The technique for estimating station time delays applies with a repetitive procedure which terminates when the difference between the observed and the theoretical times becomes insignificant. In this study, the iterations of time corrections terminate when the 1.0sec difference threshold is reached. The methodology of computing station time delays is popular for relocation purposes of shallow seismicity. It is stated that large positive or negative time delays often are a consequence of an insufficient knowledge of the geologic conditions of the Earth's or due to human error, as it has been noticed before (Akyol et al., 2006).

2.7 Magnitude Corrections

The compilation of a homogeneous final seismicity catalog in terms of magnitude properties is the last step of the data preparation process. Due to technical or scientific factors,

seismological institutions estimate earthquake magnitudes which are not identical for the same event, for this reason, variations and discrepancies between seismicity catalogs exist over the years. Such problems are common to regional and global seismicity catalogs (Mignan and Woessner, 2010; Woessner et al., 2010) and might prove misleading for committing any further seismotectonic or statistical seismicity analysis. A systematic problem is also observed in the case of the Greek seismicity catalog (Papazachos et al., 2002) and has been anticipated with the elaboration of scaling laws between different magnitudes (Papazachos et al., 1997; Baba et al., 2000; Burton et al., 2004; Leptokaropoulos et al., 2013; Michailos, 2015). In our case, the available magnitudes to be assigned to earthquakes of the seismicity catalog are reported either from the National Observatory of Athens (M_{ATH}) or from the Seismological Station of Thessaloniki (M_{THE}). Not until February 2011, an apparent differentiation between the two announced magnitudes existed, reaching even 0.5 units (Karakostas et al., 2015). Ever since, the Hutton and Boore (1987) formula is jointly applied to the earthquake waveforms of the two institutes resulting in the simulation of an equivalent Wood Anderson magnitude, referred as Local Magnitude. The approach for the elimination of the above magnitude discrepancies, focuses on the conversion of M_{ATH} into equivalent M_{THE} for the recorded earthquakes. In similar methodologies Baba et al. (2000) investigated the scaling relations between M_{ATH} and M_{THE} for the period 1964-1995 and Michailos (2015) proposed the corresponding magnitude corrections between the aforementioned institutes for the period 2000-2013, for the entire seismicity catalog. In this study the magnitude corrections were restricted to the data for each study area and the final results were compared to the general corrections found by other researchers.

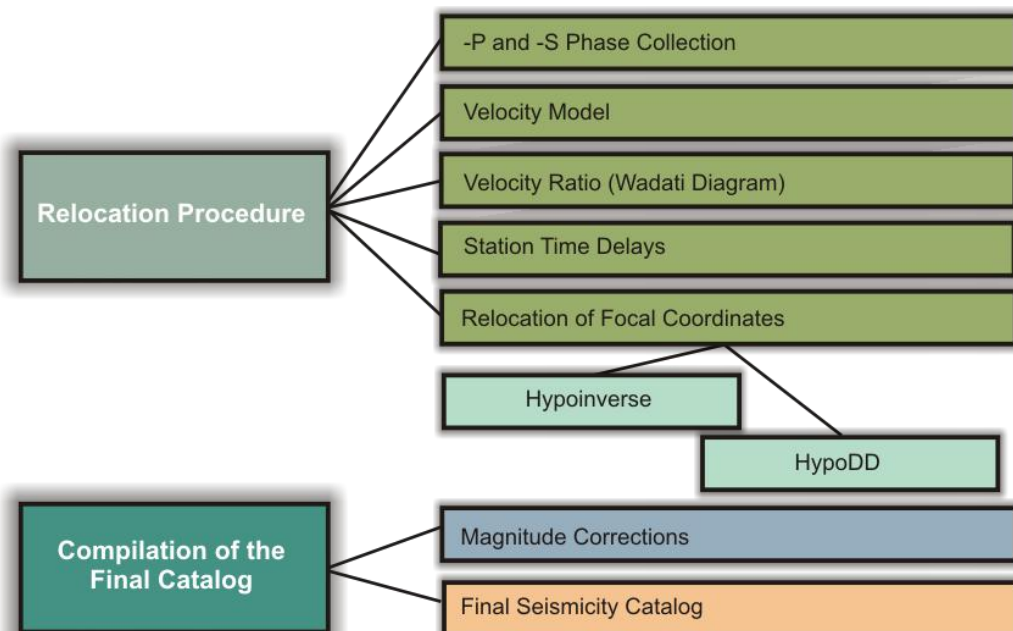
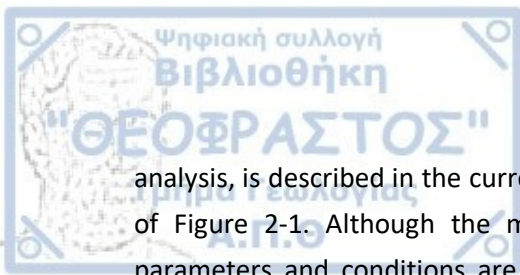


Figure 2-1 Schematic diagram of the methodology followed for the compilation of the seismicity catalogs in successive steps, as described in the paragraphs 2.2 to 2.7 in this chapter.

Summarizing, the whole procedure that is followed in this study starting from the data collection and the relocation procedure until the final seismicity catalog is compiled for further



analysis, is described in the current chapter and is schematically illustrated in the discrete steps of Figure 2-1. Although the methodology is equivalent for the two study areas, specific parameters and conditions are considered for the peculiarities of the two cases, under the framework of their seismotectonic setting and the crustal properties.

2.8 Relocation Results for Mygdonia Graben

2.8.1 Introduction

Due to the historical strong seismicity in the Mygdonian graben and its proximity to the metropolitan center of Thessaloniki, the area is being monitored by a satisfying number of seismological stations after 1978, when the strong Stivos earthquake occurred. Short term seismicity has been investigated in the past by a number of transient seismological networks as mentioned in Chapter 1, however, long term seismicity has been only once investigated by Scordilis et al. (1985; 1989) at the onset of the permanent seismological network operation and some years after, when the 1978 earthquake struck the area. A characteristic seismicity pattern and an early evidence for earthquake clustering was evident for Mygdonia in the study of Scordilis et al. (1985; 1989) even when earthquakes were studied for a short period (1981-1984). Though, an updated seismicity survey was of high significance for reaching more robust seismicity results, since the seismological network has been gradually reinforced with the addition of multiple stations around northern Greece. Earthquake recordings have been now improved and the observation period in this study is longer than the ones in the past, offering numerous data.

2.8.2 Data

The data used for the relocation processes consist of pairs of seismic wave phases for earthquakes occurring in the rectangular area comprised in between 22.80°- 23.90° meridians and 40.10°- 41.00° parallels (Fig. 1-3). In total, 2288 pairs of seismic phases were collected from January 2000 to June 2014 for earthquakes with magnitudes not exceeding 4.8. For the application of the Wadati technique and the calculation of station time delays, only a set of the most sufficient and high quality earthquake recordings are taken into consideration. This set fulfills the strict requirements that earthquakes are described by a satisfying number of recordings each ($n \geq 7$) preferably recorded by 21 seismological stations installed in a relatively short epicentral distance ($< 200\text{km}$). This data set comprises the namely optimum earthquake data set and includes 171 earthquake observations between August 2008 and June 2014. A bar plot demonstrating the total number of seismic phases per year for the period 2008 – 2014, is shown in Figure 2-2. In addition to the total number of earthquakes, Figure 2-2 shows the cumulative number of phases, which belong to the optimal earthquake data set satisfying the specific requirements is shown, shaded with blue color. Information about the spatial distribution of the seismological stations which are located in northern Greece and they belong to the permanent network of HUSN as well as the stations of neighboring countries is given in Figure 2-3. The

seismological stations which are used for the Wadati procedure and the estimation of time delays are enclosed in the red circle and it is evident that they azimuthally cover Mygdonia with satisfaction, described by a small station azimuthal coverage (GAP) meaning, the largest azimuthal distance between two adjacent seismological stations, with the exception of the southeast part of Figure 2-3 where the area is occupied by the Aegean sea, deprived of stations.

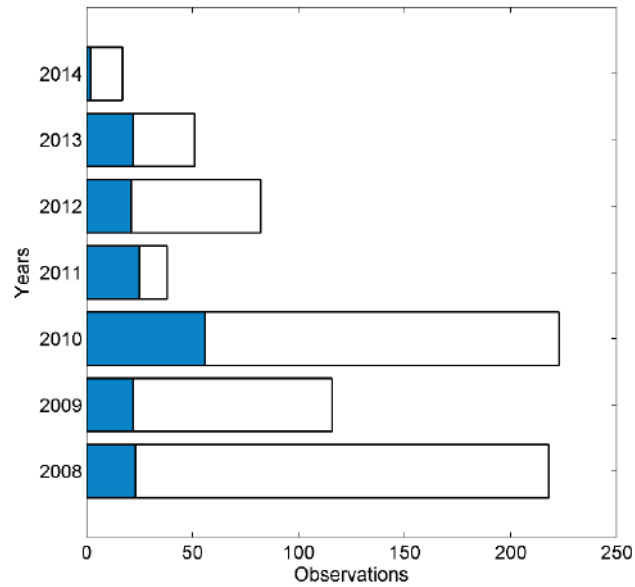


Figure 2-2 Cumulative number of seismic phases obtained from the bulletin of AUTH seismological station. Bars in blue correspond to the phases which belong to the optimum earthquake data set.

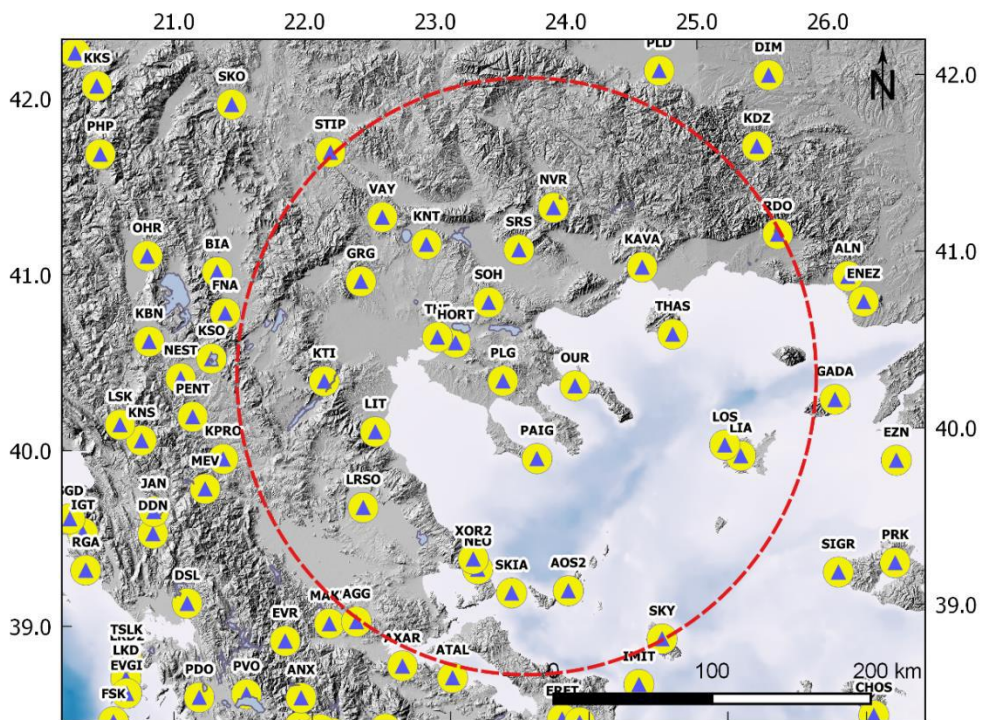


Figure 2-3 Map of northern Greece and neighboring countries with the seismological stations installed by AUTH and GI-NOA. The red circle encloses seismological stations employed for data re-processing using the methodologies for Wadati and station time delays.

The velocity model proposed by Paradisopoulou et al. (2006) is selected for this study, because it was generated from recent earthquake recordings when the seismological network was identical with the current study, hence, there is a data and methodology relevance. This model is further modified for deeper crustal layers and the half space, which is useful, when seismological stations are located in long epicentral distances. Velocity for deeper earth layers up to 30km is adopted from the mantle half-space description of Panagiotopoulos and Papazachos (1985). Detailed information on the vertical distribution of the P- velocity along with the thickness of each layer is numerically described in Table 2-1 and graphically designed in Figure 2-4, where the red and green line correspond to the models of Paradisopoulou et al. (2006) and Panagiotopoulos and Papazachos (1985) respectively.

Table 2-1. Information about velocities and depths for the adopted velocity model proposed by Paradisopoulou et al. (2006).

V_p (km/sec)	Depth (km)
4.00	0.00
5.29	1.0
5.36	1.5
5.76	2.0
5.79	3.0
6.16	4.0
6.23	6.0
6.27	8.0
6.30	10.0
6.42	20.0

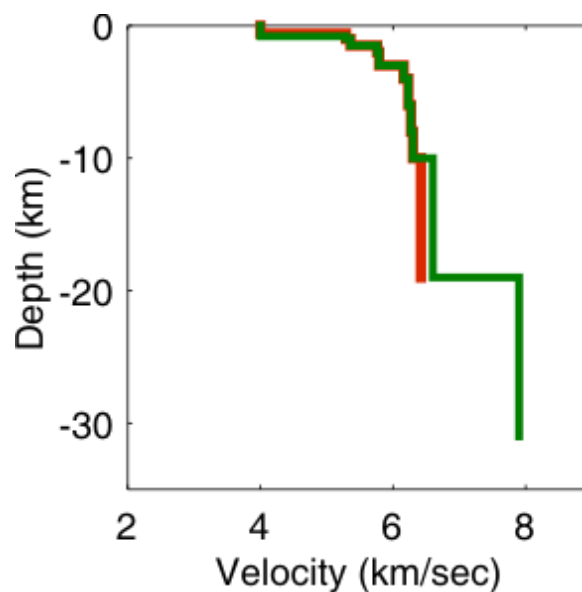


Figure 2-4 Schematic representation of the two velocity models of Paradisopoulou et al. (2006) depicted with the red line whereas the green line corresponds to the velocity model of Panagiotopoulos and Papazachos (1985).

The seismic body wave pairs which belong to the optimum earthquake data set are used for the estimation of the velocity ratios (V_P/V_S) in the region. Figure 2-5a shows the histogram for the velocity ratios of the 171 observations and it is shown that there is a good fit with the Gaussian distribution which is approximated with the red line. A cumulative Wadati diagram is also constructed for the constrained earthquake data set (Fig.2-5b) where the time difference DT between T_P and T_S is plotted against T_P for all available pairs of observations. The mean slope equals the velocity ratio, found to be $V_P/V_S=1.78\pm 0.04$, with a 95% confidence interval. There is an evident linear fit, mostly accurate for pairs of smaller or intermediate distances, whereas in longer distanced data are more diffused. It should be mentioned that earthquakes with a velocity ratio exceeding the standard deviation of the mean ratio were further excluded from the optimum data set and they were not included in the calculation of station time delays.

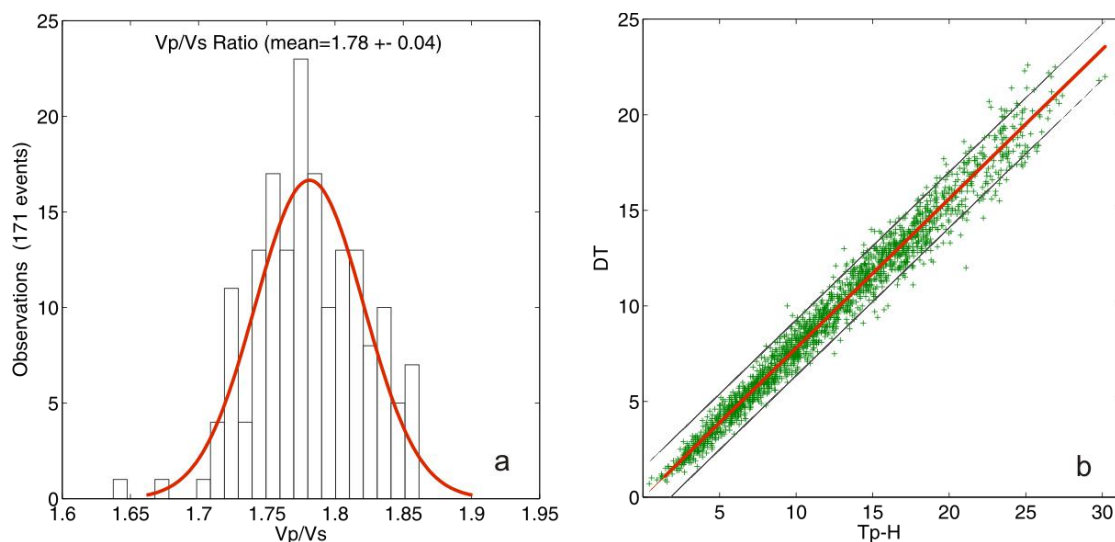


Figure 2-5 a) Histogram for 171 velocity ratios, red thick line simulates the Gaussian distribution, b) cumulative Wadati diagram indicating the linear fit (red line) between pairs of DT and T_P-H . Grey lines show the 95% standard deviation from the mean value (1.78 ± 0.04).

The calculated velocity ratio is slightly smaller than the one proposed by Soufleris et al. (1982) who calculated an average velocity ratio equal to 1.82 ± 0.12 derived from 65 well-recorded earthquakes. On the other hand, 1.78 is slightly larger than ratios like 1.74 (Hatzfeld et al., 1986/1987) and 1.76 (Paradisopoulou et al., 2006). The differences between the current and results of previous studies are reasonable and can be justified because of the long period of observations or the longer epicentral distances between earthquakes and the permanent network compared to local experiments. Temporal variations of the velocity ratio should also be considered. On the other hand, results totally agree with Scordilis (1985), who calculates $V_P/V_S = 1.77 \pm 0.07$ for three year recordings (1981-1984). The spatial distribution of V_P/V_S values across the area shown in Figure 2-6 indicated the absence of a particular characteristic pattern within the graben and the surrounding area and implies that there are no significant crustal variations in the brittle part of the crust of Mygdonia graben. Velocity ratios mostly range

from 1.72 to 1.86 and there is only a slight indication that along the area with mountainous topography of the study area the majority of the values are low (1.72 – 1.78).

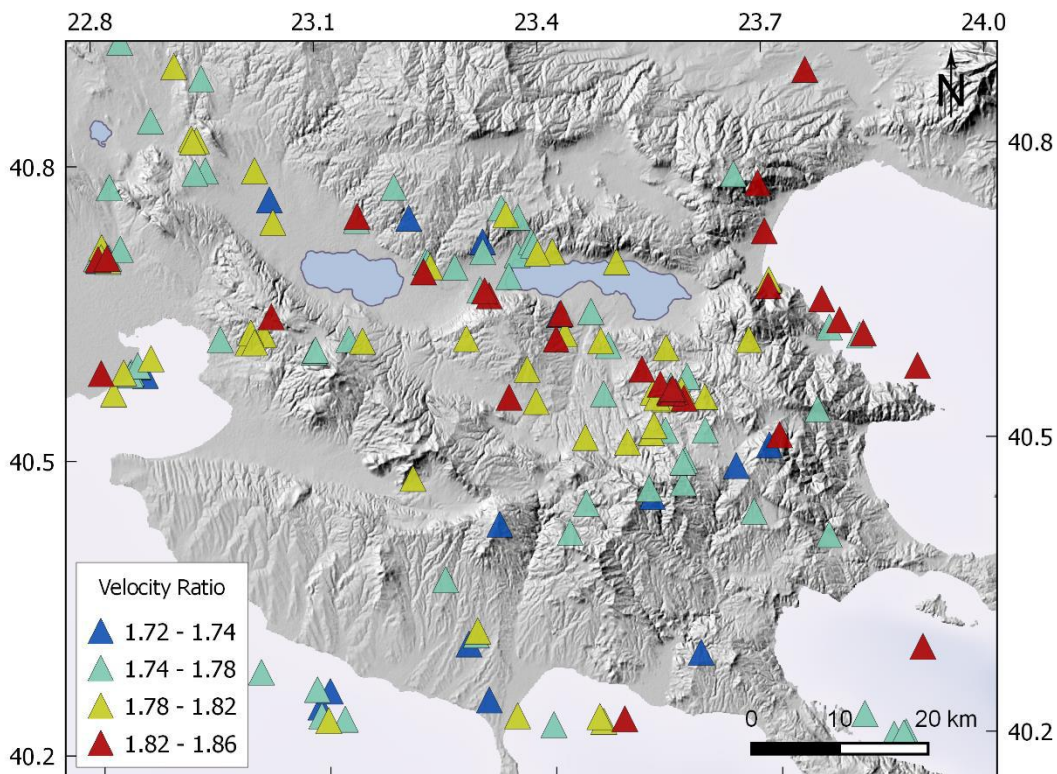


Figure 2-6 Map with the spatial distribution of the color coded velocity ratios for the optimum data set of earthquakes, where high values are indicated with the red color and lower values with blue color.

2.8.5 Station Time Corrections

Finally, station time corrections are calculated for a total number of 57 stations, which are corrected in time with the incorporation of the station delays. The obtained corrections vary between -0.7 sec and +0.7 sec for the optimum set of earthquake data. Figure 2-7 shows the spatial distribution of the derived time corrections in the broader northern Aegean which are plotted as contours. Both positive and negative station delays are calculated in Northern Greece. It is generally noticed that time corrections around the epicentral area are relatively smaller and generally show negative values in contrast to the ones estimated for stations located in longer distances (Table A-1, Appendix I).

2.8.6 Relocation process

A total number of 2288 earthquakes were finally relocated with the use of the Hypoinverse algorithm (Klein, 2000). To begin with, preliminary earthquake locations were estimated with the use of the regional velocity model and secondly they were determined with the incorporation of all the improved parameters. The two data sets were compared to each other with the use of error histograms (Fig.2-8, preliminary results: 1st row and revised results: 2nd row). There is an indication for significant improvement in the mean estimated error of the origin time

method has been used before by Rolandone et al. (2004) is adopted, for the quantification of the upper and the lower cut-off depth of the recorded seismicity. The existence of the upper cut-off depth is attributed to low normal stress and pore fluid effects, because of well-developed gouge along faults (Marone and Scholz, 1988).

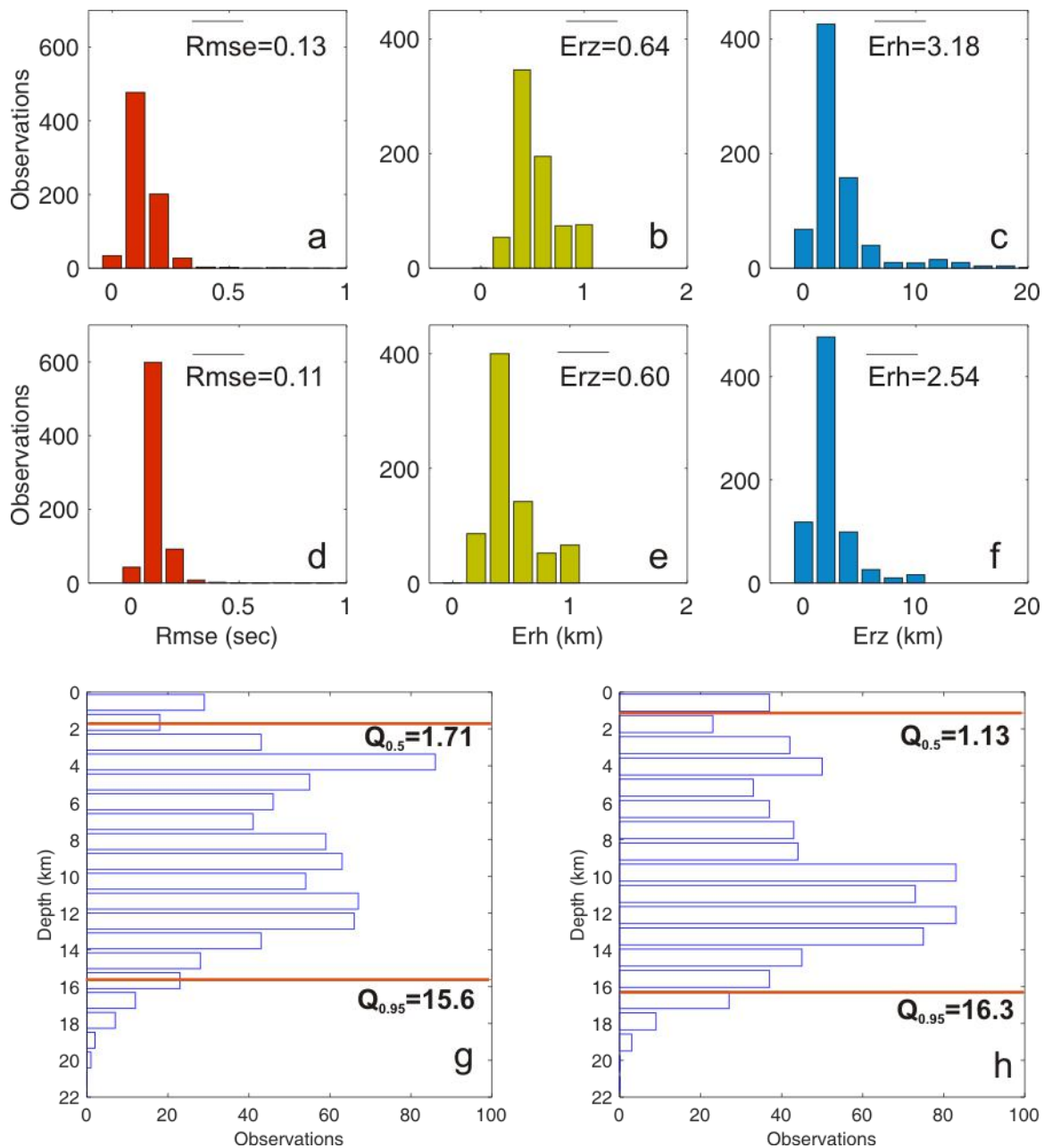


Figure 2-8 Comparison between errors for preliminary location (first row) and final relocation process (second row) for the modeled set of earthquakes. The mean values are given in each plot a) root-mean square error (Rmse), b) horizontal uncertainty (Erh), c) vertical uncertainty (Erz), d) root-mean square (Rmse), e) horizontal uncertainty (Erh), f) vertical uncertainty (Erz) and g) depth distribution, for the final results and h) depth distribution, for the preliminary results. Red lines correspond to the lower and upper cutoff where the majority of earthquakes is exhibited (90%).

Small depths are usually associated with faults, which are deprived of a well-developed gouge zones and unconsolidated lithology, in contradiction with big faults which prevent stress loading

at small depths. Marone and Scholz (1988) showed that there is an absence of hypocentres for big crustal faults (San Andreas fault in California) and that the majority of depths are distributed between 3 -15km. They also highlight the fact that the transition from the brittle to the ductile deformation occurs below the depth of the 90% foci of the shallow seismicity. In our case, there is an important number of microearthquakes at small depths distributed over the study area, whose depths do not improve even after the relocation process. The quantiles $Q_{5\%}$ (=2.6km) and $Q_{95\%}$ (=16.3km) are evaluated for preliminary and final results, implying that the width of the seismogenic part for Mygdonia area is approximately 13km. Material physics put further constrain to the maximum fault dimensions of faults, since small faults are smaller than the schizosphere and generate circular seismic sources, whereas large faults occupy the entire part of the seismogenic crust. The fault width is confined from the location of the transition zone. Faults are mostly approximated with rectangular surfaces, described by the length and the width. Since width cannot downdip extend further than the transition zone, faults favorably develop in a lateral way. The individual fault widths (W) for this study, are calculated from the width of the seismogenic crust (h), according to the equation:

$$W = \frac{h}{\sin(\delta)} \quad \text{Eq. 2-4}$$

Where δ stands for the fault dip angle. Nevertheless, the aspect ratio of the length versus the width (Scholz 1982) for thrust or for low dip faults should obey the relation: $L/W \geq 1.0$ (Lin and Stein, 2004) since only in this case faults are expected to own an important competence to trigger earthquakes on adjacent faults.

2.8.8 Earthquake Magnitude Assignment and Correction

Finally, the seismicity catalog with the relocated focal coordinates is now compiled for the area of Mygdonia and the last step to accomplish is the magnitude assignment to the corresponding events. Earthquakes for the Mygdonia region with both magnitudes M_{ATH} (NOA seismicity catalog) and M_{THE} (AUTH seismicity catalog) announced, are employed in order to define the relation between the magnitudes of the catalogs. In Figure 2-9a known pairs of M_{ATH} and M_{THE} for the same earthquakes which have both magnitudes reported, are plotted. It is evident that M_{ATH} and M_{THE} for the range of $1.0 < M \leq 3.9$ are not equivalent, a conclusion reached due to the presence of two distinctive linear trends. Furthermore, the difference $\Delta M_{Th-A} = M_{THE} - M_{ATH}$ is evaluated and plotted against the number of the events and it evidences that there is a systematic shift from zero between the two catalogues (Fig.2-9b) which is negative for the first 400 events and positive onwards. The temporal fluctuation of the discrepancies is also evident in Figure 2-10 where the average ΔM_{Th-A} for every window of 20 non overlapping events has been evaluated and plotted against the years of observations. According to the average ΔM_{Th-A} value, five observation periods are discriminated in the entire period and are the following: 1) 2000 – 2003, 2) 2004 – January 2007, 3) February 2007 – July 2008, 4) August 2008 – January 2011 and the final 5) February 2011 – 2014, for which the average ΔM_{Th-A} is quite stable. The methodology that is followed for the elimination of magnitude discrepancies, focuses on the conversion of M_{ATH}

into equivalent M_{THE} for earthquakes with magnitudes smaller than $M < 4.0$, since earthquake with larger magnitudes, although few, seem to be linearly correlated. A linear regression analysis is performed between M_{THE} and M_{ATH} for earthquake magnitudes in each time interval.

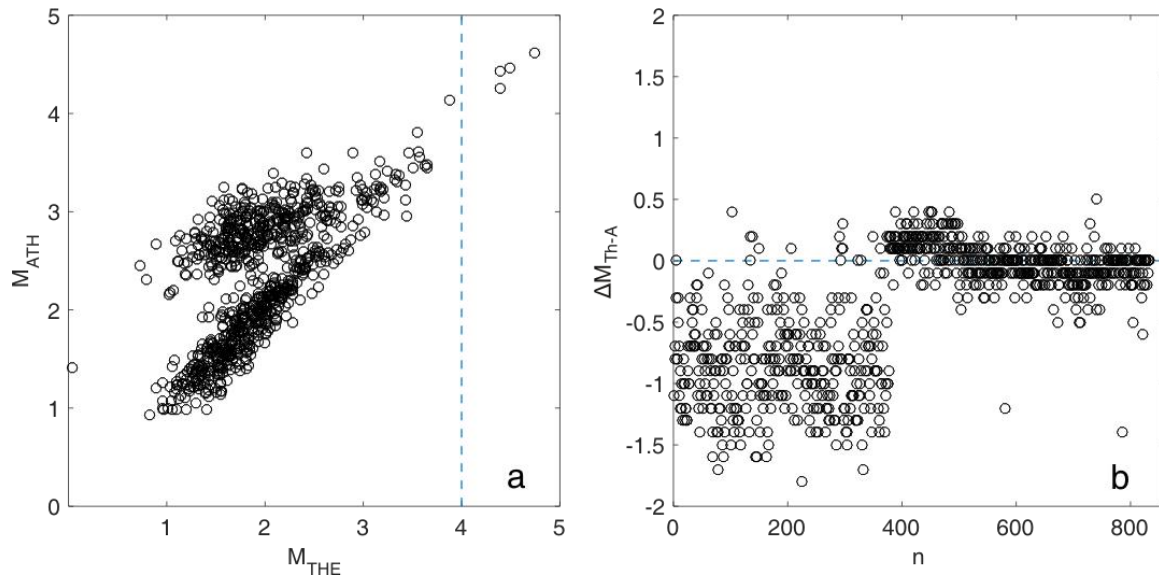


Figure 2-9 a) Correlation between pairs of magnitudes M_{THE} and M_{ATH} for the earthquakes in Mygdonia during the time interval 2008-2013 and b) The magnitude difference $\Delta M_{Th-A} = M_{THE} - M_{ATH}$ for all earthquakes.

Table 2-2. Information about the separate intervals, the results for the linear regression analysis and the final magnitude corrections applied to M_{ATH} , according to the linear regression results of **Figure 2-10**.

Period	Duration	Linear Regression	Average ΔM_{Th-A}
1	01. 2000 – 12. 2003	$a=1.254, b=0.741$	0.42
2	01. 2004 – 01. 2007	$a=2.448, b=0.368$	0.45
3	02. 2007 – 07. 2008	$a=2.707, b=0.345$	0.84
4	08. 2008 – 01. 2011	$a=2.155, b=0.344$	0.10
5	02. 2011 – 12. 2014	$a=0.013, b=1.002$	0.00

The general orthogonal regression (GOR) methodology, is applied for the linear regression, a statistical technique which is followed in several relevant cases worldwide (e.g. Castellaro and Gormann, 2007; Deniz and Yucemen, 2010; Wason et al., 2012). This analysis is preferred from the ordinary least squares methodology because no systematic errors are introduced into the regression results, since there are no uncertainties on the independent variable (Castellaro et al., 2006). Results on the regression analysis parameters (a and b-values) are shown in Table 2-2 and graphically presented in Figure 2-11. For the first interval M_{Th} is approximately 0.42 units smaller than M_{ATH} , for the second interval the distribution of ΔM_{Th-A} shows an average shift of 0.84 in magnitude differences after the year 2011. For the third period there is a 0.1 unit difference between the two magnitudes and for the forth 0.5 units.

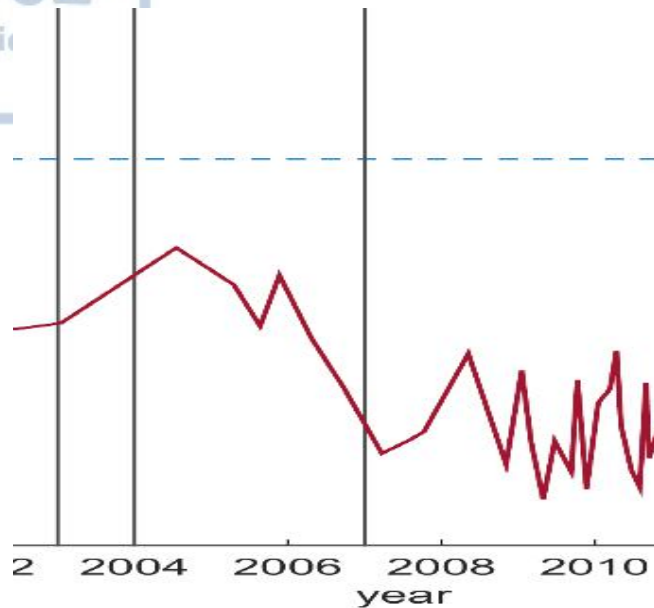


Figure 2-10 Fluctuations of the average magnitudes differences, ΔM_{Th-A} for every 20 non overlapping earthquakes for the entire time span of the observations.

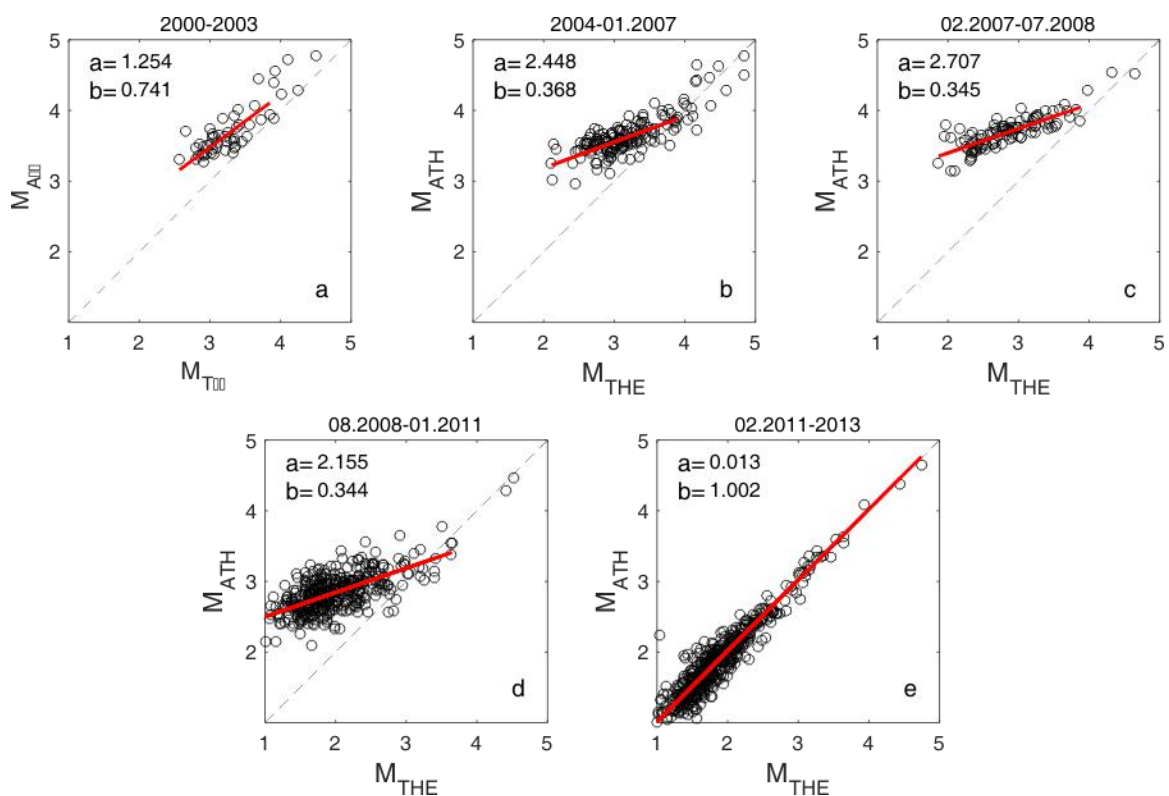


Figure 2-11 General linear orthogonal regression between M_{THE} and M_{ATH} for a) 2000 – 2003, b) 2004 – January 2007, c) February 2007 – July 2008, d) August 2008 – January 2011 and e) February 2011 – 2013. Red line corresponds to the linear fitting described by the corresponding parameters a, b.

The diagrams of Figure 2-11 show that in the last period (02.2011 to 2014) there is a good agreement between the two magnitude scales ($b=0.997$, which approximates 1.0) in contrast to all other cases, where the estimated b values are far from unity. Thus, using the scaling relations, uniform corrections were applied for the distinguished four intervals of observations and magnitudes can now be treated as a uniform time series, especially for the needs of the statistical analysis that will be accomplished in the following part of the thesis.

2.8.9 Final Seismicity Catalog

After inserting the corrected magnitudes into the catalog, the final seismicity catalog for the study area is finalized. The relocated epicenters of earthquakes for the 14 years between January 2000 and June 2014 are presented in Figure 2-12. In a quick glance, it is obvious that with the exception of the southern and the southwestern area where there is a characteristic absence of seismicity, in the rest of the area there is either scattered or clustered seismicity. During this period, seismicity is not uniform and is characterized by small and moderate size earthquakes, the majority of which is concentrated in the interior of the main Mygdonia graben or along secondary basins which are formed along the north-dipping normal and their antithetic faults. Seismic activity exists around the city of Thessaloniki, where some small excitations take place, like the west coast of Thermaikos gulf the ChMt faults and along PPF faults. Earthquake epicentres also appear at the NNW of Lagadas Lake, where approximately three clusters of epicentres are visible. Earthquake epicentres are also found around Lagadas Lake, among the faults of LAVF and AAF. A small seismic swarm is also evident in the middle of the two lakes. Moving to the east, seismicity seems to be more intense, with concentrations of earthquakes mainly distributed to the NW boundary of Volvi Lake. Significant seismic activity is additionally observed around the mountainous area of Arnea, where there is a number of clusters revealing a SE-NW or a NW-SE direction.

The target is to investigate earthquake occurrence in time and space and delineate the responsible faults so as to obtain a clear view of the seismotectonic properties of Mygdonia graben, based on recent seismicity. Firstly, there is a temporal investigation of earthquake occurrence in chronological periods, where a spatiotemporal tool is also used for extracting small dense clustering and secondly a spatial investigation is performed for assigning earthquakes to the corresponding faults, if possible. Cross sections are constructed for the investigation of the geometrical properties of faults at depth and fault plane solutions are used for ascertaining the extracted results. Results are provided on the basis of the two relocation algorithms that have been applied. In the end a combined interpretation is made for fault operation and fault activity in the area of Mygdonia.

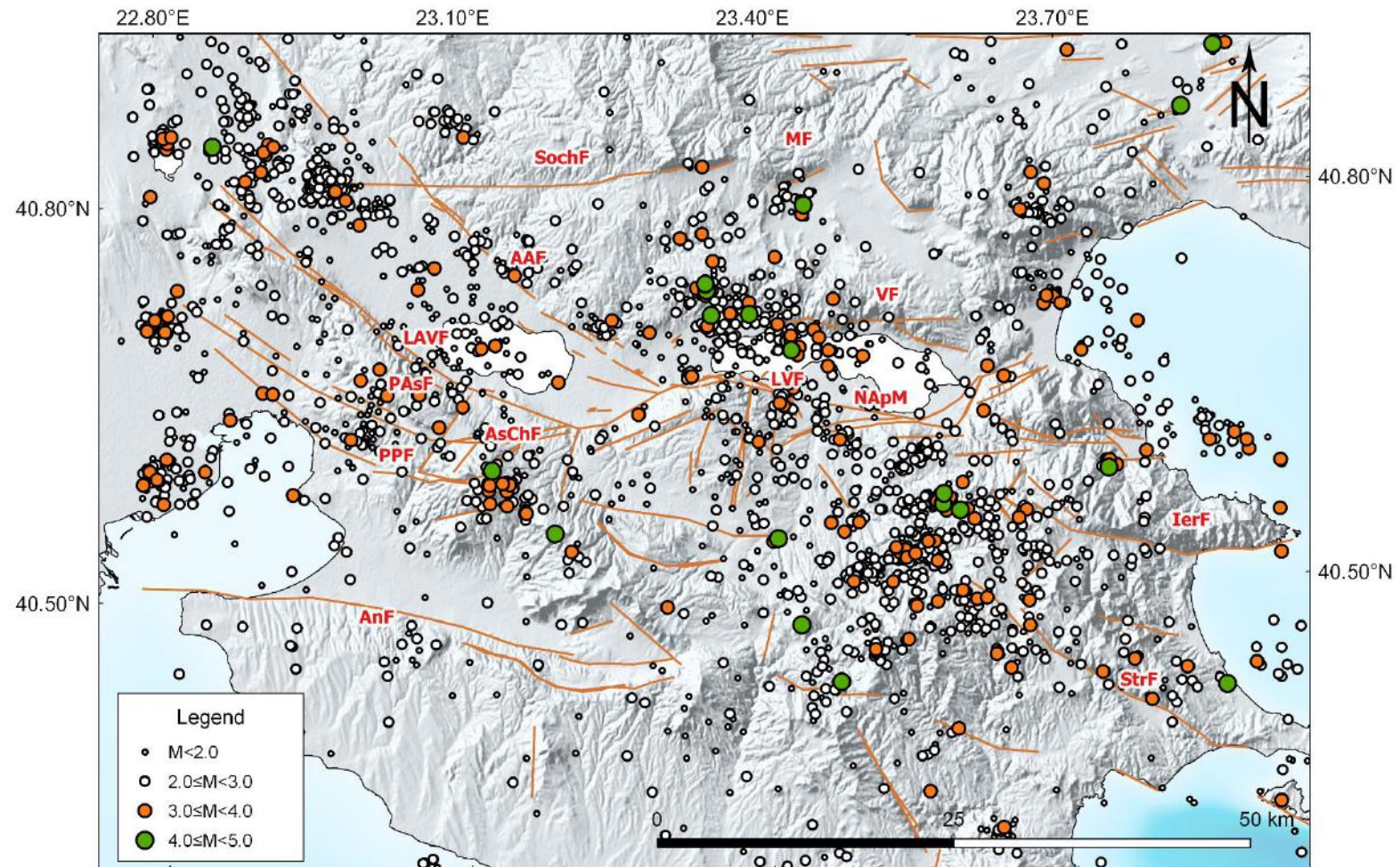


Figure 2-12 The spatial distribution of relocated earthquakes in 2000 – June 2016 in the broader Mygdonia graben. Information on the most important rupture zones is indicated by Pavlidis and Kiliyas, 1987; Tranos et al., 2003; Tranos, 2011.

A temporal and spatial analysis is further performed for the identification of the causative faults and possible microseismicity migration characteristics. A space-time plot is firstly constructed where all relocated earthquake epicentres are projected onto a 100km long vertical plane trending in an E-W direction (Fig.2-13a, SS' section, starting point: 22.80°E, 40.55°N, ending point: 23.90°E, 40.55°N), which coincides with the average strike of the dominant Thessaloniki-Gerakarou fault zone (TGFZ). In Fig.2-13b time is converted into numerical days, from January 2000 up to June 2016, earthquake magnitude is proportional to the size of the corresponding circles and distinct colors depend on geographical coordinates for clearly identifying space-time relations. In the beginning of the observations, a seismic swarm with two events of magnitudes $M \geq 4.0$ (4.5 and 4.1, 8 October 2001, with a thirty minutes lag in between) which occurred close to Chortiatis Mountain (cl.1 – in pink color) was observed and this activity lasted few days. Two more isolated events with magnitude M4.0 occurred in the same year, at the east part of Arnea, not followed by a seismic activity. The next considerable seismic concentration occurred in April 2003 (cl.2, dark red color) when a small excitation with short duration and maximum magnitude M3.3 occurred at the northern boundary of Volvi Lake. No other moderate events occurred until 2004, whereas during 2004 – 2005 seismic activity increased. The time interval between 2004 and 2008 (Julian days: 1300 – 3200) comprises a time-window where the seismicity rate is higher and it coincides with a seismic burst at the eastern part. A seismic activity initiated at the northwestern part (cl.4 – red color) which is found at approximately 8km from the start of SS' section, where some years later another group of events followed (cl.10 – red color). It is observed that at the same time there is a sequence of short seismic excitations located at the northern margin of Arnea (cl.3 – yellow color) and a subsequent concentration in Volvi lake (cl.4 – red color). In 2005, two adjacent clusters simultaneously initiated (earthquakes in light blue color, at approximately 20km from the starting point of the section and earthquakes in orange color at 18km distance), showing a constant interaction of seismicity for some years (Julian dates: 1600 - 2900). Especially in 2005, a seismic excitation (cl.6 – orange color) culminated in an earthquake with magnitude equal to 4.2 (April 2005). Regarding the cluster which occurred to the southeast of cl6 (blue color) no stronger event than M3.1 is recorded. In 2005 there is seismic activity at the northern part of Volvi lake (cl.7 – dark red color) and at the western termination of SochF, along with a number of moderate events with maximum magnitude M4.0. A seismic excitation occurred in 2007 in Thermaikos gulf (cl.9 – purple color, Julian days: 2700) with a maximum magnitude M4.4 and later in 2010 a couple of events (M4.4, M4.5) occurred around Arnea followed by a small number of aftershocks (cl.8 – green color). The last moderate event for the specific observation period took place in October 2013 and concerns a M4.4 event at the northern boundary of Volvi lake, not followed by other events. The shaded zone in Fig.2-13b (grey background zone, at approximately 45km from the beginning of the profile) represents the epicentral area of the 1978 last strong event, showing that it is not characterized by recent seismic activity.

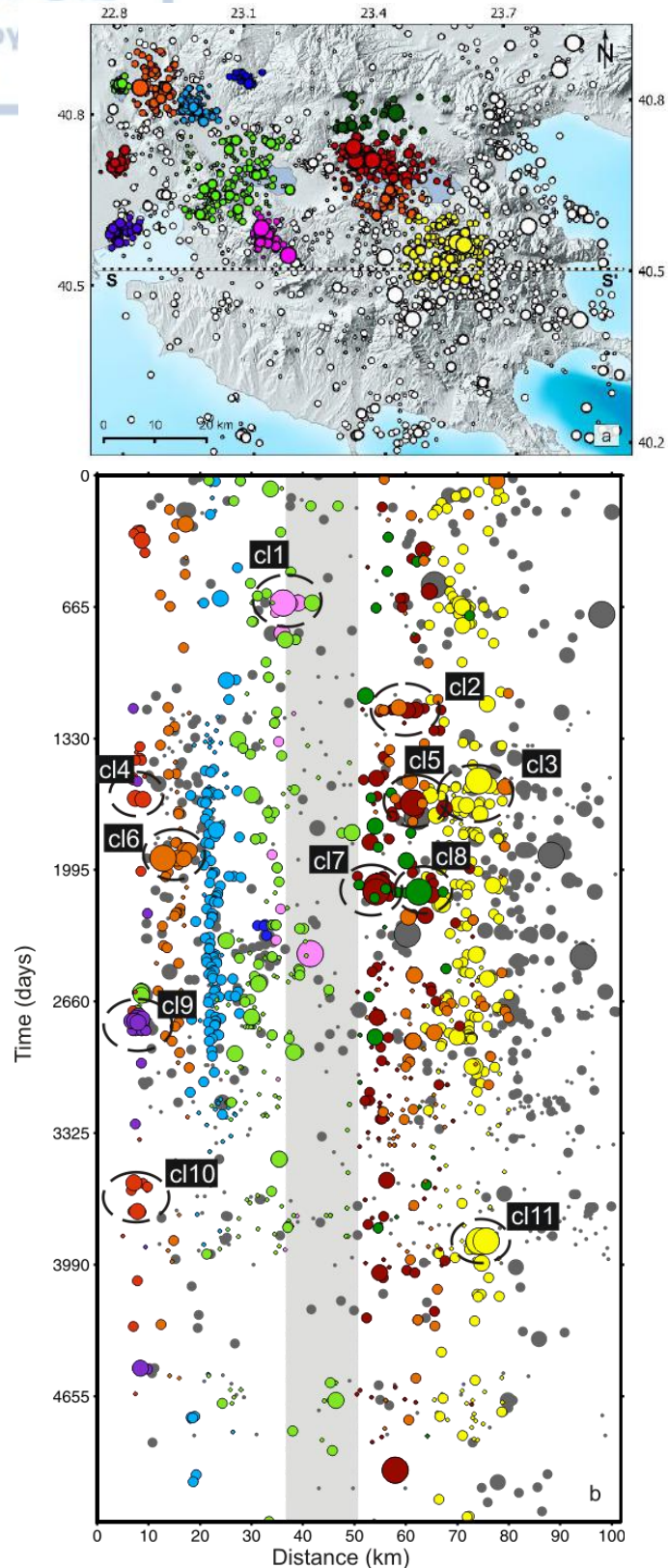


Figure 2-13 a) Spatial distribution of the relocated earthquakes. Different colors are used for a clear observation (The E-W SS' section is used for the space time plot). b) A spatial-temporal evolution plot along an E-W vertical plane, SS' , for the time period: 2000-2016. Characteristic clusters and earthquakes are enclosed in circles and they are described in the text.

In general, there is convincing evidence that triggering among fault segments is a mechanism taking place in the region of Mygdonia even if they are related to low magnitude earthquakes. The distribution of the events through time, evidences the existence of discrete prolonged earthquake bands from east to west. Parallel stripes of earthquake activity reveal a constant occurrence of a series of events around Lagadas, Volvi lakes and Arnea area. A characteristic band with scarce seismicity between Lagadas and Volvi Lakes is situated around the epicentral area of the 1978 event.

Furthermore a cluster analysis is performed with the employment of a magnitude independent space-time tool for earthquake clustering (Leptokaropoulos and Gkaraouni, 2016). This algorithm is developed in order to identify clusters, when seismicity is dense in terms of time and space compared to the background seismicity, without considering earthquake magnitudes. For a minimum number of events, a preliminary and final temporal criterion (maximum interevent time), as well as a spatial criterion (epicentral radius from the barycenter of the identified cluster) are set as inputs and constraints for the extraction of the clusters. The spatiotemporal criteria were set for a maximum interevent time between subsequent events, $Intt_{max}=3days$, maximum distance between earthquake epicentres and the cluster gravity centre, $x_{max}=8km$, for a minimum number of events, $n_{min}=10$ in each cluster and resulted in the detection of 10 seismic excitations (Table 2-3, Fig2-14). The duration of the extracted clusters lasts from 1 day to 34 days maximum in the case of the first cluster in 2001. In general, it is characteristic that in the region of Mygdonia, the duration of the clusters is short, up to 14-20 days maximum and they are comprised from a small number of events. Some of them are remote and some are swarm-like activities that occur in close distance like clusters n.5 (Fig2-14e) n.6 (Fig2-14f), n7 (Fig2-14g), which migrated along the area between Volvi lake and Sochos fault. It is characteristic that with the exception of the cluster n.9 (Fig2-14i) which is located to the west part of the study area, the other excitations dense in space and time seismic activities belong to the eastern part, around Volvi Lake.

Table 2-3. Table of the extracted clusters with the application of the spatiotemporal tool. Information is given on the number of the events, the duration of the seismic excitation and the maximum magnitude (M_{max}).

n	Date of the 1 st event	Number of events	Duration (in days)	Rank of M_{max}	M_{max}
n1	08.10.2001	34	3.49	5/34	4.1
n2	31.03.2003	20	4.87	13/20	3.3
n3	25.06.2004	15	23.10	3/15	4.0
n4	10.12.2004	8	2.63	5/8	2.8
n5	11.03.2005	11	2.83	6/11	3.4
n6	12.09.2005	8	0.29	2/8	4.8
n7	09.10.2005	14	3.84	4/14	4.0
n8	15.10.2007	12	8.45	8/12	2.6
n9	13.03.2010	8	5.81	1/8	3.2
n10	08.08.2010	20	4.36	1/20	4.5

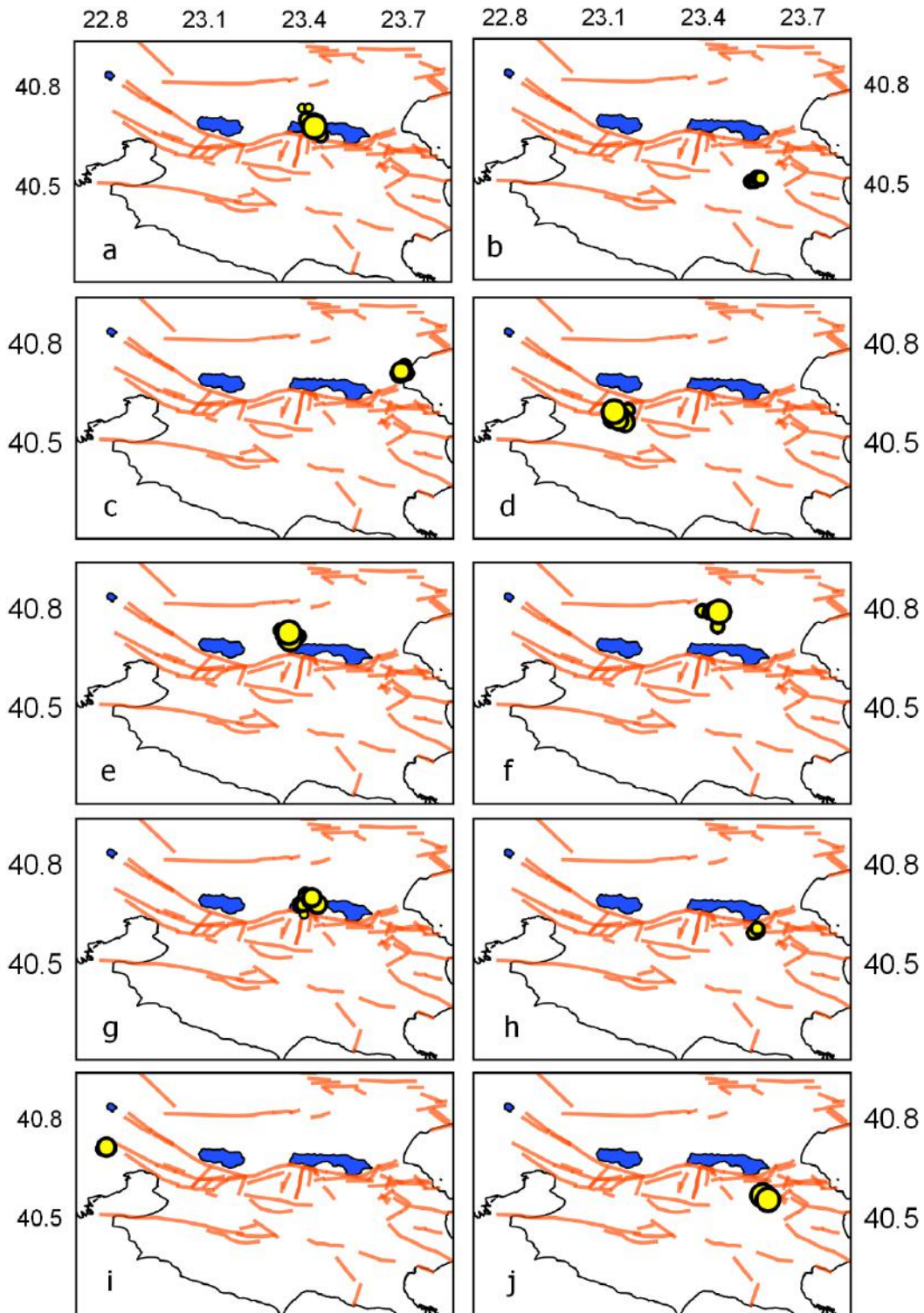


Figure 2-14. a-j) Epicentral distributions of numbered clusters n1 to n10 provided in Table 2-3, which are extracted with the use of spatiotemporal constraints for Mygdonia graben.

Relocated epicentres around Mygdonia graben are spatially analyzed for the extraction of seismicity characteristics and the possible relation of the events with their causative faults. For a more detailed inspection the study period is distinguished into the following four chronological intervals covering: i) early 2000 to July 2004, ii) July 2004 to June 2007, iii) June 2007 to June 2014 and finally iv) June 2014 to June 2016. The temporal division is simply based upon the visual inspection of seismicity on the spatiotemporal plot of the earthquake occurrence in the area (Fig.2-13b). The spatial distribution of the earthquake epicentres in chronological periods is illustrated in Fig.2-15. The contribution of the fault plane solutions is essential since they reveal the source properties and justify the interpretation of the seismotectonic setting by contributing to the identification of the responsible fault segments. Therefore, available fault plane solutions have been engaged and more information is provided in Table 2-4.

Table 2-4. A list of available fault plane solutions for small and moderate magnitude earthquakes in the time interval 2000 – 2016.

No.	Year	Time	Lat	Lon	M	Fault Plane 1			Fault Plane 2			Ref.
						ζ	dip	rake	ζ	dip	rake	
1	2001	10080450	40.59	23.15	4.5	70	34	-124	-	-	-	(1)
2	2001	10080526	40.59	23.12	4.1	74	42	-122	-	-	-	(1)
3	2003	10292115	40.58	22.76	4.5	244	46	-162	141	77	-46	(2)
4	2006	05100701	40.53	23.41	4.4	97	50	-68	-	-	-	(3)
5	2007	07181909	40.59	22.78	4.0	329	79	-31	66	60	-168	(3)
6	2010	08080900	40.56	23.58	4.4	249	54	-130	125	52	-48	(3)
7	2012	05122248	40.56	22.84	3.9	320	89	-1	50	89	-179	(3)
8	2013	10110515	40.59	23.38	4.2	287	54	-79	89	37	-105	(3)

1.Paradisopoulou et al. (2006), 2. EMSC , 3. AUTH

Figure 2-15a which corresponds to the first study period, shows that seismic activity is present around Chortiatis mountain (ChMt) where two moderate earthquakes (M4.5, M4.1, 2001.10.08) are observed. The epicentral distribution of the earthquakes corresponds to an E-W fault and they agree with the average strike derived from the fault plane solutions of shocks (N.1,2 of Table 2-4, Paradisopoulou et al., 2004) which represent a normal fault a with WNW- ESE trend ($\approx 119^\circ$) dipping with 50° to the north. The seismic activity has a short duration and no other seismic activity has struck this area ever since. In the absence of surface fault outcrops in the area, and since it occurs at the eastern termination of PPF, an association with a PPF extension to the east is has been assumed (Paradisopoulou et al., 2004). There is no more evidence in this study so as to argue this suggestion or not. Concentrations of earthquake epicenters are also met northwest than Lagadas lake and particularly at the western termination of SochF with a series of microearthquakes not exceeding M3.1. A small seismic burst is met around N. Anchialos in an NW-SE direction, also investigated in the past by Paradisopoulou et al. (2004). Two other important seismicity concentrations are observed in the eastern part of the study area, at the northwestern borders of Volvi lake and around Arnea, where a NNE-SSW trend for the epicenter concentration is visible. This area coincides with the epicentral zone of the 1995 Arnea event (Margaris and Hatzidimitriou, 1997). The fault plane solution proposed by a Harvard CMT

solution, corresponds to a fault with 260° strike, dipping with 47° to the north, characterized by a dextral strike slip component (rake=-132°).

In the second period (Fig.2-15b) seismicity is more diffuse and is mainly gathered northwest of Lagadas Lake where still there are several distinct clusters of events. There is not a characteristic trend, however in general the clusters show a NW-SE orientation. The majority of the earthquake epicentres are located between the LVF and SochF, at the northwest borders and the centre of Volvi lake where an activity is also detected after imposing the spatiotemporal constraints (Fig2.14e) as well as the burst southern than MF segment (Fig2.14f). Seismicity in Volvi area has additionally been discussed by Hatzfeld et al. (1986/1987). Moreover, there is a number of isolated moderate earthquakes with $M \geq 4.0$ and a group of events around Poligiros and Arnea. Seismic activity in this area is scarce and specific possible epicentre alignment for the justification of faults is not feasible. In general, this seismicity period appears to be the most active compared to the entire period of observations.

Seismicity in the following years, from 2007 to June 2014 (Fig.2-15c) decreases, but epicentres are distributed at approximately the same bands with the aforementioned period. There are clusters of microearthquake activity NW of Lagadas lake, in between the two lakes expressed by a minor excitation, NW of Volvi Lake as well as around Arnea. There is a seismic burst at the western margin of Thermaikos gulf where a small cluster is present with their epicentres NE-SW aligned, totally in agreement with a strike slip fault, parallel to Thermaikos gulf. In agreement with the available fault plane solutions, the seismic activity is attributed to a strike slip structure which is oblique to the faults extending into Thermaikos gulf (N.5 and N.7 of Table 2-4). The stronger seismicity is met at the area of Arnea where epicentres are spread in a NE-SW direction. The spatial distribution is in concordance with the fault plane solution for the strongest shock (N.6 of Table 2-4). The fault plane solution reveals a normal fault with a ENE-WSW azimuth with a dextral strike slip component (-130°). The epicentral distribution of the events around Volvi Lake lie in an approximately E-W trend and they are in agreement with the fault plane solution of the strongest event, which corresponds to an E-W normal fault (N.8 of Table 2-4). Small sized earthquake epicentres are also located close to the city of Thessaloniki, possibly following secondary faults in a N-S direction, highlighted also by Hatzidimitriou et al. (2001). The last two years, a number of 80 events have been recorded and they are not associated with a characteristic pattern (Fig.2-15d) with some of them exceeding $M 3.0$. There are some clustered events around Arnea showing the same epicentral distribution azimuth like the previous years but in general there is a quiescence seismicity period.

To sum up, it is observed that the spatial characteristics of earthquake distribution during the 16 years of observations reveal that there are identified similarities in epicentral concentration and clustering with the seismicity characteristics, described by previous researchers (Soufleris et al., 1982; Hatzfeld et al. 1986/1987). It is characteristic though, that there is a constant seismic activity in the area of Arnea with several epicentral trends with an absence of a clear trend as also observed for 1984 seismicity by Hatzfeld et al. (1986/1987).

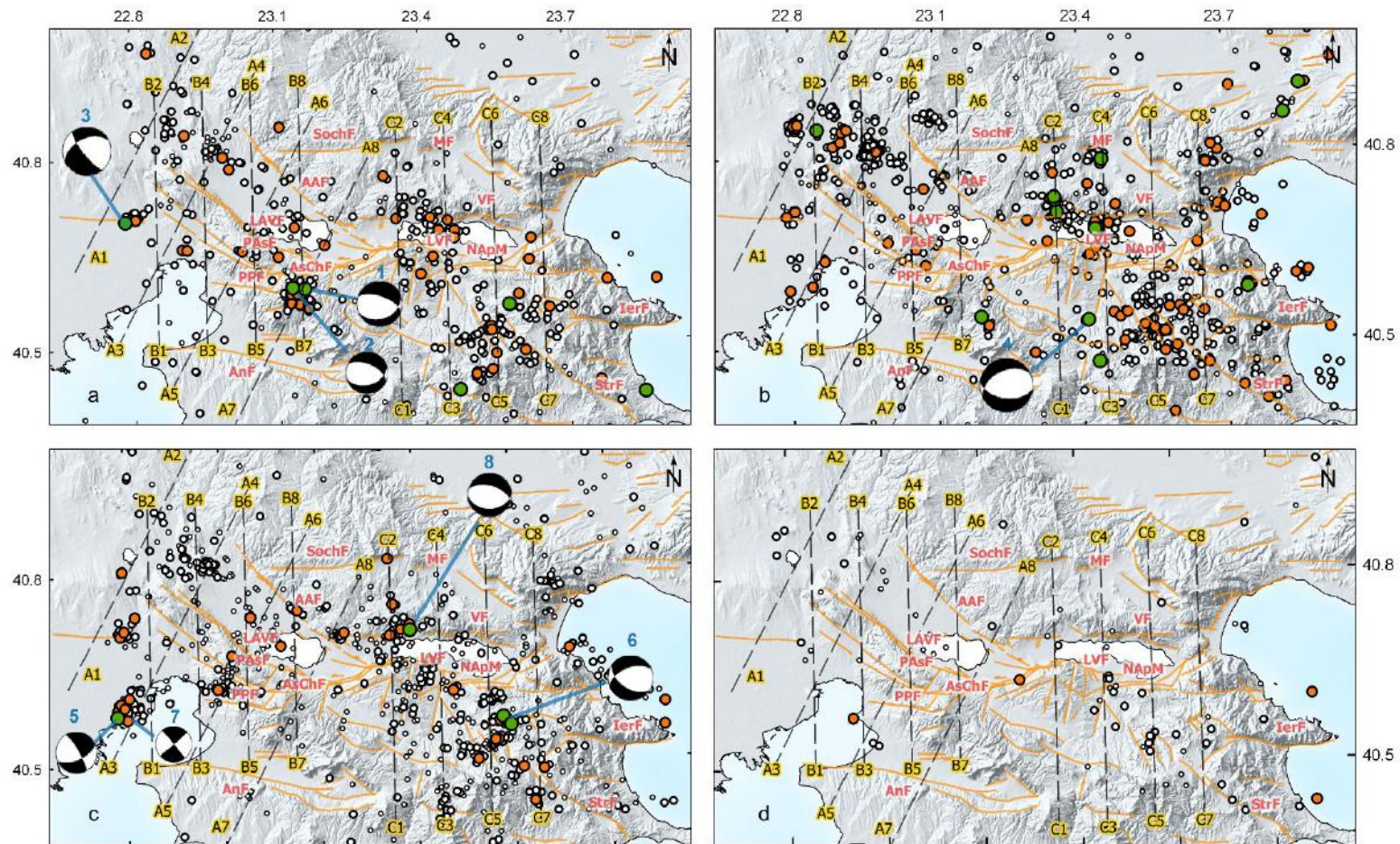


Figure 2-15 Relocated earthquake epicenters for 2000-2016 for different time intervals. Black dashed lines correspond to earthquake profiles, perpendicular and oblique to the main fault structures. Information on the fault plane solutions is shown in Table. a) earthquake epicenters for the interval 01.01.2000 – 27.03.2004, b) earthquake epicenters for the interval 27.03.2004 – 28.06.2007, c) earthquake epicenters for the interval 02.07.2007 – 10.12.2013 and d) 10.12.2013 to 06.2016

Nevertheless, the epicentral area of Stivos earthquake is deprived of seismic activity at the locations highlighted by Soufleris et al. (1982) a fact showing that the aftershock period has a rather small duration compared to other regions in the Aegean area.

Twelve successive cross sections perpendicular to the main faults are constructed for the investigation of foci association to the structures and their geometry at depth. The cross section azimuths are in accordance with the current stress field, thus, four of them are in a SW – NE direction (A_1A_2 , A_3A_4 , A_5A_6 , A_7A_8 , Fig.2-16) which is perpendicular to the general strike of the NE-SW fault that bound Lagadas sub basin. These profiles are oblique to the main E-W active faults, and perpendicular to the inherited fault network which shows a NW-SE direction. Other four S-N profiles (B_1B_2 , B_3B_4 , B_5B_6 , B_7B_8 , Fig.2-17) are normal to the most active E-W fault zones covering Lagadas fault systems, whereas, the last four South – North profiles (C_1C_2 , C_3C_4 , C_5C_6 , C_7C_8 , Fig.2-18) are normal to the most active E – W faults which extend to the eastern part of the study area (map view in Figure 2-15). Each cross section is defined with a 5km width either side, heading from south to north, whereas, the successive NE-SW sections are drawn from west to east.

Starting from west to east in Figure 2-16 a series of chronological cross sections are displayed, made in an NE-SW direction and normal to the NW-SE faults. A small cluster (in section A_1A_2) defines a fault zone that dips approximately 50° to the southeast reaching 10km in depth. This dip agrees with the fault plane solutions calculated by Paradisopoulou et al. (2004) and this zone can be associated with NAgF (Tranos et al., 2003). A swarm is found in front of the northern segment of LAVF with shallow depths and a steep dip to the north. A third swarm is observed with deeper depths up to 17km. If combined with the available fault plane solutions a zone of foci across a plane of approximately 60° dip to the southwest, is formed southern than the fault trace of AAFS. In the A_3A_4 cross section characteristic zones dipping at high angle (60°) to the south at lower depths (~ 20 km) are shown. The majority of the foci in this concentration is met around 5 and 20 km at depth. There are no characteristic fault plane solutions in the observational period, and cannot be attributed to specific fault zones. There is a high likelihood that they belong to northdipping faults in Lagadas area. A_5A_6 crosses the PPF system to the south and the SochF to the north and reveals that a rupture zone is formed up to 15km at depth, whereas a steep zone connected to SochF System. The distribution of the foci shows that both southdipping and northdipping faults seem to be activated and trigger seismicity. A_7A_8 occupies the eastern part of the section set and it crosses Chortiatis mountain to the south and SochF to the north. Through the years it seems that the majority of the foci is concentrated beyond the lakes (iii), as also seen in the section A_5A_6 .

In Figure 2-17 successive South to North profiles are constructed covering almost the same part of the fault system with the sections before but in a different angle. Although sections B_1B_2 , B_3B_4 B_5B_6 are not very representative for the NW-SE trending faults since they are positioned obliquely to them, the distribution of foci does not show an explicit differentiation at the dips of the fault planes. Section B_1B_2 reveals the existence of two seismic activations (ii and iii). A seismic

cluster is developed around 12km at depth, with the foci northern than LAVF. There is not a characteristic plane developed and the responsible fault can only be assumed. In section B₁B₂ (iii) a dense cluster is found at 10km depth. In section B₃B₄ there is a characteristic distribution of microearthquake foci which occurred within a short period of time in 2003. The fault plane is nearly vertical exhibiting a dip to the south, with foci ranging from 2-22km. The presence of fluids is considered in this case (Mesimeri et al., 2017). In section B₅B₆ seismic activity is concentrated north of PAsF. In this case the hypocentral depths range between 6-15km. A strong association of the foci with the northdipping PAsF is evident, since a northdipping fault plane (~50°) is formed. Section B₇B₈ shows that a minor excitation is presented probably attributed to the North dipping PPF, whereas earthquakes located to the north are distributed along the graben boundaries.

Figure 2-18 is useful for the at depth investigation of earthquakes around Volvi lake. Cross sections C₁C₂, C₃C₄ and C₅C₆ are normal to the E-W fault system, to the east of the fault population. Especially the earthquake foci which are projected onto C₁C₂ (ii) and C₃C₄ (ii) sections provide a robust interpretation of the responsible seismogenic faults, information that it was not clear in previous studies, since there was an absence of earthquakes during seismic experiments (Hatzfeld et al. 1986/1987; Paradisopoulou et al., 2006) or data were not enough to reach such a conclusion (Soufleris and Stewart, 1982). Volvi lake area seems more seismically active within the last years since there are plenty of epicenters distributed along the fault zones. The foci range between exhibits a southdipping plane which is associated with SochF and MF, which are evidently seismogenic. The synchronous appearance of the two seismic excitations show that there is an interaction between the two segments which are described by a stepping like fault morphology (Mountrakis et al., 1996a). A seismic plane steeply dipping to the south with 70° is characteristic. Earthquake hypocenters are mostly up to 18km at depth. In section C₃C₄ (ii) a seismic excitation delineate the fault plane dipping in 70°-80° to the south. The foci are located under Volvi Lake and they are probably attributed to SochF and MF rupture zones. The fault plane solution totally agrees with the foci geometry (89°/35°). Moving to the east, in sections C₅C₆ (i-iv) and C₇C₈ (i-iv) there are no earthquake foci northern than Volvi lake however the earthquake concentration to the south of Volvi Lake, is not able to provide clear evidence about the geometry of faults at depth and the association of the foci with faults owing a surface exposure. Arnea area is seismically active, also highlighted by Hatzfeld et al. (1986/1987) who ascertain that the seismic activity in this region has increased since Stivos event. Alternatively cross sections are made in a NW-SE direction and fault plane solutions analyzed by Hatzfeld et al. (1986/1987) have been used for the interpretation of the seismogenic pattern in the area. In this area Hatzfeld et al. (1986/1987) observed three clusters of earthquakes trending NW-SE. This is probably attributed to the activation of subsidiary faults with orientation other than E-W, so that the seismicity pattern seems to be more diffuse rather than distributed around known important faults.

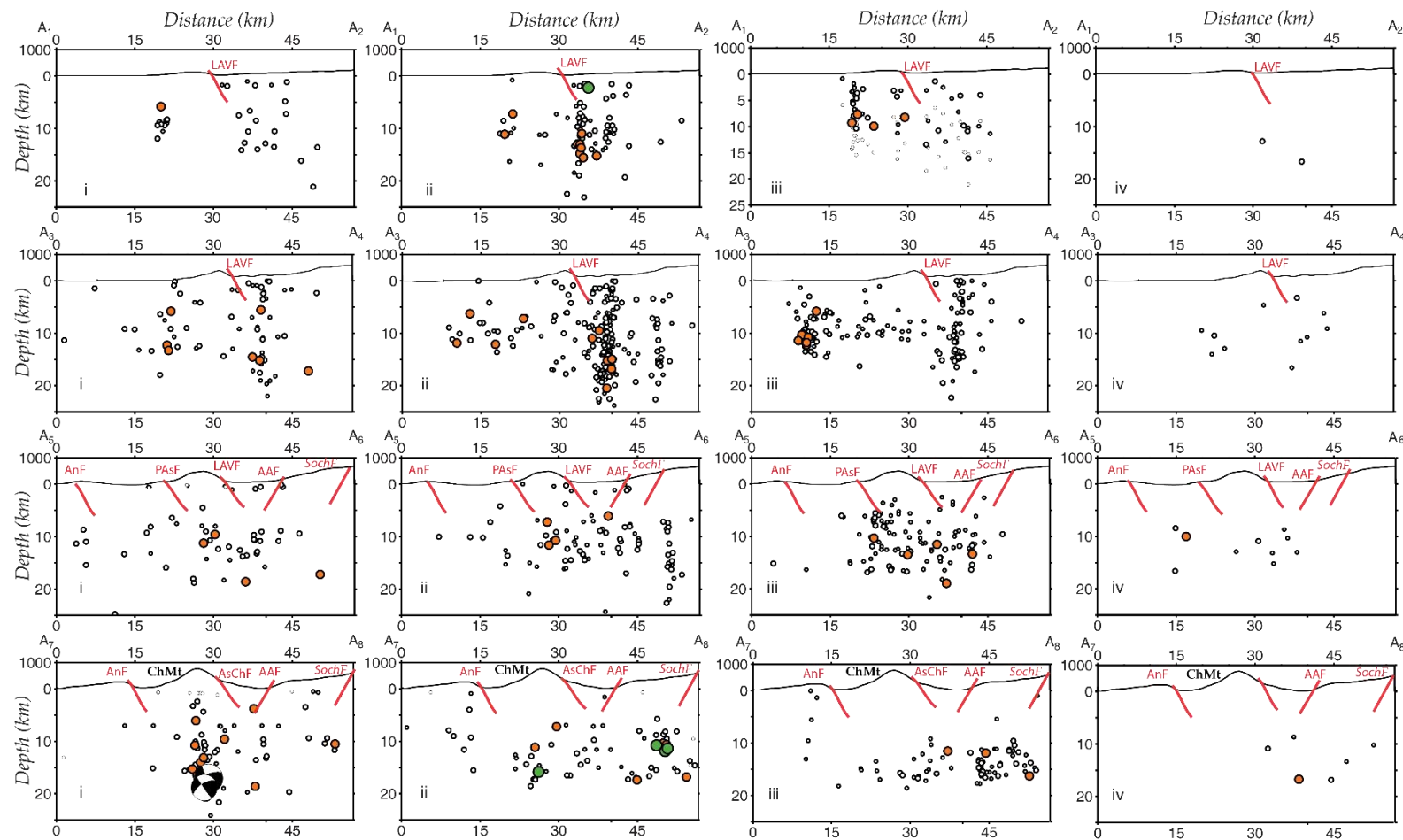


Figure 2-16 The set of cross sections, oriented perpendicular to LAV fault array (A₁A₂, A₃A₄, A₅A₆, A₇A₈) with the corresponding geomorphological profile. Relocated earthquake epicenters for 2000-2016 for different time intervals (i-iv). Colors for different earthquake magnitudes are the same as in the map view.

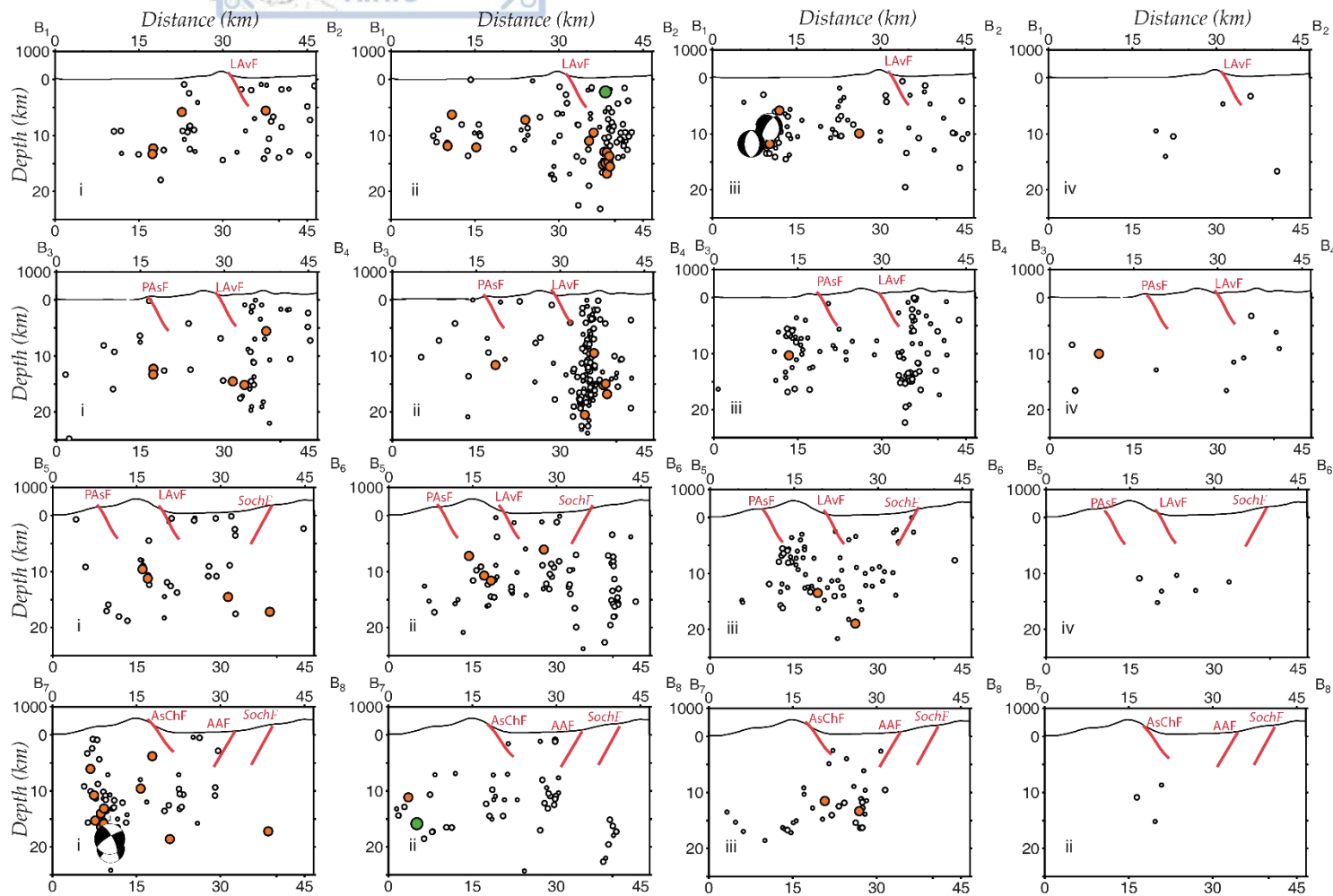


Figure 2-17 The set of N-S oriented cross sections, perpendicular to the GTFZ fault array (B₁B₂, B₃B₄, B₅B₆, B₇B₈,) with the corresponding geomorphological profile. Relocated earthquake epicenters for 2000-2016 are shown for different time intervals (i-iv). Colors for different earthquake magnitudes are the same as in the map view.

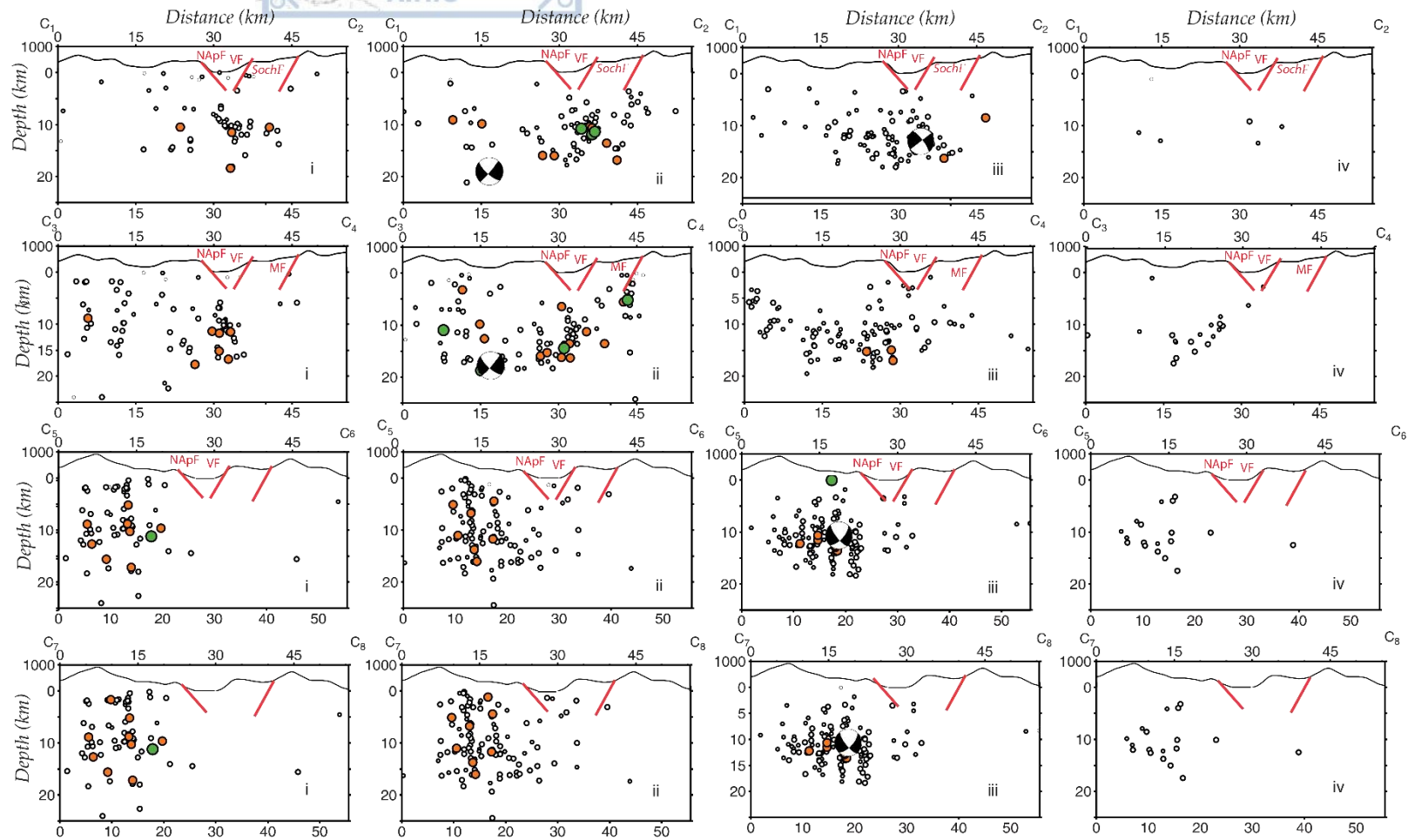


Figure 2-18 The set of cross sections, perpendicular to Volvi fault arrays (C_1C_2 , C_3C_4 , C_5C_6 , C_7C_8), with the corresponding geomorphological profile. Relocated earthquake epicenters for 2000-2016 for different time intervals (i-iv). Colors for different earthquake magnitudes are the same as in the map view.

The relocated earthquake catalog after the application of Hypoinverse algorithm is used as an input to the advanced HypoDD algorithm for obtaining more precise focal parameters for the earthquakes. The final number of events in the second case becomes considerably smaller but earthquakes are more densely distributed, shaping more accurately the fault geometry. The application of the earthquake relocation is restricted to seven well defined areas where events are already characterized with dense clustering. Results with the lowest possible uncertainties formed a relocated catalog of these areas. Figure 2-19 shows the spatial distribution of the relocated earthquakes enclosed in rectangular areas (boxes s1 to s7). Subplots below show the foci distribution of the earthquake concentrations along the sections from North to South (marked with a black line in the map).

For the clusters s1 and s2 the relocation results does not change considerably the cluster geometry. Earthquakes in subset s1 form a rupture zone up to the depth of 11km, dipping to the SE. The same depth range is observed in the s2 subset where the fault plane is dipping to the SE with 50°. This geometry coincides with the strike slip fault geometry proposed from the fault plane solutions. In s3 the seismicity between LAVF and AAF were further analyzed. The cross section shows a different foci distribution than the one obtained from the Hypoinverse algorithm (Fig.2-16, ii). Two seismic clusters are observed at depth, however there is no clear trend showing the dip of the causative fault plane. Considering the cross section s4, foci in both cases are developing zones dipping in high angles at depth.

Cluster in s5 maintains the same hypocentral properties even after the relocation process and it is characterized by the deepest foci in the entire area. There is no characteristic trend about the fault dip. In s6 rectangular area more precise important differentiations are revealed at the spatial distribution of epicenters around Volvi Lake. There is a visible gradual dipping of Sochos fault to the south, whereas now it is more evident that the seismic activity in red is associated with the northdipping normal faults (NAPF). Epicentres in orange color more clearly delineate a NNE-SSW fault zone. Subplot s7 presents the earthquake foci distribution around Arnea which is significantly improved and there is a clear indication of a fault plane dipping with 40° to the NW. The majority of the foci range between 8km and 15km, whereas s secondary fault parallel to the main rupture is formed in the front of the dipping zone. The foci distribution is also enhanced due to the fact that the profile is taken in an azimuth perpendicular to the strike of the rupture zone, as justified by the epicentres location and the available fault plane solutions.

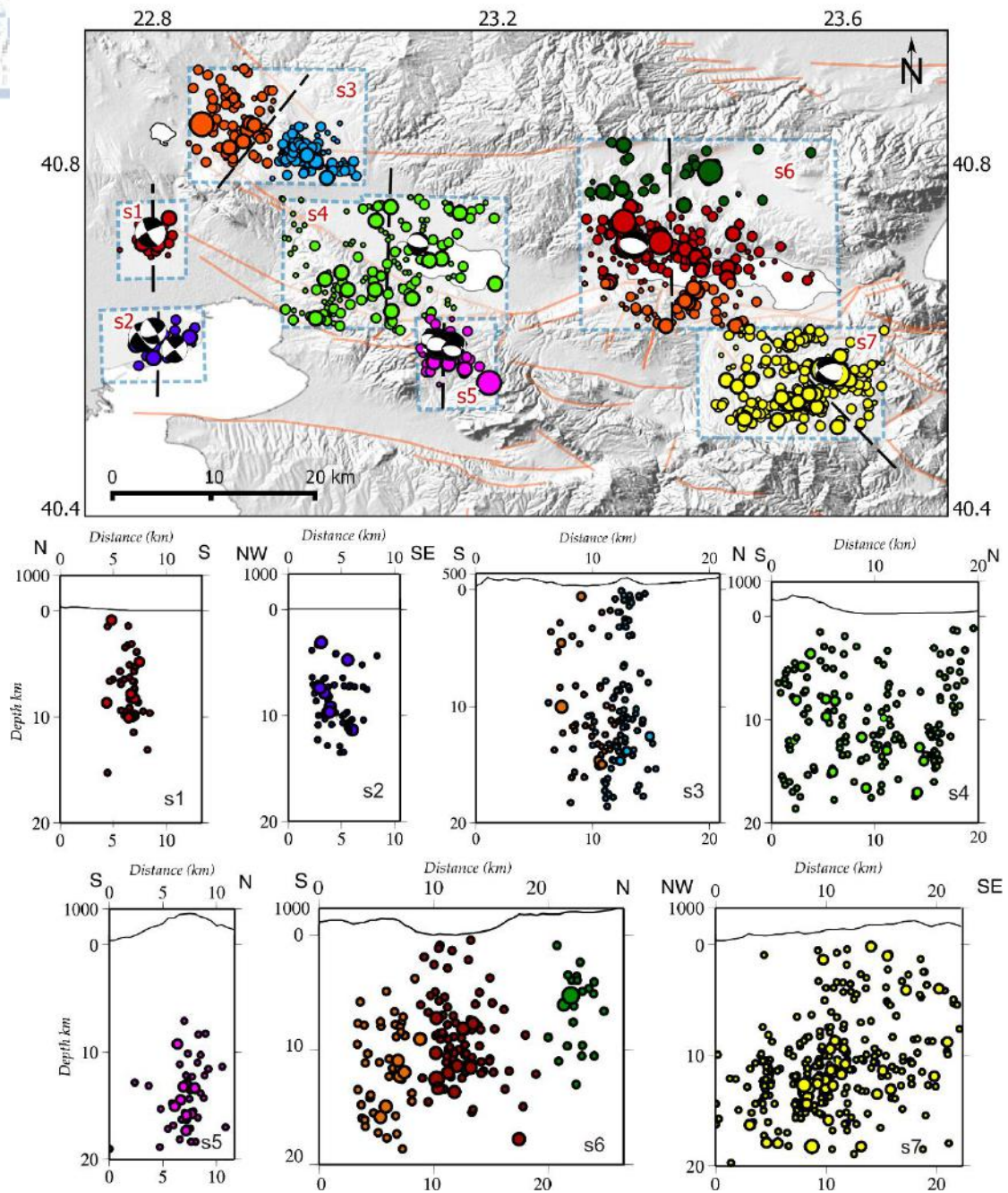


Figure 2-19. Map with the spatial distribution of epicentres in the enclosed regions and cross sections for the focal coordinates estimated with the hypoDD algorithm.

2.9 Earthquake Relocation Results for Corinth Rift

2.9.1 Introduction

The area of the Corinth rift is a broader area compared to Mygdonia graben and also more heterogeneous in the sense of the known seismicity pattern, the seismotectonic and geodetic information. Therefore, for the purposes of this study the whole area was divided into smaller zones for a more accurate approach in the seismotectonic analysis and a better understanding of the results. Six rectangular subareas were defined for assuring as much as possible homogeneity in crustal structure, during the relocation process were drawn. The scope is also to minimize the effect of the crust's heterogeneity caused by the geological interference and for reaching good earthquake locations. The division is based upon the observation of the earthquake epicenter distribution and the development of the fault segments in a consistent way with the measured strain rates, which diminish from west to east, across the area of the Corinth rift. From the western to the eastern part the subareas named by some of the characteristic locations they include, are the following: a) A₁, Mesologi area, b) A₂, Efpalio area, c) A₃, Kato Achaia area, d) A₄, Kalavrita area, e) A₅, Xylocastro area and f) A₆, Alkyonides area, all depicted with the six red rectangular boxes and their names in Figure 2-24 below.

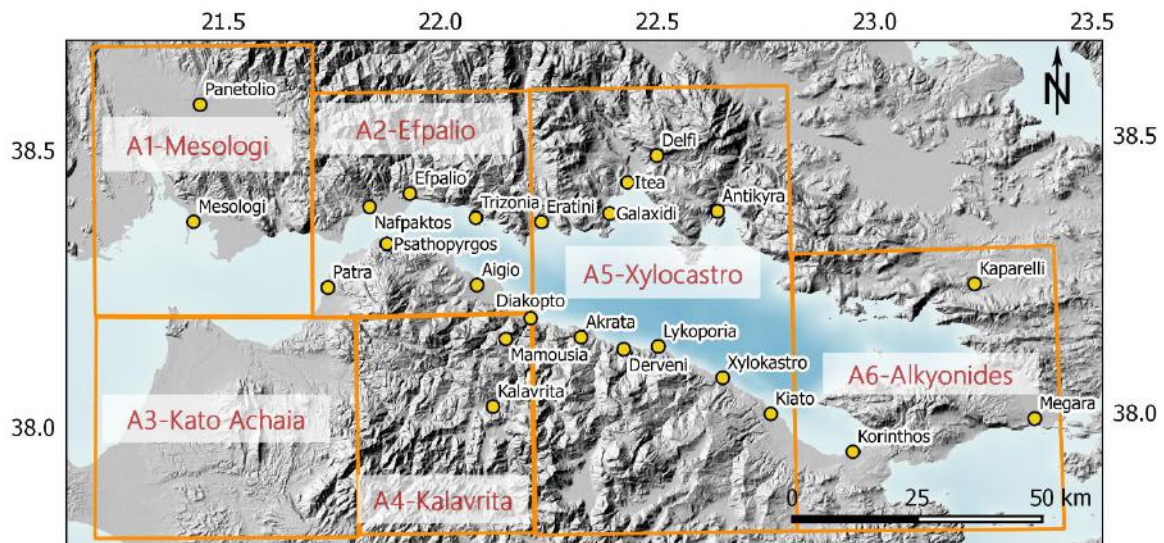


Figure 2-24 Sub areas to which Corinth rift was divided, enclosed in rectangles and they are named accordingly, along with some characteristic locations in each sub area.

The western part of the study area (A₁ zone) includes the offshore part of Patras gulf, the northern coasts of Patras gulf and the area from Mesologi to the mountainous region where Panetoliko is located, also enclosing Trichonis valley (Fig. 1-5). To the east, the A₂ rectangular area encompasses the region from Patra up to Diakopto village to the east and extends to the mountainous area northern than Efpalio, named also by the later. Although it covers the smallest area, it is profoundly the most seismogenic one, including the most recent 2008 Efpalio sequence. To the south of Mesologi and Efpalio areas the Kato Achaia area (A₃ rectangle) is expanded over the NW Peloponnese. To the east of A₃ a mountainous area around and including the village of Kalavrita,

a region with sparse seismicity is met (A₄ rectangle). To the east the A₅ Xylocastro area, expands to include the south and north margins of the central Corinth rift, including the northern coasts of Peloponnese up to Delphi ancient city. The eastern termination of the study area is enclosed in rectangle A₆ which forms the two sub basins forming Alkyonides and Lechaion gulf, a part of Megara basin and the southern margin of Thebes basin (Fig. 1-1).

2.9.2 Data

P and S phases of body wave arrivals for earthquakes recorded from the Hellenic Unified Seismological network (HUSN) were obtained from the available bulletin of AUTH seismological station and concern the entire study area bounded by 21.00°-23.40° meridians and 37.90°-38.70° parallels for the time interval between January 2008 and June 2014. The bar plots in Figure 2-25 the number of earthquake phase arrivals per year available for each subarea (plotted in white bars). In total, 2288 pairs of seismic phases were collected during this time with magnitudes not exceeding M5.4. As explained in *Methodology*, in order to apply the Wadati technique a set of the most sufficient and high quality earthquake recordings were distinguished and taken into consideration. These earthquakes correspond to the optimum earthquake data set for the Corinth rift and fulfill the following fundamental requirements: i) they consist of earthquakes recorded between August 2008 and June 2014, ii) they are described by a satisfying number of recordings ($n \geq 10$) and iii) they are preferably recorded by 21 seismological stations of the permanent network which are installed in a relatively short epicentral distance (<250km) from the geographical center of the study area. Seismic phases which belong to the optimum data set are also shown in Figure 2-25 along with the rest of the data, they are plotted in separate bar plots for each sub area and they are denoted in blue color.

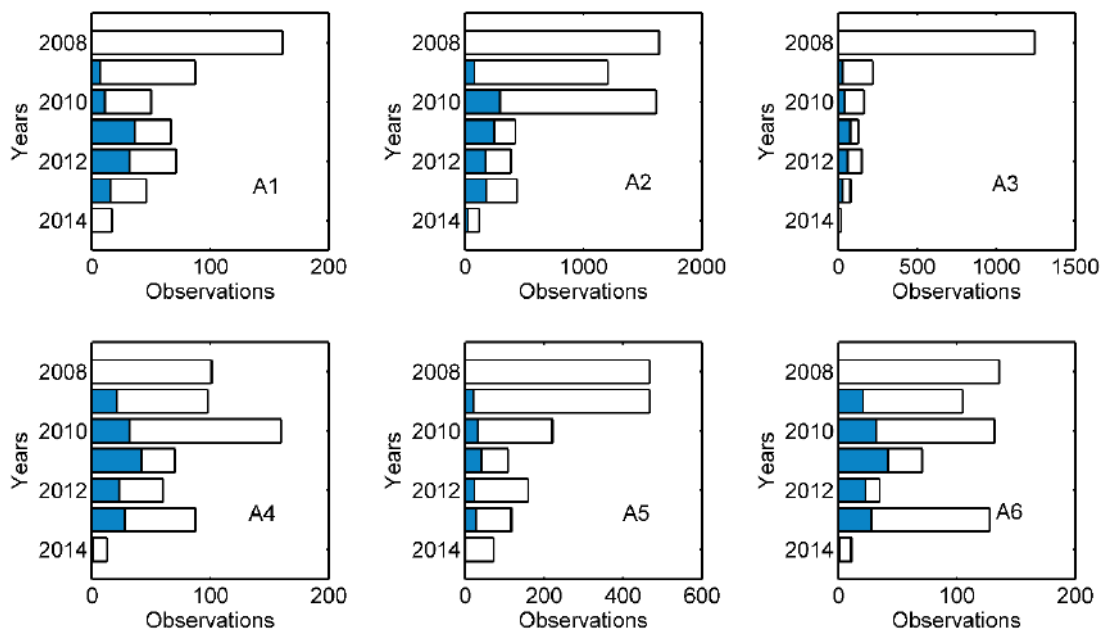


Figure 2-25 Cumulative number of seismic phases for each subarea according to the bulletin of the seismological station of AUTH. Blue shaded bars correspond to the number of observations which belong to the optimum earthquake data set and were used as an input in the Wadati procedure.

The seismological stations which were used for the relocation process in Corinth rift belong to the HUSN permanent network and they exhibit a satisfying coverage over the study area. They are installed in a distance not greater than 250km from the central Corinth rift and their locations are presented in Figure 2-26.

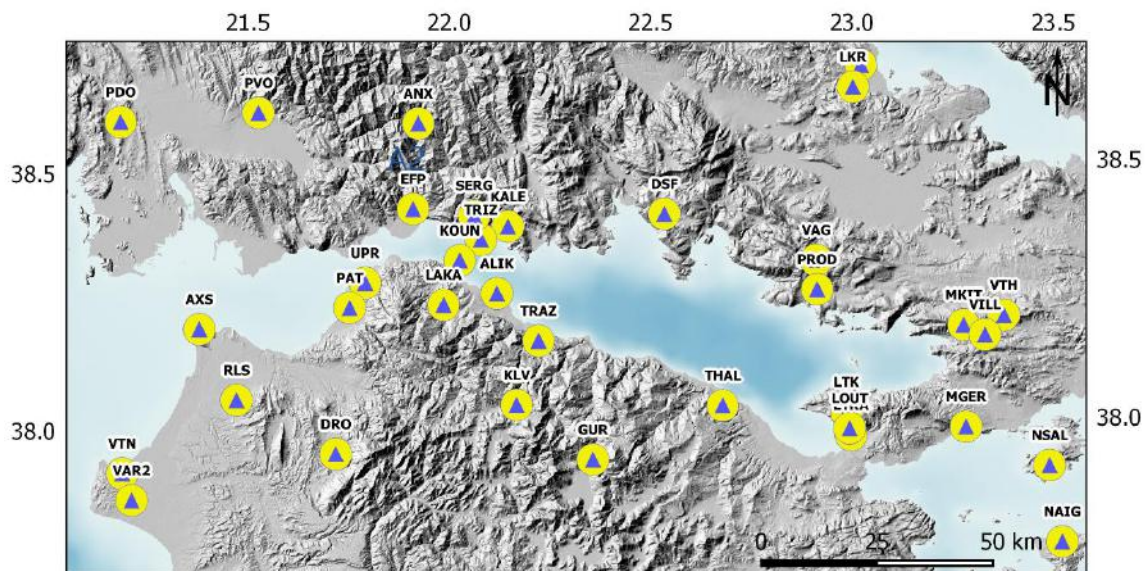


Figure 2-26 Map of the Corinth rift in central Greece with the seismological stations which are operated by HUSN and employed for data reprocessing using the methodologies for Wadati and station time delays.

2.9.3 Velocity Model

A significant number of studies for the investigation of the properties of the seismic waves velocity in Corinth rift have been accomplished, as previously described in paragraph 2.4. The models which describe the crustal properties of the chosen subareas in the Corinth rift and fit to the purpose of our studies were chosen among all. The velocity model proposed by Novotny et al. (2008) was suitable for Efpalio (A_2), Xylocastro (A_5) and Alkyonides (A_6) area, whereas the velocity model suggested by Haslinger et al. (1999) was proved to be the most suitable for Mesologi (A_1), Kato Achaia (A_3) and Kalavrita (A_4) area. Detailed information on the vertical distribution of the P velocity along with the thickness of each layer is described in Table 2-5.

Table 2-5. Information about velocities and depths for the adopted velocity models in Corinth rift proposed by Haslinger et al. (2002) and Novotny et al (2008).

Haslinger et al. (1999)		Novotny et. al. (2008)	
V_p (km/sec)	Depth (km)	V_p (km/sec)	Depth (km)
5.47	0	5.36	0.0
5.50	2.0	5.37	3.55
6.00	5.0	5.59	6.65
6.20	10.0	5.97	8.02
		6.30	10.22
		6.50	15.0
		7.00	31.0
		8.00	40.0

For comparison, preliminary earthquake locations in Corinth rift were calculated by using the velocity model proposed by Panagiotopoulos et al. (1985) which was also used in the previous study area.

2.9.4 Wadati Plots

The optimum earthquake data set defined for each area in Corinth rift, was used for the estimation of the velocity ratios for the seismic waves. In each area Wadati plots were constructed and the mean velocity ratio was extracted from the ratios of pairs of arrival times for the seismic phases which belong to the optimum earthquake data set. Results are presented with the help of histograms and cumulative Wadati diagrams where the time difference DT between T_P and T_S is plotted against T_P for all available pairs of observations in each area (Fig.2.27 to Fig.2-32). Figure 2-27a shows the velocity ratios histogram for a number of 102 earthquakes with more than 8 recorded pairs of P and S seismic arrivals in Mesologi area (A_1). The velocity ratios range between $V_P/V_S=1.62$ and $V_P/V_S=2.07$ whereas the average velocity ratio is equal to 1.81 ± 0.07 , with a 95% confidence interval. The linear fit between DT and T_P-H seems to be more accurate in the lower values of DT where there is an abundance of data, but all observations lie within the standard deviation, therefore no observations were excluded from the station delays calculations (Fig. 2-27b). To the east, in the Efpalio area (A_2) the velocity ratios for 991 earthquakes with more than 10 recordings for each earthquake range between 1.57 and 2.30 and the values show a Gaussian distribution (Figure 2-28a). The average V_P/V_S is 1.78 ± 0.06 with a 95% confidence interval is significantly smaller than the one calculated for Mesologi area and is evident that some observations lie below the standard deviation (Fig. 2-28b). Figure 2-29 shows that for the Kato Achaia area (A_3), the velocity ratios, V_P/V_S for 231 observations range between 1.60 and 2.09 with the mean ratio is 1.81 with a 95% confidence interval exhibiting the same average velocity ratio with Mesologi area to the North, but higher than Efpalio area.

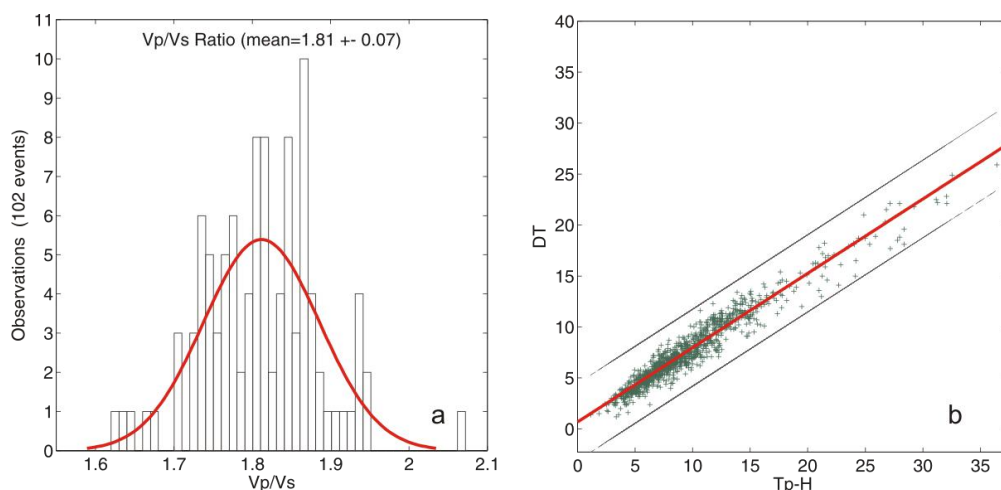


Figure 2-27 a) Histogram for 102 velocity ratios in A_1 Mesologi area, where red thick line simulate the Gaussian distribution, b) cumulative Wadati diagram indicating the linear fit (red line) between pairs of DT and T_P-H . Grey lines show the 95% standard deviation from the mean value (mean $V_P/V_S=1.81\pm 0.07$).

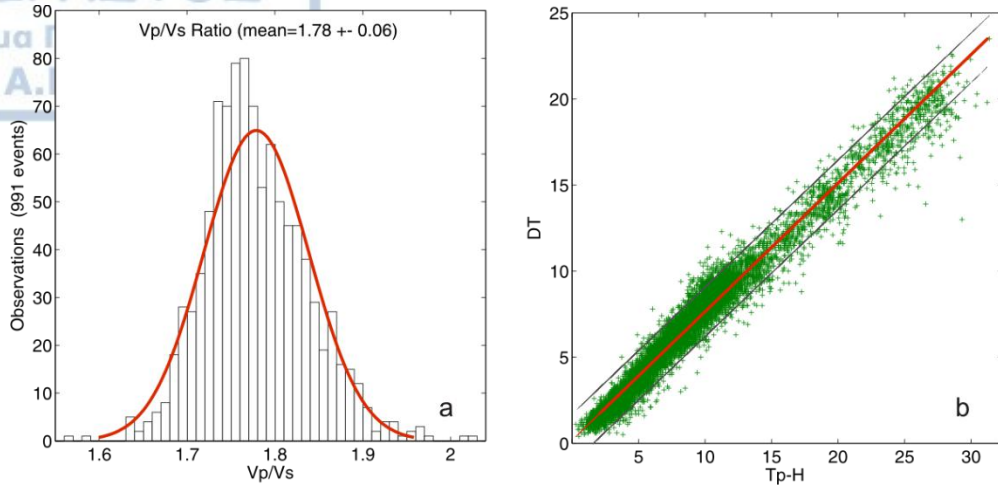


Figure 2-28 a) Histogram for 991 velocity ratios in A₂ Efpalio area, b) cumulative Wadati diagram between pairs of DT and T_{P-H}, (mean V_P/V_S=1.78±0.06) (same as Fig. 2-27).

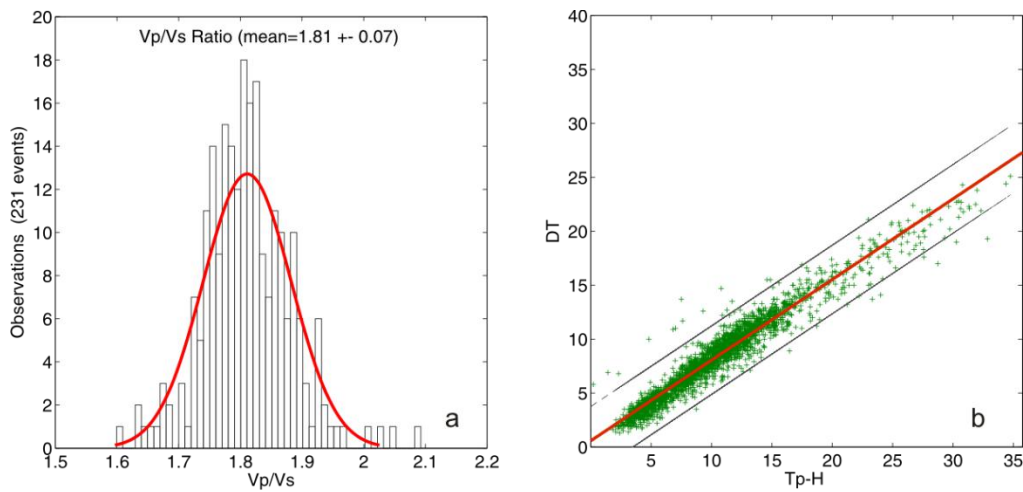


Figure 2-29 a) Histogram for 231 velocity ratios in A₃ Kato Achaia area, b) cumulative Wadati diagram between pairs of DT and T_{P-H}, (mean V_P/V_S=1.81±0.07) (same as Fig. 2-27).

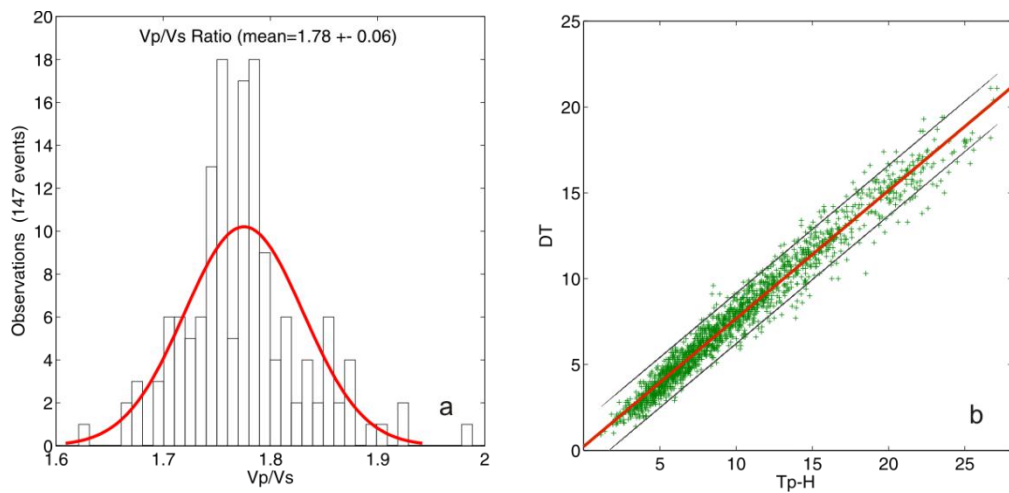


Figure 2-30 a) Histogram for 147 velocity ratios in A₄ Kalavrita area b) cumulative Wadati diagram between pairs of DT and T_{P-H}, (mean V_P/V_S=1.78±0.06) (same as Fig. 2-27).

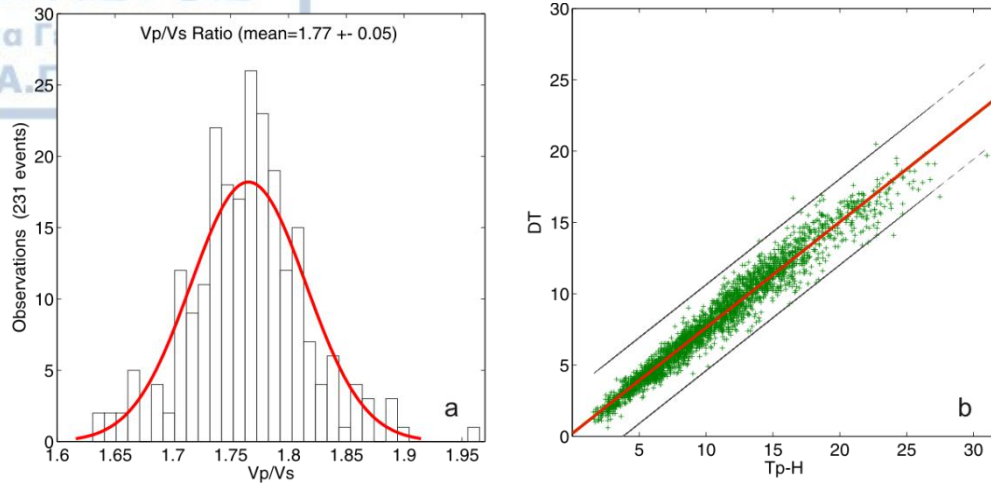


Figure 2-31 a) Histogram for 231 velocity ratios in A₅ Xylocastro area b) cumulative Wadati diagram between pairs of DT and T_p-H, (mean V_p/V_s=1.77±0.05) (same as Fig. 2-27).

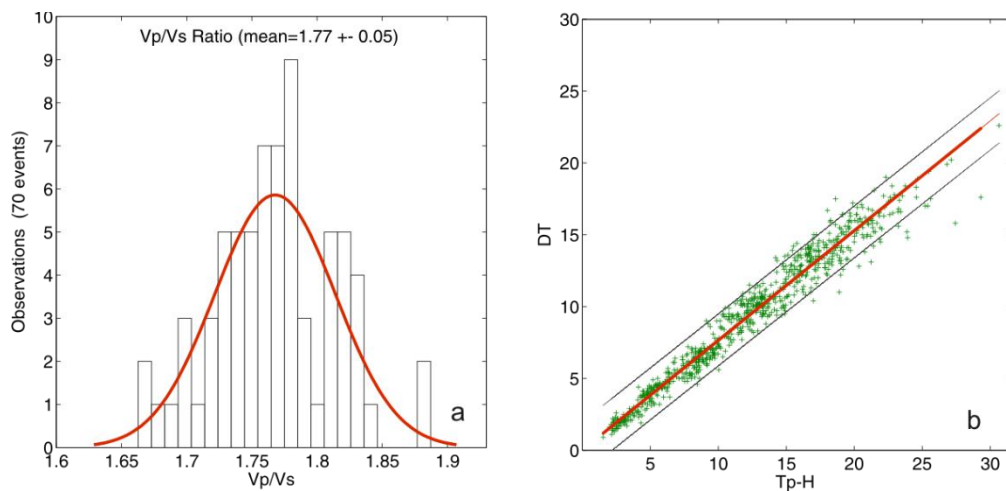


Figure 2-32 a) Histogram for 70 velocity ratios in A₆ Alkyonides area b) cumulative Wadati diagram between pairs of DT and T_p-H, (mean V_p/V_s=1.77±0.05) (same as Fig. 2-27).

Figure 2.30 depict the V_p/V_s ratio in Kalavrita area (A₄), for 147 earthquakes with ratios varying from 1.62 to 1.99 and average value equal to 1.78±0.06, which is equal to the one estimated in Efpalio area, to the North. The histogram of Figure 2.31a for Xylocastro (A₅) area shows that the velocity ratio takes values between 1.63 and 2.00, while the mean velocity ratio value is found equal to 1.77±0.05 for earthquakes recorded with more than 10 P and S wave pairs and almost all observations follow the linear fit within the standard deviation (Fig. 2-31b). Alkyonides area (A₆) to the eastern end of the Corinth rift exhibits the same average velocity ratio with Xylocastro area (1.77±0.05), calculated out of 70 earthquakes which fulfilled the requirements for the optimum earthquake data sets (Figure 2.32). Results from the Wadati diagrams are found in accordance with other studies accomplished in the region like V_p/V_s=1.83 for the area around Alkyonides gulf (King et al., 1985), 1.70-1.77 (Hatzfeld et al., 1990) or 1.77-1.83 (Melis et al., 1989; Amorese, 1993). Rigo et al. (1996) found a velocity ratio from Wadati diagrams, V_p/V_s=1.80±0.02, for the western Corinth gulf around area A₂, whereas Karakostas et al. (2012) who determined a velocity

ratio equal to 1.81 for recent seismicity. Velocity ratio is equal to $V_p/V_s=1.85$ to the NW of the study area according to Haslinger et al (1999).

Average velocity ratios in the study area range from 1.77 to 1.81 across Corinth rift with increasing values from the eastern to the western part. Velocity ratios were investigated, searching for variations in the crustal structure, beneath Corinth rift. The values of the velocity ratios which were calculated from seismic wave recordings show a slight increase from the eastern to the western part of the gulf (Fig. 2-33). This variation is probably attributed to the differentiation of the crust rheology across the Corinth rift. This observation is in accordance with previous researchers who also considered the spatial heterogeneity of V_p/V_s (Pacchiani and Lyon Caen, 2010; Karakostas et al., 2012). A three dimensional analysis has also shown a considerable velocity ratio variation at depth, a fact that also evidences the complexity of the crustal structures in Corinth rift (Lattore et al., 2004).

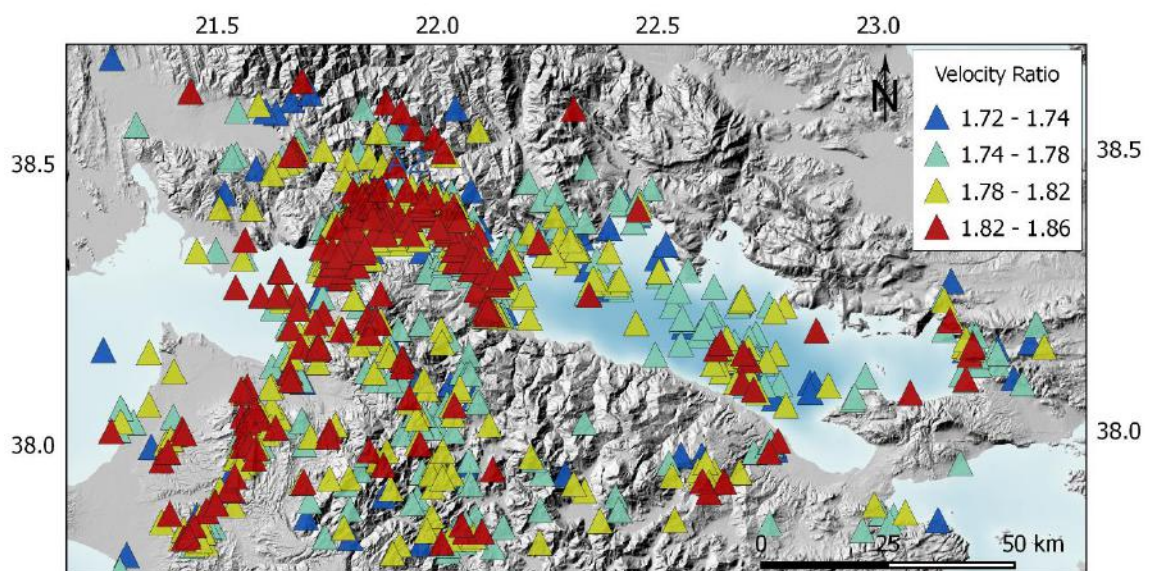


Figure 2-33 Map with the spatial distribution of the color coded velocity ratios across the Corinth rift for the optimum set of earthquakes, where high values are indicated with the red color and lower values with blue color.

2.9.5 Station Time Corrections

Station time correction were calculated individually for the seismological stations, which are found in a relatively short distance around the sub areas (<200km). The corrections were calculated for each station independently and they are the differences between the theoretical and the observed travel times. The iterative procedure for their calculation stopped when the majority of the time correction is smaller than 1sec, after which changes in time are insignificant and does not affect the earthquake focal coordinates. The scatter plot in Figure 2.34 shows the range of the station time delays (in sec) for the common seismological stations which were used in this procedure. Station values are plotted with different markers for the separate parts of the Corinth Rift. The majority of the corrections range between -0.6sec to 1.5 sec (information about

the seismological stations and their corresponding corrections is given in Tables A1.1 to A1.5 of the Appendix I).

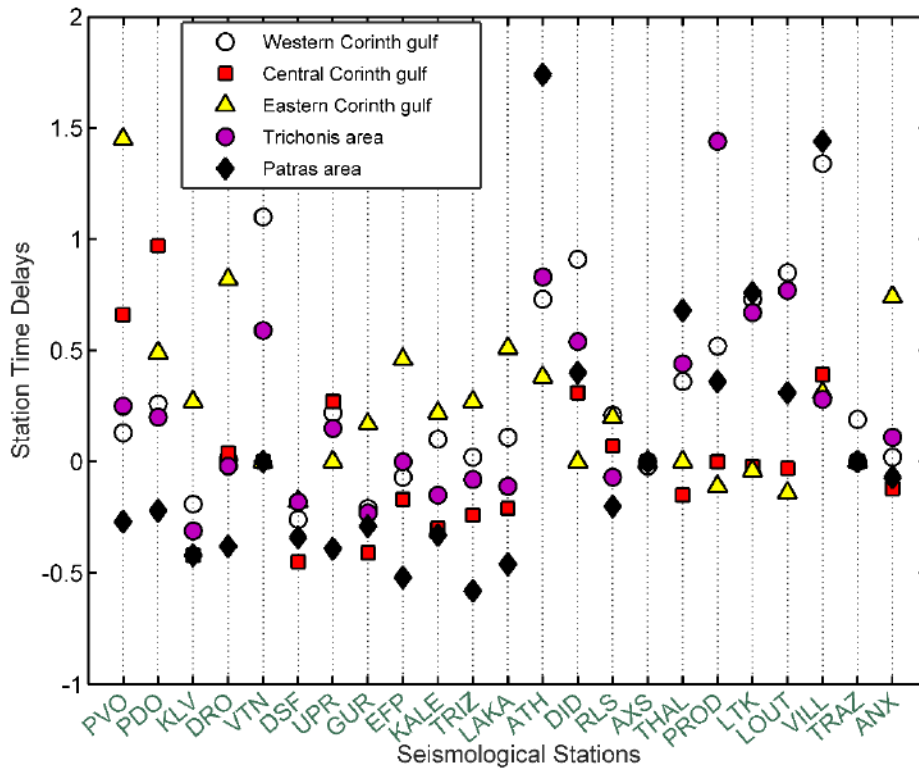


Figure 2-34. Station time delays (in sec) for all the study sub areas with the use of different symbols.

2.9.6 Relocation Process and Implications for the width of the seismogenic layer

Preliminary earthquake locations for Corinth rift were firstly computed with the use of the regional velocity model (Panagiotopoulos et al. 1985) and secondly with the incorporation of the preferred regional model for P waves, comprised of the station delays which were calculated in each case, the velocity ratio V_p/V_s and the preferred crustal model. The two data catalogs described by the preliminary and final results were compared to each other in terms of the quality parameters calculated by the Hypoinverse algorithm. In comparative histograms, the root mean square for the origin time (Rmse), the mean horizontal error (Erh) and the mean vertical error (Erz) are presented for the optimum sets of data in each region (diagrams in the first row correspond to the preliminary results whereas, data at the second row refer to results after the relocation process with the Hypoinverse algorithm). The foci distribution is also studied so as to acquire information about the width of the seismogenic layer in each case (in the first column depths before the relocation process are plotted and at the second there are the depths after the relocation process). Examining the study areas from west to east, relocation quality parameters for Mesologi area are displayed in Figure 2-35, where it is shown that there is not significant change in the estimation of the parameters (rmse, erh and erz) after the incorporation of the station delays. The 95% of the earthquake foci are distributed at large depths, between 12km and 32km (Fig2.35h). In the area of Kato Achaia and Kalavryta who were examined together average

hypoinverse results are shown in Figure 2- 36. Depths for the optimal set in this area range from 5km to 25km (Fig2.36h). An improvement is also expected at Efpalio zone (Fig.2-37). The depth distribution shows that the average depth is the lowest met in the entire Corinth rift, with the bulk of the earthquakes which belong to the optimum set of earthquakes ranging from 7.0 to 13km. In the central part of the rift, Xylocastro zone (Fig.2-38) there are significant modifications for the parameters, average uncertainties are kept similar but the depth distribution has been shifted to largest depths. In the case of Alkyonides zone (Fig.2-39) there is an indication for important improvement for the mean estimated error in origin time and the mean horizontal error after the incorporation of station delays within the relocation algorithm. Moving to the eastern part of the rift, comparative Hypoinverse histograms for the epicentral error with the use of station delays are improved in relation to the results without time corrections. Additionally the distribution of foci at depth varies in the second case and it seems that foci results exhibit a preference to higher depths.

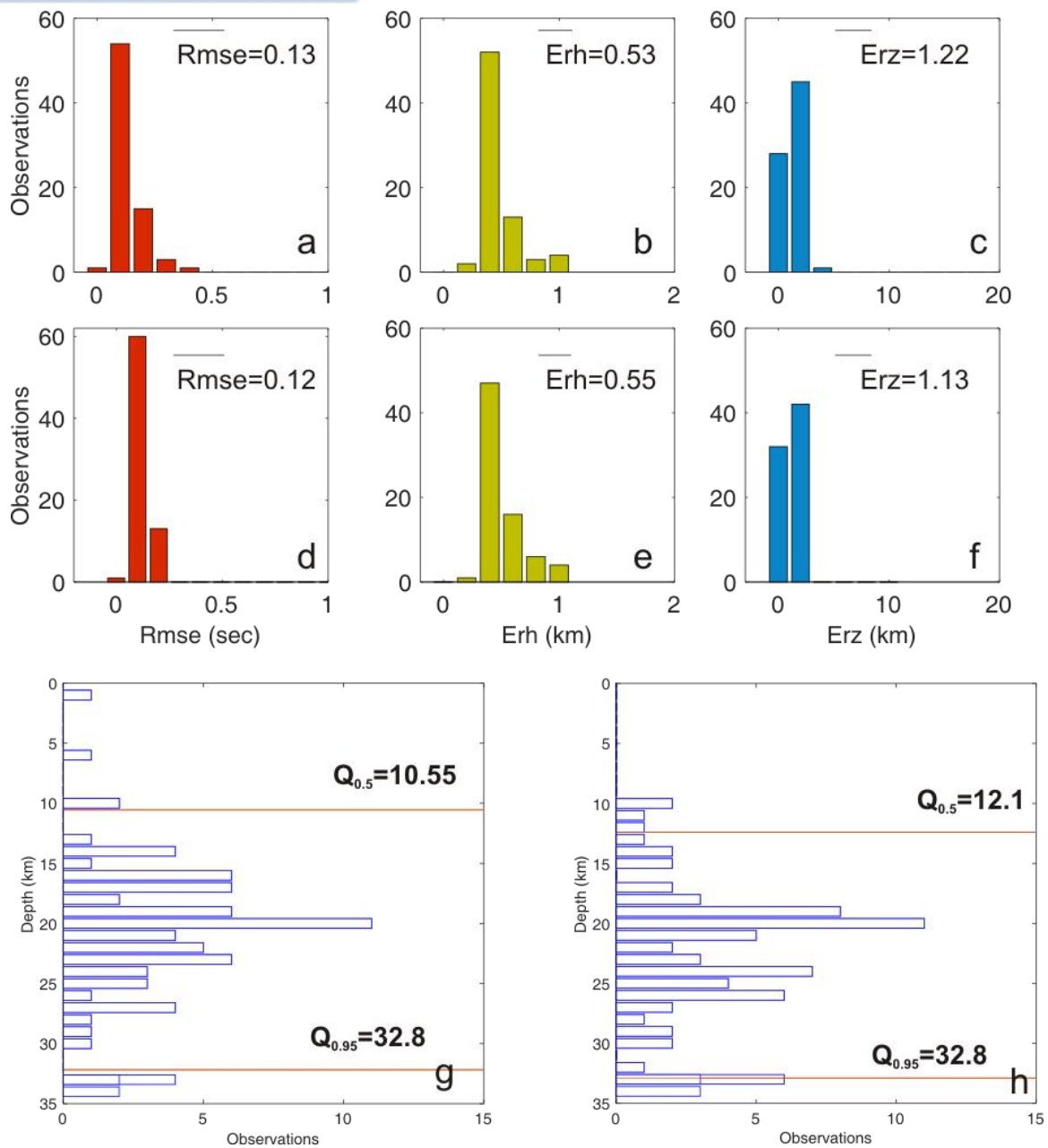


Figure 2-35 Comparison between errors for preliminary location (first row) and final relocation process (second row) for the modeled set of earthquakes in Mesologi area. The mean values are given in each plot, a) root-mean square error (Rmse), b) horizontal uncertainty (Erh), c) vertical uncertainty (Erz), d) root-mean square (Rmse), e) horizontal uncertainty (Erh), f) vertical uncertainty (Erz) and g) depth distribution for the final earthquake catalog and h) depth distribution for the preliminary results. Red lines correspond to the lower and upper cutoff where the majority of earthquakes is exhibited (90%).

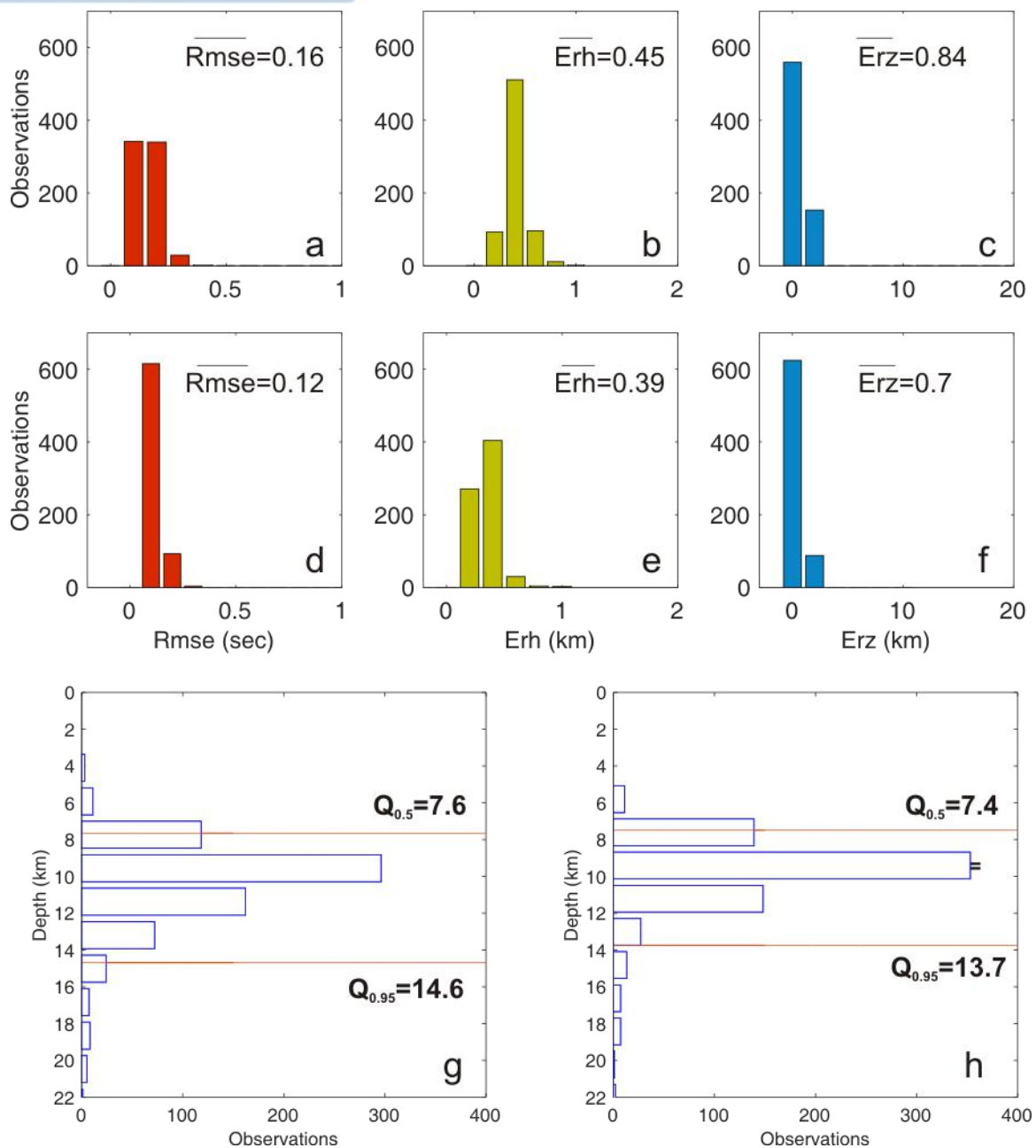


Figure 2-36 Comparison between errors for preliminary location (first row) and final relocation process (second row) for the modeled set of earthquakes in Efpalio area. The mean values are given in each plot, a) root-mean square error (Rmse), b) horizontal uncertainty (Erh), c) vertical uncertainty (Erz), d) root-mean square (Rmse), e) horizontal uncertainty (Erh), f) vertical uncertainty (Erz) and g) depth distribution for the final earthquake catalog and h) depth distribution for the preliminary results. Red lines correspond to the lower and upper cutoff where the majority of earthquakes is exhibited (90%).

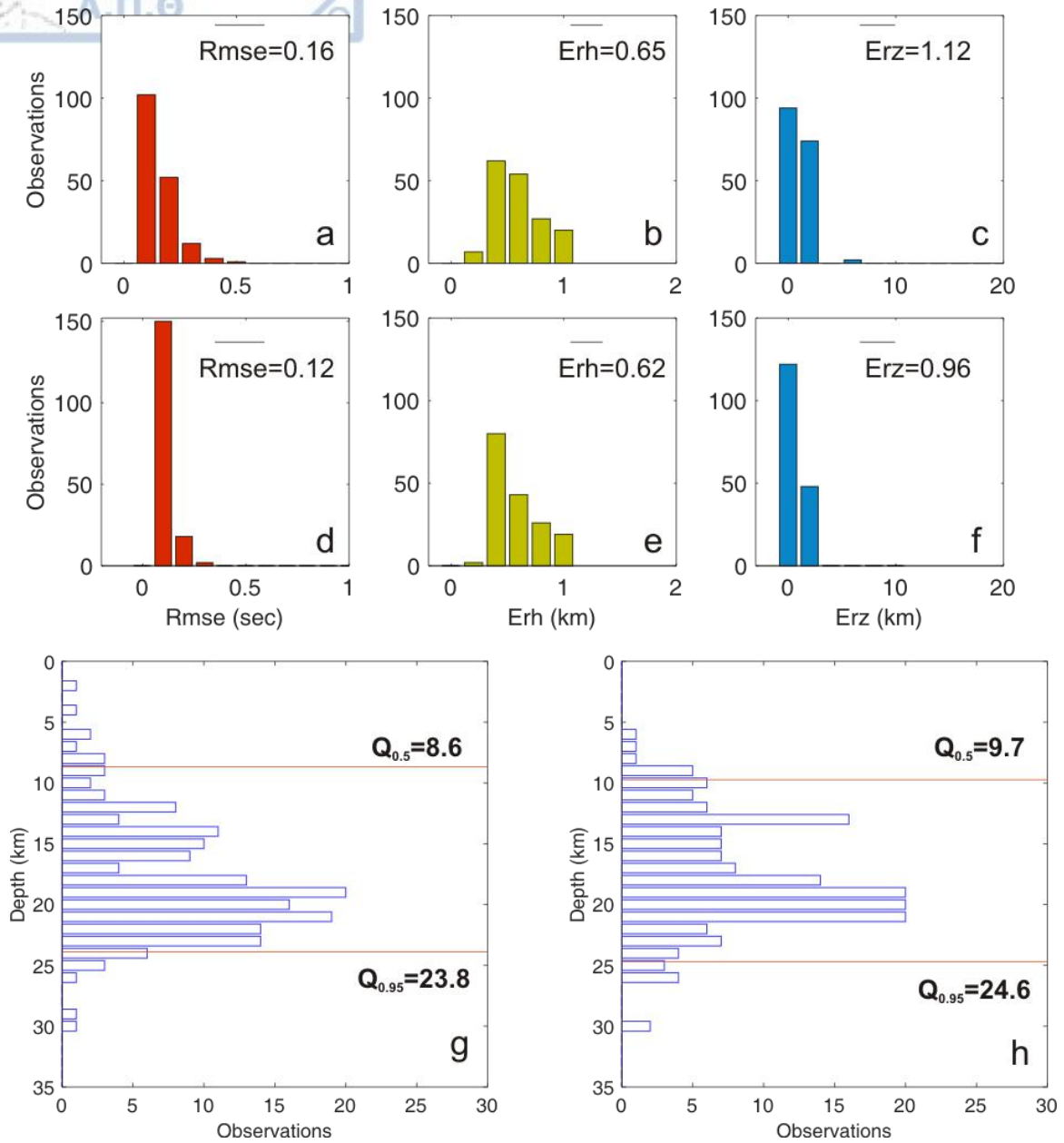


Figure 2-37. Comparison between errors for preliminary location (first row) and final relocation process (second row) for the modeled set of earthquakes in Kato Achaia and Kalavrita area. The mean values are given in each plot, a) root-mean square error (Rmse), b) horizontal uncertainty (Erh), c) vertical uncertainty (Erz), d) root-mean square (Rmse), e) horizontal uncertainty (Erh), f) vertical uncertainty (Erz) and g) depth distribution for the final earthquake catalog and h) depth distribution for the preliminary results. Red lines correspond to the lower and upper cutoff where the majority of earthquakes is exhibited (90%).

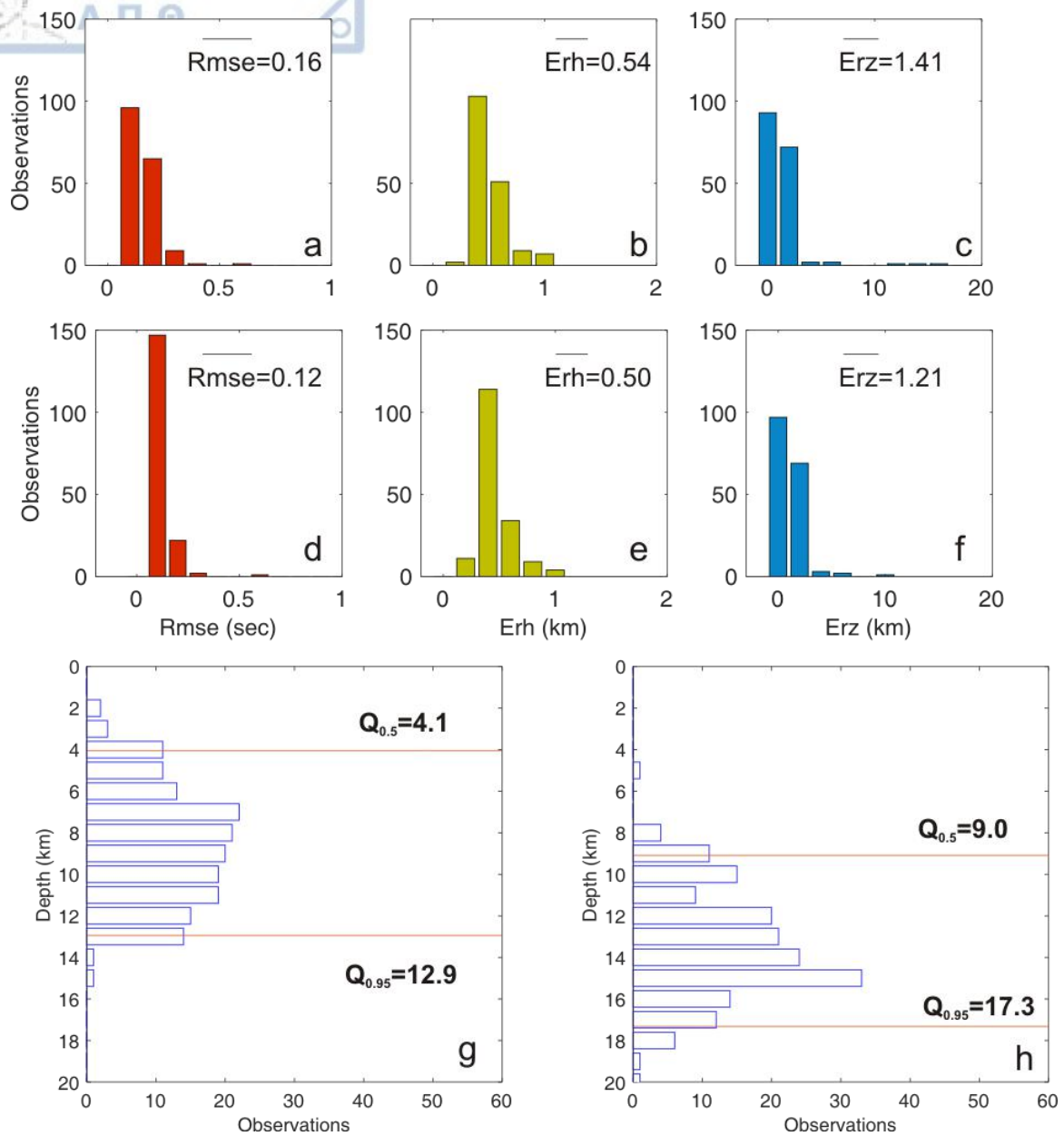


Figure 2-38 Comparison between errors for preliminary location (first row) and final relocation process (second row) for the modeled set of earthquakes in Xylocastro area. The mean values are given in each plot, a) root-mean square error (Rmse), b) horizontal uncertainty (Erh), c) vertical uncertainty (Erz), d) root-mean square (Rmse), e) horizontal uncertainty (Erh), f) vertical uncertainty (Erz) and g) depth distribution for the final earthquake catalog and h) depth distribution for the preliminary results. Red lines correspond to the lower and upper cutoff where the majority of earthquakes is exhibited (90%).

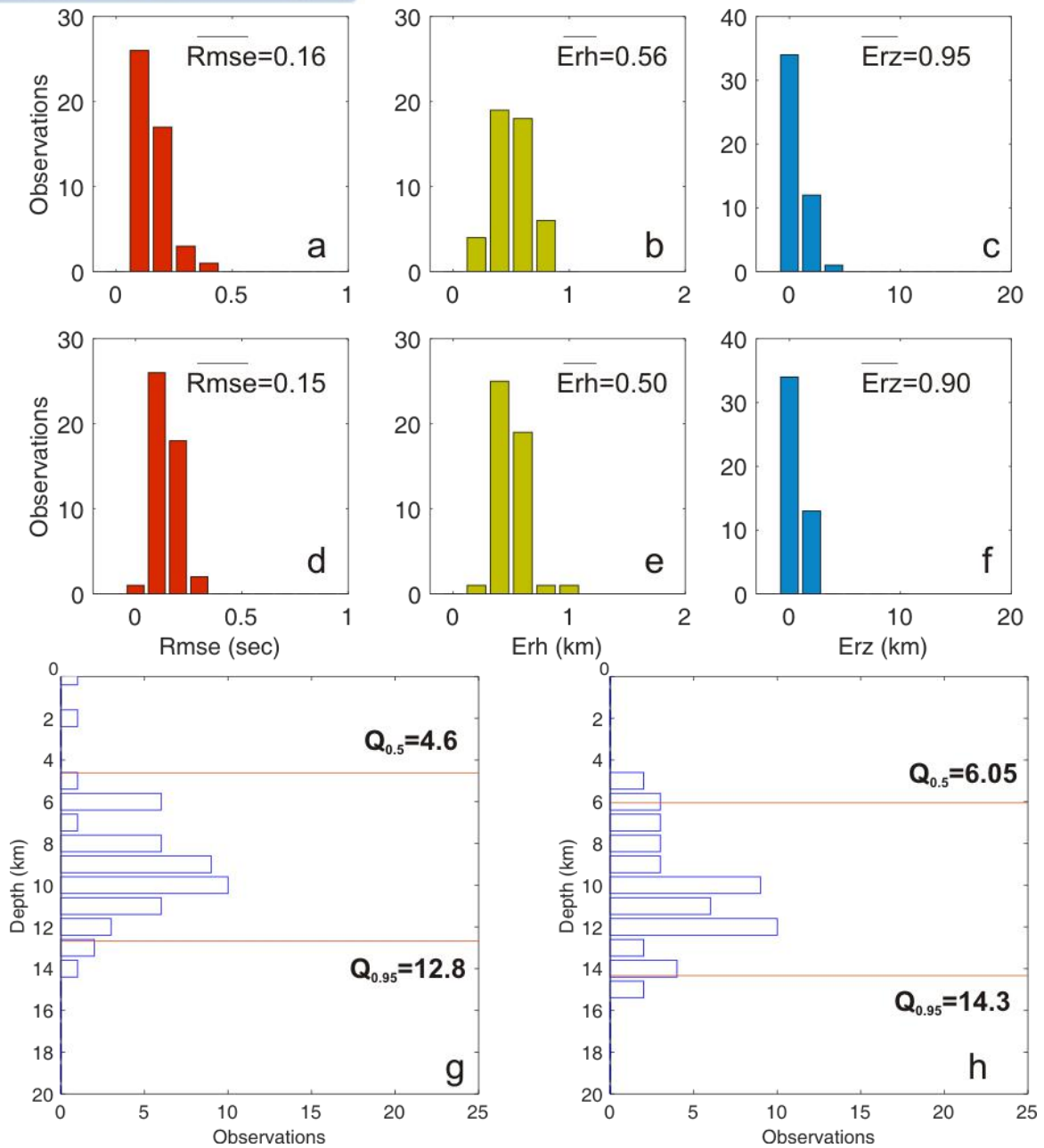


Figure 2-39 Comparison between errors for preliminary location (first row) and final relocation process (second row) for the modeled set of earthquakes in Alkyonides area. The mean values are given in each plot, a) root-mean square error (Rmse), b) horizontal uncertainty (Erh), c) vertical uncertainty (Erz), d) root-mean square (Rmse), e) horizontal uncertainty (Erh), f) vertical uncertainty (Erz) and g) depth distribution for the final earthquake catalog and h) depth distribution for the preliminary results. Red lines correspond to the lower and upper cutoff where the majority of earthquakes is exhibited (90%).

2.9.7 Earthquake Magnitude Assignment and Correction

The compilation of the final seismicity catalog magnitudes which are obtained from AUTH and GI-NOA institutes should be assigned at the relocated earthquake epicentres. Earthquakes which occur in the Corinth are reported in M_{ATH} (NOA seismicity catalog) and M_{THE} (AUTH seismicity catalog) magnitudes. Similar discrepancies with magnitude in Mygdonia were identified. Figure 2-40 shows that the association for magnitudes pairs reported by M_{THE} and M_{ATH} during 2008-2014 is problematic. The figure clearly shows the existence of the two linear trends for magnitudes $M < 4.0$ revealing that the two magnitude catalogs are not equivalent. In Fig.2-40b $\Delta M_{Th-A} = M_{THE} - M_{ATH}$ is plotted against the number of the events and evidences the systematic shift between the two catalogues (Fig.2-9b) which is negative for the first 4000 events and slightly positive onwards.

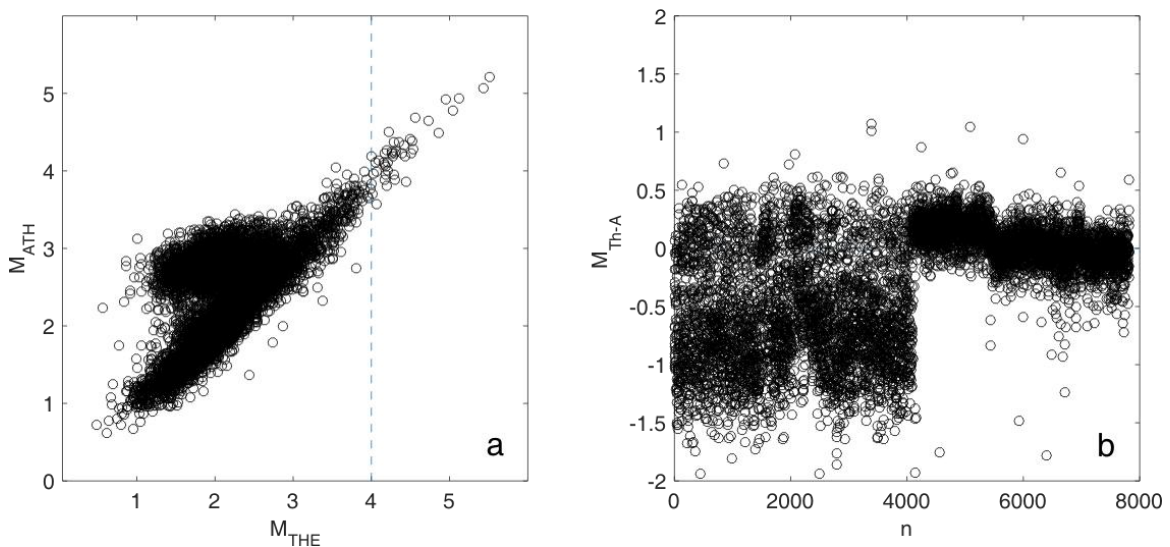


Figure 2-40 a) Correlation between pairs of magnitudes M_{THE} and M_{ATH} for the earthquakes in Corinth rift during the time interval 2008-2014 and b) The magnitude difference $\Delta M_{Th-A} = M_{THE} - M_{ATH}$ for all earthquakes.

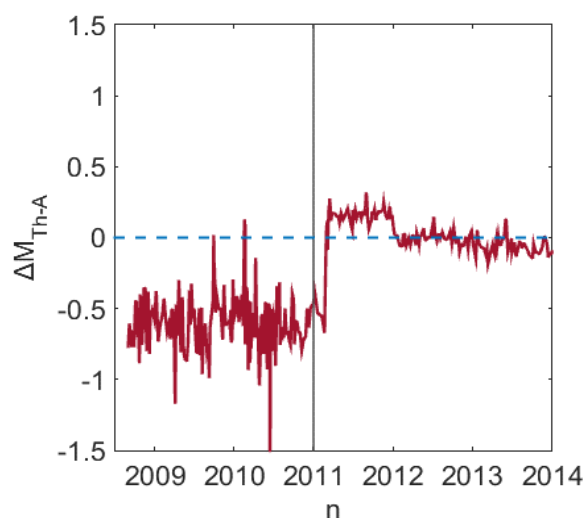


Figure 2-41 Fluctuations of the average magnitude differences, ΔM_{Th-A} for every 20 non overlapping earthquakes for the entire time span of the observations.

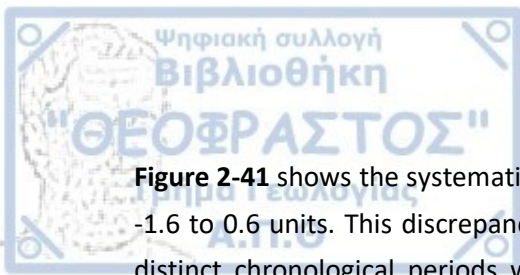


Figure 2-41 shows the systematic temporal variation between the two magnitudes ranging from -1.6 to 0.6 units. This discrepancy is anticipated with the adoption of magnitude corrections in distinct chronological periods with the conversion of M_{ATH} into equivalent M_{THE} . Magnitude corrections for the Corinth Rift were obtained from Karakostas et al. (2015) and Mesimeri (2018). The methodology for the elimination of magnitude discrepancies, was applied for $M < 4.0$ earthquakes since M_{ATH} and M_{THE} for larger magnitudes, although they are few they follow a linear correlation.

2.9.8 Final Seismicity Catalog

The relocated seismicity catalog for Corinth Rift was finalized with the implementation of the Magnitude corrections. The relocated epicenters of earthquakes for the 14 years between January 2000 and June 2014 are presented in Figure 2-42. Relocated seismicity in Corinth rift is investigated in time and space for the identification of seismicity and seismotectonic characteristics. Space-time plots along with successive chronological maps are the tools which are employed for the analysis and the interpretation of the seismicity evolution in time. Cross sections were constructed for the investigation of the geometrical properties of faults at depth and fault plane solutions are used for ascertaining the extracted results. There is significant seismicity during the study period and forms specific seismicity bands across the Corinth Rift. The largest shock during this period was the 2008 M6.4 Achaia earthquake which occurred in Kato Achaia which was followed by the M5.0 strongest aftershock. The 2010 Efpalio doublet with the M5.5 and M5.4 earthquakes and numerous aftershocks which lasted for three months occurred at the central part of the study area. Four more earthquakes with magnitudes $M > 5.0$ and shallow focal depths occurred in the broader area, a M5.0 earthquake in 2008 in Xylocastro area, a M5.1 earthquake occurred in Kato Achaia in 2011, and two M5.5 and M5.2 earthquakes in the area of Kalavryta which were not followed by aftershocks. The seismic activity in Mesologi area is sparse compared to the other regions in the Corinth Rift and exhibits magnitudes $M < 4.0$. Detailed seismotectonic analysis was conducted for Efpalio, Kato Achaia, Xylocastro and Alkyonides area which exhibit significant seismicity.

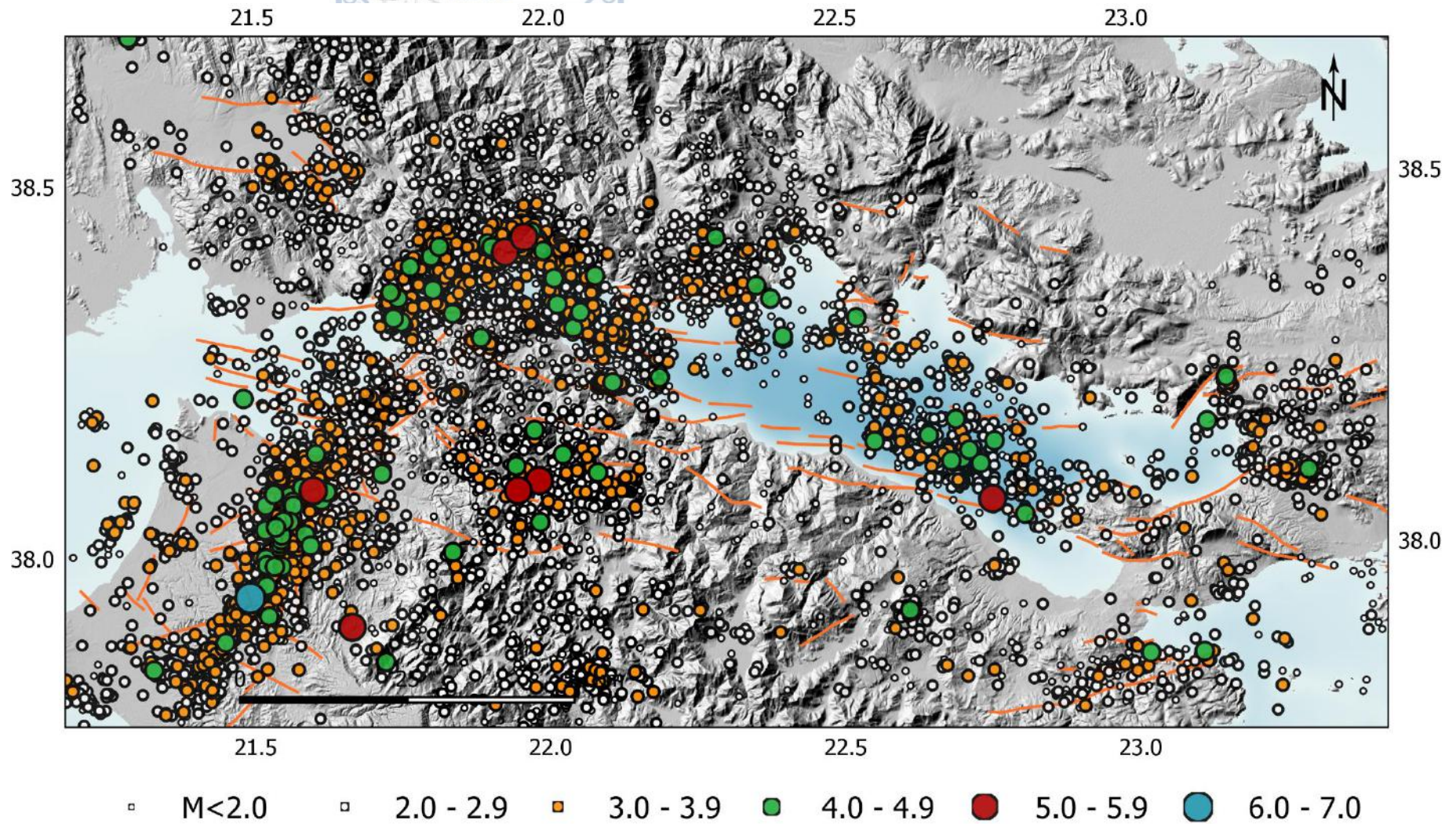


Figure 2-42 The spatial distribution of the relocated earthquakes for 2008 – 2014 in Corinth Rift

Spatiotemporal Seismicity Analysis

Efpalio area exhibits the highest seismicity rate within the Corinth Rift. The most notable activity is the occurrence of the 2010 Efpalio earthquake doublet (owing magnitudes M5.5 and M5.4) and the rich aftershock sequence (Karakostas et al., 2012; Sokos et al., 2012; Ganas et al., 2012). The seismicity catalog for Efpalio area consists of 5.914 relocated earthquakes with magnitude $1.2 \leq M < 5.5$ that occurred from 2008 to 2014. The spatiotemporal seismicity evolution is investigated with the use of a space time plot where the relocated epicenters are projected onto an E-W 42 km long vertical plane (section SS') which is parallel to the dominant strike of the major rupture zones of the Efpalio area. A seismicity map where the location of the SS' profile is mapped is shown in Figure 2-43a. Figure 2-43b shows the space time distribution, where time is converted into numerical time (days) from the beginning of the study period. Corresponding colors between the map and the space-time plot denote the corresponding event clusters and contribute to a clear view of the evolution of earthquake clustering in time. A M4.2 earthquake (2008.07.02) followed by few aftershocks (cl1, green color). Four days later, increased seismic activity was observed close to Efpalio, with a M4.0 event (2008.07.06) and the seismicity propagated 4km to the northeast, where hundreds of events followed in the next years (cl2, red color). Simultaneously, a short seismic burst (cl3, yellow color) with maximum magnitude equal to M4.4 (2008.07.23) occurred at the southern part of the rift, north of Sella village. Seismicity cascaded offshore, west of Psathopyrgos Fault, PsF when in 2009 an earthquake with magnitude M4.0 (2009.03.10) occurred and was followed for more than a month with numerous aftershocks (cl4, purple color). By the end of 2009 the seismic activity was intense both onshore and offshore in the Corinth Rift. In 2009 seismicity became more intense at the eastern termination of PsF, offshore (cl5, blue color) and at the same time a seismic cluster with minor magnitudes not exceeding M3.2 struck Logos village at the southern boundary of Corinth rift (cl6, dark green color). Microseismicity of small magnitudes migrated to the eastern edge of Efpalio subarea (cl7, white color). In 2010, a seismic burst with moderate events started at the northern boundary of the gulf. A doublet of earthquakes with similar magnitude and 4 days lag between them occurred (the first M5.5 event occurred on January 18th and the second M5.4 on January 22nd) and a bulk number of aftershocks followed for months, considerably increasing the seismicity rate across this zone (cl8, red color). Seismicity expanded both to the west and the east of Efpalio rupture zone, where a number of clusters were formed from 2008 to 2011 with synchronous triggering of events to the west of the Efpalio epicentral area (cl9, green color and cl11, orange color). A M4.5 event (2010.03.08) additionally occurred to the east, around Trizonia islands (cl10, yellow color). The seismic activity of cl.11 migrated towards southwest (cl.12, blue color). The activity further migrated to the east (cl.13, green color) where two earthquakes with magnitudes M4.3 (2011.07.28) and M4.2 (2011.07.29) occurred close in time.

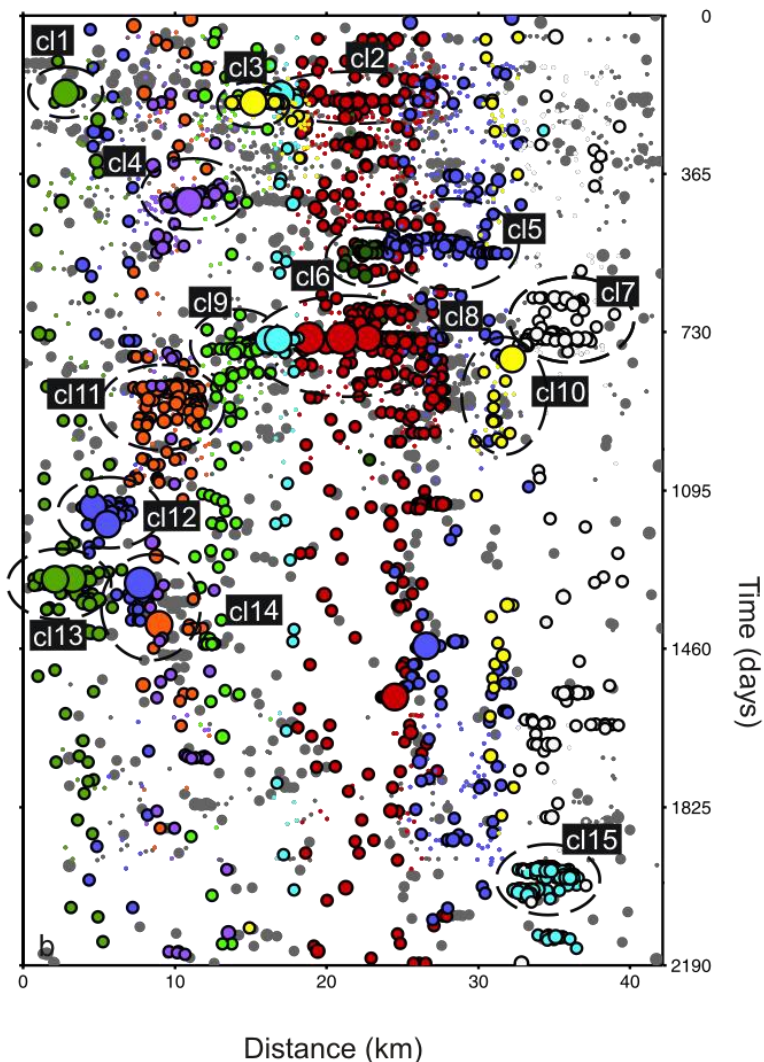
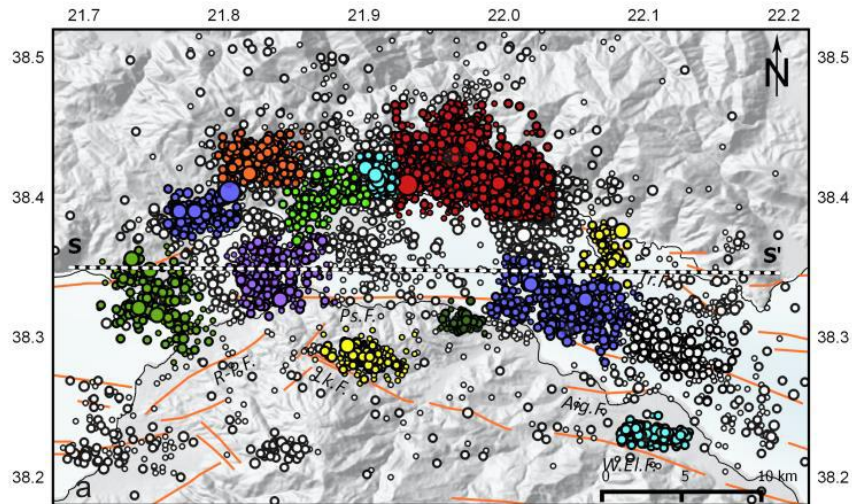


Figure 2-43. a) Map view of the relocated seismicity for 2008 - 2014 in Efpalio area. SS¹ line shows the profile along which the space time plot is constructed, b) Space-time plot of the seismicity distribution, where earthquake epicenters are projected onto the vertical plane along SS¹. Corresponding colors are used between the map view and the section.

A seismic excitation culminated in the occurrence of a M5.0 earthquake (2011.08.20) close to Nafpaktos city (cl14, blue color) with a number of aftershocks striking the epicentral area,

among which a M4.7 event (2011.11.10). Two earthquakes with $M \geq 4.0$ followed (M4.0, 2011.12.29, M4.3, 2012.04.25). In May 2013 a seismic excitation occurred close to Logos village with maximum magnitude equal to M3.7 and lasted for 19 days (cl15, light blue color). Seismic activity expanded to the west and another swarm of events with 14-days duration occurred. The spatiotemporal pattern of seismicity (Fig.2.43b), reveals that during the last years seismicity is diffuse and characterized by several seismic excitations either having short and long duration. Most of them are associated with moderate earthquakes ($M \geq 4.0$) whereas, there is a small fraction of moderate events which is deprived of aftershock activity. The major part of the seismic activity, is evidently found along the hanging wall, where there is a simultaneous scatter of activity to both directions. The expanding of the seismic activity is strongly triggered from the Efpalio doublet in the central part of the study area, forming a continuous deformation zone. There are some clusters at the southern boundary of the Corinth Rift, in an area where there is a relative absence of seismicity and this activity is limited in time.

The magnitude independent space-time tool for earthquake clustering (Leptokaropoulos and Gkarlaouni, 2016) was also applied for the cluster identification. The spatiotemporal criteria were set for a maximum interevent time between subsequent events, $Intt_{max} = 3days$, maximum distance between earthquakes epicentres and the cluster gravity centre, $x_{max} = 10km$, for a minimum number of events, $n_{min} = 20$ in each cluster. Information about the number of events, the duration and maximum magnitude of the 14 identified clusters which fulfilled the given criteria are described in Table 2-6 and their spatial distribution is plotted in Fig2-44. The most numerous seismic excitation detected is the Efpalio sequence (n8) which shows a strong clustering in time and space, lasted for 48.2 days and includes 422 events. The cluster of 224 events (n4) which occurred at the western termination of the Psathopyrgos fault was also detected (cl4 in Fig.2.43)

Table 2-6 Table of the extracted clusters with the application of the spatiotemporal tool. Information is given on the number of the events, the duration of the seismic excitation, the maximum magnitude (M_{max}) and its ranking.

n	Date of the 1 st event	Number of events	Duration (in days)	Rank of M_{max}	M_{max}
n2	01.07.2008	127	27.77	54/127	3.6
n1	29.07.2008	167	16.93	2/167	3.7
n3	20.10.2008	167	16.93	2/167	3.7
n4	09.02.2009	224	41.65	158/224	4.0
n5	04.08.2009	29	12.16	28/29	2.8
n6	27.10.2009	22	4.43	1/22	3.8
n7	19.12.2009	99	41.26	42/99	3.3
n8	07.01.2010	422	48.28	3/422	5.5
n9	03.04.2010	23	9.10	22/23	3.5
n10	11.02.2011	37	6.21	2/37	4.2
n11	22.07.2012	64	20.45	20/64	4.3
n12	21.06.2012	31	16.28	4/31	2.9
n13	21.05.2013	104	19.02	81/104	3.7
n14	13.07.2013	43	13.95	23/43	3.7

with maximum magnitude 4.0 which lasted about 42 days. Smaller clusters were also detected at the southern part of the study area (n12, n13, n14 in Fig.2.44 l,m,m subsets) which lasted <20

days each. Characteristic was the seismic swarm that started on 21.05.2013 and evolved into two smaller clusters in time and space which lasted 19.02days and 13.95days in an area not known for exhibiting seismicity before.

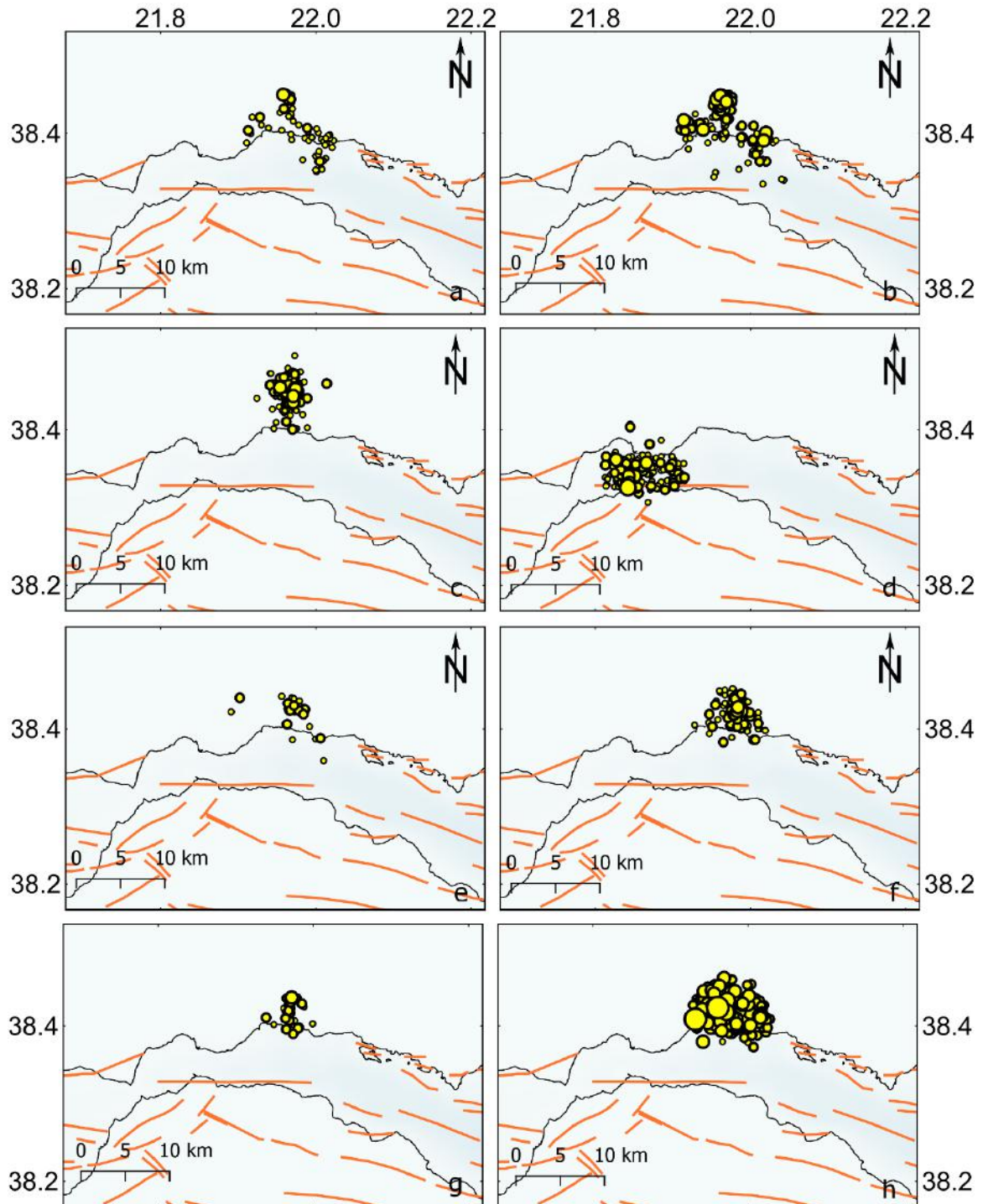


Figure 2-44. a-h) Epicentral distributions of numbered clusters a) n1 cluster, b) n2 cluster, c) n3 cluster, d) n4 cluster, e) n5 cluster, f) n6 cluster, g) n7 cluster and h) n8 cluster, which are extracted with the use of spatiotemporal constraints for the Efpalio area (information provided in Table 2-6).

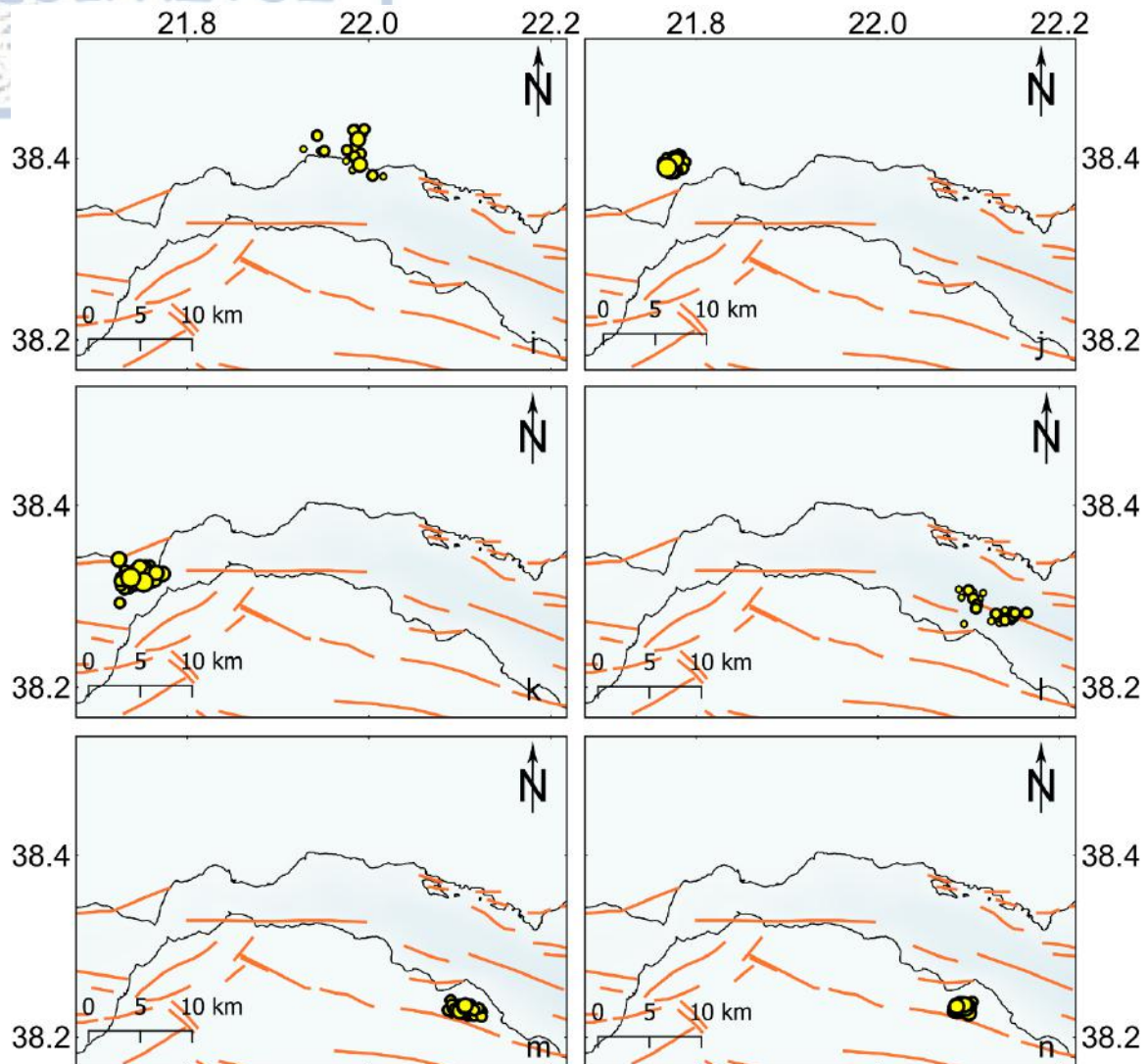


Figure 2-44 (continued). i-h) Epicentral distributions of numbered clusters n9 to n10 provided in Table 2-6, which are extracted with the use of spatiotemporal constraints for the Efpalio area.

2.9.9.2 Spatial Seismicity Analysis

The first striking impression obtained from the epicentral distribution of earthquakes is the seismicity band along the northern coasts of the rift as well as offshore in the area southern of Nafpaktos (Fig. 2-45). There is a characteristic aseismic area, with the characteristic absence of earthquake epicentres at the central part of the study area, northern than Pspathopyrgos fault (Psf). At the north coasts of the Corinth Rift the seismic activity is intense and strong and corresponds to the epicentral area of the devastating Aigion event (1995, M6.5). In the eastern part, dense seismic activity is evident, forming an arc-shaped pattern and covering the central zone of the gulf, aligned with the coast. Strong earthquake are equally distributed along the aforementioned seismicity patches. The epicentral distribution of the relocated earthquakes is investigated in successive chronological intervals which were preferably selected based on the spatiotemporal analysis of seismicity. The distinctive chronological periods are: i) January 1st 2008 – July 25th 2008, ii) July 25th 2008 – June 08th 2009, iii) June 08th 2009 – January 23rd 2010, iv) January 23rd 2010 – November 18th 2011 and the last v) November 18th 2011 – 1st June 2014. For defining

the geometry of the activated structures at depth, eleven vertical profiles are constructed with azimuths ranging from NNW – SSE to NNE – SSW retaining normality to the strike of the main fault trend (dashed grey lines in Fig.2-45). The coverage of the earthquake foci that can be projected onto cross sections is equal to 3km either side of the vertical planes and marked with a rectangular shaded zone. Figures 2-46 to 2-50 depict the spatial distribution of seismicity in successive chronological maps along with the respective cross sections. Available fault plane solutions for earthquakes with magnitude $M \geq 4.0$ are also added (Table 2.7).

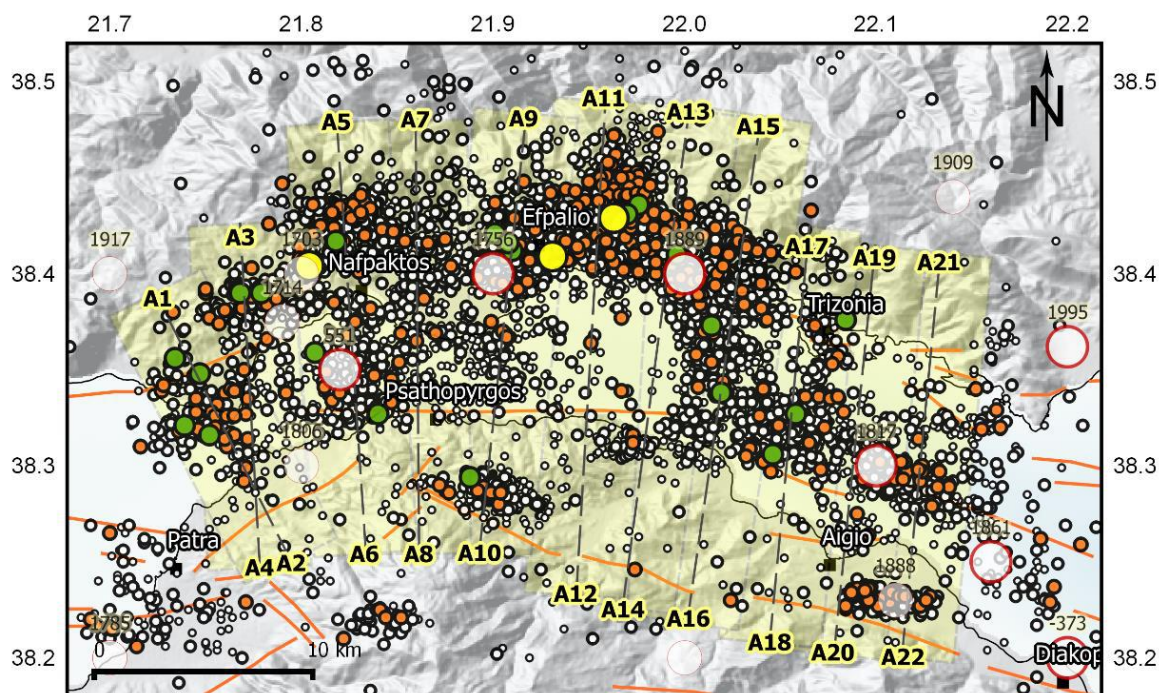


Figure 2-45 Relocated seismicity for Efpalio area. Earthquakes are ranked by magnitude. White circle corresponds to strong historical events, while dashed lines in shaded rectangles mark the location and the coverage of the cross sections. The locations of the strongest historical earthquakes ($M \geq 6.0$) are also shown (red circles).

Table 2-7. Available fault plane solutions for small and moderate magnitude earthquakes in the time interval 2008 – 2014.

No.	Year	Time	Lat	Lon	M	Fault Plane 1			Fault Plane 2			Ref.
						ζ	dip	rake	ζ	dip	rake	
1	20080702	161851.3	38.32	21.79	4.0	275	90	76	185	14	180	(1)
2	20090607	090006.1	38.312	22.050	4.4	100	31	-88	277	59	269	(1)
					4.4	279	50	-92	101	40	-88	(2)
					5.1	103	40	-73	261	52	256	(1)
					5.2	271	48	-100	107	43	-79	(2)
3	20100118	155609.0	38.404	21.961	4.9	82	46	-115	296	49	-66	(3)
					5.5	255	50	-120				(4)
					5.2	270	77	-79	48	17	230	(1)
4	20100118	203656.7	38.435	21.996	4.2	255	50	-60				(4)
					4.2	270	77	-79	48	17	230	(1)
5	20100122	004656.7	38.432	22.007	5.2	87	48	-85	260	43	265	(1)
					5.4	280	50	-105				(4)
6	20100122	105332.6	38.426	21.915	4.2	277	78	-71	39	23	214	(1)
					4.2	265	50	-120				(4)
7	20100122	105916.1	38.396	21.940	4.4	123	52	-31	233	66	223	(1)

					4.5	245	50	-120				(4)
8	20100221	014241.0	37.910	21.456	4.4	211	75	163	305	74	14	(1)
9	20100308	131202.9	38.357	22.111	4.5	320	42	-47	89	59	-122	(1)
					4.5	300	40	-60				(4)
10	20110211	175656.1	38.378	21.779	4.2	310	84	-93	155	6	-65	(1)
11	20110728	091810.3	38.322	21.781	4.3	315	89	23	225	66	179	(1)
12	20110729	195226.8	38.322	21.756	4.2	321	85	15	230	74	175	(1)
13	20110807	143534.5	38.410	21.812	4.7	250	42	119	107	53	-66	(1)
					5.0	285	39	-54	62	59	-115	(3)
38	20110820	020024.5	37.924	21.705	4.9	328	80	-11	59	78	-171	(1)
					5.1	149	67	-23	249	69	156	(3)
14	20111110	172540.2	38.418	21.818	4.7	98	70	-78	247	22	-120	(1)
					4.6	79	47	-107	283	46	-72	(2)
41	20111229	151935.8	38.341	22.020	4.0	285	45	-91	105	44	-89	(1)
43	20120425	103412.0	38.397	21.992	4.3	117	63	-79	275	28	-110	(1)

1. NOA, 2. AUTH, 3. GCMT – HRV, 4. Karakostas et al (2012)

The epicentral distribution for the first period (January 1st 2008 – July 25th 2008) and the section locations are presented in Figure 2-46 and the foci distribution for each cross section is displayed at sections (i) to (xii). Earthquake foci are plotted from North to South on vertical planes. The geomorphological profile is also imprinted along the cross section where a slight exaggeration is added to the geomorphological profile for better visibility. It is observed, that with the exception of the seismicity concentration which is located onshore and along the southern coast of the Corinth Rift, seismic activity during this period is mostly expressed by clusters located offshore and along the north coasts. Seismicity is sparse at the western part of the area and two moderate events ($M > 4.0$) occurred close to Antirio. Foci profiles A_1A_2 (i subplot), A_3A_4 (ii subplot) and A_5A_6 (iii subplot) outline the at-depth geometrical properties where the earthquake foci indicate a plane gently dipping (30°) to the north. This agrees with the fault plane solution for the M4.0 (2008.07.02) which indicates a low 14° angle to the North (A_1A_2 , Table 2-9). Further to the east, two clusters around Efpalio southern than Psathopyrgos are imprinted on profiles A_7A_8 (iv subplot) and A_9A_{10} (v subplot) hypocentres reach 10 km at depth. The cluster at the southern coast of the Corinth rift is developed at relatively lower depths but the fault plane dip is not clear. This seismic burst culminated in a moderate earthquake with magnitude M4.4 (Sela earthquake) located at the western tip, not exceeding 7km at depth. The seismic activity coincides with the strike of the northward dipping Lakka fault (LkF) (A_9A_{10}) (Ford et al., 2013). The northern cluster located close to Efpalio (A_9A_{10}) includes a M4.0 at 10km depth. 4km to the NE a minor magnitude cluster exists. The N-S $A_{11}A_{12}$ section (vi subplot) depicts the foci distribution which form an almost horizontal zone at 11km depth, slightly dipping to the North. Moving to the east, seismicity is mostly concentrated onshore and along the northern coast of the Corinth rift. Earthquake foci along $A_{13}A_{14}$ section (vii subplot) form two distinctive gently dipping planes reaching the depth of 10km. A 30° dipping fault plane is also formed along section $A_{15}A_{16}$ (viii subplot). At the eastern edge of the zone seismicity is scarce and at sections $A_{17}A_{18}$ (ix subplot), $A_{19}A_{20}$ (x subplot) and $A_{21}A_{22}$ (xi subplot) earthquake foci range from 4km to 10km at depth forming a semi-horizontal plane with a gentle dip to the North.

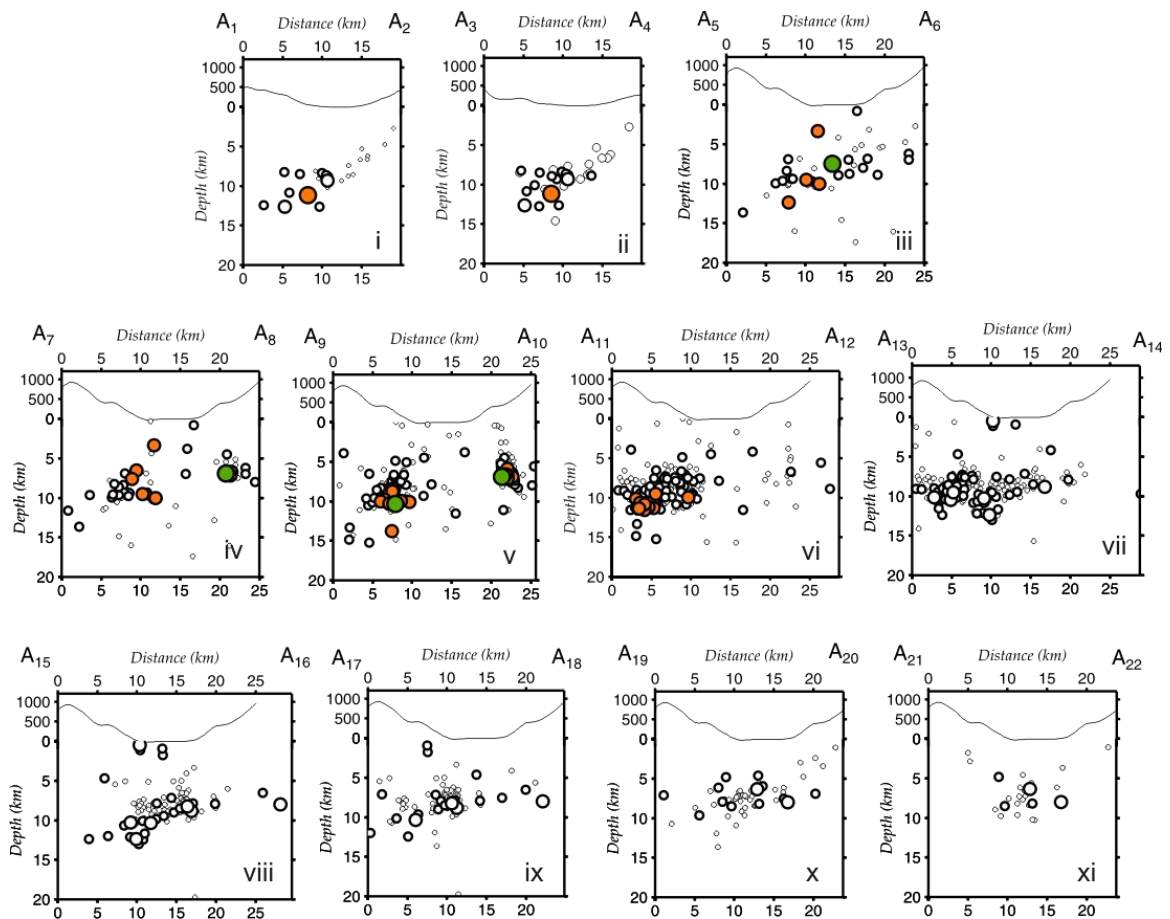
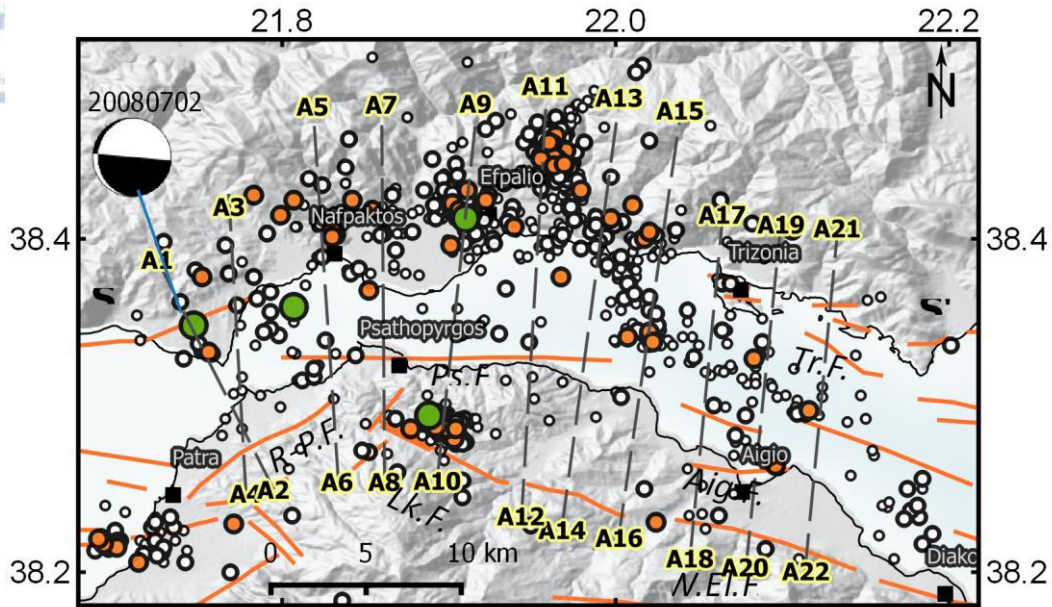


Figure 2-46 Relocated seismicity for the 1st period (01 January 2008 – 25 July 2008) in Efpalio area along (i) section A₁A₂, (ii) section A₃A₄, (iii) section A₅A₆, (iv) section A₇A₈, (v) section A₉A₁₀, (vi) section A₁₁A₁₂, (vii) section A₁₃A₁₄, (viii) section A₁₅A₁₆, (ix) section A₁₇A₁₈, (x) section A₁₉A₂₀ and (xii) section A₂₁A₂₂. Different colors correspond to different earthquake magnitudes but into agreement with the ones used in the maps

The seismicity in map view and cross sections for the second chronological period (July 25th 2008 – June 08th 2009) is depicted in Figure 2-47. In this single year period there is an apparently denser concentration of earthquake epicentres compared to the first period, to the southern and northern part, as well as offshore. An ongoing seismic activity exists with the majority of the epicentres around Antirion exhibiting magnitudes $M < 4.0$. Foci distribution retains the same characteristics with the earlier period and sections A_1A_2 (i subplot) and A_3A_4 (ii subplot) exhibit a fault plane dipping with 30° angle to the North. There is a slight increase of the dipping angle to the East where intense activity now exists. Epicentres are located over the sea between Nafpaktos and the western termination of PsF where there is a seismic cluster with a $M4.0$ (2009.03.10) strongest earthquake at 7km depth. In sections A_5A_6 (iii subplot) and A_7A_8 (iv subplot) the foci distribution shapes a nearly horizontal rupture zone, with hypocenters distributed in less than 10km depths. There is an aftershock seismic activity, after the $M4.4$ Sella event (this period begins soon after the occurrence of Sella sequence main event) which is highly clustered, delineating a rupture area approximately equal to 5km in length and shallow depths $< 11\text{km}$ (A_9A_{10}). Seismicity is also shifted to the south of Efpalio ($A_{11}A_{12}$) where seismic excitations are found in depths $< 10\text{km}$. The seismic activity at the central part of the area, onto the northern coasts of Corinth rift is intense. Earthquake hypocenters are concentrated at 10km depth as shown in sections $A_{11}A_{12}$ (vi subplot) and $A_{13}A_{14}$ (vii subplot). To the east, seismic activity at the central part of the rift along $A_{15}A_{16}$ (ix subplot) and $A_{17}A_{18}$ (x subplot) are concentrated along the horizontal plane, where foci are slightly shifted to larger average depth close to the northern termination of the sections. Southern than Trizonia island an earthquake equal to $M4.4$ (2009.06.07) occurred (ix subplot), defining a fault plane with a 279° strike dipping to the north with a 50° dip indicating a normal rupture zone (rake= 92°) according to the AUTH fault plane solution. The seismic activity at the eastern tip of the study area is described by sections $A_{19}A_{20}$ (xi subplot) and $A_{21}A_{22}$ (xii subplot), which cross the Aigion fault and the foci distribution is clustered and less than 10km at depth.

The 3rd observation period (08 June 2009 – 23 January 2010) covers seven months and coincides with the evolution of the seismic activity in Efpalio area (Figure 2-48). During this period there are numerous aftershocks concentrated around the area of Efpalio, along the northern coasts of the Corinth rift. Seismicity is also present offshore along Aigio fault with seismicity $M < 4.0$. No significant seismicity is observed at the western part of the area, therefore profiles A_1A_2 (i subplot), A_3A_4 (ii subplot), A_5A_6 (iii subplot), A_7A_8 (iv subplot) do not provide any additional seismotectonic information. In addition the seismic activity which was previously spotted along A_9A_{10} section because of the activation on Lakka fault has also ceased. In Efpalio, the first event ($M5.5$, 2010.01.18) occurred on January 18th, 2010 and some days after, the second stronger event ($M5.4$, 2010.01.22) followed. The spatio-temporal properties of this sequence have been already been discussed by several previous researchers (Jansky et al., 2011; Ganas et al., 2012; Karakostas et al., 2012; Novotny et al., 2012; Sokos et al., 2012), Ganas et al., 2012; Kapetanidis, 2017). There is a number of proposed fault plane solutions which

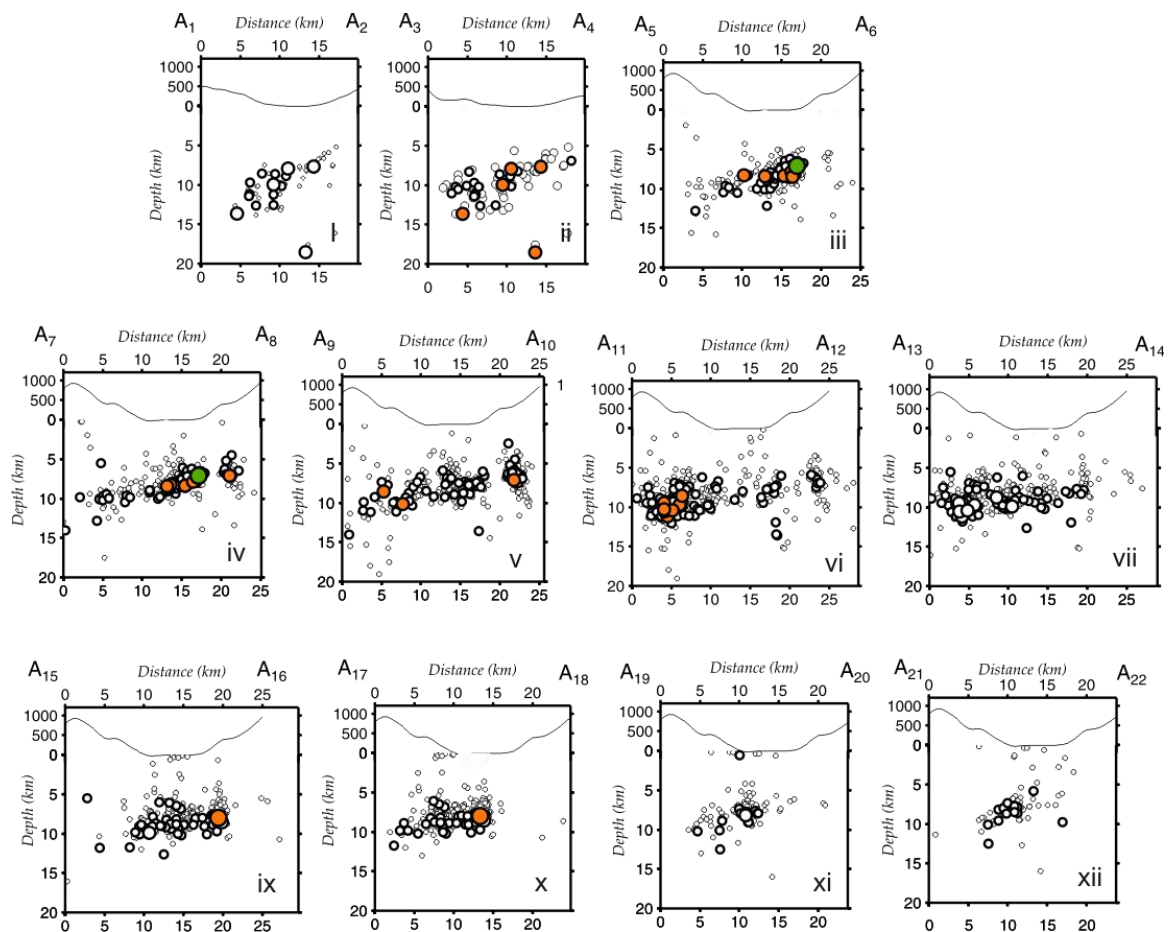
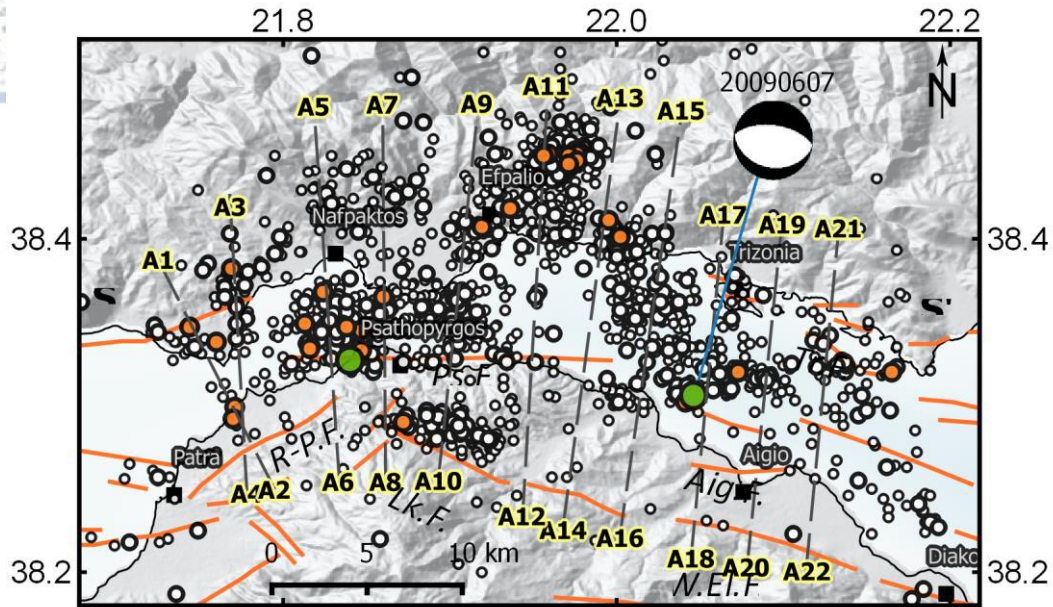


Figure 2-47 Relocated seismicity for the 2nd period (January 2008 – 25 July 2008) in Efpalio area (i) section A₁A₂, (ii) section A₃A₄, (iii) section A₅A₆, (iv) section A₇A₈, (v) section A₉A₁₀, (vi) section A₁₁A₁₂, (vii) section A₁₃A₁₄, (viii) section A₁₅A₁₆, (ix) section A₁₇A₁₈, (x) section A₁₉A₂₀ and (xii) section A₂₁A₂₂.

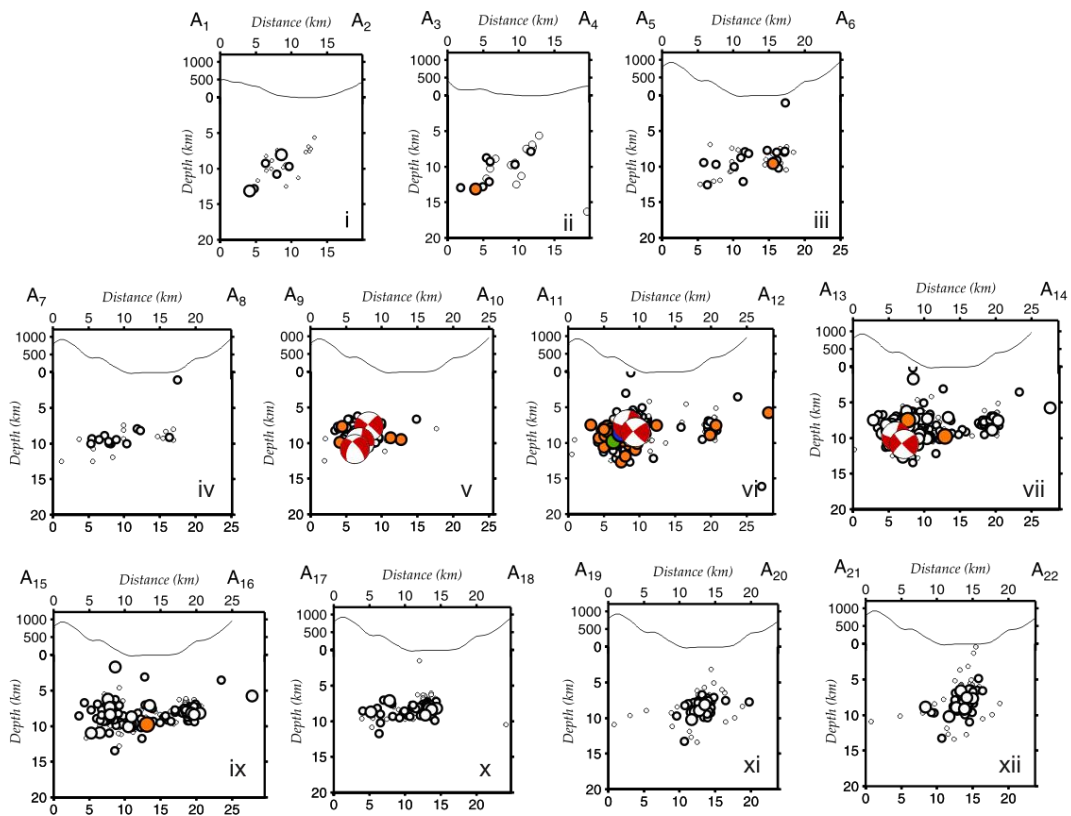
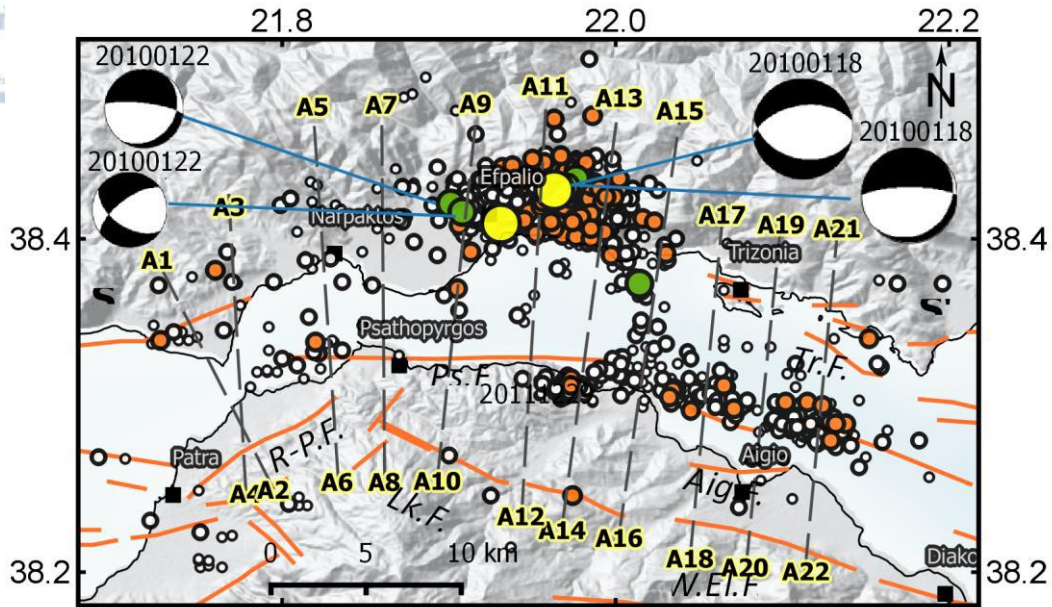


Figure 2-48. Relocated seismicity for the 3rd period (08 June 2009 – 23 January 2010) in Efpalio area along (i) section A₁A₂, (ii) section A₃A₄, (iii) section A₅A₆, (iv) section A₇A₈, (v) section A₉A₁₀, (vi) section A₁₁A₁₂, (vii) section A₁₃A₁₄, (viii) section A₁₅A₁₆, (ix) section A₁₇A₁₈, (x) section A₁₉A₂₀ and (xii) section A₂₁A₂₂.

indicate a normal rupture zone at approximately 170° with 50° dipping to the North. (Table 2-7). The seismic outburst was also extracted with the spatiotemporal tool (Fig.2-44h) according to which lasted 48.8 days. The two strong earthquakes are located in about 3.5 km distance between each other, with the first event to be south of the subsequent one. The earthquake foci distribution is visible at Sections A_9A_{10} (v subplot), $A_{11}A_{12}$ (vi subplot) and $A_{13}A_{14}$ (vii subplot), where the fault plane solutions of the largest shocks are also plotted. The depths are found at the similar depth with the preexisting seismicity range between 6km and 13km, which agrees with other studies (eg Karakostas et. al., 2012). In Sections $A_{13}A_{14}$ a small cluster is visible to the south of Psathopyrgos fault defining a 2km rupture zone along the direction of the coast with maximum magnitude M3.2 (2009.07.04). In sections $A_{15}A_{16}$ (ix subplot) and $A_{17}A_{18}$ (x subplot) the horizontal fault zone at around 10km is clearly delineated. In sections $A_{19}A_{20}$ (xi subplot) and $A_{21}A_{22}$ (xii subplot) earthquakes are clustered and indicate a steeper plane that was not identified before, the cluster ranges from 5km to 10km at depth.

During the 4th period which lasts for 22 months (January 23rd 2010 – November 18th 2011) seismicity is remarkably high along the northern boundary of the Corinth rift and forms an arc-shaped seismic zone from Antirion to Trizonia islands to the east. A cascade of moderate events occurs from west to east as already highlighted from the spatiotemporal seismicity investigation. In Figure 2-49 it is observed that there is a migration of seismicity offshore, where a cluster of moderate earthquakes occur with two maximum magnitude shocks M4.3 (2011.07.28) and M4.2 (2011.07.29). Epicentres in section A_1A_2 are few but define a plane dipping to the North with hypocentres ranging from 5km to 14km. In 2011 (August 20th) a M5.0 earthquake occurred in Nafpaktos. The fault plane solution corresponds to a strike slip fault with a rake equal to -115° according to HRV-GCMT. The seismic activity at Nafpaktos is observed in sections A_3A_4 (subplot ii) and A_5A_6 (iii subplot). The M4.5 (2010.03.08) is observed along the section $A_{17}A_{18}$ (x subplot) at 11.8km depth and its fault plane solution computed by Karakostas et al. (2012) defines a fault plane with 300° strike, dipping with 40° to the North and -60° rake. Seismicity along $A_{19}A_{20}$ (xi subplot) and $A_{21}A_{22}$ (xii subplot) is sparse but clustered defining a horizontal plane with depths <10 km.

During the last observation period (November, 18th 2011 – June, 1st 2014) seismicity rate has diminished in Efpalio. Southern than Efpalio clustered seismic activity defines a linear seismic zone. Seismicity is mostly located offshore, with exception of two seismic clusters east of Aigio where a swarm occurred in 2013 (Fig.2-50). To the west of the study area, there are dispersed small earthquake concentrations and their projection along A_1A_2 (i subplot), A_3A_4 (ii subplot) and A_5A_6 (iii subplot)) accurately delineate fault planes dipping with a 30° - 20° angle to the north. The characteristic angle lowering to the east is visible from section A_7A_8 (iv subplot) to section $A_{13}A_{14}$ (vii subplot) showing the clusters at depth, and the formed fault plane coincides with the fault plane solution for the M4.3 (2012.04.25) which corresponds to a low angle normal fault with 275° strike and 28° dip according to NOA fault plane solution. To the eastern part of the study area seismicity is more increased and it is characterized by the occurrence of a number of

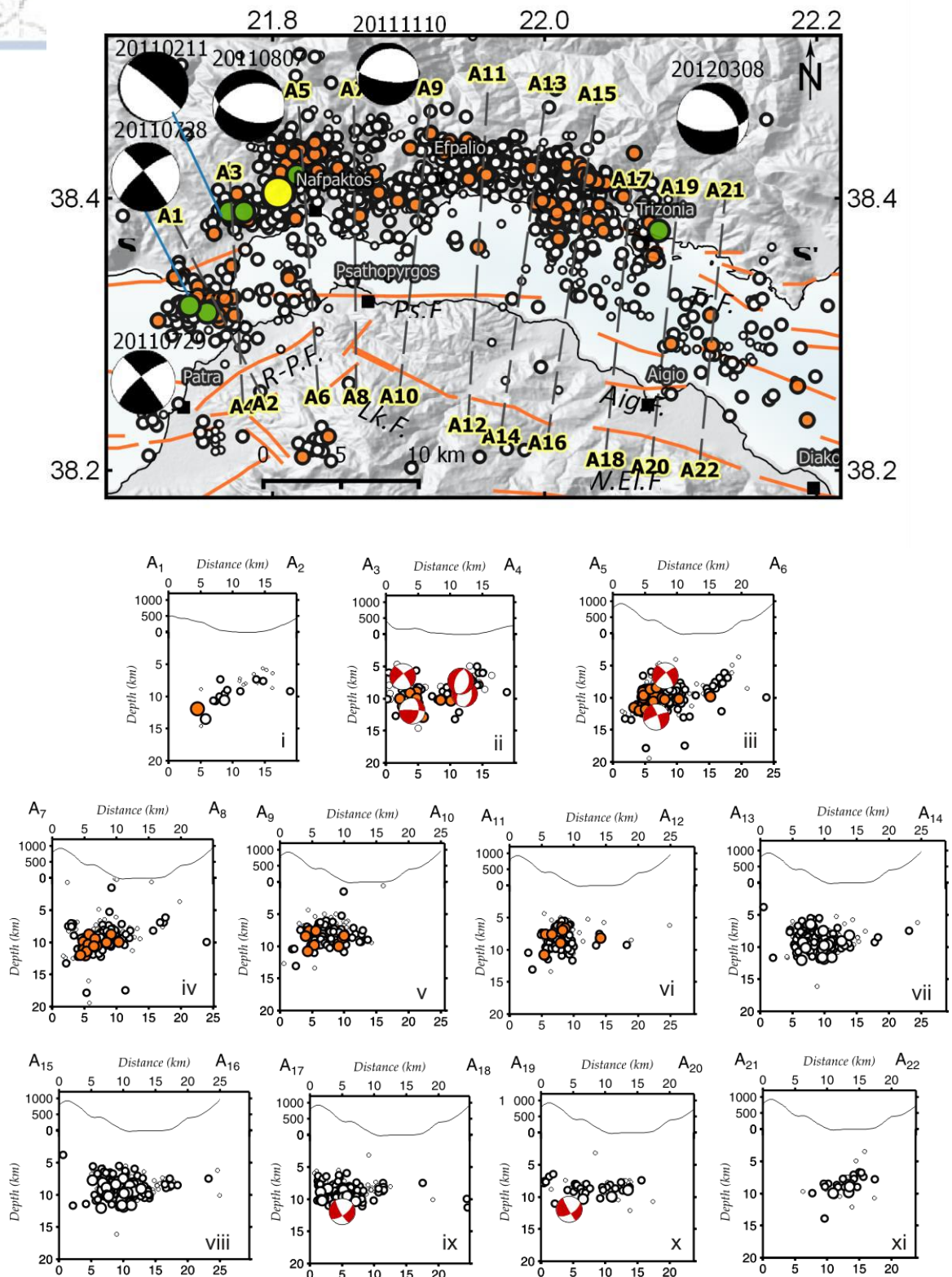


Figure 2-49 Relocated seismicity for the 4th period: January 23rd 2010 – November 18th 2011), in the western Corinth rift, foci distribution along (i) section A₁A₂, (ii) section A₃A₄, (iii) section A₅A₆, (iv) section A₇A₈, (v) section A₉A₁₀, (vi) section A₁₁A₁₂, (vii) section A₁₃A₁₄, (viii) section A₁₅A₁₆, (ix) section A₁₇A₁₈, (x) section A₁₉A₂₀ and (xi) section A₂₁A₂₂.

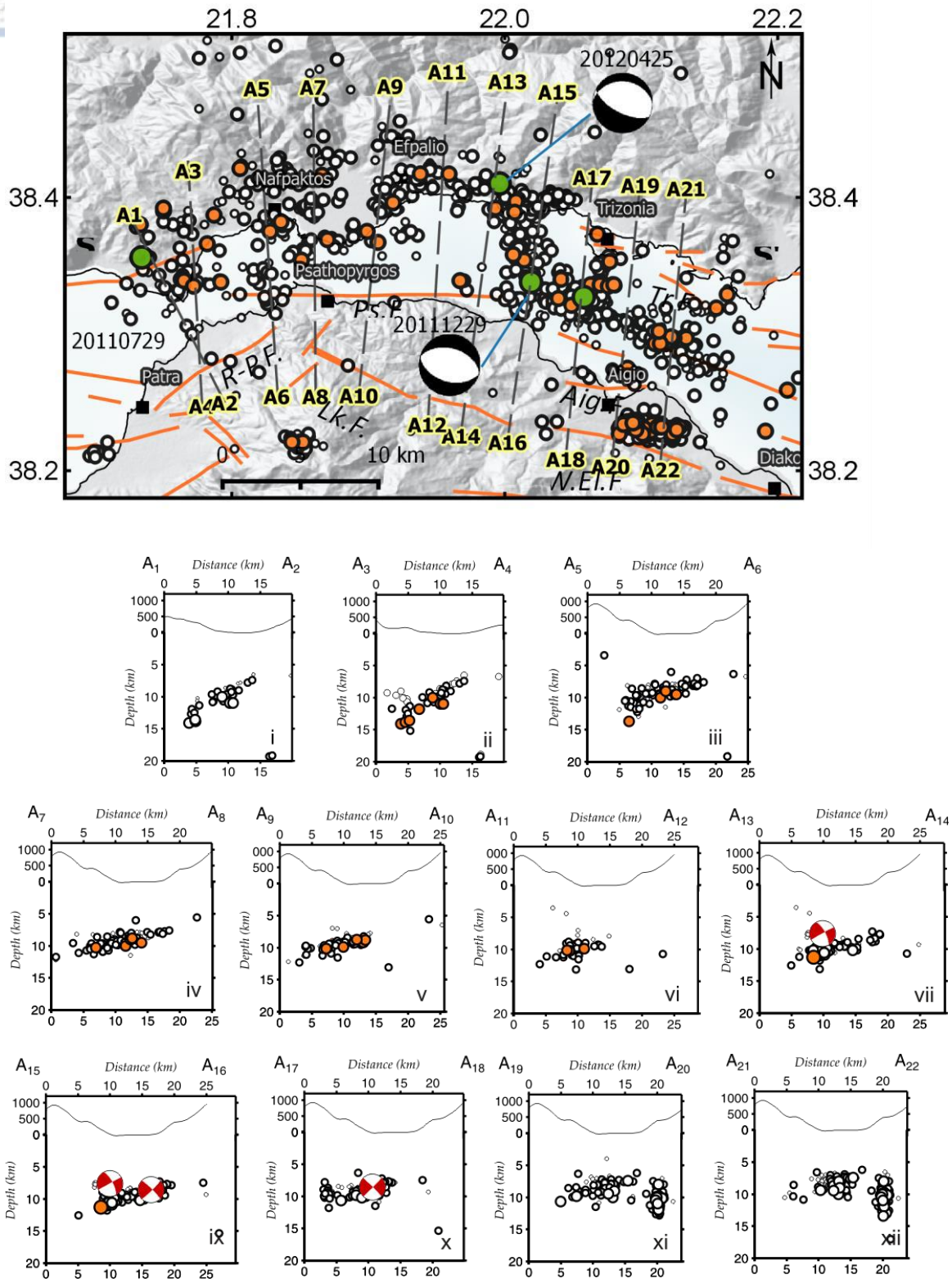


Figure 2-50 Relocated seismicity for the 5th period (November 18th 2011 – 1st June 2014), in the western Corinth rift, foci distribution along (i) section A₁A₂, (ii) section A₃A₄, (iii) section A₅A₆, (iv) section A₇A₈, (v) section A₉A₁₀, (vi) section A₁₁A₁₂, (vii) section A₁₃A₁₄, (viii) section A₁₅A₁₆, (ix) section A₁₇A₁₈, (x) section A₁₉A₂₀ and (xii) section A₂₁A₂₂.

moderate events with $M \geq 4.0$. There is an uncertain indication of a south dipping rupture in section A₁₇A₁₈ (x subplot). Moving to the eastern part an earthquake cluster which occurred in the summer of 2013 and two earthquakes with magnitude M3.9 occurred. The seismic cluster southeast from Aigio which started on 2013.05.21 and lasted for 3 months delineates an almost E-W fault zone. Earthquake foci are projected at sections A₁₉A₂₀ (xi subplot) and A₂₁A₂₂ (xii subplot) where a high angle dipping fault plane is formed. Foci range from 7km to 14km at depth. This feature is considerably different compared to the rest seismicity characteristics at the central part of the Corinth rift and is probably related to the west Heliki fault. Mesimeri et al. (2015) proposed that the earthquake foci range between 9 and 11km, forming a 2km long plane at 40°-50° to the North and according to them the seismic swarm was divided into four distinctive clusters triggering each other.

In order to refine coordinates of earthquakes which form clusters the hypoDD algorithm was further applied. The individual subsets used for this purpose are presented in the following Figure. The best-fit velocity model of Novotny et al (2002) was used for the relative relocation procedure. For each cluster presented in the Figure, a number of calculation iterations were performed so as to optimize the parameters involved in the algorithm. Different factor values like damping and maximum and minimum cluster distances were tested. Best HypoDD results are presented in the following Figure. In most of the cases the distance threshold for the neighboring events was set equal to 5km with a minimum of 8 observations for each cluster. A number of iterations were made in order to reject earthquakes with a small probability to belong to the clusters. The corresponding cross sections are presented in Figure 2.51. Results show significant depth variations for the studied seismicity only in some cases compared to the Hypoinverse results. For example, the depth distribution in subset (c) retains the same depth ranges forming a fault plane dipping with a 30° to the North (Fig2-50, subset iii). Seismicity at the Efpalio which includes the Efpalio sequence (subset f) shows a depth range 4km to 11km which are slightly shallower (Fig.2-48, vi). It should be mentioned that Sokos et al. (2012) and Jansky et al. (2012) suggest a 6km to 9km depth range, which is slightly shallower than the ones calculated in this study. The relocated offshore seismicity to the east of the study area (subsets l and j) exhibit the same depths as before (3km to 10km) forming a thick almost horizontal fault plane dipping gently to the North. The earthquake cluster of subset l with the use of hypoDD is shifted to more shallow depths ranging from 2km to 8km. There is not clear evidence for the fault plane which probably shows a high angle dipping to the North.

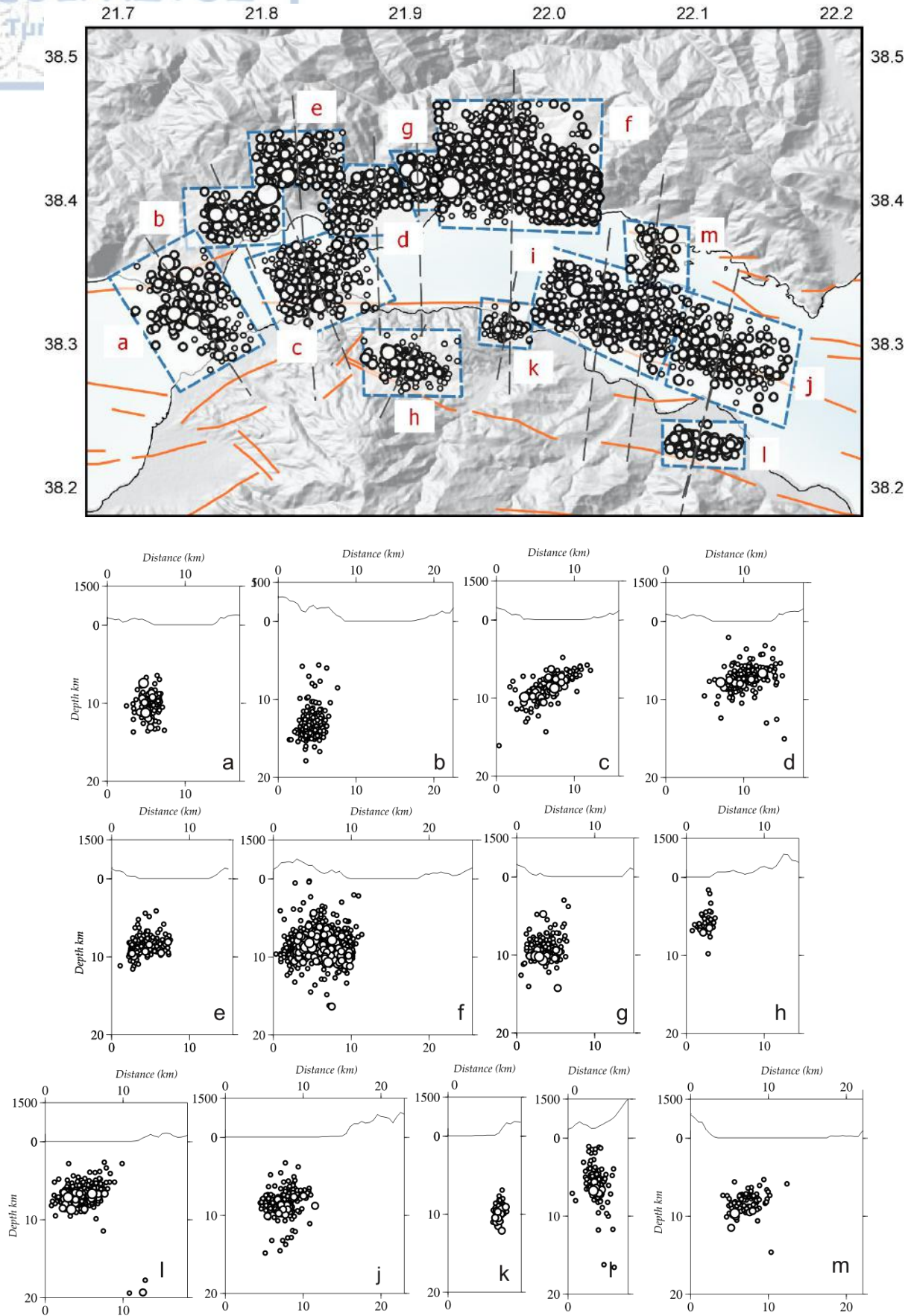


Figure 2-51. Cross sections for HypoDD estimations in the region of Efpalio

2.9.10 Seismicity investigation for Kato Achaia area

2.9.10.1 Spatio-Temporal Seismicity Analysis

The Kato Achaia area encloses the western part of the Corinth rift and the northwestern Peloponnese and constitutes a transition zone between the Corinth Rift and the Hellenic arc. Strong historical seismicity in the area was only known to the north of this region. During the study period the strong 2008 June 8 M6.4 Achaia earthquake and its aftershocks struck this area, which was previously characterized as a low seismicity region. The causative fault according to computed fault plane solutions for this event (HRV-GCMT, $209^{\circ}/83^{\circ}/164^{\circ}$) is a right lateral strike slip fault with high dipping angle, which is in contrast with the E-W normal faults dominating in the Corinth rift. Relocated earthquake epicentres in Figure 2-52a indicate that the majority of seismicity during this period is distributed along an elongated thick zone aligned in a NNE-SSW direction. The epicentral distribution defines a 46km long zone which is strongly confined to the southern part of the zone and becomes wider with diffused epicentres, northern than the M6.4 main shock. Both the mainshock and the strongest M5.0 aftershock which occurred 17 minutes after the mainshock, are aligned in the same zone. The spatiotemporal evolution of earthquakes is presented in a space-time diagram (Fig. 2.52b) in the direction of the seismicity zone (SS' profile which) alongside which, all earthquakes in 20km distance are plotted on a vertical plane and its location is displayed in Figure 2.52a. The vast majority of the earthquakes occurred within few months after the mainshock happened, whereas seismicity in the following years is more frequent at the northern part of the zone. Seismicity is generally decreased and exhibits low magnitudes ($M < 4.0$). A M5.1 earthquake (2011.08.20) which occurred in 15km distance from the M6.4 seismic zone, is the strongest earthquake to occur, deprived of any foreshock or aftershock activity. High clustering in time and space during this period was examined with the employment of the MYSTIC spatiotemporal tool for specific spatiotemporal criteria.

Different criteria were applied for the seismic sequence when earthquake occurrence was highly clustered. For the three months after the main shock, the spatiotemporal criteria were set for a maximum interevent time between subsequent events, $Intt_{max} = 1.8\text{day}$, maximum distance between earthquakes epicentres and the cluster gravity centre, $x_{max} = 8\text{km}$, for a minimum number of events, $n_{min} = 10$ in each cluster. Two clusters were defined for this case, (n1, n2, Table 2-8). The clusters are located to the NNW of the mainshock within the aftershock seismic zone (Figure 2.53). n1 cluster initiated 15 minutes after the main shock (12:40:54), consists of 234 events which occurred in 8.33days with maximum magnitude, $M_{max} = 4.8$ and includes 15 earthquakes with magnitude $M \geq 4.0$. They are distributed in a N-S direction. n2 cluster which initiated one day after, consists of 74 events which evolved in 30.47days and they are located slightly northern than n1 cluster. Two events have magnitudes with $M \geq 4.0$ and $M_{max} = 4.8$, and the epicentral distribution has an almost N-S trend. Both clusters are presented in Figure 2-48a and 2.48b and they are parts of the M6.4 aftershock activity.

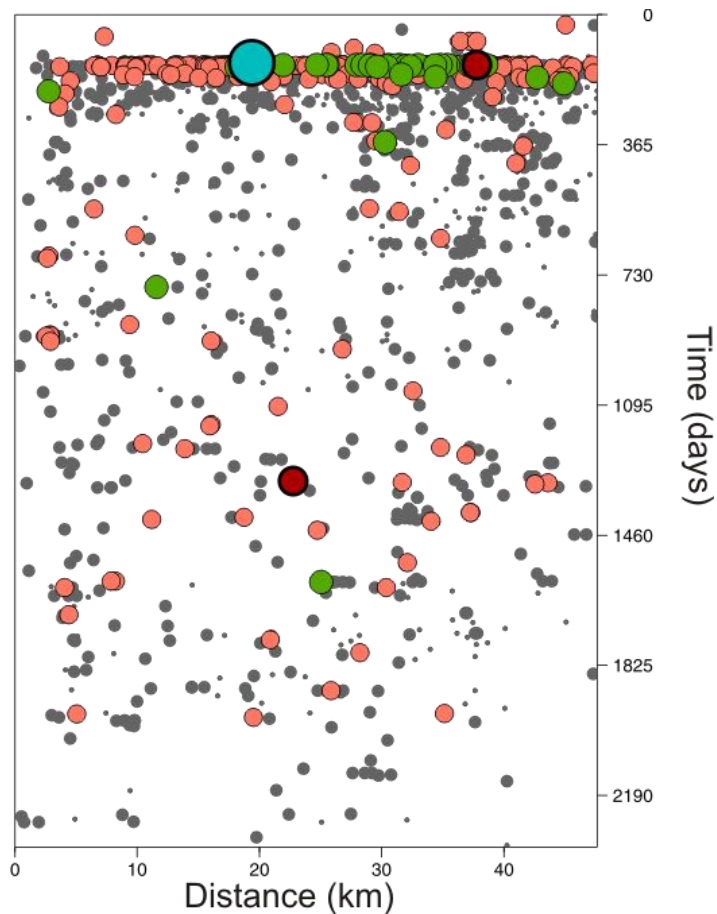
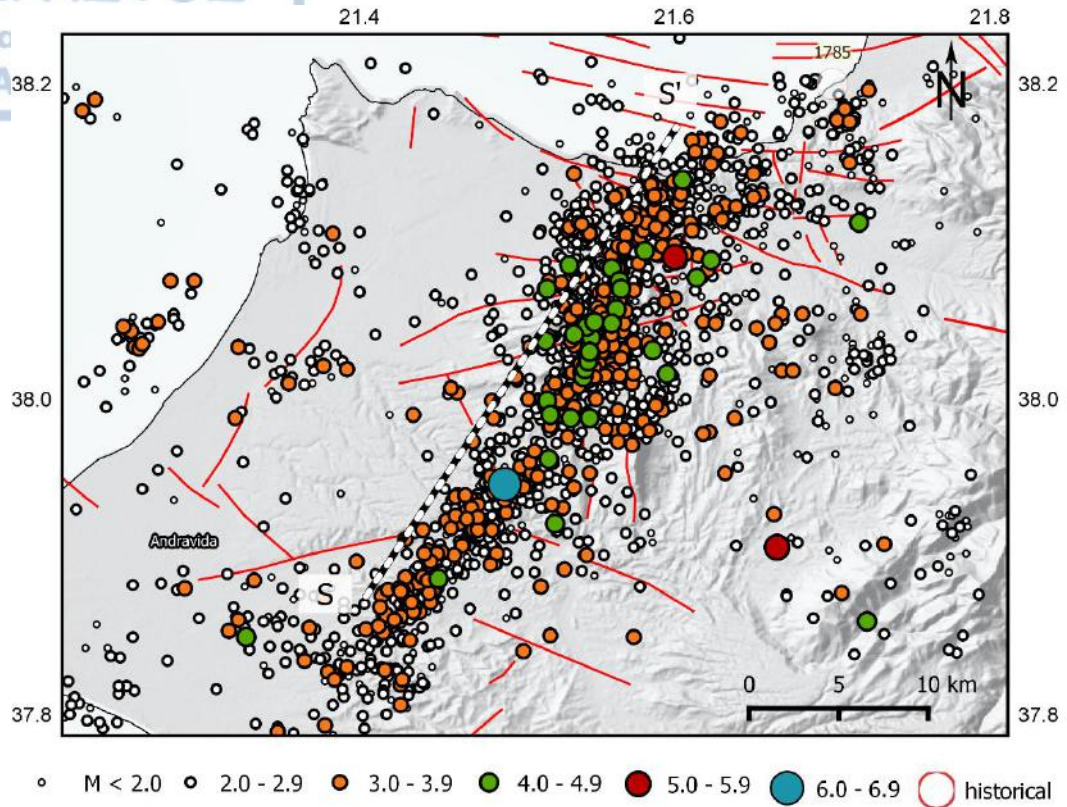


Figure 2-52 a) Relocated seismicity for Patras area. Information for faults in Kato Achaia area obtained from Flotte et al. (2005) b) Space-time plot of the seismicity distribution, where earthquake epicenters are projected onto the vertical plane along SS'.

Table 2-8 Information on the extracted clusters with the application of the spatiotemporal tool (MYSTIC) for Kato Achaia area. Information is given on the number of the events, the duration of the seismic excitation and the maximum magnitude (M_{max}).

n	Date of the 1 st event	Number of events	Duration (in days)	Rank of M_{max}	M_{max}
n1	2008.06.08	234	8.33	51/234	4.6
n2	2008.07.01	74	30.47	16/74	4.8
n3	2010.07.06	11	3.75	9/11	3.5
n4	2012.01.19	14	5.93	11/14	3.1
n5	2012.05.28	8	2.61	1/8	4.3
n6	2013.03.29	11	0.11	5/11	3.4

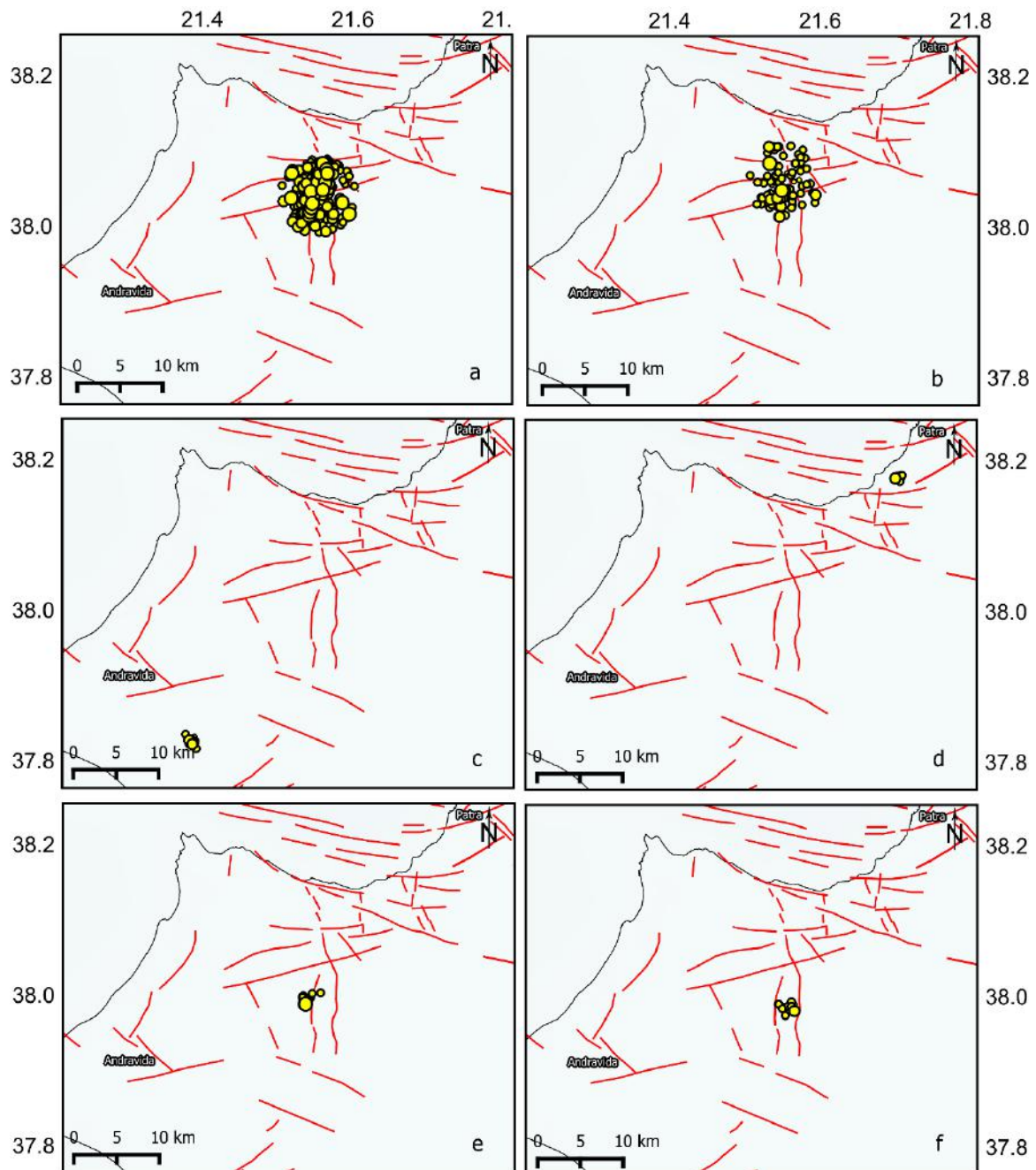


Figure 2-53. a-f) Epicentral distributions of numbered clusters n1 to n6 provided in Table 2-8, which are extracted with the use of spatiotemporal constraints for Kato Achaia area.

For the following years, criteria were set equal to $\text{Intt}_{\max}=3\text{days}$, $x_{\max}=10\text{km}$ and $n_{\min}=8$ for which, two more clusters were identified (clusters n3, n4, n5, n6, Table 2-8). Contrary to the previous, these clusters have a short time duration lasting from 0.11 days to 5.93 days and they consist of 8 to 14 events, while $M_{\max}=4.3$ (cluster n5). Seismicity in the area is not highly clustered with the exception of the period of the seismic sequence.

The chronological evolution of the seismicity in the area is also presented in Figure 2.54, where seismicity is plotted in three different intervals i) 01.01.2008 – 16.08.2008, ii) 17.08.2009 – 31.12.2008, iii) 01.01.2009 -01.01.2014 along with available fault plane solutions described in Table 2-9. In the first interval which lasts 10 days after the M6.4 earthquake occurred seismicity is distributed into two spatial concentrations, one 16km long NE-SW southern than the main shock and one 19km N-S zone to the north. The majority of the strongest earthquakes with $M>4.0$ occurred during the first 10 days (Fig. 2-54a) and they are located at the N-S seismogenic zone. Fault plane solutions for the main shock indicate a NNE-SSW strike slip fault plane. For the second chronological interval seismicity is distributed with the same pattern but low magnitude earthquakes are dominant (Fig. 2-54b). For 2009- 2014 (Fig. 2-54c) seismicity zones are more confined and elongated forming small clusters. The earthquake distribution at depth is investigated with vertical cross sections normal to the NNW-SSE trend of the seismogenic zone, in chronological intervals. The locations of the four cross sections, presented in Figure 2.54 cover the seismic zone from South to North.

Depth distribution at B_1B_2 cross section which encompasses events at the southern part of the zone ranges between 3km and 22km with the vast majority of hypocentres at around 15km for the first two chronological periods. In the last period there is seismic activity with foci ranging at larger depths between 18km and 24km, with the strongest earthquake of the observed seismicity at the largest depth point of the distribution. The foci delineating an almost vertical fault plane dipping to the west. The same pattern is displayed for all the chronological periods (i), (ii), and (iii). Earthquake depths in B_3B_4 (i) section shows a deeper range of hypocentres, with the stronger earthquakes reaching 23km at depth with the majority of the hypocentres found between 5km and 16km. The main shock is found at the 28.4km depth. This depth is deeper than the one calculated by Karakostas et al. (2017) at 25km. The minor seismicity foci of the second chronological period exhibit the same depth range and outline a fault plane dipping for more than 80° . Foci after 2009 are few and mostly gathered at 20-24km.

Sections B_5B_6 and B_7B_8 cover the northern seismicity patch which exhibits stronger earthquakes with magnitudes $M>4.0$. Aftershock depths in section B_5B_6 (i) are mainly distributed between 5km and 24km and a foci cluster is also observed at 19km depth (i). The same depth distribution pattern is retained for the subsequent chronological periods (ii) and (iii). Section B_7B_8 (i) includes the stronger aftershock hypocentres at 14.8km depth (i). The majority of the foci is strongly clustered at larger depths at 17km, while a number of foci reach 26km at depth. In section B_7B_8 (ii) seismicity is dispersed and is mainly distributed between 6km and 25km.

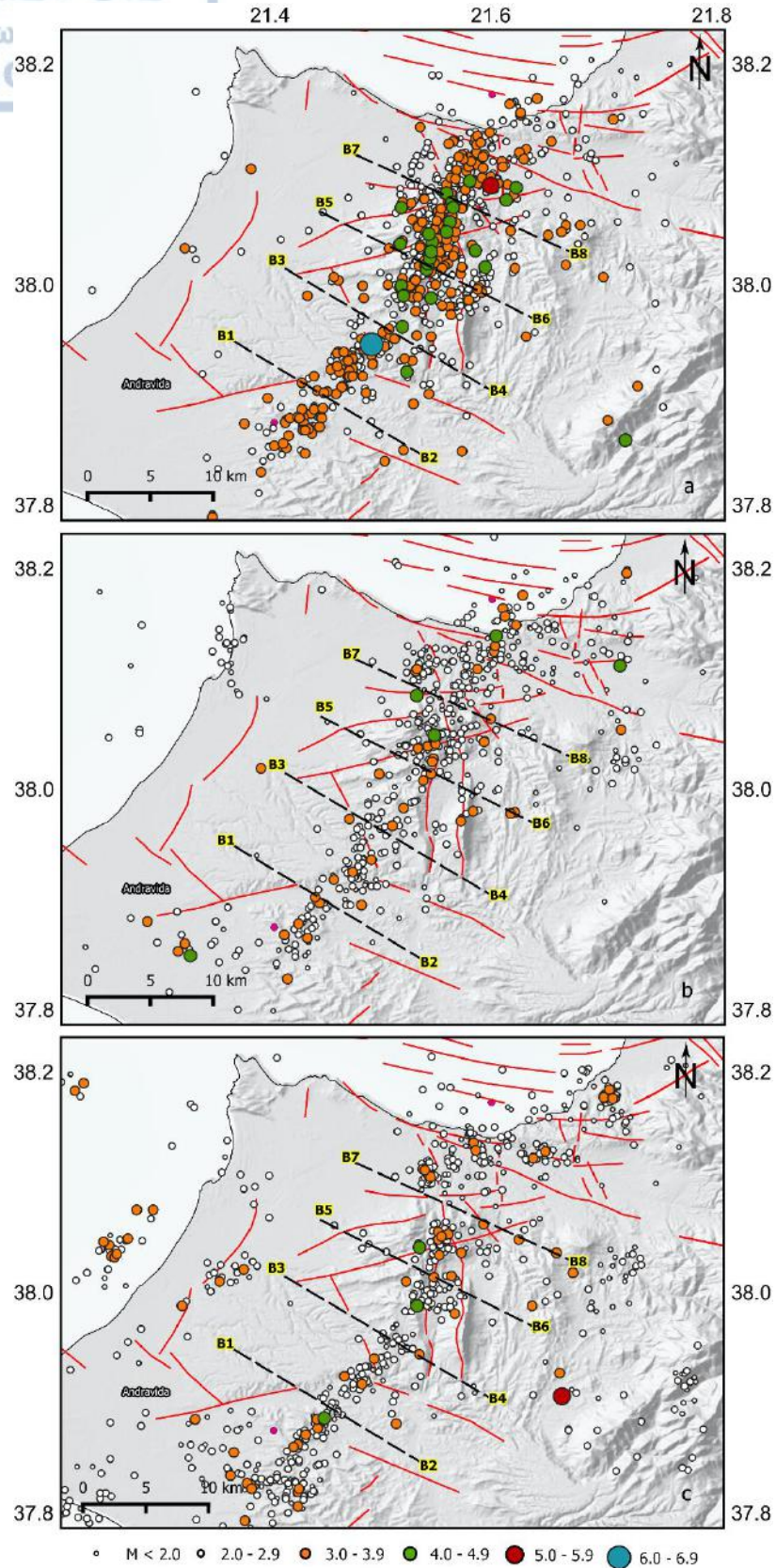


Figure 2-54 Relocated seismicity for Kato Achaia area for the chronological periods a) 01.01.2008 – 16.08.2008, b) 17.08.2009 – 31.12.2008, c) 01.01.2009 -01.01.2014, Locations of the cross sections are also shown.

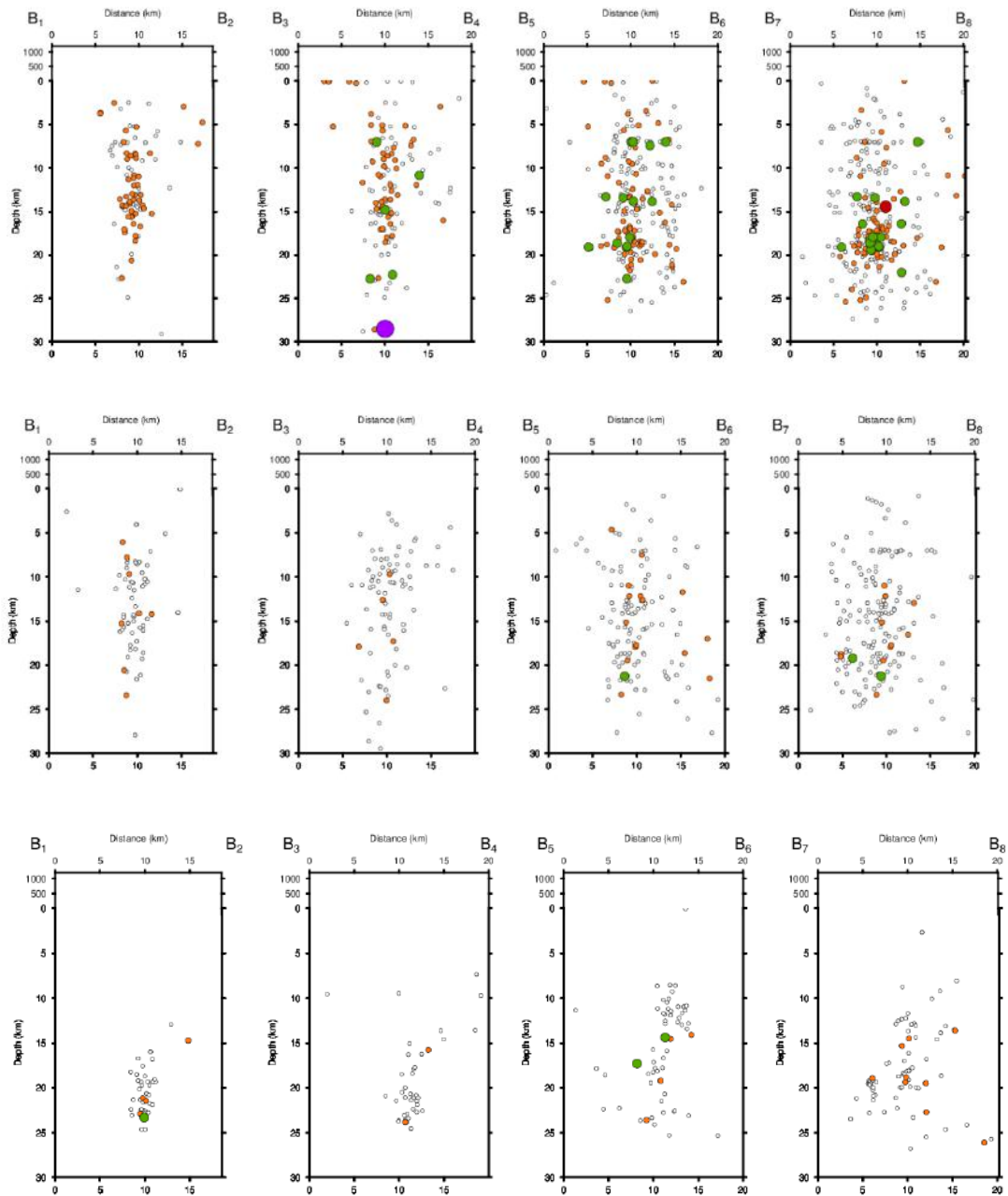


Figure 2-55 Cross sections for Kato Achaia area for the chronological periods (i) 01.01.2008 – 16.08.2008, upper row, (ii) 01.01.2008 – 16.08.2008, middle row and (ii) 2009.01.01 -01.01.2014, lower row, along section B₁B₂, section B₃B₄, section B₅B₆ and section B₇B₈. Cross section locations are mapped in Figure 2.54.

2.9.11 Seismicity Analysis for the Xylocastro area

2.9.11.1 Spatiotemporal Seismicity Analysis

Xylocastro is situated to the east of Efpalio area and is an expanded offshore part of central Corinth rift, extending from Eratini to Kiato (Fig.2-56a). This area includes major seismogenic rupture zones to the south coast, aligned with the general azimuth of the rift, such as the western part of W.El.F, Akr.F, onshore and offshore Xyl.F, which shape a significant part of the rift footwall. At the northern coast there is a synthesis of geomorphological complexities including small gulfs and peninsulas formed by small but also seismogenic faults such as Del.F which has been associated with important earthquakes e.g. the strong historical earthquake of 1870 (M6.0). The seismicity catalog for Xylocastro area consists of 1611 relocated earthquakes with magnitude $1.2 \leq M < 5.0$ ranging from 2008 to 2014. The spatial distribution of the relocated epicentres (Fig. 2.56a) shows the existence of two main seismicity bands, one to the NW of the study area, at Galaxidi and Eratini coasts and another band to the SE, at the offshore Xylocastro area. Seismicity is plotted in a space-time diagram (Fig.2.56b) and projected onto the SS' section (starting point: 22.248°E, 38.346°N, ending point: 23.271°E, 37.933°N, section mapped in Fig.2.50a). The spatiotemporal profile is characterized by the presence of the two discrete seismicity zones separated with a zone where seismicity is sparse. Seismicity is constant along the two bands through the whole study period. In the beginning of 2008, the earthquake activity is located around Eratini and Galaxidi (*cl1 – blue color*) where a moderate event with M4.0 (2008.07.09) occurred. At the same time an offshore seismic activity northern than Xylocastro area occurred, along a NE – SW rupture zone where there was a number of earthquake clusters close in time (*cl2 – orange color, cl3 – yellow color, cl4 – red color and cl5- orange color*). This seismic activity is characterized by a cascade of moderate events with magnitudes $M \geq 4.0$ (M4.2, 2008.10.23 and M4.0, 2009.01.12) and some months later a triplet of moderate events (M4.9, M4.2, M4.5) followed. Two earthquake groups are found to the north of Xyloxastro band (*cl6 – blue color*) offshore, where no other seismicity was noticed before (*cl7-green color*). The strongest earthquake in this study period occurred at the southeast termination of the zone, in 2012.09.22 when an earthquake with magnitude M5.0 occurred and was followed by a small number of aftershocks (*cl8*). At the north coasts of Itea, after the 2009 swarm (*cl4 – red color*) the next seismic activity continued in 2013, when a cluster (*cl9 –yellow color*) of moderate magnitudes occurred.

Seismic excitations in the sense of a dense spatiotemporal activity were studied using the temporal criterion where the criteria were for a maximum interevent time between subsequent events, $\text{Intt}_{\max} = 3\text{days}$, maximum distance between earthquakes epicentres and the cluster gravity centre, $x_{\max} = 10\text{km}$, for a minimum number of events, $n_{\min} = 10$ in each cluster. The identified clusters are shown in Table 2-9 and plotted in the subsets of Figure 2.57 (a to e). In total five clusters fulfilled the introduced temporal and spatial criteria which were selected for extracting short excitations. The duration of the seismic bursts range from 9.76 to 15.77 days with the maximum Magnitude to be found mostly in the beginning of the excitations. The majority of the

clusters occurred at the eastern part of the study area and most of them are associated with Xylocastro fault (Fig.2.57 b, c, d). The most notable seismic cluster which occurred includes 48 events with $M_{\max}=4.9$ within 9.76 days at the central part of Xylocastro fault (Fig. 2-57d).

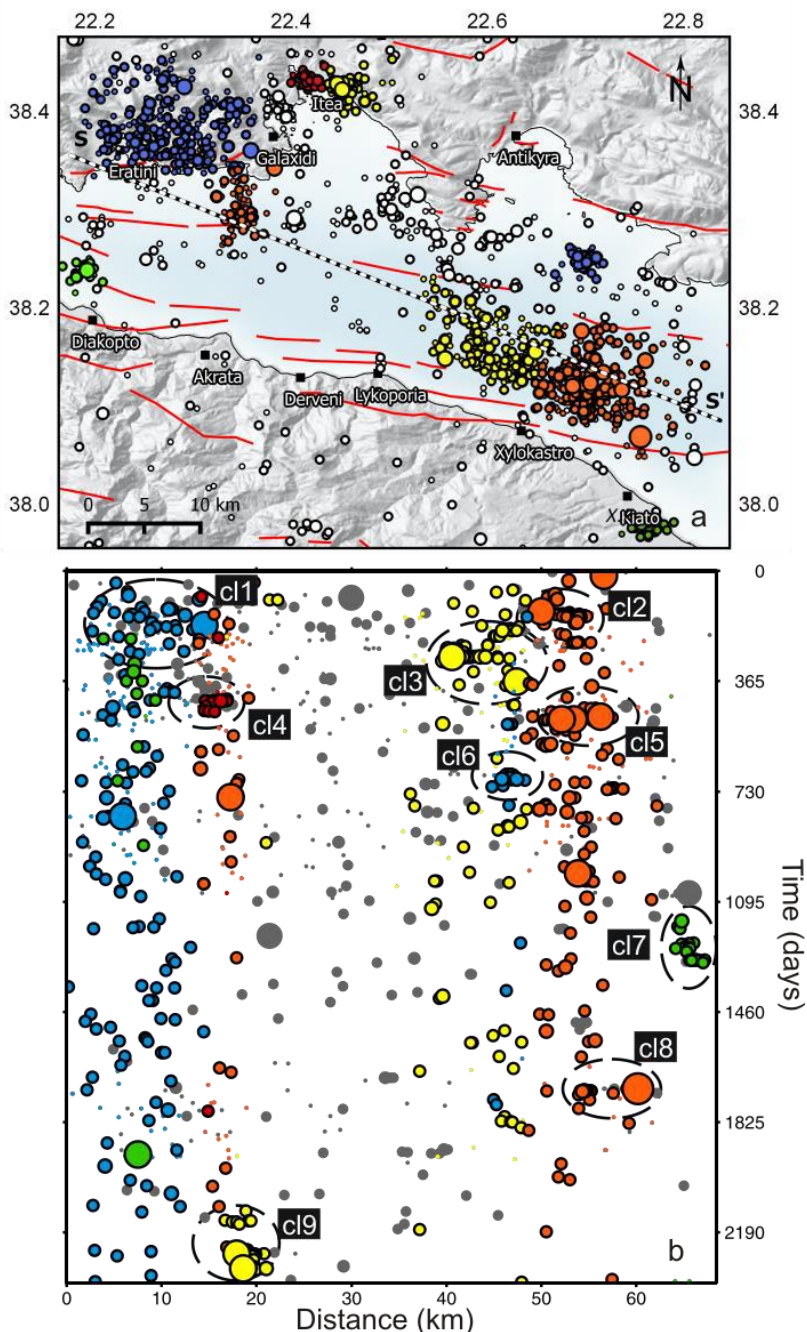


Figure 2-56. a) Map view of the relocated seismicity for 2008 - 2014 in Xylocastro area. SS' line shows the profile along which the space time plot is constructed, b) Space-time plot of the seismicity distribution, where earthquake epicenters are projected onto the vertical plane along SS'. Corresponding colors are used between the map view and the section.

Table 2-9. Table of the extracted clusters with the application of the spatiotemporal tool. Information is given on the number of the events, the duration of the seismic excitation and the maximum magnitude (M_{max}).

n	Date of the 1 st event	Number of events	Duration (in days)	Rank of M_{max}	M_{max}
n1	18.09.2008	11	14.21	4/11	3.6
n2	12.01.2009	35	13.50	1/35	4.0
n3	27.04.2009	14	15.77	9/14	4.3
n4	12.05.2009	48	9.76	9/48	4.9
n5	16.11.2009	29	4.2	6/29	3.7

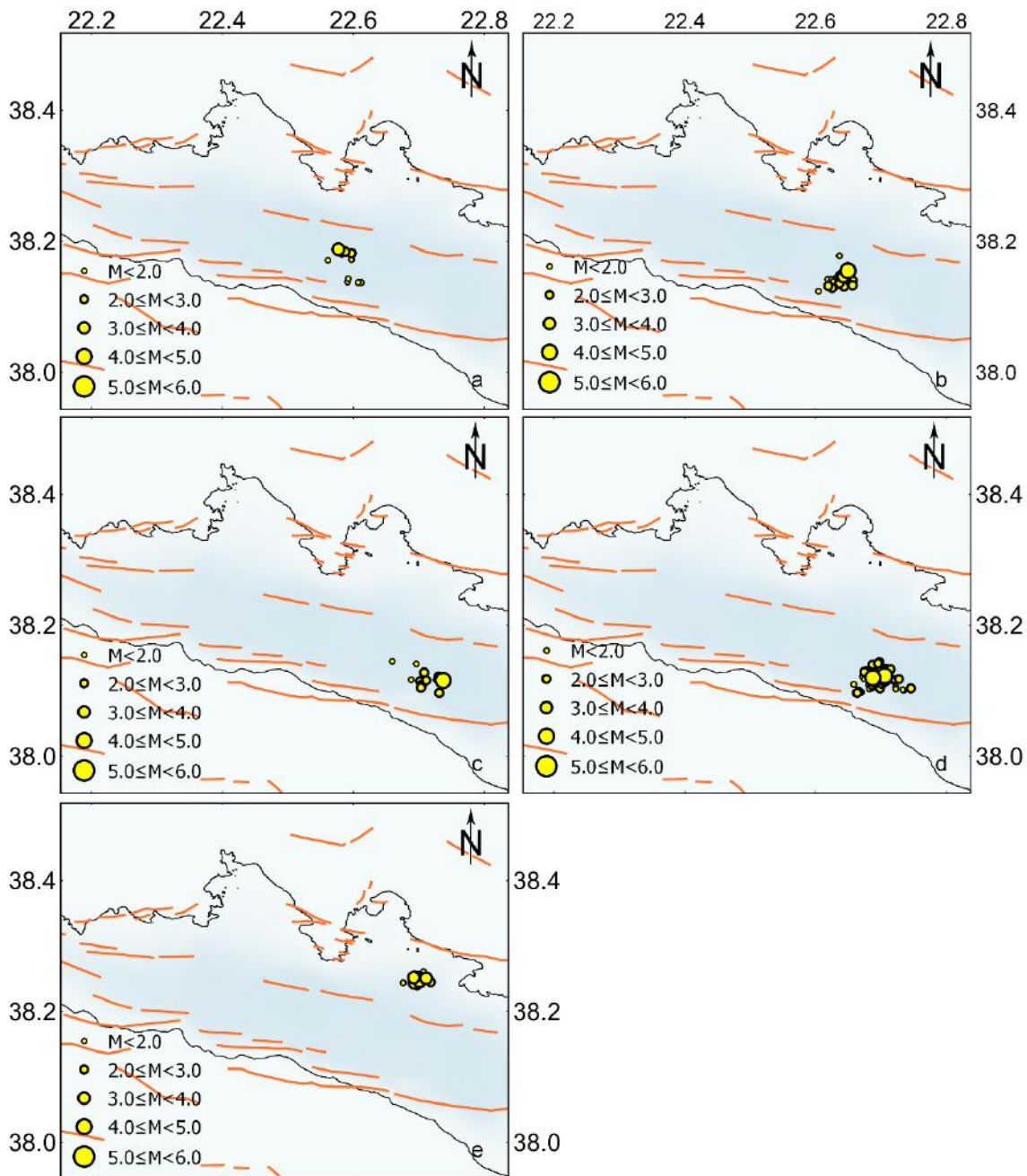


Figure 2-57. a-e) Epicentral distributions of numbered clusters n1 to n5 provided in Table 2-9, which are extracted with the use of spatiotemporal constraints for Xylocastro area.

The earthquake spatial distribution and the distribution at depth is important for revealing fault characteristics. N-S oriented cross sections were constructed in Figure 2-58, with 7km either side (yellow shaded zones). The sections are perpendicular to the active rupture zones in the area. In addition, the evolution of seismicity, although not as intense as at the western part of the rift, is highlighted with the chronological subsets. Seismicity is analyzed into the following periods: i) 01 August 2008 – 17 May 2009 (Fig.2-59a), ii) 17 May 2009 – 07 October 2010 (Fig.2-59b) and iii) 08 October 2010 up to 2014 (Fig.2-59c). As indicated from the previous paragraph, earthquake epicenters during the study period are mainly gathered in two main spatial clusters, the one northern than Xylokastro village and the second one along the northern coast of Corinth rift, between Itea and Eratini. It is also evident that there is a characteristic absence of seismicity between these two locations where Der.F is developed. The western earthquake concentrations at depth are investigated with the use of C₁C₂ and C₃C₄. In C₁C₂ section a cluster of foci is shown at the depth of 15km. The low dip of this zone coincides with the fault plane solution for the M4.5 earthquake (304°/52°/-62°). An indication of south dipping faults are highlighted with the distribution of foci under the mainland southern coasts. This area is associated with the M5.9 Galaxidi earthquake in 1992 with its epicentre southern of Galaxidi.

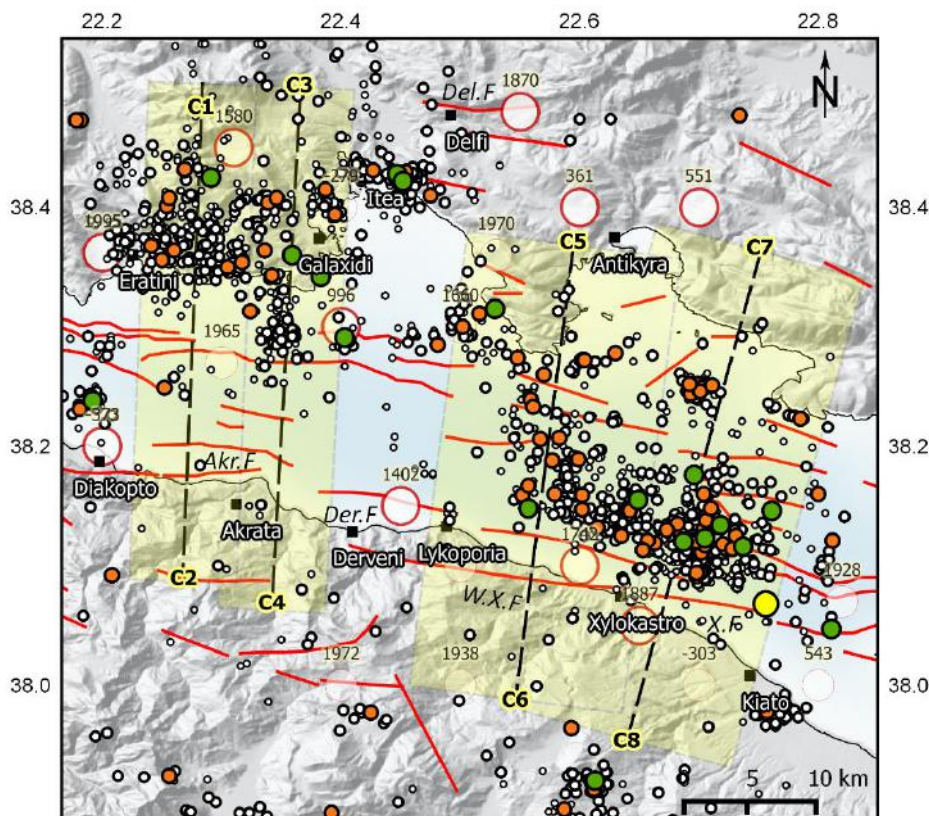


Figure 2-58. Relocated seismicity for Xylokastro area. Dashed lines correspond to the cross sections and the transparent rectangles to the width of its section which is equal to 7km in each side. Red circles correspond to the strong earthquakes with $M \geq 6.0$ which have occurred since 480BC (Papazachos and Papazachou, 2003)

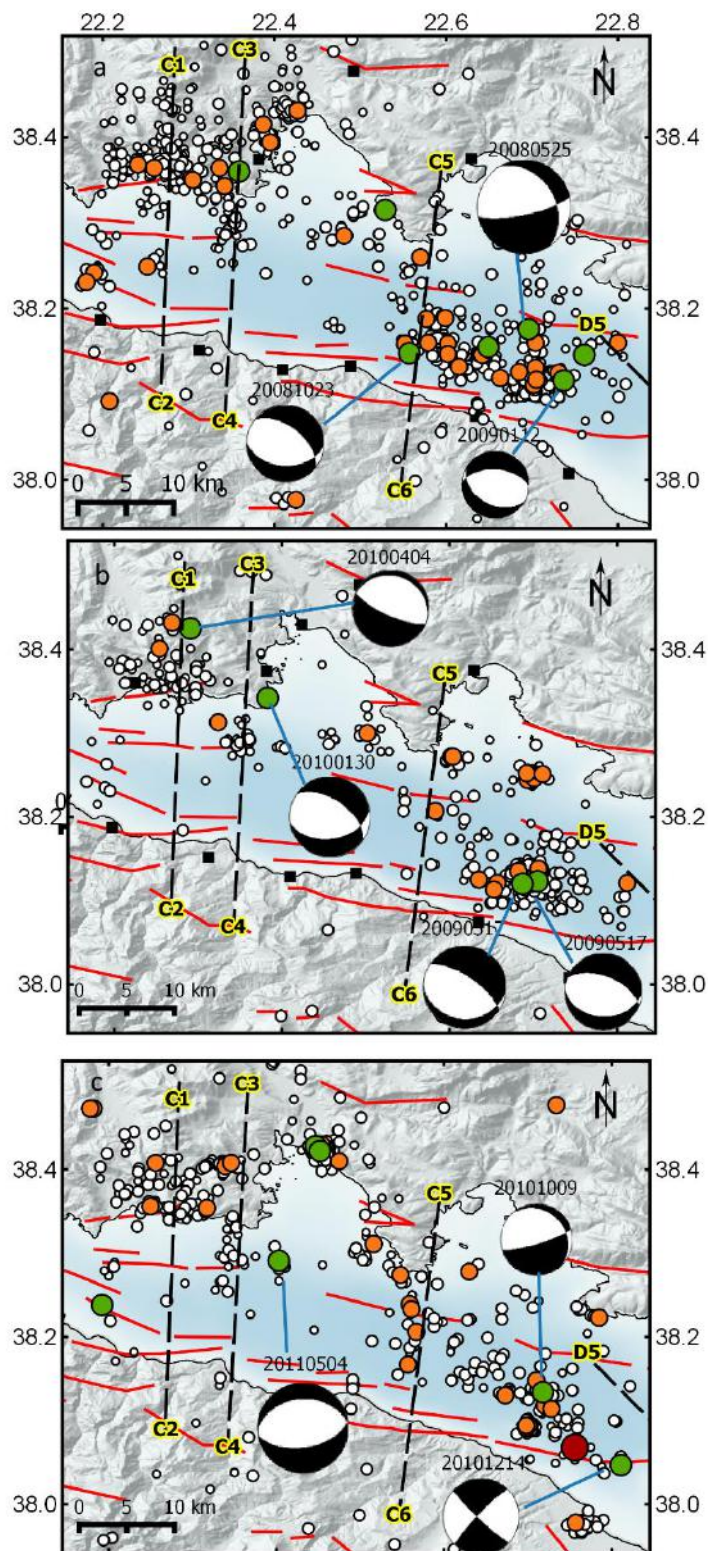


Figure 2-59 Epicentral distribution of earthquakes in Xylocastro area, along with the location of the cross sections for a) August 2008 – 17 May 2009, b) 18 May 2009 – 07 October 2010, c) 08 October 2010 up to the end of 2013. Dashed lines present vertical cross sections with 10km width.

Table 2-10 A list of available fault plane solutions for small and moderate magnitude earthquakes in the time interval 2008 – 2014.

No.	Year	Time	Lat	Lon	M	Fault Plane 1			Fault Plane 2			Ref.
						ζ	dip	rake	ζ	dip	rake	
1	20080525	151137.9	38.214	22.808	4.8	327	34	-25	78	77	239	(1)
2	20081023	021710.1	38.169	22.455	4.2	308	54	-67	92	42	242	(1)
3	20090110	222623.8	37.995	21.575	4.3	282	48	-9	18	84	222	(1)
4	20090112	201208.5	38.162	22.652	4.0	119	40	-70	274	52	-106	(1)
5	20090509	014602.9	38.126	22.726	4.3	279	48	-78	81	43	257	(1)
6	20090517	115903.6	38.127	22.690	4.5	291	57	-80	94	35	255	(1)
					4.6	282	49	-91	103	41	-89	(2)
					4.9	298	35	-75	101	56	-100	(3)
7	20090517	223926.4	38.123	22.680	4.2	304	69	-78	91	24	240	(1)
					4.2	273	48	-85	85	43	-96	(2)
8	20100130	134738.7	38.329	22.387	4.5	304	55	-62	82	42	-124	(1)
9	20100404	220556.7	38.401	22.319	4.1	114	74	-89	292	15	-92	(1)
10	20101009	190449.7	38.152	22.720	4.5	316	20	-29	74	81	253	(1)
11	20101214	135852.9	38.068	22.788	4.1	133	84	-7	224	83	186	(1)
12	20110504	123943.5	38.275	22.427	4.0	81	54	-93	265	35	-86	(1)
13	20110714	084156.1	37.823	22.611	4.2	253	79	59	146	32	159	(1)
14	20121209	012306.2	37.929	22.609	4.1	97	59	-87	271	31	-95	(1)
					4.3	289	46	-81	96	45	-99	(2)
15	20130428	044957.0	38.257	22.222	4.3	128	80	78	358	16	139	(1)

1. NOA, 2. AUTH

Hatzfeld et al (2000) who analyzed the seismic sequence suggested that the earthquake as well as the aftershock sequence is attributed to an ESE-WNW normal fault plane dipping 30° to the north. The depth is assigned to 7.5km, whereas the aftershock foci range between 6 and 15km. Hatzfeld et al (2000) inferred that the causative fault for that sequence was consistent with Aigion fault.

The construction of C₅C₆ and C₇C₈ sections contributes to the identification of the structures to the east. Seismic activity is mainly attributed to a north dipping fault where a number of earthquakes stronger than M4.0 occur during a seismic swarm. The seismogenic layer is ranging from 5 to 16km. It seems that compared to the western part of Corinth rift, seismogenic depths are larger and dips are steeper. To the east of the area, there is a small number of earthquakes, the same as in 1965 Erateini fault and probably it is related to an asperity between Helike and Xylocastro fault (Hatzfeld et al., 1996). The maximum earthquake which struck the area was equal to Mw5.0 and occurred in 2012, May 23rd close to Kiato, to the northern boundaries of Peloponnese. Especially in Xylocastro, the seismic activity culminated in the strong event of May 23. HypoDD was also used for the relocation of earthquakes which were also analyzed with the use of HypoDD algorithm. HypoDD was applied in specific clusters and the results are depicted in the following figure for the four aforementioned sections.

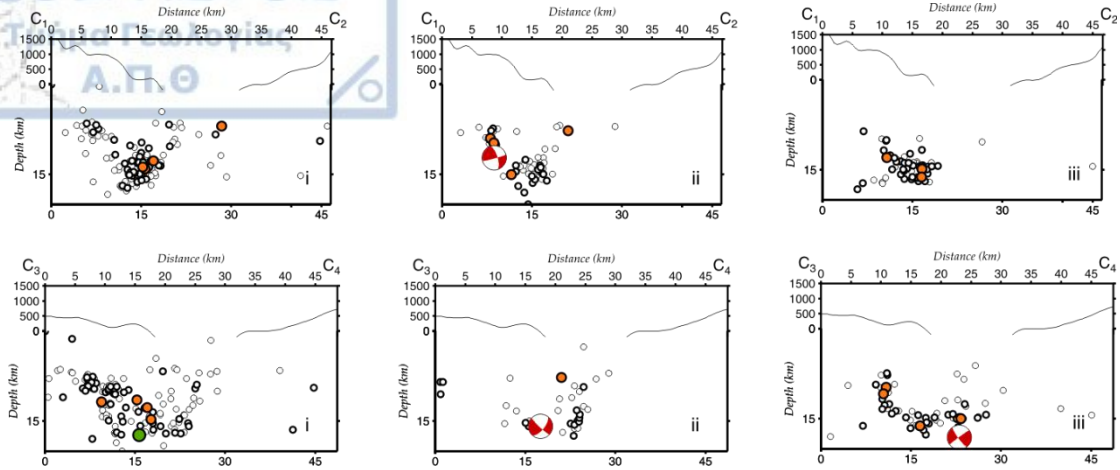


Figure 2-20. Successive chronological cross sections in Xylocastro area, along the profiles C_1C_2 and C_3C_4 for different time intervals (i, ii and iii).

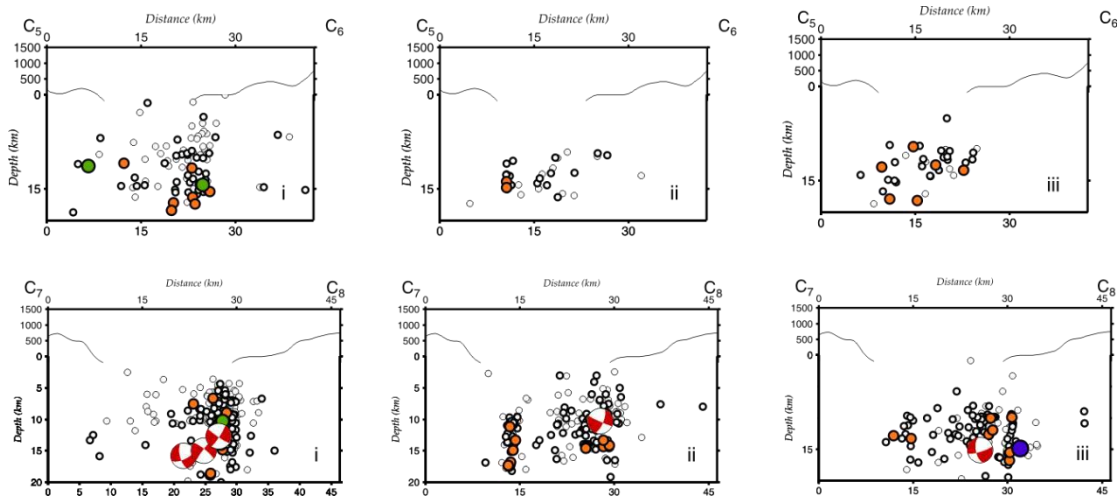


Figure 2-61. Successive chronological cross sections in Xylocastro area along the profiles C_5C_6 and C_7C_8 for different time intervals (i, ii and iii).

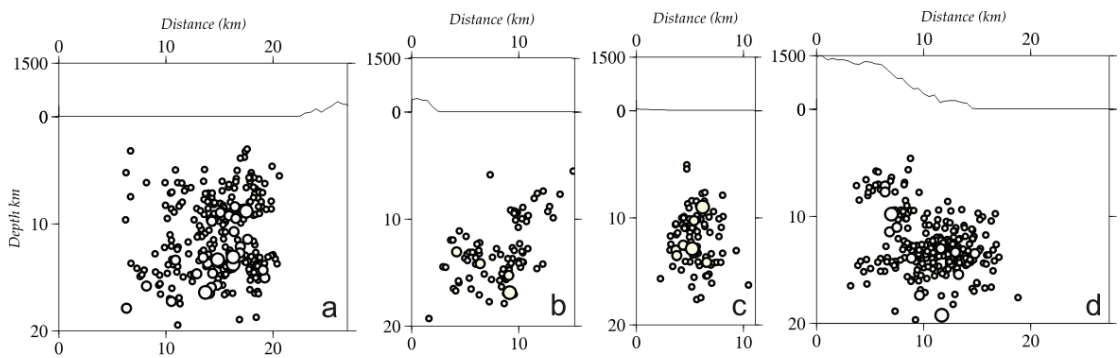


Figure 2-62. HypoDD results for the sections, a) C_1C_2 , b) C_3C_4 , c) C_5C_6 and d) C_7C_8 in Xylocastro area.

2.9.12 Seismicity investigation for the Alkyonides area

2.9.12.1 Spatiotemporal Seismicity Analysis

The easternmost part of the study area comprises the termination of Corinth rift to the east, where it is subdivided into two semi-parallel gulfs, the Alkyonides and Lechaion gulfs and encloses the coastal northeast Peloponnese and southern central Greece, the Megara basin and the footwall of Theves basin. This part is associated with strong earthquakes and it is especially well known for the recent triplet of Alkyonides in 1981 February (M_w 6.2 and M_w 6.7) and March (M_w 6.4). An array of normal faults synthesizing the footwall of the Corinth rift with Perachora offshore, Skinos, Aleporchori and Kaparelli faults along with the sub-basins fault boundaries in Alkyonides gulf from north and south, whereas Kechries onshore fault is also associated with strong earthquakes.

The spatiotemporal earthquake distribution in Alkyonides area, was investigated with a seismicity space – time diagram ranging from 2008 to 2014 (Fig.2-63b). The 68km long section (SS') along which earthquake epicentres are plotted as a function of time and space, extends in a NW-SE direction following the coastal morphology (Figure 2-63a). The interpretation of the distribution is facilitated with the use of different colors for the corresponding clusters in both the map view and the section. In the beginning of 2008, earthquake activity is mainly located at the northern boundary of Megara basin, at the northern part of Peloponnese coasts and at Perachora peninsula, offshore. Seismicity at the north boundary of Megara basin is manifested with the occurrence of two clusters close in time. The first cluster consists of events with small magnitudes (cl1 – green color) and maximum magnitude M 3.2, lasts for some months and culminates in a second cluster (cl2- green color) with maximum magnitude M 4.4 (2009.09.02) followed by fewer events. Seismicity there defines a rupture zone with 7km in length. In 2010 (2010.09.02) a M 4.2 earthquake occurs (cl3 - orange color) close to Kaparelli village and it is followed by a small number of aftershocks. There is a synchronous earthquake occurrence with rather steady rate at the northeastern part of Peloponnese, along the rupture zone of Kechries fault (epicentres in blue color) where a moderate magnitude event occurs in 2012 (2012.02.17) (cl4 – blue color). An adjacent event of large depth (M 4.2) which is also depicted in the map, occurred (not involved in the relocation process). In 2013 (2013.09.20) a M 4.4 event occurred offshore in Alkyonides gulf, after a seismic excitation which preceded in 6km distance (cl5 – red color) and lasted for few days. During the entire study period, there is also a band of seismic activity offshore, along Perachora fault with a steady occurrence of minor events (yellow color). The temporal distribution of seismicity at the easternmost part of the Corinth rift shows the existence of small magnitude clusters with short duration. Perachora peninsula and Korinthos experience seismicity which lasts for a long period, exhibiting a low seismicity rate. Seismicity is concurrent at both the northern and the southern boundaries of the study area, while short excitations are mostly concentrated at the onshore area of central Greece. High clustering compared to seismicity rates in this area were searched with the MYSTIC spatiotemporal criterion of Leptokaropoulos and Gkarlaouni (2016) for which the given spatiotemporal criteria for maximum inter-event time between

subsequent events equal to 3 days, maximum distance between earthquakes epicentres and the cluster gravity centre equal to 8, for a minimum number of 10 events in each cluster five clusters were defined (Table 2-11, Figure 2.64). The clusters which are all located at the NW part of the study area, are short in time lasting from 3.47days to 8.74days and they consist of 10 to 24 events. Maximum magnitude is $M_{max}=3.5$ for cluster n4 lasting 6.67 days along the southdipping Megara fault (Fig.2-64d).

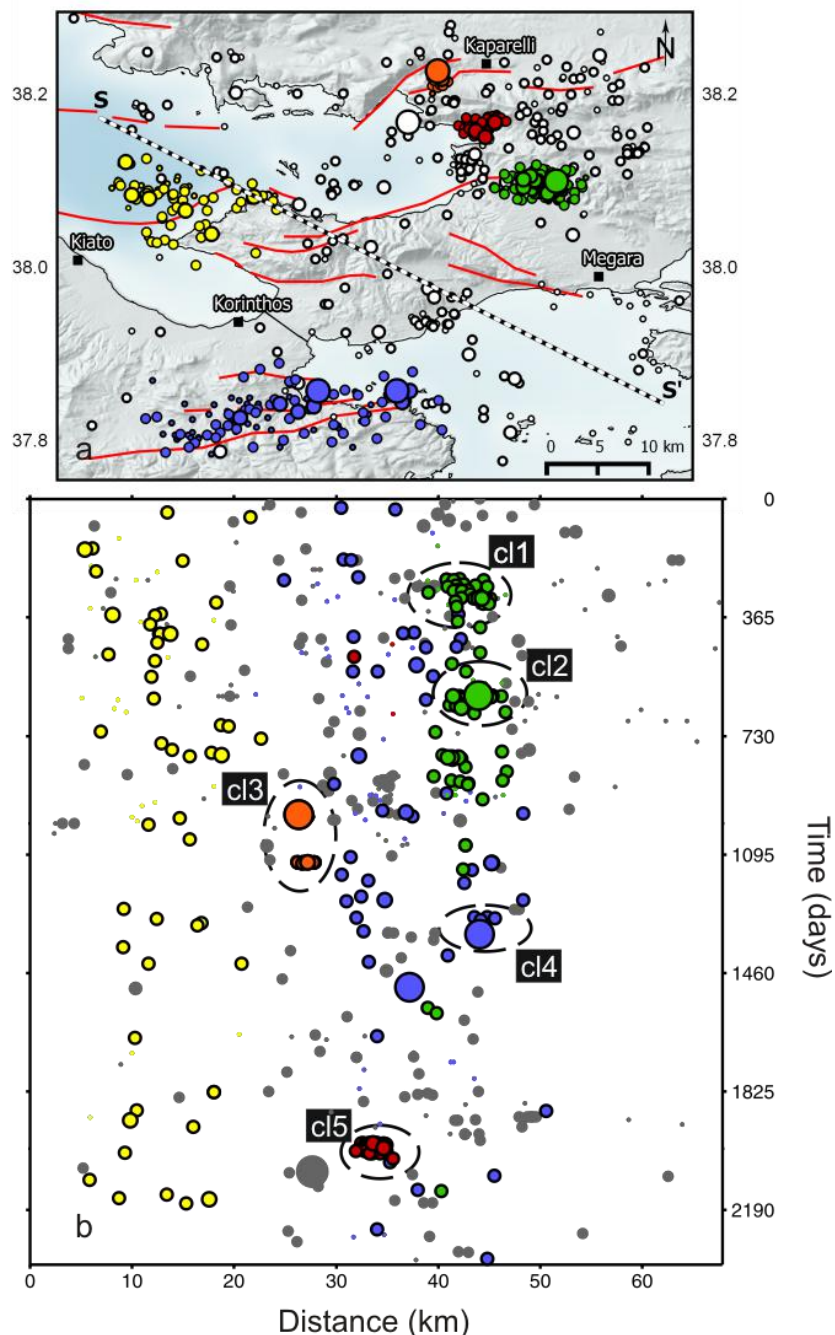


Figure 2-63 a) Map view of the relocated seismicity for 2008 - 2014 in Alkyonides area. SS' line shows the profile along which the space time plot is constructed, b) Space-time plot of the seismicity distribution, where earthquake epicenters are projected onto the vertical plane along SS'. Corresponding colors are used between the map view and the section.

Table 2-11 Table of the extracted clusters with the application of the spatiotemporal tool (MYSTIC). Information is given on the number of the events, the duration of the seismic excitation and the maximum magnitude (M_{max}).

n	Date of the 1 st event	Number of events	Duration (in days)	Rank of M_{max}	M_{max}
n1	28.09.2008	10	4.02	4/10	3.2
n2	08.10.2008	10	8.74	6/10	2.7
n3	11.06.2013	19	6.67	5/19	3.5
n4	22.06.2013	24	3.47	20/24	3.2

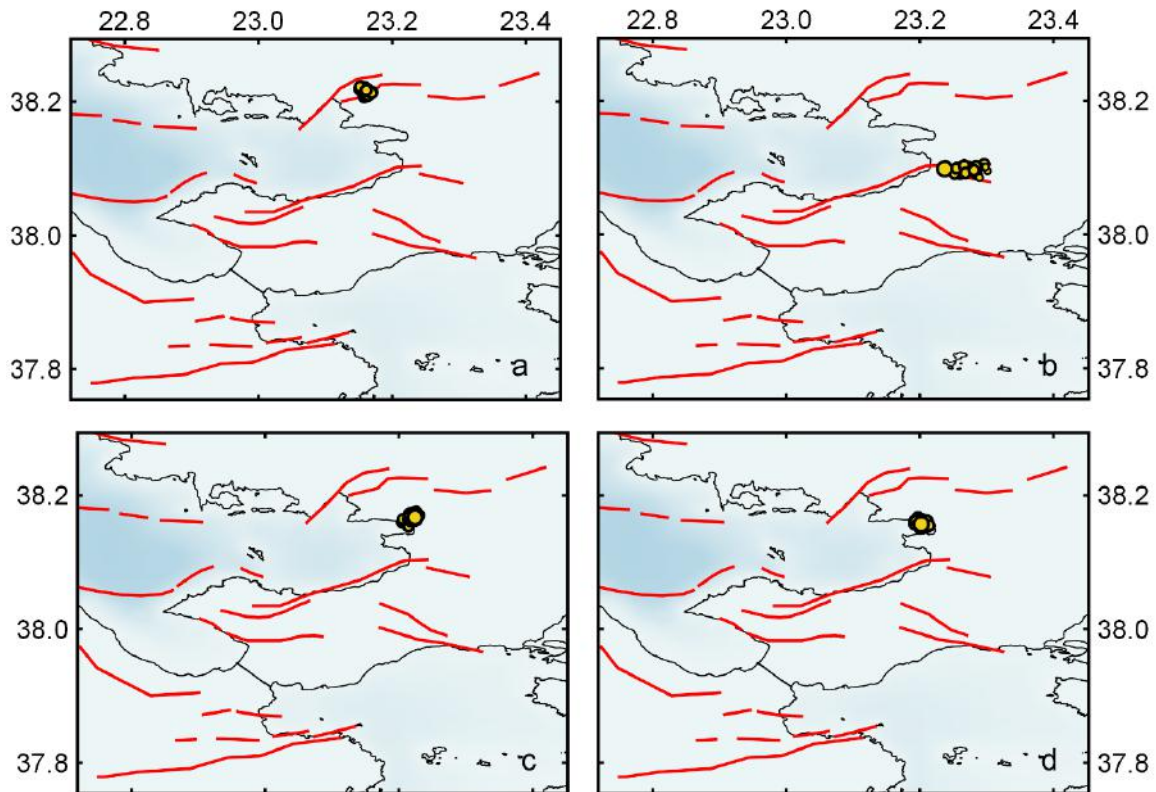


Figure 2-64. Spatial distributions of the clusters n1 to n4 extracted with MYSTIC spatiotemporal tool (Table 2-2). Cluster information is given in Table 2-11 with a) n1, b) n2, c) n3 and d) n4 cluster.

The criterion shows that high clustering occurs only in the southdipping fault of this area, whereas at the northdipping faults seismicity is constant through the time studied.

2.9.12.2 Spatial Seismicity Analysis

For the period 2008-2014, the earthquakes with relocated coordinates with maximum magnitude equal to $M_{4.4}$, were redefined exhibiting a much lower seismicity rate compared to the other parts in the rift. The strongest earthquake is a $M_{4.8}$ event which occurred in 2008 in NE Peloponnese an earthquake with large depth not included in the investigation of the present study. Relocated with the Hypoinverse algorithm earthquakes are displayed in Figure 2-65 where strong historical and instrumental earthquakes which have occurred since 480BC summarized in Papazachos and Papazachou (2003) and the locations of cross sections are displayed. No strong earthquakes occurred during this time. Seismicity in Alkyonides is localized, forming specific bands along rupture zones and small earthquake clusters confined in the northeastern part of the study

area. There is an absence of seismicity along the seismogenic faults of the Alkyonides seismic sequence and in the broader Alkyonides Gulf, with the exception of seismicity existence between Livadostras and Kaparelli faults.

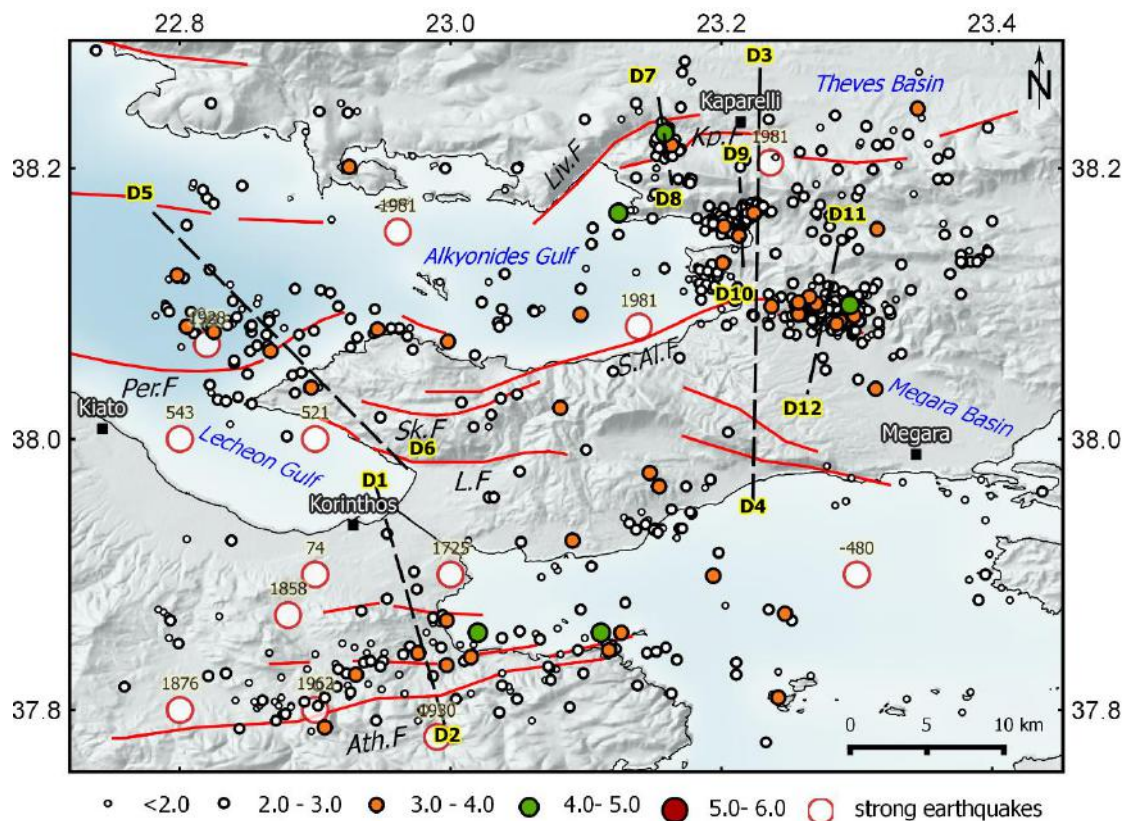


Figure 2-653 Map with relocated seismicity for Alkyonides area. Dashed lines represent the cross sections whose width is equal to 15km alongside. Red circles correspond to the strong earthquakes with $M \geq 6.0$ which have occurred since 480BC (Papazachos and Papazachou, 2003) (Kech.F.: Kechries, Per.F: Perachora, Sk.F: Skinos, S.Ak.: South Alkyonides, Liv: Livadostras, Kp: Kaparelli, fault information according to Bernard et al., 2006).

Table 2-12. Available fault plane solutions for small and moderate magnitude earthquakes in Alkyonides area for 2008 – 2014.

N _o	Year	Time	Lat	Lon	M	Fault Plane 1			Fault Plane 2			Ref.
						ζ	dip	rake	ζ	dip	rake	
1	20100902	035304.5	38.229	23.167	4.2	264	54	-88	81	36	267	(1)
					3.9	98	79	-33	195	58	-167	(2)
2	20120217	080504.6	37.862	23.019	4.0	121	42	-87	297	47	-93	(1)
3	20130920	020519.9	38.168	23.130	4.4	217	46	-113	69	49	-68	(1)

1.NOA, 2. AUTH

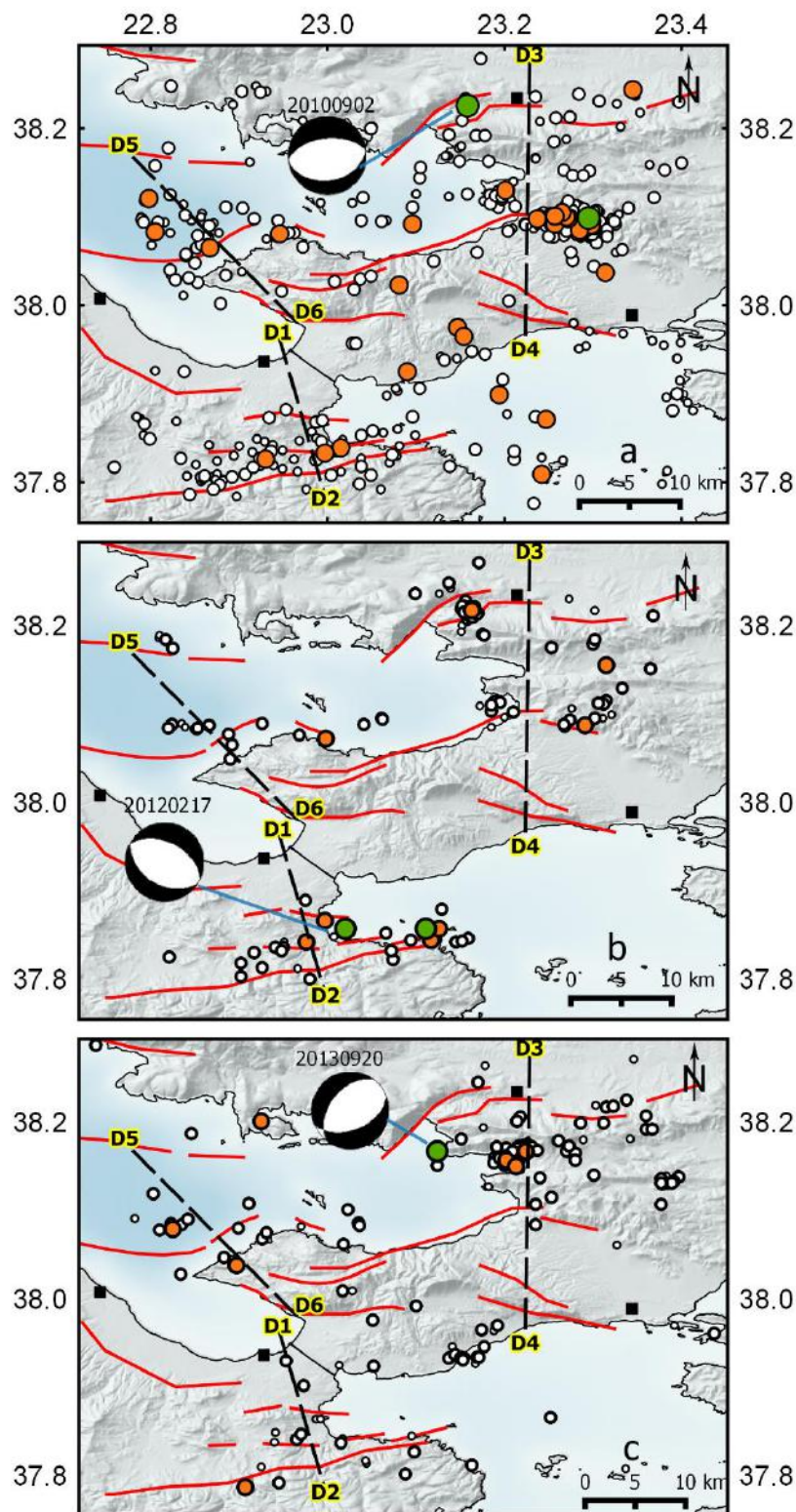


Figure 2-66 Successive chronological maps of seismicity in Alkyonides area for a) August 2008 – 03 September 2010, b) 03 September 2010 – 20 February 2012, c) 20 February 2012 to June 2014. Available fault plane solutions (information in Table 2-12) and the locations of cross sections for relocated seismicity with Hypoinverse algorithm are also plotted.

Chronologically the period is divided into three successive time intervals for: i) August 2008 – 03 September 2010 (Fig2-66a), ii) 03 September 2010 – 20 February 2012 (Fig2-66b) and iii) 20 February 2012 - June 2014 (Fig2-66a) for a better understanding of the seismicity evolution. Available fault plane solutions are also added (Table 2-12). Seismic activity in the first interval is relatively higher compared to the next intervals (Fig. 66-a). Earthquakes are distributed along Kechries fault and their epicentral distribution defines a 24km long rupture zone. Seismicity is rich at the northern boundaries of Megara basin with the M4.4 event in a 7km long rupture zone defined by the spatial distribution of the earthquake cluster. A M4.2 earthquake occurs close to Kaparelli village whose aftershock activity is presented in Figure 2-2-66b. The available fault plane solution corresponds to a normal fault (rake: 267) with 81° strike dipping 36° to the south. In the following two chronological intervals, seismicity is sparse, characterized from activity forming small clusters. During the second interval (Figure 2-66b) the aftershock sequence of Kaparelli earthquake shortly continues, while the bulk of seismicity is met along Kechries fault where the event of M4.0 occurs. According to the fault plane solution, the earthquake is attributed to a normal fault (rake=-93°) with a 297° strike, being in good agreement with the geomorphological outcrop of Kech.F. The distribution of minor earthquakes define an active zone of approximately 25km in length. During the third time - interval a seismic burst occurs southern than Kaparelli fault (Figure 2-66c) while, after the end of this excitation, as shown at the space time plot, a M4.4 event occurs (strike= 69°, dip=49°, rake=-68°).

For the most accurate description of seismicity at depth, and the association with causative faults, a number of chronological cross sections are constructed perpendicular to the strikes of the main faults, such as Kech.F, Kp.F and Liv.F as well as Per.F (Figure 2-67). The width of the cross sections is 5km alongside. In detail, D₁D₂ cross section in NW-SE direction is perpendicular to Kech.F. The angle dip is higher than 46°, estimated with the fault plane solution but it is consistent with the geometry properties of Kechries fault also given by geological observations.

D₃D₄ cross section lies in a NS direction and is almost normal to the northern boundaries of Megara basin and Kp.F. Foci distribution in all subsets generally shows an antithetic geometry to the Corinth rift footwall. Clusters cl.1, cl.2, cl.3 and cl.5 are investigated with the use of D₃D₄ section. The distribution of the earthquake foci in (i) and (ii) chronological sections define a rather narrow and steep rupture zone dipping to the North. In subset (i) the M4.2 earthquake is depicted. The earthquake depth is 16km whereas the aftershocks depths vary from 6-13km (ii) defining a fault dipping steeply to the south, probably attributed to Liv.F. In addition with Kaparelli aftershocks subplot (ii) depicts a group of earthquake foci with minor magnitudes which exhibit a slight dip to the North. Finally in subset (iii) the depth distribution of the cluster cl.5 is shown. A southward dip of the causative fault zone is indicated. Most of the focal depths are ranging between 3-14km. Finally the fault plane mechanism of M4.4 earthquake is plotted however the absence of aftershocks gives no clear impression for the causative fault. It is characteristic that both earthquakes that occurred in the area originated at the same depth. There is indication that dipping planes correspond to both southdipping and northdipping faults. Results come into

agreement with Hatzfeld et al. (2000) who established a transient deployment and suggest that both southdipping and northdipping faults in the area are seismically active and there is no clear evidence of the dipping planes. An impression of Perachora peninsula seismicity is gained with the construction of D_5D_6 where seismicity is constant without seismic excitations. It is clear that in this cross section the distribution of depths ranges between smaller depths and shows a stronger similarity to the depth distribution of earthquakes at the central and the western part of the gulf.

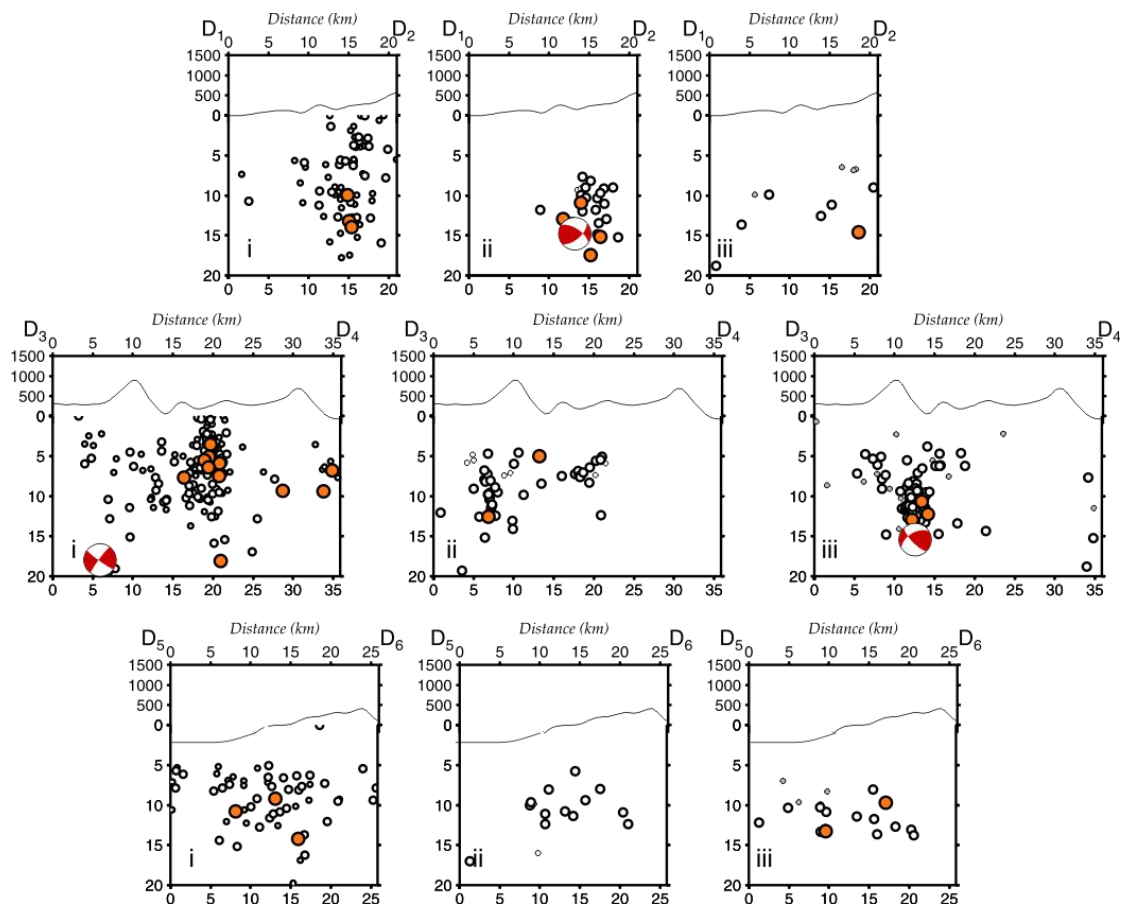


Figure 2-67 Chronological cross sections with earthquake depths for the eastern part of the Corinth rift for the sections D_1D_2 and D_3D_4 and D_5D_6 for three distinctive (i), (ii) and (iii) periods which agree with Fig.2-66, where the exact location of the cross sections are demonstrated.

HypoDD relocation results for specific seismicity clusters were compiled based on the clusters cl1, cl2, cl3, cl4 and cl5. After the first relocation procedure, where an impression was gained about the structures at depth, the HypoDD algorithm was additionally applied. Results show that there is an improvement in the relocation analysis for this part of the Corinth rift and cross sections are used to highlight this differentiation of the results. To the south of the study area, D_1D_2 cross section (Fig. 2.67a) which is normal to Kechries fault shows a denser HypoDD hypocentre concentration at depth compared with Hypoinverse depths. The majority of the hypocentres range from 8 to 12km and they define a rupture plane which is less steep dipping to the North than what Hypoinverse results indicated. D_5D_6 cross section (Fig. 2.67b) which is normal

to the eastern termination of Perachora fault exhibits a shift of hypocentres to shallower depths and the cluster indicates a low angle fault plane dipping to the North and they are in accordance with the fault properties of Perachora fault. The geometry of the northeastern part seismicity at depth was described in D₃D₄ cross section, whereas for a detailed representation it is now substituted from sections D₇D₈ (Fig 2.67c), D₉D₁₀ (Fig 2.67d) and D₁₁D₁₂ (Fig 2.67e). Seismicity cluster presented in D₇D₈ is confined between Livadostras Fault and the western termination of the Kaparelli Fault. Although the dipping plane is poorly constrained there is an indication of the cluster dipping to the south. The distribution of depths for earthquakes included in D₁₁D₁₂ cross section is shallower compared to the other cross sections of the same area and they range between 3km and 10km with few foci reaching 12km at depth. Seismicity is associated with small structures in the area.

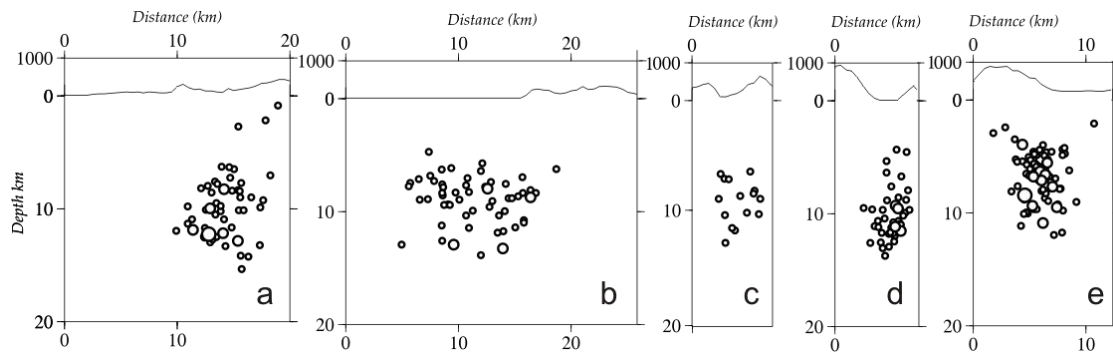


Figure 2-68 Cross section on relocated seismicity with the use of HypoDD algorithm. a) section D₇D₈ b)section D₉D₁₀, c) section D₁D₂ d) section D₁₁D₁₂ e) section D₅D₆

2. 10 Conclusions and Discussion

The investigation of earthquake properties regards a fundamental tool for constraining the geometric properties of the activated structures (fault segments or fault systems) (Kagan and Jackson, 1998) especially in the case of faults which lack a surface expression. In this study, long term seismicity between 2000 and 2016 in Mygdonia was relocated and an accuracy improvement was achieved in order to unveil the properties of the associated fault population. The incorporation of the best well-fitted velocity model, the calculation of station time delays and the velocity ratio, were prerequisite and individually contributed to diminish earthquake coordination errors. The microearthquake study in the area of Mygdonia, has contributed to a better understanding on fault activation and their properties, taking advantage of the epicentral and foci distribution of the relocated seismicity. Although this area has often been struck by disastrous earthquakes, there is considerable lack of assurance regarding the estimated macroseismic epicentres and magnitudes of the historical earthquakes. Taking for instance the 1902 Assiros earthquake there is a disagreement about the causative fault segment, with Papazachos and Papazachou (2003) suggesting a Sochos fault reactivation whereas Pavlides (1996) considered the Gerakarou fault segment for a seismic activation. Geological evidence out of paleoseismological information is also inadequate to shape the pattern of earthquake occurrence along northdipping segments due to the complexity in the segmentation of the studied rupture zones (Chatzipetros, 1998). Therefore the accurate location of the strong earthquake epicentres is crucial and for this reason microseismicity was engaged to configure seismic faults. The previous research was based on limited local network data are now extended after a long-term seismicity observation. The stress field in Mygdonia graben shows a general N – S extension, exhibiting a spatial variation of the least stress axis orientation from NNW – SSE to NNE – SSW which also agrees with the "S-shaped" basin formation (Vamvakaris et al., 2006; Mountrakis et al., 2006). The widespread extension has been measured by different studies and in every case the fault plane solutions totally agree with the foci distribution and the geometry of the active faults. The barrier raised for the clear determination of fault seismogenesis is connected with the fact that the fault network is composed of a synthesis of fault orientations whose strike is aligned with the stress tensor in the region and secondary faults which exhibit an NW-SE activation that corresponds to older structures which are seismogenic.

Our perception about the width of the brittle crust and the dips of the active faults was enhanced by investigating the hypocentral distribution with the use of successive profiles, normal to the major faults strike. The majority of the foci depth range between 3km and 16km, defining the width of the seismogenic zone. Seismogenic structures, especially the ones which are strongly influenced from the previous seismotectonic episodes comprise inherited structures with low seismicity forming fault planes with high dipping angles. The complex seismotectonic episodes have been imprinted on the structures after the clockwise rotation of the region and consequently a relative rotation of the active stress field (Pavlides et al., 1988; Kissel et al., 1985). The epicentral

distribution of the earthquakes is in a good agreement with the fault trends and the minimum stress axis (σ_3) calculated with the use of seismological data (Vamvakaris et al., 2006).

A striking observation as deduced from the temporal and spatial analysis is that seismicity is not evenly distributed in the entire area but occurs along deformation bands in space and time. There are not significant seismic sequences observed during the study period, with the exception of some well- defined small clusters with a small number of earthquakes and a short temporal duration, extracted with the use of strict spatiotemporal criteria. There is an evidence that minor clusters are also triggered in adjacent faults like in the case of clusters N°5, N°6, N°7 and N°8 (Fig.2-14) exhibiting a migration of clusters from the western termination of NApF to SochF and then to the eastern termination of NApF. The cascade of moderate events at the northern margin of Volvi Lake shows that there is an indication of interaction between the north and southdipping faults in this part of the graben.

There are large areas which are deprived of seismicity such as Anthemountas basin, central Chalkidiki, and eastern Chalkidiki. It is generally inferred that there are zones that although have the potential to generate earthquakes they are lacking seismicity in the last years, like the epicentral area of 1978 earthquake sequence, probably attributed to the widespread stress release which hinders the possibility of earthquake occurrence along this fault, a suggestion also stated by Tranos et al. (2003). It is questioned if moderate slip rates accommodated with approximately 1mm/yr (Kotzev et al., 2001) are efficient to recover stress values after the last strong event across TGFZ to a new critical point for a new strong earthquake occurrence. On the other hand, it is observed that Arnea region which suffered the last strong earthquake in 1995, exhibits a constant occurrence of minor earthquakes, with magnitudes $M \leq 4.8$ that seems to be a direct consequence of lateral stress increase after the 1978 strong event. In the fourth chapter of the study, more light is shed into the possible reasons why seismicity in this part of the study area has been increased based on the Coulomb stress changes in the area.

Earthquake occurrence in the instrumental period is mainly concentrated in a broad zone running from Assiros through the Lagada and Volvi Lakes to the sea at Stratoni. Seismicity in the western part of the area is mainly located west than Assiros, around Asvestochori and to the north of Lagadas Lake, with minor clusters. Seismicity in this part is adjusted to the coexistence of two characteristic sets of faults that accommodate stress. It is evident that a big amount of earthquakes is generated along the NW-SE sub-basin of Lagadas Lake bounded from AAF and LAVF fault zone, with a likelihood that both boundaries are seismogenic. Evidence is not very clear for the antithetic LAV fault due to the vertical or nearly vertical fault planes which are observed in the foci profiles.

Earthquake epicenters are also located at the conjunction of SochF and AAF, implying that a possible propagation of SochF to the west is probably causing the activation of AAF, whose general strike is not oriented in accordance to the least principle stress axis. The earthquake foci planes dipping to the southwest are formed in large dips with approximately 70°- 80°, a fact which is in agreement with the statement of Pavlides and Kiliadis (1987) who affirmed that especially the south dipping faults are closely related to high angle normal faults, a fact also noticed for Sochos

fault. Around Asvestochori area there is an earthquake concentration probably showing a NE-SW trend, however it is not clear whether they are attributed in a fault of this direction. Foci distribution below in Lagadas Lake as it can be ascertained shows a gradual reduction of dip and an association is confirmed with both northdipping and southdipping faults.

As far as the eastern part of the study area is concerned, it is clear that seismicity shows a strongly clustered pattern and a tendency for migration between moderate earthquakes and minor earthquakes clusters. Numerous earthquakes are located at the western and northwestern edge of Volvi Lake, at the conjunction of NAp fault segment with Stivos segment and to the south of Arnea. Fault plane solutions for Volvi area in general correspond to normal faulting with high angles and they are mostly attributed to the E-W trending north dipping fault system. The seismic activity of MF segment which is a segment of Sochos linked with a stepping like morphology is ascertained by the occurrence of a minor cluster which clearly shows a southdipping fault plane. Moderate seismic excitations are attributed to "Sochos" fault with foci reaching 17km in depth, whose fault plane is well-defined (Fig.2-69). The structure of SochF at depth has not been revealed before. The southern zones are also seismogenic, exhibiting lower dip angles. Diffuse off fault seismicity is also evident especially in Arnea, to the northeast of Poligiros where uncorrelated moderate events, not followed by an aftershock sequence, occasionally occur. The relocated foci after the employment of hypoDD algorithm show a clear view of the causative fault plane dipping to the northwest at approximately 45°-50° and it is about 10km long.

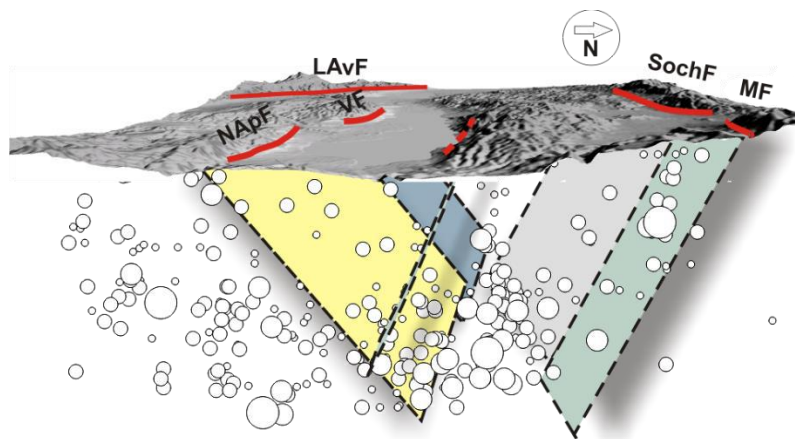


Figure 2-69 Three dimensional representation of the eastern part of Mygdonia graben.

The study area is characterized by the existence of horsts and graben and could be approximated with a basin-and-range like topography. According to Goldsworthy et al. (2001) there is a preferential migration of fault activity to the hanging wall of the basins in Greece. The foci distribution in the area of Mygdonia reveals the profound activation of both southdipping and northdipping normal faults. SochF and Assiros where seismicity is detected are not purely antithetic to the TGFZ, it bounds the study area, setting a strong geomorphological boundary to the north.

The analysis at depth generally reveals that fault planes indicate steep plane dipping with high angles, which are either vertical or nearly vertical. There are many other areas that vertical

faults within extensional environments have been identified such as in the East African Rift, in Iceland, in Canyonlands National Park, Utah. Several reasons can be responsible for such a fault evolution. Firstly, vertical planes might be either attributed to the fact that faults have been reactivated as inherited structures. The fault network has been activated with a different orientation of the least stress axis. The second reason for the existence of steep faults is probably related with the crust friction properties, since the fault dip development strongly depends on the static friction coefficient of rocks. Experiments have shown that in a given seismotectonic environment where the extension rate is constant, the higher the friction is, the steeper the faults become. According to Doglioni et al. (2015) the high friction areas are in demand of higher energy for reaching failure, so strain rate is higher and there is a likelihood for earthquakes with stronger magnitude to occur, when this threshold is exceeded. In the case of Mygdonia area faults are formed in the Serbomacedonian massif which contains crystalline rocks (gneiss, marbles, amphibolites, etc) with an expected high rock friction and fault planes at depth exhibit nearly vertical zones where a significant amount of gravitational energy is accommodated, that should not be neglected (Thompson and Parsons, 2016). The existence of fluids at the interior of the study zone, is also an additional factor that may influence earthquake occurrence (Mesimeri et al., 2017).

All the available earthquake seismic phases recorded from the permanent network since 2008 to 2014 were processed and relocated for the Corinth Rift. Good accuracy earthquake coordinates is a basic requirement for the precise description of the active fault population in the Corinth Rift, where faulting structures are complex. The preliminary results of earthquake coordinates were redefined by reducing the uncertainties which are involved in earthquake analysis with a series of successive techniques. For the best approximation of the crust characteristics different crust models were used and the variation of the velocity ratio across the Rift was taken into consideration for our calculations, observations which signify the seismotectonic variability across the Corinth Rift. In contrast to Mygdonia graben where seismicity for 2008-2014 is sparse, in the case of the Corinth rift, there is significant seismic activity with strong earthquake $M > 5.0$. Seismic activity with moderate size earthquakes clustered in time and space, along with minor events swarms of short duration are observed, mostly constrained along the north coasts are the main expressions of the last seismicity. The seismicity pattern investigated only over few years, is not totally representative of the seismogenic volume and does not fully describe the fault population and the properties, but gives a sufficient impression of the active fault locations. Recent seismicity in some parts of the Rift in general follows a similar pattern with the one described by previous researchers (Rigo et al., 1996 and Hatzfeld et al., 2000), however there is additional information demonstrated in seismicity for 2008-2014.

Rigo et al. (1996) investigated a $M4.5$ earthquake sequence (July 3rd, 1991) close to Helike fault and observed the low-angle fault plane solutions for this part of the gulf, suggesting that north dipping faults root into the low angle detachment zone. The seismic swarm of 1991 was located in the same area with the 2013 seismic swarm in Efpalio area. Rigo et al. (1996) suggested

that the 1991 seismic swarm is probably attributed to the roots of Mamousia and W. Heliki northdipping faults which interact with the detachment zone at around 10km depth. Pacchiani and Lyon Caen (2010) investigated the M4.3 Agios Ioannis earthquake swarm (April 8th, 2001) proposing that the responsible fault was beyond the already known faults and a new hidden fault Kerinitis Fault, a traverse dextral oblique-slip normal fault with 230° is playing an important role in stress transferring among the parallel north dipping faults. There is not observed seismicity in this fault during this period. Seismicity for 2000-2007 in the western part of the rift has been undertaken by Lambotte et al. (2014) and Kapetanidis (2017), whereas Mesimeri (2018) studied the spatiotemporal properties of swarms in 2008 to 2014.

In central Corinth rift earthquake seismicity is located offshore, trending parallel to Xylocastro fault and at onshore, at the northern coast of Corinth gulf. An array of northdipping en echelon faults exists in this areas with Xylocastro fault system to be associated with the epicentral area of the majority of strong historical earthquakes (1742, 1887). There is synchronous spatiotemporal occurrence of seismicity, with frequent clustered earthquakes with magnitudes $M \geq 4.0$. Most of the clusters are located along Xylocastro fault. The depth distribution shows high dipping angles (45°) to the North (Fig.2.62a) with depths reaching 17km. A zone of seismic quiescence extends for 17km between the two seismicity patches, confined between Xylocastro offshore and Eliki faults. The 2012 seismic excitation with the strongest magnitude M4.8 occurred along the southern coast of the gulf.

Active fault segmentation in the eastern termination of the gulf shows that there is an absence of seismicity at locations where the 1981 Alkyonides strong earthquakes occurred, in the broader area of the Alkyonides gulf, Megara basin and along Kaparelli fault. Minor seismicity clusters are extracted, with magnitudes $M < 4.0$ mostly found onshore and one associated with the southdipping fault segment linking Livadostras fault and Kaparelli faults. Results for the eastern Alkyonides area show that earthquake foci are distributed between 5 and 13km at depth and is in agreement with Hatzfeld et al. (2000) who suggest a depth range between 4km and 14km on this area. Moderate seismicity is also observed along Athikia/Kechries fault forming a high angle fault plane with hypocentres ranging between 8km and 12km at depth. According to the limited information provided by the scarce seismicity and the spatiotemporal analysis in this part of the gulf, there is weak seismicity with small clusters which occur on secondary small faults and there is the implication that fault dips are steeper than the other parts of the gulf.

Kato Achaia area resembles a strike slip dominating area where the seismogenic ruptures dip in high angles and the foci distribution reveals that the seismogenic crust extends from 5km to 29 km where the strong M6.4 Andravida earthquake originated. The majority of aftershocks is clustered at the depth of 15km in one of the two seismogenic ruptures probably activated during the earthquake. The spatiotemporal analysis showed that the majority of the strongest earthquakes with $M > 4.0$ occurred in 10 days after the mainshock. Seismological information proved to be significant for revealing the blind seismogenic fault with long recurrence times.

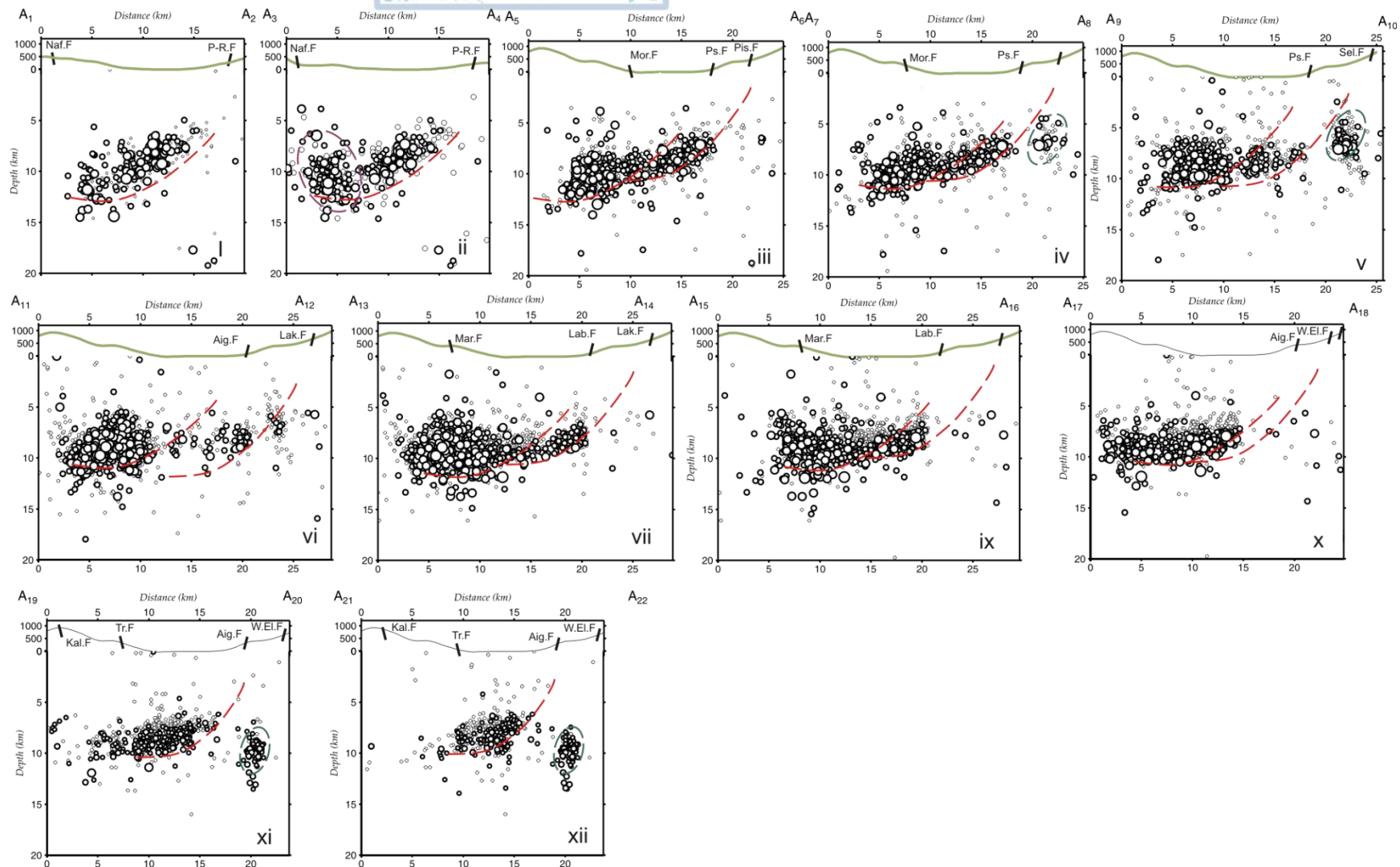
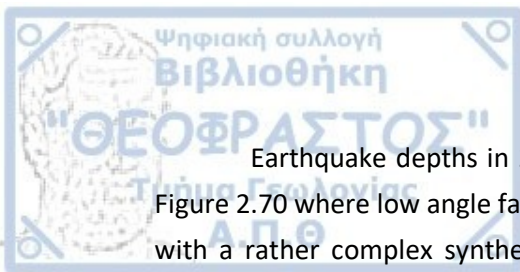


Figure 2-70 Characteristics of the fault population as discussed in the earthquake analysis.



Earthquake depths in 2008-2014 in Efpalio are summarized in the cross sections of Figure 2.70 where low angle faults are dominant. A northward low dipping detachment zone with a rather complex synthesis which does not easily reveal the existence of antithetic southdipping structures (eg. Fig.2-70ii) where the northern cluster ranging between 7km and 13km could be associated with a southdipping fault, possibly Nafpaktos fault. Rare indications exist for south dipping faults in this area. The characteristic feature highlighted by previous studies is the identification of the geometry of the detachment zone can be observed. Cross sections along the western Corinth gulf clearly shows the distribution of the foci in an east – west direction, where the boundary between the ductile and the brittle zone of the crust under the Corinth gulf is located around 7km to the east of the area and around 9 km to the western part. The bulk number of earthquakes indicated by cross sections along the rift is generally restricted at depths 5-12km. This distribution comes in agreement with the observations of Hatzfeld et al. (2000). In depths smaller than 5 km foci are totally absent. There is a successive dip transition from the western to the eastern part, from 30° angle to horizontal planes which define the transition from the brittle to the ductile part. The association of seismic clusters with fault geometry at surface is difficult, an issue also addressed by other studies. Fluid involvement is of crucial importance in the interpretation of the foci distribution. Seismicity occurs in spatial and temporal clusters which interact. The most significant indication is the interrelation of seismicity between the Efpalio cluster which occurred at the eastern tip of Psathopyrgos fault. The investigation of background seismicity is underlined in this study since results provide an important contribution to the study of fault interaction at depth, seismotectonic zoning in areas where background seismicity is an important process. This approach reveals additional information on the development of the seismogenic structures deprived of clear surface trace, that exist within an active seismotectonic environment such as the seismically active grabens that are met in Greece.



Chapter 3

Statistical Analysis

3.1 Introduction

3.1.1 Statistical analysis of seismicity

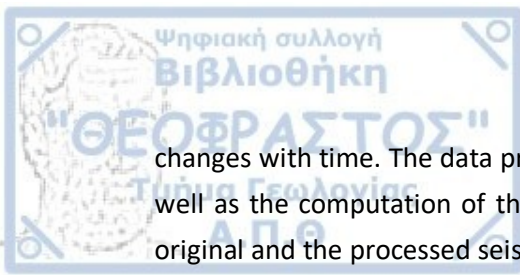
Active faults are associated with earthquakes which may migrate along faults, trigger adjacent faults due to stress transfer or cause periods of quiescence. This collective behavior of seismicity is attributed to earthquake interaction even in the case of small earthquakes and to the mutual interactions between active faults. Seismicity properties are not measured directly but they are strongly imprinted on earthquake catalogs. Earthquake occurrence or absence is assumed to be a complex spatiotemporal phenomenon, which is described by nonlinear dynamics. The partially random seismic process cannot be fully described from a deterministic point of view, but it can be approximated with the use of stochastic means (Vere-Jones et al., 2005; Zhuang et al., 2012). Thus, natural processes are approximated with stochastic - probabilistic models for indirectly studying the occurrence of earthquakes in time and space. According to Console et al. (2006) stochastic analysis stems from the scientific need to exploit the restricted earthquake catalogs in order to model the weakly known earthquake physical processes and determine the obedience of seismicity properties to specific characteristics which might be universal. This approach is additionally encouraged by the fact that seismicity corresponds to a time-dependent marked point process in which, each observation corresponds to an earthquake (described by size, time, space, etc) and can be decomposed into a set of time series including magnitude, epicentral location, occurrence time, interevent time or interevent distance between consecutive events.

The use of stochastic means for studying this process has been highlighted by a number of studies (Kossobokov et al., 2000; Holliday et al., 2008, among others). The quantification of the theoretical stochastic models is directly applied for forecasting purposes, although their application aims not only to describe the seismicity patterns but also to clarify the underlying physical process and provide constrains (Console et al., 2006). A number of scaling laws describe the behavior of the decomposed seismicity components and try to specify the existence of complexities and clustering in time, space and size. Clustering in the occurrence probability is the increasing trend for earthquakes close in time and space compared to other events (Console et al., 2006). The spatial or the temporal characteristics of seismicity are related with the elastic and dynamic features of the crust, as well as with the dominance of certain seismotectonic structures and the recurrence rate of strong seismicity. Therefore, the stochastic analysis of all the above parameters is related to earthquake predictability. The incorporation of statistical tools according to Ben-Zion (2008) enables an integrated investigation for revealing common intrinsic features of the collective systems of earthquakes and faults which inevitably affect seismic hazard and earthquake prediction.

A. The occurrence of earthquakes reveals a process where earthquakes are dependent from their predecessors or they have an impact at the following ones, which is a crucial matter of earthquake forecast. After the main seismogenic sources in the two study areas are defined, the next step is to unveil collaborative characteristics of the seismic process. An attempt is made to identify and quantify clustering properties among earthquakes, search prevailing spatiotemporal or size properties of the seismic process and describe memory characteristics which influence the occurrence of the next earthquake in the case of a dependent process. These effects have a strong impact on the seismic cycle and their investigation is expected to contribute to the better understanding on the seismicity process and consequently seismic hazard in these areas. Particular datasets had to be defined and processed, as described in the following paragraphs so that they can be used in the statistical analysis.

The aim is to investigate seismicity behavior in a wide range of earthquake magnitudes, so as to search for differences between strong ($M \geq 6.0$) moderate ($M \geq 4.0$) and minor earthquakes ($M \geq M_c$, where M_c is the earthquake completeness threshold) covering different time spans, accordingly. This dataset combination offers a complementary perspective for all possible earthquake dynamics. Seismicity complexity in the two study areas is investigated for magnitudes (hereafter mentioned as M) and interevent times (hereafter mentioned as IET). The seismicity pattern extracted from the seismotectonic analysis (Chapter 2) implied the localization of earthquake epicenters along specific fault zones and a temporal concentration of events to specific seismicity bands. Statistical tools are employed for quantifying the short-term and long-term interrelations of earthquakes the clustering degree and search if this behavior of seismicity is associated with the existence of seismicity bursts or it is connected to the background seismic activity across the fault zones. The Hurst coefficient (Hurst, 1951) and the autocorrelation coefficient are employed for indicating the persistence or antipersistence of the seismic process as well as the dominance of the memory content. The spatiotemporal distribution of the Hurst coefficient is further investigated, in an attempt to pinpoint areas of high or low correlation degree. The temporal Hurst fluctuations which have given controversial results in previous works are also examined in this study in comparison with the variations of the b value to test the significance of Hurst coefficient for earthquake predictability. Clustering effects are examined with the Coefficient of Randomness since clustering is essential not only in the case when an aftershock or a foreshock sequence happens, but also in cases of background seismicity.

The compilation of homogeneous data is beforehand the most crucial step for performing any statistical analysis. For this reason a series of tests have been conducted in order to divide seismicity data into certain seismicity periods including consistent and complete sets of earthquakes. Different sets of earthquakes for the two study areas are compiled in a way to include an adequate number of earthquakes for a reliable statistical analysis and at the same time to secure catalog completeness, since magnitude completeness



changes with time. The data processing includes the declustering of the seismicity catalog as well as the computation of the best available magnitude thresholds for the data sets. The original and the processed seismicity catalogs along with the data processes are described in the next paragraphs.

3.2 Data Sets and Data Process

3.2.1 Data Resources

The reliability of statistical methodologies is susceptible to a variety of factors on the quality and the homogeneity of the input information, which in the case of seismology are the seismicity catalogs. Catalogs incorporate heterogeneous information since they are compiled in successive time intervals, during which, science and technology rapidly advances. A variety of factors regarding their compilation, human artifacts (instrumentation, methodologies, algorithms, spatial differentiations in the existing seismological network) as well as the interference of geological factors (seismotectonic setting, seismic excitations) or the duration of the time span, all of them result to discrepancies in the statistical analysis, not associated with the physics of seismogenesis (Mignan and Woessner, 2010; Woessner et al., 2010). Therefore, it is a prerequisite for seismological catalogs to be searched for their consistency and their homogeneity before any statistical analysis. The earthquake catalog which was elaborated for the scopes of the study is obtained from the Department of Geophysics, Aristotle University of Thessaloniki, available at the following webpage: <http://geophysics.geo.auth.gr/ss/>. This catalog includes earthquake information from the historical times up to now, covering the area of the Aegean and the adjacent regions. Strong earthquakes from historical times (550 BC – 1899 AD) are described by historical documentation on macroseismic effects (information summarized by Papazachos and Papazachou 2003). Until 1981 earthquake recordings are based on the seismicity network of the National Observatory of Athens, which was the first seismological network established in Greece. In 1978 the seismological network of the Seismological Station in Thessaloniki launched its operation and the number of earthquake recordings was increased. In August 2008 the Unified National Seismologic Network of Greece (HUSN) came into force and the unification of the seismological networks, offered a satisfying coverage in the area of the Aegean leading to a lower M_c for the seismicity catalogs. The magnitude of the events corresponds to the Local Magnitude (M_L) and since 2008 is estimated by applying the methodology of Hutton and Boore (1987) on simulated Wood Anderson earthquake recording. Due to the repeated changes in the seismological network geometry, the earthquake catalog is not homogeneous and cannot be studied in its entire range, but only in separate time intervals which can be characterized from a relative homogeneity in the recording process.

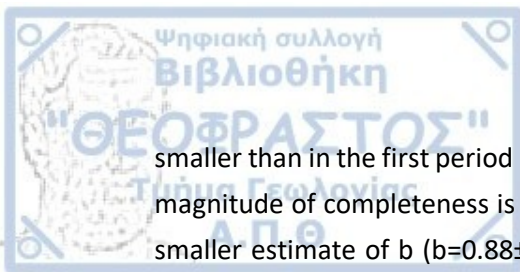
Complete earthquake catalogs are important not only for the process itself but also for the interpretation of the stochastic results. Complete data sets were compiled on the methodology proposed by Wiemer and Wyss (2000) who take into account the self-similarity characteristics of earthquake occurrence, with the application of the Modified Goodness-of-Fit-Test (MGFT-Leptokaropoulos et al., 2013). Magnitude threshold is estimated after performing goodness-of-fit tests in Gutenberg-Richter power law distributions derived from real and synthetic datasets which are produced by Monte Carlo simulations. b value is determined in all cases under the assumption that the magnitude distribution obeys a G-R law. b value provides a sufficient indication of the distribution characteristics even if the magnitudes do not follow a power law distribution. The statistical estimate of b based on the maximum likelihood estimator (MLE) is derived from the methodology proposed by Aki (1965) and also suggested by many researchers and is given by:

$$b = \frac{1}{\ln(10)[\langle M \rangle - (M_c - \Delta M / 2)]} \quad \text{Eq. 3-1}$$

where $\langle M \rangle$ is the average magnitude in the sample (Ak.i, 1965; Utsu, 1966). If N is the number of the observations then, b accuracy is described by the standard error, σ_b , expressed by:

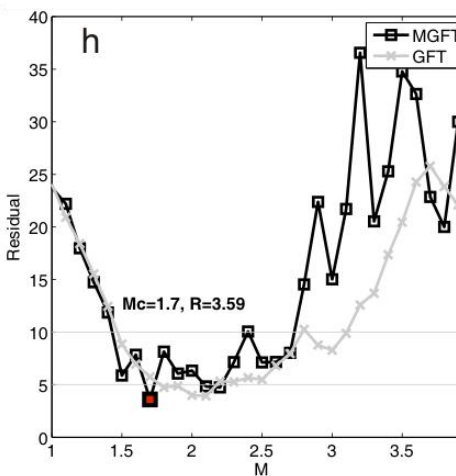
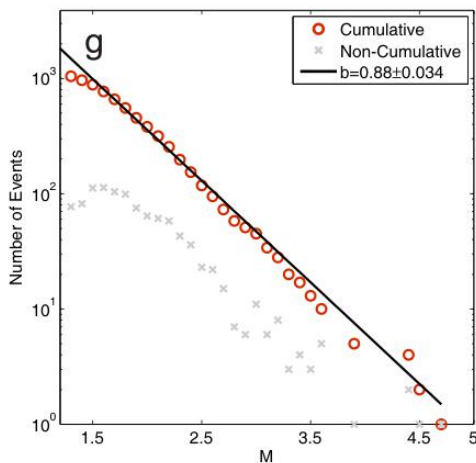
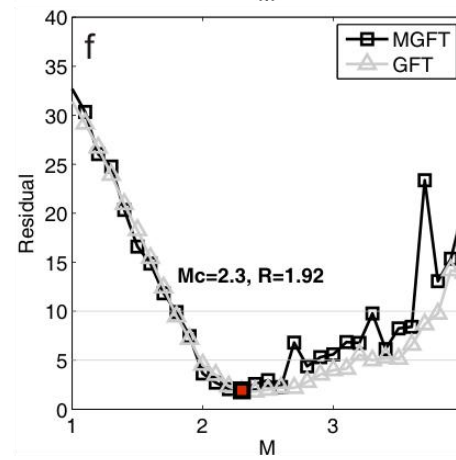
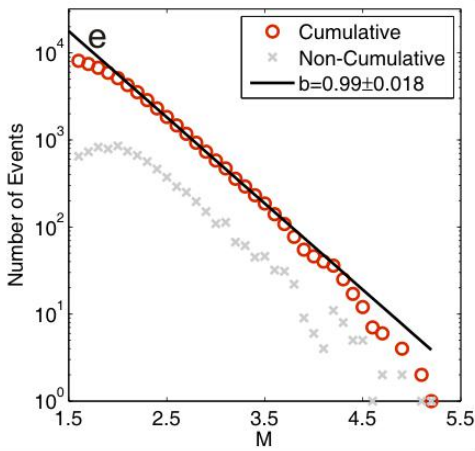
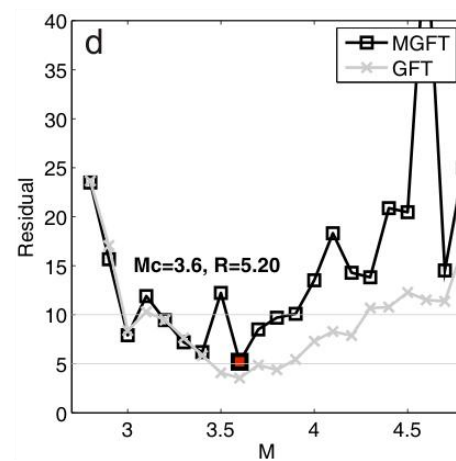
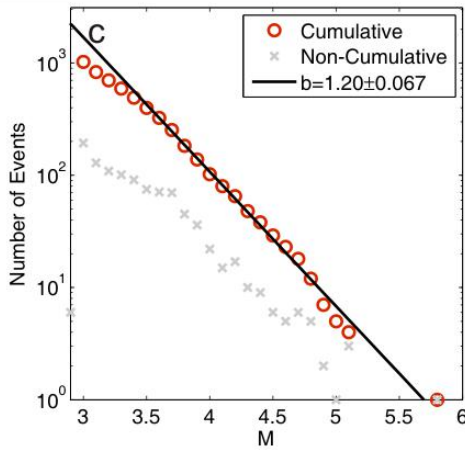
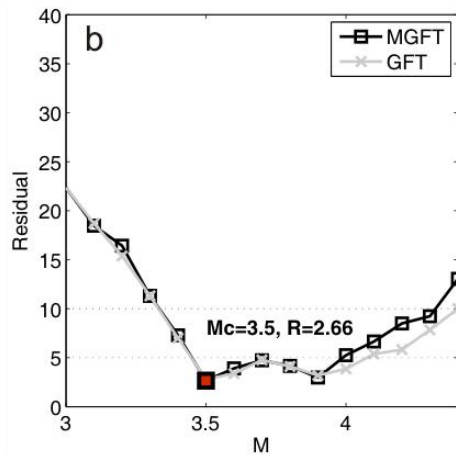
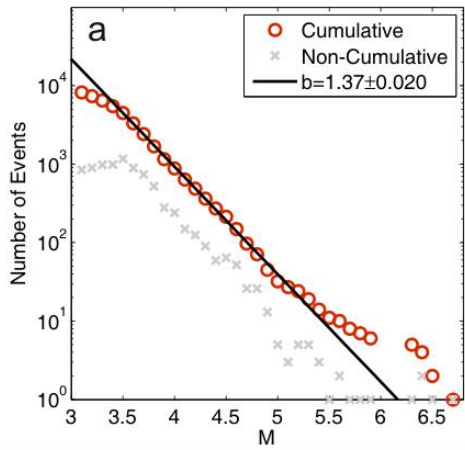
$$\sigma_b = b / \sqrt{N} \quad \text{Eq. 3-2}$$

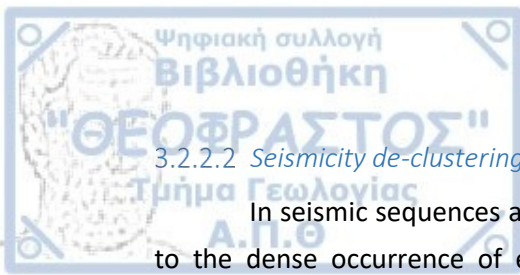
Where N is the sample size. This technique is based on the assumption that magnitudes follow an exponential distribution and M_{\max} is infinite. Estimations for Corinth Rift and Mygdonia regions have been performed for the time intervals i) January 1981– October 2014 and ii) August 2008– October 2014. Figure 3-1 shows the results on magnitude completeness for the final earthquake catalogs. In the first column, the cumulative number (red circles) and the incremental number (grey crosses) of earthquakes are presented along with the best linear fit (black line) for the magnitude threshold, calculated in each case. The second column depicts the average difference (errors) between the observed data and 1000 synthetic catalogs of random events generated by the MGFT (black line) and the GFT (grey line) proposed by Wiemer and Wyss, (2000). The smaller error, R (red rectangle) represents the smaller difference, for which the magnitude of completeness value is considered to provide the most reliable estimation for M_c . Horizontal lines correspond to the residual of deviation from the power law distribution at 5% and 10% confidence interval. Figure 3-1 a and b describes the completeness magnitude threshold for the period January 1981 to October 2014 in Corinth gulf. For the least error ($R=2.66$) M_c is estimated equal to $M_c=3.5$ with $b=1.37\pm 0.02$ (Eq. 3-5) while for the Mygdonian graben the best indications for the magnitude threshold corresponds to $M_c=3.6$ ($R=5.20$) with a b equal to 1.20 ± 0.02 (Figure 3-1 c, d). In the second case (August 2008 – October 2014) the magnitude threshold is apparently shifted to lower values for both study areas, upgrading the information on the seismicity catalogs. For the least residual ($R=1.92$) the magnitude cut-off is equal to $M_c= 2.3$ for the Corinth Gulf, whereas b value is



smaller than in the first period $b=0.99\pm 0.018$. On the other hand, in the case of Mygdonia, the magnitude of completeness is equal to $M_c=1.7$ for the best fit with $R=3.59$, also exhibiting a smaller estimate of b ($b=0.88\pm 0.03$) than the first case (Figure 3-1 e, f). In the second time interval earthquake magnitudes range between $1.7\leq M < 4.8$, evidencing the total absence of strong events during the last years in the region of Mygdonia (Figure 3-1 g, h).

Figure 3-1 Cumulative number of earthquakes for different study periods along with the best fitting curve as it was based on methodology proposed by Wiemer and Wyss (2000) and the Modified Goodness of Fit (MGFT) technique by Leptokaropoulos et al. (2013) (left column) and b value, in each case. The black line (right column) indicates the average difference between the observed data and the 1000 synthetic catalogues of random events following the aforementioned power law. a) Magnitude completeness for Corinth Rift for 01.1981 – 10.2014, equal to $M_c=3.5$, b) Errors estimated for the corresponding completeness threshold, c) Magnitude completeness for Mygdonia seismicity, $M_c=3.6$ for the same period as in 3a, d) Least error related to the suggested threshold, e) Magnitude completeness for Corinth Rift seismicity, $M_c=2.3$ for 08.2008 – 10.2014, f) error curve for the magnitude completeness results, g) Magnitude completeness for Mygdonia, $M_c=1.7$ for 08.2008 – 10.2014 h). Least error related to the suggested threshold.





3.2.2.2 Seismicity de-clustering process

In seismic sequences and swarms the degree of clustering is naturally amplified due to the dense occurrence of earthquakes in time and space. When long-term clustering properties of seismicity are investigated, the dense earthquake occurrence due to seismic excitations is misleading, especially when it comes to hazard assessment (Frankel, 1995) or seismicity rate studies (Wiemer and Wyss, 1994) and dependent events should be removed. In declustering methodologies earthquakes are classified as mainshocks (independent events) or aftershocks (dependent events) and dependent events are removed. There is a broad range of declustering methodologies that are based on the spatiotemporal proximity of the seismic events developed according to deterministic (Gardner and Knopoff 1974; Reasenber, 1985) or stochastic approaches (Zhuang et al., 2004 etc).

Reasenber declustering algorithm (Reasenber, 1985) was applied to initial catalogs for the compilation of data sets deprived of aftershock sequences. Reasenber algorithm is used for identifying aftershock clusters based on a two-parameter earthquake interaction model producing a Poissonian declustered earthquake catalog which is deprived of correlated events. Parameters used to define the dependent earthquakes are described in Table 3-1, where τ_{\min} and τ_{\max} correspond to the minimum and the maximum suggested time for which the next earthquake is expected to occur with a probability, p_1 while x_k is the magnitude threshold for completeness, x_{xmeff} is a component which characterizes the main event and finally r_{fact} is equal to the length of the area radius within which the next aftershock is expected (according to Kanamori and Anderson, 1975). The declustering algorithm was applied only for the recent seismicity catalogs (2008-2014). For the Corinth Rift approximately 2000 dependent earthquakes were identified and removed from the original catalog, whereas less than 500 aftershocks were removed from the initial seismicity catalog of Mygdonia. For comparative reasons M_c was further estimated for the declustered seismicity catalogs with the Modified Goodness of Fit (MGFT) technique (Leptokaropoulos et al., 2013) and the results are presented in Figure 3-2. Magnitude completeness for the declustered seismicity catalog in the Corinth Rift for the period 2008 to 2014 is set to $M_c=2.2$ ($b=0.94\pm 0.018$) (Figure 3-2 a, b) for the best fit ($R=1.63$) whereas the corresponding cut-off magnitude for Mygdonia is $M_c=1.7$ ($b=0.82\pm 0.034$) (Figure 3-2 c, d) for $R=3.86$. Results on the magnitude completeness and the b values for the declustered catalogs slightly differ from the ones in the original catalogs of seismicity. The declustered seismicity catalogs in Corinth Rift and Mygdonia study areas are deprived of seismic excitations and aftershocks sequences such as the M6.7 2008 Achaia earthquake or the 2010 Efpalio sequence in the Corinth Rift, so the impact of dense occurrence due to stronger earthquakes has been eliminated. Since the ability of the stochastic tools to provide information is strongly based on the abundance of data the declustering process is expected to change the characteristics of the statistical sample in Corinth Rift. In Mygdonia where there is an absence of strong events during the study period declustering is expected to have a small impact on the results. However in all cases results for the declustered catalog are always compared to the results obtained without declustering.

Table 3-1 Range of values for the parameters incorporated into Reasenberg's model and the typical values that were used in the study.

Parameters	Typical Value	Minimum Value	Maximum Value
τ_{min}	1	0.5	2.5
τ_{max}	10	3	15
ρ_1	0.95	0.9	0.99
χk	0.5	0	1
χ_{meff}	1.5	1.6	1.8
r_{fact}	10	5	20

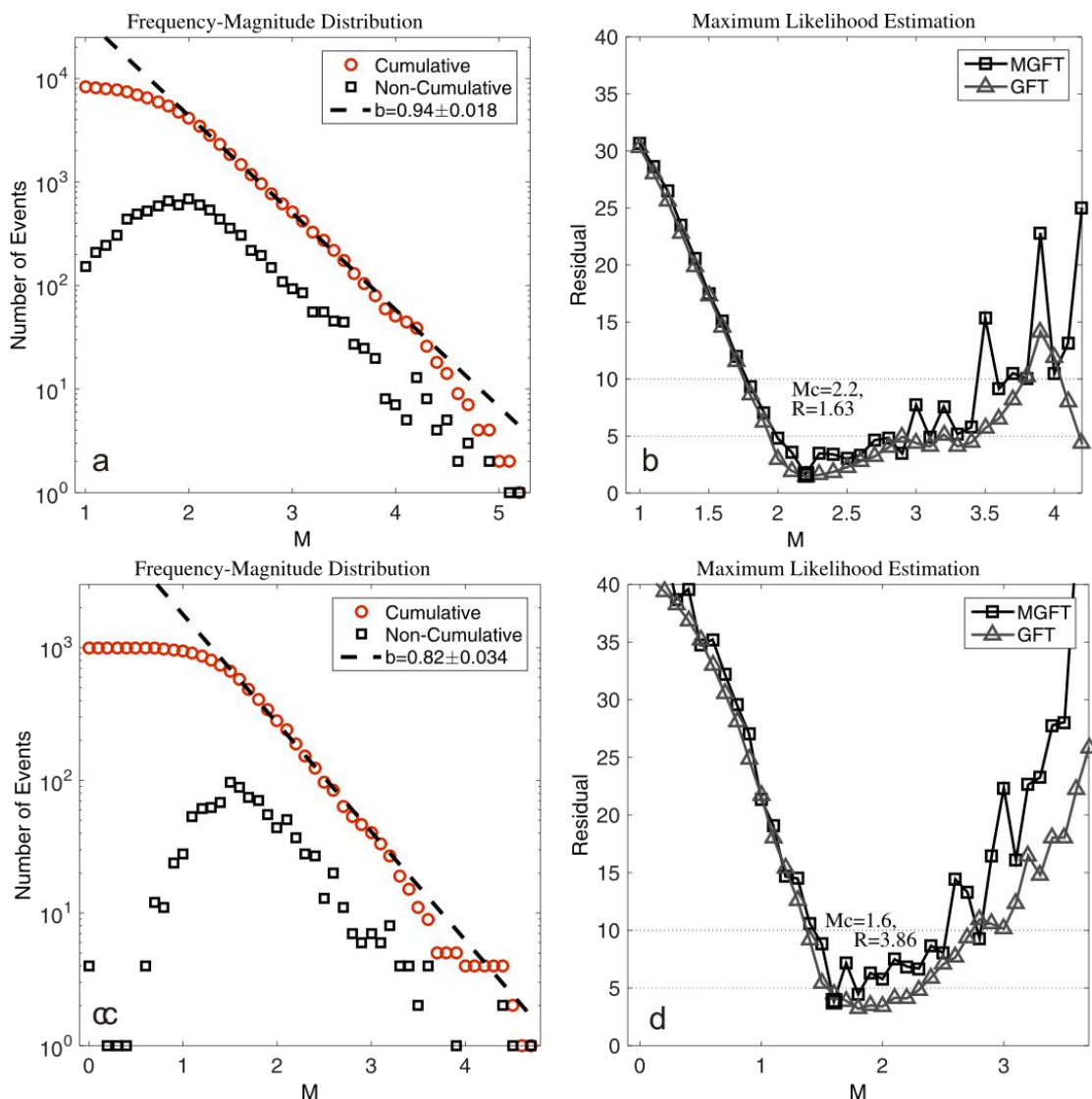


Figure 3-2 a) Magnitude completeness for the declustered catalog of the Corinth Rift for 2008 – 2014, equal to $M_c = 2.2$, b) Errors estimated for the corresponding completeness threshold, c) Magnitude completeness for Mygdonia seismicity, $M_c = 1.6$ for the same period, d) Least error related to the suggested threshold.

The earthquake datasets used correspond to three separate magnitude groups (Table 3-2). Details for the time duration, the number of events N , the minimum magnitude M_{\min} and maximum magnitude M_{\max} of the datasets are provided in detail in Table 3-2. The first dataset (A catalog) includes all strong earthquakes ($M \geq 6.0$) which have occurred in the Corinth Rift from 1700 till present (Fig. 1-4) since when the catalog was found to be complete for this interval (Console et al., 2013 and references therein). The almost complete historical information recorded by the constant habitation in the Corinth Rift also supports the assumption that the seismic catalog is complete for earthquakes with magnitude $M \geq 6.0$ after 1700. This set includes both historical information (summarized by Papazachos et al 1982; 1997) who compiled an atlas of isoseismal maps by gathering all the available information on macroseismic intensity for strong earthquakes in Greece, as well as from recent strong instrumental data. Earthquake magnitudes refer to moment magnitudes, M_w . In total, 45 strong earthquakes have been identified and these were used as an input to the statistical analysis. Mygdonia is struck by a limited number of strong earthquakes ($M \geq 6.0$) since 1700 (7 earthquakes) (Papazachos et al 1982; 1997) a fact that hinders any robust statistical analysis for Mygdonia (Fig. 1-3).

Table 3-2 Information on the three sets of earthquake catalogs, where N is the number of observations and M_{\min} , M_{\max} are the minimum and maximum magnitudes.

Code	Study area	Time interval	N	M_{\min}	M_{\max}
A	Corinth Rift	1700 - 2014	45	6.0	6.7
B ₁	Corinth Rift	1981 - 2014	815	4.0	6.7
B ₂	Mygdonia graben	1981 - 2014	100	4.0	5.8
C ₁	Corinth Rift	2008 - 2014	3192	2.3	5.2
D ₁	Corinth Rift	2008 - 2014	2288	2.2	5.2
C ₂	Mygdonia graben	2008 - 2014	560	1.7	4.7
D ₂	Mygdonia graben	2008 - 2014	485	1.6	4.7

The second group of datasets (B₁ and B₂ catalogs) includes moderate instrumental seismicity for both areas recorded in the period 01.1981–10.2014 with magnitudes $M \geq 4.0$. These two datasets comprise parts of the complete earthquake catalogs for the specified time (Fig.3-2a,c). 815 earthquakes for the Corinth Rift (B₁ catalog) with magnitudes ranging between $4.0 \leq M < 5.8$ and 100 earthquakes for Mygdonia graben (B₂ catalog) with magnitudes between $4.0 \leq M < 4.8$ are found. The third dataset regards recent seismicity information for 08.2008–10.2014 as recorded by HUSN, with magnitudes above the completeness threshold as specified in each case (C₁ and C₂ catalogs). The recent seismicity period coincides with the most recent improvement for the permanent regional seismological network, which resulted in a significant onward lowering of the magnitude threshold and advanced earthquake detectability. Therefore, 3192 earthquakes with magnitudes $2.3 \leq M < 5.8$ were extracted for the Corinth Rift (C₁ catalog) whereas 560 complete earthquakes with magnitude $1.7 \leq M < 4.8$

were detected for the graben of Mygdonia (C_2 catalog) in the same time interval. The complete datasets which were declustered with the process described in the previous paragraph provided the declustered catalogs (D_1 and D_2 catalogs for Corinth Rift and Mygdonia, respectively).

For building a stochastic model, each point in the process represents a single earthquake with a magnitude M , a certain time of occurrence converted into decimal days and geographical coordinates [longitude, latitude], which for the scope of the statistical analysis are converted into Euclidian coordinates $[x, y]$ in a given time (x_i, y_i, t_i, M_i) . Depth is neglected from the spatial coordinates due to the uncertainties it carries compared to the other parameters. Therefore, the seismic process can be decomposed into the three following different marked point processes:

1. Earthquake Magnitude, M which, for strong earthquakes is a moment magnitude (M_w) and M_L for moderate seismicity and microseismicity.
2. Interevent time, IET, which is the lapse time between two successive earthquakes, ($IET = t_{i+1} - t_i$) in a chronological order, independently of their size. Considerable research has been performed on the analysis of the interevent times of earthquakes and according to Jonsdottir et al. (2006) their employment is beneficial in relation to the origin time, since it is deprived of relative errors that origin-time carries. In addition, interevent time is assumed to form a collaborative property which depends on the study area and its seismic behavior.
3. Interevent distance, IED, which corresponds to the two dimensional spatial difference between two successive events ($IED = r_{i+1} - r_i$).

The aforementioned marked point processes (IET, IED and M) have been elaborated for all catalogs described in Table 3-2 A_1 (Appendix, Fig.II-1) for B_1 (Appendix, Fig.II-2), C_1 (Appendix, Fig.II-3) and D_1 catalog (Appendix, Fig.II-14) in the Corinth Rift, B_2 (Appendix, Fig.II-5), C_2 (Appendix, Fig.II-6) and D_2 catalog (Appendix, Fig.II-7) in Mygdonia graben. All marked point processes which describe seismicity were investigated for their population, temporal and spatial and size properties with the scope to obtain an integrated description of seismicity in all magnitude ranges.

3.2.3 Long Term Memory Analysis

3.2.3.1 Rescaled Range Analysis - Methodology

The long memory features of the seismic process are investigated in an attempt to seek for whether earthquakes depend on their predecessor events or influence the time and the location of the following ones. "Memory" or "persistence" in a given stochastic process expresses the element reliance to one or more elements over a specific lag. Rescaled Range Analysis (R/S) is applied for defining the tendency of seismicity to maintain temporal, spatial or size features. Long-term memory systematics are often associated with power law distributions and they are expressed as the Hurst law or Hurst effect. The Hurst effect is known since 1951, when the hydrologist H. E. Hurst, introduced the Hurst coefficient or Hurst exponent, H (Hurst, 1951) and quantifies the memory content or a process randomness. He performed a temporal analysis of the Nile's reservoirs capacity and seasonal flooding over a long period of time, implying the memory characteristics of the process. Mandelbrot and Wallis (1969) suggest that in self-similar process the fractal dimension, D , is related to Hurst, despite the fact that the fractal dimension has local characteristics whereas H is global. In a n -dimensional space the two relation between the two coefficients is given by:

$$D = n - H \quad \text{Eq. 3-3}$$

Theoretical values of the H estimate range between 0 and 1 implying either long memory or random properties. When $0.5 < H < 1.0$ the process is persistent with a long range dependence between elements, a long-memory correlation between events exists (a low fractal dimension is implied). This state describes a time-series which is long-term positively autocorrelated with its elements depending upon the previous ones, so that a past trend is more likely to be continued than to be inverted in the future. Memory persistence in seismicity signifies the dependence of earthquakes upon previous or future ones. When $0 \leq H < 0.5$ a memoryless or an antipersistent procedure is signified (higher fractal dimensions are dominant) and a trend reversion is more probable than the trend continuation. A Brownian motion (random and uncorrelated procedure) is implied when $H=0.5$ a phenomenon observed in a wide range, in nature, where the examined process does not possess long memory (it has independent increments). In the case of seismicity parameters the results for such an investigation are interpreted in terms of identification of seismicity systematics evidencing the appearance or the lack of clustering and time persistence.

The most common methodology to estimate the Hurst exponent is the Rescaled Range (R/S) analysis which was firstly introduced by Hurst (Hurst, 1951). The method for distinguishing correlated from random time series was later developed by Mandelbrot and Wallis (1969) and Feder (1988) who further improved the analysis. Despite the method's effectiveness it was sensitive to short-range dependent correlations and for this reason Lo (1991) developed a modified R/S Analysis, doubted by a number of researchers. In this study the classical R/S analysis is engaged for the identification of long range seismicity features. According to this method, the set of n observations $X \in \{X_1, X_2, \dots, X_n\}$ is subdivided into

d non overlapping sub series of X , $(X_{(k-1)s+1}, X_{(k-1)s+2}, \dots, X_{k,s})$, $k = 1, 2, \dots, d$ with individual lengths equal to $s = n/d$. The rescaled range $(R/S)_s$ of the set is expressed by:

$$(R/S)_s = \frac{1}{d} \sum_{k=1}^d (R_{k,s} / S_{k,s})_s \quad \text{Eq. 3-4}$$

where, the range $R_{k,s}$ corresponds to the largest measured difference between the maximum positive and maximum negative cumulative deviation of $Y_{k,s}$ from its mean $\bar{X}_{k,s}$ and is given by:

$$R_{k,s} = \max_{1 \leq i \leq s} \{(Y_{k,s})_i\} - \min_{1 \leq i \leq s} \{(Y_{k,s})_i\} \quad \text{Eq. 3-5}$$

where $Y_{k,s}$ is given by:

$$(Y_{k,s})_i = \sum_{j=1}^i (X_{(k-1)s+j} - \bar{X}_{k,s}), \quad i = 1, \dots, s \quad \text{Eq. 3-6}$$

And $\bar{X}_{k,s}$ is the average value:

$$\bar{X}_{k,s} = \frac{1}{s} \sum_{i=1}^s X_{(k-1)s+i} \quad \text{Eq. 3-7}$$

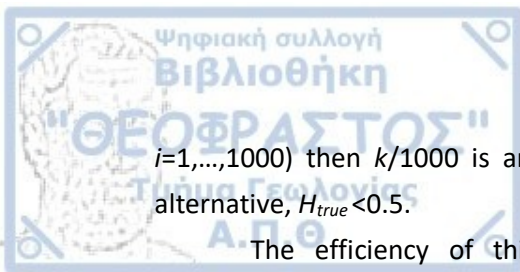
$S_{k,s}$ refers to the standard deviation of the same value given by:

$$S_{k,s} = \sqrt{\frac{1}{s} \sum_{i=1}^s (X_{(k-1)s+i} - \bar{X}_{k,s})^2} \quad \text{and} \quad k=1, \dots, d \quad \text{Eq. 3-8}$$

Finally, the rescaled range is connected with the Hurst coefficient according to the following equation where H_{obs} expresses the Hurst coefficient estimate (according to Weglarczyk and Lasocki, 2009):

$$\log(R/S)_s = \text{const} + H_{\text{obs}} \log s \quad \text{Eq. 3-9}$$

The above equation provides an estimate \hat{H} of the true H , which for real data will hereafter be mentioned as H_{obs} . The Hurst exponent (H_{obs}) is estimated from the original data sets, with direct application of Eq. 3-9. The significance of H_{obs} estimate is determined by its deviations from 0.5, which indicates randomness. A null hypothesis is set, according to which, the population is long memory free. H -estimate is compared to 1000 estimates obtained from random permutations of the original time series. Random permutations of a time series elements destroy the causality in the series, despite the fact that the values that describe the effect remain the same. If this hypothesis is true, then H_{obs} will not differ significantly from H -estimates obtained from the actual memory-free samples. A distribution of the Hurst coefficient, provided the null hypothesis is true, results from H -estimates obtained from 1000 randomly permuted series. The resultant 1000 H values, H_i , $i=1, \dots, 1000$, are finally compared with H_{obs} . When $H'_{k+1} > H_{\text{obs}} > H'_k > \text{mean}(H_i, i=1, \dots, 1000)$ and $H'_k, k=1, \dots, 1000$ are H_i values sorted in the ascending order, then $(1000-k)/1000$ is an approximate significance of the null hypothesis, with the alternative, $H_{\text{true}} > 0.5$. To the contrary, when $H'_{k+1} > H_{\text{obs}} > H'_k < \text{mean}(H_i,$



$i=1, \dots, 1000$) then $k/1000$ is an approximate significance of the null hypothesis, with the alternative, $H_{true} < 0.5$.

The efficiency of this method, has been widely underlined in the field of environmental, health, economic and seismological sciences. An R/S earthquake analysis was firstly implemented by Lomnitz (1994) who analyzed earthquake slip data. Correig et al. (1997) analyzed the temporal occurrence of seismicity at Deception Island in Antarctica, which exhibited persistence. Long memory persistence was identified for the occurrence of moderate–strong earthquakes in the Mediterranean area by Xu and Burton (2001). The same authors (Xu and Burton, 2006) applied R/S analysis along with Monte Carlo simulations in sub-zones of Greece revealing different characteristics for the involved parameters. Cisternas et al (2004) used Hurst analysis in order to forecast the site of an anticipated large earthquake in Marmaras Sea and suggested the persistency of seismicity. The correlation between Hurst exponent for slip and waiting time data of real earthquake series in Taiwan and Italy is investigated by Chen et al. (2008) and Lee et al. (2012) respectively. Weglarczyk and Lasocki (2009) applied the R/S analysis to interevent times, interevent epicentral distances and event sizes of mining induced seismicity data and revealed a long memory process. Interrelations between the occurrence of future and past events are strongly highlighted in the majority of the studies above, especially concerning seismicity properties in time domain. Possible long range memory features for the IET, the IED and M between consecutive pairs of earthquakes are investigated for all catalogs in the Corinth Rift and Mygdonia graben and results are separately described.

3.2.3.2 Results for the Corinth Rift

R/S analysis results for the Corinth Rift for real and synthetic data (H_{obs} , $\langle H \rangle$) are summarized in Table 3-3, where the significance value (p value) which approximates the probability to fail when rejecting the null hypothesis is also given. Results for the real (upper row) and reshuffled data (lower row) of strong earthquakes are schematically displayed in Figure 3-3. The corresponding values for H_{obs} which are estimates of the linear fit (red line) of $\log(R/S)_s$ versus $\log(s)$ as it was explained before, are given in the upper row. The second row displays the frequency histogram of H-estimates when the actual value of H is 0.5 stemming from 1000 synthetic random datasets. Red line is an approximation of the histogram by the Gaussian distribution, the red dot indicates the estimated H_{obs} while the black dot indicates the mean H, $\langle H \rangle$, obtained from the memoryless sample. The vertical dashed line indicates the upper limit of the 99% confidence interval of H-estimates for a memoryless sample.

R/S analysis was firstly applied on the historical catalog comprising strong ($M \geq 6.0$) earthquakes (catalog A), where H_{obs} values for all parameters considered (IET, IED and M) are found around 0.5 ($H_{obs}=0.511$, $H_{obs}=0.496$ and $H_{obs}=0.452$, respectively) close to the average H values extracted from the synthetic datasets. This fact implies that strong event occurrence approximated by the three aforementioned parameters is likely to be a random process,

rather deprived of a memory content. For moderate events (B_1) results are profoundly different, in terms of H_{obs} with $H_{obs} > 0.5$ for IET (Fig.3-4, 1st column) and IED (Fig.3-4, 2nd column), revealing the presence of a memory content. IET is the parameter exhibiting strong interdependence in the seismic process ($H_{obs} = 0.908$). IED also shows a strong dependence ($H_{obs} = 0.802$) with an insignificant probability to fail if rejecting the hypothesis of randomness, whereas for magnitudes it is less significant ($H_{obs} = 0.551$) (Fig.3-4, 3rd column). The results for Corinth gulf reveal strong persistency in IET and IED with IET to be the most dependable parameter, whereas there are no grounds to reject randomness of event magnitudes.

For catalogs C_1 (Fig.3-5) and D_1 (Fig.3-6) it is generally observed that the abundance of the samples offers smaller uncertainties. H_{obs} for IET takes the largest value among all cases ($H_{obs} = 0.841$) with a probability much less than 1% for the process to exhibit no memory, meaning that it is highly probable that consecutive IET tend to retain similar values through the seismic process (Fig.3-5, 1st column). A smaller but significant property clustering is evidenced in the space domain with H_{obs} for IED to be equal to 0.790 (Fig.3-5, 2nd column). Magnitudes at last exhibit a lack of long-term memory ($H_{obs} = 0.582$) (Fig.3-5, 3rd column). Moving to the declustered catalog, (D_1) one can observe that the inclusion of dependent events in the data samples, which are identified as aftershocks and removed, imposes a significant effect on the results of the R/S analysis. The presence of aftershocks increases the values of Hurst exponent estimates. IET retains its memory content in a significant level ($H_{obs} = 0.727$) (Fig.3-6, 1st column). For IED significant correlations have been reduced to minor correlations with $H_{obs} = 0.599$ (Fig.3-6, 2nd column) and for magnitudes the significance of long-term correlations has dropped down from weakly significant to insignificant $H_{obs} = 0.569$ (Fig.3-6, 3rd column).

Table 3-3 R/S analysis results for Corinth gulf datasets. H_{obs} denotes the estimated Hurst exponents for the real catalog, whereas $\langle H \rangle$ is the mean value of H for $N=1000$ random permutations of the original data series. The p value approximates the probability to fail if the null hypothesis is rejected.

Code	IET			IED			M		
	H_{obs}	$\langle H \rangle$	p	H_{obs}	$\langle H \rangle$	p	H_{obs}	$\langle H \rangle$	p
A_1	0.511	0.595	0.740	0.466	0.612	0.850	0.452	0.608	0.860
B_1	0.908	0.546	≤ 0.001	0.802	0.545	≤ 0.001	0.551	0.543	0.420
C_1	0.840	0.532	≤ 0.001	0.790	0.527	≤ 0.001	0.582	0.532	0.076
D_1	0.727	0.530	≤ 0.001	0.599	0.530	0.031	0.569	0.533	0.150

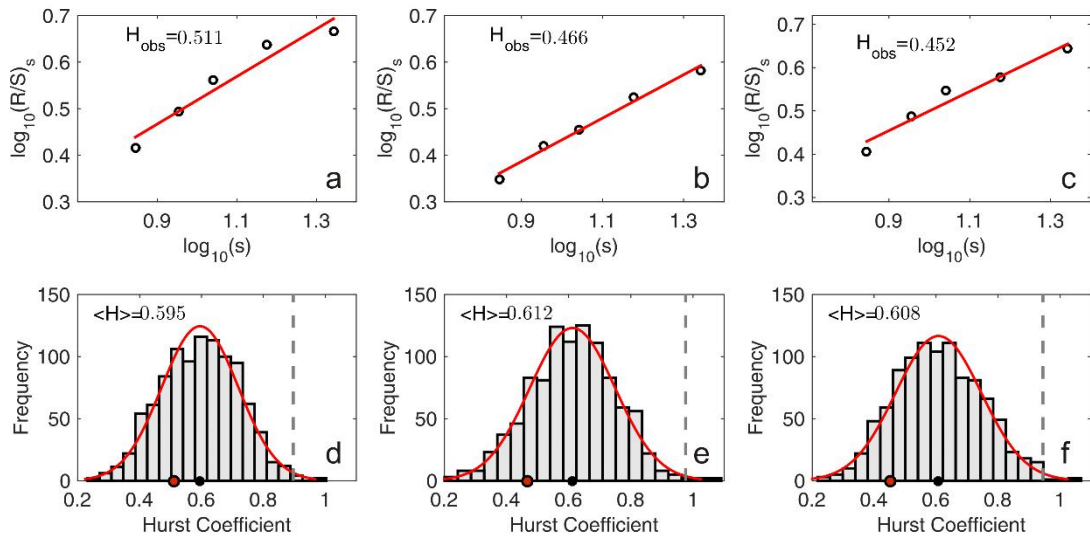


Figure 3-3 R/S analysis results for strong earthquakes with magnitude $MW \geq 6.0$ since 1700 for the case of Corinth Gulf. Upper row: Logarithmic values for the rescaled ranges are plotted against the number of the subseries logarithms. The regression line (red line) for real observations, along with the estimated Hobs are presented. Lower row: frequency histograms for 1000 H values calculated from random samples. Red line is an approximation of the histogram by the normal distribution, red dot indicates the estimated Hobs, black dot indicates the mean H, $\langle H \rangle$, from random samples. The first column is related to IET, the second to IED and the third to magnitude.

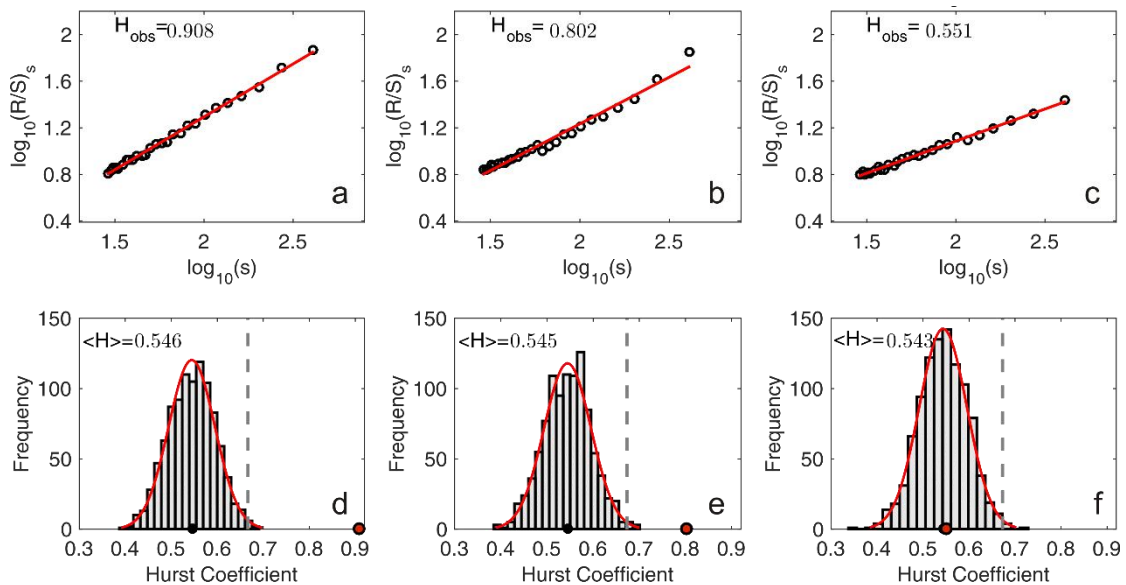


Figure 3-4 Rescale Range analysis results for earthquakes with magnitude $MW \geq 4.0$ for 1981–2012 for Corinth rift (Symbols are described in Fig.3-3). The first column is related to IET, the second to IED and the third to magnitude.

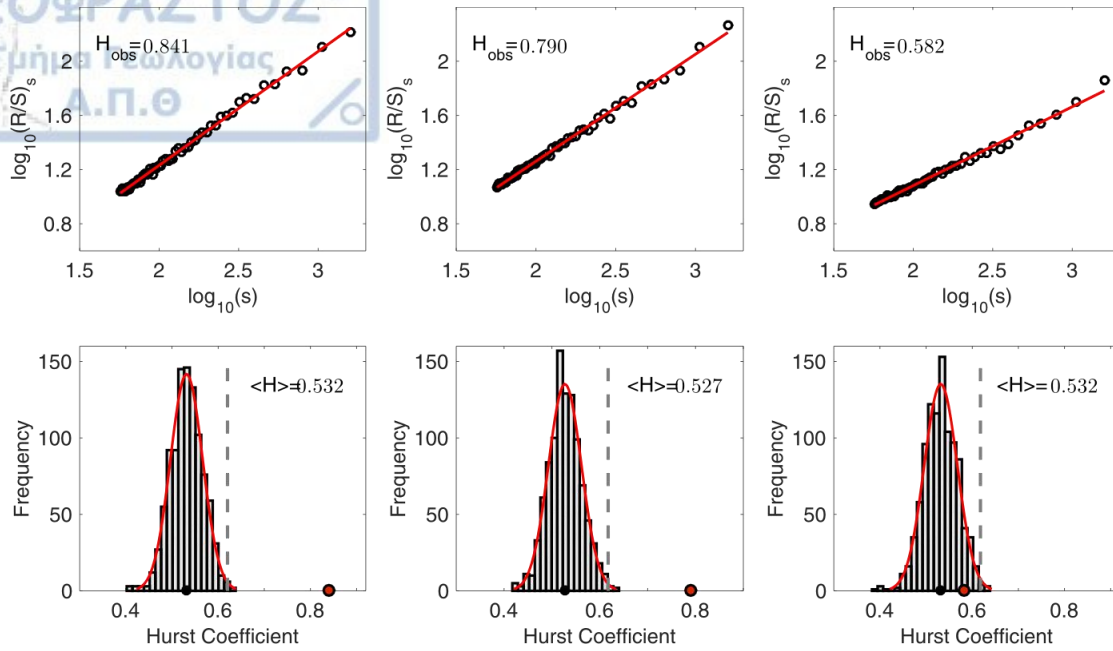


Figure 3-5 Rescale Range analysis results for earthquakes with magnitude $M_w \geq 4.0$ for the full complete catalog of the Corinth rift (Symbols are described in Fig. 3-3). The first column is related to IET, the second to IED, and the third to magnitude.

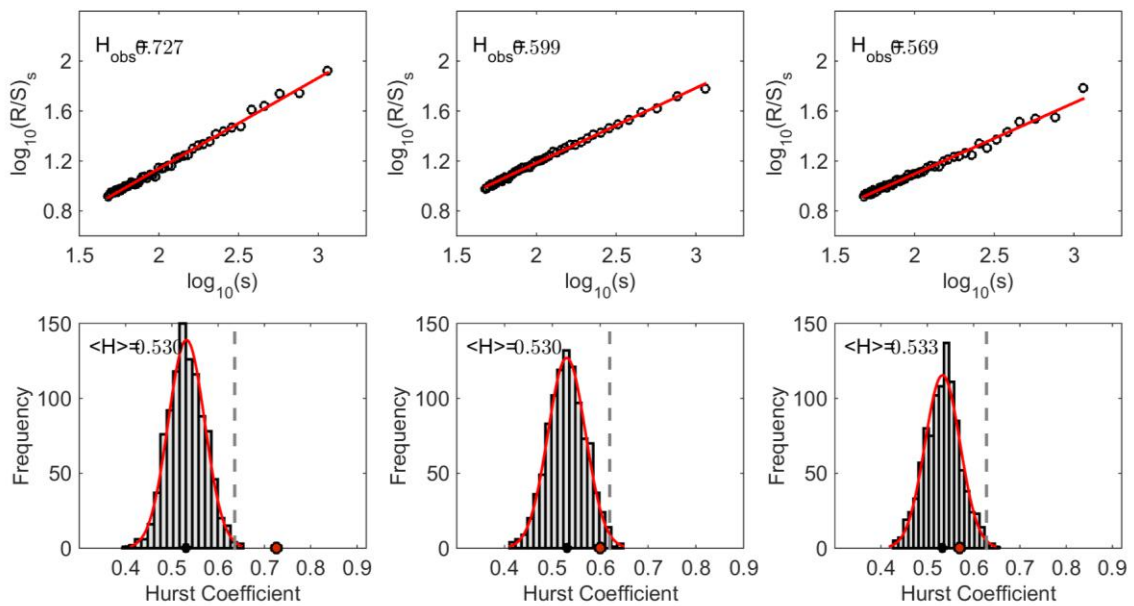


Figure 3-6 R/S analysis results for earthquakes with $M \geq 2.4$ in Corinth Gulf (Symbols are described in Fig. 3-3). The first column is related to IET, the second to IED and the third to magnitude.

3.2.3.3 Results for Mygdonia graben

All results for Mygdonia R/S analysis are depicted in Table 3-4. For B_2 data set, Hurst exponents are in all cases smaller than in Corinth gulf, but larger than 0.5 (IET, $H_{obs}=0.773$; IED, $H_{obs}=0.631$ and M, $H_{obs}=0.699$). For IET, H_{obs} obtains the highest value among all cases showing that moderate earthquakes spanning 1981-2014 exhibit strong interdependence in time (Fig.3-7, 1st column). In cases of IED (Fig.3-7, 2nd column) and magnitude (Fig.3-7, 3rd column) larger than 0.5 (IED, $H_{obs}=0.631$; magnitude, $H_{obs}=0.699$), however, the p-values are found 0.299 and 0.10, respectively, provided only a weak suggestion, yet stronger for magnitudes, which may exhibit some persistency. An interpretation of Mygdonia results should also take into account the small sample size ($N=100$), which makes statistical inference based on R/S analysis, uncertain. Nevertheless, IET seems to be the most dependable parameter in the entire seismic process.

Table 3-4 R/S analysis results for Mygdonia basin. H_{obs} denotes the estimated Hurst exponents for the real catalog, whereas $\langle H \rangle$ is the mean value of H for $N=1000$ random permutations of the original data series. The p value approximates the probability to fail if the null hypothesis is rejected.

	IET			IED			M		
Code	H_{obs}	$\langle H \rangle$	p	H_{obs}	$\langle H \rangle$	p	H_{obs}	$\langle H \rangle$	p
B_2	0.773	0.573	0.013	0.631	0.585	0.299	0.699	0.582	0.100
C_2	0.674	0.547	0.008	0.691	0.546	0.006	0.692	0.551	0.006
D_2	0.619	0.549	0.128	0.505	0.550	0.076	0.695	0.551	0.006

Moving to C_2 and D_2 catalogs (Fig.3-8 and Fig.3-9, in respect) it is observed that for all examined parameters an interdependence is clearly implied. IET and IED exhibit memory properties, though weaker than in the case of the Corinth rift, in particular when the dataset is declustered. For the full but complete catalog, Hurst estimates for IET (Fig.3-8, 1st column) and IED (Fig.3-8, 2nd column) which are $H_{obs}=0.674$ and $H_{obs}=0.691$, in respect, are not memoryless processes and they own an insignificant probability to fail when rejecting the null hypothesis, that the sample is random. Magnitudes are also correlated ($H_{obs}=0.692$, Fig.3-8, 3rd column).

For D_2 dataset all Hurst estimates are larger than 0.5 but slightly reduced for IET ($H_{obs}=0.619$, Fig.3-9 – 1st column) and significantly reduced for IED ($H_{obs}=0.505$, Fig.3-9 – 2nd column) with the exception of magnitudes which remains almost the same with the non declustered data sets ($H_{obs}=0.695$, Fig.3-9 – 3rd column). It seems that the declustering effect is more intense in Mygdonian data than the case before, correlating with the fact that the declustering procedure has removed greater part of the Mygdonia dataset than that of the Corinth rift dataset. For two parameters of the earthquake series from Mygdonia, IET and IED, the significance of long-term correlations has changed from very significant to weakly significant (IED) or insignificant (IET). However, the magnitude series possess a strong long-term correlation, both in the original and the declustered sample.

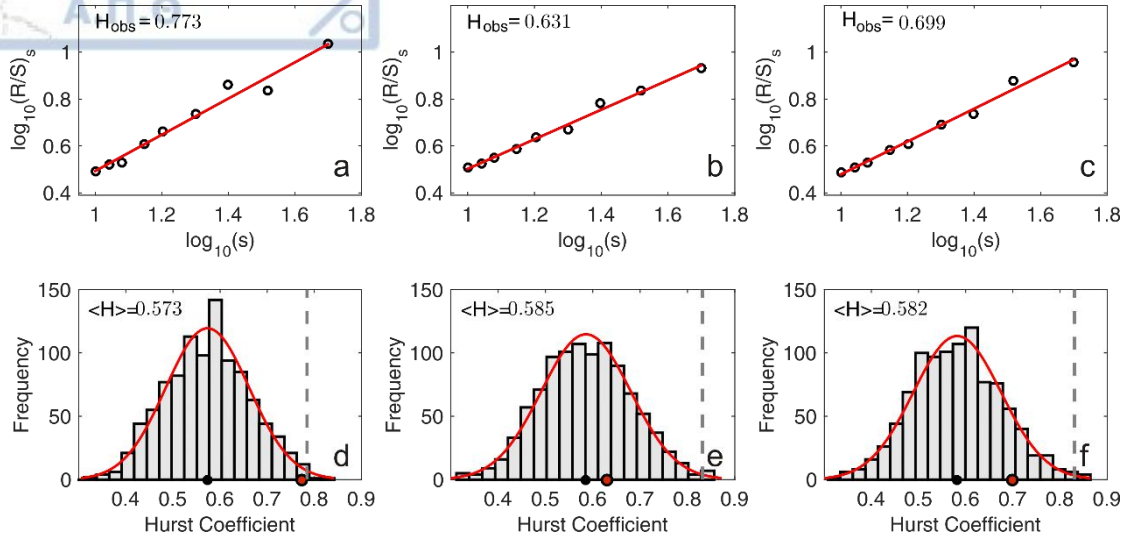


Figure 3-7 Rescale Range analysis results for earthquakes with $M \geq 4.0$ in Mygdonian basin for 1981–2012 (Symbols are described in Fig. 3-3). The first column is related to IET, the second to IED and the third to magnitude.

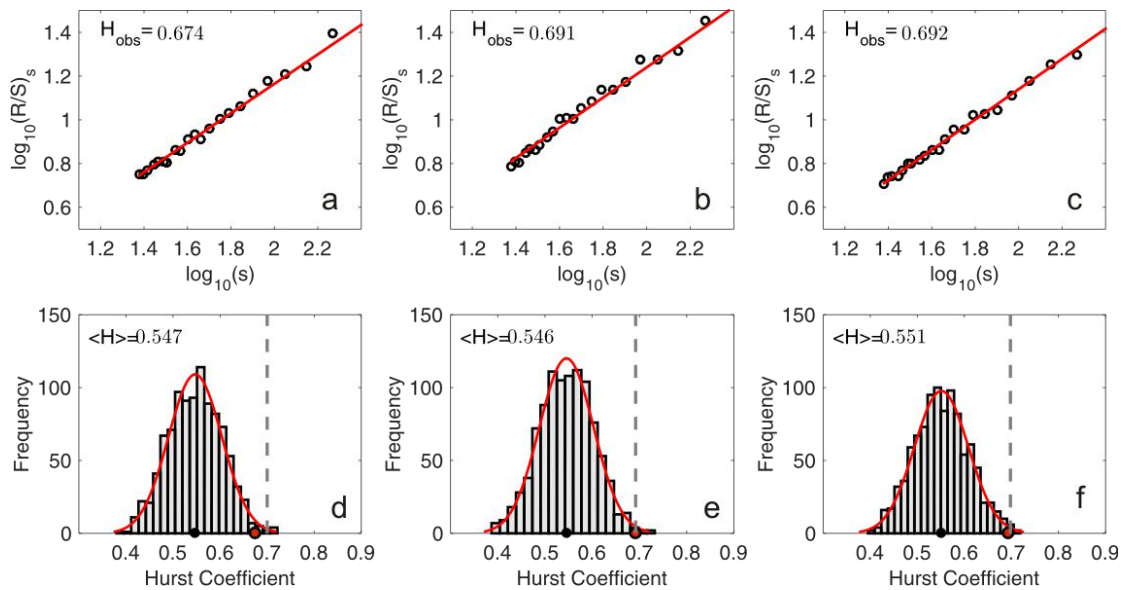


Figure 3-8 Rescale Range analysis results for earthquakes with $M \geq 2.4$ in Mygdonia for 2008–2014 (Symbols are described in Fig. 3-3). The first column is related to IET, the second to IED and the third to magnitude.

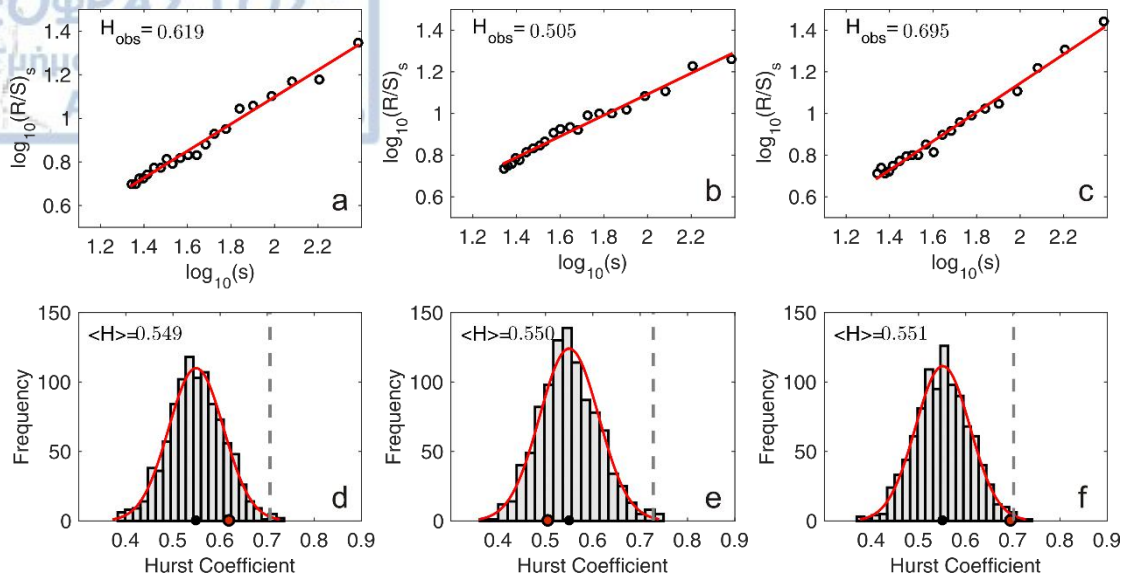


Figure 3-9 Rescale Range analysis results for earthquakes with $M \geq 1.7$ in Mygdonia for 2008–2014 (Symbols are described in Fig. 3-3). The first column is related to IET, the second to IED and the third to magnitude.

3.2.3.4 Temporal variations of the Hurst exponent

H estimate variations for real series of the seismicity parameters are investigated in space and time, seeking for possible correlation with a strong event occurrence or changes in seismicity rate. b-value variations before stronger earthquakes have been observed and their precursory potentials have been studied since long (Rikitake, 1976; Imoto, 1991) without robust conclusions (El-Isa et al., 2014). Ponomarev et al. (1997) discovered a negative correlation between the Gutenberg-Richter b-value and Hurst temporal variations for acoustic emissions generated in rocks. A negative correlation between b and H for earthquake sizes was also derived from the long-range connective sand pile model applied to seismicity (Lee et al., 2009) and then experimentally confirmed (Lee et al., 2012). If it holds true, H is expected to show a predictive potential similar to that possessed by the b-value.

R/S analysis showed that among all seismic parameters, the IET time-series holds the most significant memory content, for this reason it is introduced in the temporal analysis. The best populated 2008-2014 data sets are favoured against the other catalogs because of the lower magnitude cut-off that makes them more detailed. For investigating the temporal fluctuations of Hurst coefficient and following Imoto (1991) concurrent time-changes of H for the IET and time changes for the b-value according to Eq. 3-1 are calculated. Both parameters are calculated with a rolling window of 200 events and sliding every 15 events. This methodology causes H estimates to lose their initial notion of an objective indicator for long-term memory when the numbers of events in the moving window vary considerably. However, in this analysis we detach H exponent from its initial notion and treat it only as a candidate for the indicator of time-changes of the earthquake process. In Figure 3-10 estimates of H (red line), b-value (dashed line) and the ratio H/b (blue line) as a means of measurement between these two components have also been estimated for the same windows. Events with

magnitudes $M > 4.0$ are also plotted against time. There is a fluctuation of the Hurst exponent for IET mostly between 0.5 and 0.8 with few values staying out of these boundaries. Interevent time seems to regard a memory process through the entire period although dependent events are theoretically removed. Interestingly, there is an indication that strong earthquake occurrences are correlated with decreasing trends of b/H . In the case of the first group of stronger events from the beginning of 2010, the decreasing trend of b/H results mostly from the decreasing trend of b -value. However, at the second stronger event group from around midst of 2011, b -values exhibit an increasing tendency but the increasing trend of H is stronger, which results in the decreasing trend of b/H . The last decreasing trend of b/H , to which the $M4.9$ in the second half of 2012 might be linked, is due to combined effects of the slight decreases of b and H . If H and b -value, are negatively correlated as shown in Lee et al. (2009) for laboratory samples, then b/H ratio should only enhance concordant signals issued by b and H . Here, however, the mentioned b/H decreasing trend can be attributed to a distinct decrease of b -value only once; in two other cases it results from more complex interactions of b and H changes.

The variation of Hurst in time is insufficient for Mygdonia area since there is a shortage of data that can offer a study in detail (Fig.3-11). However, there is a variation in Hurst values between 0.5 and 0.7 through time, thus the seismic process especially for microearthquakes can be characterized as persistent in all range. Events are by all means less correlated than earthquakes in the Corinth rift.

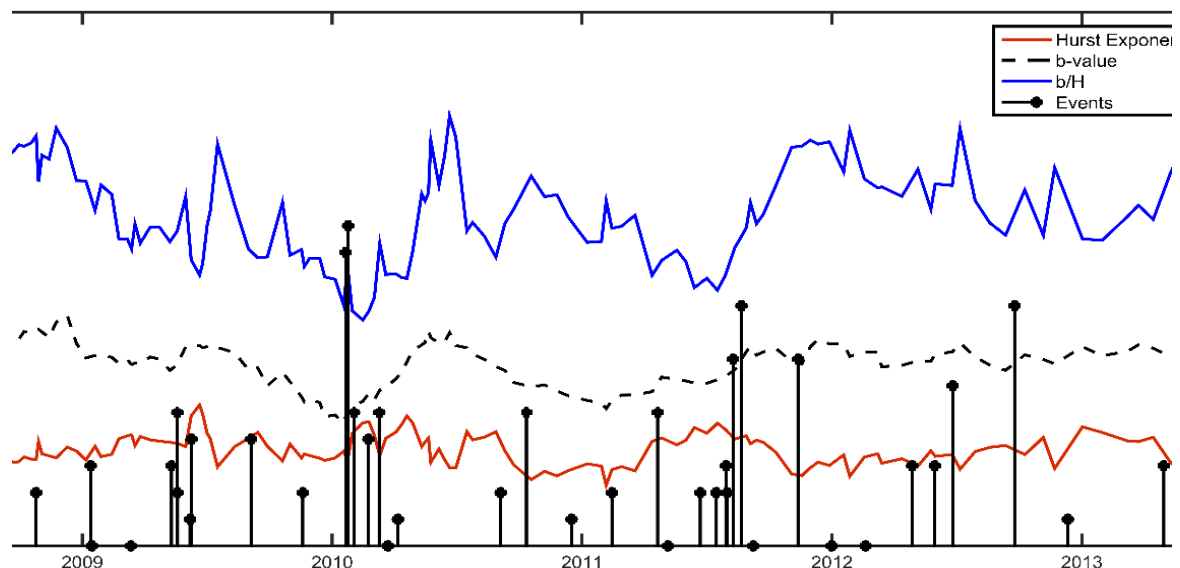


Figure 3-10 Hurst temporal variations (2008-2014) for the Hurst exponent computed for the rolling window of 200 events per 15 events for the Corinth Rift (red line) along with b variations (dashed line) and the b/H ratio (blue line). Earthquakes stronger than 4.0 are also plotted against time.

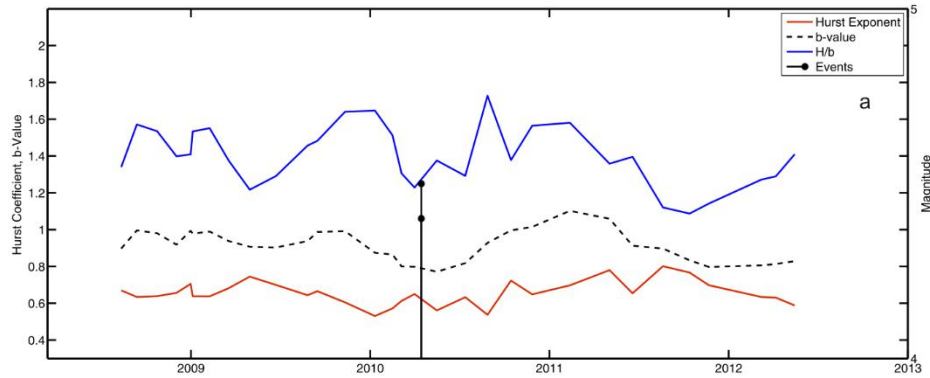


Figure 3-11 Hurst temporal variations (2008-2014) computed for the rolling window of 50 events per 10 events for Mygdonia (red line) along with b variations (blue line) and the ratio b/H (dashed line). Earthquakes stronger than 4.0 are visible.

3.2.3.5 Spatial variation of the Hurst exponent

Along with the temporal investigation, the spatial variations of Hurst are also investigated to detect the spatial concentration of the memory content in both study areas. A grid with circular cells is superimposed on the study areas with 20 km (spatial windows) spacing analysis was performed for the last period that our data cover, i.e. 2008–2014. At each node the data encompassed in a circular area 30–km radius were taken into account only if the earthquake number inside each circle is equal to or larger than 80 events, IET (Fig. 3.12a), IED (Fig. 3.12b) and M (Fig. 3.12c). For IET, H exhibits a variance of values mainly ranging between 0.5 and 0.8, which are all spatially distributed. The distribution of Hurst for the interevent time presents a high degree of correlation (0.812) however, it is clear that high values of H are mainly concentrated in the central part of the Corinth gulf, whereas at the two ends lower values of H are found. This variation shows that there is a synthesis of higher and lower degree correlation areas. It should be emphasized that earthquakes supposed to belong to aftershock sequences have been removed from the calculations, therefore background seismicity properties are mainly indicated. The spatial analysis is also performed in Mygdonia graben (IET - Fig. 3.13a, IED - Fig. 3.13b and M - Fig. 3.13c). Using the same spatial input parameters the pattern that was emerged in Mygdonia shows a uniform pattern for the Hurst exponent spatial variations with the majority of values ranges between 0.6 and 0.8. Higher values are met at the western part of the area and the main tectonic structure of the area (TGfZ – Thessaloniki Gerakarou Fault Zone) whereas to the eastern part interdependencies expressed by the Hurst component seem to be lower. The above results indicate that the seismicity in both areas have in general an heterogeneous pattern, showing regions of relatively high correlation and uncorrelated regions.

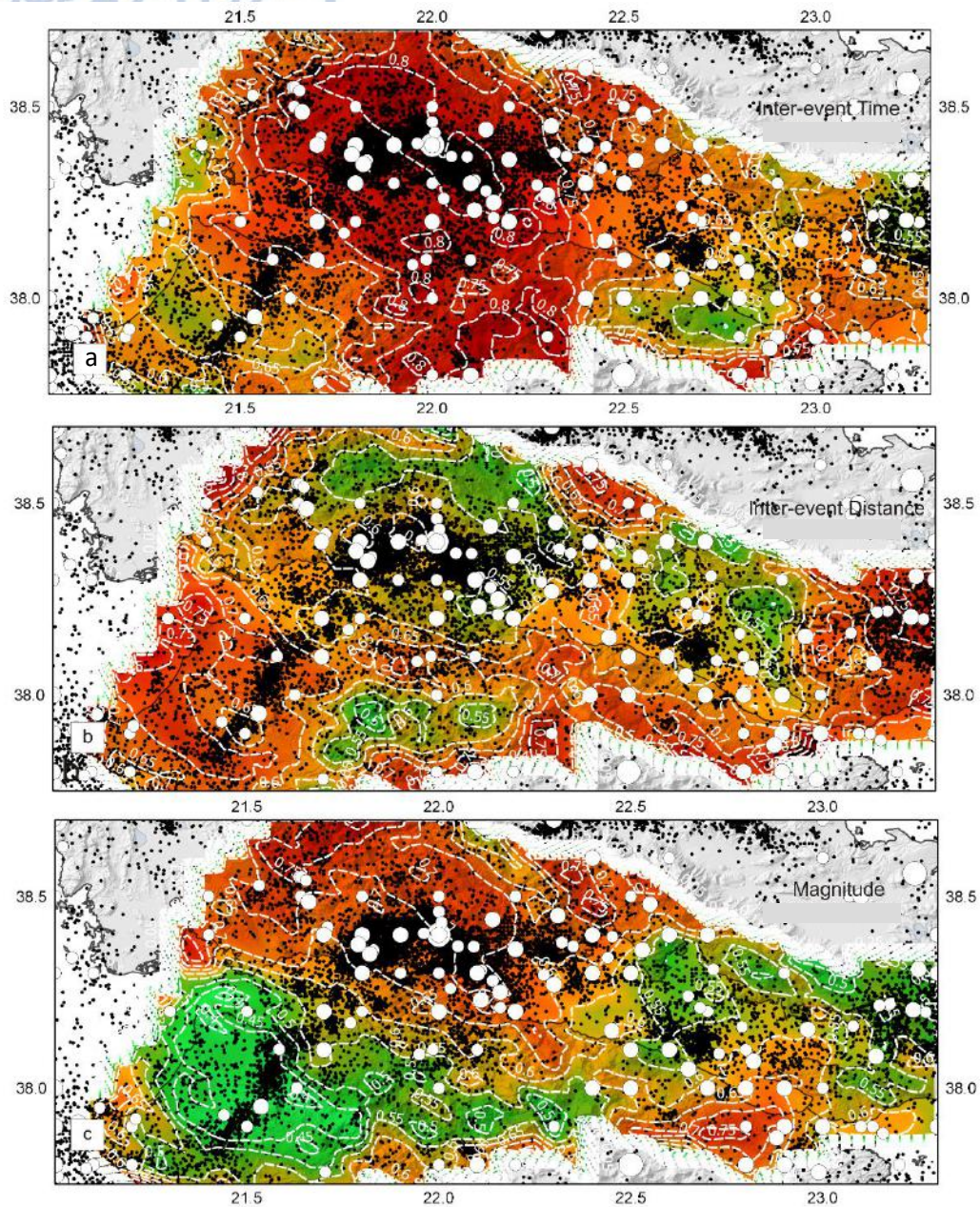


Figure 3-12 Spatial distribution of the Hurst exponent computed from IET for the region of the Corinth rift for the period 2008–2014. The most important faults from west to east are depicted: Psathopyrgos fault (Ps.F), Aigio Fault (Aig.F), Eliki fault (El.F), Akrata fault (Akr.F) and to the eastern part Xylocastro fault (Xyl.F), and Perachora fault (Per.F), Skinios fault (Sk.F) and Alkyonides fault (Alk.F), Athikia fault (Ath.F), Patras fault, Achaia Fault (Ach.F), Trichonida Fault (Trich.F) and the antithetic Delphi fault (Del.F.) a) for IET, b) for IED, c) for M.

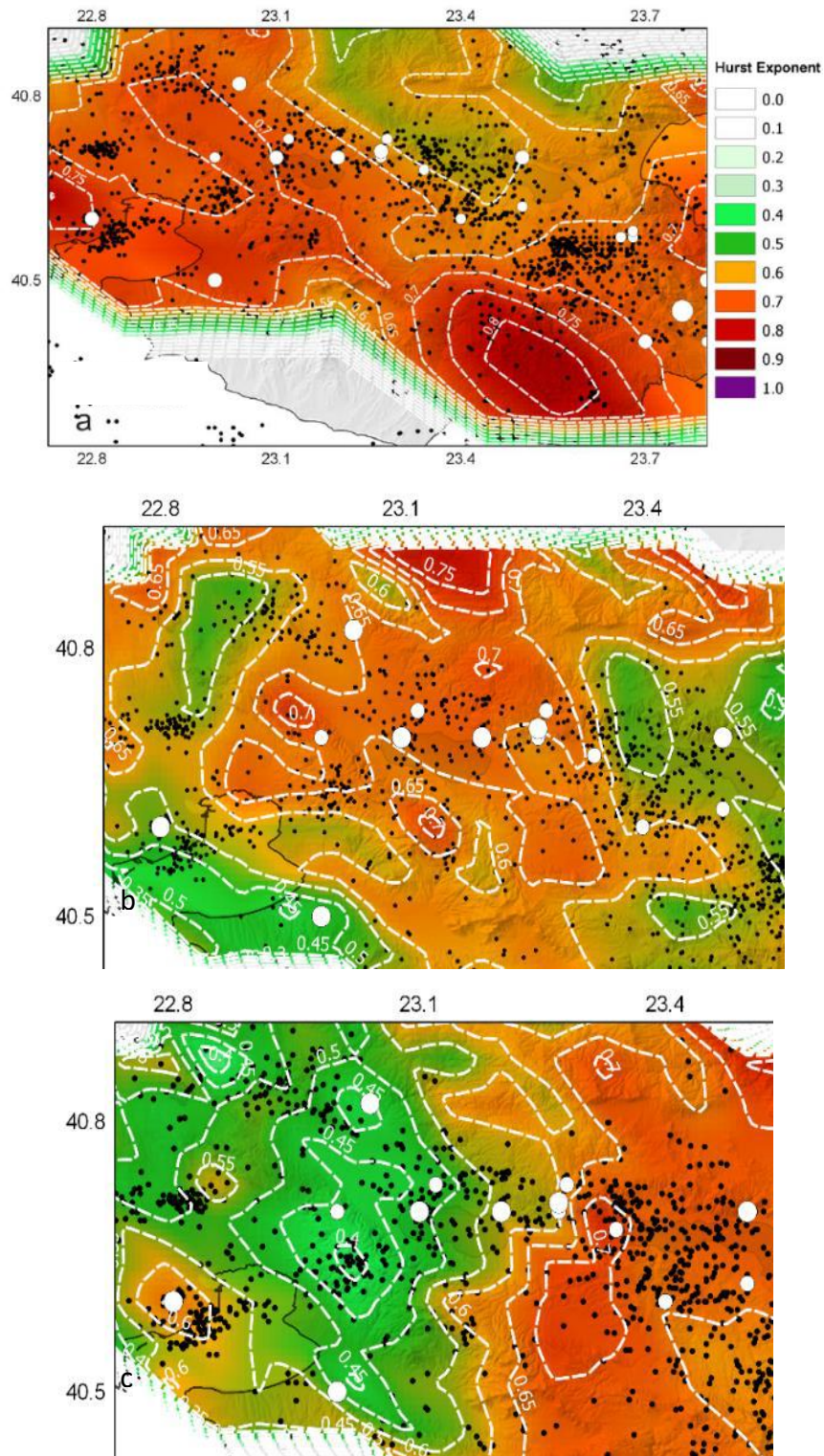


Figure 3-13 Spatial distribution of Hurst exponent computed for the IET for the region of Mygdonia graben for the period 2008–2014 a) for IET, b) for IED, c) for M

In addition to the long-term correlations expressed with Hurst coefficient, short term correlations were investigated, in terms of autocorrelation. The degree of autocorrelation over a specific lag is measured with the autocorrelation function \hat{ACF} which defines that stationarity in a process is expected when \hat{ACF} which is provided by:

$$\hat{ACF}(k) = \frac{E[(X_i - E[X])(X_{i+k} - E[X])]}{E[(X_i - E[X])^2]} \quad \text{Eq. 3-10}$$

where $E[X]$ denotes the expectation operator, is summable, for example $\sum_{k=-\infty}^{\infty} |\hat{ACF}(k)| < \infty$

Non summability corresponds to a power decay when the function decays exponentially for large lag times. Stationarity implies a short-range memory condition, an absence of earthquake excitations or aftershock occurrence, a state which generally describes the background regular seismicity. This function is used to highlight the autocorrelation degree under the means of \hat{ACF} , that expresses the relation between two observations which belong to the same stochastic process and they lag for k . This coefficient is used for stationary processes and expresses their short or finite memory. The autocorrelation coefficient for a known stochastic process $X_i, i=1, \dots, n$, is given by the following function:

$$\hat{ACF}(k) = \frac{\sum_{i=1}^{n-k} (X_i - \bar{X})(X_{i+k} - \bar{X})}{\sum_{i=1}^n (X_i - \bar{X})^2}, \quad k = 0, 1, \dots, K \text{ and } \bar{X} = \sum_{i=1}^n X_i \quad \text{Eq. 3-11}$$

where the parameter k is the adopted truncation lag (lag length) of \hat{ACF} . The coefficient varies from -1.0 to 1.0, however due to autocorrelation function symmetricity, \hat{ACF} positive values are considered only. \hat{ACF} is used for the identification of preserved short-term memory for IET, IED and M in all earthquake catalogs described in Table 3.2 Weglarczyk and Lasocki (1999) applied this methodology to induced seismicity and their results strongly suggest short memory existence for lapse time and distance in induced microseismicity catalogs. \hat{ACF} results are presented in correlograms/autocorrelation plots. Confidence intervals with an $\alpha=0.05$ significance approximating the Gaussian distribution bound \hat{ACF} values. Autocorrelation at and beyond a given lag is rejected (null hypothesis) at $\alpha=0.05$ significance level, when \hat{ACF} values exceeds the upper or the lower bound.

3.2.4.2 Results for the Corinth Rift

The autocorrelation function technique was applied in IET, IED and M for all seismicity catalogs for Corinth Rift in order to investigate whether and for which parameters the earthquake process preserves short memory characteristics. Results for Corinth rift are graphically depicted in Figure 3-14, where \hat{ACF} values for the 40 first successive lags are plotted against the respective lags. \hat{ACF} values for IET, IED and M for strong earthquakes

(A₁ catalog) are confined within the confidence bounds [-0.32, 0.32] and assumingly they are deprived of short memory attributes, exhibit randomness (Fig.3-14a,b,c). Short memory characteristics for moderate earthquake (B₁ catalog) and microseismicity (C₁ catalog) exhibit a largely different behavior. In moderate seismicity, IET (Fig.3-14d) and IED (Fig.3-14e) hold higher values which indicate the presence of short memory properties in the examined process over a lag that is defined by the number of the observations above the Gaussian threshold [-0.042, 0.042]. Magnitude autocorrelation analysis shows an increased value for the first measurement and the rest values ranging between the confidence bounds, indicating the absence of correlation in short lags (Fig.3-14f).

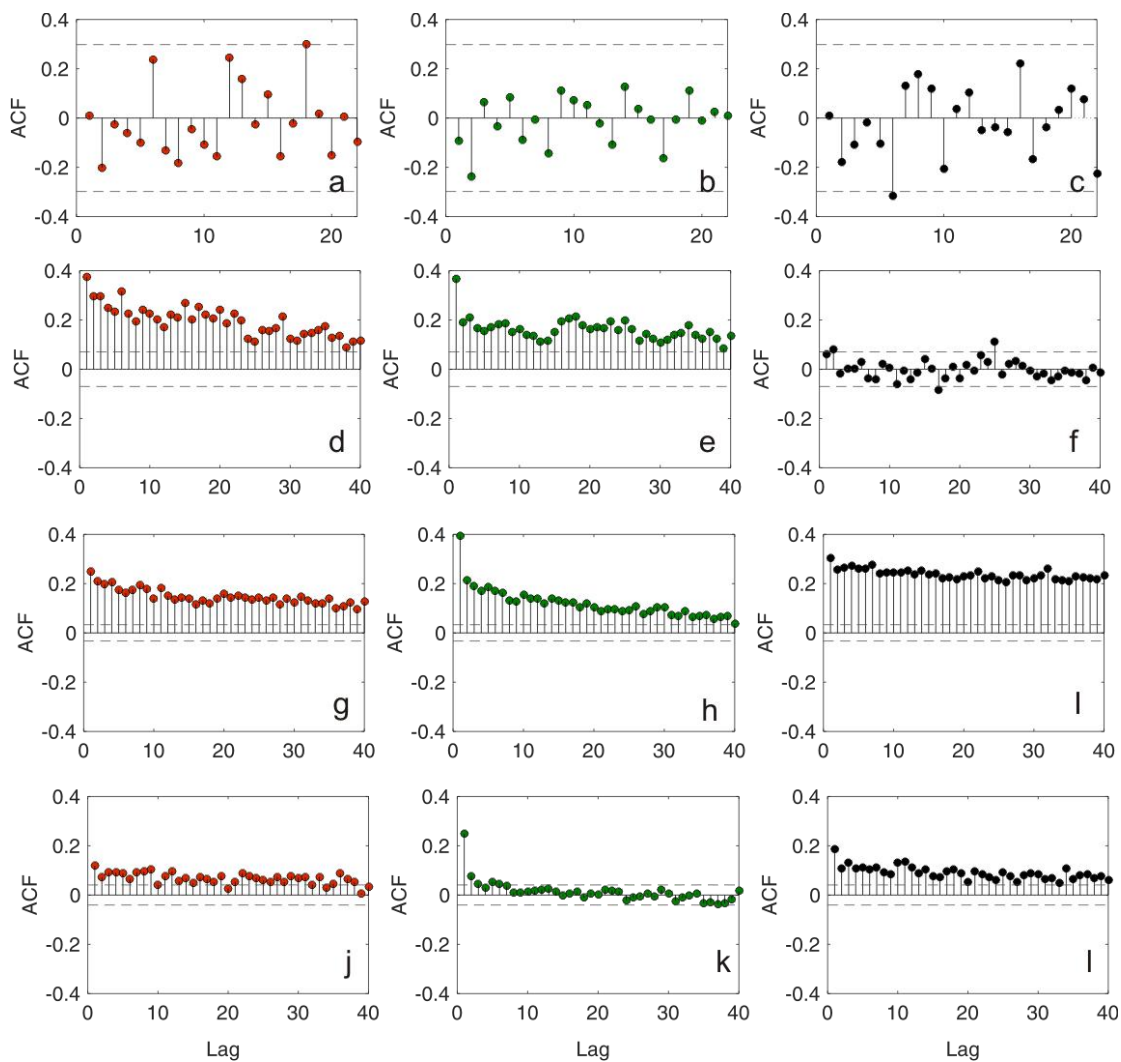
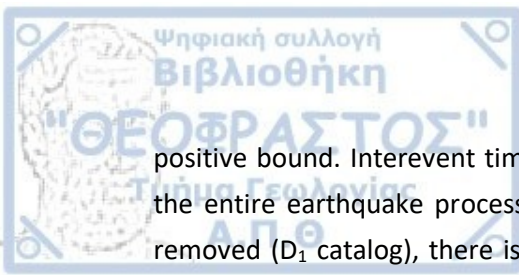


Figure 3-14 ACF results for all data sets of Corinth gulf. The first column corresponds to calculations on IET, the second to IED and the third to Magnitudes. In particular a) IET for A₁ data set, b) IED A₁ data set, c) Magnitude for A₁ data set, d) IET for B₁ data set, e) IED B₁ data set, f) Magnitude for B₁ data set, g) IET for C₁ data set, h) IED C₁ data set, i) Magnitude for C₁ data set, j) IET for D₁ data set, k) IED D₁ data set, l) Magnitude for D₁ data set.

Strong autocorrelation during the entire process is indicated for IET (Fig.3-14g), IED (Fig.3-14h), and M (Fig.3-14i) non declustered microseismicity (and Fig.3-14h) showing a dominant short memory pattern for seismicity. \hat{ACF} values in time show a totally different behavior than any other examined parameter since almost all the first 40 values exceed the 0.042



positive bound. Interevent time in Corinth possesses strong short memory behavior during the entire earthquake process. When a significant portion of dependent earthquakes are removed (D_1 catalog), there is an impact on the seismic process that loses strong memory content but still preserves short memory characteristics (Fig.3-14j). IED varies between the interval bounds with the exception of the first three positive values, indicating that the process afterwards turns into a random procedure without preserving memory after three lags of observations (Fig.3-14k). Magnitudes also retain the memory content for the first twenty lags of the process (Fig.3-14l).

3.2.4.3 Results for Mygdonia graben

Figure 3-32 shows the $A\hat{C}F$ results for IET, IED and M analysis in Mygdonia. For the moderate seismicity catalog (B_2 catalog) where $A\hat{C}F$ values are bounded between [-0.085, 0.085] interevent times show important indications of short memory characteristics at the first two lags of the process (Fig.3-15a) in contradiction with IED (Fig.3-15b) and M (Fig.3-15c) for which the null hypothesis is confirmed up to the 40th lag of the seismic process for the confidence interval [-0.2 0.2]. $A\hat{C}F$ for recent microseismicity (C_2 catalog) preserves strong short memory properties, with autocorrelations values ranging in the confidence boundaries of [-0.085, 0.085]. Interevent time exhibits extremely high autocorrelation values denoted at the first three lags of the process, while the next values up to the 40th lag are bounded within the confidence intervals (Fig.3-15d). Significant short term characteristics describe IED (Fig.3-15e) and M (Fig.3-15f) where short memory is expected for four and three subsequent lags of the earthquake process, in respect. Short memory decay exists for the rest of the process. Aftershock removal in D_1 catalog shows a slight variation for IET which still holds short term memory for the first three lags of the process (Fig.3-15g). When it comes to interevent distance, short memory is non-significant since $A\hat{C}F$ values beyond the first lag do not exceed the upper and lower limit [-0.085, 0.085] (Fig.3-15h). $A\hat{C}F$ for magnitudes while there are only some values which exceed the upper confidence interval, especially the first value, meaning that there are not strong indications for short memory effect (Fig.3-15i). Mygdonia contains significant short memory content and the time occurrence of the events is strongly related to the occurrence time of the previous events. Interevent time is the most important parameter possessing memory, whereas magnitudes are not mutually related and distances are dependent in two or three lags after of which no short memory is possessed. Short memory characteristics follow the same behavior and only quantitatively differentiate between each other.

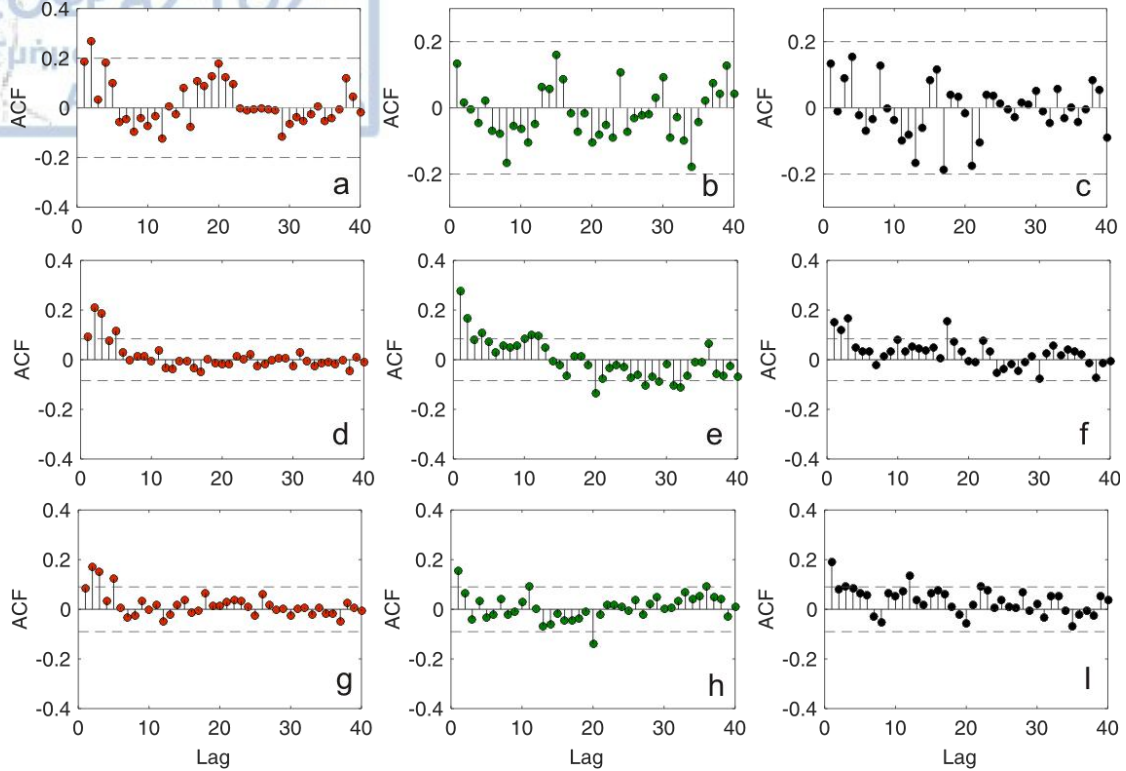


Figure 3-15 R/S analysis results for all data sets of Mygdonia. The first column corresponds to calculations on IET, the second to IED and the third to magnitudes. In particular a) IET for B₂ data set, b) IED B₂ data set, c) Magnitude for B₂ data set, d) IET for C₂ data set, e) IED C₂ data set, f) Magnitude for C₂ data set, a) IET for D₂ data set, b) IED D₂ data set, c) Magnitude for D₂ data set.

Matsumura coefficient of randomness, C_R , introduced by Matsumura (1984) was employed for measuring the quantification of earthquake clustering and interaction in time, space and size domain. The coefficient is expressed with a simple formula, which accounts for the first two statistical moments, the mean and the mean of the squares:

$$C_R = \frac{[MEAN(\tau)]^2}{MEAN(\tau^2)} \quad \text{Eq. 3-12}$$

where τ stands for the vector of the given seismicity parameter and $MEAN(\cdot)$ is the average value of the given sample. Mutsumura coefficient values range between 0 and 1 and when is equal to $\pi/4 (\cong 0.785)$ it signifies the existence of a completely random sample described by a Poisson process. For $C_R < \pi/4$ a seismicity pattern with high event clustering is implied and when $C_R > \pi/4$ there is indication for a regular process (e.g. a periodic or a quasi-periodic). The coefficient depends on the general pattern of seismicity according to the two moments, despite the parameters theoretical distribution and classifies the seismic activity accordingly. Matsumura (1984) applied this method on a central California microearthquake catalog for space, time and magnitude and showed that seismicity is random or slightly clustered with the exception of two important seismic bursts where clustering was dense. He suggested the application of this methodology in a wider range of magnitudes like moderate and strong earthquakes, which is conducted in the current study. Kijko (1993) who applied C_R as a function of apparent stress for induced seismicity cases in gold mines of South Africa suggested that when C_R implies randomness, stress is increased. In addition, he showed that strong events are described by a decreased C_R value, implying an enhancement of dense clustering between events.

Olszewska et al. (2017) applied this technique in interevent times for an induced seismicity catalog of Rudna mines, in Poland and showed the tendency of C_R to obtain values close to 0.5 with small events removal. In this study, C_R was used as an additional unbiased criterion of earthquake dense occurrence. The coefficient of randomness was investigated for all cases of strong, moderate and minor seismicity for IET, IED and M in Mygdonia and the Corinth Rift (Table 3-2). In all cases, the coefficient was estimated for the real data and synthetic samples were additionally compiled for further validating and comparing results between the two regions. N=10000 surrogate samples were generated with Bootstrap resampling from real data, a methodology which relies on random resampling with the replacement of real data. 95% confidence intervals were calculated from the synthetic samples with the use of Matlab toolkit. Results are described for the two study areas separately.

3.2.5.2 Results for the Corinth Rift

Results for randomness coefficient in Corinth Rift are summarized in Table 3-5 and schematically presented in Figure 3-16. $C_{R(IET)}$, $C_{R(IED)}$ and $C_{R(M)}$ correspond to the randomness coefficient values on real data for IET, IED and M respectively. It is observed that amongst all seismicity catalogs, the lowest values ($C_R < 0.5$) are met for the IET, whereas higher values with $C_R > 0.785$ are calculated for M, meaning that earthquake magnitudes exhibit a non random occurrence ($C_R \approx 1.0$). The highest $C_{R(IET)}$ value among interoccurrence event times corresponds to the one obtained for strong earthquakes (A₁ catalog) ($C_{R(IET)} = 0.487$), which implies moderate to weak clustering. A weaker correlation exists for interevent distance ($C_{R(IED)} = 0.685$), whereas magnitude shows a rather periodic repetition ($C_{R(M)} = 0.998$) (Fig. 3-16 a,b,c). IET clustering is significant for moderate events (B₁ catalog) ($C_{R(IET)} = 0.238$) and recent seismicity (C₁ catalog) ($C_{R(IET)} = 0.276$) whereas $C_{R(IED)}$ for both catalogs follows a similar weak correlation trend (≈ 0.5). IET for the declustered dataset of recent seismicity (D₁ catalog) shows that randomness coefficient is increased compared to the value obtained from the full catalog ($C_{R(IET)} = 0.381$) and clustering is discouraged with aftershock removal. However, the remaining background seismicity is not expected to have a random occurrence, contrary to Kijko (1993) findings. Matsumura coefficient for interevent distance, holds a value around 0.5 ($C_{R(IED)} = 0.586$) which shows that interevent distance clustering remains the same for the majority of the introduced datasets. Figure 3-16 shows the values on real data compared with synthetic values. The big range for bootstrap confidence intervals in catalog A₁, are related to the abundance of the sample.

Table 3-5. Information about the randomness coefficient for IET, $C_{R(IET)}$ IED, $C_{R(IED)}$ M, $C_{R(M)}$ in the Corinth Rift for all seismicity catalogs. C_R values obtained from real data are given along with the upper and lower Bootstrap confidence intervals calculated from 10.000 values for the synthetic data-set in each case.

Catalog	IET		IED		M	
	Real Data $C_{R(IET)}$	Bootstrap Confidence Interval	Real Data $C_{R(IED)}$	Bootstrap Confidence Interval	Real Data $C_{R(M)}$	Bootstrap Confidence Interval
A ₁	0.487	[0.326, 0.601]	0.685	[0.588, 0.760]	0.998	[0.997, 0.998]
B ₁	0.238	[0.213, 0.262]	0.510	[0.486, 0.532]	0.993	[0.991, 0.994]
C ₁	0.276	[0.261, 0.290]	0.544	[0.443, 0.467]	0.970	[0.968, 0.971]
D ₁	0.381	[0.351, 0.401]	0.586	[0.571, 0.601]	0.973	[0.9715, 0.975]

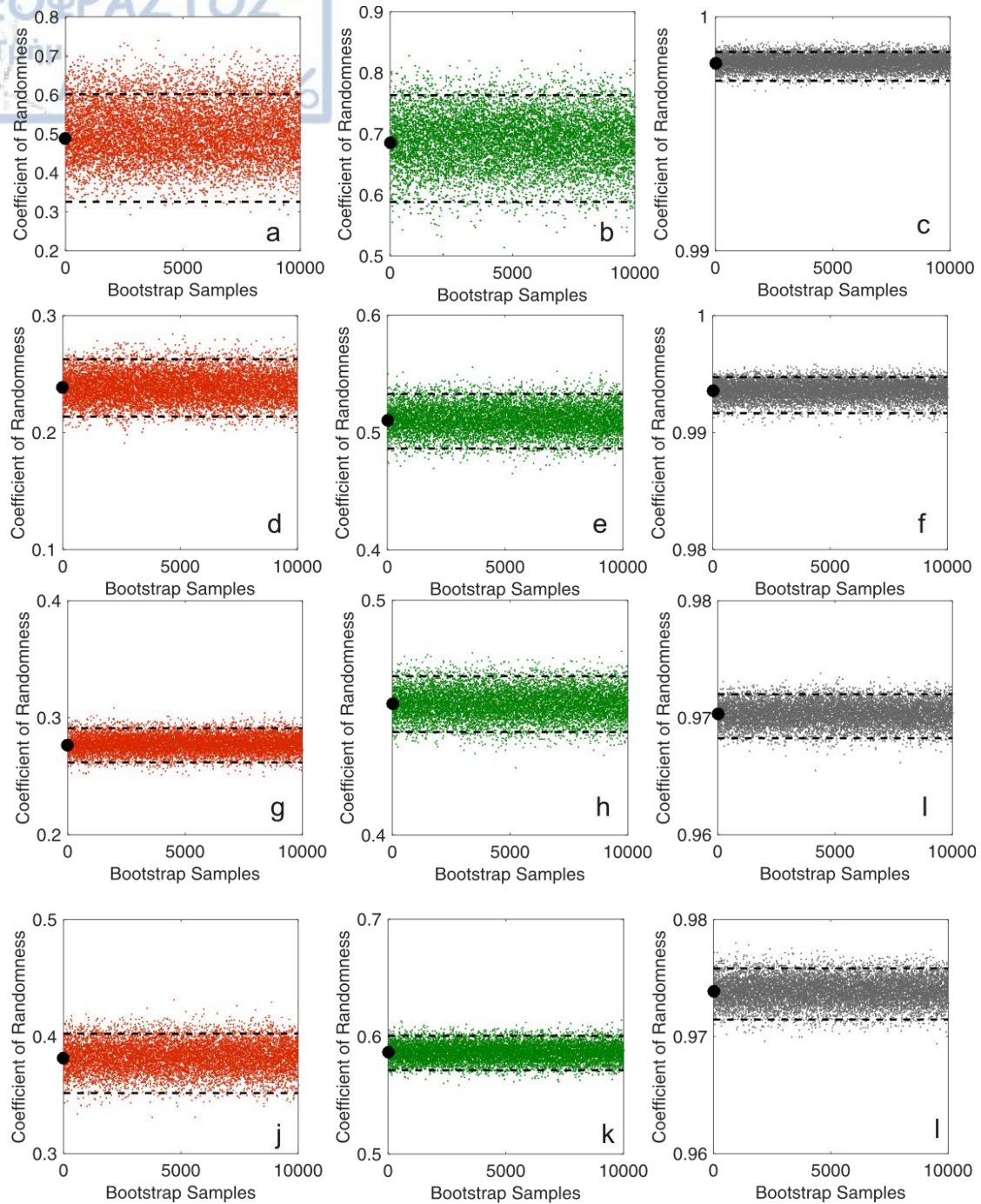


Figure 3-16 Results for the coefficient of randomness in the Corinth Rift considering IET (*left column*), IED (*central column*) and M (*right column*) displayed with the black dots, whereas dots in colors stand for the synthetic data sets. Confidence intervals produced by the synthetic samples are also shown with dashed lines. Calculations are performed for the seismicity catalog for strong earthquakes A (a, b, c), moderate earthquakes B₁ (d, e, f), recent earthquakes C₁ (g, h, i) and declustered recent earthquakes D₁ (j, k, l).

3.2.5.3 Results for Mygdonia graben

Estimations of the randomness coefficient, C_R in Mygdonia datasets are presented in Table 3-6 and plotted in Figure 3-17 where values on real data (black marker) along with the respective confidence bounds (dashed lines) produced by $N=10000$ values of randomness coefficient for synthetic data are displayed. The randomness coefficient lowest values are obtained for IET, where $C_{R(IET)} < 0.4$ (Fig.3-17 a, d, g), for B_2 catalog ($C_{R(IET)} = 0.241$) for C_2 catalog ($C_{R(IET)} = 0.279$) and slightly increased for the declustered D_2 catalog ($C_{R(IET)} = 0.399$) exhibiting a behavior theoretically closer to the background seismicity, which tends to be more random and less clustered.

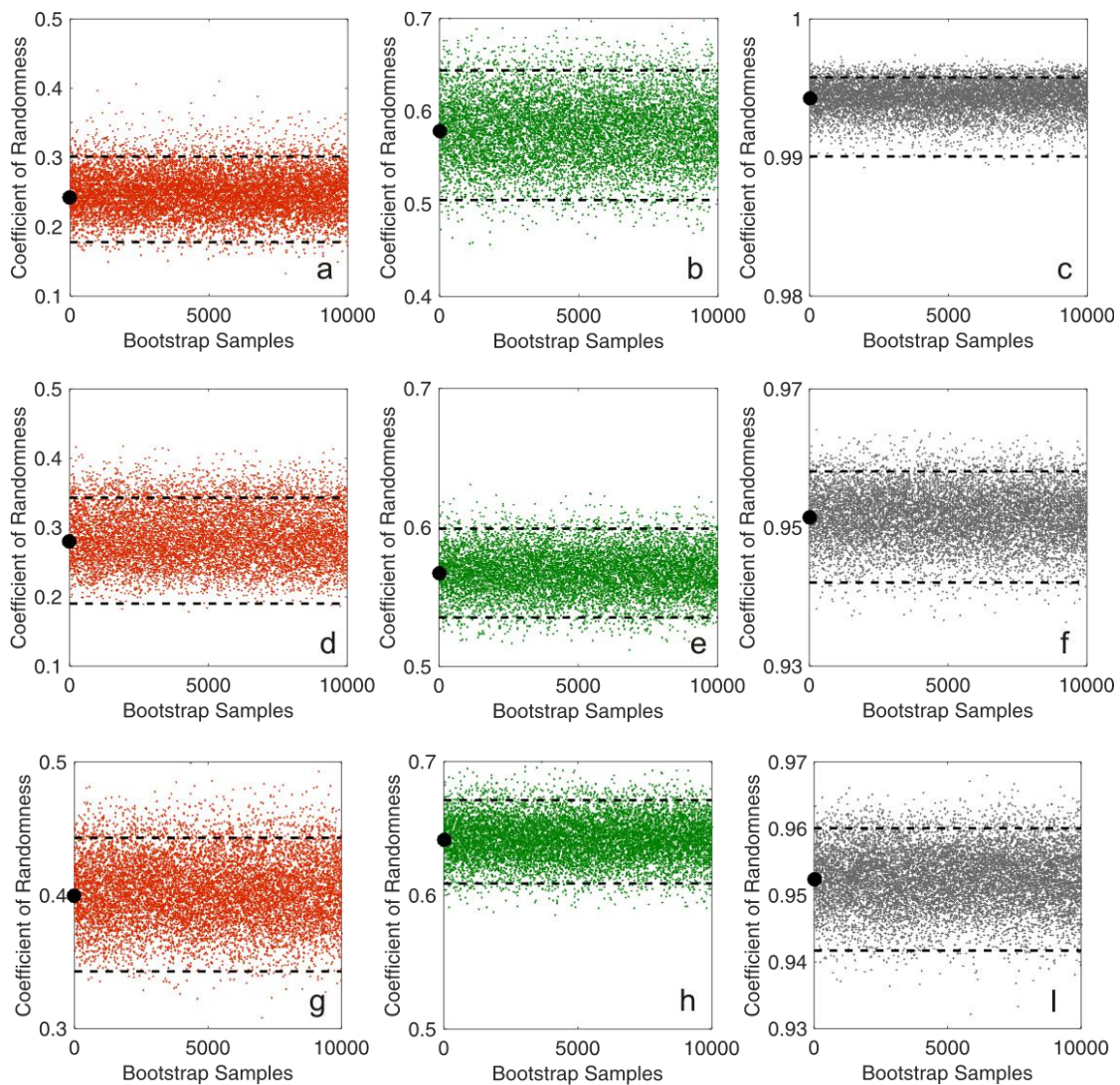
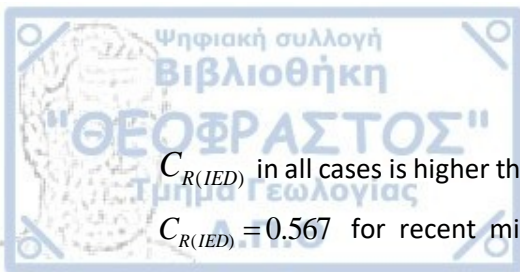


Figure 3-17 Results for the coefficient of randomness, in Mygdonia graben considering IET (left column), IED (central column) and M (right column) displayed with the black color, whereas dots in color stand for the synthetic data sets. Confidence intervals produced by 10.000 bootstrap samples are also shown with dashed lines. Calculations are performed for moderate earthquakes B_2 (a, b, c), recent earthquakes C_2 (d, e, f), and declustered recent earthquakes D_2 (g, h, i).



$C_{R(IED)}$ in all cases is higher than 0.5, $C_{R(IED)} = 0.578$ for moderate earthquakes (Fig. 3-17b), $C_{R(IED)} = 0.567$ for recent microseismicity (Fig.3-17e) and the highest value amongst all $C_{R(IED)} = 0.641$ for declustered microseismicity (Fig. 3-17h), indicating a rather random behavior in all cases. $C_{R(M)} \approx 1.0$ for all catalogs signify periodicity or a characteristic absence of interrelations between magnitudes within dense confident intervals (Fig. 3-17 c, f, l). Similarly with the Corinth Rift, randomness coefficients for IET declare that the strongest clustering degree between events is possessed in the time domain with the moderate events to prevail.

Table 3-6. Information about the randomness coefficient for IET, $C_{R(IET)}$ IED, $C_{R(IED)}$ M, $C_{R(M)}$ in Mygdonia for all seismicity catalogs. C_R values from real data are given along with the upper and lower Bootstrap confidence intervals calculated from 10.000 values for the synthetic data-set in each case.

Catalog	IET		IED		M	
	Real Data $C_{R(IET)}$	Bootstrap Confidence Interval	Real Data $C_{R(IED)}$	Bootstrap Confidence Interval	Real Data $C_{R(M)}$	Bootstrap Confidence Interval
B₂	0.241	[0.177, 0.301]	0.578	[0.504, 0.643]	0.994	[0.990, 0.995]
C₂	0.279	[0.190, 0.342]	0.567	[0.535, 0.599]	0.951	[0.942, 0.958]
D₂	0.399	[0.342, 0.443]	0.641	[0.608, 0.671]	0.952	[0.941, 0.959]

3.1 Synthesis of the results - Discussion

The stochastic approach of seismicity parameters reveals hidden information of the seismic process. The contribution of the current analysis is the exhaustive exploitation of all available data from historical catalogs up to most recent microseismicity and the analysis from different perspectives but with compatible and collaborative methodologies. The analysis is performed for a specific seismotectonic environment connected with two extensional fault systems, which cannot be completely isolated from the general seismotectonic regime but they form two distinct fault populations with specific properties, each one of them. The scope of the study was not to identify universal characteristics of seismicity, but to search for systematic behaviors on two specifically seismogenic regions in Greece exhibiting intense seismicity. The degree of interaction and presence of clustering which is raised between earthquakes, is the result from the interdependence mechanisms between faults and cannot be studied without considering fault properties. The objective for the overall analysis is set to the identification of differences, temporal or spatial differentiation in the analysis of distinct datasets which form a unique seismic pattern. A considerable effort has been put for the elaboration of different catalogs and magnitude ranges according to the magnitude thresholds in each case. The magnitude of completeness which has been calculated with significant accuracy, comprises a vital parameter for the magnitude investigation and also for

the interevent times of the consecutive events which characterize each catalog. The analysis has been achieved at all magnitude scales and for full and declustered earthquake catalogs, since different laws are expected to dominate in the case when dependent features are removed from mainshocks even with the application of arbitrary to some extent declustering procedures. The most striking conclusive remarks for complexity, short- and long- range memory and clustering, inferred from the aforementioned statistical processes, are summarized in Table 3-3 and Table 3-4 for both areas. The memory content within the seismic process composed by IET, IED and M was investigated. The degree of dependence and interrelations between events through the seismic process are well documented by the use of the Hurst exponent tool and the employment of the rescaled range analysis, which is applied in a wide range of sciences for analysing time-series. In the current thesis, R/S analysis targets to specific fault zones, sharing common seismotectonic properties, where the associated seismicity is mostly concentrated at the center of the grabens, bounded by normal antithetic faults. The new component in this approach is that details of the seismicity properties are sought in a smaller scale comparing with previous studies (Xu and Burton, 2006) thus avoiding over smoothing in the analysis or identification of gross characteristics which are evident when large areas are examined.

Hurst results for strong seismicity could be achieved only in Corinth rift due to limited available data and show a hint of independence in the occurrence of earthquakes with $M > 6.0$. Low values of H for interevent time and distance show almost Brownian attributes with the absence of clustering in the occurrence of these events. However, results from the synthetic data express a slightly higher value of H adding a small amount of clustering in the seismic process. Independence of strong events has also been proposed by Shadhkoo et al. (2009) for California earthquakes and strong ones seem to behave in a less correlated way, than smaller earthquakes. However, Cisternas et al. (2004) stated a strong correlation for a number of historical earthquakes along the North Anatolia Fault in Turkey. It seems that the occurrence of strong events is still under debate. On the other hand, there is evidence that smaller earthquakes do not occur randomly but they exhibit strong clustering in time and space even if dependent events are removed. The most dependent seismicity parameter is time and especially the lapse time which intercedes between successive events. Memory in time and distance is evident in both study areas, since H has a range of values exceeding 0.5 in all cases. A high value of H is determined for the interevent time in Corinth Rift showing that there is a significant dense occurrence of earthquakes. The reliability of H estimations can be deduced from the synthetic data set that they are in accordance with the behavior of a random sample. Corinth Rift experiences higher H values for interevent time for 1981-2014 and 2008-2014 with the discrepancy in the completeness threshold for each catalog. In general a strong dependency among the following and the past events is revealed as far as interevent time and distance are concerned. The dependence of earthquake occurrence with the previous events is also strong for Mygdonia where the majority of the data correspond to small magnitudes distributed along the deformation zones. It is observed that all the calculated coefficients both



for real and synthetic data exhibit values higher than 0.5 indicating long memory characteristics for the given state of the individual components which parameterize the earthquake process, showing that future states depend on the previous one and consequently share the same characteristics. These results agree with Shadkhoo et al. (2009) who suggest that Hurst exponent increases for smaller magnitudes and is obvious in the study areas. However, it seems that in all cases earthquakes in the Corinth gulf show a higher dependence compared to Mygdonia seismic fault zone. Based on the results for the moderate earthquakes and the recent seismicity, we observe that the Corinth rift seismicity reveals a more persistent behavior in IET and IED parameters than Mygdonia seismicity. The persistence of the Corinth rift earthquake series appears the best in the IET and next in the IED series. However, the Mygdonia magnitude data seem to be persistent whereas the Corinth rift data do not. In both cases magnitudes cover nearly the same range, of about 3 magnitude units, but the range for Mygdonia events begins from M1.7, whereas the Corinth rift from M2.3. This suggests that magnitudes of weaker events are more correlated.

For statistical efficiency, the temporal and spatial analysis of the Hurst estimates is performed only for the more abundant data series in the two study areas (D_1 and D_2 datasets) for IET, IED and magnitudes. A spatial analysis was done in order to associate H variations with the fault network. H values range between 0.5-0.8 in Corinth rift showing a spatial pattern with high values ($H \sim 0.8$) along Pspathopyrgos (Ps.F) and Aigion faults (Aig.F) in the central part of the Rift (Figure 3-18). Microseismicity around these areas is spatially highly clustered but also reveals areas where earthquake occurrences are likely uncorrelated ($H \sim 0.5$, greenish parts). Faults associated with high H values are mainly the Ps.F and the Aig.F. Microseismicity along these faults is triggered by the Efpalio sequence in 2010. High values are further observed along Eliki fault (El.F.), exhibiting a weak remote interaction. A magnitude independent space-time clustering algorithm is applied at the seismic catalog of the Corinth rift and thus significant seismic bursts that occurred during this period are also mapped shown with higher contrast. Three distinct parts are formed, according to the significance of high Hurst values, which are the western Corinth rift (up to 22.50 longitude), the eastern Corinth rift and the NW Peloponnese area (longitude: 21.0–21.6) (Fig. 3-18). IET time series in these three parts are depicted in Fig. 3-19 for comparison. Western Corinth rift experiences the occurrence of more numerous and more close in time earthquakes, than eastern Corinth and NW Peloponnese, showing that there is a higher tendency for the seismicity of the western part to keep persistent characteristics. A stronger dependence degree of earthquake occurrence times is evident in the first case. Earthquakes of the eastern part are not strongly related, meaning that short interevent times are probably followed by long interevent times, probably due to the interference of subsequent earthquakes in the western part of the rift. As far as short time analysis is concerned, results are different for the two study areas. It seems that there is an independence of strong earthquakes in Corinth gulf. The situation is different for moderate and small events where especially for moderate events a long term memory is highlights during the entire process especially for interevent time and distance.

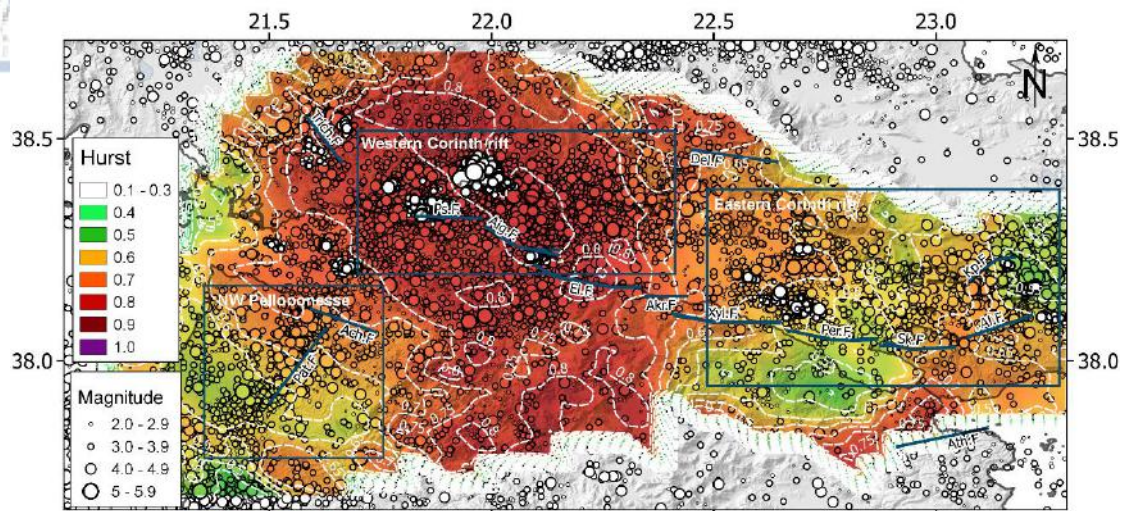


Figure 3-18 Spatial distribution of the Hurst exponent computed from IET for the region of the Corinth rift for the period 2008–2014. The most important faults from west to east are depicted: Psathopyrgos fault (Ps.F), Aigio Fault (Aig.F), Eliki fault (El.F), Akrata fault (Akr.F) and to the eastern part Xylocastro fault (Xyl.F), and Perachora fault (Per.F), Skinos fault (Sk.F) and Alkyonides fault (Alk.F), Athikia fault (Ath.F), Patras fault, Achaia Fault (Ach.F), Trichonida Fault (Trich.F) and the antithetic Delphi fault (Del.F.).

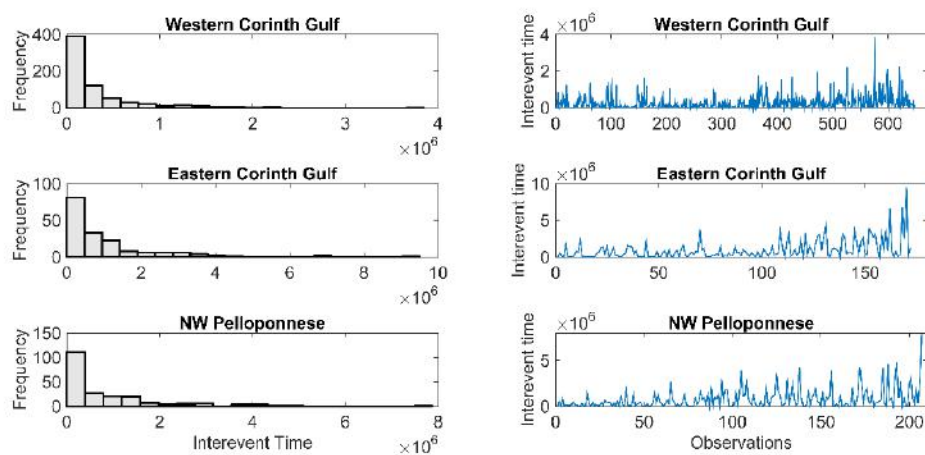


Figure 3-19 The frequency histogram of the IET series (left-hand-side column) and the time-series diagram (right-hand-side column) for the western Corinth rift, the eastern Corinth rift and NW Peloponnese.

The spatial analysis is also performed in Mygdonia graben. Hurst exponent spatial variations show that the majority of values ranges between 0.6 and 0.8 (Fig. 3-20). Higher values are met at the western part and the main tectonic structure of the area (TGFZ – Thessaloniki Gerakarou Fault Zone) whereas to the eastern part interdependencies expressed by the Hurst component seem to be lower. For the same values of tuning parameters as in the previous analysed case of Corinth rift seismicity the pattern is now more uniform. The

investigation of magnitude does not exhibit clear results, since the Magnitudes of the recent period seems to be more correlated than the ones in 20 years duration.

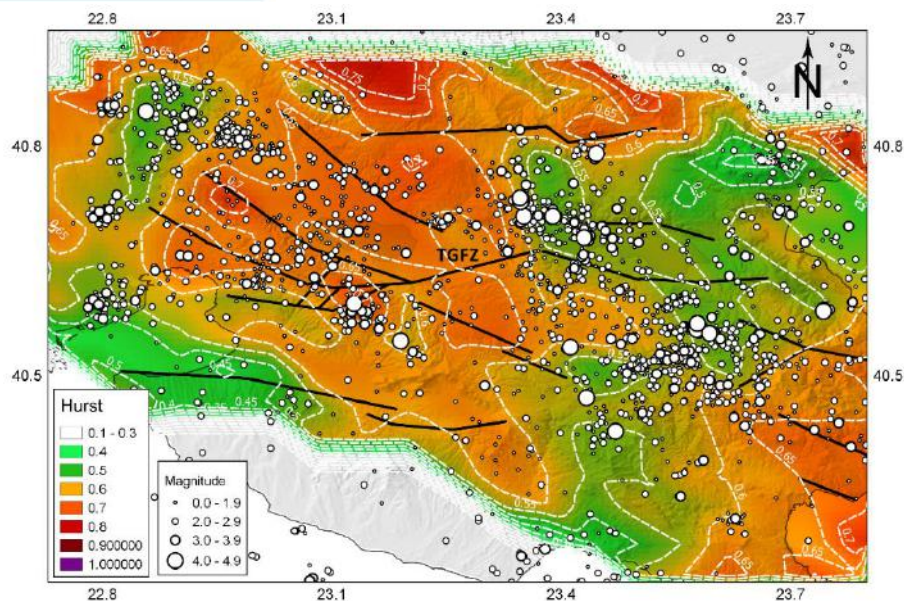


Figure 3-20 Spatial distribution of Hurst exponent computed for the IET for the region of Mygdonia graben for the period 2008–2014. The most important fault zones are mapped. Two separate areas are distinguished in the eastern and the western part of the Mygdonia graben.

On the other hand, Mygdonia area shares short term memory characteristics in all cases. Seismicity catalogs of different areas and periods exhibit a wide range of properties behaving either with randomness (Gardner and Knoppof, 1974), periodicity (Rikitake, 1976) or high clustering depending on geological and seismotectonic factors. In this study the statistical criteria for the detection of subtle variations concerning occurrence in seismicity was the Coefficient of Randomness, Cr. Long term interaction of strong earthquakes has been suggested for a long time (seismic cycle, seismic gap, Fedotov, 1965; Mogi, 1969). There are studies indicating that the long-term correlation of strong earthquakes over long periods (tens of years or centuries) is a characteristic phenomenon. (Kagan and Jackson, 1991a; b) suggest that in periods with a high seismicity rate, there is a high probability of an anticipated event and in cases where periods of quietness have a smaller than usual probability for an earthquake occurrence. In our case, the number of the strong events is statistically inadequate. Small earthquakes are not directly associated with hazard assessment due to their minor societal impact, however, they can be exploited as indicators which highlight the future candidates where larger earthquakes are likely to happen. The dense spatial distribution and the increased frequency are often observed in the vicinity of strong earthquakes, so it delineates zones where strong events are anticipated. Kafka and Levin (2000) showed that future earthquakes have a tendency to occur in the vicinity of past



earthquake concentrations more frequently than would be expected for a random distribution of future earthquakes.

Summing up, characteristics in the successive earthquake occurrence reflect the characteristics of the interaction of faults and the associated seismicity. Even in the case of minor earthquake occurrence investigation, the ascertained memory is linked to the causative fault population. Detection of memory holding processes enables predictability of future earthquakes. Therefore, the stochastic analysis performed in this study in addition to the description and interpretation of the seismicity behavior, provides an additional component for seismic hazard assessment. It is expected that these new findings are effective and will provide further contribution to the future seismic hazard assessment in the study areas. Nevertheless, there are some discrepancies that hinder the analysis and even more problems that need to be answered and to be further investigated. It is susceptible to a number of factors such as the seismotectonic environment of the study area, the data sample, the homogeneity and the consistency of the catalogue as well as the time period that the data refer to, and all of them affect the results. The results obtained from the application of the stochastic analysis help us to provide an interpretation of seismicity behavior as well as they denote a further insight into the physical mechanisms generating either a high or a low current seismicity state in the two study regions of Greece.



Chapter 4

Coulomb Stress Analysis

4.1 Introduction

4.1.1 Earthquake, fault interaction and tectonic deformation

Earthquake occurrence is a process evolving on active faults. The strong connection between earthquakes and faults became clear with the introduction of the elastic rebound theory (Reid, 1910) showing that earthquakes and faults reflect the way crustal deformation builds up. Aspects of the seismic process such as earthquake interaction, earthquake migration, hypocentral distribution, spatio-temporal clustering can be interpreted in terms of stress transfer between seismogenic sources (Ben-Zion and Sammis, 2003). It has been widely shown by a large number of studies that earthquake interaction is a dominant feature of seismicity (King et al., 1994; Toda et al., 1998; King and Cocco, 2001, Scholtz, 2002). The occurrence of a strong earthquake causes a redistribution of stress around the epicentral area and coseismic static stress changes. In stress increase areas seismicity is triggered, whereas in areas of stress decrease future earthquake occurrence is hindered (Harris, 1998; Stein, 1999). After a strong earthquake, a fault relaxation period follows where stress values recover under the long-term tectonic loading due to plate movements. It is assumed that changes in stress even in the order of 0.1bar are efficient enough to trigger a future event (Reasenberg and Simpson, 1992; King et al., 1994) meaning that even small stress change increments are capable of influencing the location and timing of the following earthquake.

Faults represent elastic dislocations within the brittle crust where strain accumulation is the driving agent that makes them grow, link and dislocate. Faults in nature exist within fault populations comprising a complicated synthesis of isolated, segmented or linked faults (Ben-Zion and Sammis, 2003). A fault initiates when strain values reach a critical level and lead to gradual coalescence and linkage of smaller faults to large ones. Fault growth is assumed to be the result of the lateral propagation of the fault tips where stress exceeds the yield strength of the elastic medium and the linkage between adjacent faults when they start propagating (Scholz, 2002). Fault segments which start to be linked with each other, merge into longer structures and act as a single fault with maximum displacement and length (acquiring soft or hard linkage). These interaction processes are dominant in extensional seismotectonic environments like the areas in this study. It is assumed that populations of faults and earthquakes are self-organizing (e.g., Sornette and Sornette 1990) and their physical, geometric and statistical characteristics evolve with increasing deformation. Therefore, deformation reveals the evolutionary stage and the tectonic maturity of the fault populations also affecting seismogenesis. Hardacre and Cowie (2003) suggested that the higher the strain builds in a region, the longer the fault zones evolve, indicating faulting localization. Regarding the correlation between increasing strain and fault evolution it has been experimentally shown that fractures are enhanced as a function of strain and fracture density (Spyropoulos et al. 1999). Strain accumulation also indicates strong or weak localization of faulting associated with the geometrical and structural properties of faults and is often related to

different statistical scaling fits. Low strain regions are related to fault populations with power-law scaling fits, whereas higher strain areas where the major amount of strain is accommodated by slip on certain long faults, lead to exponential laws (Bonnet et al., 2001; Cowie et al., 1993). In addition to this observation Scholz and Cowie (1990) suggest that the majority of strain accumulation in a region is mainly associated with the largest faults of the population and the contribution of small structures is rather negligible. According to Jackson and McKenzie (1988) when slip rates along faults are significant (especially along plate boundaries where crustal deformation is fast) short seismic rate released by the instrumental seismicity is sufficient enough in order to construct the regional strain pattern. The amount of strain is controlled by a variety of geological factors including rock strength, crustal rheology, presence of fluids, fault healing rate, structure and mechanical properties of the brittle crust. The total amount of the interseismic strain accumulation in the crust is attributed both to continuing seismic and aseismic processes, so there is a consistency between the strain produced by plate movements and long term earthquake moment release. This long term process is caused by the coseismic dislocations during strong earthquakes and the relative plate motion which evolves between strong earthquakes. Ambraseys and Jackson (1990) suggested that in seismogenic areas like Greece a significant proportion of strain is of aseismic origin (almost 50% of total strain) or is accumulated due to low magnitude earthquake occurrence ($M < 5.8$).

4.1.2 Objective of the study

The objective of this study is to investigate earthquake and subsequently fault interaction in terms of stress transfer and identify the driving mechanism of seismogenesis. The study is restricted to the specific fault systems described in Chapter 1 and where the influence of earthquakes and faults close to the borders of the study areas, is considered insignificant. The first scope is to examine if under the known regime of deformation, strong earthquakes ($M > 6.0$) that occurred from 1700 until 2014 in Corinth rift and from 1677 until 2014 for Mygdonia graben have caused faults to move closer or further from failure and whether there is an interrelation between strong earthquakes. The Coulomb fracture criterion is adopted for the calculation of the static stresses on target from the source faults which in this study are called rupture models and faults are approximated as rectangular planes dipping into the seismogenic crust. The construction of the source models is significant because the stress tensor depends on the geometrical parameters of the source and target fault that is resolved onto. The rupture models for the strong pre-instrumental and instrumental earthquakes are assessed and constraints are based on geological and seismological criteria. Scaling laws have also been elaborated in the absence of relevant seismotectonic information. The contribution of the total deformation, seismic and aseismic due to constant lithospheric movements is studied. The current stress field as well as the gradual stress perturbations after the occurrence of each strong earthquake are modelled by adding the effects of the co-seismic changes due to the coseismic slip and the long-term tectonic loading which is accumulated

along major faults. This study is conducted in order to examine the overall dependence of recent seismicity on previous strong activity under the current stress pattern. For the estimation of the interseismic strain accumulation around the major fault zones the methodology of the "virtual dislocation model" is adopted which presupposes the estimates of the slip rates along the major regional faults acquired from geological or geodetic studies. The stress model is applied in evolutionary stages for the two study areas starting from 1700 until present. A number of tests on the probable value of the coefficient of friction, μ , and Skempton's coefficient, B , which are embodied into the analysis are performed and alternative values for the apparent coefficient of friction have been tested in order to detect possible variations of the stress pattern. The association between the current stress field and microseismicity clusters are also investigated. The portion of the aseismic and seismic strain is a driving mechanism which leads to earthquake occurrence and stress release in the fast deforming grabens of the Aegean sea and the different viscous properties of the crust are also responsible for the differences in the seismotectonic pattern and the seismic activity. Differences expected between these two amounts of strain are considered in addition to interpret results from the seismotectonic and the statistical analysis and possibly explain how deformation affects the seismicity pattern and if there is a systematic stress behavior of the study areas. The scientific targets of the study are graphically described in Figure 4-1.

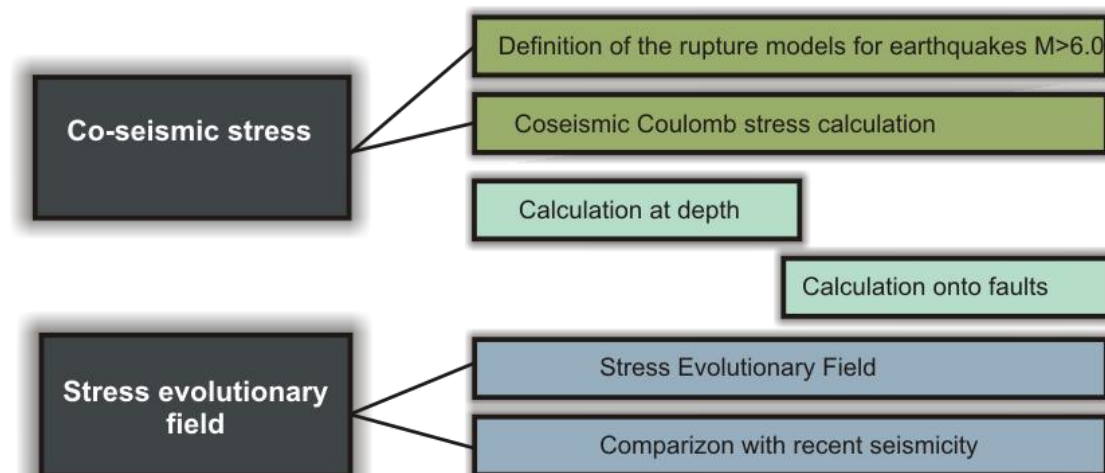


Figure 4-1. Graphical description of the targets for Coulomb stress analysis.

4.2 Coulomb Stress Changes

4.2.1 Methodology

Static stress changes influence the location and timing of subsequent strong earthquakes or aftershock activity (King et. al., 1994; Parsons et al., 2002). Changes in the evolving stress field arise due to the coseismic stress changes induced by the occurrence of strong earthquakes ($M \geq 6.0$), along with long-term stress accumulation on major faults. The interaction of earthquakes by studying the evolution of the stress field in the two study areas is attempted. The methodology that is followed relies on elastic rebound theory, according to which the stress released in an area existed prior to the event and the applied technique follows Deng and Sykes (1997). According to this technique, stress is a tensor varying in space and time and is elastically transmitted within the brittle crust of the Earth, while the brittle crust is approximated as an elastic single-layer crust over a homogeneous ductile half space. The cumulative change in stress is the combined result of the seismic deformation (coseismic dislocations) and the slow aseismic deformation due to the relative plate motions. For calculating the interseismic strain accumulations the "virtual dislocation" concept is introduced. The model suggests that the stress released in an earthquake preexists in the crust brittle part before the event and is determined by assuming that the fault slips backwards powered by constant lithospheric loading, the energy that generates earthquakes. The aseismic deformation which occurs along the major faults from their free surface to the seismogenic depth is quantified with their slip rates. The fault source models for the coseismic and virtual dislocations are approximated with a planar orthogonal fault surface, Σ , with finite dimensions, embedded in an elastic half space (Okada, 1992). The displacement, u_k , across the surface of the fault for an arbitrary uniform dislocation, U is determined from the following equation (Steketee, 1958):

$$u_k = \frac{U_i}{8\pi G} \iint_{\Sigma} w_{ij}^k v_j d\Sigma \quad \text{Eq. 4-1}$$

where U_i is the i^{th} component of U and G is the shear modulus, v_j are the direction cosines of the normal to the surface, and w_{ij}^k are the six sets of Green 's functions. The computation of the elastic stress, s_{ij} derives from the strain tensor, e_{ij} following Hooke's law for an isotropic medium, as follows:

$$s_{ij} = \frac{2G\nu}{1-2\nu} \delta_{ij} e_{kk} + 2Ge_{ij} \quad \text{Eq. 4-2}$$

where ν is the Poisson's ratio and δ_{ij} is the Kronecker delta. It is assumed that Earth is as an elastic structure where post seismic deformation is almost negligible. Absolute values of acting stress on faults cannot be measured directly but they can effectively be inferred from strain values.



Earthquakes occur when the stress exceeds the fault strength and the Coulomb Failure Function criterion examines the conditions under which failure occurs on brittle rocks (Scholz, 2002). According to it, earthquakes occur along a plane when shear stress exceeds rock strength. Changes in Coulomb Failure Function (ΔCFF) depend on the changes in shear stress, $\Delta\tau$ and normal stress, $\Delta\sigma$, resolved onto the earthquake's fault plane:

$$\Delta CFF = \Delta\tau + \mu'\Delta\sigma \quad \text{Eq. 4-3}$$

where μ' is the apparent coefficient of friction. The change in normal stress, $\Delta\sigma$, is positive for increasing normal stress and shear stress, $\Delta\tau$, is positive for increasing shear stress in the direction of the fault slip. Positive ΔCFF values denote a high likelihood for failure, therefore locations with advanced stress changes indicate areas close to rupture in the direction of the relative slip on the target fault, whereas negative values indicate that fault failure is prevented. Subsequent earthquakes preferentially occur on positive ΔCFF locations whereas negative values are seismic quiescence areas. The spatial correlation between aftershock seismicity and Coulomb stress has been highlighted by a number of studies (Reasenber and Simpson, 1992; Kagan and Jackson, 1998) showing that the main shock promotes the occurrence of the subsequent seismicity in bright areas. The criterion cannot indicate when the consecutive earthquake will occur, however, it reveals if the failure has been advanced. The insufficiency of friction laws to fully explain fault properties lays on the fact that fault strength is strongly affected by the presence of pore fluids in rocks. Pore fluids mechanically reduce the effective normal stress and consequently cause a reduction in shear stress. Fault strength is also affected from the occurrence of chemical reactions when the temperature level along the shear zone is elevated (Hickman et al., 1995). The role of the pore fluids expressed with the failure function criterion on triggered seismicity has been thoroughly studied (Harris, 1998; Stein 1999). When the effect of pore fluids is considerable, Eq 4-3 takes the form:

$$\Delta CFF = \Delta\tau + \mu(\Delta\sigma + \Delta P) \quad \text{Eq. 4-4}$$

where μ corresponds to the friction coefficient which for dry models ranges between 0.6 and 0.8 (Byerlee, 1978). For a homogeneous isotropic poroelastic model ΔP is the pore pressure change within the fracture, expressed by $\Delta P = -B\Delta\sigma_{kk}/3$ (Rice and Cleary, 1976) where B is the Skempton's coefficient and $\Delta\sigma_{kk}$ is the summation of the stress tensor trace and corresponds to the change in effective normal stress. When a change in fluid presence occurs there is a sudden change of $\Delta\sigma$ and a subsequent change to both ΔP and $\Delta\sigma_{kk}$ making all parameters dependent on time. Skempton's coefficient theoretically varies between 0 and 1.0 depending on the rock pores and the filling material. For air filled pores, B is almost zero, for water ranges between 0.5 and 1.0 and in the case of fluid and soil saturated rock it takes values around 1.0 (Rice and Cleary 1976). There is a variance of B for granites, sandstones or

marbles, between 0.5 and 0.9. Robinson and McGinty (2000) propose that B is obtained between 0.5 and 0.75, whereas Scholz (2002) suggests that immediately after an earthquake $B \approx 2/3$ but it can also be equal to zero if fluids drain off the fault zone. The apparent coefficient of friction, μ' is related to the Skempton and friction coefficient under the expression $\mu' = (\mu - \alpha)(1 - B)$ for the special conditions where $\Delta\sigma_{11} = \Delta\sigma_{22} = \Delta\sigma_{33}$ and then $\mu' = \mu(1 - B)$. μ' describes the effect of the pore pressure change due to pore fluid and is either treated as a material constant or a time dependent parameter varying before and after a strong earthquake (Harris and Simpson 1998). Low μ' values are related to weak fault zones with a well-developed gouge often saturated with fluids (Stein, 1999). μ' values for dry materials range between 0.5 and 0.8 (Harris, 1998). According to Parsons et al. (1999) the apparent coefficient of friction is low for long fault zones ($\mu' < 0.2$) whereas it is high for small ones ($\mu' > 0.8$). King et al. (1994) suggested that substantial variations from 0.4 do not impose significant alterations in stress changes and following them, Nalbant et al. (2002) as well as Toda et al. (1998) obtained $\mu' = 0.4$ for their studies in eastern Turkey and Japan, respectively. For the Loma Prieta earthquake Reseanberg and Simpson (1992) identified that for $\mu' = 0.2$, they achieved the best dependence between positive stress values and aftershock locations. King et al (1994) suggested that even if μ' varies essentially it does not alter the stress distribution in adjacent area of the seismic source. Lin and Stein (2004) suggested the value of 0.4 for long rupture zones like Saint Andreas fault in California as well as for subduction zones. For reverse faults Parsons (2005) introduced different values of the apparent coefficient of friction into the calculations and concluded that results are not strongly susceptible to the variations of μ' . For studies in the Aegean area, Papadimitriou and Sykes (2001) employed $\mu' = 0.6$ while Papadimitriou (2002) considered $\mu' = 0.4$ after testing different values for the apparent coefficient which showed insignificant effect in stress results for the central Ionian islands. Paradisopoulou et al. (2010b) investigated the effect of pore pressure by using different values of B and observed differences particularly around the fault tips, for onto fault stress calculations.

For the calculation of static stress changes, source models are constrained to approximate the rupture geometry. Stress caused by the occurrence of an earthquake is computed according to the properties of the receiver fault by resolving the stress on a preferable plane defined by the focal mechanism of the earthquake. Fault outcrops show rugged surfaces and this approximation is followed by some researchers at depth (Mildon et al., 2019) however, a simplified geometry also followed by other researchers is accepted in this study. Despite their heterogeneity, faults can be simply approximated with planar rectangular geometric structures, which dip into the brittle part of the crust. Except of small earthquakes which they correspond to circular seismic sources, strong earthquakes are assumed to extend from the lower part of the brittle crust to the surface (Scholtz, 2010).

The geometrical parameters such as the fault length (L) the fault width (w) the coseismic displacement (u) and the fault plane solution given by the strike (ζ) dip (δ) and rake (λ) adequately describe the rectangular rupture models and they are used as input for stress change evaluation (Fig. 4-2). These parameters are deduced from the available geological or seismological information and in the absence of this information, parameters are computed with the application of empirical relationships relating earthquake moment magnitude with fault length and average displacement. Several such empirical relations have been proposed for regional and global data (Wells and Coppersmith, 1994; Ambraseys and Jackson, 1998; Papazachos et al., 2004; Pavlides and Caputo, 2004). The necessity for the use of scaling laws especially in this study lies to the fact that the majority of the strong events have a pre-instrumental origin. The scaling laws proposed by Papazachos et al. (2004) who collected worldwide structural data with the area of Greece included in the data set, were used. The relationships for dip slip continental faults (Eq. 4-5) and strike slip faults (Eq. 4-6) are described by the following forms for fault length (in km):

$$\log L = 0.50M - 1.86 \quad \text{Eq. 4-5}$$

$$\log L = 0.59M - 2.30 \quad \text{Eq. 4-6}$$

Jackson and White (1989) showed that the maximum length for individual normal faults is not capable of exceeding 20-25km, this assumption is also considered in this study. Empirical laws for the estimation of the average coseismic displacement, u (in m) for dip slip continental faults (Eq. 4-7) and strike slip faults (Eq. 4-8) are accordingly expressed by (Papazachos et al., 2004):

$$\log u = 0.82M - 3.71 \quad \text{Eq. 4-7}$$

$$\log u = 0.68M - 2.82 \quad \text{Eq. 4-8}$$

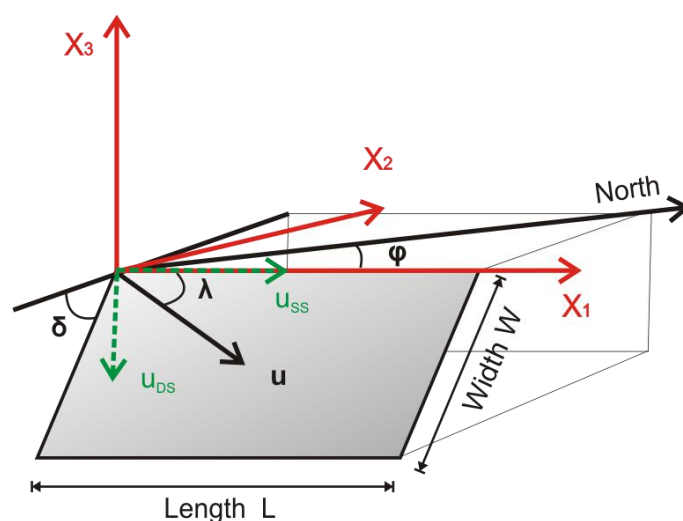


Figure 4-2 Graphical representation of the sources which are approximated with rectangular surfaces along with their descriptive parameters.

Fault width is calculated from $w = h/\sin(\delta)$ where δ is the dip angle of the fault and h is the down-dip distance from the surface to the lower edge of the fault. The value of the aspect ratio (fault length/fault width, L/W) is taken into consideration for shallow dip faults. According to Lin and Stein (2004) the efficiency of one fault to trigger an earthquake is related to the shadow zone around the strike of the fault, meaning that short thrust ruptures are efficient in triggering other thrust events of similar size along the strike of the rupture plane, while long ruptures inhibit thrust faults in a large region perpendicular to the rupture plane. The constraint for the aspect ratio $L/W \geq 1.0$ is maintained especially when low dip angle faults are investigated (Mildon et al., 2016). In cases of instrumental recordings where seismic moment (M_0) is known, the average coseismic displacement, \bar{u} (in cm) can be directly calculated from:

$$M_0 = G\bar{u}wL = G\bar{u}S \quad \text{Eq. 4-9}$$

where G is the shear modulus in the seismic source, which is approximately estimated equal to $3.3 \cdot 10^{11} \text{ dyn} \cdot \text{cm}^{-2}$ (Stein et al., 1997) and S corresponds to the fault area. For historical earthquakes where there is a significant uncertainty in the estimation of magnitude, the

equation $\bar{u} = \frac{\pi^2}{32} \frac{\Delta\sigma}{\mu} (WL)^{1/2}$ proposed by Console et al. (2008) has been also taken into

account, where the seismic moment is completely omitted from the calculations and where μ is the shear modulus of the elastic medium ($3.3 \cdot 10^{11} \text{ dyn} \cdot \text{cm}^{-2}$; Scholtz, 2002) and $\Delta\sigma$ is the stress drop ($3 \cdot 10^6 \text{ Pa}$; Console and Catalli, 2006). The vertical and the along strike components of the displacement vector (u_{SS}, u_{DS}) are geometrically computed as shown in Figure 4-2. The seismic moment is assumed to be the most representative seismic parameter for the quantification of the source size for instrumentally recorded earthquakes (Aki, 1967) and it is fundamental in strain estimation. For historical earthquakes for which the seismic moment is unknown, the scaling law by Hanks and Kanamori (1979) was used according to which the logarithmic scalar seismic moment for each earthquake M_0 is linearly related to the moment magnitude according to:

$$\log M_0 = 1.5M_w + 16.01 \quad \text{Eq. 4-10}$$

where M_0 is expressed in $\text{dyn} \cdot \text{cm}$ and M_w has been inferred from macroseismic information derived from seismological and geological data (Papazachos and Papazachou, 2003) or recordings. Furthermore, it is important to define the width of the seismogenic crust in which brittle properties prevail and where the stress is accommodated. The seismogenic part is indicated by the distribution of the relocated foci at depth obtained from the seismotectonic analysis of Chapter 1. For Mygdonia graben the depth is obtained equal to 15km (3-18km) which is in agreement with previous studies (Tranos et al., 2003; Papadimitriou

and Sykes, 2001) and in the case of Corinth rift the average width of the seismogenic crust is considered to be slightly thinner and it is taken equal to 3-12km.

4.2.2 Seismic Sources

The seismic sources which are encompassed in Stress Coulomb analysis regard strong earthquakes ($M \geq 6.0$) from 1677 until present in Mygdonia graben and Corinth rift. Historical earthquakes only for the last four centuries were incorporated in the study in an attempt to minimize uncertainties produced by imperfectly known and limited information on strong past seismicity. Epicentral and size uncertainties as well as the correlation of events with the causative faults are increasing by going back in time, with subsequent uncertainties rising especially when it comes to the estimation of seismic moment. The seismic sources are described by fault geometrical properties which are approximated with the procedure described in methodology and the fault plane solutions which are crucial for the definition of the stress field since the variation of these parameters strongly affects the final stress pattern. A considerable number of historical events from the late 17th century until present, with the only exception of the instrumental 1978 earthquake, have occurred in Mygdonia. Strong seismicity information on their assumed or reported fault plane solutions is summarized in Table 4-1 and Figure 4-3. The focal mechanisms for the six earthquakes are attributed to Papazachos and Papazachou (2003) and Ambraseys (2009) and are inferred from fault geometry whereas the epicentral locations are speculated from isoseismal maps (Papazachos and Papazachou, 2003; Paradisopoulou et al., 2016).

Table 4-1 Information on fault plane solutions for Mygdonia strong earthquakes ($M \geq 6.0$) for the period 1677 - present. Fault planes used in this study are highlighted in bold letters. Magnitudes with asterisks are approximations of M_w based on historical macroseismic information (Papazachos and Papazachou, 2003). In the absence of instrumental measurement, seismic moment is theoretically calculated with Eq. 4-10.

n	Time Year	Epicenter		Depth (km)	M_w	M_0 ($\cdot 10^{25}$)	Fault Plane Solution			Ref.
		Latitude (ϕ°)	Longitude (λ°)				Strike (ζ°)	Dip (δ°)	Rake (λ°)	
1	1677	40.500	23.000	-	6.2*	2.04	278	53	-93	(1), (2)
2	1759	40.600	22.800	-	6.3*	2.88	278	53	-93	(1), (2)
3	1902	40.820	23.040	-	6.5*	8.13	90	53	-93	(1), (2)
4	1932	40.450	23.760	-	7.0*	30.9	93	53	-93	(1), (3)
5	1932	40.790	23.440	-	6.2*	2.04	90	53	-93	(1), (4), (2)
6	1933	40.659	23.545	-	6.3*	2.88	278	46	-70	(1), (4), (2)
7	1978	40.729	23.254	7.0	6.5	5.20	278	46	-70	(5)
						4.24	271	42	-74	(6)
						3.50	257	41	-96	(7)
						2.70	286	43	-88	(8)

1: Papazachos and Papazachou (2003); 2: Hanks and Kanamori (1979), 3: Taymaz et al. (1991), 4: Paradeisopoulou et al. (2016); 5: Soufleris and Stewart (1981), 6: Liotier (1989); 7: Braunmiller & Nabelek (1996); 8: HRV-GCMT.

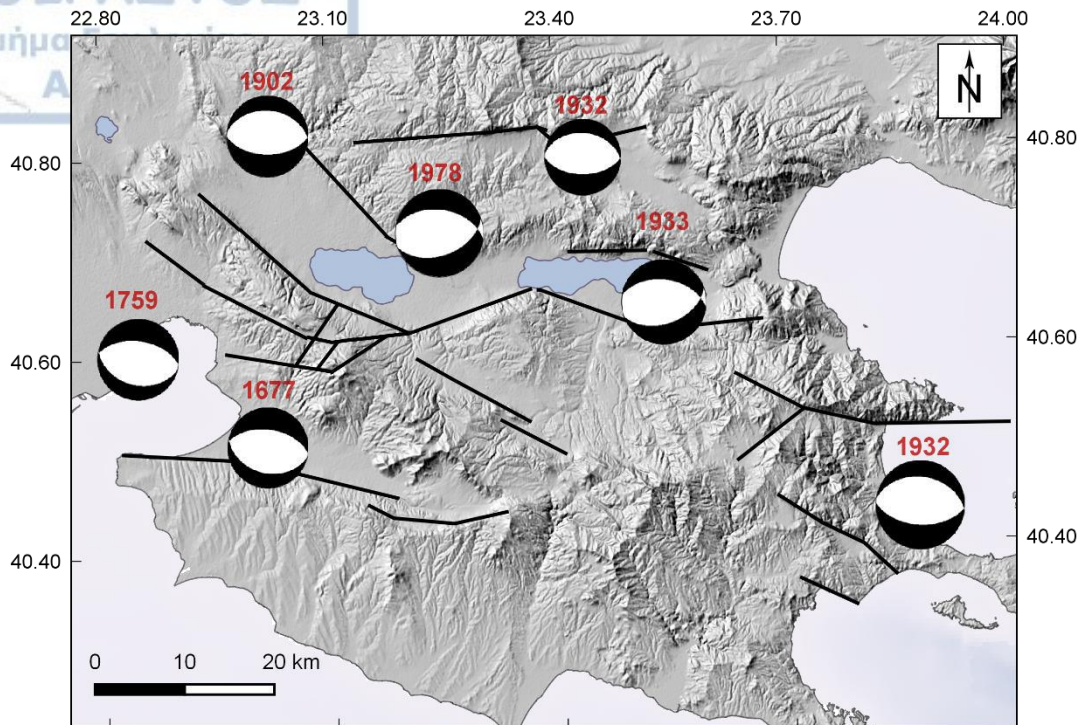


Figure 4-3 Fault plane solutions for the strong ($M \geq 6.0$) earthquakes in the period 1700 until present in Mygdonia graben (Table 4-1) shown as equal area lower hemisphere projections where compressions quadrants are shown in black. The occurrence year is on the top of the beach balls.

Jackson and McKenzie (1988) and Ambraseys and Jackson (1990) agree that 30 years of observation are adequate for studying the long term moment release rate in the fast deforming Aegean area. Figure 4-4 shows the cumulative scalar seismic moment M_0 released in Mygdonia area for the study period, as a function of time. Individual M_0 for the strong earthquakes ($M \geq 6.0$) are computed with Eq. 4-10 apart from the 1978 earthquake which is obtained from Soufleris and Stewart (1981). The total released seismic moment is equal to $5.53 \cdot 10^{26}$ dyn-cm and the seismic moment distribution exhibits an uneven distribution in time, when the knowledge of all the earthquakes shows a long recurrence time for these earthquakes and long stress built-up. The sharp increase of the seismic moment after 1900 implies that a possible overestimation of magnitude for the earthquakes which occurred in 1932 and 1933. The eigenvalues of the seismic moment tensor are computed according to the equation set of Aki and Richards (1980) and the six elements of the individual and total seismic moment tensors are listed in Table III-1 of the Appendix III. M_{33} seismic moment component ($M_{33} = -53.14 \cdot 10^{25}$ dyn-cm) ascertains the thinning of the crust width, in North – South direction while positive values in the horizontal directions reflect the extensional deformations in both axes, as expected. The strain tensor is obtained from the equations of Kostrov (1974) who suggested that if regional strain is seismic then it is approximated with the sum of moment tensors released by faults or earthquakes. According to Kostrov theorem for a given crustal volume V , the average strain rate ϵ_{ij} during a specific time window T (not including rotational deformations) that is produced by N earthquakes is given by the sum of the released seismic



moments produced by strong earthquakes which have occurred in the study area for the given time, as shown below:

$$\varepsilon_{ij} = \frac{1}{2\mu VT} \sum_{k=1}^N M_o^k m_{ij}^k \quad \text{Eq. 4-1101}$$

where M_o is the scalar seismic moment. m_{ij}^k is the ij unit component of moment tensor of the k^{th} earthquake and μ is the elastic shear modulus of rigidity for the elastic medium ($3 \cdot 10^{11} \text{ dyn/cm}^2$). The area undergoing deformation is calculated for a 12km width single-layer brittle crust, for the range of $T=343$ years of strong seismic observations. The average strain for the strain tensor principle components is approximately equal to $5.31 \cdot 10^{-8}$. The elements of the strain tensor evidence that the maximum deformation which is almost in a N-S direction is extensional ($3.8 \cdot 10^{-8}$) while deformation in the E-S direction ($-2.4 \cdot 10^{-11}$) is insignificant. The negative value of e_{33} ($-3.8 \cdot 10^{-8}$) indicates a thinning of the crust, which is compatible with the stress field in Mygdonia area.

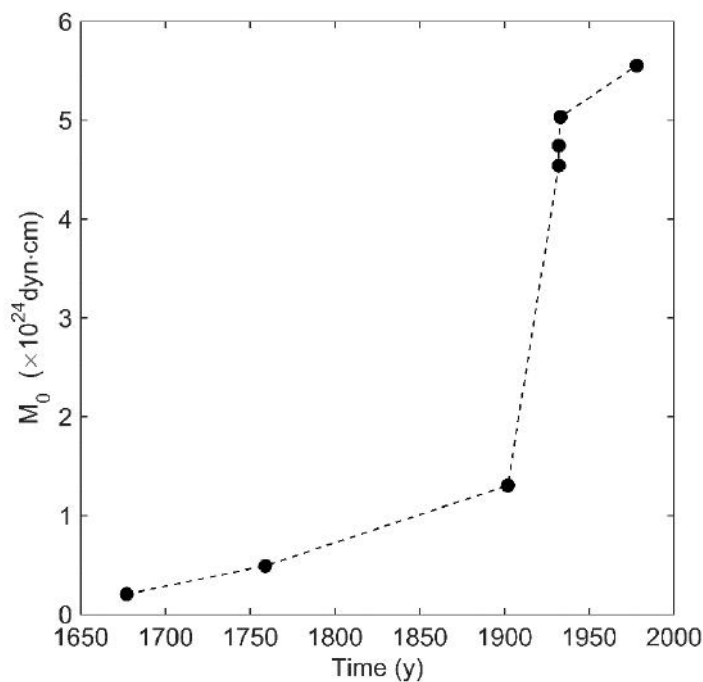


Figure 4-4 Cumulative seismic moment M_0 (in dyn-cm) released in Mygdonia area for the historical and instrumental strong earthquakes ($M > 6.0$) from 1677 to 2020.

There is a record of 30 historical and instrumental strong earthquakes which struck the area from 1700 onwards in the Corinth Rift. Information on earthquake fault plane solutions and their resources is summarized in Table 4-2 whereas they are depicted in Figure 4-5. Focal mechanisms of strong earthquakes show that normal fault plane solutions are dominant in the entire area which is associated with the N-S extension except in the western part in Patras gulf and the Northwestern Peloponnese where strike slip faulting prevails.

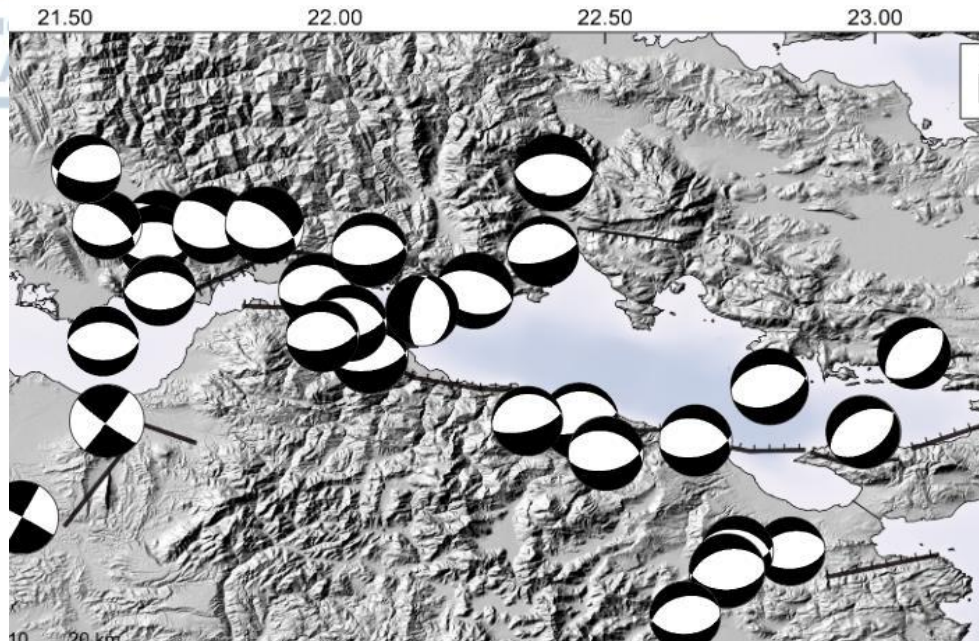


Figure 4-5 Fault plane solutions for the strong ($M \geq 6.0$) earthquakes in the period 1700 to today in Corinth rift (information is given in detail in Table 4-2) shown as equal area lower hemisphere projections. Compression quadrants are shown in black.

The scalar seismic moment, M_0 , estimates until 1965 are based on the scaling law of Hanks and Kanamori (1979) since there in the absence of other sources. The cumulative seismic moment released by all earthquakes with $M \geq 6.0$ in Corinth gulf as a function of time is graphically shown in Figure 4-6. The number of historical and instrumental strong seismicity over the 300 years is considerable and the rate is relatively steady, indicative periods of high activity around 1800 and 1980 and there is no indication for missing earthquake information. The cumulative seismic moment release in the Corinth rift is $1.62 \cdot 10^{27}$ dyn-cm with the M_{33} seismic moment component equal to $1.32 \cdot 10^{27}$ dyn-cm. (Eq. III-1, Appendix III). The estimation of the seismic strain in Corinth rift is based on the above information for $T=337$ years. The strain tensor shows that it is clear that the maximum deformation which is almost in a N-S direction is extensional ($5.77 \cdot 10^{-8}$), while deformation in the E-S direction is less significant ($e_{22} = -1.5 \cdot 10^{-8}$) and the negative value of e_{33} ($e_{33} = -5.59 \cdot 10^{-8}$) is in accordance with the undergoing extension and crust thinning (Table III-1, Appendix III).

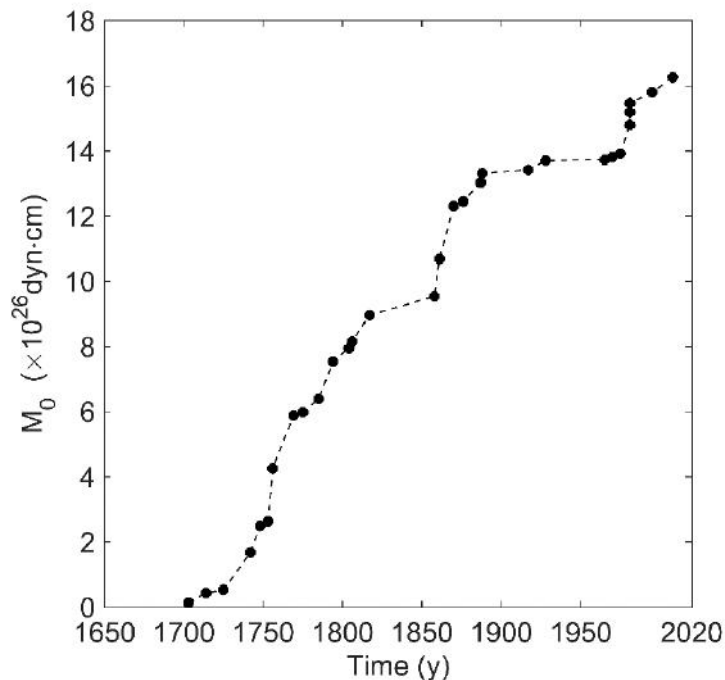


Figure 4-6 Cumulative seismic moment M_0 (in dyn-cm) released in Corinth rift for the historical and instrumental strong earthquakes ($M > 6.0$) from 1700 to 2020.

Table 4-2 Information on fault plane solutions for Corinth rift strong earthquakes ($M \geq 6.0$) for the period 1700 - 2020. Fault planes used in this study are highlighted in bold letters. Magnitudes with asterisks are approximations of M_w based on historical macroseismic information (Papazachos and Papazachou, 2003). In the absence of instrumental measurement, seismic moment is theoretically calculated with Eq. 4-10.

Time		Epicentre			Fault Plane Solution					
n	Year	Latitude (ϕ°)	Longitude (λ°)	Depth (km)	M_w	M_0 (10^{25})	Strike (ζ°)	Dip (δ°)	Rake (λ°)	Ref.
1	1703	38.400	21.800	Naf.F	6.1*	1.44	85	40	-125	(1), (2)
2	1714	38.375	21.790	Ps.F.	6.2*	2.88	270	45	-90	(2), (3)
3	1725	37.900	23.000	Naf.F	6.0*	1.02	255	43	-100	(1), (2)
4	1742	38.100	22.600	Xyl.F.	6.7*	11.4	265	23	-81	(1), (2)
5	1748	38.200	22.200	Aig.F.	6.6*	8.12	277	33	-76	(1), (2)
6	1753	38.100	22.500	Xyl.F.	6.1*	1.44	265	23	-81	(1), (2)
7	1756	38.400	21.900	Naf.F	6.8*	16.21	85	40	-125	(1), (2)
8	1769	38.400	22.000	Naf.F	6.8*	16.21	85	40	-125	(1), (2)
9	1775	37.900	22.900	Per.F.	6.0*	2.04	285	40	-70	(1), (2), (3)
10	1785	38.200	21.700	Ach.F.	6.4*	1.02	331	73	-35	(2), (4)
11	1794	38.300	22.400	Er.F	6.7*	11.48	106	40	-90	(1), (2)
12	1804	38.100	21.700	Ps.F.	6.4*	4.07	270	45	-90	(2), (3)
13	1806	38.300	21.800	Ps.F.	6.2*	2.04	270	45	-90	(1), (2)
14	1817	38.300	22.100	Aig.F.	6.6*	8.12	277	33	-76	(2), (3)
15	1858	37.870	22.880	Kech.F.	6.5*	5.75	255	43	-100	(1), (2)
16	1861	38.250	22.160	El.F.	6.7*	11.40	281	34	-71	(2), (3)
17	1870	38.480	22.550	Del.F.	6.8*	16.21	91	40	-90	(1), (2)
18	1876	37.800	22.800	Kech.F.	6.1*	1.44	255	43	-100	(1), (2)
19	1887	38.050	22.650	Per.F.	6.5*	5.75	285	40	-70	(2), (3)
20	1888	38.230	22.110	Aig.F.	6.3*	2.88	277	33	-76	(2), (4)
21	1917	38.400	21.700	Naf.F	6.0*	1.02	85	40	-125	(1), (2)

Time		Epicentre		Fault Plane Solution							Ref.
Year		Latitude (φ°)	Longitude (λ°)	Depth (km)	M _w	M ₀ (10 ²⁵)	Strike (ζ°)	Dip (δ°)	Rake (λ°)		
22	1928	38.070	22.820	Per.F.	6.3*	2.88	285	40	-70	(2), (3)	
23	1965	38.270	22.300	Er.F.	6.3	0.18	191	65	-79	(2)(5)	
						-	270	14	-90	(6)	
						1.67	281	34	-71	(7)	
24	1970	38.360	22.530	Xyl.F.	6.2	-	278	20	-85	(6)	
						0.9	265	23	-81	(8)	
						0.91	75	67	-94	(9)	
25	1975	38.486	21.661	Trich.F.	6.0		236	39	-125	(10)	
						1.13	316	71	-26	(11)	
26	1981	38.153	22.961	Sk.F.	6.7	8.9	285	40	-70	(5)	
						8.75	264	42	-80	(9)	
						10.5	268	39	-76	(12)	
						9.0	285	37	-64	(13)	
						13.0	287	58	-43	(14)	
27	1981	38.083	23.139	Al.F.	6.4	3.8	250	42	-80	(5)	
						3.97	241	44	-85	(9)	
						3.5	246	44	-84	(12)	
						3.8	264	37	-64	(13)	
28	1981	38.204	23.236	Kp.F.	6.3	2.8	68	47	-82	(5)	
						2.7	230	45	-90	(9)	
						-	50	45	-90	(12)	
						2.8	258	42	-60	(13)	
						2.9	272	48	-31	(15)	
29	1995	38.362	22.200	Aig.F.	6.5	3.38	277	33	-76	(14)	
						6.0	265	43	-103	(13)	
						3.3	276	34	-73	(16)	
30	2008	37.952	21.537	P.F.	6.4	-	29	89	-178	(17)	
						4.6	209	83	164	(13)	
						2.5	297	84	6	(15)	

1: Papazachos and Papazachou (2003); 2: Hanks and Kanamori (1979), 3: Console et al. (2006), 4: Karakostas (1994), 5: Ambrasseys & Jackson (1990), 6: McKenzie, 1978; ; 7: Baker et al., 1997, 8: Liotier (1989); 9: Taymaz et al. (1991); 10: Papazachos et al. (1975); 11: Kiratzi et al., 2008 12: Braunmiller & Nabelek (1996); 13: HRV-GCMT catalog; 14: Bernard et al. (1997); 15: PDE – PDE/GS; 16: NEIC, 17: A.U.Th

4.2.3 Fault segmentation and long term slip rate constraints

The calculation of the stress evolutionary model requires the incorporation of the lithospheric deformation which is accommodated in an aseismic manner along the major faults. The long-term slip rates along faults can be estimated by using a variety of methodologies. It is characteristic that there is an inconsistency between the slip rates inferred from different methodologies like paleoseismological methods (trenching and dating faults), geomorphic observations (scarps or triangular facets), or geodetic (GPS) and seismological measurements biasing seismic hazard analysis (Cowie and Roberts, 2001). In addition to the measurement variations, the fault slip rates are not stable but they vary in space along faults, from the centers to the tips and they also vary in time in association with the fault population stage and the linkage stages during the evolutionary process. The slip variations in time are associated with the strong event occurrence and the recurrence time

distribution. Cowie and Roberts (2001) also suggest that especially for the Corinth rift geodetic measurements overestimate slip rates along major faults. In this study in order to maintain a homogeneity we consider an average slip rate for each fault derived only from geodetic measurements. In the Aegean area the continuous extension is intense and is controlled by the westward extrusion of the Aegean microplate, the North Aegean Trough, the subduction and the rolling back of the eastern Mediterranean slab, implying that there are vast heterogeneities on the deformation pattern over the entire area. There is a successive increase in the relative motion of the Aegean lithosphere against the stable European plate from the north to the Hellenic trench led by the westward extrusion of the Aegean microplate along the North Aegean Trough, up to its overthrust along the Hellenic arc. The Anatolian plate is moving westwards along the NAF, with an average velocity of about 24 mm yr^{-1} which is accommodated by an additional N–S deformation of 11 mm yr^{-1} in the Aegean due to the rollback of the subducting plate, resulting in a total SW motion of 41 mm yr^{-1} of the southern Aegean relative to Eurasia. The Aegean moves almost uniformly in a SSW direction with an average velocity of 30 mm yr^{-1} . The velocity increases from 25 mm yr^{-1} in the central and southern part of the western coast of Turkey to $30\text{--}35 \text{ mm yr}^{-1}$ near the southwestern part of the Hellenic arc (Papazachos 1999).

High strain rates have been the objective for several researchers who have measured the crustal velocity field by different means (McKenzie 1972; Le Pichon et al., 1995; Davies et al., 1997; McClusky et al., 2000; Reilinger et al., 1997; Reilinger et al., 2006; Kotzev et al., 2006). Particularly, at the northern Greek mainland and the south Balkans, Kotzev et al. (2006) measured the velocity field and suggests a slip rate equal to 1 mm yr^{-1} for the whole area, while Tranos et al. (2003) suggest a very small slip rate along faults equal to 0.4 mm yr^{-1} based on geological data. Especially after the occurrence of the 1978 triplet Martinod et al. (1997) established a geodetic network in the macroseismic area and during the 20 years of experiments an amount of extension equal to 5.7 mm yr^{-1} was measured in a narrow zone at the southern margin of Mygdonia graben, interpreted as a combined effect between post seismic relaxation and continuous aseismic extension. Evaluating the geodetic and geological measurements a slip of 1 mm yr^{-1} was attributed to all the well-defined faults of the area.

Estimation of the strain accumulation on the most important zones requires their classification into separate segments, according to available seismotectonic studies. Since strain is accommodated from the most important faults the selection of the segments was based on seismotectonic information. The most important fault segments employed for the construction of the evolutionary model in Mygdonia are presented in Figure 4-7. Information about the fault segments regarding the fault length (L), mean coordinates (λ and ϕ), azimuth (ζ), dip (δ), horizontal (u_{SS}) and along dip direction displacement (u_{DS}) is listed for all the 28 distinct fault segments ($S_1\text{--}S_{28}$) in Table 4-3. The fault segments are Lagina- Agios Vasileios (LAV, $S_1\text{--}S_2$), Pilea-Peristera (PP, $S_3\text{--}S_4$), Asvestochori-Chortiatis (AsCh, S_{23}), Thessaloniki-Gerakarou fault zone, comprised of three segments ($S_7\text{--}S_9$) and in the south Anthemountas – Skepasto fault (AnF, $S_{10}\text{--}S_{11}\text{--}S_{21}$). At the northern part there are the Sochos (SF, S_{16}) and

Mavrouta fault (MvF, S₁₇) whereas at the eastern part Stratoni Fault (StF, S₂₈-S₁₅) and Gomati-lerissos (IF, S₁₉-S₂₀) and in the central part Arnea Fault (ArF, S₁₈), Zagliveri fault (ZF, S₁₂) and Geroplatanos fault (GF, S₂₇) which show a geomorphological continuation of the LAV fault to the east.

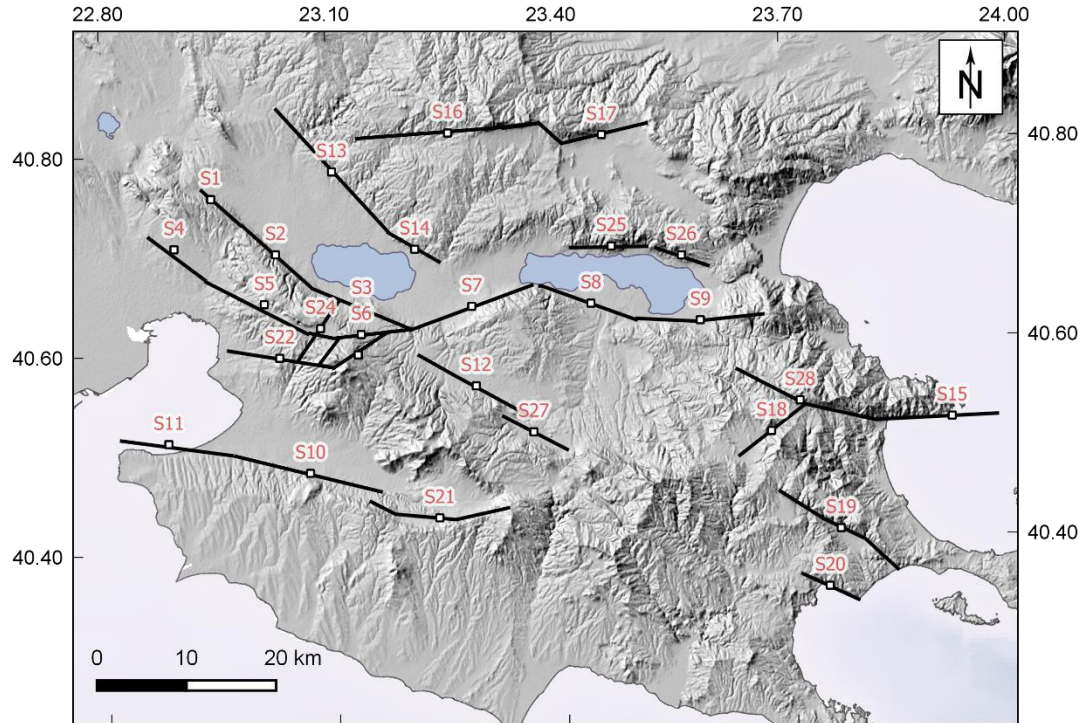


Figure 4-7 Black lines depict the inferred surface traces of fault segments which were introduced in the stress evolutionary model with their code names written on top. Information about their geometric properties of the fault segments is given in **Table 4-3**.

Table 4-3. Geometrical properties and long-term slip rates on the major fault segments for Mygdonia. Slip rates have been assigned based on Kotzev et al. (2006).

No	Segment number	Fault Name	Length (km)	Mean coordinates		Azimuth (°)	Dip (°)	Slip Rate (myr ⁻¹)	
				(λ°)	(φ°)			u _{SS}	u _{DS}
1	S ₁	Lag1	8,8	22.944	40.756	310	45	0	0.5
2	S ₂	Lag2	10	23.029	40.699	310	45	0	0.5
3	S ₃	Lag3	11,6	23.140	40.643	300	45	0	0.5
4	S ₄	PP	12,9	22.891	40.733	310	45	0	0.5
5	S ₅	PAs	12,8	23.009	40.657	310	45	0	0.5
6	S ₆	AsCh	11,3	23.139	40.617	278	46	0	0.5
7	S ₇	Ger	14,6	23.286	40.643	278	46	0	0.5
8	S ₈	Nap	11,3	23.442	40.642	270	46	0	0.5
9	S ₉	NAP	14	23.586	40.623	260	46	0	0.5
10	S ₁₀	Anth1	17,0	23.094	40.477	278	53	0	0.3
11	S ₁₁	Anth2	15.0	22.907	40.503	278	53	0	0.3
12	S ₁₂	Zagl	14,4	23.289	40.561	310	45	0	0.5
13	S ₁₃	Ass1	18,5	23.104	40.781	130	53	0	0.5
14	S ₁₄	Ass2	6,2	23.214	40.701	110	53	0	0.5
15	S ₁₅	Str	17,8	23.920	40.518	90	53	0	0.5
16	S ₁₆	Sch	20	23.258	40.817	90	53	0	0.5

No	Segment number	Fault Name	Length (km)	Mean coordinates		Azimuth (°)	Dip (°)	Slip Rate (myr ⁻¹)	
				(λ°)	(φ°)			u _{SS}	u _{DS}
17	S ₁₇	Mv	9,7	23.471	40.813	90	53	0	0.5
18	S ₁₈	Arn	9	23.675	40.509	230	45	0	0.5
19	S ₁₉	Ier	16	23.763	40.410	130	45	0	0.5
20	S ₂₀	Sig	6,8	23.747	40.351	130	45	0	0.5
21	S ₂₁	Anth3	16	23.220	40.431	278	53	0	0.3
22	S ₂₂	N	15	23.031	40.594	45	80	0	0.5
23	S ₂₃	N	8,5	23.133	40.595	45	80	0	0.5
24	S ₂₄	N	9	23.085	40.624	45	80	0	0.5
25	S ₂₅	V1	11,3	23.470	40.698	90	45	0	0.5
26	S ₂₆	V2	8,2	23.563	40.688	90	45	0	0.5
27	S ₂₇	Ger	9,8	23.362	40.515	130	45	0	0.5
28	S ₂₈	Str	16	23.714	40.538	110	53	0	0.5

Corinth rift stands as one of the most rapidly extending regions worldwide, with an 8-14mm yr⁻¹ opening rate (Armijo et al., 1996). Characteristic feature of the rift is the strong variance of the extensional rate between the western and the eastern part of the gulf, a common observation for geodetic and seismological data. Extension rates at the eastern part of the gulf vary from 5mm yr⁻¹ and increase rapidly to the west (Davies et al., 1997; Clarke et al., 1998; Briole et al., 2000; Avallone et al., 2004) where currently an average rate of 15 mm yr⁻¹ is measured (Briole et al., 2000). It is characteristic that further west a 2-3 cm yr⁻¹ slip rate is estimated along the Cephalonia Fault (Cocard et al., 1999). Geological evidence from Armijo et al. (1996) demonstrated a N-S extensional rate around 7-16 mm yr⁻¹ at the western and the central part of the gulf. Uplifting is measured up to 1.5 mm yr⁻¹ since the late Middle Pleistocene, as it was deduced from marine terraces (Westaway 2002 and references therein). Long term slip rates along faults in the Corinth rift have been measured with different methodologies (geomorphological interpretation, geodetic measurements, paleoseismicity trenches). Based on GPS data, Bernard et al. (2006) give a mean slip for Psathopyrgos fault (S₁) equal to 6 mm yr⁻¹. Pantosti et al. (2004) suggested a mean slip rate of 6.3 mm yr⁻¹ for Aigion fault (S₂) and Bernard et al. (2006) give a slightly smaller estimation (5 mm yr⁻¹). Bernard et al. (2006) also suggest that the central northdipping faults of the gulf (Helike, Aigion and Trizonia faults) share a total slip rate 2 mm yr⁻¹. For Elikei fault (S₃) a slip rate equal to 1.5 mm yr⁻¹ is suggested by Stewart and Vita-Finzi (1996) for the last 3ka. Armijo et al. (1996) suggest a slip rate of 3-8 mm yr⁻¹ and Briole et al. (2000) give higher slip rates approximately equal to 4-10 mm yr⁻¹. For offshore Akrata (S₄) Bell et al. (2009) have calculated a slip rate equal to 3-5 mm yr⁻¹. There are various assumptions for Xylocastro fault (S₅) where Armijo et al. (1996) suggest 6-7mm/yr and 6mm/yr is estimated by Bernard et al (2006). For offshore Perachora (S₆) Console et al. (2013) used a 4 mm yr⁻¹ slip rate in their study.

The Gulf of Alkyonides shows decreasing N-S extension rate across the gulf, starting from 5-3 mm yr⁻¹ to the west and about 1mm yr⁻¹ to the east, geodetically measured (Clarke

et al., 1998). The displacement rate along South Alkyonides is considered equal to 2-3mm yr⁻¹ (Leeder et al., 1991). For Kaparrelis fault (S₁₀) Benedetti et al. (2003) measured a 0.2 mm yr⁻¹ slip rate from cosmogenic dating on the 1981 March earthquake fault scarp. Ganas et al. (2007) estimated a 0.3mm yr⁻¹ mean slip rate from paleoseismological data. These results are in agreement with Armijo et al. (1996) assumptions that almost 10% of the total strain should be attributed to the antithetic southdipping faults within a graben. Skinos (S₇) has a 2 mm yr⁻¹ slip rate according to Hatzfeld et al. (1996). Paleoseismological trenching indicated a slip rate between 0.7 and 2.5 mm·yr⁻¹ for Skinos fault alone (Collier et al., 1998). For Alepochori fault (S₈) Console et al. (2013) suggest 3 mm yr⁻¹ while Armijo et al. (1989) suggest 1.8 mm yr⁻¹. Kechries (S₉) and the broader area of Corinth city display a Holocene slip rate in the order of 0.15 mm yr⁻¹ according to the measurements of Koukouvelas et al. (2017).

At the northern coast of Corinth rift for the Delfi (S₁₁) fault segment Piccardi et al. (2008) estimated about 0.1–0.2mm yr⁻¹, under the framework of the present-day stress regime (last 1 Ma) whereas Piccardi et al. (2000) had earlier reported a higher rate (0.5 – 0.7mm yr⁻¹). Valkaniotis (2009) suggested a slightly higher average slip rate about 0.8 – 1.2mm yr⁻¹ for the last 1 Ma considering the cumulative fault throw on Delphi fault. For Nafpaktos – Marathias faults (S₁₂ and S₁₃) InSAR data have documented slip along the Nafpaktos fault with 2 mm yr⁻¹ normal motion and dextral motion as well (Elias, 2013). To the northwest, geodetic measurements of Lyros et al. (2019) performed around Trichonis Lake showed that deformation accommodates with a 3mm yr⁻¹ slip rate along the Trichonis fault system (S₁₄). For Erateini fault Bell et al. (2008, 2009) give a 1.0-1.9 mm yr⁻¹ Late Quaternary slip-rate and Beckers et al (2015) 0.17-0.23 mm yr⁻¹. To the south, Achaia (S₁₅), the Rion – Patras fault zone has a comparable deformation pattern. InSAR data additionally suggest that the fault is creeping with about 4mm yr⁻¹ normal slip and some right-lateral motion (Elias, 2013; Parcharidis et al., 2013).

The above available information was used in order to assign average slip rates along the faults in the broader area of the Corinth rift (Table 4-4). The faults were grouped into two categories (Model 1 and Model 2). Model 1 includes only the major northdipping normal faults which bound the southern part of the gulf (S₁ – S₉) along with the strike slip zone responsible for the strong Achaia earthquake (S₁₀). Model 2 involves all the faults which are responsible for strong seismic activity in the study area. This division was done in order to investigate the impact of the southdipping faults on the overall stress field in Corinth rift. Faults which were used for the construction of the fault network and calculation of the evolutionary model in Corinth rift are presented in Figure 4-8. Information on the geometrical properties and the slip rates along the faults are summarized in Table 4-4.

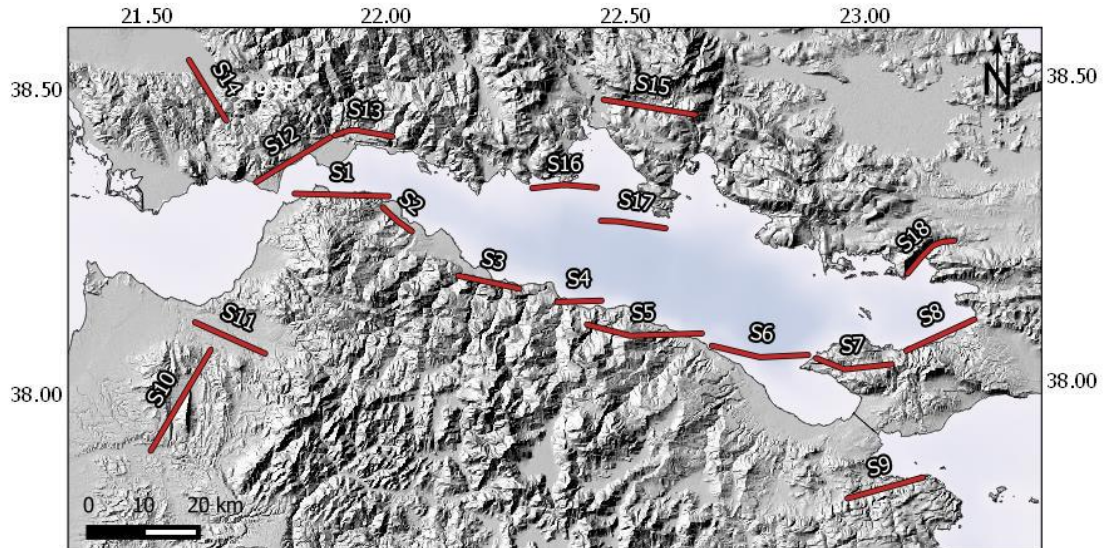


Figure 4-8 Red lines depict the inferred surface traces of fault segments which were introduced in the stress evolutionary model with their code names written on top. Information about their geometric properties of the fault segments is given in **Table 4-4**.

Table 4-4 Geometrical properties and long-term slip rates on the major fault segments for the case of the Corinth Gulf.

No	Segment number	Fault Code	Length (km)	Mean coordinates		Azimuth (°)	Dip (°)	Rake	Slip Rate (mm yr ⁻¹)			Model
				λ°	φ°				u	u _{SS}	u _{DS}	
1	S ₁	Psathopyrgos	15	21.900	38.322	270	45	-90	6.0	0	0,63	MODEL 1
2	S ₂	Aigio	16	22.054	38.257	277	33	-76	6.0	0.15	0.58	
3	S ₃	Eliki	22	22.205	38.175	281	34	-71	6.0	0.20	0,57	
4	S ₄	Akrata offshore	8	22.394	38.143	270	30	-81	5.0	0,09	0,59	
5	S ₅	Xylokaastro	20	22.521	38.088	265	23	-81	5.0	0,08	0,49	
6	S ₆	Perachora	18	22.756	38.048	285	40	-70	4.0	0,14	0,38	
7	S ₇	Skinos	19	22.962	38.025	264	42	-80	3.0	0,05	0,30	
8	S ₈	Alepochori	13	23.138	38.078	261	44	-85	3.0	0.03	0,30	
9	S ₉	Kechries	19	22.923	37.807	255	43	-100	0.15	0.0002	0	
10	S ₁₀	Achaia1	19.6	21.566	37.991	209	83	164	4.0	0.004	0.001	
11	S ₁₁	Achaia2	15	21.673	38.084	331	73	35	3.0	0.003	0.002	
12	S ₁₂	Nafpaktos1	15	21.806	38.382	45	45	-90	0.2	0	0.2	
13	S ₁₃	Nafpaktos2	10	21.950	38.424	45	90	-90	0.2	0	0.2	
14	S ₁₄	Trichonida	14	21.622	38.495	316	71	-26	3.0	0.002	0.001	
15	S ₁₅	Delphi	16	22.550	38.459	91	40	-90	0.6	0	0.6	
16	S ₁₆	Desfina	12.4	22.364	38.335	90	45	-90	0.2	0	0.2	
17	S ₁₇	Itea offshore	12	22.508	38.270	90	45	-90	0.2	0	0.2	
18	S ₁₈	Kaparelli	13	23.121	38.216	50	45	-90	0.2	0	0.2	

4.2.4 Coseismic Coulomb stress changes for Mygdonia

Rupture models for source and receiver faults are approximated as rectangular planes embedded in the brittle crust (3-18km) and are determined for the seven strongest earthquakes ($M > 6.0$) that occurred in the first study area from 1677 until present. An illustration of the numbered rupture models projected onto the earth's surface is presented in Figure 4-9 where the northdipping faults are plotted in white color and southdipping in red. The geometrical properties namely azimuth, dip, rake, length, width, horizontal and along dip slip (in m) which describe the rupture models along with seismic moments (M_0) are given in Table 4-5. All rupture models correspond to normal faults striking at an almost E-W direction and ΔCFF for every model is calculated on a planar surface resolved onto the receiver fault. Stress changes are computed at 8km depth, which is chosen to be several kilometers above the locking depth in the evolutionary model. Coseismic changes associated with the earthquakes are illustrated in Figures 4-10 to 4-16, where ΔCFF is color coded and denotes negative (blue colors) and positive (red colors) stress increments which imply an inhibition or an enhancement of seismicity triggering. Each map depicts the activated fault for which the stress pattern is calculated (white color), the epicenter of the respective earthquake (big marker) and the subsequent strong earthquake (small marker) and causative fault (green color). A brief description for each calculation and the parameters selection are discussed, shear modulus, G , and Poisson's ratio, ν , are fixed as $3.3 \cdot 10^5$ bars and 0.25, in respect.

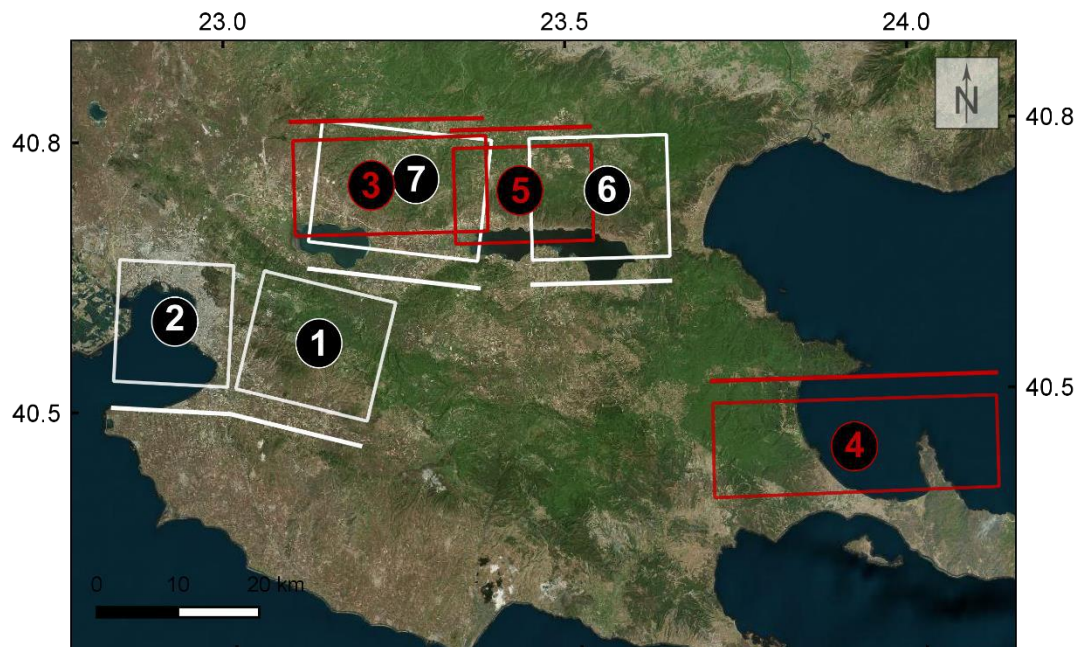


Figure 4-9 The rupture models for main earthquakes in Mygdonia area. White color represents northdipping faults, while south-dipping faults are red colored. Details about the models are given in Table 4-2.

Table 4-5 Rupture models for earthquakes with $M \geq 6.0$ from 1677 until 2020 in Mygdonia graben.

Time		Epicenter		Fault Geometry			Fault Plane Solution			Average Displacement				
n	Year	Latitude ϕ°	Longitude λ°	Fault Code	M_w	M_o ($\cdot 10^{25}$)	L (km)	W (km)	Z ($^\circ$)	Dip ($^\circ$)	Rake ($^\circ$)	u (m)	u_{SS} (m)	u_{DS} (m)
1	1677	40.500	23.000	An.F	6.2*	2.04	17	15	278	53	-93	0.44	-0.01	0.24
2	1759	40.600	22.800	An.F	6.3*	2.88	15	15	278	53	-93	0.52	-0.02	0.38
3	1902	40.820	23.040	So.F	6.5*	8.13	23	15	90	53	-93	0.72	-0.04	0.71
4	1932	40.450	23.760	Ier.F	7.0*	30.9	25	15	93	53	-93	1.96	-0.11	2.07
5	1932	40.790	23.440	So.F	6.2*	2.04	17	15	90	53	-93	0.44	-0.01	0.24
6	1933	40.659	23.545	NA.F	6.3*	2.88	15	15	278	46	-70	0.52	0.12	0.33
7	1978	40.729	23.254	TG.F	6.5	5.20	21	16	278	46	-70	0.45	0.15	0.42

1677, Vasilika earthquake ($M^*=6.2$)

The available historical information on the 1677 Vasilika earthquake, which caused severe damages at Vasilika village (Maximum Intensity, $I_{max}=VIII$, Vasilika) infers an association of this earthquake with Anthemountas fault (AnF) (Fig.4-10). The suggested by Papazachos and Papazachou (2003) fault plane solution was employed for the construction of the rupture model. It corresponds to a representative for the area northdipping normal fault (strike= 278° , dip= 53° and rake= -93°) and is in agreement with the properties of the AnF western fault segment. The rupture length deduced from scaling laws and topography, is equal to 17km and 15km in width. The average displacement calculated from Eq. 4-10 and Eq.4-9 ($M_0 = 2.04 \cdot 10^{25}$ dyn-cm) is equal to 0.19m. Figure 4-10 displays the coseismic stress changes induced by the 1677 event. The location of the following M6.3 earthquake is found in areas with more than 0.1 bars stress increase. Thermaikos Gulf to the west and Central Chalkidiki to the east of the causative fault are additionally reinforced by static stress enhancement. The westward along-strike AnF fault prolongation which is strongly encouraged by positive stress, 82 years later gave a subsequent of the same size earthquake, revealing that the occurrence of the 1759 earthquake was probably promoted due to 1677 earthquake on the adjacent AnF segment.

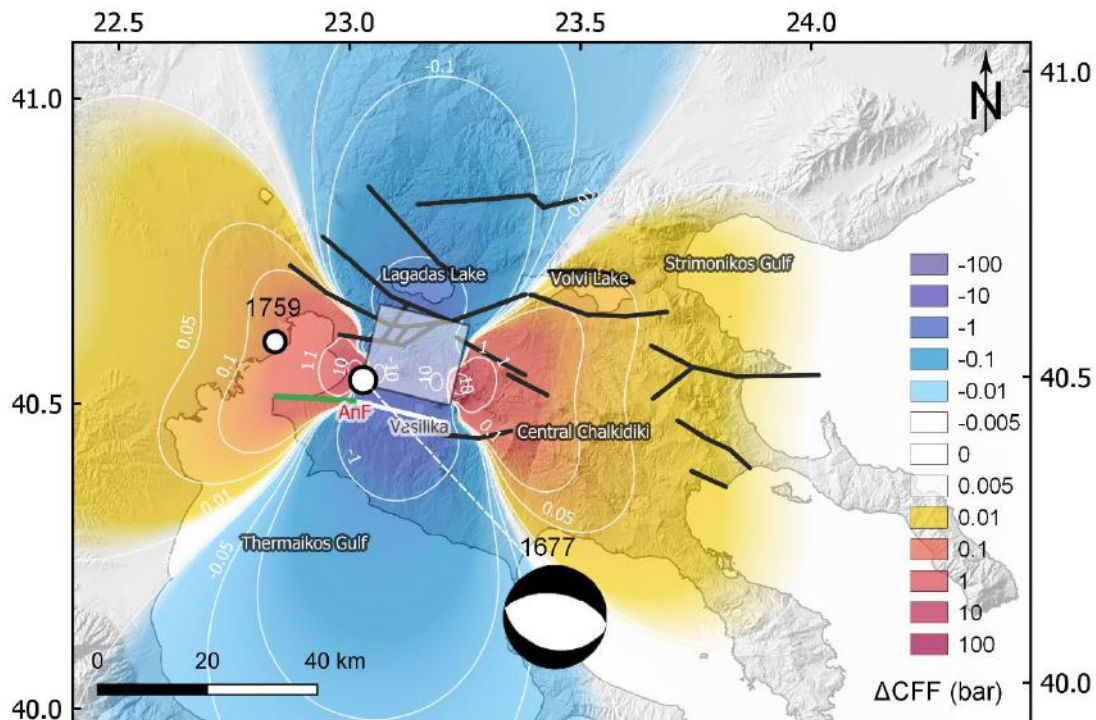


Figure 4-10 Spatial distribution of the coseismic Coulomb stress changes calculated at 8.0km depth, caused by the occurrence of the 1677 Vasilika earthquake (big circle) on the AnF eastern segment. The white line shows the surface projection of the causative fault and the rectangular area represents the horizontal fault projection. The earthquake epicenter along with the corresponding equal area lower hemisphere projection of the fault plane solution are shown. The consecutive M6.3 earthquake (small circle) associated with the western AnF fault segment (green color line) are also shown. The stress distribution shows that Thermaikos Gulf and Central Chalikidiki areas accept stress enhancement after the 1677 earthquake occurrence. Stress changes are plotted with the use of a colored scale in bars.

1759, Thessaloniki earthquake ($M^*=6.3$)

The 1759 earthquake caused disastrous consequences in the city of Thessaloniki ($I_{\max}=IX$, Thessaloniki). This event was probably associated with the western E-W AnF segment (Fig.4-11) and likely to be triggered from the occurrence of the preceding 1677 earthquake. According to Papazachos and Papazachou (2003) the fault plane solution is considered similar to the 1677 earthquake ($278^\circ/53^\circ/-93^\circ$). Geological data and scaling relations infer that the fault is 15km long and 15km wide and the average displacement is 0.31m ($M_0=2.88 \cdot 10^{25}$ dyn-cm, Eq.4-9). The co-seismic stress pattern corresponds to the one generated by a pure normal fault (Fig.4-11) and the distribution of stress indicates an advance of positive $\Delta CFFs$ to the east and west of the causative fault, particularly over Central Chalkidiki and the west coasts of Thermaikos Gulf. Stress changes are further reinforcing the existing positive stress increments due to the preceding earthquake. The occurrence of 1677 and 1759 earthquakes resulted in the overall rupture of the two AnF branches in a relatively short time and a seismic quiescence followed, whereas further seismicity occurred off fault as shown in the following paragraphs. The subsequent M6.6 earthquake in 1902 was located 30km north of the 1759 event, and its causative fault was partially inhibited by a stress shadow zone at 8km depth. The earthquake might not have strongly triggered the 1759 earthquake occurrence but part of the causative fault seems to have receive positive stress increase, leading to an impending fault failure.

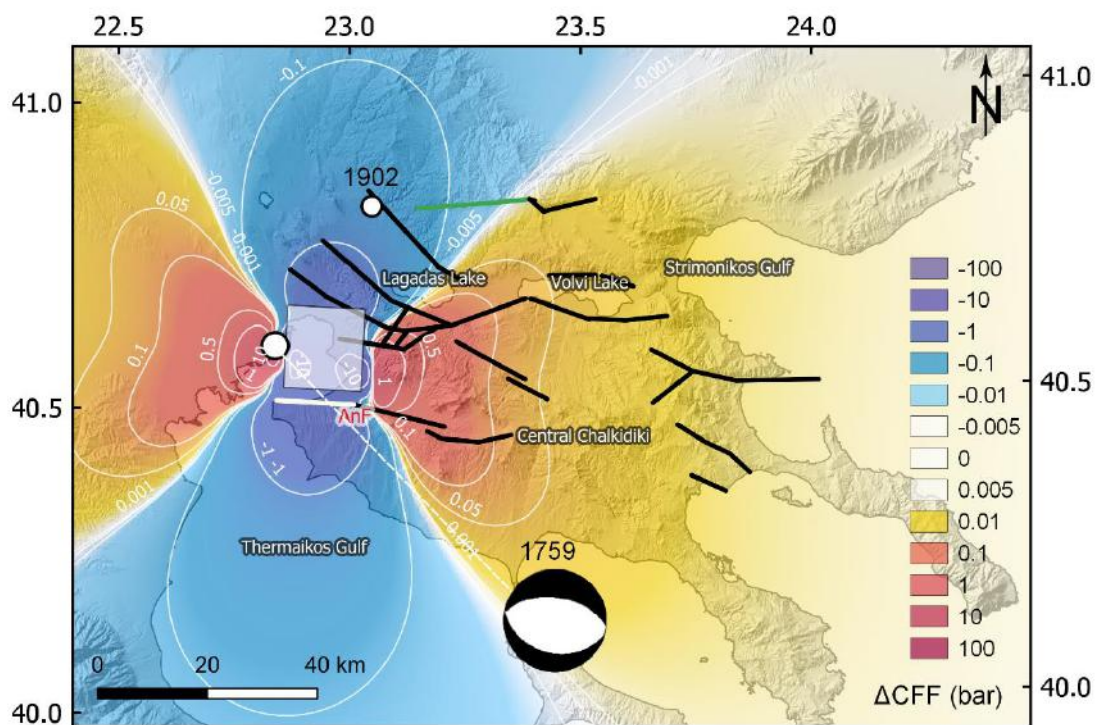


Figure 4-11 ΔCFF spatial distribution of the 1759 Thessaloniki earthquake calculated at 8.0km depth along with the epicenter and the corresponding fault plane solution. The white line shows the surface projection of the causative fault and the rectangular area represents the horizontal fault projection. The location of the next 1902 M6.6 earthquake and its causative fault (green color) are shown. (Symbols same with Figure 4-10).

1902, Assiros earthquake ($M^*=6.6$)

The severe 1902 earthquake ($I_{\max}=IX$, Assiros) caused the extensive collapse of buildings and chimneys in Assiros and Lagadas villages. Epicentral uncertainties are significant for this earthquake. Papazachos and Papazachou (2003) suggest that Sochos normal fault (SochF, Fig.4-12) is the causative fault for this earthquake (strike= 90° , dip= 53° and rake= -93°) and was adopted in this study. Paradisopoulou (2009) obtain a 23km long fault and Papazachos et al. (2001) consider an 27km long fault zone. Mouratidis (2010) also suggested a 20-27km long fault based on remote sensing analysis of the fault topography. Comparing geological and seismological data fault length was considered 23km, the width 15km and the average slip equal to 0.72m ($M_0=8.13 \cdot 10^{25}$ dyn-cm). Coseismic stress pattern shows that a N-S shadow zone was cast over a large area in central Mygdonia but positive stress changes accumulated to the eastern part of the study area where the next M7.0 Ierissos earthquake occurred 30 years later. In the central region an extensive stress shadow is developed in a North – South orientation and encompasses an important portion of the fault population in Mygdonia. Considering the uncertainties around the causative fault, if the hypothesis on the source model regarded an antithetic northdipping normal fault, the spatial ΔCFF distribution would be identical, since the fault mechanism shapes the geometry of the stress field changes. The Stratonis fault responsible for the subsequent earthquake is situated in an area enhanced by positive stress because of the 1902 event but also amplified from preceding earthquakes.

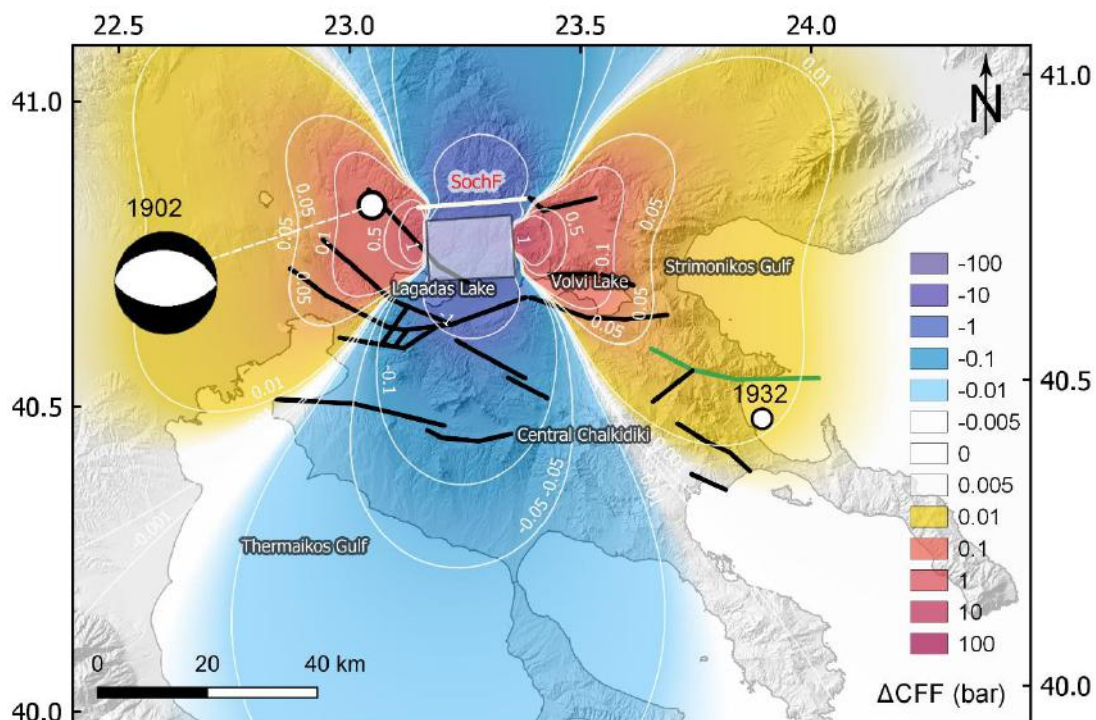


Figure 4-12 Spatial redistribution of coseismic stress Coulomb changes caused by the 1902 earthquake. The stress patterns reveals positive stresses along strike and a broad shadow zone is casted over central Chalkidiki. The subsequent 1932 earthquake is distant but the causative Str.f lies in a bright stress zone.

1932, September 26, Ierissos earthquake ($M^*=7.0$)

The Assiros earthquake was followed in 1932 by the Ierissos M7.0 ($I_{max}= X$, Ierissos) devastating earthquake to the east, which is the strongest instrumental earthquake in the study area with $m_b7.0$ (Engdahl et al., 1998). The broader Chalkidiki peninsula suffered extensive damage, along with the complete destruction of Ierissos city and Stratoni village. Several macroseismic effects were reported and there was indications for a small tsunami along the eastern coasts of Chalkidiki peninsula (Papazachos and Papazachou, 2003). The earthquake is attributed to the E-W south dipping Stratoni fault (Strf), where surface ruptures were visible in alignment with the fault scarp. The suggested fault plane solution by Papazachos and Papazachou (2003) show a normal southdipping fault ($90^\circ/53^\circ/-93^\circ$). Surface ruptures with 2.0m vertical displacement were observed in an east-west direction for more than 7.0km length. The expected length according to scaling laws is 43km, however Nalbant et al. (1998) considered a 25km long rupture. Considering the geomorphology of the fault scarp, the on land fault length, is approximately equal to 15km (Pavlidis and Tranos, 1991), however a 10km seaward extension is proposed. In previous research the length is considered equal to 50km (Papazachos et al., 2001; Papadimitriou et al., 2006) and 44km (Paradisopoulou et al., 2009). Here, a fault length equal to 25km and fault width equal to 15km were obtained. Nalbant et al. (1998) suggested a 2.0m average coseismic displacement similar to the value (1.96m) extracted from Eq.4-9 ($M_0=3.09 \cdot 10^{26}$ dyn-cm, Taymaz et al., 1991).

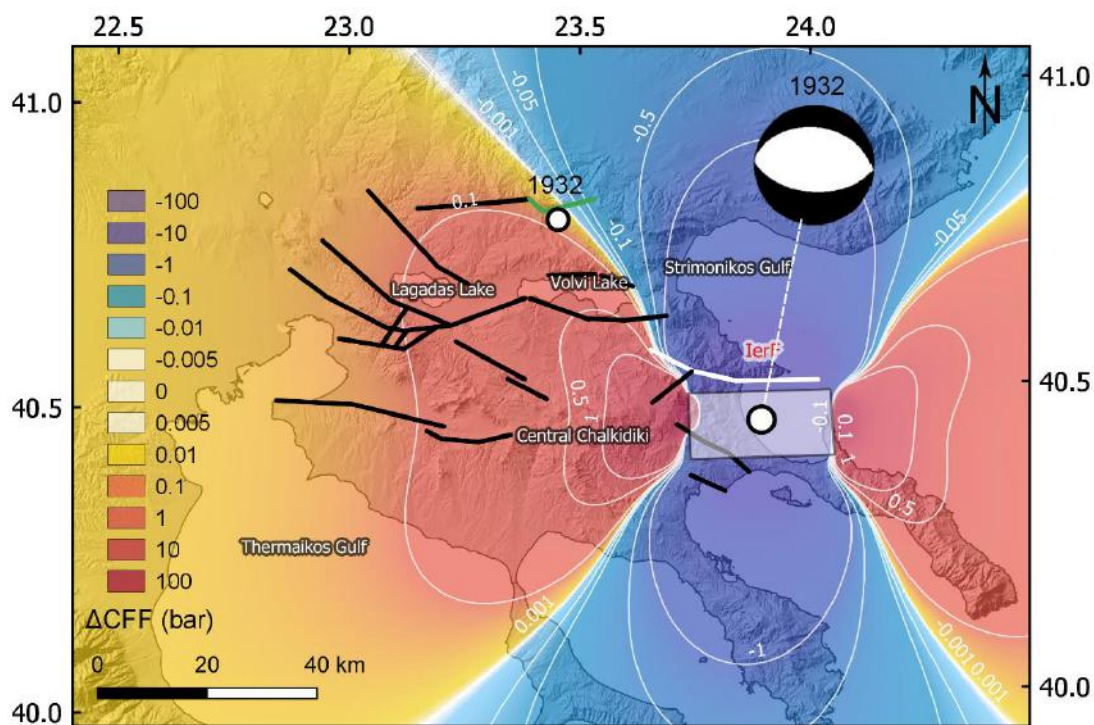


Figure 4-13. ΔCFF distribution after Ierissos 1932 earthquake where the corresponding fault plane solution is also visible. An additional broad stress increase is imposed in the entire Mygdonia area, whereas a wide shadow zone is casted over a broader area in N-S direction. The next 1932 earthquake, shortly after Ierissos event is located in the vicinity of increased stress values. Stress changes strongly affect the central part where strong seismicity follows.



The fault plane solution for a recorded M4.8 (1983, August 26th) earthquake which occurred in the same location and exhibited a fault plane solution: strike=72°, dip=73° and rake=-168° (Ekstrom and England, 1989) confirms the rupture properties. Figure 4-13 illustrates the coseismic stress changes pattern associated with the Ierissos earthquake. Extensive areas of Δ CFF enhancement are formed located at the west termination of Stratonis fault and the central area of Mygdonia graben where three strong earthquakes followed among which the M6.5 1978 earthquake. The broader area has been positively affected with stress changes >0.5 bars and faults in this area are highly likely to be advanced towards failure because of the severe 1932 event. The following smaller 1932 earthquake probably along the southdipping Sochos fault north of Stratonis fault and is half located within the western bright Δ CFF lobe.

1932 September 29, Sochos earthquake ($M^*=6.2$)

In 1932 a M6.2 shock occurred northern than the epicentral area of the preceding event. The epicentral coordinates have been determined according to the macroseismic intensities acquired from historical information and the application of Bakun and Wenworth (1997) methodology applied by Paradisopoulou et al. (2016). The epicenter is located close to Sochos and is attributed to the activation of the eastern segment of Sochos fault (Sochf). The suggested fault plane is a pure south dipping normal fault (strike=90°, dip=53° and rake=-93°, by Papazachos and Papazachou, 2003). The fault length was estimated equal to 17km (Eq.4-5) the fault width was taken equal to 15km and the average slip equal to 0.19m according to the calculated seismic moment ($M_0=2.04 \cdot 10^{25}$ dyn·cm, Eq.4-10). Figure 4-14 depicts the distribution of the coseismic static stress changes and the location of the following earthquake at the southern margin of Mygdonia graben, in an area where positive stress increments encourage portion of the seismogenic fault.

1933, Volvi earthquake ($M^*=6.3$)

According to Papazachos and Papazachou (2003) and the macroseismic of Paradisopoulou et al. (2016) the 1933 M6.3 earthquake was likely to be located at the southern boundary of Volvi Lake and is associated with Nea Apollonia fault (NAf). The fault plane solution by Papazachos and Papazachou (2003) was employed for the construction of the rupture model which regards a north dipping normal fault with strike= 278°, dip=53° and rake=-93°. The length and width of the rupture were taken equal to 15km (Eq.4-5) and the average displacement equal to 0.26m ($M_0=2.88 \cdot 10^{25}$ dyn·cm, Eq.4-10). Figure 4-15 displays the Δ CFF result for the 1933 Volvi earthquake. It is notable that the geometry of the coseismic stress field for Volvi and the predecessor 1932 Sochos earthquake are similarly evolved along the two antithetic fault zones and they impose cumulative stress increments at the central part of Mygdonia graben where the subsequent and last strong earthquake occurred in 1978. The dense occurrence of these the 1932 Ierissos, the 1932 Sochos and the 1933 Volvi earthquakes indicate an interactive mechanism between the causative antithetic faults and a successive westward migration of the epicentres, from the edges of Mygdonia fault population to the central part.

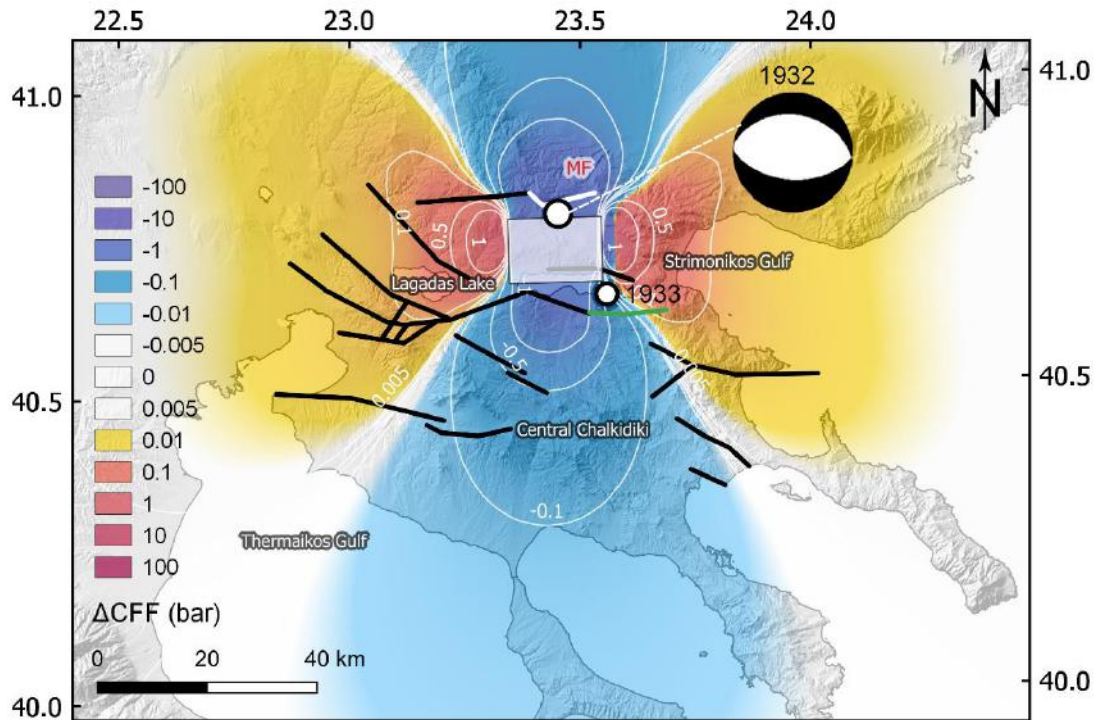


Figure 4-14 Spatial distribution of stress because of lerissos 1932 earthquake along with its corresponding fault plane solution. An additional stress increase is imposed, in the entire Mygdonia area, whereas a shadow zone is cast over a broader area in N-S direction. The following earthquake was located in the vicinity of the increased values.

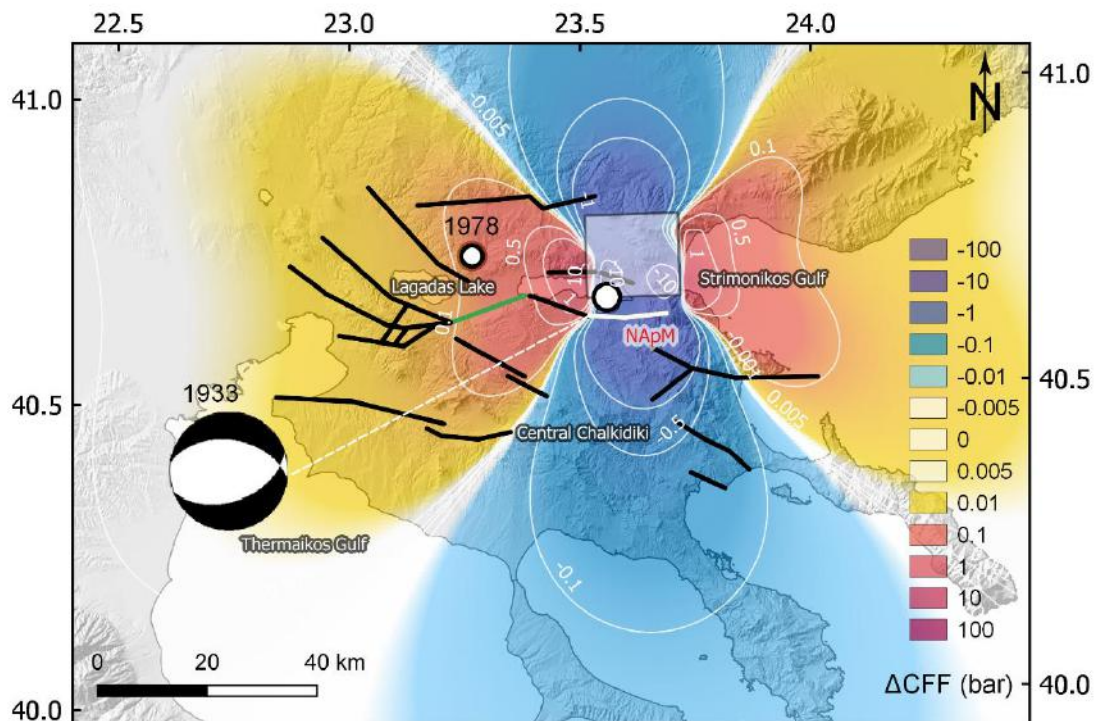


Figure 4-15 Stress spatial distribution because of Volvi 1933 earthquake and its corresponding fault plane solution. The Coulomb stress pattern is similar to the 1932 earthquake according to which positive stress changes are shed over the central part of Mygdonia graben where the following 1978 earthquake occurred.

1978 June 20, Stivos earthquake (M=6.5)

Stivos M6.5 earthquake was the last recorded earthquake in Mygdonia graben ($I_{\max} = VIII+$, Stivos). The epicenter was located between Lagadas and Volvi Lakes, 30km far from the Thessaloniki city, which experienced severe building damage and human losses due to one building collapse. A rich literature exists, concerning the seismic sequence and extensive field work has been undertaken since 1978 (Papazachos et al., 1979; Soufleris and Stewart, 1981; Soufleris et al., 1982; Mercier et al. 1983; Hatzfeld et al., 1986/87; Mercier and Carey-Gaihardis, 1989; Scordilis et al., 1989; Hatzidimitriou et al., 1991). Stress changes for the 1978 earthquake sequence have also been calculated by Tranos et al. (2003) and Paradisopoulou et al. (2009). The causative fault is a north dipping normal fault bounding the graben from the south and extensive field research revealed the existence of surface ruptures in the interior of the basin in an E-W direction up to 12km in length (Papazachos et al., 1979). The fault is related to Stivos-Gerakarou (SGf) segment which is situated in the central part of the Thessaloniki - Gerakarou rupture zone. The fault plane solutions and the seismic moment ($M_0 = 5.20 \cdot 10^{26}$ dyn-cm) computed by Soufleris and Stewart (1981) for a normal fault with WNW – ESE strike (strike=278°, dip=46° and rake=-70°) were obtained for building the dislocation model. Mean coseismic displacement is equal to 0.45m (Eq.4-10) for a 21km long and 16km wide fault (Tranos et. al., 2003). Figure 4-16 depicts the resulting stress field geometry. Positive ΔCFF stress changes are located at the eastern and the western fault termination, promoting future failure to the NE-SW trending faults, northern than Thessaloniki where the

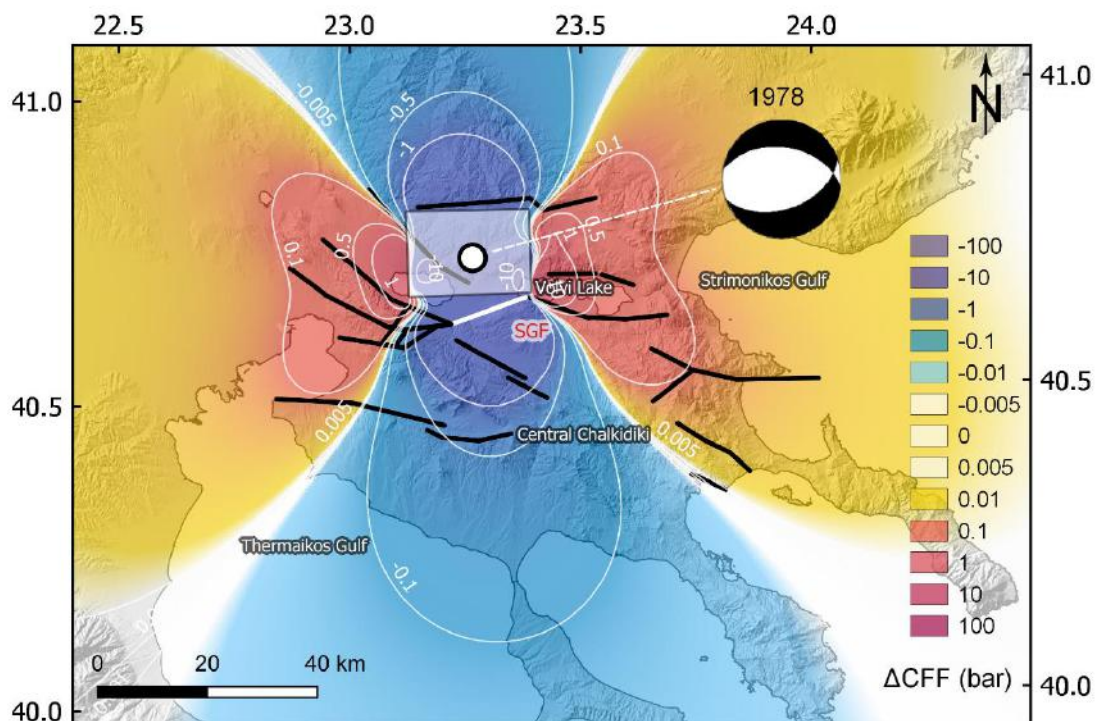
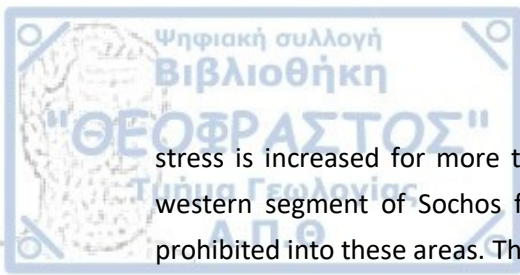


Figure 4-16 Spatial distribution of the coseismic stress changes imposed by the occurrence of the 1978 Stivos earthquake. Stress changes have been calculated for an E-W normal fault. Stress enhanced regions are developed along the fault strike in an E-W direction whereas stress shadows are N-S casted.



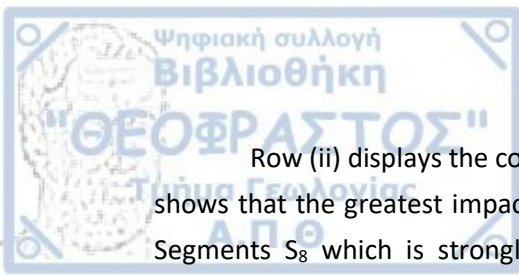
stress is increased for more than 1.0 bars while the area of Anthemountas fault and the western segment of Sochos fault remain in stress shadow, and earthquake triggering is prohibited into these areas. The earthquake is located in an area where it has been gradually affected with successive stress enhancement by strong earthquakes during the studied period.

4.2.4.2 *Onto-fault Δ CFF calculations*

The cumulative coseismic stress changes along a rupture zone were used in order to investigate fault stress interaction when earthquakes occur on adjacent, distant faults or antithetic faults of the same fault population and understand the role of fault mechanics. The characteristic feature of this fault population is that the major faults which contribute to seismic and aseismic strain accommodation are adjacent fault segments with the same strike, have parallel or semi parallel strike or they are antithetic faults. Normal fault plane mechanism for strong earthquakes is dominant, creating similar geometry in an horizontal plane at the mid depth of the seismogenic layer. Knowing the significant Coulomb stress variation with depth, onto fault plane coseismic stress changes were computed along the Thessaloniki - Gerakarou - Nea Apollonia fault zone (TG-Nap FZ). The receiver fault segments for which stress changes were calculated along their dipping planes are the Pilea-Peristera fault, PPF (S_5), Asvestochori-Chortiatis fault AchF (S_6), Stivos fault St.F (S_7), Gerakarou fault GerF (S_8) and Nea Apollonia fault NAF (S_9) from west to east (Figure 4-16). Stress due to the co-seismic impact of strong earthquakes is resolved onto the fault segment planes which are approximated with rectangles embedded into the brittle crust. Table 4-3 and Table 4-5 contain the faults and earthquake source models respectively. The accumulated stress changes are calculated according to the faulting type of the next strong. Stress changes are calculated for depths 1.0 -20 km along slip direction, within the brittle crust. Results are shown in the sub plots of Figure 4-17 where Coulomb stress calculations are progressively described from i to v.

Subsets along row (i) exhibit the collaborative effect of the 1677 M6.2 and 1759 M6.3 earthquakes associated with the eastern and western Anthemountas fault segments on the TGNAp five fault segments. Stress distribution along slip shows that segments S_7 and S_8 are mostly influenced by this occurrence and they are embedded in high negative Δ CFF values at the biggest part of the seismogenic crust. Distant fault segments are receiving small but positive stress increments.

The stress changes due to the occurrence of the 1902 M6.6 earthquake on the antithetic Sochos fault (SochF) is shown along row (ii). The coseismic stress imposes considerable stress disturbances on the zone producing positive Δ CFF and in particular a positive stress enforcement from 10 to 20km in Stivos S_7 , which is the central part of the rupture zone (row ii). Small is the stress effect at the eastern termination of the zone (S_8 and S_9 fault segments).



Row (ii) displays the coseismic result of the 1932 M7.0 Ierissos earthquake. Modelling shows that the greatest impact is a stress increase onto the eastern part of the fault zone, Segments S_8 which is strongly advanced toward failure and S_9 , which partially receives enhanced stress changes. There is no evidence for a significant along slip impact on the stress field of the central and the western part of the TGNAp fault zone.

The cumulative impact of the 1932 M6.2 Sochos and 1933 M6.3 Volvi earthquakes is shown along (iv) row. Stress has been released along NApF and GerF (S_7 and S_8) and there is enforcing of positive stress changes to the west towards the 1978 causative fault (S_7) and to the east. Indications derived from the application of the Coulomb Failure Criterion show that the consecutive stress changes in the area caused failure to Stivos fault.

The occurrence of the 1978 M6.5 earthquake S_7 is shown along (v) row. Stress release causes an extensive shadow zone at the seismogenic depth of segment S_7 and the adjacent segments. The shadow zone is expanding along the rupture zone which bounds Mygdonia graben from the south, inhibiting a future earthquake occurrence along the zone. Patches of increased Coulomb stress changes exist to the east and the western areas of the zones.

Spurious stress values close to the tips of the faults according to Ishibe et al (2011) are attributed to the simplified source geometry and slip distribution is for this reason local high ΔCFF values and loading along faults was neglected. It is shown that for the satisfying study period for 300 years Coulomb stress which explains the failure on faults showed the progressive stress built-up along the fault zone due to the coseismic stress changes and revealed the stress triggering mechanisms at depth. It is notable that after the occurrence of the last 1978 earthquake seismic stress has been released along the fault planes for the given rupture models.

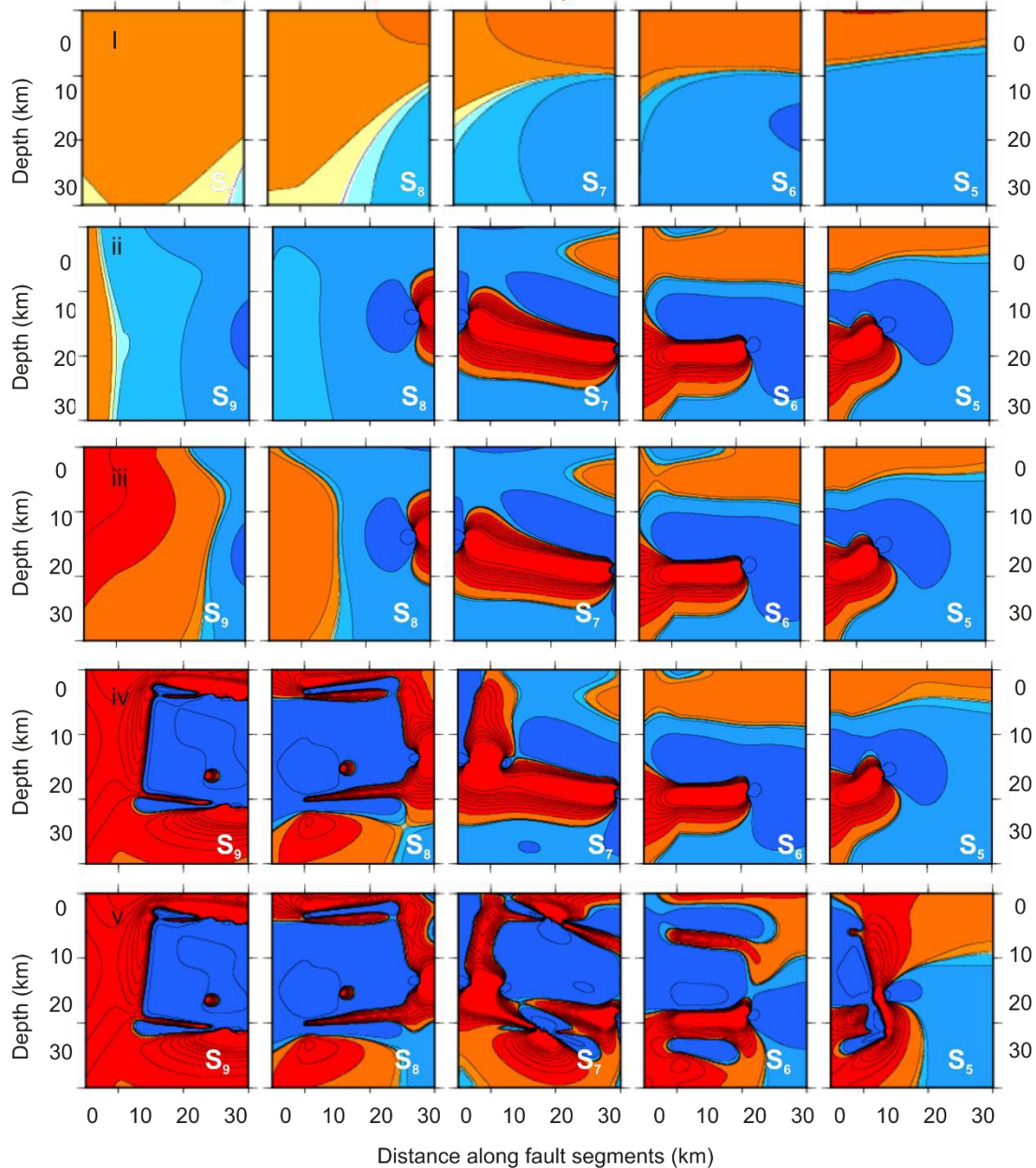


Figure 4-17 At the top, the hanging wall relief of TGNAp rupture zone with view from the North. View from the North Successive snapshots of Coulomb stress changes onto the segments of TGNAp FZ (S5-S9), i) The 1st row shows the coseismic stress changes after the 1677 and 1759 earthquakes along An.F, ii) the 2nd row presents the stress changes after 1902 Assiros event. iii) the 3rd row shows the effect of 1932 Ierissos earthquake, iv) the 4th row shows the stress changes after the 1932 Sochos and 1933 Volvi earthquakes, v) finally in the 5th row the stress field after the occurrence of the 1978 Stivos earthquake is calculated.

Coseismic Coulomb stress changes were calculated for the 30 strong earthquakes (Table 4-2) which struck the Corinth rift from 1700 until 2008 when the last strong ($M \geq 6.0$) earthquake occurred. The construction of the models is more complicated than in Mygdonia graben due to the seismotectonic complexity of the area. Historical and seismotectonic information were examined for the rupture model construction. Figure 4-18 depicts the horizontal projection of the rupture planes which are approximated as rectangular planes. They are plotted in accordance to the geometric properties described in Table 4-6 where information like azimuth ($^{\circ}$), dip ($^{\circ}$), rake ($^{\circ}$), length (km), width (km), horizontal and vertical slip (m) and seismic moment (M_0) is included. Rupture models for fault segments dipping to the south are red colored whereas the ones dipping to the North are white colored for clarity. ΔCFF is calculated for an horizontal layer at 8km depth. Figures 4-19 to 4-27 display the coseismic stress changes after the occurrence of each earthquake in a chronological order. In every case the epicentre, the activated fault (white color) the fault plane solution of the investigated earthquake are shown along with the epicentre and the fault segment (green color) of the following earthquake. Shear modulus, G and Poisson's ratio, ν , are also taken equal to $3.3 \cdot 10^5$ bars and 0.25, respectively, like in Mygdonia study area. A brief description of the source models and the Coulomb stress planar pattern is discussed below.

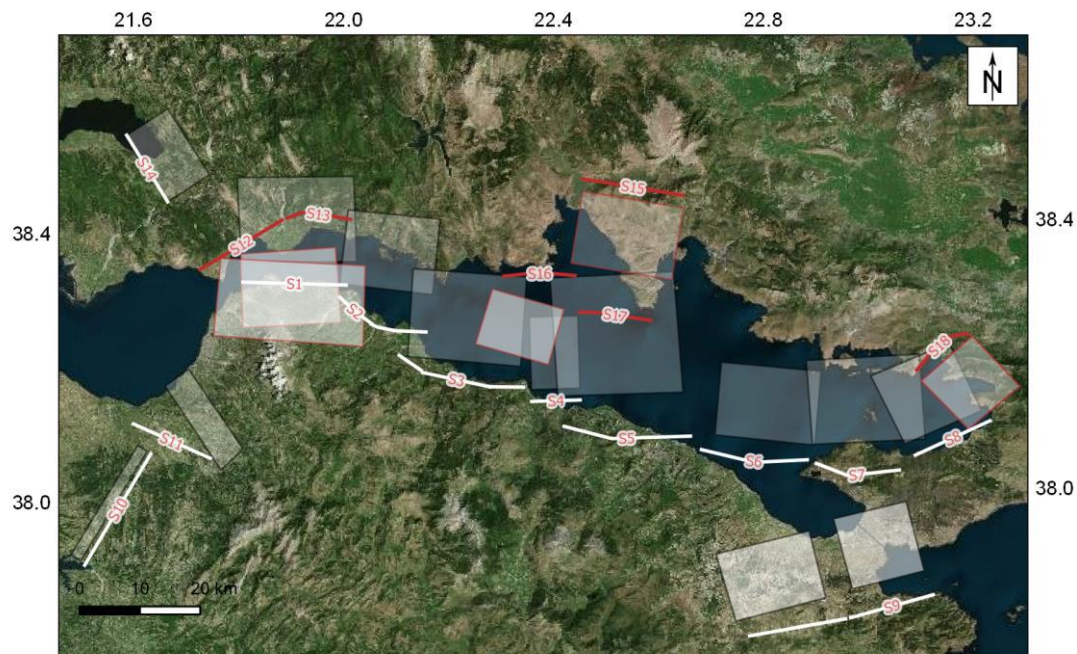


Figure 4-18 Surface projections for main faults in the Corinth rift. Rectangles correspond to the horizontal projection of the fault planes embedded in the brittle crust (3-15km). White color represents northdipping faults, while south-dipping faults are red colored. Details about the models are given in **Table 4-6**.

Table 4-6 Rupture models for strong earthquakes ($M \geq 6.0$) from 1700 until present in the Corinth Rift

Epicenter				Fault Geometry			Fault Plane Solution					Average Displacement		
n	Year	Latitude (φ°)	Longitude (λ°)	Fault Code	M _w	M ₀	L (km)	W (km)	Z (°)	Dip (°)	Rake (°)	u (m)	u _{ss} (m)	u _{DS} (m)
1	1703	38.400	21.800	Naf.F	6.1*	1.44·10 ²⁵	15	10	85	40	-125	0.37	-0.214	0.306
2	1714	38.375	21.790	Ps.F.	6.2*	2.88·10 ²⁵	17	16	270	45	-90	0.44	0	0.441
3	1725	37.900	23.000	Kech.F	6.0*	1.02·10 ²⁵	13.8	10	255	43	-100	0.31	-0.055	0.311
4	1742	38.100	22.600	Xyl.F.	6.7*	11.4·10 ²⁵	20	17	265	23	-81	1.00	0.159	1.00
5	1748	38.200	22.200	Aig.F.	6.6*	8.12·10 ²⁵	16	10	277	33	-76	0.85	0.020	0.830
6	1753	38.100	22.500	Xyl.F.	6.1*	1.44·10 ²⁵	20	17	265	23	-81	0.37	0.058	0.369
7	1756	38.400	21.900	Naf.F	6.8*	16.21·10 ²⁵	27	15	85	40	-125	1.19	-0.683	0.976
8	1769	38.400	22.000	Naf.F	6.8*	16.21·10 ²⁵	20	15	85	40	-90	0.72	0	0.724
9	1775	37.900	22.900	Per.F.	6.0*	2.04·10 ²⁵	18	16	285	40	-70	0.31	0.108	0.297
10	1785	38.200	21.700	Ach.F.	6.4*	1.02·10 ²⁵	17	12	331	73	35	0.57	0.474	0.332
11	1794	38.300	22.400	Er.F	6.7*	11.48·10 ²⁵	14	14	106	40	-90	0.32	0.000	0.316
12	1804	38.100	21.700	Ps.F.	6.4*	4.07·10 ²⁵	15	10	270	45	-90	0.61	0	0.614
13	1806	38.300	21.800	Ps.F.	6.2*	2.04·10 ²⁵	15	10	270	45	-90	0.44	0	0.441
14	1817	38.300	22.100	Aig.F.	6.6*	8.12·10 ²⁵	16	10	277	33	-76	0.85	0.207	0.830
15	1858	37.870	22.880	Kech.F.	6.5*	5.75·10 ²⁵	24	17	255	43	-100	0.72	-0.126	0.713
16	1861	38.250	22.160	El.F.	6.7*	11.4·10 ²⁵	22	12	281	34	-71	1.00	0.329	0.954
17	1870	38.480	22.550	Del.F.	6.8*	16.21·10 ²⁵	17	17	91	40	-90	1.19	0.000	1.191
18	1876	37.800	22.800	Kech.F.	6.1*	1.44·10 ²⁵	15	10	255	43	-100	0.37	-0.065	0.368
19	1887	38.050	22.650	Per.F.	6.5*	5.75·10 ²⁵	18	16	285	40	-70	0.72	0.248	0.681
20	1888	38.230	22.110	Aig.F.	6.3*	2.88·10 ²⁵	16	10	277	33	-76	0.52	0.126	0.505
21	1917	38.400	21.700	Naf.F	6.0*	1.02·10 ²⁵	13.	10	85	40	-125	0.31	-0.128	0.183
22	1928	38.070	22.820	Per.F.	6.3*	2.88·10 ²⁵	18	16	285	40	-70	0.52	0.104	0.285
23	1965	38.270	22.300	Er.F.	6.3	0.18·10 ²⁵	19.5	12.5	191	65	-79	0.52	0.169	0.492
24	1970	38.360	22.530	Xyl.F.	6.2	0.91·10 ²⁵	17	15	75	67	-94	0.24	0.038	0.239
25	1975	38.486	21.661	Trich.F.	6.0	1.13·10 ²⁵	13.8	13	316	71	-26	0.15	0.142	0.069
26	1981	38.153	22.961	Sk.F.	6.7	8.75·10 ²⁵	19	17	264	42	-80	1.06	0.186	1.053
27	1981	38.083	23.139	Al.F.	6.4	3.97·10 ²⁵	13	13	241	44	-85	0.72	0.064	0.727
28	1981	38.204	23.236	Kp.F.	6.3	2.7·10 ²⁵	13	13	50	45	-90	0.51	0.0	0.516
29	1995	38.362	22.200	Aig.F.	6.5	3.38·10 ²⁵	16	10	277	33	-76	0.64	0.155	0.621
30	2008	37.952	21.537	Pat.F.	6.4	4.6·10 ²⁵	25	12	209	83	-164	0.46	-1.274	-0.045

1703 February, Nafpaktos earthquake ($M^*=6.1$)

The first considered historical earthquake in the 18th century is documented in 1703 and its epicenter is given close to Nafpaktos ($I_{max}=VII$, Nafpaktos). According to Ambrasseys and Jackson (1997) this earthquake caused limited damage in Nafpaktos and other locations around the Corinth Rift. It is highly probable that its magnitude is overestimated and it does not exceed $M6.0$. Bernard et al. (2006) and Karakostas et al. (2012) assume that the causative fault is an antithetic to the main rupture zone of Corinth rift normal fault as also suggested by Papazachos and Papazachou (2003) who associated this event with the Nafpaktos south dipping E-W fault (strike= 85° , dip= 40° , rake= -125°). The suggested fault plane solution used for the reconstruction of the Nafpaktos rupture model is described in Table 4-6. Considering the scaling laws, the rupture model has a 15km length (Eq.4-7, $M_0 = 1.44 \cdot 10^{25}$ dyn-cm) which is in agreement with geomorphological expression and owns an average displacement 0.37m (Eq. 4-7). The ΔCFF stress field associated with its coseismic slip is shown in Figure 4-19a where the consecutive 1714 earthquake and its causative fault segment eleven years later are also shown. Bright zones are created on Patras gulf and the central Corinth Rift.

1714 July 29, Nafpaktos earthquake ($M^*=6.2$)

The 1714 earthquake ($I_{max}=VIII$, Nafpaktos) that caused extensive damage from Nafpaktos to Patras is attributed by Papazachos and Papazachou (2003) to Nafpaktos fault segment but Console et al. (2013) proposed Psathopyrgos fault, a hypothesis also considered in this study. The rupture model is a north dipping normal fault (strike= 270° , dip= 45° and rake= -90°). For the geometric properties of the model the fault length is set equal to 17km (Console et al., 2013) and the slip 0.44m (Eq. 4-7) ($M_0 = 2.88 \cdot 10^{25}$). Figure 4-19b shows the coseismic Coulomb stress pattern where positive stress accumulation is formed to the eastern part along S_2 fault, where the 1948 $M6.6$ earthquake occurred and the western part of the Corinth Rift, whereas the central area is covered by the N-S stress shadow lobes. The next 1725 $M6.0$ earthquake happened to the west end of the Corinth Rift where there is no evidence for stress interaction.

1725, Corinth earthquake ($M^*=6.0$)

The 1725 $M6.0$ earthquake occurred in the proximity of the city of Corinth ($I_{max}=VIII$) where a tower collapsed (Ambrasseys and Jackson, 1997). Information on the fault plane solution has been obtained from Papazachos and Papazachou (2003) who associated it with a normal northdipping fault (strike= 255° , dip= 43° and rake= -100°). The suggested responsible fault is the Kechries northdipping normal fault connected with strong earthquakes during Holocene (Copley et al., 2018). The rupture length was calculated for a $M6.0$ earthquake according to Eq.4-5 and is equal to 13.8km and the slip equal to 31cm (Eq. 4-7), whereas the seismic moment according to Eq.4-10 is $M_0 = 1.02 \cdot 10^{25}$ dyn-cm. ΔCFF spatial distribution shows that positive $\Delta CFFs$ are distributed to the SE part of the study area, affecting the northdipping major faults (Fig.4-19c). The following $M6.7$ earthquake occurred 17 years later in 1742 at the

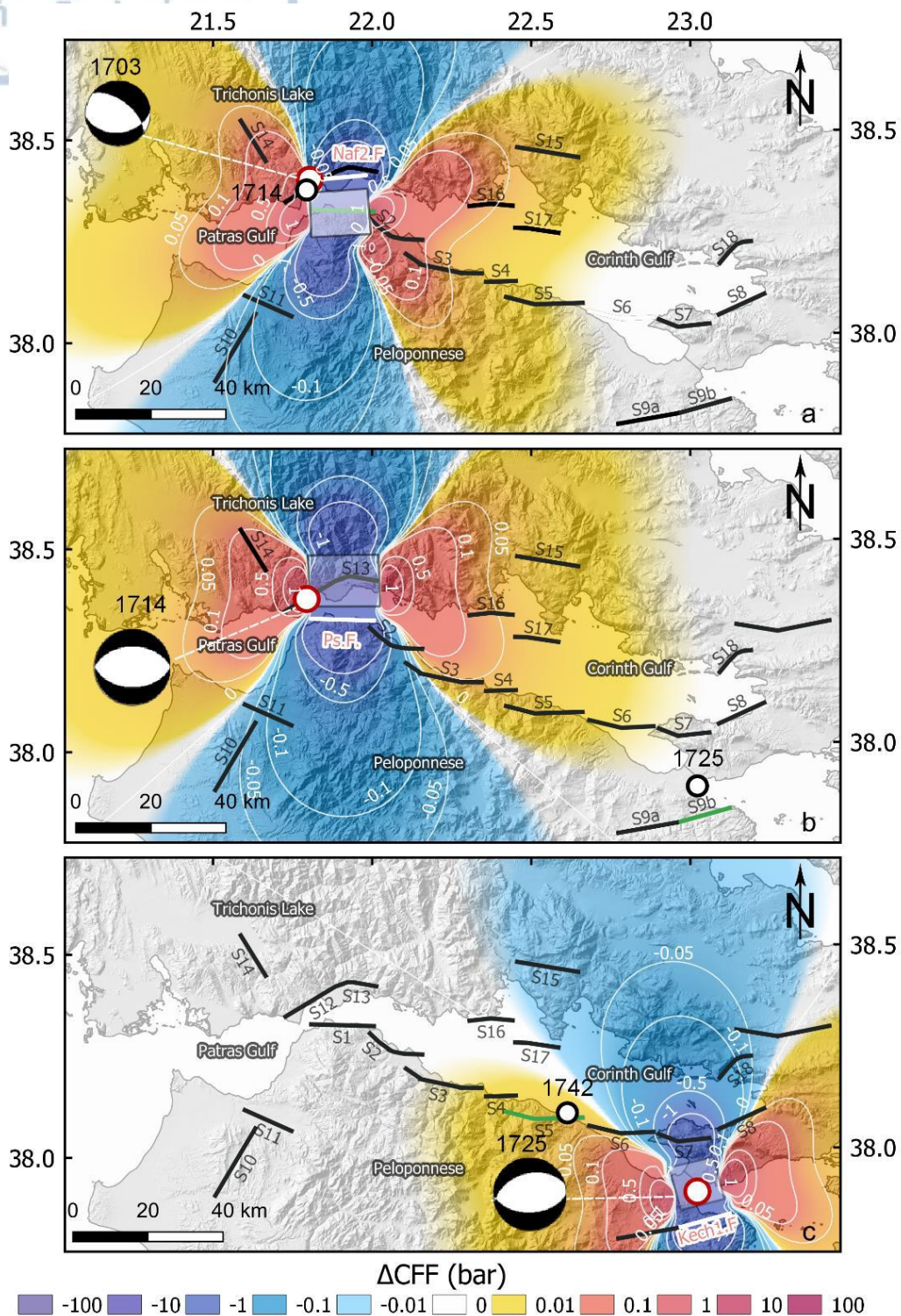


Figure 4-19 a) The spatial distribution for ΔCFF caused by the occurrence of the 1703 earthquake b) The coseismic stress Coulomb changes caused by the 1714 earthquake. c) ΔCFF changes caused by the occurrence of the 1725 earthquake (figure annotation like Figure 4-10).



Xylocastro fault segment (S_5), where failure along fault is promoted due to the 1725 earthquake occurrence (Figure 4-19c).

1742 February 21, Xylocastro earthquake ($M^*=6.7$)

The Xylocastro earthquake affected a large area along the central Corinth rift with the city of Corinth sustaining major damage ($I_{\max}=\text{VIII}+$ Trikala). A large number of fatalities and injuries were reported and buildings were destroyed in several villages located near the city of Corinth. There was also information for tsunami waves. According to Papazachos and Papazachou (2003) the causative fault was the Xylocastro fault segment (strike= 265° , dip= 23° and rake= -81°) and the rupture model was built according to the above fault properties. The length was taken equal to 20km as proposed from Console et al. (2013) whereas the average coseismic displacement approximately 1.0m in accordance with the scaling law (Eq. 4-7) ($M_0= 11.4 \cdot 10^{25}$ dyn-cm, Eq.4-10). Bright zones are created in an E-W direction (Fig. 4-20a) encompassing the majority of the major faults in the Corinth Rift. Adjacent faults like Aigion (S_2) and Eliki (S_3) faults are strongly reinforced with an increasing likelihood for a potential earthquake occurrence. The Eliki fault was activated after 6 years, causing the 1748 M6.6 earthquake, possibly triggered by the 1742 earthquake.

1748 May 25, Aigion earthquake ($M^*=6.6$)

In 1748 a M6.6 earthquake ($I_{\max}=\text{X}$, Aigion) caused severe damages in the city of Aigion which was evacuated for a long time. Historical documentation for a tsunami occurrence in the gulf was also reported. The association with Eliki fault (S_3) is proposed by Papazachos and Papazachou (2003) whereas Aigion fault is suggested by Console et al. (2013), an assumption adopted in this study (strike= 277° , dip= 33° and rake= -76°). For constraining the rupture model the length and the displacement of the fault are taken equal to 16km (Console et al., 2013) and 85cm (Eq.4-7) respectively ($M_0= 8.12 \cdot 10^{25}$ dyn-cm). The 1748 earthquake (Fig. 4-20b) created a stress pattern whose geometry shows a promotion of earthquake occurrence along strike over the majority of the northdipping faults that bound the Corinth Rift from the south. Location and time of the M6.1 1753 earthquake which occurred on Xylocastro fault segment (S_5) is likely to be advanced by the 1748 earthquake.

1753 March 6, Xylocastro earthquake ($M^*=6.1$)

Eleven years after the 1742 earthquake another earthquake (M6.1) occurred in 1753 ($I_{\max}=\text{VII}$, Zacholi) in close distance to the previous one according to a monastery archives. The rupture model for this earthquake which is attributed to Xylocastro fault was constrained according to the fault properties given by Papazachos and Papazachou, (2003) and Console et al. (2013) (strike= 265° , dip= 23° and rake= -81°). The fault length is based on scaling laws and set equal to 15.5km (Eq.4-5) and the average coseismic displacement is 37cm (Eq.4-7) ($M_0=1.44 \cdot 10^{25}$ dyn-cm). Positive ΔCFFs are cast over the eastern part of the rift, further enhancing the area to the west termination of the gulf (Fig. 4-20c). A migration of strong seismicity follows with no indication for interaction between the 1753 and the following 1756

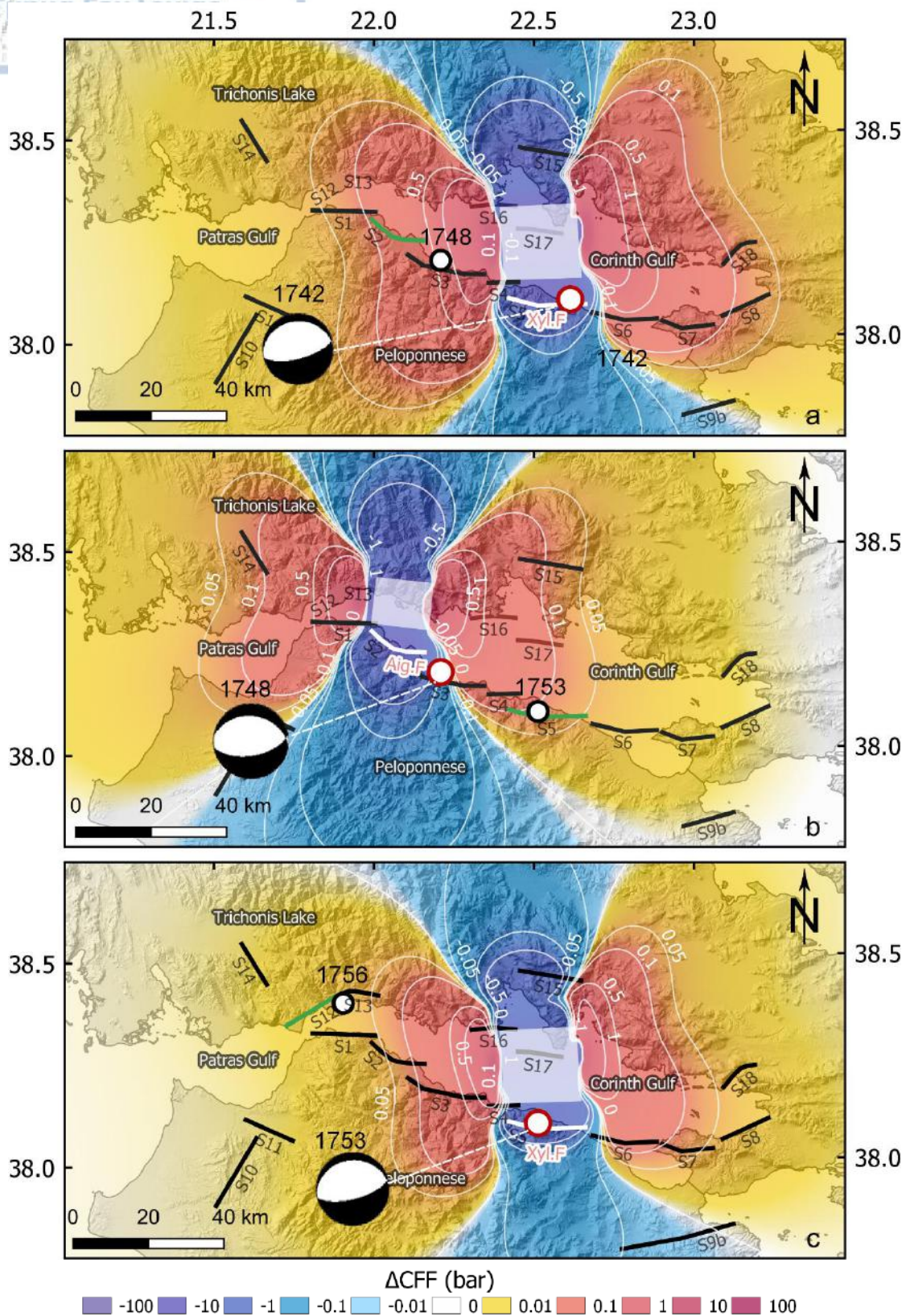


Figure 4-20 a) The spatial distribution of the coseismic stress Coulomb changes due to the 1742 earthquake b) Stress Coulomb changes caused by the occurrence of the 1748 earthquake and c) Coulomb changes caused by the occurrence of the 1753 earthquake on Xylocastro fault.

earthquake which occurred around Nafpaktos, at the western termination of the Corinth gulf. Significant stress enhancement along strike is imposed possibly associated with the 1775 M6.0 earthquake on Perachora fault (S_6).

1756, Nafpaktos earthquake ($M^*=6.8$)

The 1756 M6.8 event destroyed Nafpaktos city ($I_{max}=VIII+$) and was widely felt in the broader area, with the northern part of the study area to be mostly affected (Ambraseys, 2009). Papazachos and Papazachou (2003) consider Nafpaktos as the causative fault, also accepted in this study (strike= 85° , dip= 40° and rake= -125°). According to the magnitude and the geomorphologic expression on the faults the length is taken equal to 27km (Eq.4-5) and the average coseismic displacement during the earthquake was calculated equal to 119cm (Eq.4-7) ($M_0= 16.21 \cdot 10^{25} \text{ dyn}\cdot\text{cm}$). Coseismic stress distribution depicted in Figure 4-21a is developed over a broad area of the western Corinth Rift by significantly promoting failure along the rift. The subsequent earthquake which occurred in 1769 is closely located to areas of interference and might have been advanced by its predecessor, but the correlation between these two events remains uncertain.

1769, Desfina earthquake ($M^*=6.8$)

30 years after the occurrence of the 1756 Nafpaktos earthquake, the next strong event struck the north coasts of the gulf and caused the majority of the damage at Desfina and Galaxidi ($I_{max}=VIII$, Desfina). Papazachos and Papazachou (2003) consider that the Nafpaktos fault is also responsible for this earthquake. Due to the distribution of the damages other authors consider that this earthquake is rather smaller than 6.8 and associated with other faults to the east of Nafpaktos. For modelling the rupture, length was taken equal to 20km (Eq.4-5) and the fault properties similar to the south dipping normal faults of the central part of the gulf (strike= 85° , dip= 40° and rake= -90°). The displacement was estimated equal to 72cm (Eq.4-7) and $M_0= 16.21 \cdot 10^{25}$ (Eq.4-10). The stress distribution (Fig. 4-21b) shown little impact on the following strong earthquake, which is related to the stress perturbations caused by previous seismicity at the eastern part of the study area.

1775, Corinth earthquake ($M^*=6.0$)

The 1775 earthquake ($I_{max}=VIII$, Corinth) had a great impact on the city and it was even felt in Patras and Zakynthos. Papazachos and Papazachou (2003) suggested that the activated fault is a north dipping normal fault and the earthquake was located around the Corinth city whereas Console et al. (2013) suggest that the seismogenic fault is offshore Perachora fault segment, also accepted in this study (strike= 285° , dip= 40° and rake= -70°). The length of the rupture is taken equal to 18km (Console et al., 2013) and the average displacement according to Eq.4-7 is equal to 31cm ($M_0= 2.04 \cdot 10^{25} \text{ dyn}\cdot\text{cm}$, Eq.4-10). The spatial distribution of the coseismic stress changes is shown in Figure 4-21c. ΔCFF distribution shows that the advance of earthquakes occurrence at the eastern part of the rift is quite significant.

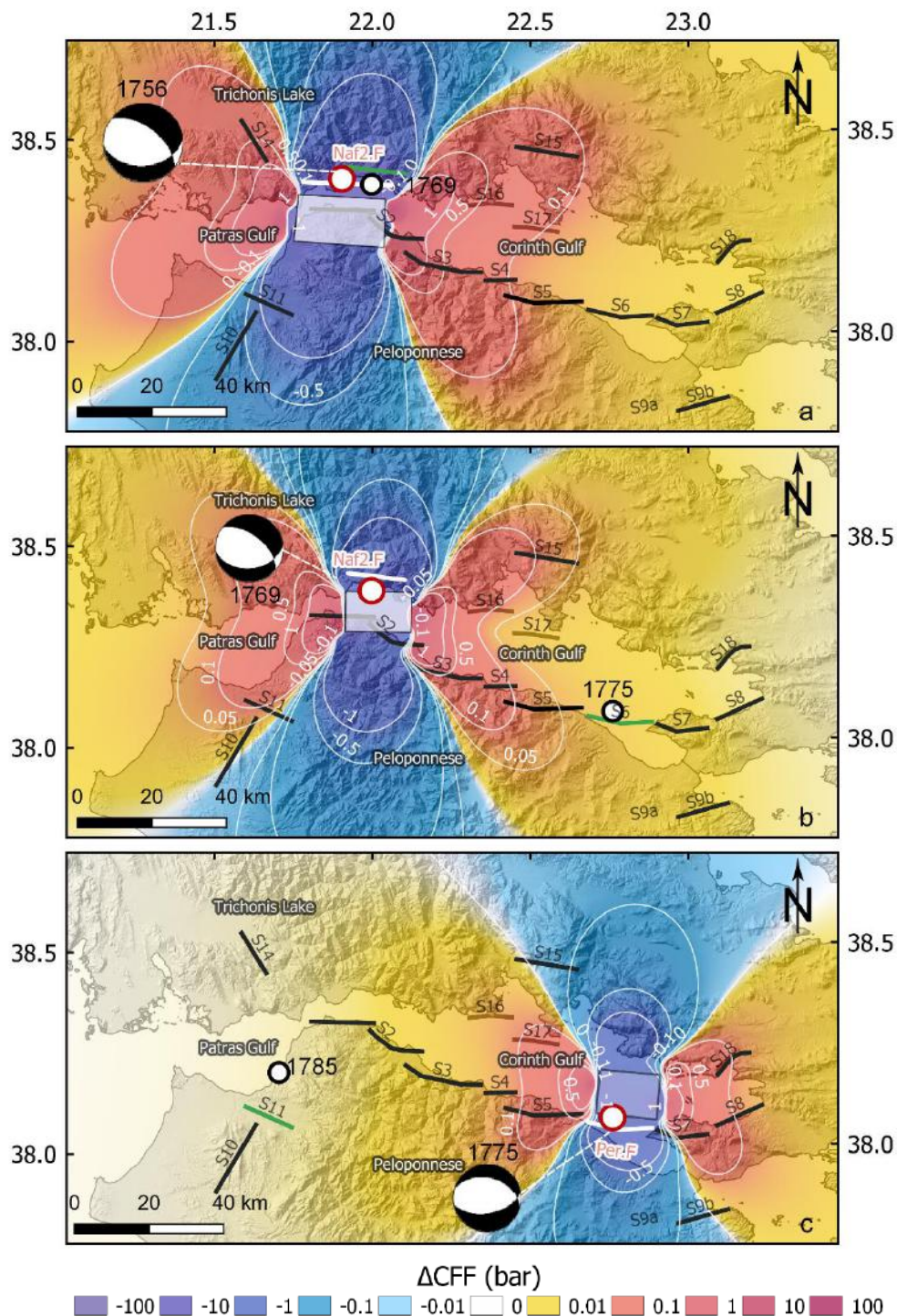
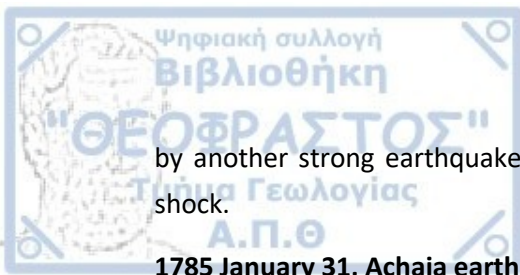


Figure 4-21 a) Coulomb changes due to the 1756 event b) The spatial distribution of the coseismic stress Coulomb changes caused by the occurrence of the 1769 earthquake c) The spatial distribution of the coseismic stress Coulomb changes caused by the occurrence of the 1775 earthquake.

The epicentre of the 1785 earthquake that followed occurred at the western termination of the gulf. However strong seismicity in less than twenty years the broader area was struck again



by another strong earthquake in its vicinity which might have been triggered by the 1775 shock.

1785 January 31, Achaia earthquake ($M^*=6.4$)

In 1785 a $M_{6.4}$ earthquake was felt near the city of Patras ($I_{\max}=\text{IX}$, Patras) causing numerous ruins and casualties. Papazachos and Papazachou (2003) suggested that the activated fault was a strike slip vertical fault with strike= 37° , dip= 89° and rake= -174° . The 1988 $M_{5.9}$ Patras which occurred in the proximity of the 1785 earthquake was used for constraining the rupture model for a NNW–SSE striking fault plane (Karakostas et al., 1994, strike= 331° , dip= 73° and rake= -35°). The fault was considered 17km in length with an average displacement 57cm obtained for strike slip faults according to Eq.4-9 and M_o ($M_o= 4.07 \cdot 10^{25} \text{dyn}\cdot\text{cm}$). Positive ΔCFF changes are cast over the epicentral area of the 2008 Achaia earthquake in NW Peloponnese and over the central part of the gulf where the 1794 $M_{6.7}$ earthquake subsequently occurred (Fig. 4-22a).

1794, Galaxidi earthquake ($M^*=6.7$)

The 1794 $M_{6.7}$ earthquake was mostly felt around Galaxidi where several macroseismic effects like mud flows or sea waves occurred ($I_{\max}=\text{VII}$, Galaxidi). Papazachos and Papazachou (2003) associated the occurrence of this earthquake with an antithetic to the main rupture zone, southdipping fault. Valkaniotis (2009) based on geomorphological and seismotectonic observations suggested the existence of an offshore seismogenic fault southern of Itea city that is associated with this earthquake. The rupture model is described by 14km in length and 31cm slip with fault properties according to Papazachos and Papazachou (2003) strike= 106° , dip= 40° and rake= -90° ($M_o= 1.14 \cdot 10^{26} \text{dyn}\cdot\text{cm}$). Figure 4-22b depicts the geometry of the ΔCFF field in the central part of the Corinth Rift. Along the strike of the Itea offshore fault (It.off.F) the area is stress enlightened, and rupture is also promoted on the western S_1 and S_2 segments where the next three earthquakes occurred.

1804 June 8, Patras earthquake ($M^*=6.4$)

In 1804 a strong earthquake occurred in Patras area ($I_{\max}=\text{IX}$, Patras) but also felt to the west. There is limited information about this earthquake for which Papazachos and Papazachou (2003) suggest the Achaia fault that was last activated in 1785 to be the responsible fault but Console et al. (2013) associate it with Psathopyrgos fault and this suggestion is obtained in the study (strike= 270° , dip= 45° and rake= -90°). The rupture length is 15km and the average displacement equal to 61cm according to Eq.4-10 ($M_o= 4.07 \cdot 10^{25} \text{dyn}\cdot\text{cm}$). The earthquake may probably regard a foreshock of the 1806 earthquake that followed after two years and is probably associated to the same fault because of the existence of a fault asperity (Fig. 4-22c). Stress bright zone covered the central and north part of the western part of the Corinth Rift.

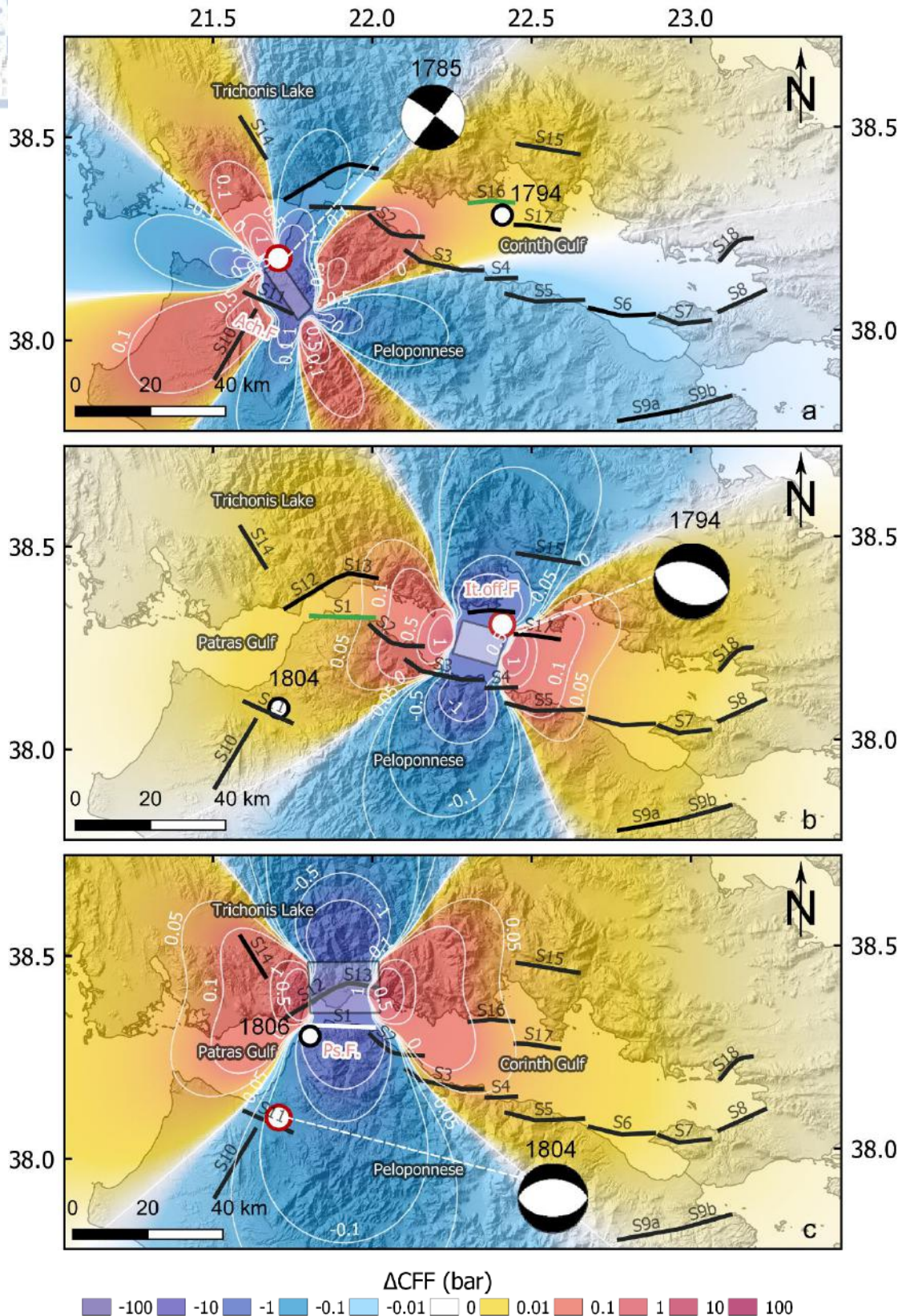
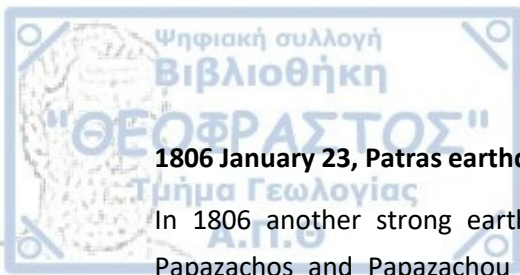


Figure 4-22 a) The spatial distribution of the coseismic stress Coulomb changes caused by the occurrence of the 1785 earthquake, b) spatial distribution of the coseismic stress Coulomb changes caused by the occurrence of the 1794 earthquake c) The spatial distribution of the coseismic stress Coulomb changes caused by the occurrence of the 1804 earthquake.



1806 January 23, Patras earthquake ($M^*=6.2$)

In 1806 another strong earthquake caused severe damage in Patras ($I_{\max}=\text{VIII}$, Patras). Papazachos and Papazachou (2013) associated the occurrence of this earthquake with Nafpaktos fault and Console et al. (2013) attributed the event to Psathopyrgos fault. The association with Psf was also accepted in this study and thus the 1806 rupture model shares the same characteristics with the 1804 event which preceded. The slip introduced in the rupture model of the event is equal to 44cm and the rupture length equal to 15km (Eq.4-10, $M_o= 2.04 \cdot 10^{25}$ dyn-cm). The spatial distribution of the Coulomb stress changes broadly cumulatively affected the western and central part of the gulf as shown in Figure 4-23a, by advancing failure along the adjacent faults like the S2 Aigion fault where the next earthquake M6.6 occurred 11 years later.

1817 August 23, Aigion earthquake ($M^*=6.6$)

The 1817 Aigion earthquake destroyed the two thirds of the city of Aigion ($I_{\max}=\text{IX}$, Aigion) killed many people and triggered a tsunami. The activated fault by Papazachos and Papazachou (2003) is the Eliki fault, whereas Console et al. (2013) suggest Aigion fault which was last activated in 1748. Aigion fault plane properties and length (16km) proposed by the latter authors were used for the construction of the rupture model (strike= 277°, dip=37° and rake=-76°) and the average displacement 85cm according to Eq.4-7 ($M_o= 8.12 \cdot 10^{25}$ dyn-cm). The coseismic stress pattern shows that positive ΔCFF are shed over the central part of the study area strongly affecting the majority of the north dipping faults by encouraging an impending earthquake along them (Fig.4-23b). The next earthquake occurred at the eastern part and shows not direct association with stress changes induced by the 1817 event.

1858 February 21, Corinth earthquake ($M^*=6.5$)

The 1858 earthquake is the third strong historical earthquake that is associated with Kechries fault (Koukouvelas et al., 2017) at the southeastern part of the Corinth Rift ($I_{\max}=\text{IX}$, Corinth). It was widely felt over the Greek mainland and the surrounding islands and there is tsunami information and a rich archive for damages associated with this shock and the abundant aftershocks. The rupture length was taken equal to 25km (Eq. 4-5) and the slip equal to 72cm ($M_o= 5.75 \cdot 10^{25}$ dyn-cm). Similar fault plane solution with the two previous events caused by Kechries fault was used (strike=255°, dip=43° and rake=-100°). Figure 4-23c shows the eastern and western part of the study area covered with extensive stress enhanced zones. Seismicity migrated to the centre with the M6.7 1861 earthquake to be the next, along Eliki (S_3) fault.

1861 December 26, Eliki earthquake ($M^*=6.7$)

The 1861 severe earthquake (Valimitika, $I_{\max}=\text{X}$) caused casualties, surface ruptures up to 13km, tsunami waves and liquefaction phenomena. According to Papazachos and Papazachou (2003) the causative fault segment is the Eliki fault (S_3). The rupture model has strike= 270°,

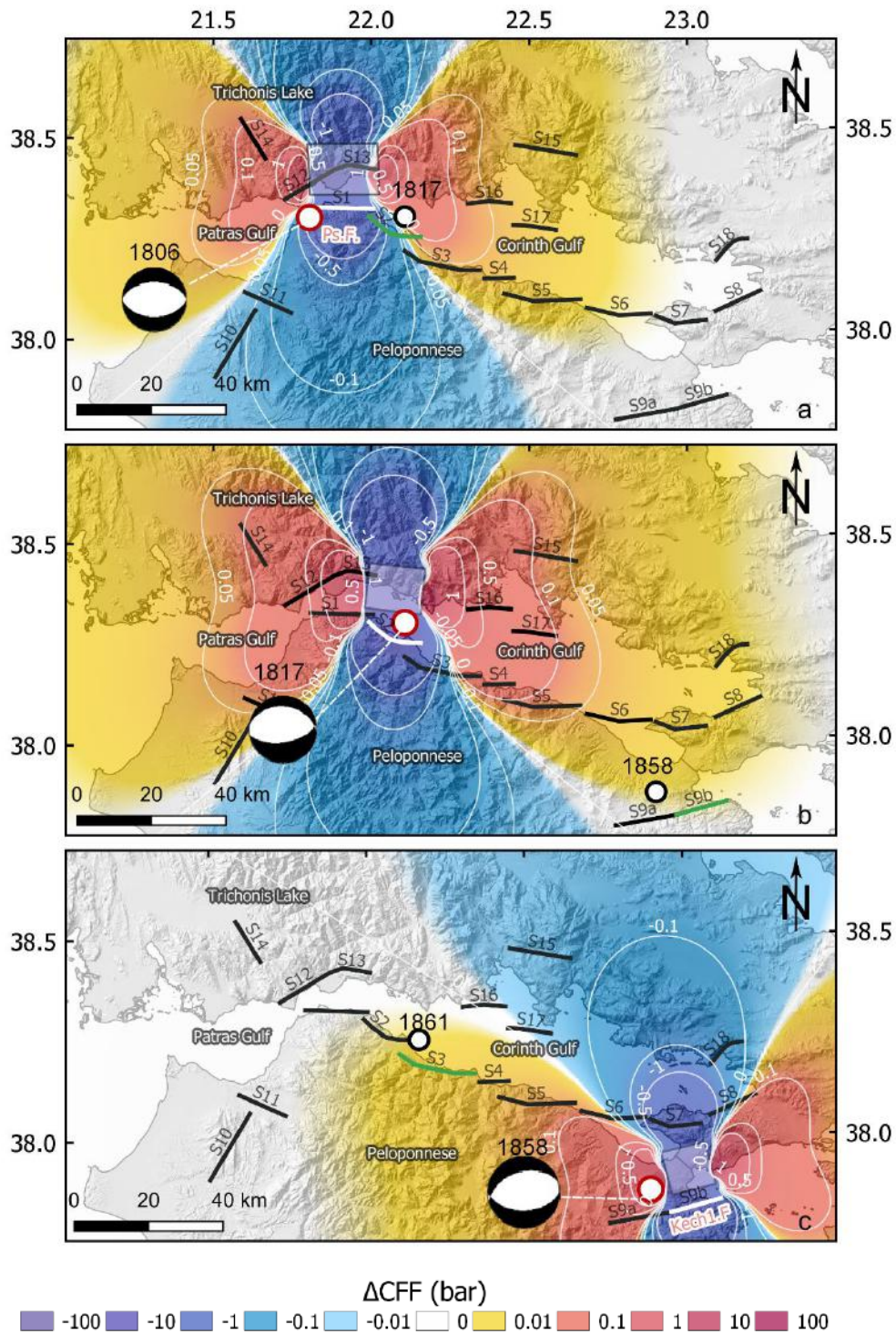
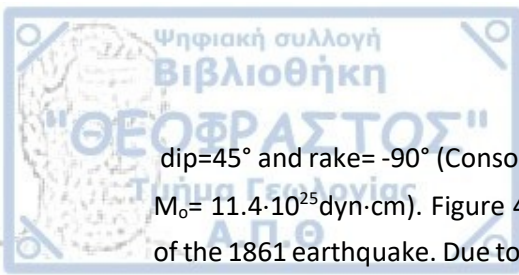


Figure 4-23 a) The spatial distribution of the coseismic stress Coulomb changes caused by the occurrence of the 1806 earthquake. b) The spatial distribution of the coseismic stress Coulomb changes caused by the occurrence of the 1817 earthquake c) The spatial distribution of the coseismic stress Coulomb changes caused by the occurrence of the 1858 earthquake



dip=45° and rake=-90° (Console et al., 2013), 22km length and 100cm displacement (Eq.4-10, $M_0= 11.4 \cdot 10^{25}$ dyn·cm). Figure 4-24a illustrates the stress changes induced by the occurrence of the 1861 earthquake. Due to the earthquake size, positive stress changes encompass a large area over the central part of the Corinth Rift where stress is increased along the strike of the dominant northdipping fault zone. The next earthquake was located at the north coast of Corinth gulf, in a stress enhanced more than 1.0bars lobe because of the 1861 event.

1870 August 1, Arachova earthquake ($M^*=6.8$)

The 1870 earthquake ($I_{max}=IX$, Arachova) was described in many historical resources because of the severe casualties and damages at the northern part of the Corinth Rift. Ambraseys and Pantelopoulos (1989) describe a rich sequence with strong foreshocks ($M5.3$) and five strong aftershocks with magnitude $M \geq 5.4$, showing a westward epicentral migration. A surface rupture with a 2.0m vertical displacement regards a surface indication of the fault location, whereas other geological observations were similar to the 1965 Eratini earthquake. Delphi fault is the causative fault according to Ambraseys and Jackson (1998), Papazachos and Papazachou (2003) and Pavlides and Caputo (2004). The suggested fault plane solution is an E-W south dipping normal fault (strike=91°, dip=40° and rake=-90°). The length is obtained from measurements on the segmented fault zone of Delphi 25km (Valkaniotis, 2009) and is equal to 17km and the average displacement equal to 119cm (Eq.4-10, $M_0= 16.2 \cdot 10^{25}$ dyn·cm). Stress results are displayed in Figure 4-24b, where the significant impact especially on the northern part of the study area is visible.

1876 June 26, Nemea earthquake ($M^*=6.1$)

According to Papazachos and Papazachou (2003) the 1876 Nemea earthquake caused the vast damages in Nemea ($I_{max}=VII$) but it was felt in a broad area. Based on the damage distribution, the western segment of Kechries fault is assumed to be the causative fault which was also responsible for the 1858 Corinth earthquake (Kech2.F). Information on the fault plane solution has been obtained from Papazachos and Papazachou (2003) according to which, strike=255°, dip=43° and rake=-100°. The rupture length was 15km (Eq. 4-5) and slip, $u=37$ cm (Eq.4-10, $M_0= 1.44 \cdot 10^{25}$ dyn·cm). The ΔCFF spatial distribution is displayed in Figure 4-24c and shows that the subsequent $M6.0$ earthquake is not favored by the 1887 earthquake occurrence, since its epicentre is located in the shadow zone produced by the Nemea earthquake.

1887 October 3, Xylocastro earthquake ($M^*=6.3$)

The 1887 earthquake ($I_{max}=VIII$, Xylocastro) caused building collapses along the south coast of the central Corinth Rift over Xylocastro and Perachora faults. Papazachos and Papazachou (2003) associated this earthquake with the Xylocastro fault segment, however Console et al. (2013) related it with Perachora offshore fault segment. The latter rupture model was used in order to calculate the coseismic stress changes resolved for a fault with strike=285°, dip=40° and rake=-70°. The rupture length was taken equal to 18km and the average slip equal to 72cm ($M_0=5.7 \cdot 10^{25}$ dyn·cm). Results on the distribution of positive and negative ΔCFF changes

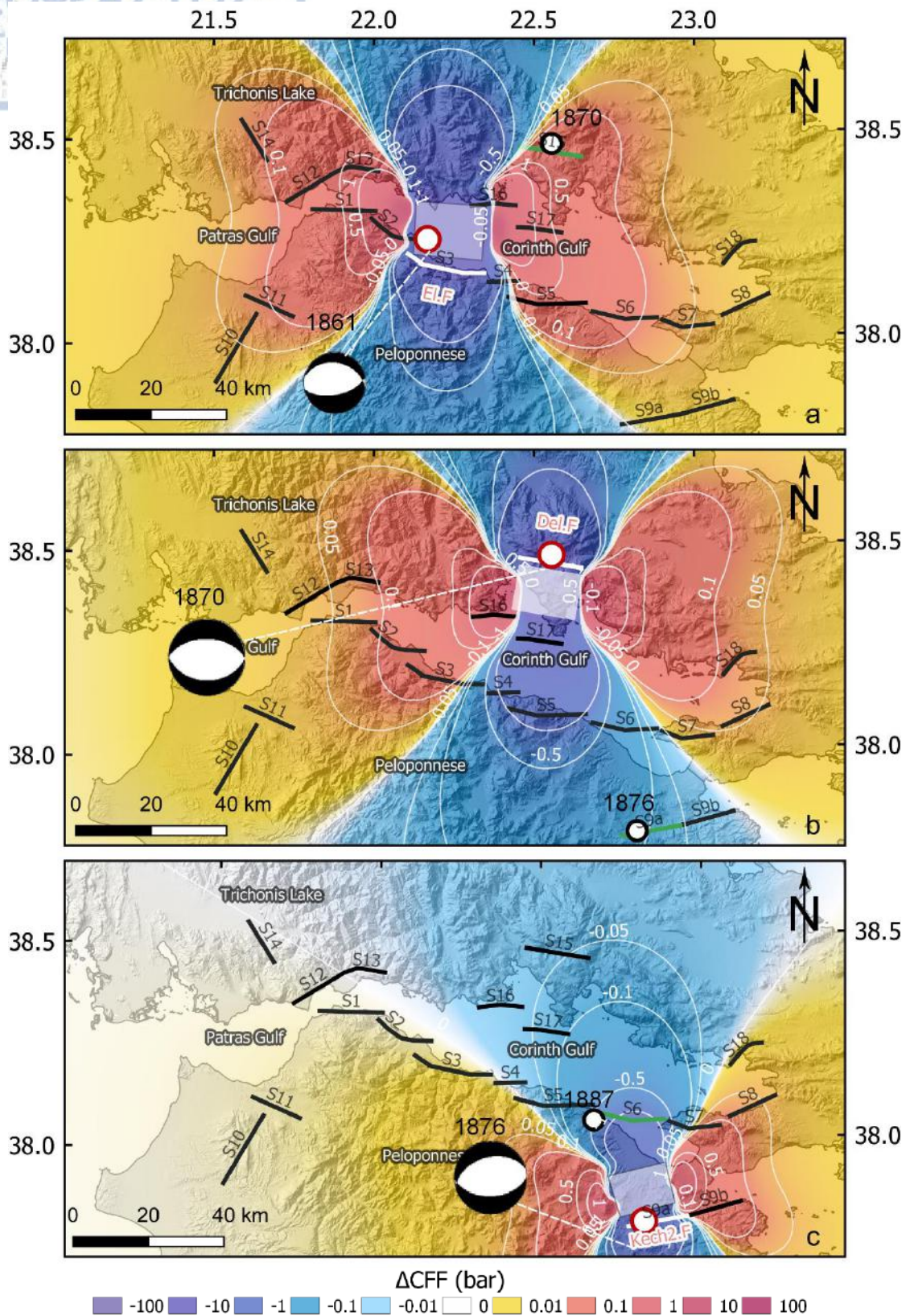


Figure 4-24 a) The spatial distribution of the coseismic stress Coulomb changes caused by the 1861 occurrence at the ancient city of Delphi. b) The spatial distribution of the coseismic stress Coulomb changes caused by the occurrence of the 1870 earthquake, c) The spatial distribution of the coseismic stress Coulomb changes caused by the occurrence of the 1876 earthquake

are shown in Figure 4-25a. A significant stress enhancement >1.0 bars is induced at the eastern part of the rift along S_7 , S_8 and the antithetic S_{18} faults, causative faults for the 1981 seismic sequence. There is a high likelihood that these faults have been brought closer to failure because of the 1887 on Perachora fault. Increased stress are also imposed on S_5 , S_4 and S_3 faults where the following seismicity occurred.

1888 September 9, Aigio earthquake ($M^*=6.3$)

The 1888 Aigion earthquake was very destructive for Aigio and Valimitika ($I_{max}=IX$) and according to historical information it was felt 150km away from the proposed epicentral area. Macroseismic effects such as landslides and a tsunami were observed. Previous researchers consider Aigion fault responsible for this earthquake (Galanopoulos 1953; Console et al., 2013). The rupture model has strike= 277° , dip= 33° and rake= -76° , 52cm slip and 16km length (Eq. 4-5) ($M_0=2.88 \cdot 10^{25}$ dyn·cm). Figure 4-25b displays the coseismic ΔCFF distribution and the location of the next M6.0 1917 earthquake to the NW Aigio fault and within the strong influence of the positive ΔCFF values (>1.0 bars). Triggering of the 1917 event because of the preceding 1888 earthquake is possible.

1917 December 24, Nafpaktos earthquake ($M^*=6.0$)

The 1917 earthquake struck the northern coast of the Corinth Rift and the suggested causative fault according to isoseismal contours generated by Papazachos and Papazachou (2003) indicated the activation of Nafpaktos fault. The rupture model is described by parameters typical for the southdipping normal fault of Nafpaktos (strike= 84° , dip= 40° and rake= -125°), 14km length and 31cm average slip ($M_0=1.02 \cdot 10^{25}$ dyn·cm). Coseismic stress changes are shown in Fig. 4-25c and mainly affect the central study area and especially S_2 , S_3 and S_{14} faults, which were activated in 1995, 1965 and 1975 in respect. The next M6.3 shock in 1928 migrated at the eastern Corinth Rift, where more strong earthquakes followed.

1928 April 22, Corinth earthquake ($M^*=6.3$)

The 1928 earthquake struck the eastern part of the study area. According to Papazachos and Papazachou (2003) the earthquake was caused by Kechries fault but Console et al. (2013) suggested that Perachora fault is the responsible seismogenic fault (strike= 285° , dip= 40° and rake= -70°). For the construction of the rupture model, the fault length was considered equal to 18km (suggested by Console et al., 2013) and the slip $u=52$ cm according to Eq.4-10 ($M_0=2.88 \cdot 10^{25}$ dyn·cm). The earthquake occurrence caused a positive stress accumulation to the eastern and the western part of the study area, whereas the central area is covered by the stress shadow lobes (Fig. 4-26a). The causative faults for the 1981 seismic sequence S_7 , S_8 and the antithetic S_{18} fault received an additional stress enhancement. The next earthquake in 1965 occurred at the central part of the gulf.

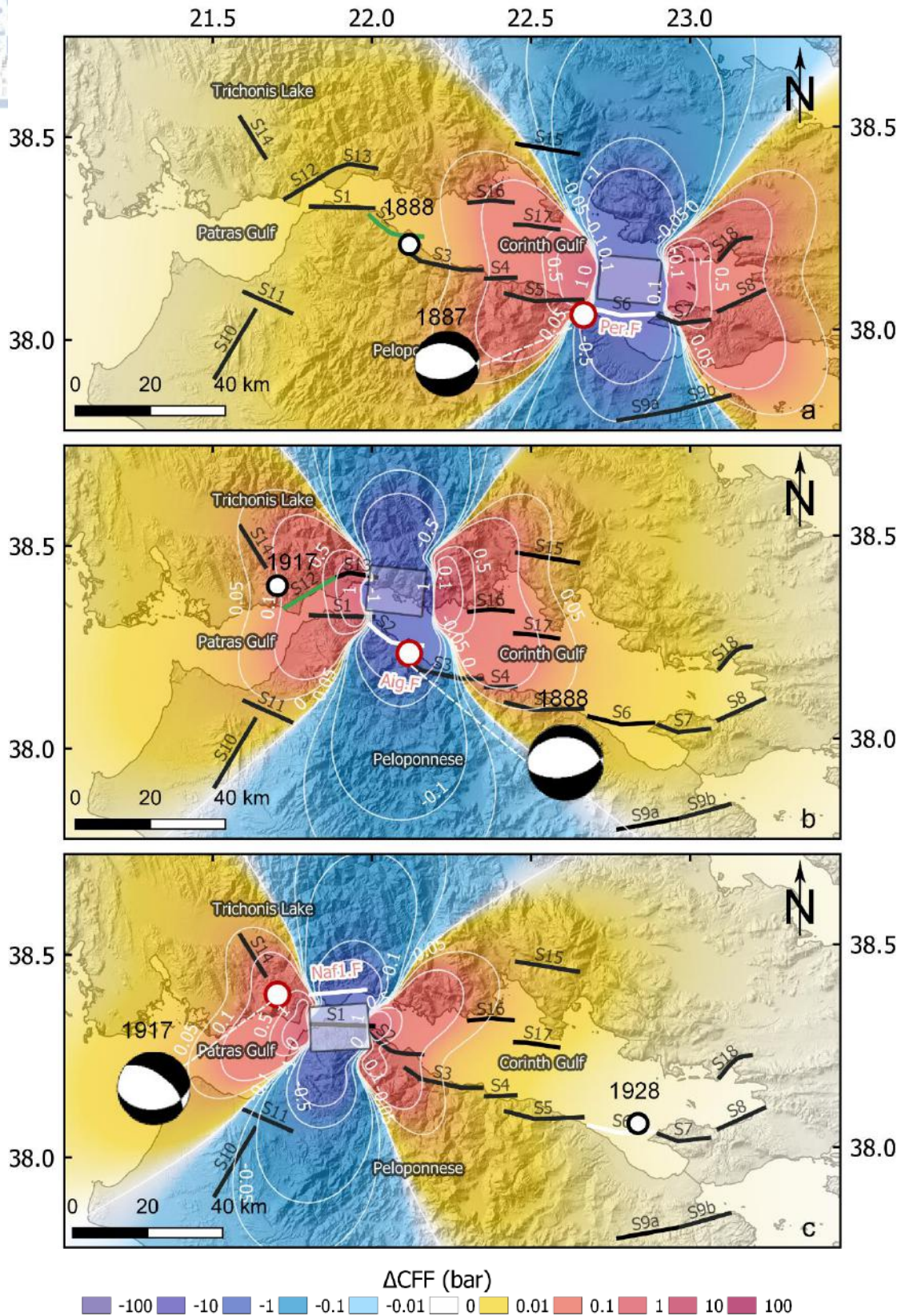


Figure 4-25 The spatial distribution of the coseismic stress Coulomb changes caused by the occurrence of the 1887 earthquake b) The spatial distribution of the coseismic stress Coulomb changes caused by the occurrence of the 1888 earthquake c) The coseismic stress Coulomb changes caused by the occurrence of the 1917 earthquake



1965 July 6, Eratini earthquake ($M^*=6.3$)

The 1965 severe earthquake in Erateini ($I_{\max}=\text{VIII}+$) based on the macroseismic distribution of the damages is attributed to Eratini fault. Papazachos and Papazachou (2003) associated the occurrence of this earthquake with an antithetic southdipping fault (strike= 106° , dip= 40° and rake= -90°). The length of the rupture is considered 19km and the average displacement is 52cm according to Eq.4-10 ($M_0=1.62 \cdot 10^{26}$ dyn-cm). The earthquake occurrence caused a positive stress distribution to the eastern and the western part of the study area, whereas the central area was covered by stress shadow lobes (Fig. 4-26b).

1970 April 8, Antikyra earthquake ($M_w=6.2$)

The 1970 earthquake occurred at the eastern part of the study area with maximum macroseismic intensity VII in Antikyra. The fault plane solution is obtained from Taymaz et al. (1991) for constraining the rupture model for the event (strike: 75° , dip: 67° and rake -94°) and it is associated with the Xylocastro active fault. The rupture length is taken equal to 17km whereas the slip is 21cm as deduced from the seismic moment ($M_0=0.9 \cdot 10^{25}$ dyn-cm). The earthquake occurrence causes positive stress changes to the eastern and the western part of the study area, whereas the central area is covered by the stress shadow lobes (Fig. 4-26c).

1975 December 31, Trichonis earthquake ($M_w=6.0$)

In June – December 1975 a seismic sequence with a M6.0 shock occurred in Trichonis Lake, causing damage to old buildings (Delibasis and Carydis, 1977). According to seismological data and previous seismotectonic studies Kiratzi et al. (2008) suggested that the causative fault is a NNW-SSE north dipping normal fault with sinistral strike slip motion (strike= 316° , dip= 71° and rake= -26°), a fault controlling the southern boundary of Trichonis basin. They also relocated the focal coordinates of the earthquake and this data is used in the construction of the rupture model. The fault length is equal to 14km (by Papazachos et al., 2001), and the average displacement is 15cm derived from the seismic moment ($M_0=1.13 \cdot 10^{25}$ dyn-cm, HRV-GCMT). ΔCFF spatial distribution mainly covers the northwestern part of the study area (Fig. 4-27a). In 2007 a seismic cluster with a triplet of moderate earthquakes (M5.0, M5.2, M5.2) occurred within an hour in the same area. The distribution of these events is in agreement with the causative 1975 fault. Kiratzi et al. (2008) suggested that this swarm was enhanced from the 1975 event since it occurred NW of the 1975 rupture within a bright zone and generally activated a 25km zone. This event is the only one affecting the northwestern part of the study area (S_{12} and S_1 faults).

1981 February 24, Alkyonides earthquake ($M_w=6.7$)

In 1981 February 24th a M6.7 earthquake occurred at the eastern part of Corinth rift strongly felt by citizens in the Greek capital and it was the first of the Alkyonides strong earthquake triplet. The strong seismic sequence resulted in human fatalities with 20 people killed and more than 500 injured, building collapsed and severe damages. Liquefaction effects,

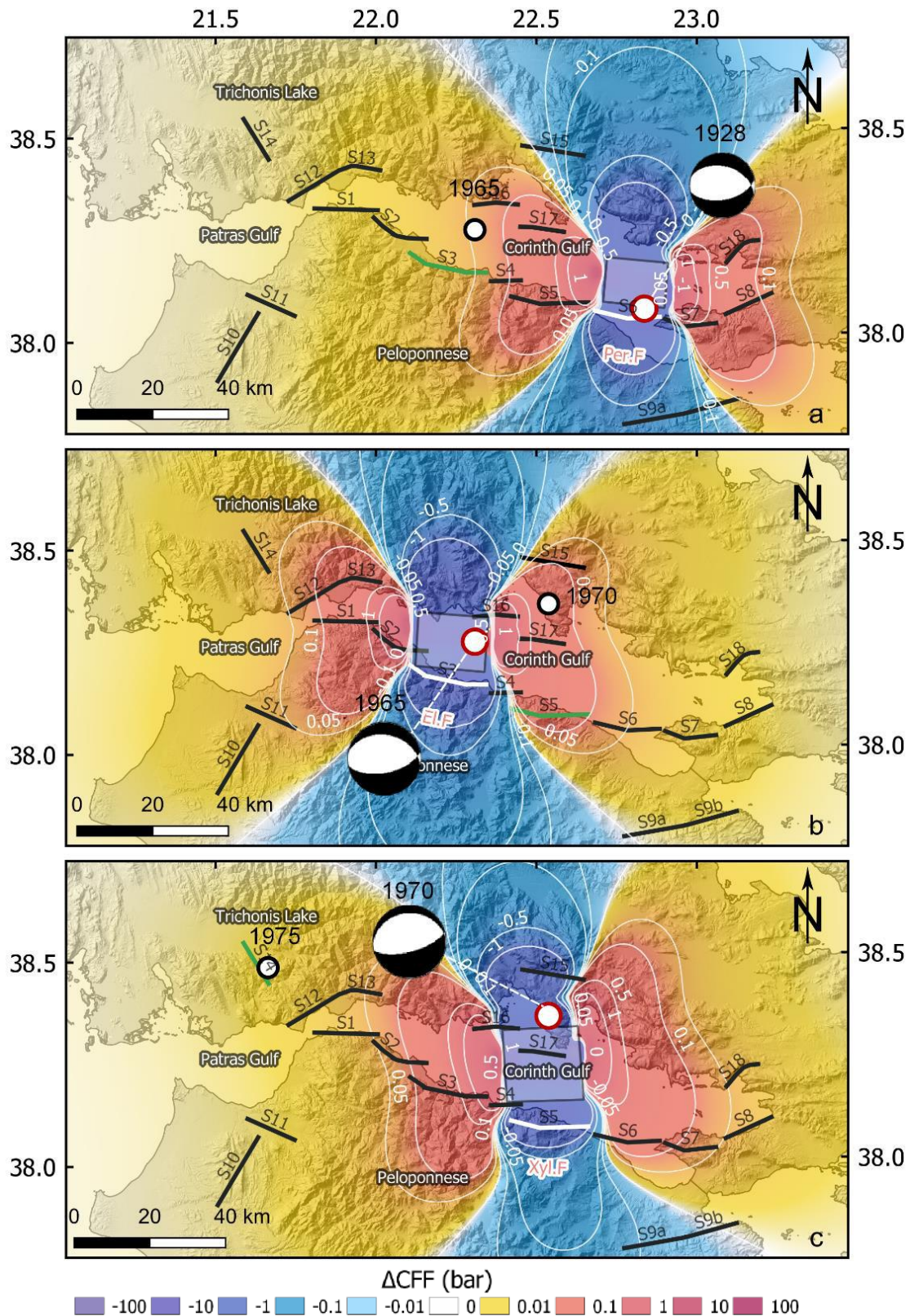


Figure 4-26 The spatial distribution of the coseismic stress Coulomb changes caused by the occurrence of the 1965 earthquake b) The spatial distribution of the coseismic stress Coulomb changes caused by the occurrence of the 1970 earthquake c) The coseismic stress Coulomb changes caused by the occurrence of the 1975 earthquake

surface ruptures and uplifts along the coast of Perachora peninsula and a local 1m high tsunami were also observed (Jackson et al., 1982). All the reported fault plane solutions (Table 4-2) indicate a north-dipping low angle fault. The coseismic rupture model was based on the solution given by Taymaz et al. (1991) which is similar to other results. The assumed fault plane is a north dipping normal fault plane with 264° strike, 42° dip and $\lambda=-80^\circ$. According to Console et al (2013) the length of the rupture is equal to 19km, slightly longer than the one suggested by Hubbert et al. (1996) but in agreement with the length range suggested by Armijo et al. (1996). The average coseismic slip is equal to 2.96m and is obtained from $M_0= 1.1 \cdot 10^{26}$ dyn-cm. The coseismic stress distribution in Figure 4-27b shows the two broad bright zones created along strike and positively enforces S_8 segment responsible for the February 25th earthquake. The epicentre of the second earthquake occurred in an area where the Coulomb stress change is equal to 1bar and is probably advanced by the first earthquake.

1981 February 25, Alkyonides earthquake ($M_w=6.4$)

One day after the first Alkyonides earthquake the second $M_w6.4$ earthquake occurred. The causative fault is the Alepochori fault (S_8). Fault plane solutions have been given by Jackson et al., 1982; Taymaz et al. (1991) as given in Table 4-2. The rupture is modelled based on Taymaz et al. (1991) for an E-W oriented fault with 241° strike and rake= -85° ($M_0= 3.97 \cdot 10^{25}$ dyn-cm) 13km long and 72cm average displacement. From the stress field geometry it is observed that S_{18} fault has been brought closer to failure because of the second earthquake which probably triggered the occurrence of the March 4 earthquake (Fig. 4-27c). There is evidence for a successive advance of earthquake occurrence along the adjacent faults.

1981 March 4, Alkyonides earthquake ($M_w=6.3$)

The $M6.3$ third Alkyonides earthquake occurred 7 days later, northeast of the second event. Jackson et al (1982) found south dipping surface ruptures at the north part of the gulf after the occurrence of the third earthquake therefore this shock is attributed to the south dipping Kaparelli/Livadostras fault a pure dip slip normal fault. The fault plane solution for constraining the rupture model was taken from Braunmiller and Nabelek (1996) and corresponds to a normal fault striking 50°, dipping 45° and owing -90° rake. The rupture is 13km long and the displacement 51cm based on the radiated seismic moment ($M_0=2.88 \cdot 10^{25}$ dyn-cm). Figure 4-28a shows the ΔCFF spatial distribution and the location of the following $M6.0$ earthquake on Aigio fault. The Alkyonides epicentral cascade among adjacent and antithetic faults highlights the significance of interaction mechanisms between strong earthquakes. It is believed that the time and location of the earthquakes are strongly encouraged by the successive accumulation of stress at the eastern part of the gulf and the triplet earthquakes are stress correlated.

1995 June 15, Aigio earthquake ($M_w=6.0$)

The 1995 Aigio earthquake was disastrous for Aigio city ($I_{max}=VIII$) and the surrounding areas since 26 people died due to collapsed buildings most of which located in the city of Aigio. The

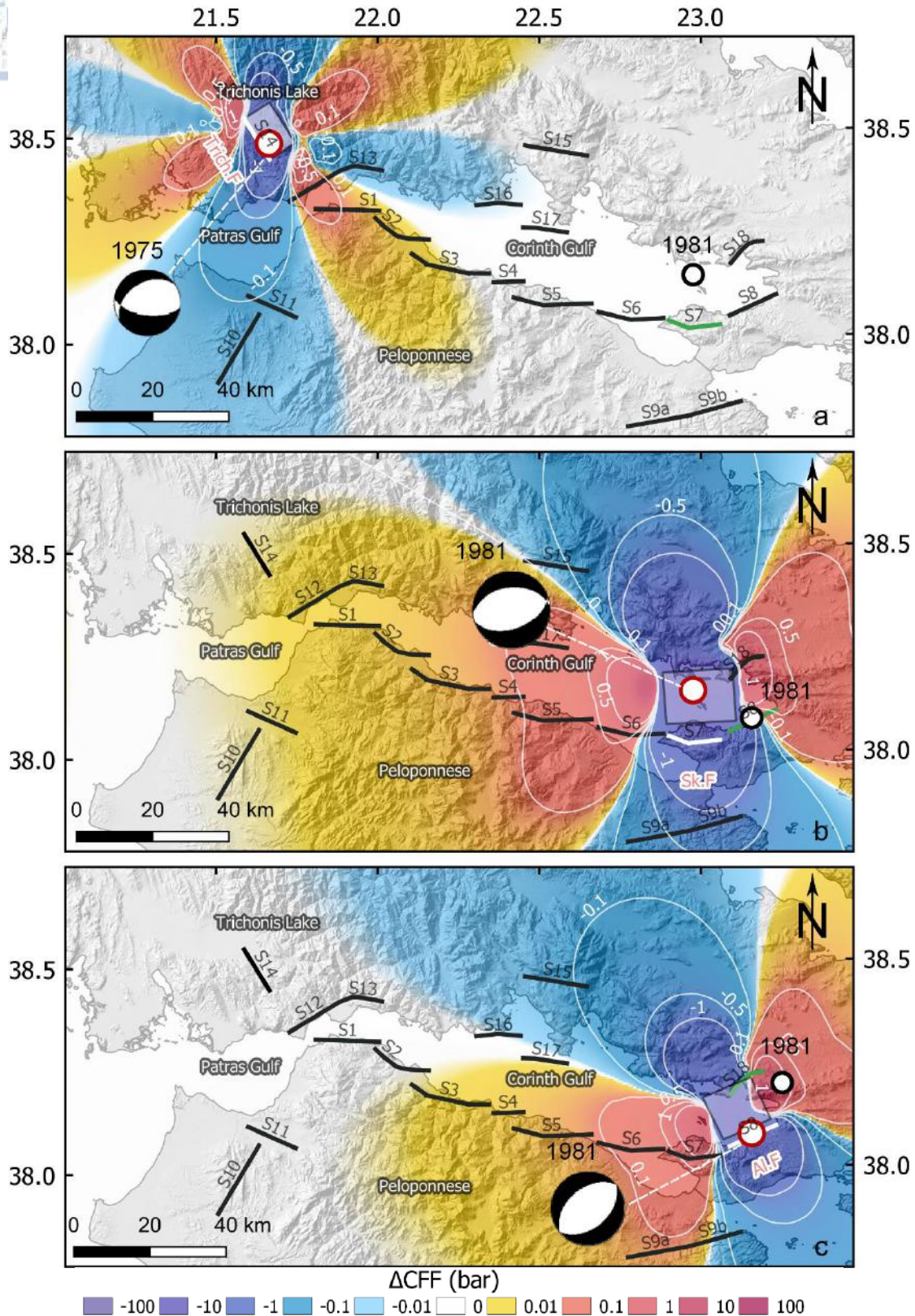


Figure 4-27 a) The ΔCFF spatial distribution caused by the occurrence of the 1975 earthquake in Trichonis basin, b) The spatial distribution of the coseismic stress Coulomb changes caused by the occurrence of the February 24th 1981 earthquake, c) The spatial distribution of the coseismic stress Coulomb changes caused by the occurrence of the February 25th 1981 earthquake

reported fault plane solutions define a low angle E-W normal fault (HRV-GCMT; Bernard et al., 1997; PDE-PDE/GS). Bernard et al. (1997)(Table 4-2) solution was adopted for constraining the rupture model for a fault with 277° strike, 33° dip, -76° rake ($M_0=3.38 \cdot 10^{25}$ dyn-cm). Aigion fault was the causative fault (Bernard et al., 1997; Console et al., 2013) the length of the which in this study is presumed to be 16km (Console et al., 2013 and references therein) smaller than the length calculated from scaling laws (25km) but in accordance with the geomorphological fault expression. The earthquake which nucleated at 10km depth was followed by a large number of aftershocks with hypocentres between 8 and 12km and the strongest aftershock (M5.6) some minutes after the main shock. Based on the above information the average coseismic slip was taken equal to 63cm (Eq.4.9) smaller than the one proposed by Bernard et al. (1997) (87cm). Figure 4-28b exhibits the pattern of the coseismic stress distribution computed at 8km depth. Δ CFF imposes positive changes in both sides of the fault tips over the entire Corinth rift, increasing the stress deficit in the broader area. The subsequent 2008 strong earthquake occurred in Achaia as denoted with the black marker at the border of the bright stress lobe created by the 1995 earthquake (Figure 4-28b).

2008 June 8, Achaia earthquake ($M_w=6.4$)

The 2008 Achaia earthquake was the strongest recent earthquake that struck the study area and caused the death of two people, human injuries and extensive building damage. The low instrumental seismicity and the absence of strong historical seismicity in the specific area along with the lack of knowledge for active faults raised the scientific interest and a significant number of studies have been published ever since for improving the location of the seismic sequence (Konstantinou et al., 2009; Roumelioti et al., 2013; Serpetsidaki et al. 2014; Karakostas et al., 2017) investigating the rupture properties (Gallovic et al., 2009; Feng et al., 2010) the stress transfer and the deformational pattern of the rupture zone (Koukouvelas et al., 2009; Stiros et al., 2013; Segou et al., 2014, Karakostas et al., 2017). The majority of the reported fault plane solutions refer to strike slip faults and the chosen in this study is reported from GCMT and corresponds to a nearly vertical fault with a dextral strike slip component (strike= 209° , dip= 83° , rake= 164° and seismic moment, $M_0=4.6 \cdot 10^{25}$ dyn-cm). The NNE-SSW fault strike is in accordance with the aftershock distribution (Konstantinou et al., 2009; Karakostas et al., 2017). The average fault slip (46.06cm) was extracted from fault properties (Eq. 4.9) considering a fault length equal to 25km which approximates the length of the aftershock epicentral distribution defined by Konstantinou et al. (2009) and fault width is taken equal to 12km. The main shock is located at the deepest part of the brittle zone (Gallovic et al. 2009; Ganas et al. 2009; Konstantinou et al. 2009) as also shown in the seismotectonic analysis of Chapter 2. In Figure 4-28c it is observed that the Δ CFF spatial distribution reveals the existence of a stress enhanced zone in a NNE direction over Patras rift and Psathopyrgos fault and along a SE-NW lobe over northern Peloponnese. The 2010 M5.6 and M5.5 Efpalio earthquakes are located into a stress enhanced zone and probably favored by the 2008 earthquake occurrence even if the Coulomb stress change is smaller than 0.1 bars.

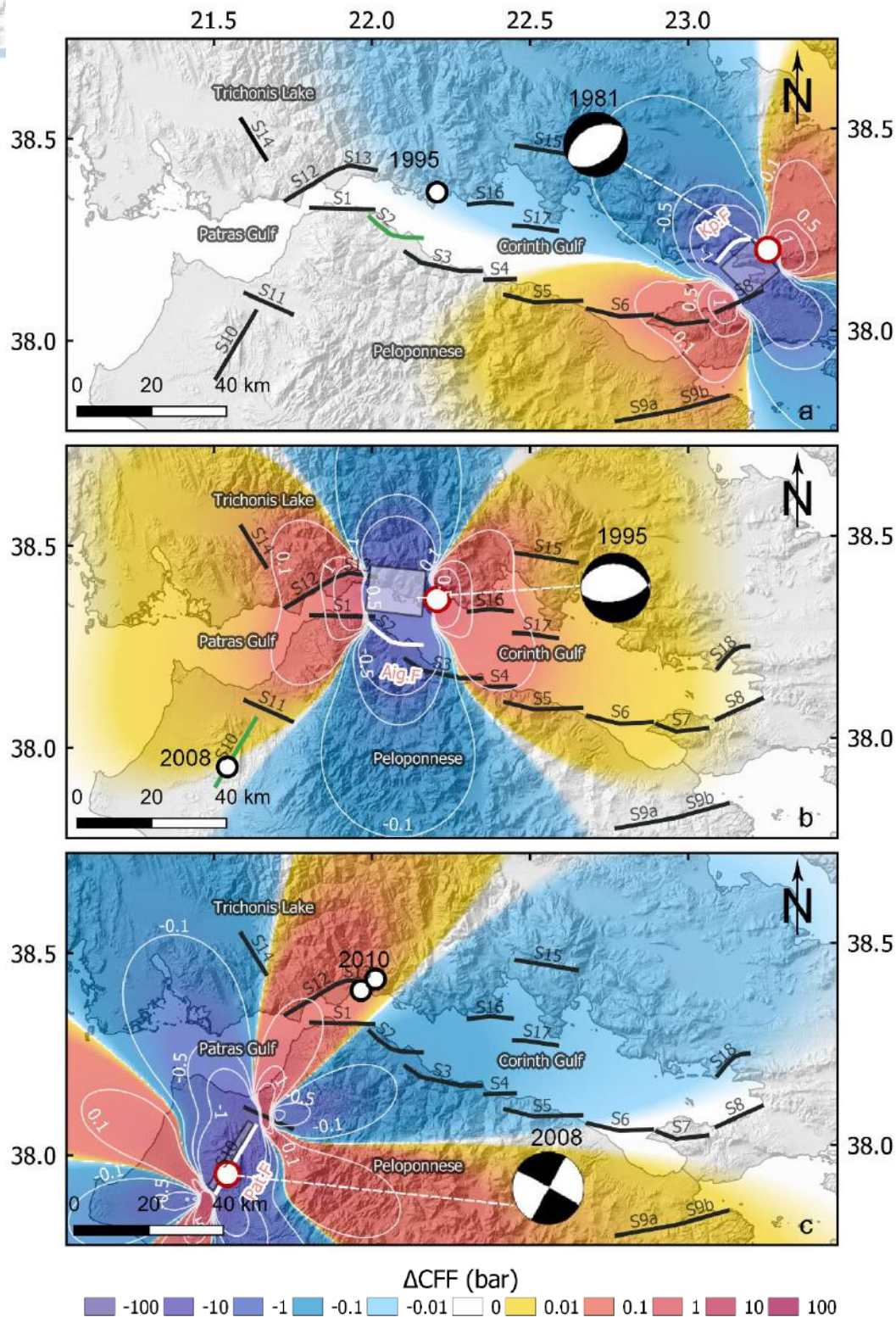


Figure 4-28 a) Coulomb stress pattern caused by the March 4th 1981 earthquake, b) ΔCFF distribution due to the 1995 Aigio earthquake, c) ΔCFF distribution after the 2008 Achaia earthquake, which is the last strong shock in Corinth gulf. The locations of the 2010 Efpalio doublet are also shown.

A. In addition to the coseismic stress changes which are imposed by strong earthquakes, the long-term tectonic loading along major faults was added in order to reconstruct the stress evolutionary model for the last 300 years. The successive estimations of the stress evolutionary states can shed light into correlations among strong earthquakes and activated faults in respect to the deformation field and can provide information about the current stress state. Evolutionary models indicate regions expected to hold increased stress changes, which are areas with high potential for an impending earthquake, but can also be used for studying interrelations between the stress changes caused by strong earthquakes and recent moderate and small seismicity. The successive time intervals for which the stress evolutionary field are defined prior the occurrence of each earthquake. In each stage, ΔCFF is calculated onto the rupture plane of the next inspected event, so changes in shear and normal stress of an earthquake are resolved according to the properties of the subsequent event's faulting type. Stress values are computed at 8 km depth approximately in the middle of the brittle crust and stress changes are presumably zero before the initial strong event. Results are shown in snapshots and stress changes for positive and negative stress changes are color coded as previously.

4.2.6.1 Evolutionary stress model for Mygdonia Graben

Stress calculations for the reconstruction of the evolutionary model in Mygdonia initiated in 1677 when the first Vasilika earthquake happened, before which stress is considered zero. Results are presented in the successive snapshots of Figure 4-29(a-g) where the reconstructions of the evolutionary model are successively depicted for different intervals. The most important fault zones with their properties described in Table 4-3 were considered for the estimation of the accumulated interseismic strain. Figure 4-29a exhibits the initial stress state, which is the coseismic stress change caused by the occurrence of the 1677 event in the eastern segment of Anthemountas fault (S_{10}). The generated ΔCFF pattern exhibits positive stress change lobes along the strike of Anthemountas fault where failure is enhanced. Thermaikos gulf and central Chalkidiki are the areas mainly influenced from the increasing values of stress caused by the 1677 event. It is assumed that there is a positive interaction between the two segments of the fault zone. The along strike prolongation of the rupture to the west creates a bright zone of positive stress changes where after 82 years, in 1759 the next strong earthquake with the same magnitude occurs. Figure 4-29b shows the stress pattern before the 1759 Thessaloniki which occurred at the prolongation of Anthemountas fault to the west (S_{11}). The result incorporates the cumulative effect of the 1677 earthquake along with the tectonic loading on faults for 82 years resolved according to the properties of the 1759 receiver fault. The causative fault for the 1759 lies in a stress enhanced area and probably failure has been advanced by the previous earthquake.

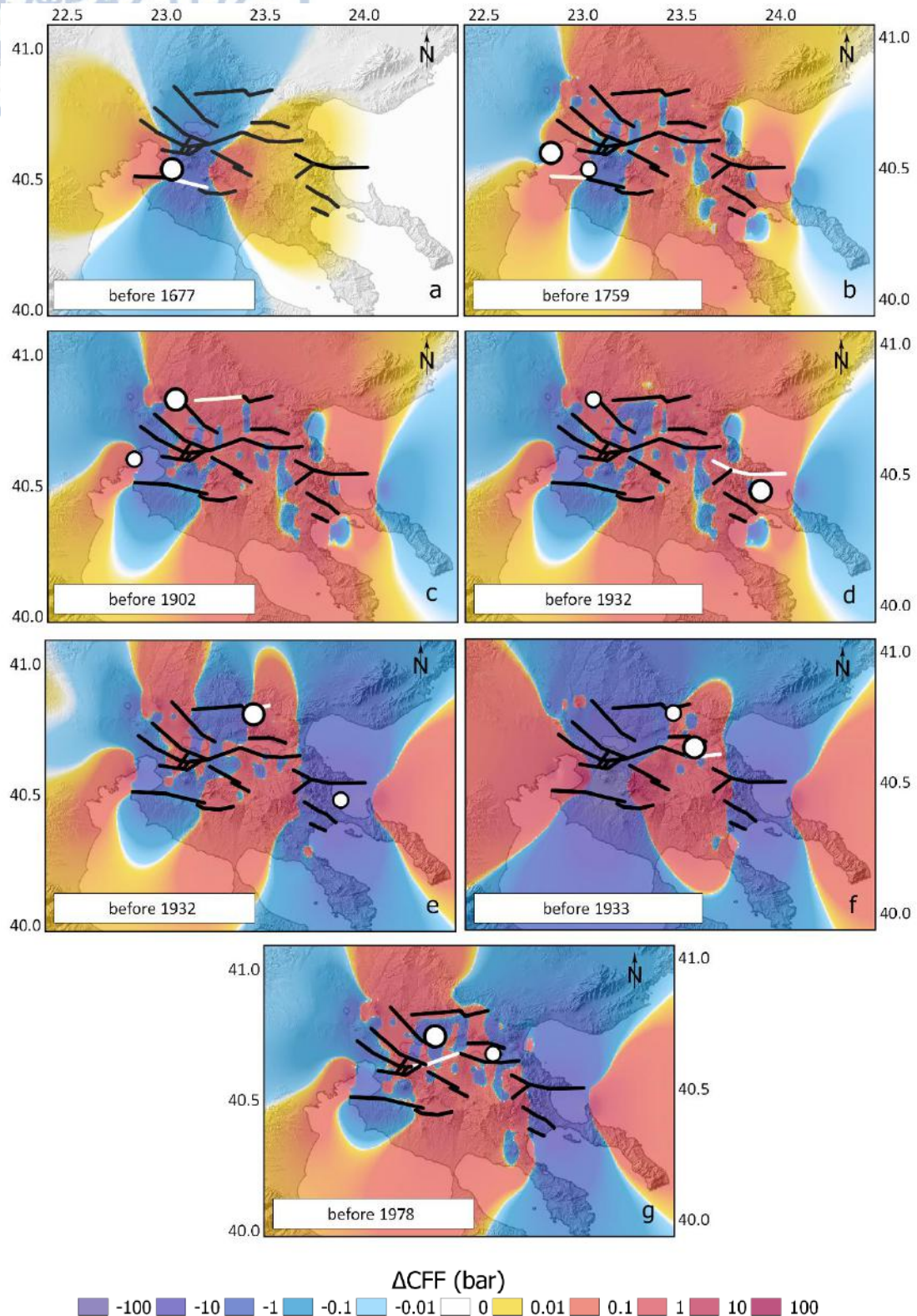
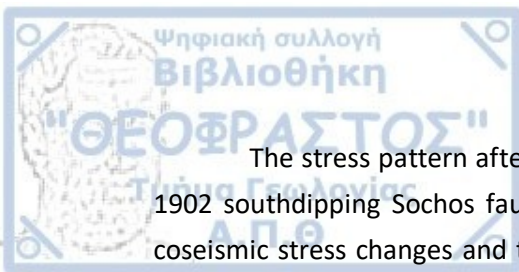


Figure 4-29 Evolutionary Coulomb stress in Mygdonia. Coulomb stress changes are calculated for 8km depth. a) Coseismic stress changes associated with the 1677 event, b) Stress changes before the 1759 earthquake c) Stress changes before the 1902 event, d) Stress changes before the 1932 earthquake, e) Stress changes before 1933, f) Stress changes before the 1978 triplet, g) stress field after the last strong earthquakes.



The stress pattern after the occurrence of the 1759 event resolved according to the 1902 southdipping Sochos fault is displayed in Figure 4-29c. The cumulative effect of the coseismic stress changes and tectonic loading shows a reinforcement of the positive stress existence over the central part of Mygdonia. The shadow zones only affect Anthemountas basin and Thessaloniki area. In Figure 4-29d the stress field after the occurrence of the 1902 stress effect and before the occurrence of the 1932 Ierissos event, calculated for its own source properties, is shown. It is characteristic that 1902 Assiros earthquake further increases the positive stress accumulation to the eastern part of the study area where the next earthquake occurs 30 years later. Figure 4-29e demonstrates the stress impact of the devastating Ierissos earthquake after which, a broad shadow zone where the occurrence of future earthquakes is prohibited. On the contrary, positive ΔCFF stresses are reinforced in the central part of the study area. The two following small earthquakes in 1932 and 1933 whose epicentral accuracy is on debate, are considered to be aftershocks and they also occurred around the western stress bright lobe, caused by the 1932 event. The stress pattern before the occurrence of the 1932 (Fig. 4-29e) and the 1933 (Fig. 4-29f) comply with epicentral distribution of these earthquakes and it is strongly believed that they have been triggered because of the severe 1932 earthquake. Eventually, extensive areas of stress enhancement exist in the central area of Mygdonia graben, where in 1978, 46 years later the last recorded strong shock occurs. In Figure 4-29g the stress field calculated for the fault properties of the last Stivos strong earthquake. The distribution of stresses is calculated for a northdipping normal fault typical for Mygdonia area. Stresses are significant in the central part of Mygdonia, while the area of Anthemountas fault and the western segment of Sochos fault remain in stress shadow, prohibiting earthquake triggering in these areas.

4.2.6.2 *Evolutionary Coulomb stress model for Corinth rift*

The reconstruction of the successive evolutionary Coulomb stress stages for the Corinth Rift initiated in the early 18th century, in 1703, with the occurrence of the M6.1 Nafpaktos earthquake and extends for including the coseismic effects of Patras 2008 earthquake, the last strong earthquake to occur. In the meantime, 28 earthquakes with magnitude $M \geq 6.0$ have occurred to the best of the historical knowledge and they have individually affected the stress field. The tectonic loading for this time period has been quantified with the constant slip along the major faults which show a dominant activity along the rift. The cumulative result of these two mechanisms was investigated and searched for interrelation behaviors between strong seismicity and their causative seismogenic faults. As mentioned before, two different models (model I and model II, Table 4-5) have been proposed in order to investigate the impact of the rift antithetic faults. In both models the interseismic strain is regarded zero before the 1703 event after which chronological stress stages are gradually constructed before the occurrence of each strong earthquake. In all cases stress has been analyzed for the preferred plane with the fault properties of the subsequent earthquake at 8km depth. Uncertainties on the exact epicentral location and magnitude of the historical earthquakes have been considered in the analysis and the interpretation of the results. Stress results are presented in snapshots (Figures 4-30(a-j), 4-31(a-j) and 4-32(a-j) for model 1 and Figures 4-33(a-j), 4-34(a-j) and 4-35(a-j) for model 2, where the same colors are used for denoting the positive and negative stress changes.

In Figure 4-30(a-j) the successive stress changes between 1703 and 1785 are shown in chronological snapshots. Figure 4-30a shows the coseismic pattern of the 1703 Nafpaktos earthquake (similar to Fig. 4-19a) resolved for on its own causative fault, for a southdipping E-W normal fault close to the west termination of the Corinth Rift. Positive ΔCFF changes due to the event are shed towards Patras-Rion gulf and the central part of the Corinth rift where the next earthquake occurred in an adjacent area in 1714. In Figure 4-30b the model shows the stress state before the occurrence of the second Nafpaktos earthquake in 1714 whose occurrence has presumably been advanced by the nearby 1703 event and the tectonic loading along faults over the mediating 11 eleven years. The exact location of the earthquakes is unknown due to considerable historical uncertainties, but it is presumed that the 1714 epicentre is located at the western tip of Nafpaktos fault where increased ΔCFF are caused by the 1703 event at the adjacent normal fault. Following, in Figure 4-30c the stress state before the occurrence of the subsequent M6.0 Corinth earthquake in 1725 is shown, resolved onto the fault properties of the associated Kechries segment. At this point the entire central and eastern Corinth rift can be described as a stress enhanced area. In 1742 strong seismicity migrated northern close to the south coast of Corinth rift when the M6.7 Xylocastro earthquake occurred. The stress changes before the 1742 earthquake are displayed in Figure 4-30d where the stress pattern is estimated for the source properties of Xylocastro fault.

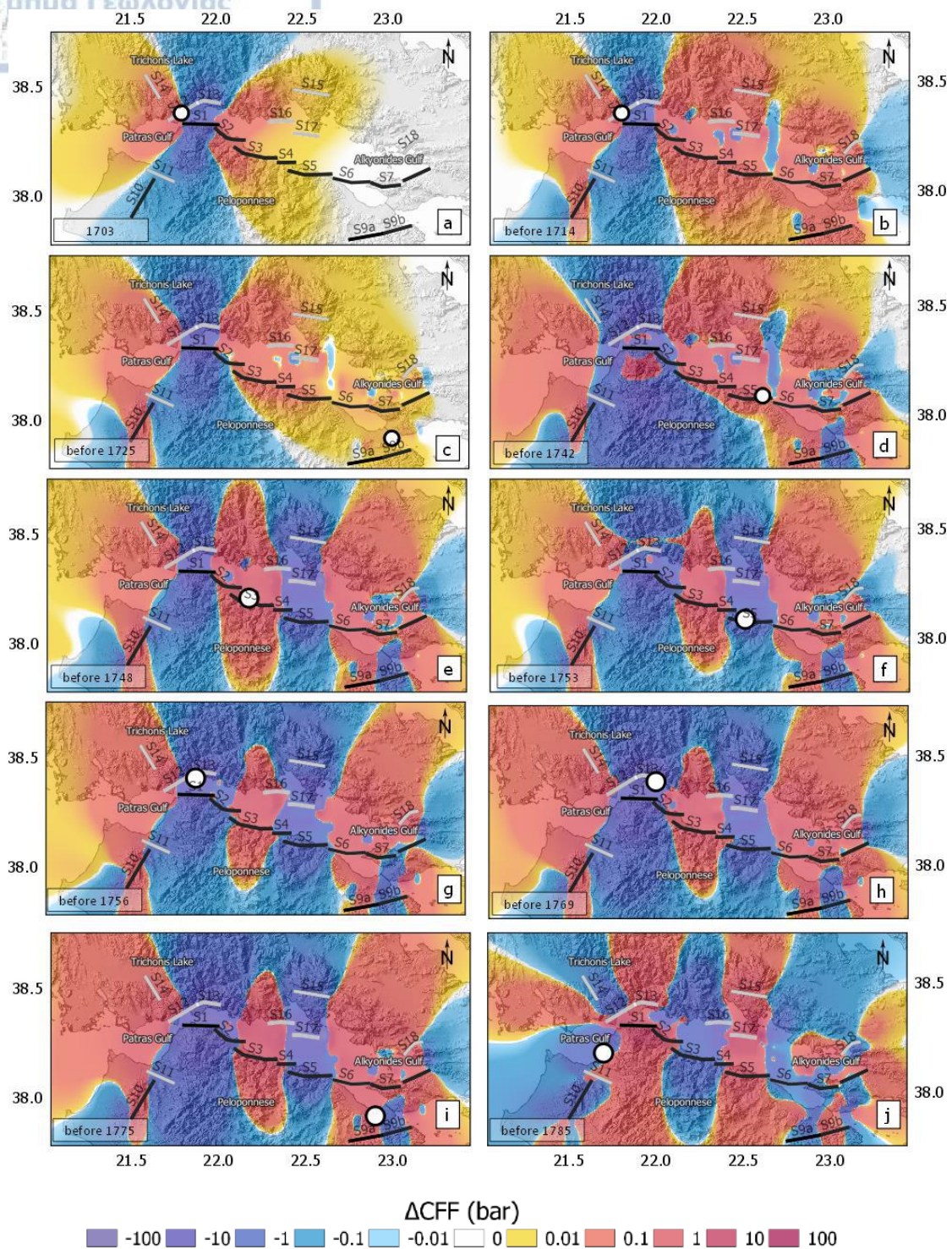
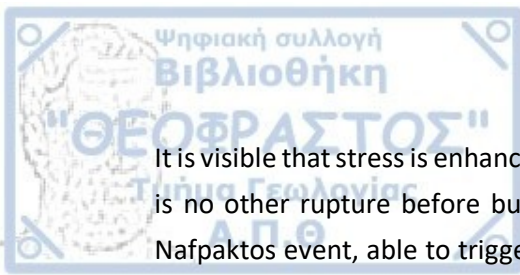


Figure 4-30 Model 1 - Evolutionary Coulomb stress states, in Corinth rift for Model 1. Coulomb stress changes are calculated for a horizontal plane at 8km depth showing a) coseismic stress changes associated with the 1703 event, b) stress changes before the 1714 earthquake, c) stress changes before 1725, d) stress changes before the 1742 earthquake, e) stress changes before 1748, f) stress changes before the 1753 event, g) stress pattern before 1756, h) the stress state before the 1769 earthquake, i) stress changes before the 1775 event, and j) stress changes before the 1785 earthquake.



It is visible that stress is enhanced at the central part of the Corinth Rift not only because there is no other rupture before but because it is additionally increased with the occurrence of Nafpaktos event, able to trigger the strong earthquake of 1742. The next strong earthquake occurred 6 years later, to the west of the 1742 rupture. The distribution of stress values before the 1748 Aigion earthquake are resolved onto the Aigion fault, which is found in positive ΔCFF as presented in Figure 4-30e. The occurrence of the previous events especially in 1742 and 1714 has bounded a bright zone around the epicenter of the 1748 earthquake. Figure 4-30f describes the stress pattern after the occurrence before the 1753 Xylocastro earthquake. This earthquake is probably a predecessor of the 1742 earthquake at Xylocastro fault and its epicentre is located onto a stress shadow zone, created by the first earthquake. The stress pattern before the M6.8 Nafpaktos 1756 earthquake is depicted in Figure 4-30g. The rupture is located at the same epicentral area with the 1703 and 1714 earthquakes, probably having ruptured the eastern part of the zone. The location is not justified by the calculations of the stress field in this stage, since the Nafpaktos fault lies in negative stress changes. 30 years later, the stress field is estimated before the 1769 Desfina fault characteristics (Figure 4-30h). There are extended low stress values created by the strong earthquakes of the northdipping Aigion fault and it seems that the exact locations of these epicentres are on debate. In Figure 4-30i the stress field has been estimated before the 1775 Perachora earthquake, for a northdipping normal fault. The model shows that the cumulative impacts from the beginning of the century until that moment, three patches of stress enhancement existed to the west, to the east and along a central N-S zone. The 1775 earthquake struck the eastern part of the rift where Perachora fault has probably been advanced by the current stress state. In the last snapshot (Figure 4-30j) the stress situation 10 years after or the right lateral strike slip fault which is believed to be responsible for the 1785 M6.4 earthquake at the northwestern part of Peloponnese. According to the model the fault seems to be reinforced with positive stress changes which can trigger a failure along the fault.

Snapshots of Figure 4-31(a-j) illustrate the stress evolutionary stages chronologically from 1794 until before the 1888 earthquake. After the occurrence of the 1785 Achaia earthquake another strong earthquake followed in 1794 at the central part of the Corinth gulf. Figure 4-31a exhibits the effect of the coseismic stress changes prior the 1794 event and the tectonic loading long faults since 1703 when the initial event occurred. It can be observed that the previous events have caused the formation of a bright zone around the Galaxidi epicentre, which could trigger a future event. The next earthquake was the 1804 Patras earthquake. The stress calculations approximated for a faulting mechanism similar to the 1804 earthquake which is attributed to Psathopyrgos northdipping fault are described in Figure 4-31b. The historic information is not adequate enough in order to define the exact location of the epicentre and its relation with the following event, two years later, in 1806 when another earthquake along Psathopyrgos fault occurred. The stress pattern after the 1804 strong shock is shown in Figure 4-31c. Following the two above earthquakes that occurred close in time the

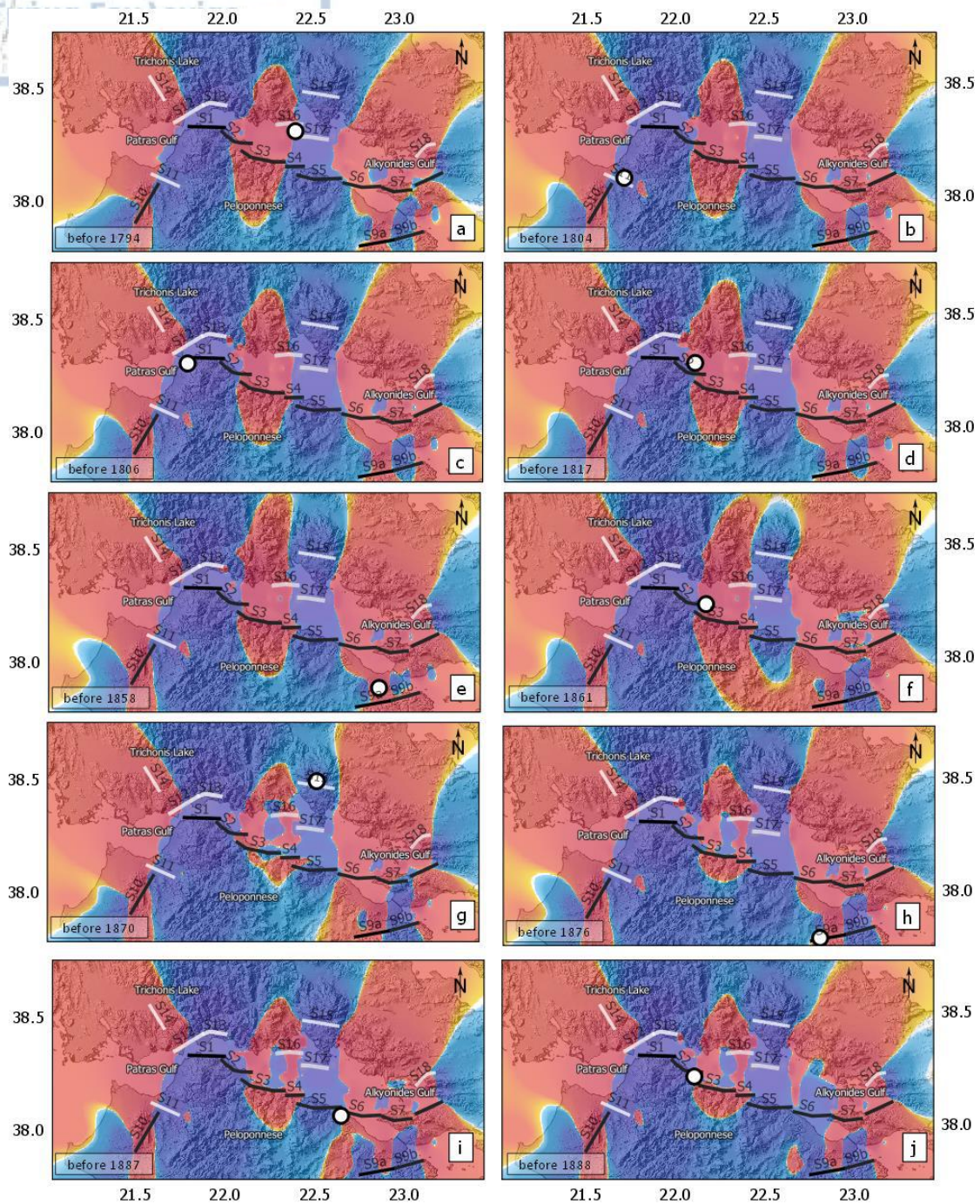


Figure 4-31 Model 1 - Evolutionary Coulomb stress states, a) ΔCFF before the 1794 event, b) stress changes before the 1804 earthquake, c) the stress state before 1806, d) stress changes before the 1817 event, e) ΔCFF changes before the 1858 event, f) the stress state before 1861, g) stress changes before the 1870 event, h) stress changes before the 1876 earthquake, i) stress pattern before the 1887 earthquake and j) stress changes before the 1888 event.

seismic activity migrated toward the east continuation of Psathopyrgos fault, something which comes with agreement with the fact that the previous two earthquakes contributed to the stress increase at tips of the fault zone in a E-W strike. Therefore the stress field before the 1817 Aigio earthquake which ruptured the Aigio fault can be seen in Figure 4-30d. The next earthquake happened at the western Corinth rift in 1858. Figure 4-31e depicts the stress field just before the 1858 Corinth earthquake and it is calculated for a north dipping normal fault. Some years later the seismicity migrated to the central part and in Figure 4-31f the stresses are estimated for before the occurrence of the 1861 Eliki earthquake which happened in an area where no other rupture was reported until 1861. The Eliki fault lays in a stress positive crust and the probably been brought closer to failure by the occurrence of the nearby strong earthquakes along Aigio and Xylocastro faults. The following strong earthquake was the Arachova 1875 earthquake which occurred to the north of the study area. Figure 4-31g shows the calculated stress changes resolved onto the normal southdipping Delphi segment. A broad shadow zone is cast over the epicentral area of the 1870 event. Therefore the model fails to associate the occurrence of this earthquake with a bright zone. In Figure 4-31h the stress field prior to the 1876 Nemea earthquake shows that there is a small part that has not been ruptured in the past and might have been advanced. The following strong earthquake occurred in 1887 because of Perachora fault which was last ruptured in 1775 but stress built-up along with the interaction of the nearby seismicity advanced the fault to a new rupture. Figure 4-31i presents the Coulomb stress field prior to the 1887 earthquake at the eastern part of the rift where the causative fault for which the stresses have been calculated is positively stressed. In a short time another strong earthquake happened in 1888 along Aigio fault at the west of the rift. The stress evolutionary model before the 1888 Aigio earthquakes is presented in Figure 4-31j where there is a combination of positive and negative values.

In Figure 4-32(a-j) results are shown for the chronological stress stages from 1917 until 2008 which is the last strong earthquake in the study area. Figure 4-32a depicts the Δ CFF pattern before the 1917 Nafpaktos earthquake resolved onto the properties of southdipping normal Nafpaktos segment. According to the historical data this area was last struck by a strong earthquake 161 years ago in 1756. The model shows that before the 1917 earthquake stress bright zones are mostly dominant at central Corinth rift, the western and eastern termination of the gulf. Figure 4-32b shows the stress changes before the 1928 Corinth earthquake caused by the cumulative stress changes after the 1917 Nafpaktos earthquake together with the constant tectonic loading on the major faults as defined for model 1. Stress was resolved onto the Perachora northdipping normal faults found at the eastern part of the rift. According to the model the broader area remains covered in negative stress changes which were developed after the last strong earthquakes that struck the eastern part of the rift. The following earthquake occurred in 1965 and Coulomb stress changes before the 1965 Eratini earthquake are presented in Figure 4-32c. In this case stress has been analyzed for a southdipping normal fault similar with the one

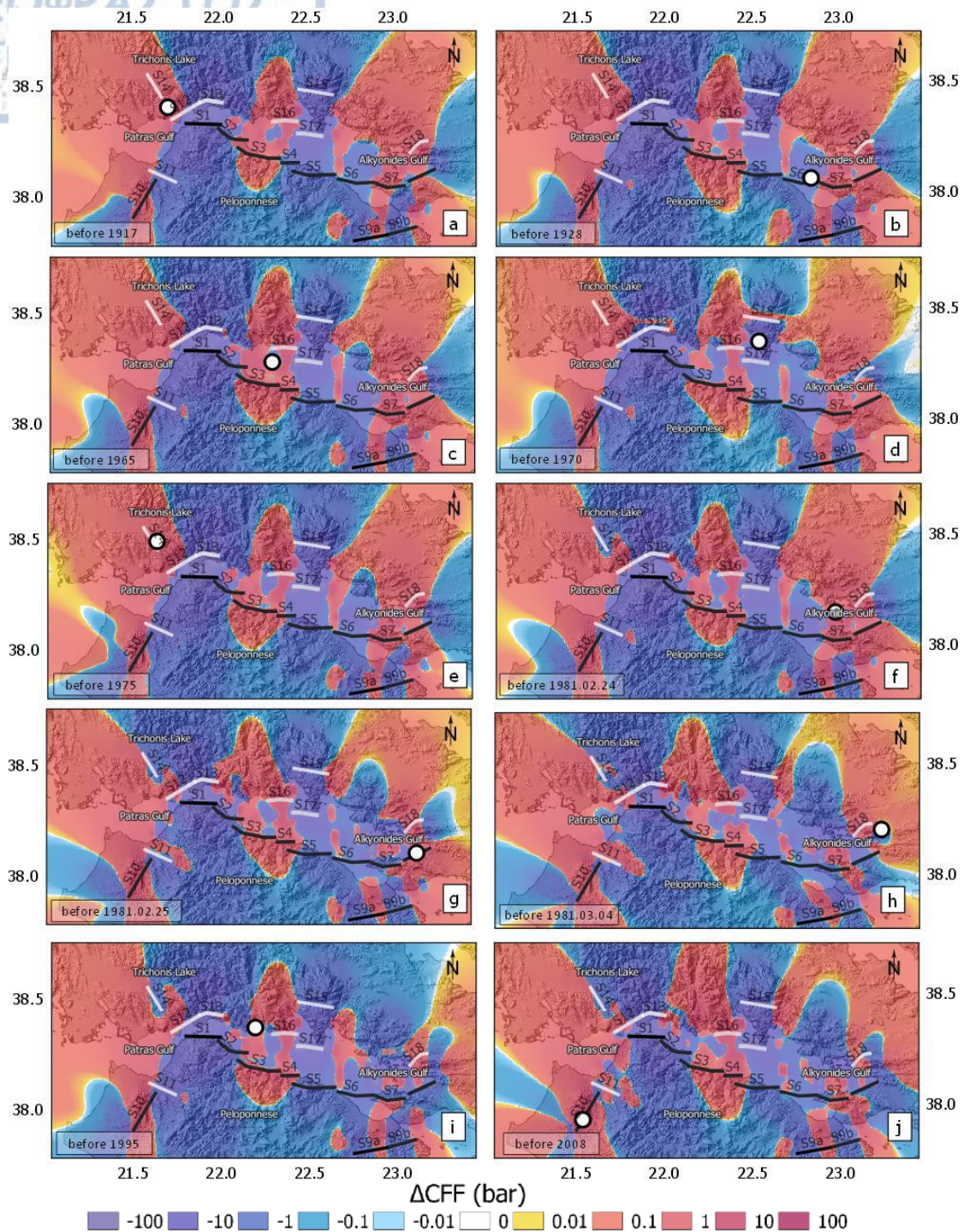


Figure 4-32 Model 1 – Evolutionary Coulomb stress states, a) stress changes before the 1917 event, b) stress changes before the 1928 earthquake, c) stress changes before 1965, d) stress changes before the 1970 event, e) stress changes before the 1975 event, f) the stress state before the first earthquake of the 1981 sequence, g) the second earthquake of the sequence, h) the stress state before the third 1981 earthquake, i) ΔCFF before the 1995 event and j) stress changes before the 2008 event.

responsible for the 1965 earthquake. A broad zone where the 1965 hypocentre is defined corresponds to a stress bright zone where no important earthquakes have occurred until this time and can be triggered by the Coulomb changes. Only five years after 1965 earthquake another strong earthquake occurred in 1970 to the east of the Eratini epicentre. The accumulated stress changes before the 1970 M6.2 Antikyra earthquake was estimated and presented in Figure 4-32d. It is observed that there are negative stress changes around the northeastern coasts of Corinth gulf when the epicentre is located. In 1975 strong seismicity migrated to the west part of the study area where the M6.0 Trichonis earthquake occurred. Since no other strong earthquake is included in the model for this area, there is appositive stress increment and a continually stress built-up until 1975 as shown in Figure 4-32e. Some years later in 1981, the Alkyonides seismic sequence occurred at the eastern part of the rift. The cumulative stress state prior to the seismic triplet is shown in Figure 4-32f where ΔCFF have been calculated for the northdipping Skinos fault responsible for the first M6.7 earthquake. The epicentral area is characterized by a positive stress increment. The stress field changes after the co-seismic stress changes of the first earthquake and the cumulative stress result just before the second M6.4 earthquake is visible in Figure 4-32g. The effect of the coseismic changes induced by the second earthquake of the triplet was then calculated for a south dipping normal fault similar to the one responsible for the last earthquake of the sequence and the result is presented in Figure 4-32h. It is shown that the fault responsible for the M6.3 strong event lies in a stress enhance area and is highly probable that it has been triggered by the preceding earthquakes. Figure 4-32i presents the cumulative stress field before the M6.0 Aigio earthquake which occurred in 1995. The stress field is estimated for a northdipping normal fault. Finally Figure 4-32j presents the stress changes before the last strong earthquake that struck the study area in 2008. The stress changes are now oriented for the strike slip fault with properties similar to the ones that caused the 2008 earthquake. The stress pattern prior to the event shows that area is significantly stress enhanced and hosts the occurrence of the strong earthquake.

The evolutionary stress states before the occurrence of strong earthquakes has also been calculated considering the tectonic loading along the southdipping faults which have been associated with historical seismicity. The fault properties and slip rates for the additional selected seismogenic faults are described in Table 4-4. The stress evolutionary stress results for model 2 are presented in Figure 4-33 (a-j) for the chronological states from 1703 to 1785, in Figure 4-34 (a-j) from 1794 to 1888 and in Figure 4-35 (a-j) from 1917 to 2008. In an attempt to compare the two different models it is believed that the southdipping faults because of their small slip rates compared to the prevailing fast deforming south faults impose an insignificant impact on the final stress field, since the induced changes are covered by the coseismic stress changes during the strong earthquakes.

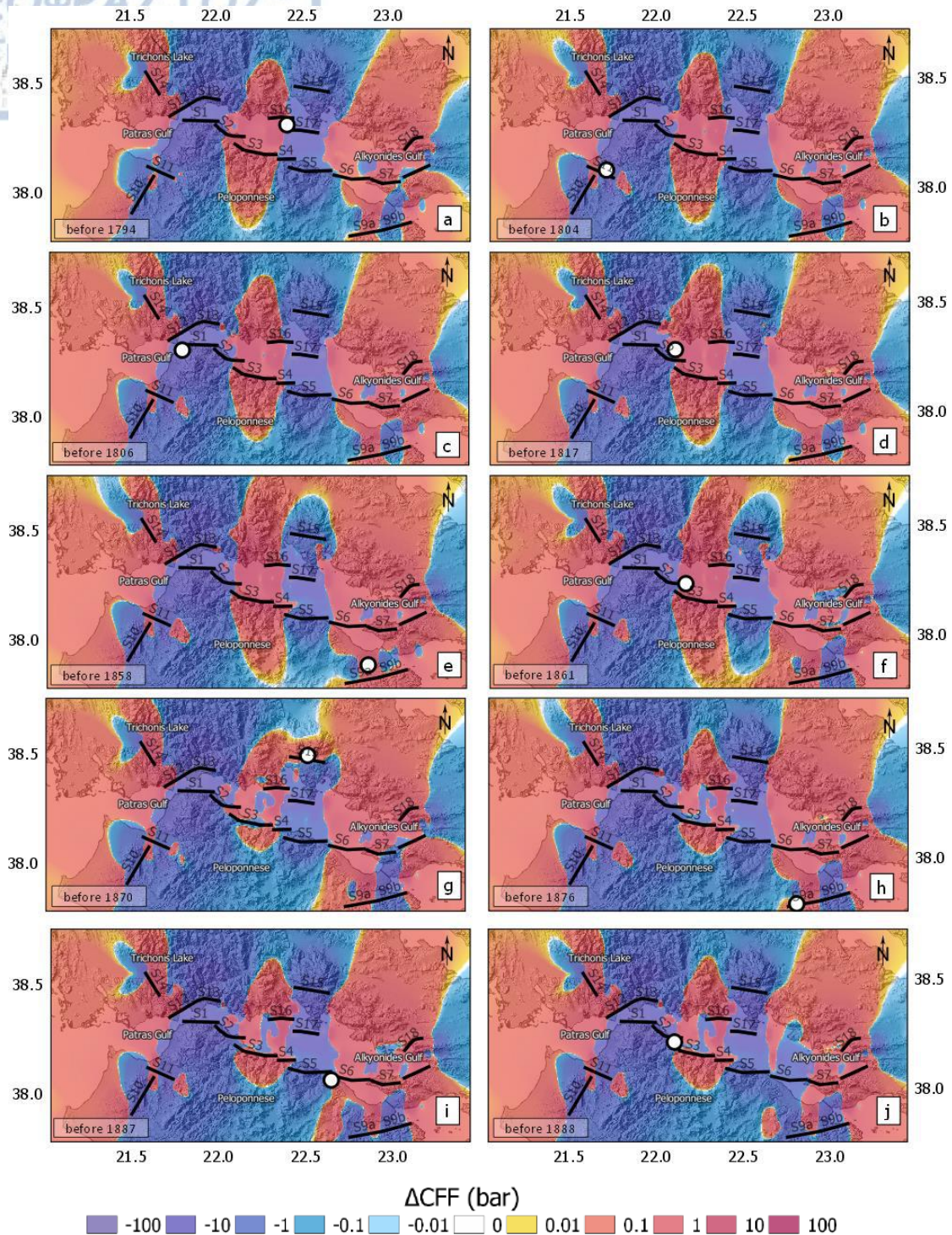


Figure 4-34 Model 2 - Evolutionary Coulomb stress states, a) ΔCFF before the 1794 event, b) stress changes before the 1804 earthquake, c) the stress state before 1806, d) stress changes before the 1817 event, e) ΔCFF changes before the 1858 event, f) the stress state before 1861, g) stress changes before the 1870 event, h) stress changes before the 1876 earthquake, i) stress pattern before the 1887 earthquake and j) stress changes before the 1888 event.

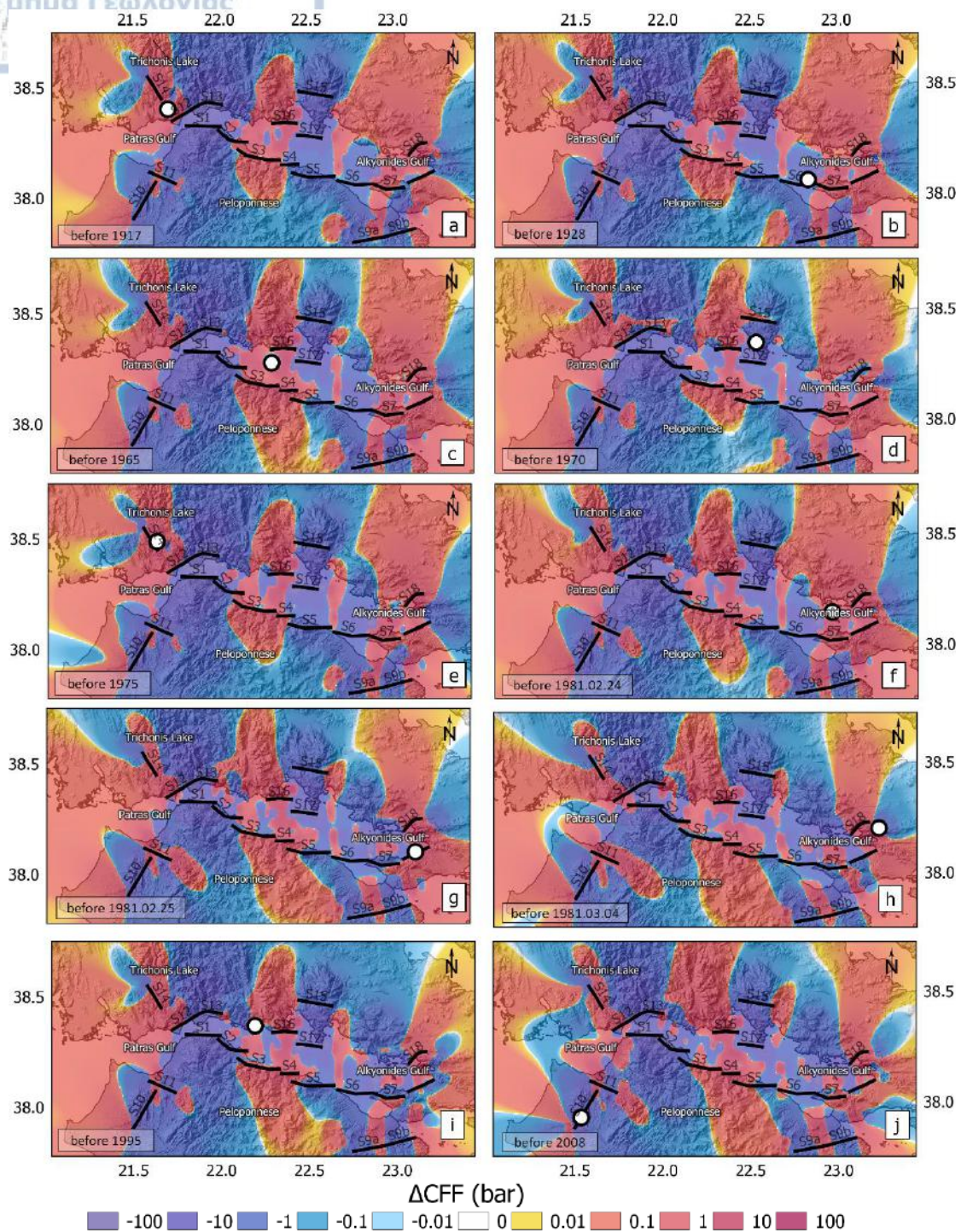


Figure 4-35 Model 2 - Evolutionary Coulomb stress states, a) stress changes before the 1917 event, b) stress changes before the 1928 earthquake, c) stress changes before 1965, d) stress changes before the 1970 event, e) stress changes before the 1975 event, f) the stress state before the first earthquake of the 1981 sequence, g) the second earthquake of the sequence, h) the stress state before third 1981 earthquake, i) ΔCFF before the 1995 event and j) stress changes before the 2008 event.

4.2.7 Correlation between Stress Coulomb and Seismicity

4.2.7.1 Current evolutionary stress state and friction properties

The positive correlation between Coulomb stress changes and aftershock spatial distribution is affirmed by previous studies, with aftershock activity to be promoted due to mainshock increased stress changes (King et al., 1994; Stein, 1999). Deng & Sykes (1997) showed a satisfying correlation between positive ΔCFF and the distribution of large historical strong, moderate earthquakes in the past decades and microearthquakes. Kagan and Jackson (1998) suggest that aftershock spatial distribution depends on the values of friction coefficient. A substantial suppress of seismicity and seismicity rate decrease was found in stress shadows for the $M_w 7.6$ Chi-Chi aftershocks in China (Ma et al. (2005). Ishibe et al. (2011) identified a significant correlation only in the case of four out of nine historical earthquakes in dependence with receiver fault plane solutions, for Japan strong earthquakes ($M \geq 6.5$) and background seismicity. Karakostas et al. (2014) explained the existence of aftershock activity on secondary adjacent faults with positive stress changes related to crustal frictional properties for the $M 5.8$ N. Aegean, 2013, earthquake in Greece. In this study the correlation between the ΔCFF distribution and past seismicity was also studied and the friction model parameters were investigated. The analysis is based on the above assumptions that earthquakes preferentially occur on areas which experience a static stress enhancement (King et al., 1994).

Coulomb stress changes were individually calculated at the focus of each earthquake, for earthquakes with magnitude $M \geq 4$ which occurred in the period 1981-2014 in Mygdonia and for the relocated microseismicity for 2008-2014 with magnitude $M \geq 2.0$. ΔCFF s on earthquake foci was the result of the cumulative coseismic stress changes after the occurrence of strong seismicity and the constant tectonic loading along faults until 1981 for the moderate earthquakes and until 2014 for smaller earthquakes. ΔCCF was calculated not only at the epicentral coordinates for each earthquake but also at the specific focal depth where each earthquake originated. The percentage of the earthquakes with positive ΔCFF at their foci was investigated as a function of the frictional parameters, μ and B . ΔCFF was repeatedly calculated for all available combinations between the friction coefficient, μ (0.1 to 0.9) and Skempton coefficients, B (0.1 to 0.9). The scope is to identify the friction parameters which best describe the mechanical properties of Mygdonia fault population, for which seismicity is adequately explained by the geometry of the stress pattern. The earthquake percentage with positive stress changes (encouraged by stress distribution) was calculated in each case over the whole number of earthquakes. Results on the percentage of earthquakes with positive ΔCFF values on their locations, depending on B and μ iterations are summarized in Table 4.7 and they are plotted in Figure 4-36. This sensitivity test is performed based on the criterion that the majority of earthquakes are preferentially promoted because of positive perturbations of Coulomb stress. Positive ΔCFF percentages systematically increase when

friction parameter increase, from 0 to 1. The highest percentages of positive ΔCFF s for all possible combinations between B and μ are met for B=0.1, that best describes the crust properties. Small values of B show higher percentages and especially for B<0.5, scores are higher than 58%, with B=0.1 exhibiting percentages more than 60% for $\mu \geq 0.4$. Smaller percentages indicate a weaker combination between seismicity and friction parameters. Percentages up to 85% of earthquakes with positive ΔCFF at focus, were found for 2 years period after M9.2 (2004) and M8.7 (2005) shocks in Sumatra-Andaman Sea (Cattin et al., 2009). Karakostas et al. (2014) found earthquake percentage equal to 70% for all calculations

Table 4-7. Percentage of earthquake foci with positive ΔCFF for all possible pairs of friction coefficient, μ and Skempton coefficient, B.

		Skemtons coefficient, B								
		0.1	0.2	0.3	0.4	0.5	0.6	0.7	0.8	0.9
Friction coefficient, μ	0.1	55.48	55.34	55.04	54.82	54.67	55.11	54.97	55.11	54.97
	0.2	56.37	56.08	56.15	55.93	55.63	55.34	54.82	55.11	55.11
	0.3	57.71	57.27	56.89	56.37	56.08	55.93	55.48	54.82	54.97
	0.4	59.34	58.53	57.93	57.27	56.67	56.08	55.93	55.34	55.11
	0.5	60.75	60.08	59.05	58.45	57.49	56.67	56.083	55.63	54.67
	0.6	61.57	61.12	60.31	59.34	58.45	57.27	56.37	55.93	54.82
	0.7	62.09	61.57	61.12	60.31	59.05	57.93	56.89	56.15	55.04
	0.8	62.53	62.09	61.57	61.12	60.08	58.53	57.27	56.083	55.34
	0.9	62.98	62.53	62.09	61.57	60.75	59.34	57.71	56.37	55.48

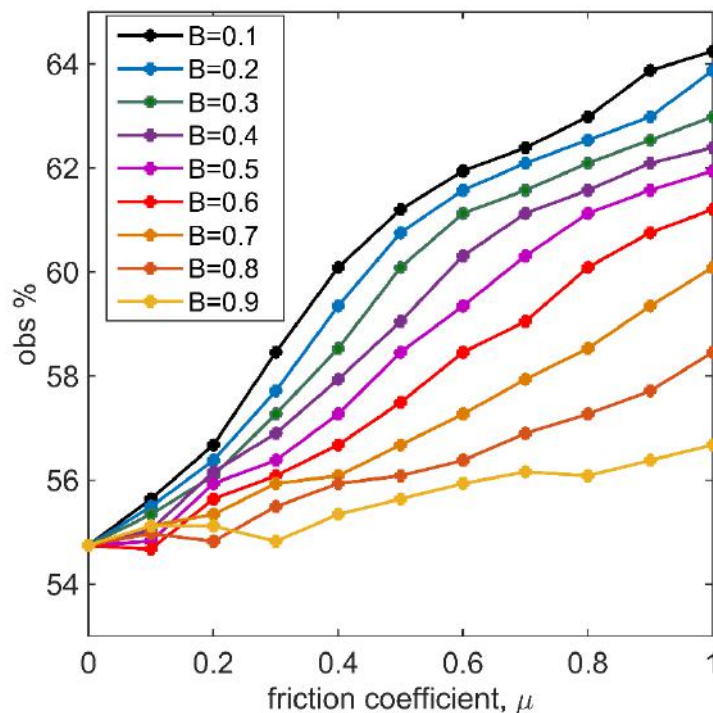


Figure 4-36 Percentage of earthquakes in locations with $\Delta CFF > 0$ as a function of friction coefficient, μ , for all possible values of Skempton coefficient, B.

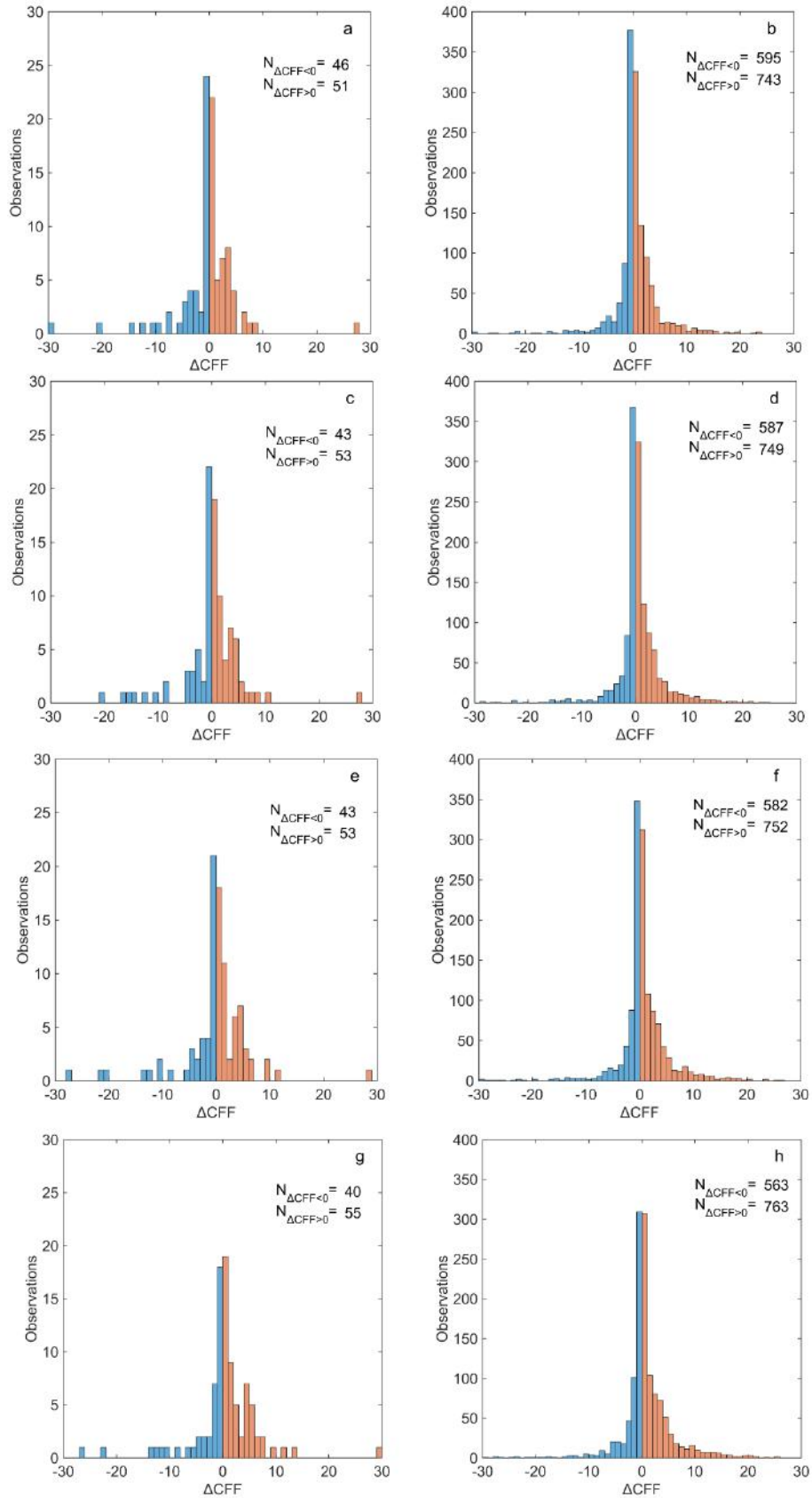
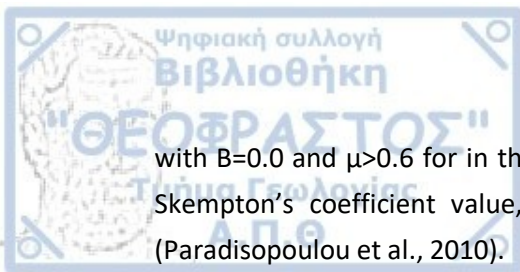


Figure 4-37. Histograms of Coulomb stress changes at earthquakes foci, when Skempton's coefficient, $B=0.1$ and a) magnitude $M \geq 4.0$ and friction coefficient, $\mu=0.2$, b) $M \geq 2.0$, $\mu=0.2$, c) $M \geq 4.0$, $\mu=0.4$, d) $M \geq 2.0$, $\mu=0.4$, e) $M \geq 4.0$, $\mu=0.6$, f) $M \geq 2.0$, $\mu=0.6$, g) $M \geq 4.0$, $\mu=0.8$ and h) $M \geq 2.0$, $\mu=0.8$. The number of earthquakes with $\Delta CFF > 0$ (red color) and $\Delta CFF < 0$ (blue color) is indicated.



with $B=0.0$ and $\mu>0.6$ for in the case of the North Aegean aftershocks. The selection of the Skempton's coefficient value, B , can cause up to 0.2bar changes in stress calculation (Paradisopoulou et al., 2010).

Keeping the value of the Skempton's coefficient steady, $B=0.1$, ΔCFF was again calculated for a range of friction coefficient values, $\mu=0.2$, $\mu=0.4$, $\mu=0.6$ and $\mu=0.8$ so as to identify the improvement of the frictional model with the higher portion of earthquakes in enhanced stress Coulomb changes. In Figure 4-37 histograms of the percentages for the two seismicity catalogs are shown, with earthquakes $M\geq 4.0$ (left column) for 1981 to 2014 and $M>2.0$ (right column) for 2008 to 2014. Histograms show that there is a systematic increase of the number of promoted earthquakes with increasing μ . The highest scores are shown for $\mu=0.8$ where the number of positive ΔCFF locations for moderate earthquakes is $N_{\Delta CFF<0}=40$ and negative ΔCFF locations $N_{\Delta CFF>0}=55$ (Fig.4-37g) and in the case of microseismicity $N_{\Delta CFF<0}=563$ and $N_{\Delta CFF>0}=763$ (Fig.4-37h). The correlation between positive and negative stress changes in locations of moderate earthquakes is almost steady with μ changes, but the systematic increase of microseismicity favored by stress increase, with the increase of μ , is evident. The spatial extend of earthquake epicentres close to the map boundaries beyond the defined faults increases the number of earthquakes with holding negative ΔCFF . The frictional state of faults in Mygdonia is best explained for $B=0.1$ and $\mu=0.8$. Frictional parameters partially describe the strength of faults according to the Byerlee's law (Byerlee, 1978) which defines the stress demand to slip with friction coefficient ranging between 0.6 and 1.0. $B=0.1$ characterizes an almost dry crust with air filled pores. Robinson and McGinty (2000) assume $B=0.5$ and $\mu=0.75$ for a dry fault model and for Harris (1998) dry models range between 0.6 and 0.8. The strength of faults is also explained with frictional properties and it is expected that low μ values correspond to weak faults which yield in environments related to heat flow. Results favor the existence of strong rupture zones with the absence of pore fluids in Mygdonia.

The spatial distribution of earthquakes and the correlation with the stress field are depicted in Figure 4-38. Earthquake epicentres are colored white if Coulomb stress is positive ($\Delta CFF>0$) at the earthquake foci and alternatively ($\Delta CFF<0$) colored black and they are plotted over the stress evolutionary field calculated at 8km depth. Visual inspection ascertains a good correlation between seismicity and spatial distribution of the positive stress values, since the majority of the microseismicity clusters are located in stress bright areas. Areas with significant positive ΔCFF show abundant seismicity with most of the events to be positive on their foci. Notably, earthquakes especially to the northeast and northwest of the study area, might be affected by other seismotectonic faults which they don't belong to the fault population but can laterally affect it by stress. Earthquakes with negative ΔCFF might be also be attributed to different fault plane solutions with the preferred fault plane, for which stress is calculated. There are patches of negative stress changes where seismicity is inhibited, compared to nearby areas. For example, seismicity is not encouraged along Ierissos, Stivos fault as well as along Anthemountas fault. The occurrence of recent strong earthquakes and

the slow aseismic tectonic loading along faults is probably not adequate to positively recover stress along these faults. The example of the cluster west of the Volvi lake which is found in a negative stress zone might be attributed to reasons like the overestimation of the Assiros earthquake and the additional negative stress changes that this earthquake has imposed. In slowly deformed tectonic areas, like Mygdonia, the aftershock activity can last for hundreds of years after the mainshock (Stein and Liu, 2009).

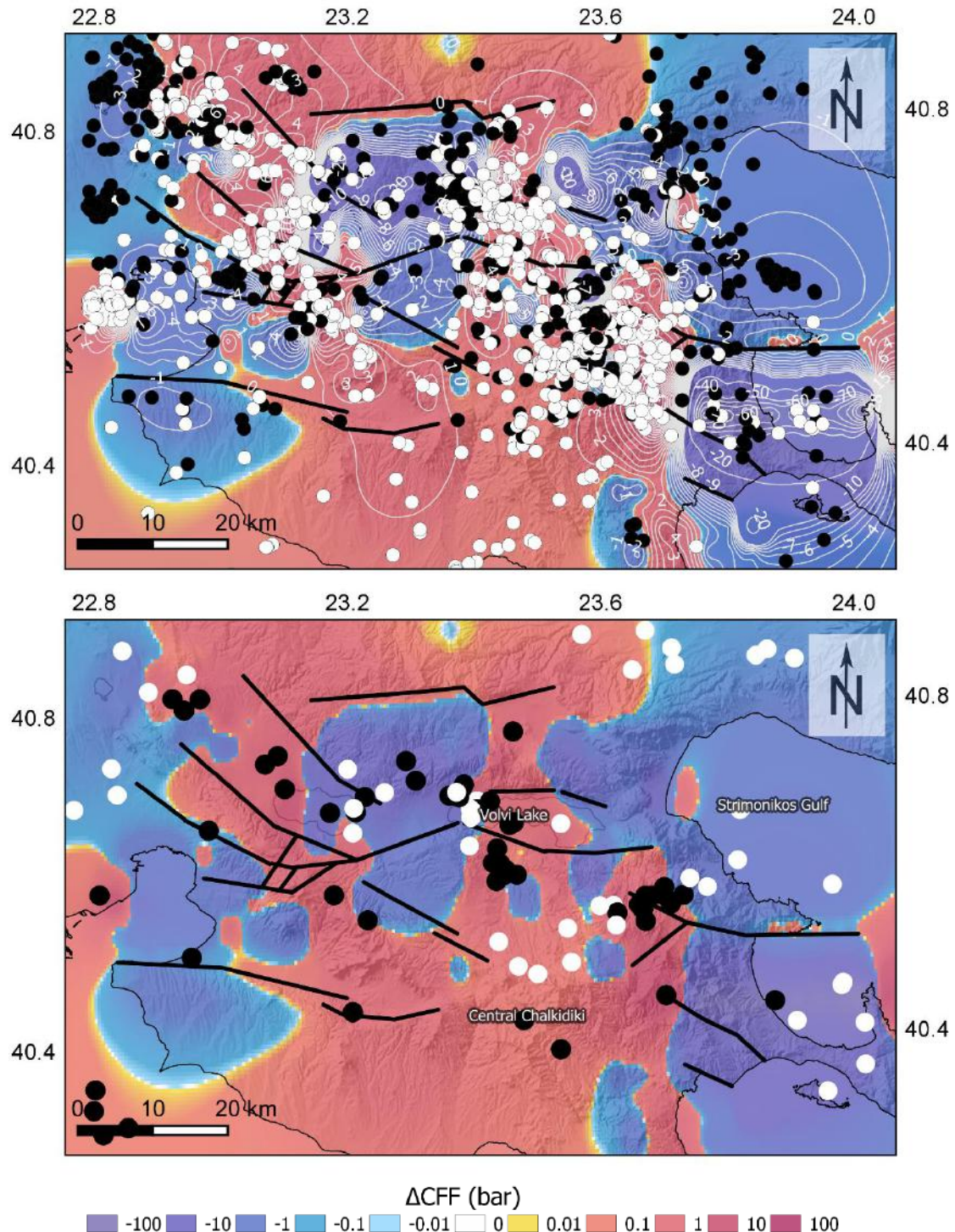


Figure 4-38 Current stress field with the relocated recent seismicity, for $\mu=0.8$ and $B=0.1$ (up) and moderate magnitudes (1981-2014) (down). Earthquakes with a positive ΔCFF on their foci are white colored, whereas black colored earthquakes correspond to negative ΔCFF values.

4.2.7.2 Extrapolated stress evolutionary model for 2050

A. The Coulomb stress evolutionary model in Mygdonia was further extrapolated for 30 years, so as to investigate faults which will be brought closer to failure in terms of stress enhancement. Supposing the absence of future strong seismicity, the existing coseismic stress changes and interseismic deformation on the 28 individual fault segments from 1700 to 2050 were considered for the model extrapolation. Normal and shear stress were resolved onto two preferred fault plane solutions, characteristic for the seismotectonic regime of Mygdonia.

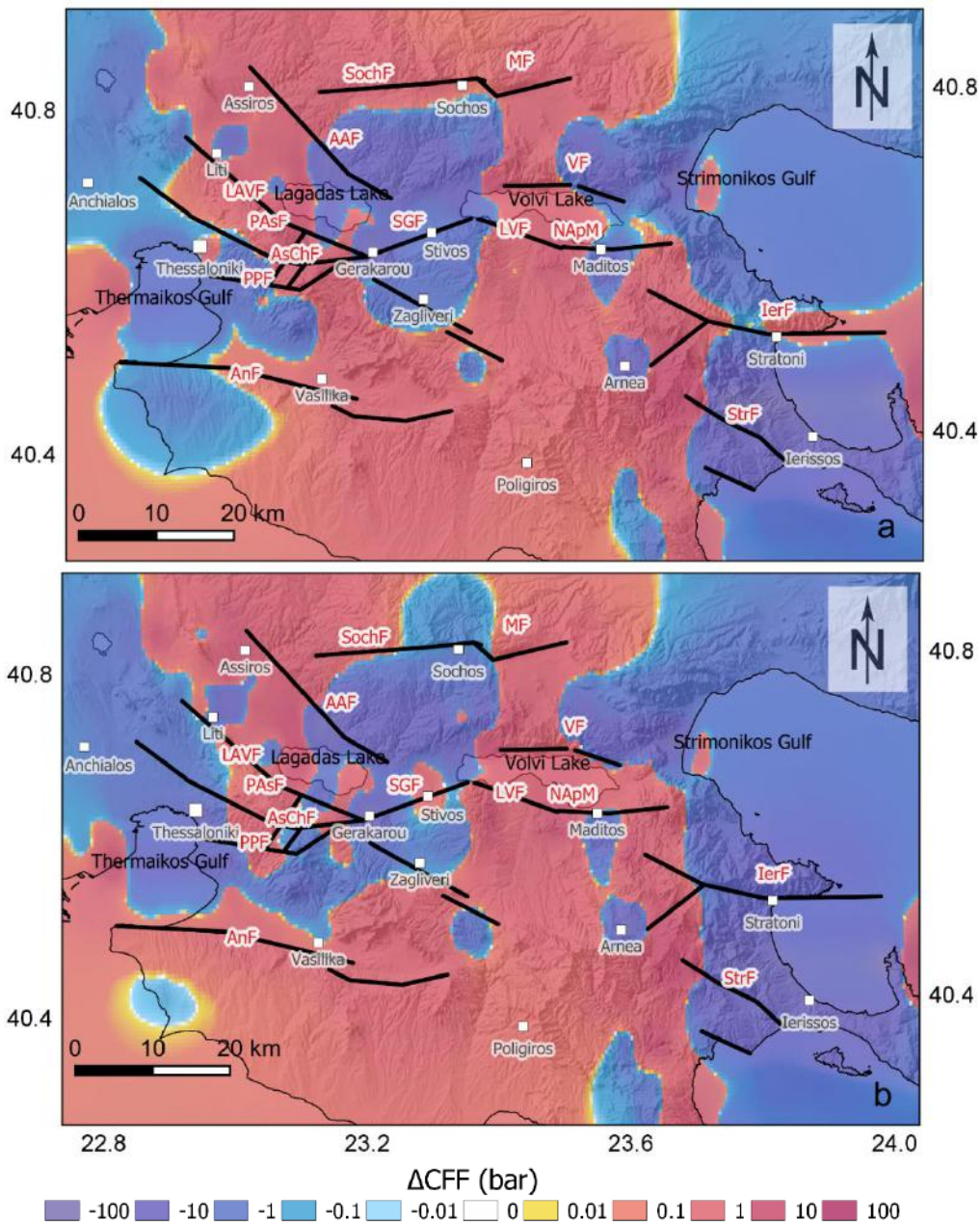
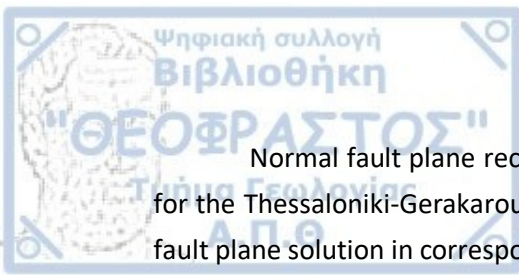


Figure 4-39 The current stress field with the relocated seismicity, for $\mu=0.5$ and $B=0.5$ calculated for a fault plane with $278^\circ/46^\circ/-70^\circ$ and b) and for a fault plane with $90^\circ/45^\circ/-90^\circ$



Normal fault plane receivers a) with 278° strike, 46° dip and -70° rake, characteristic for the Thessaloniki-Gerakarou fault zone and Anthemountas fault, and b) antithetic normal fault plane solution in correspondence with Sochos and Lerissos fault (90° strike, 53° dip and -93° rake) were used. For modelling friction the most suitable frictional parameters were obtained. Stress is calculated at 8km depth and frictional parameters are friction coefficient, $\mu=0.5$ and Skempton's coefficient, $B=0.5$. Stress field simulation for a north dipping normal fault (Figure 4-39a) shows that stress shadows have not been eliminated with constant tectonic loading and still occupy the central part of Mygdonia graben. A negative ΔCFF patch covers the western segment of Anthemountas fault and Thermaikos gulf. There is no likelihood of a strong earthquake occurrence in these areas. Seismicity is also inhibited to the eastern part of the study area. Parts of Lerissos fault are receiving positive stress changes, meaning that stress recovery is expected, considering a slip rate of 1mm/yr. Sochos and Mavrouda faults are also located in a bright zone. A stress enhanced zone is running through the LAVF and PASF where future seismicity is encouraged. Positive stress changes are shed over LVF and NAPMF, part of which had ruptured in 1933 Volvi earthquake.

Coulomb stress changes analyzed for a south dipping normal fault show a similar distribution of positive and negative ΔCFF over Mygdonia, exhibiting some changes in the geometry of the field (Fig. 4-39b). Impending seismicity is likely to be hindered to the biggest part of the Thessaloniki – Stivos - Gerakarou fault zone, as well as to part of Sochos fault to the north. Lerissos fault shows a decreased likelihood of fault rupture, since, it lays in a dark stress zone, with its western termination to be located into positive stress changes. Anthemountas fault is also receiving positive stress changes when the stress is calculated for an antithetic normal fault. The central part of Chalkidiki is deprived of significant faults that can accommodate strain, for this reason stress is not released and the model shows a continuous accumulation of stresses. In addition the northeastern part of the area, where Strymonikos gulf is located, is covered by stress decrease, but it can be slightly affected from the deformation due to adjacent fault, which are beyond the study area boundaries.

4.2.7.3 *Current evolutionary stress state and friction properties, Corinth rift*

The association between positive Coulomb stress changes and the spatial distribution of seismicity in Corinth rift was investigated in three different stages because of the strong earthquakes in between. The recent 1981 Alkyonides, the 1995 Aigio and the 2008 Achaia earthquakes which mark the end of strong seismicity until now, substantially disturbed the Coulomb stress field driven by their coseismic impact. ΔCFF at the hypocentral coordinates was calculated for all earthquakes with magnitude $M \geq 4.0$ which belong to the periods i) 03.1981 – 06.1995 after the occurrence of the 1981 triplet, ii) 06.1995 – 2008, including the coseismic changes of the 1995 earthquake and iii) 2008 to 2014 incorporating the 2008 impact. Stress has been resolved onto a fault receiver similar with the typical low dip north dipping normal faults that bound the south part of Corinth rift ($278^\circ/46^\circ/-70^\circ$) for all pairs of

B and μ . The percentage of earthquakes with positive stress changes at foci was calculated in each case over the whole number of earthquakes. In the first period 508 earthquakes occurred with magnitude $M > 4.0$. Results on the percentage of earthquakes with positive ΔCFF values on their locations, for B and μ iterations are given in Table 4.8 and plotted in Figure 4-40. Earthquake percentages exhibit the highest scores for $B > 0.5$ where they exceed 60% by increasing μ . For $0.1 \leq B \leq 0.4$ the behavior of B is not systematic and μ increase caused the decrease of the percentage of earthquakes promoted by enhances stress changes. Although the range is small, for $B = 0.5$ the increase is systematic in all the range of the friction values. Thus, $B = 0.5$ best describes the positive correlation between moderate seismicity and stress changes. In Figure 4-41 histograms of the percentages for the two seismicity catalogs are shown, with earthquakes $M \geq 4.0$ for 03.1981 – 06.1995 for different values of μ , $\mu = 0.2$ (Fig.4-41a), $\mu = 0.4$ (Fig.4-41b), $\mu = 0.6$ (Fig.4-41c) and $\mu = 0.8$ (Fig.4-41d). Histograms show that there is not significant systematic increase of the number of promoted earthquakes with changing μ . The highest scores are shown for $\mu = 0.6$ where the number of positive ΔCFF locations for moderate earthquakes is $N_{\Delta CFF > 0} = 290$ and negative ΔCFF locations $N_{\Delta CFF < 0} = 186$, but the correlation positive stress and locations based on this earthquake sample is uncertain. Percentages of the 206 earthquakes which belong to the period 06.1995 – 2008, 206 earthquakes are given in Table 4.9 and plotted in Figure 4.42. The number of earthquakes is small and there is a scarce correlation between the spatial distribution and stress increase, since the relatively maximum positive percentage is met for different values for $B \leq 0.5$. Thus, $B = 0.5$ that more clearly described the increase in positive correlation between moderate seismicity and stress changes was kept steady and different values of μ were tested for this sample $\mu = 0.2$ (Fig.4-43a), $\mu = 0.4$ (Fig.4-43b), $\mu = 0.6$ (Fig.4-43c) and $\mu = 0.8$ (Fig.4-43d). The sensitivity of the percentages of positive ΔCFF is low and no significant changes are observed in the ratio between percentages of positive and negative ΔCFF the second period. The third period includes 81 earthquakes occurred with magnitude $M > 4.0$ and the positive correlations between earthquake locations and positive stress changes is 25%. $B = 0.5$ and $\mu = 0.75$ have been obtained for Patras area (Karakostas et al., 2017) and Efpalio area (Karakostas et al., 2012).

The spatial distribution of locations of moderate earthquakes with $\Delta CFF > 0$ (white color) and $\Delta CFF < 0$ (black color) at their focus are shown in Figure 4-44 for the three separate intervals. Moderate earthquakes for 03.1981 – 06.1995 (Fig.4-44a) are plotted over the pattern of the stress evolutionary model after the occurrence of the 1981 triplet. The majority of the earthquake epicentres belong to 1981 aftershocks and are clustered at the eastern part of the study area. A large number are triggered by the stress changes induced by the strong triplet. Stress enhanced areas are also found at the central part of the gulf where the following strong earthquake occurred. Locations of moderate earthquakes for the time period 06.1995 – 2008 are compared to the stress field that is the cumulative stress loading on loading along faults and the coseismic stress changes until the 2008 Achaia earthquake (Fig4-44b).

Table 4-8. Percentage of earthquake foci with positive ΔCFF for all possible pairs of friction coefficient, μ and Skempton coefficient, B , for moderate earthquakes $M \geq 4.0$ between 03.1981 – 06.1995

		Skemtons coefficient, B								
		0.1	0.2	0.3	0.4	0.5	0.6	0.7	0.8	0.9
Friction coefficient, μ	0.1	57.87	57.48	57.28	57.28	57.48	57.48	57.28	57.48	57.28
	0.2	57.67	57.87	57.48	57.87	57.67	57.48	57.28	57.49	57.48
	0.3	57.67	57.87	57.67	57.66	57.69	57.83	57.87	57.28	57.28
	0.4	58.85	58.07	57.67	57.87	57.87	57.87	57.87	57.48	57.48
	0.5	59.05	59.05	58.46	58.07	57.87	57.87	57.69	57.67	57.47
	0.6	60.23	59.64	58.66	58.85	58.07	57.87	57.67	57.87	57.28
	0.7	60.62	60.62	59.84	58.66	58.46	57.67	57.68	57.48	57.28
	0.8	59.84	60.43	60.62	59.60	59.05	58.07	57.87	57.88	57.48
	0.9	59.84	59.84	60.62	60.23	59.05	58.85	57.67	57.67	57.86

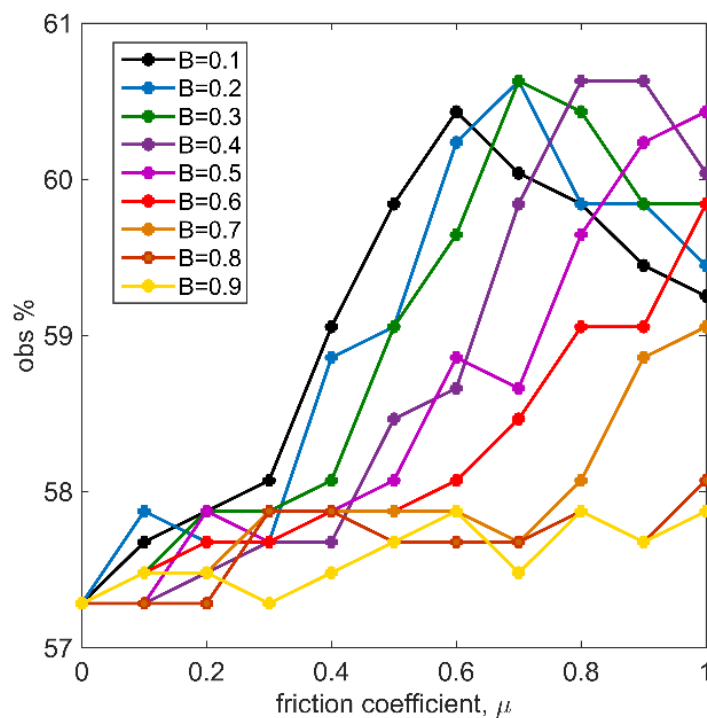


Figure 4-40 Percentage of earthquakes with $\Delta CFF > 0$ calculated for all possible combinations of Skempton coefficient, B and the friction coefficient μ .

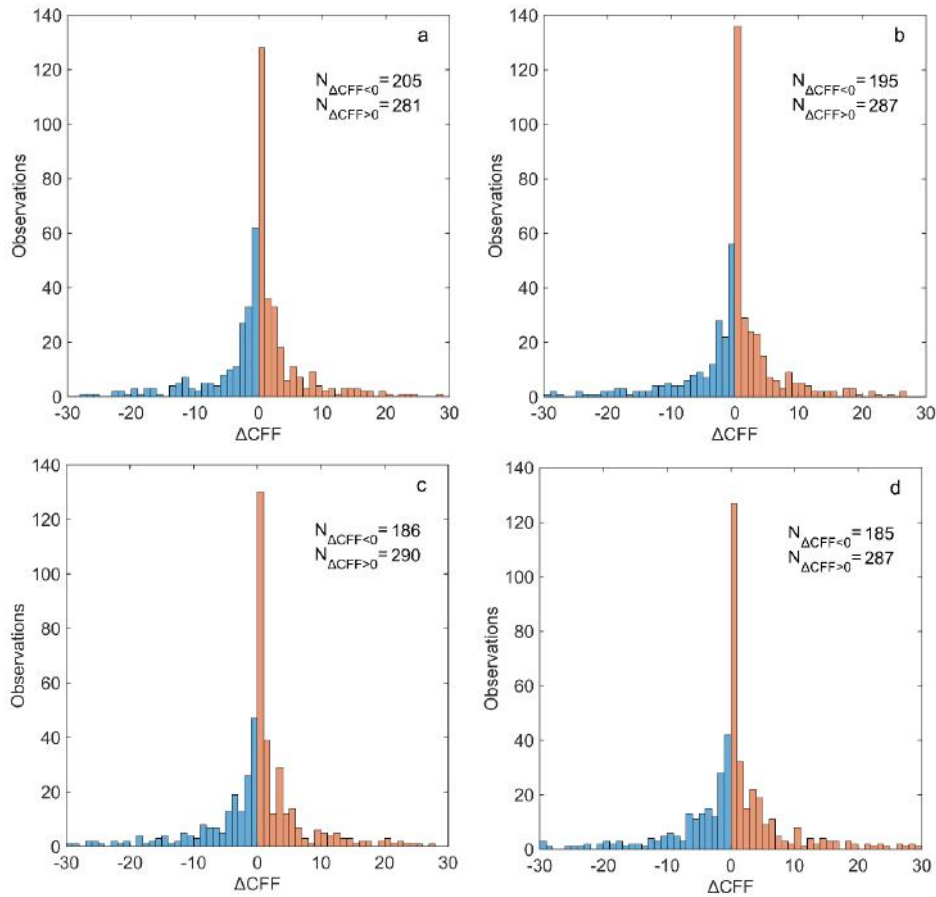


Figure 4-41. Histograms for $\Delta CFF > 0$ and $\Delta CFF < 0$ for moderate earthquakes $M \geq 4.0$ between 03.1981 – 06.1995 and $B=0.5$ a) for $\mu=0.2$, b) for $\mu=0.4$, c) for $\mu=0.6$, d) for $\mu=0.8$.

Table 4-9. Percentage of earthquake foci with positive ΔCFF for all possible pairs of friction coefficient, μ and Skempton coefficient, B , for moderate earthquakes $M \geq 4.0$ between 06.1995 – 2008

		Skempton's coefficient, B								
		0.1	0.2	0.3	0.4	0.5	0.6	0.7	0.8	0.9
Friction coefficient, μ	0.1	46.60	47.08	47.57	47.57	47.57	47.08	46.60	46.60	46.60
	0.2	47.57	48.54	48.05	48.05	47.57	47.08	47.57	47.08	46.60
	0.3	48.54	49.51	50.00	48.54	48.05	48.05	47.57	47.57	46.60
	0.4	50.00	50.00	50.00	49.51	49.51	48.54	48.05	47.08	47.08
	0.5	50.00	50.48	50.00	49.51	50.00	49.51	48.05	47.57	47.57
	0.6	50.97	50.97	50.98	50.00	49.51	49.51	48.54	48.05	47.57
	0.7	50.97	50.97	50.97	50.97	50.00	50.00	50.00	48.05	47.57
	0.8	51.94	51.94	50.98	50.97	50.48	50.00	49.51	48.54	47.08
	0.9	51.94	51.94	51.94	50.97	50.97	50.00	50.00	48.54	47.57

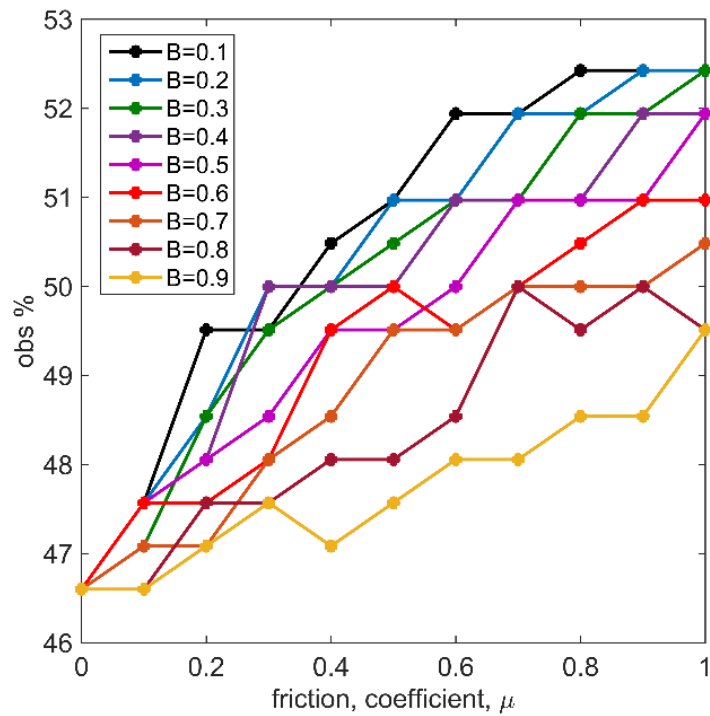


Figure 4-42 Percentage of earthquakes with $\Delta CFF > 0$ calculated for all possible combinations of Skempton's coefficient, B and the friction coefficient μ .

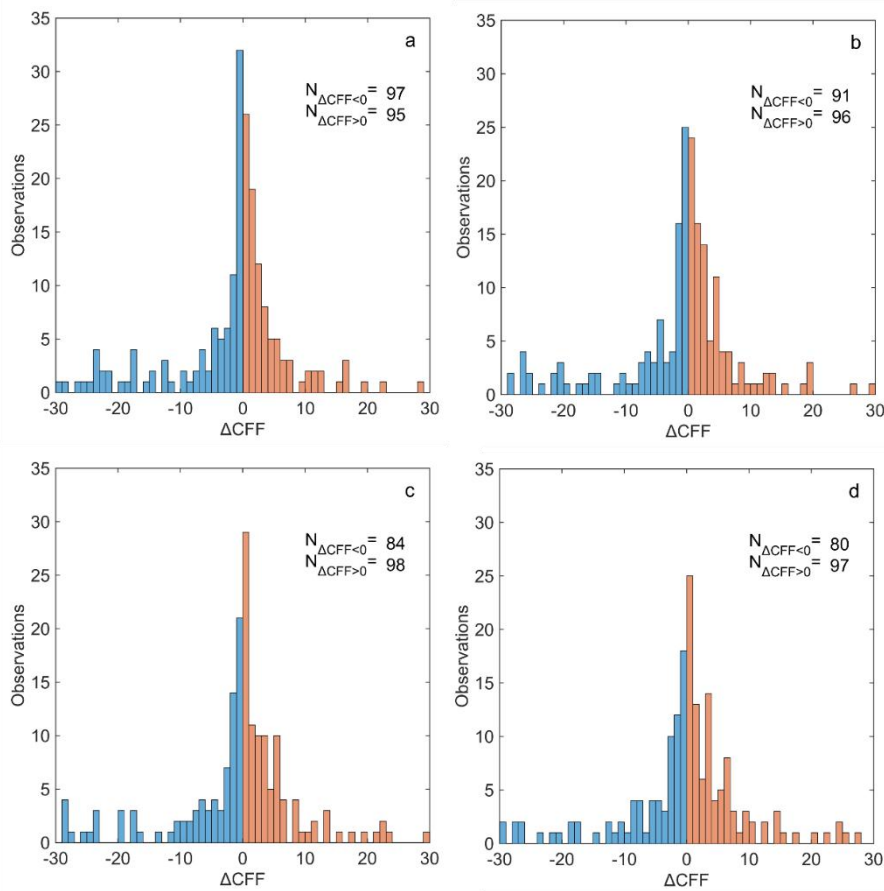


Figure 4-43. Histograms for $\Delta CFF > 0$ and $\Delta CFF < 0$ for moderate earthquakes $M \geq 4.0$ between 06.1995 – 2008 and $B=0.5$ a) for $\mu=0.2$, b) for $\mu=0.4$, c) for $\mu=0.6$, d) for $\mu=0.8$.

The stress is resolved onto the receiver strike slip fault of the Achaia earthquake. Locations in the central part of the gulf are favored, whereas there is a significant number of earthquake which are located in the area mostly affected by the shadow zones which are created by the multiple ruptures on Psathopyrgos fault (S_1 fault). Considering the coseismic stress effect of the 1995 earthquake occurrence has triggered the occurrence of moderate earthquakes mostly to the east of the fault, compared to the western fault area. In Figure 4-44c the locations of moderate earthquakes after the occurrence of the 2008 with positive and negative ΔCFF are plotted on top of the stress evolutionary field created after the 2008 earthquake. The scarce seismicity is concentrated along Achaia fault where the aftershock sequence took place, where the majority of the aftershocks are characterized of negative ΔCFF on their foci. Reasoning for this result can be given to the fact that aftershocks foci are ranging in larger depths (15-20km) compared to seismicity across Corinth rift and the evolutionary field is calculated at 8km depth and due to the fact that stress has been resolved for the northdipping normal faults of the Corinth Rift. With the exception of the 2008 sequence the majority of the moderate earthquakes in the Corinth rift, including the Efpalio sequence that followed in 2010, received a stress enhancement after the last strong earthquake in the area, having positive ΔCFF values.

The spatial distribution of recent seismicity and the correlation with the stress field in the Corinth Rift in shown in Figure 4-45. The stress field incorporates the changes induced by all the strong seismicity in the Corinth Rift along with the effect of the lithospheric loading until 2008 and is calculated for a fault type with 278° strike, 46° dip and -70° rake ($B=0.5$ and $\mu=0.6$). The positive correlation between seismicity and spatial distribution of the positive stress values varies across the study area. since the majority of the microseismicity clusters are located in stress bright areas. Areas with significant positive ΔCFF show abundant seismicity with most of the events to be positive on their foci. Earthquakes with absolute ΔCFF values > 30 bars and < -30 bars have been omitted. Earthquake locations in areas where constantly belong to stress shadows keep receiving negative stress increments as it can be observed in Fig.4-46. The extend of seismicity to distant areas from loading faults, like in the case of the Northwestern Peloponnese increases negative ΔCFF percentages.

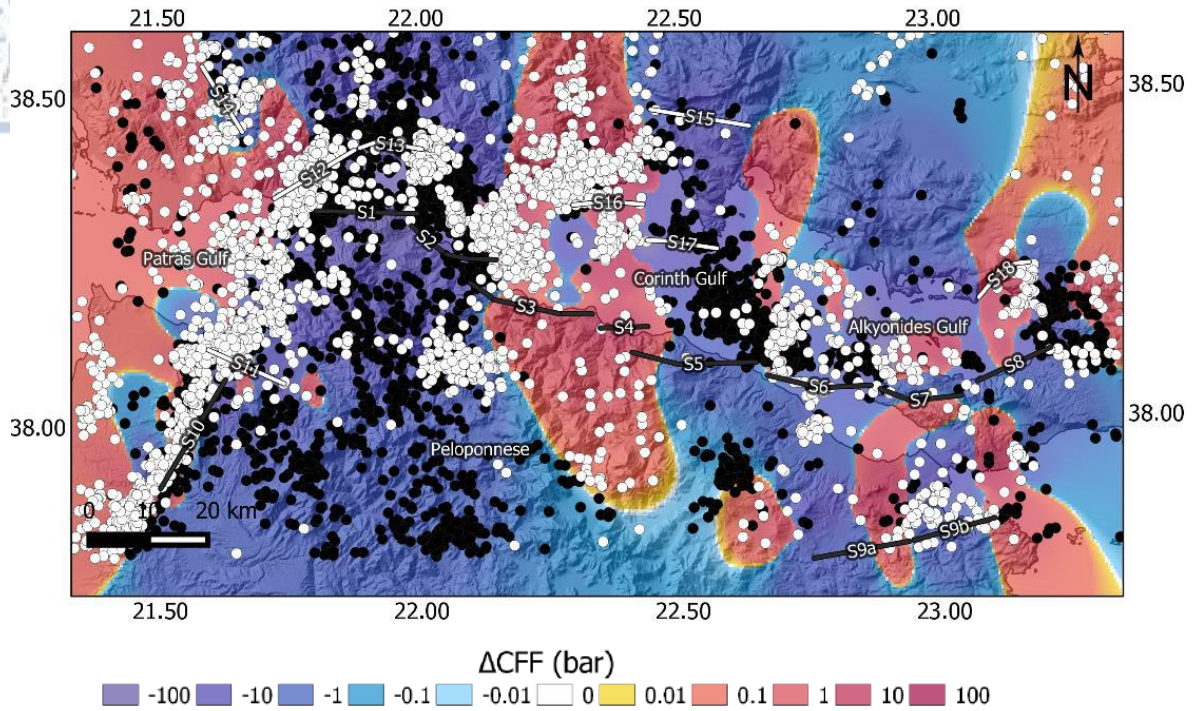


Figure 4-45 Current stress field with the relocated seismicity, for $\mu=0.6$ and $B=0.5$ for earthquakes with $M>2.3$ after 2008.

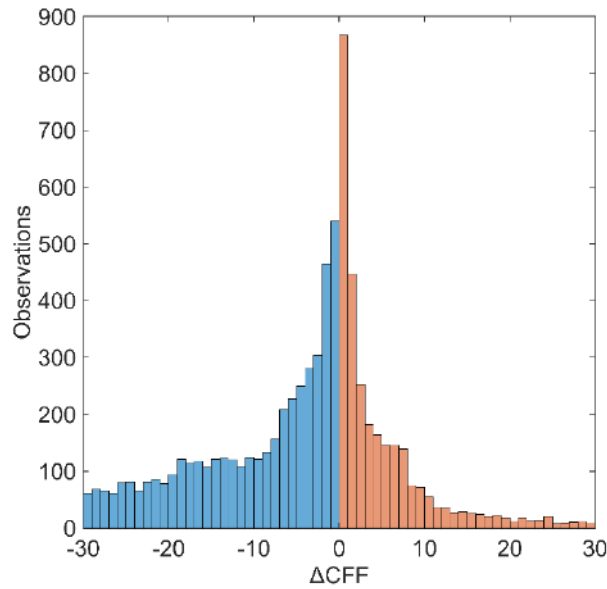


Figure 4-46. Histograms for $\Delta CFF > 0$ (blue color) and $\Delta CFF < 0$ (red color) for earthquakes with $M \geq 2.3$

4.2.7.4 Extrapolated stress evolutionary model for 2050

The stress evolutionary model in Corinth rift was extrapolated for 2050 for determining the areas with enhanced stress increments where impending seismicity is expected, considering no other strong earthquake has occurred in the meantime. The satisfying interpretation of strong earthquake localities in terms of positive ΔCFF allows us to extrapolate results for future fault movements to failure. Stress was analyzed for a normal fault plane with $(273^\circ/45^\circ/-70^\circ)$ for faults in model 1 (Figure 4-47a) and for Model 2 (Figure 4-47b) taking $B=0.4$ and $\mu'=0.5$. The stress field was calculated at the depth of 7km for the seismogenic crust. No significant changes exist between the two models, because the southdipping faults accommodate strain insignificantly, compared to the northdipping active faults. Stress extrapolation indicates a fault relaxation period for many of the faults in Corinth rift since, meaning that stress along faults has not yet recovered, considering the assumed slip rates on major faults.

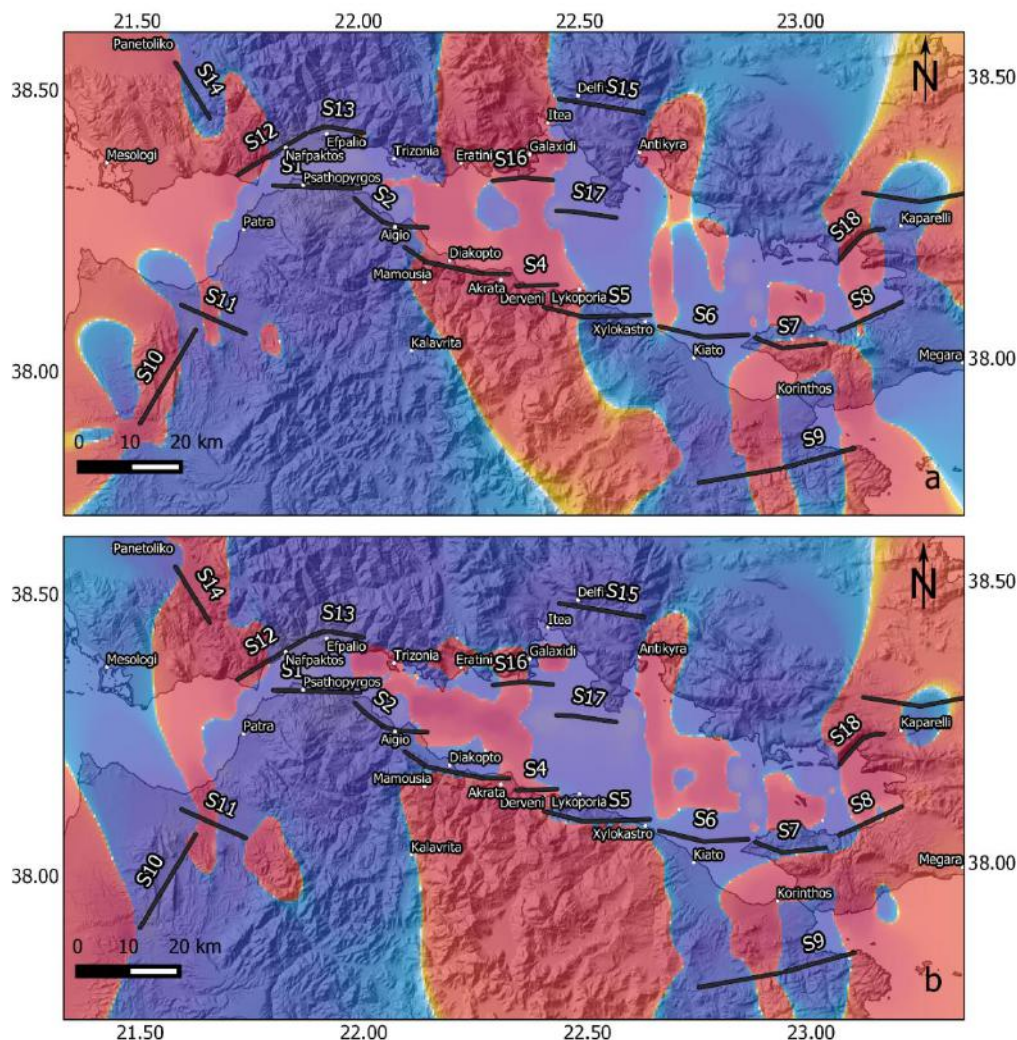
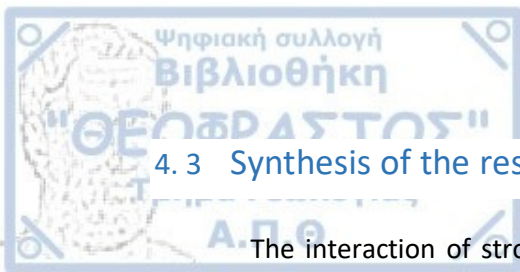


Figure 4-47 The extrapolated stress field for 2050, for $\mu=0.6$ and $B=0.5$ calculated for $278^\circ/46^\circ/-70^\circ$ fault plane faults included in a) model 1 and b) model 2.



4.3 Synthesis of the results and discussion

The interaction of strong ($M \geq 6.0$) earthquakes and their dependence on Coulomb static stress transfer between seismogenic faults for a 300 years record of historical and instrumental seismicity was the scope of this study. The evolution of the Coulomb stress changes was based on the cumulative impact of coseismic stress changes of strong earthquakes and tectonic loading in the fault populations of Mygdonia graben and the Corinth Rift. For modelling the interseismic deformation on faults, only the most active faults were considered significant for strain accumulation and stress release. Evolutionary stress models adequately explain the occurrence of strong earthquakes on stress enhanced areas (Deng and Sykes, 1997; Papadimitriou and Sykes, 2001). Insufficient results and model failure to interpret earthquake occurrence is attributed to misleading factors and inherited issues ought to be considered before the interpretation of the analysis results. Contrary to our assumption that Coulomb stress changes which pre exist the onset of the studied seismicity are zero, stress state is poorly known and its ignorance biases the initial condition of our models (Mildon et al., 2019). Historical earthquakes carry uncertainties like magnitude overestimations or underestimations and the impact on the calculated stress field is not the one anticipated. Fault slip is not uniform, as assumed, but varies from centre to fault tips and can notably alter the pattern and values of the evolving stress field. When it comes to the approximation of the interseismic loading, slip rates along faults are not steady but vary through time and their geological or geodetic origin shows significant discrepancies. Despite the above heterogeneities and the simplification of the real process, the stress evolutionary models effectively describe strong earthquake occurrence. Dynamic and post seismic deformation are not incorporated in this study, but they are not expected to alter approximations of the interseismic deformation because the time that intervenes between earthquakes in most cases is long. Post seismic effects if existing, reinforce the positive stress changes and reduce the negative stress changes imposed by coseismic slip, without affecting the geometry of the stress field (Jaumé, 1994). Coulomb stress analysis in the two areas which exhibit differences in respect to their seismicity, seismotectonic properties, deformation and crustal properties shows a different interactive behavior.

In Mygdonia, interaction through stress transfer between the strong seven earthquakes in the range of 301 years is effectively confirmed with Coulomb stress analysis. The loading process is accommodated with a slow rate equal to 1mm/year (Kotzev et al. 2001) giving a slow stress recovery procedure and long earthquake recurrence times on faults. Consequently there is a small number of strong earthquakes in the 3 last centuries, which corresponds to a long enough historical seismological record. Stress triggering is dominant in all cases since earthquake epicentral locations or parts of the causative faults are located into relatively highly positive stress values. Strong earthquakes which occur in Mygdonia are strongly influenced by the locations of the past events. Migration of strong seismicity on adjacent or antithetic faults, mostly in an E-W direction is also highlighted by the stress



Coulomb analysis. Stress transfer among adjacent faults is dominant in the case of the two Anthemountas events, and in between the antithetic faults of Sochos and Stivos faults. The westward migration of the 1677 and 1769 earthquake epicentres along Anthemountas fault within 82 years, is an indication of fault interaction between the two adjacent segments. The occurrence of the 1677 on Anthemountas eastern segment (Anth1.F) caused positive ΔCFF of the order of 0.15 to 10.0bars at the western segment fault edge (Anth2.F) moving it closer to failure and probably advancing the occurrence time. Failure on Anthemountas fault has caused the relaxation of this fault which shows no association with strong seismicity nowadays and currently experiences seismic quiescence. The extrapolation of the evolution of the stress field for 2050 shows that the shadow zone is eliminated in the future for Anthemountas fault. The 1902 Assiros earthquake shows the most enigmatic origin, since the epicentre is questioned. There is no geological evidence to justify the occurrence of this earthquake, which by no means has contributed to the increase of stress at the central part of the study area, the migration of seismicity to the east and the increase of ΔCFF in the central part of the zone, where faults are positively loaded. The 1932 M7 Ierissos significantly reinforces positive stress changes greater 0.1bar at the central part and western termination of the Thessaloniki-Gerakarou Fault zone and encouraged sequential strong seismicity at the central part of Mygdonia area (1932 Sochos earthquake, 1933 Volvi and 1978 M6.5 Stivos earthquake) and recent microseismicity in Arnea area where a bright patch is created. The interaction of the seismogenic faults due to the stress field is evident at the onto fault coseismic stress field calculations which show the influence of the stress disturbances even when the distance between faults there is more than 30km and the north dipping rupture zone which bounds Mygdonia graben from the south showed that there are considerable interrelations in adjacent and parallel fault segments.

The strong association between bright zones and strong or minor earthquakes occurrence is a characteristic feature in Mygdonia. The current seismicity pattern exhibits a strong relevance with the stress changes imposed by the strong historical and instrumental earthquakes. The spatial variability of the positive Coulomb stress changes shows that microseismicity and especially clustered microseismicity is strongly encouraged by the locations of the strong earthquakes and the spatial distribution is affected by the occurrence of strong earthquakes. The methodology followed is based on the Coulomb failure criterion which is significantly based on the crustal and friction properties. The correlation also is associated with the spatial extend of the study area which increases negative ΔCFF values and is visible at the spatial distribution of Figure 4-38. The frictional properties are outlined (dry crust with $B=0.1$) with the absence of fluids and the prevalence of strong faults with high angles.

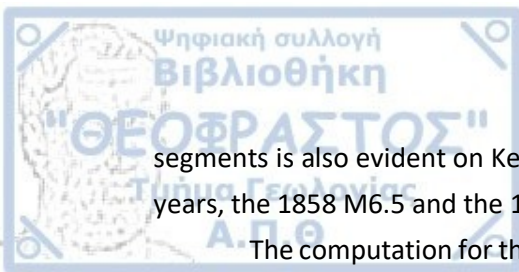
Positive stress increments do not declare subsequent epicenter location but correspond to the segment efficient to fail because it has reached high stress level and is close to failure. For this reason, the stress evolutionary model was extrapolated and shows that

apart from the main part of the rupture zones that have recently been activated, the stress has been generally increased by bringing faults close to their stress levels just prior rupture.

The double objective of this work is the exploitation of the historical seismicity and their impact on the stress field and the constant loading on faults obtained from geodetic data. Current stress enhanced areas with an increased likelihood for earthquake occurrence are identified at the western part of Mygdonia and central Chalkidiki. Recent seismicity in the time interval 2000 until 2014 with relocated focal coordinates show that most of the earthquakes are concentrated in locations with increased stress values for a stress field oriented for a typical north dipping normal fault. The stress evolutionary model for Mygdonia, evaluates a positive correlation between bright stress zones and earthquake occurrence and serve as a tool in seismic hazard assessment.

Results for seismicity interrelations based on the Coulomb stress changes induced by strong earthquakes in the Corinth Rift showed opposing results. Deformation in Corinth rift is fast accommodated with significant slip rates on faults and frequent earthquakes. Thirty strong historical earthquakes, comprising a complete set, were modeled and were searched for their capacity of interacting. The effect of long-term lithospheric loading on two groups of faults comprising model 1 and model 2 was also added to the resulting stress. Although the earthquakes are considered to be complete significant uncertainties exist for their location and the size, considering even 20km epicentral errors (Papazachos and Papazachou 1997). Misfits in stress computation can also be attributed to the seismotectonic complexity and the existence of minor faults with various faulting types, when the crust is multi-segmented.

The prevailing normal fault type in Corinth Rift cause an accumulative negative stress impact, inhibiting earthquake occurrence in elongated N-S shadow zones, whereas they enhance faulting along their strikes in an E-W direction encouraging failure on adjacent fault. Triggering of adjacent faults is short time is frequent. The 1965 Eratini earthquake occurrence along Eliki fault was followed in 1970 by the Antikyra earthquake, on the adjacent Xylocastro fault. The 1817 M6.6 earthquake on Aigion fault was probably promoted by the 1804 M6.4 earthquake on the adjacent Psathopyrgos fault. The interaction between Aigion and Xylocastro faults with the 1742 Xylocastro earthquake, the 1748 Aigion earthquake and the 1753 M6.1 Xylocastro earthquake on strong events which are triggered alongside of Xylocastro fault. It is worth noting that a clustering of strong seismicity is evident in Corinth Rift. Strong earthquakes at the western part of the Corinth rift are often clustered in time and space. The 1703 M6.1 and the 1714 M6.2 earthquakes that were caused because of the activation of Psathopyrgos fault within 9 years and the 1756 M6.8 and 1769 M6.8 earthquakes which occurred within 13 years on Nafpaktos fault, the 1804 M6.4 and the 1806 M6.2 earthquakes with 2 years interevent time on Psathopyrgos fault are characteristic examples. For the eastern Corinth Rift the sequential interaction between Skinos, Alepochori and Kaparelli faults in 1981 sequence is characteristic, exhibiting a constant migration of seismic activity to the east, whereas 53 years earlier the M6.3 earthquake occurred in Perachora fault, implying the eastward migration of fault ruptures within 53 years. The activation of separate



segments is also evident on Kechries fault where two strong earthquakes occurred within 18 years, the 1858 M6.5 and the 1876 M6.1 earthquake.

The computation for the stress evolution for two different models, the one comprised from the main northdipping fault zone and the second including the northdipping faults that are associated with strong seismicity showed that there is not significant alteration in the stress field for explaining the locations for impending strong earthquakes. However the existence of the southdipping faults contribute to a better understanding of the microseismicity spatial distribution. The evolutionary model adequately explains the location for the 17 out of the 29 cases, in which the epicentre or the causative fault is stress enhanced, and the model has succeeded in interpreting earthquake interrelations. For the rest of the cases, for which epicenters are located in stress shadows, stress interaction is doubtful. This fact can also be attributed to fault interaction that inhibits faults to complete a seismic cycle and they rupture before approaching the required maximum stress or different seismic cycles (Console et al., 2010). Characteristic is the example of Psathopyrgos fault for which the model fails to explain any of the associated strong seismicity eg. the 1756 (Fig. 4-30g) the 1804 (Fig. 4-31b), the 1806 (Fig4-31c) earthquakes. This can be attributed to misleading seismicity information in terms of location and size or additional mechanisms or additional healing mechanisms for Corinth Rift that require further research. (Armijo et al., 1992) suggests that in Corinth rift there are fault scarps showing large displacements, but their origin might not be seismogenic. The complex way that strain is accommodated along the Corinth Rift in seismic or aseismic manner influences the results of the stress evolutionary model.

The correlation between moderate, recent earthquakes and strong seismicity provided uncertain results. There is a fair to good correspondence between moderate seismicity and strong earthquake occurrence, taking into consideration the recent strong seismicity which also occurred. However there is an important portion of earthquakes which are not favored by positive stress and cannot be explained by the stress evolutionary model. Mechanisms like stress diffusion, fluid presence or post seismic behavior of rupture (Ishibe et al., 2011) are responsible so that moderate seismicity rate cannot be sufficiently explained in respect to long term earthquake occurrence. In addition earthquake depth variation and earthquakes owing different fault plane solutions contribute to the increase of negative ΔCFF in Corinth Rift.



Chapter 5

Concluding Remarks

The interpretation of earthquake phenomenology demands a pluralistic approach for the best understanding of its behaviour. In this thesis, interaction mechanisms between faults through their stress fields, being associated with strong, moderate and minor seismicity, were identified. The selected methodology was effectively applied in two active fault populations in the Aegean area, which share common seismotectonic properties, since they are both related to extensional back-arc regime, and at the same time significantly different as far as the deformation rate and seismicity level are concerned. Results for the two study regions highlight the strong impact of the fault population development on the overall seismicity behaviour and are summarized below:

1) Findings regarding microseismicity occurrence and fault properties:

- The comparatively uniform spatial distribution of the velocity ratio ($V_P/V_S=1.78$) that was determined for Mygdonia implies a structural homogeneity for the entire study area. On the other hand, a striking observation for the Corinth Rift is the velocity ratio variability from the west to the eastern part, declaring the structural heterogeneity across the rift, a fact additionally imprinted on the spatiotemporal properties of seismicity from W-E.
- In the absence of strong seismicity during the study period, relocated microseismicity delineated the existence of smaller active faults, which develop within the fault population. Microseismicity is clustered and localized, forming seismogenic bands and bands of seismic quiescence along seismogenic faults known to have caused strong earthquakes in the past. The spatial distribution of seismicity clusters is effectively explained by the Coulomb stress evolutionary model, with the majority of the recent seismicity located where increasing positive static stress changes are calculated. Recent earthquake occurrence is significantly favored by the occurrence of strong seismicity in Mygdonia.
- The foci spatial distribution shows that the majority of the earthquake foci for Mygdonia are placed between 3km and 16km, defining the seismogenic layer, which is in agreement with previous studies (Hatzfeld et al., 1986/1987). There is a variability of the width of the seismogenic layer across the Corinth Rift, moving from deep to shallow depths from the eastern to the western part of the Rift.
- The hypocentral distribution is indicative of the different way deformation is accommodated in the two study areas. The distribution of earthquake foci in Mygdonia delineates fault planes with steep angles at depth. According to Bell et al. (2008) seismogenic faults with high angles ($>45^\circ$) form new basins which experience high strain. The seismicity is associated with both northdipping and southdipping faults. High fault angles can be attributed to preexisting fault planes (Pavlidis and Kiliyas, 1987) or to high friction values (Doglioni et al., 2015) also confirmed with the frictional coefficient values. However the spatiotemporal distribution of the seismic clusters

north of Lagadas Lake indicates that fluid influence should be seriously considered (Mesimeri et al., 2017). Fluid presence Corinth Rift is an area where both low angle and high angle faults are found. Low angle north dipping faults is the outstanding characteristic of the central Corinth Rift. There are slight indications for south dipping structures, however their role in stress accommodation remains uncertain. High angle dipping faults are dominant in Northwestern Peloponnese in contradiction to the low angle faulting of the central Corinth rift.

- The activation of both south and north dipping faults is characteristic in the area of Mygdonia. South dipping high angle faults seem to be significant although they don't alter the accommodation of strain which is mainly attributed to the normal northdipping faults and a migration of seismicity between antithetic faults has been evidenced for small earthquakes.

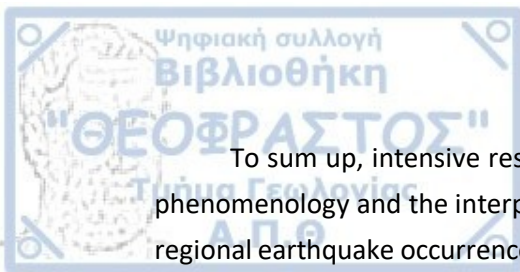
2) Results for interrelation features of strong moderate and minor seismicity:

- The existence of memory features for earthquake interevent time, interevent distance and magnitude is achieved with the exploitation of all earthquakes in all magnitude ranges and different time periods. Strong ($M \geq 6.0$), moderate ($M \geq 4.0$) and recent complete seismicity catalogs (declustered and non declustered) were investigated for interaction and randomness. The employment of the above catalogs with different properties in earthquake size and coverage provides a complementary perspective of the seismic process.
- Temporal and spatial distribution of seismicity along with the stochastic seismicity analysis showed the dominance of clustering and interactive mechanisms in the areas of Mygdonia and Corinth rift. There is a contradiction in the seismicity pattern with the region of the Corinth Gulf to shape a stronger persistence than Mygdonia area.
- Independence it time, space and magnitude is indicated in the occurrence of strong earthquakes with $M > 6.0$ in the Corinth Rift, an issue that is still under debate and further research is required (Cisternas at al., 2004; Shadkhoo et al., 2009).
- Smaller earthquakes do not occur randomly but they exhibit strong clustering in time and space and tend to retain similar features through the seismic process, even if dependent events are removed. The most persistent seismicity parameter is time between successive events, whereas magnitudes are in general memory free.
- Earthquake interevent time and interevent distance holds a significant short and long memory content in Corinth Rift, while magnitude is a less interrelated parameter. In Mygdonia the memory content is less significant, however existing both for long term and short term correlations.
- The diverse properties of fault populations in the two study areas, reveal different spatiotemporal aspects of seismicity, with Mygdonia to be more distributed along small faults, compared to Corinth rift where clustering is dense.

3) Results on the interaction of strong earthquakes through their Coulomb stress field:

- In an effort to investigate the extent to which Coulomb stress changes are efficient to reveal locations of incoming strong earthquakes, the evolutionary Coulomb stress model was applied and showed that triggering is dominant for all strong earthquakes in Mygdonia and for 19 out of 29 strong earthquakes in the Corinth Rift.
- In the Corinth Rift there is a significant tendency for strong earthquakes to trigger or advance the time of subsequent strong earthquakes in adjacent faults (Psathopyrgos and Aigio faults) or segments of the same fault (Kechries fault) or antithetic faults (eg, 1981 seismic sequence). The same tendency is observed in Mygdonia (eg. the Anthemountas fault zone, 1932 Sochos and 1933 Volvi earthquakes).
- There is indication for an eastward migration of earthquake epicentres to the east part of the Corinth Rift, with the sequential interaction between Perachora fault, Alepochori, Skinis and Kaparelli faults.
- According to the stress evolutionary model strong earthquake clustering is favored in the Corinth Rift (1804 and 1806 Psathopyrgos earthquakes, 1756 and 1769 Nafpaktos earthquakes, 2010 Efpalio seismic doublet). The quantification of strong earthquake clustering through statistical analysis carries uncertainties due to restricted data.
- There is a strong interrelation between strong earthquakes and the spatial distribution of moderate seismicity and microseismicity in Mygdonia basin.
- The extrapolation of the stress evolutionary model in Corinth Rift shows that major north dipping faults associated with the strongest earthquakes are currently "locked" considering the given geodetic slip rate, with the exception of Eliki fault. For Mygdonia graben although the annual interseismic deformation is accommodated with slow slip rates (1mm/yr) along faults, stress built-up is indicated for Anthemountas and Stratoni faults, while the hazardous Stivos fault remains negatively stressed.

Gradual strain build up fault zones evolve towards faulting localization and fault coalescence (Hardacre and Cowie, 2003) which is a main characteristic of Corinth rift (e.g., Armijo et al., 1996; Hubert et al., 1996). Results show that the different degree of localization of deformation into the two study areas is imprinted on seismicity. The stronger localization of strain in the Corinth Rift is responsible for the strong indications of clustering and long memory content for interevent time and distance, meaning that seismicity mostly occurs along the main fault zones. On the other hand, a relatively more distributed deformation pattern in Mygdonia graben, compared to Corinth Rift, where subsidiary small faults, are brought into failure due to the occurrence of strong past earthquakes. The aseismic deformation accommodated on faults in Mygdonia is slow due to slow slip rates and seismicity exhibits a weaker degree of spatiotemporal memory and clustering with traces of similar trend in magnitude occurrence.



To sum up, intensive research work is conducted for the interpretation of earthquake phenomenology and the interpretation of the spatial, temporal and size features of global or regional earthquake occurrence through stochastic approaches. A variety of statistical models were introduced, so as to resemble best to the seismic activity and associate it with the hazardous active fault systems. The stochastic approach on good quality seismicity catalogs along with deformation studies share the satisfactory determination of potential seismic threat in a seismogenic region. It is evident that the analyses of seismicity on the basis of stochastic methodologies provides insights on the hidden properties of the seismic process and the assessment of the seismic hazard.

Appendix AI. Station time delays

Table AI.1. Station time delays calculated in Mygdonia for the seismological stations in distance ≤ 200 km.

n	Station code	ϕ°	λ°	elevation	Time Delay
1	KAVA	4059.65N	2430.71E	95	-0.10
2	OUR	4020.04N	2358.74E	60	-0.33
3	NVR	4121.00N	2351.72E	595	-0.38
4	SRS	4107.03N	2335.53E	400	-0.64
5	SOH	4049.30N	2321.23E	670	-0.51
6	VAY	4119.26N	2234.20E	168	-0.12
7	KNT	4109.72N	2253.88E	380	-0.23
8	GRG	4057.40N	2224.08E	560	0.21
9	LIT	4006.05N	2229.40E	480	0.44
11	THE	4037.93N	2257.90E	70	-0.33
12	HORT	4035.87N	2305.98E	933	-0.29
13	NEO	3918.40N	2313.41E	500	0.24
15	XOR	3921.97N	2311.52E	500	0.31
16	SKIA	3909.99N	2327.97E	325	0.30
17	AOS	3910.20N	2352.80E	200	-0.04
18	PLG	4022.43N	2326.73E	580	-0.36
19	LOS	3957.83N	2504.15E	389	0.67
20	LIA	3953.88N	2510.98E	60	0.00
21	PAIG	3955.63N	2340.78E	140	0.30

Table AI.2. Station time delays calculated in Efpalio area for the seismological stations in distance ≤ 200 km.

n	Station code	ϕ°	λ°	elevation	Time Delay
1	PVO	3836.96N	2131.50E	184	0.13
2	PDO	3835.92N	2111.00E	227	0.26
3	KLV	3802.62N	2209.38E	758	-0.19
4	DRO	3757.12N	2142.60E	465	0.01
5	VTN	3754.96N	2111.10E	52	1.10
6	DSF	3824.67N	2231.63E	701	-0.26
7	UPR	3817.02N	2147.18E	138	0.22
8	GUR	3756.18N	2220.54E	1080	-0.21
9	EFP	3825.61N	2154.35E	135	-0.07
11	KALE	3823.47N	2208.39E	760	0.10
12	TRIZ	3821.93N	2204.36E	57	0.02
13	LAKA	3814.41N	2158.71E	505	0.11
15	ATH	3758.33N	2343.00E	95	0.73



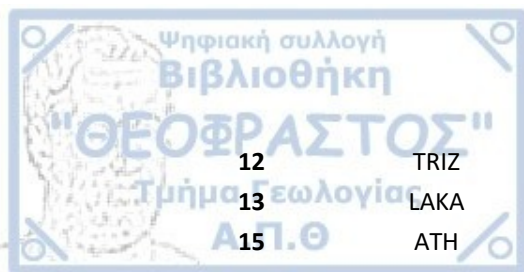
16	DID	3730.22N	2314.12E	553	0.91
17	RLS	3803.47N	2128.00E	100	0.21
18	UPR	3817.02N	2147.18E	138	0.22
19	AXS	3811.46N	2122.34E	97	-0.02
20	THAL	3802.13N	2239.47E	129	0.36
21	PROD	3815.32N	2253.59E	350	0.52
22	LTK	3801.22N	2258.01E	407	0.73
23	LOUT	3759.16N	2258.27E	307	0.85
24	VILL	3809.51N	2318.43E	650	1.34

Table AI.3. Station time delays calculated in Patras area for the seismological stations in distance ≤ 200 km.

n	Station code	ϕ°	λ°	elevation	Time Delay
1	PVO	3836.96N	2131.50E	184	0.25
2	PDO	3835.92N	2111.00E	227	0.20
3	KLV	3802.62N	2209.38E	758	-0.31
4	DRO	3757.12N	2142.60E	465	-0.02
5	VTN	3754.96N	2111.10E	52	0.59
6	DSF	3824.67N	2231.63E	701	-0.18
7	UPR	3817.02N	2147.18E	138	0.15
8	GUR	3756.18N	2220.54E	1080	-0.23
9	EFP	3825.61N	2154.35E	135	0.00
11	KALE	3823.47N	2208.39E	760	-0.15
12	TRIZ	3821.93N	2204.36E	57	-0.08
13	LAKA	3814.41N	2158.71E	505	-0.11
15	ATH	3758.33N	2343.00E	95	0.83
16	DID	3730.22N	2314.12E	553	0.54
17	RLS	3803.47N	2128.00E	100	-0.07

Table AI.4. Station time delays calculated in Xylocastro area for the seismological stations in distance ≤ 200 km.

n	Station code	ϕ°	λ°	elevation	Time Delay
1	PVO	3836.96N	2131.50E	184	0.66
2	PDO	3835.92N	2111.00E	227	0.97
3	KLV	3802.62N	2209.38E	758	-0.42
4	DRO	3757.12N	2142.60E	465	0.04
5	VTN	3754.96N	2111.10E	52	0.00
6	DSF	3824.67N	2231.63E	701	-0.45
7	UPR	3817.02N	2147.18E	138	0.27
8	GUR	3756.18N	2220.54E	1080	-0.41
9	EFP	3825.61N	2154.35E	135	-0.17
11	KALE	3823.47N	2208.39E	760	-0.30



12	TRIZ	3821.93N	2204.36E	57	-0.24
13	LAKA	3814.41N	2158.71E	505	-0.21
15	ATH	3758.33N	2343.00E	95	0.83
16	DID	3730.22N	2314.12E	553	0.31
17	RLS	3803.47N	2128.00E	100	0.07
18	UPR	3817.02N	2147.18E	138	0.27
19	THAL	3802.13N	2239.47E	129	-0.15
20	PROD	3815.32N	2253.59E	350	0.00
21	LTK	3801.22N	2258.01E	407	-0.02
22	LOUT	3759.16N	2258.27E	307	-0.03

Table AI.5. Station time delays calculated in Alkyonides area for the seismological stations in distance ≤ 200 km.

n	Station code	ϕ°	λ°	elevation	Time Delay
1	PVO	3836.96N	2131.50E	184	1.45
2	PDO	3835.92N	2111.00E	227	0.49
3	KLV	3802.62N	2209.38E	758	0.27
4	DRO	3757.12N	2142.60E	465	0.82
5	VTN	3754.96N	2111.10E	52	0.00
6	DSF	3824.67N	2231.63E	701	-0.18
7	GUR	3756.18N	2220.54E1	1080	0.17
8	EFP	3825.61N	2154.35E	135	0.46
9	KALE	3823.47N	2208.39E	760	0.22
11	TRIZ	3821.93N	2204.36E	57	0.27
12	LAKA	3814.41N	2158.71E	505	0.51
13	ATH	3758.33N	2343.00E	95	0.38
15	DID	3730.22N	2314.12E	553	0.00
16	RLS	3803.47N	2128.00E	100	0.20
17	THAL	3802.13N	2239.47E	129	0.00
18	PROD	3815.32N	2253.59E	350	-0.11
19	LTK	3801.22N	2258.01E	407	-0.04
20	LOUT	3759.16N	2258.27E	307	-0.14

Appendix AII. Statistical analysis

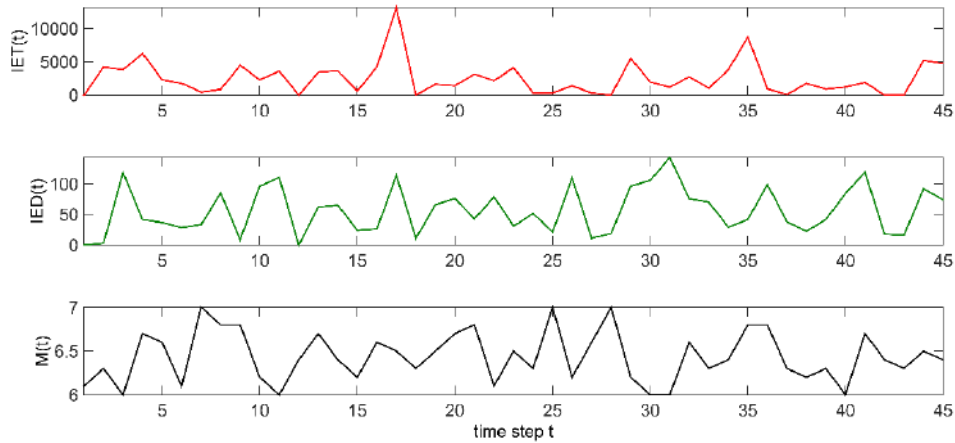


Figure AII.1. Time series for strong earthquakes in the Corinth rift (A catalog) with IET in decimal numbers (upper row), IED (central row) and magnitudes (lower row).

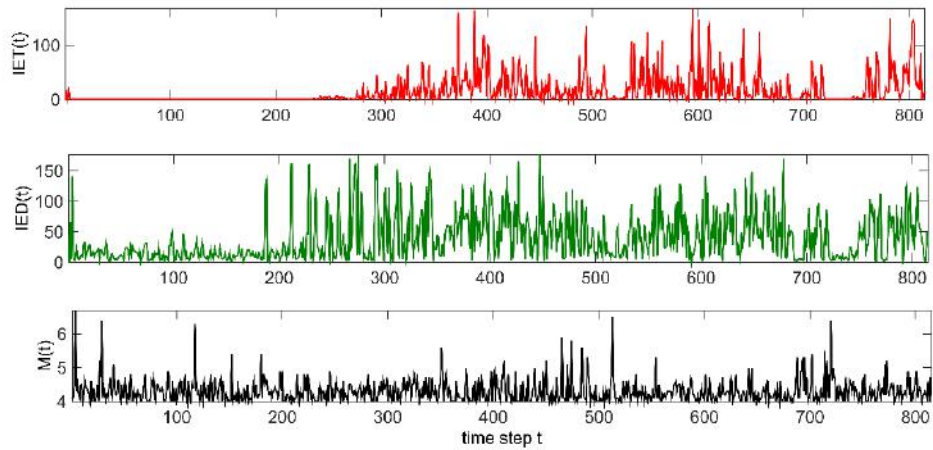


Figure AII.2. Time series for moderate earthquakes in the Corinth rift (B_1 catalog) with IET in decimal numbers (upper row), IED (central row) and magnitudes (lower row).

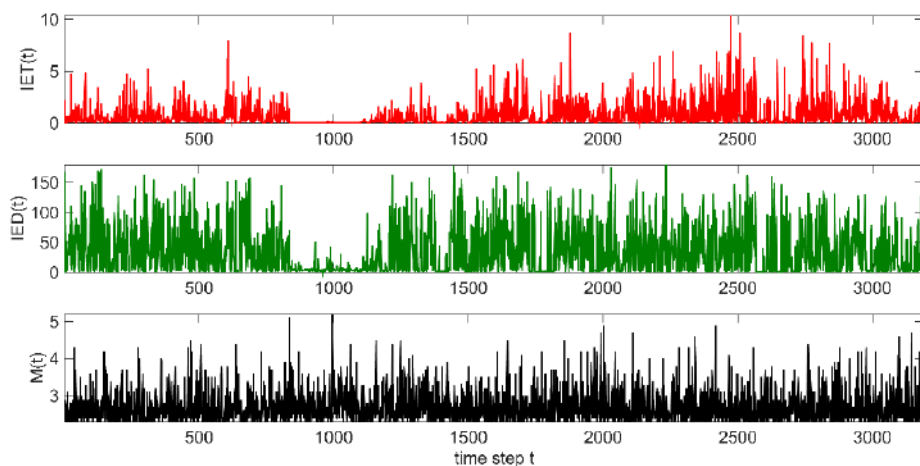


Figure AII.3. Time series for complete earthquakes in the Corinth rift (C_1 catalog) with IET in decimal numbers (upper row), IED (central row) and magnitudes (lower row).

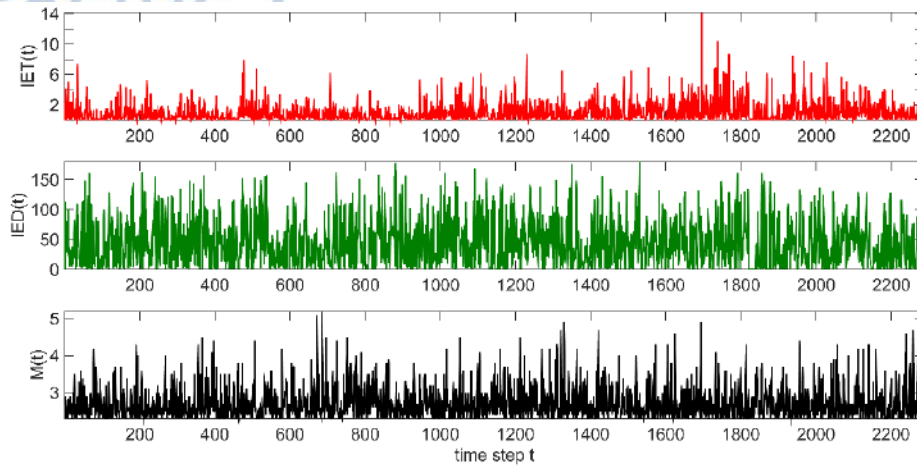


Figure AII.4. Time series for the declustered recent catalog in the Corinth rift (D_1 catalog) with IET in decimal numbers (upper row), IED (central row) and magnitudes (lower row).

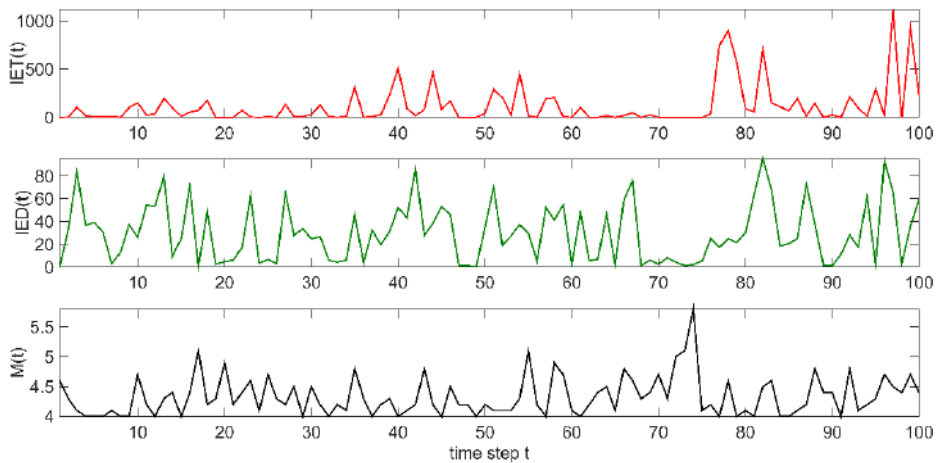


Figure AII.5. Time series for moderate earthquakes in Mygdonia graben (B_2 catalog) with IET in decimal numbers (upper row), IED (central row) and magnitudes (lower row).

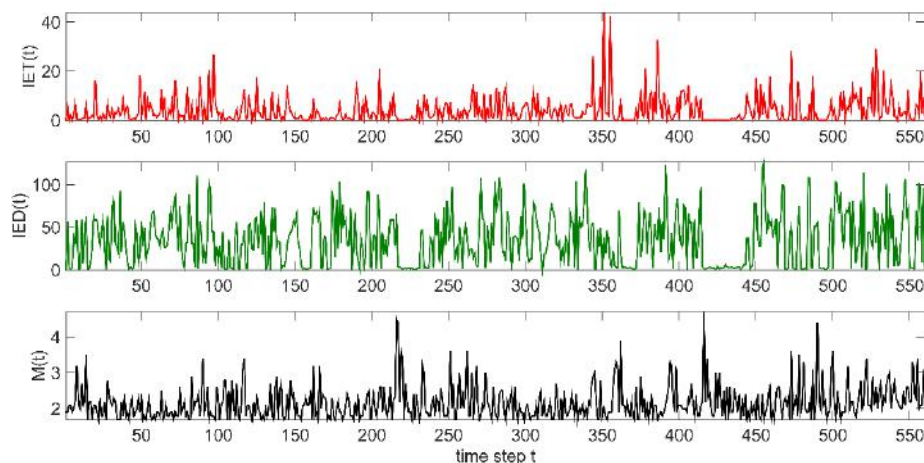


Figure AII.6. Time series for complete earthquakes in Mygdonia graben (C_2 catalog) with IET in decimal numbers (upper row), IED (central row) and magnitudes (lower row).

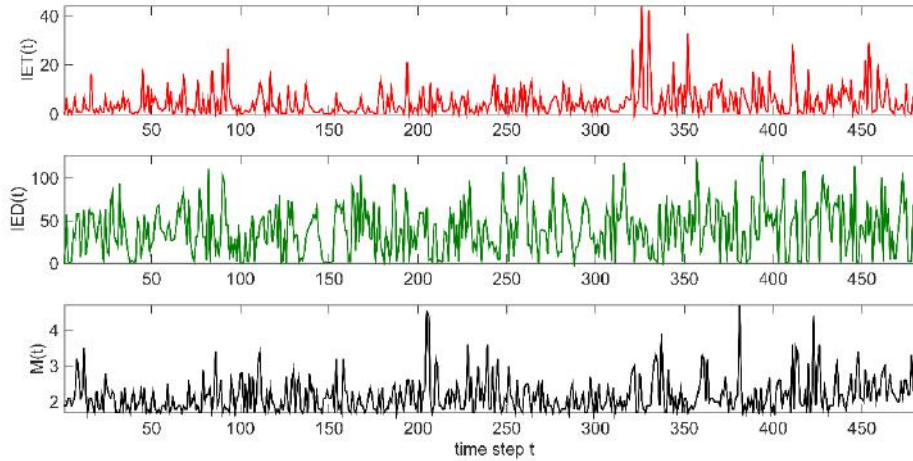


Figure All.7. Time series for the declustered catalog in Mygdonia graben (D_2 catalog) with IET in decimal numbers (upper row), IED (central row) and magnitudes (lower row).

Appendix All. Seismic moment tensor and strain calculation

Table III.1 Information on the six seismic moment tensor elements for Mygdonia strong earthquakes. M_{11} , M_{22} , M_{33} component are principal whereas, $M_{12}=M_{21}$, $M_{13}=M_{31}$, $M_{23}=M_{32}$ are the shear components (Aki and Richards, 1980).

N	Year	M_0	Moment Tensor Elements ($\cdot 10^{25}$) dyn-cm ²					
			M_{11}	M_{22}	M_{33}	M_{12}	M_{13}	M_{23}
1	1677	2.04	1.8985	0.0615	-1.9600	0.3522	0.5655	0.0145
2	1759	2.88	2.6817	0.0869	-2.7685	0.4974	0.7988	0.0205
3	1902	8.13	7.8081	-0.0053	-7.8027	0.2716	-2.2351	0.2755
4	1932	32.4	30.8367	0.2265	-31.0632	2.9686	-8.9484	0.5516
5	1932	2.04	1.9613	-0.0013	-1.9600	0.0682	-0.5614	0.0692
6	1933	2.88	2.8516	-0.1431	-2.7085	-0.3088	-0.0017	0.6917
7	1978	5.2	5.1415	-0.2580	-4.8834	-0.5568	-0.0031	1.2472
ΣM			53.1793	-0.0330	-53.1462	3.2925	-10.3854	2.8703

Table III.2 Information on the six seismic moment tensor elements for Corinth rift strong earthquakes. M_{11} , M_{22} , M_{33} component are principal whereas, $M_{12}=M_{21}$, $M_{13}=M_{31}$, $M_{23}=M_{32}$ are the shear components (Aki and Richards, 1980).

N	Year	M_0	Moment Tensor Elements ($\cdot 10^{25}$) dyn-cm ²					
			M_{11}	M_{22}	M_{33}	M_{12}	M_{13}	M_{23}
1	1703	$1.44 \cdot 10^{25}$	1.2497	-0.0837	-1.1660	0.4236	0.2602	0.6148
2	1714	$2.88 \cdot 10^{25}$	2.8821	0.0002	-2.8823	0.0252	0.1006	0.0009
3	1725	$1.02 \cdot 10^{25}$	0.9985	0.0067	-1.0053	-0.1464	-0.1015	-0.1073
4	1742	$11.4 \cdot 10^{25}$	7.9736	0.1838	-8.1574	-1.3994	-7.7035	2.3336
5	1748	$8.12 \cdot 10^{25}$	7.3571	-0.1521	-7.2050	-0.1676	-3.3849	1.2459
6	1753	$1.44 \cdot 10^{25}$	1.0038	0.0231	-1.0270	-0.1762	-0.9698	0.2938
7	1756	$16.21 \cdot 10^{25}$	14.0222	-0.9389	-13.0833	4.7526	2.9192	6.8978
8	1769	$16.21 \cdot 10^{25}$	14.0222	-0.9389	-13.0833	4.7526	2.9192	6.8978
9	1775	$2.04 \cdot 10^{25}$	0.9960	-0.0490	-0.9470	0.0419	-0.2307	0.2158
10	1785	$1.02 \cdot 10^{25}$	3.8993	-3.8845	-0.0149	-1.1237	-0.1996	0.3824
11	1794	$11.48 \cdot 10^{25}$	10.4480	0.8591	-11.3071	2.9959	1.9165	0.5496
12	1804	$4.07 \cdot 10^{25}$	3.8993	-3.8845	-0.0149	-1.1237	-0.1996	0.3824
13	1806	$2.04 \cdot 10^{25}$	2.0403	0.0002	-2.0405	0.0178	0.0713	0.0006

14	1817	$8.12 \cdot 10^{25}$	7.3571	-0.1521	-7.2050	-0.1676	-3.3849	1.2459
15	1858	$5.75 \cdot 10^{25}$	5.6152	0.0380	-5.6532	-0.8231	-0.5710	-0.6036
16	1861	$11.4 \cdot 10^{25}$	10.4821	-0.4166	-10.0655	-0.0528	-4.5833	2.2661
17	1870	$16.21 \cdot 10^{25}$	15.9668	0.0049	-15.9717	0.2787	2.8158	0.0492
18	1876	$1.44 \cdot 10^{25}$	1.4105	0.0095	-1.4200	-0.2068	-0.1434	-0.1516
19	1887	$5.75 \cdot 10^{25}$	5.6010	-0.2758	-5.3252	0.2357	-1.2972	1.2133
20	1888	$2.88 \cdot 10^{25}$	2.6104	-0.0540	-2.5564	-0.0595	-1.2010	0.4421
21	1917	$1.02 \cdot 10^{25}$	0.8847	-0.0592	-0.8255	0.2999	0.1842	0.4352
22	1928	$2.88 \cdot 10^{25}$	2.8072	-0.1382	-2.6689	0.1181	-0.6501	0.6081
23	1965	$0.18 \cdot 10^{25}$	-0.0067	0.1421	-0.1354	0.0035	0.0359	-0.1087
24	1970	$0.91 \cdot 10^{25}$	0.6385	0.0145	-0.6530	-0.1126	-0.6027	0.1872
25	1975	$1.13 \cdot 10^{25}$	1.0024	-0.7262	-0.2762	0.1684	0.0302	0.4623
26	191	$8.75 \cdot 10^{25}$	8.2696	0.3052	-8.5748	-1.8864	-0.7782	1.2178
27	1981	$3.97 \cdot 10^{25}$	2.8197	1.1328	-3.9525	-1.8033	-0.0001	0.2846
28	1981	$2.7 \cdot 10^{25}$	1.5680	1.1319	-2.6999	-1.3323	0.0107	0.0128
29	1995	$3.38 \cdot 10^{25}$	3.0593	-0.0632	-2.9961	-0.0697	-1.4076	0.5181
30	2008	$4.6 \cdot 10^{25}$	-3.8819	3.7819	0.1000	2.4534	0.1902	0.6432
ΣΜ			137.0159	-4.1997	-132.816	5.8760	-16.137	28.4156

Strain tensor calculation

For Mygdonia, the final strain tensor according to Kostrov's theorem (Eq.4-11) for T=337 years, within a rectangle area and for a crust depth approximately equal to 12km yields (shear modulus is taken equal to $\mu=3 \cdot 10^{11} \text{dyn}\cdot\text{cm}^2$):

$$\varepsilon_{ij} = \begin{bmatrix} 3.8290 & 0.2371 & -0.7478 \\ 0.2371 & -0.0024 & 0.2067 \\ -0.7478 & 0.2067 & -3.8266 \end{bmatrix} \cdot 10^{-8}$$

Positive strain values indicate an extension of the area, while negative values reveal a crust shortening in general. Therefore, $\varepsilon_{11}=3.8 \cdot 10^{-8}$ (N-S), while $\varepsilon_{33}=-3.82 \cdot 10^{-8}$ is vertical and indicates crust thinning, which is compatible with the stress field in Mygdonia. Eigen analysis of the strain-tensor matrix gives the eigenvalues. For the Corinth Rift, the final strain tensor for the time period of T=311 years, within a rectangle area and for a crust depth equal to 12km is given by:

$$\varepsilon = \begin{bmatrix} 5.775 & 0.248 & -0.680 \\ 0.248 & -1.5224 & 1.198 \\ -0.680 & 1.198 & -5.598 \end{bmatrix} \cdot 10^{-8}$$

In a N-S direction in the Corinth Gulf, the deformation taking place is $\varepsilon_{11}=5.77 \cdot 10^{-8}$ and along the depth $\varepsilon_{33}=-5.59 \cdot 10^{-8}$ is showing a more important crustal thinning than Mygdonia.

- Ackermann, R., Schlische, R.W. and Withjack, M.O. (2001). The geometric and statistical evolution of normal fault systems: an experimental study of the effects of mechanical layer thickness on scaling laws, *J Struct. Geol.*, **23**, 1803 – 1819.
- Aki, K. (1965). Maximum likelihood estimate of b in the formula $\log N = a - bM$ and its confidence limits, *Bull. Earthquake Res. Inst., Tokyo Univ.*, **43**, 237–239.
- Aki, K. (1967). Scaling law of seismic spectrum, *J. Geoph. Res.*, **72**, 1217-1231, doi:10.1029/JZ072i004p01217.
- Aki, K. and Richards, P.G. (1980). *Quantitative Seismology*. Freeman, San Francisco.
- Akyol, N., Zhu, L., Mitchel, J., Sözbilir, H. and Kekovali, K. (2006). Crustal structure and local seismicity in Western Anatolia. *Geophys. J. Int.*, **166**, 1259-1269.
- Ambraseys, N. and Pantelopoulos, P. (1989). The Fokis earthquake of 1 August 1870, *J. Europ. Earthq. Eng.*, **3**, 10-18.
- Ambraseys, N.N. and Jackson, J.A. (1990). Seismicity and associated strain of central Greece between 1890 and 1988, *Geophys. J. Int.*, **101**, 663–708.
- Ambraseys, N.N. and Jackson, J.A. (1997). Seismicity and associated strain in the Gulf of Corinth (Greece) since 1694, *J. Earthq. Engin.*, **1**, 433–474.
- Ambraseys, N.N. and Jackson, J.A. (1998). Faulting associated with historical and recent earthquakes in the Eastern Mediterranean region, *Geophys. J. Int.*, **133**, 390–406.
- Ambraseys, N.N. (2009). *Earthquakes in the Mediterranean and Middle East: a multidisciplinary study of seismicity up to 1900*. Cambridge University Press, 947, ISBN 978 0 521 87292 8.
- Amorese, D. (1993). *Sismotectonique et dkformation actuelle de la terminaison nord occidentale de l'Arc Egken (Iles Ioniennes, Acharnanie, Epire, Grece)*, PhD Thesis, Universite Joseph Fourier, Grenoble, France.
- Angelier, J., Tarantola, A., Manoussis, S. and Valette, B., (1982). Inversion of field data in fault tectonics to obtain the regional stress, *Geophysical Journal of the Royal Astronomical Society* **69**, 607–621.
- Armijo, R., Meyer, B., King, G.C.P., Rigo, A. and Papanastassiou D. (1996). Quaternary evolution of the Corinth Rift and its implications for the Late Cenozoic evolution of the Aegean, *Geophys. J. Int.*, **126**, 11–53.
- Armijo R., B. Meyer, A. Hubert, and A. Barka (1999). Westwards Propagation of the North Anatolian Fault into the Northern Aegean: Timing and kinematics, *Geology*, **27**, 267-270.
- Avallone, A., Briole, P., Agatza-Balodimou, A.M., Billiris, H., Charade, O., Mitsakaki, C., Nercessian, A., Papazissi, K., Paradissis, D. and Veis, G. (2004). Analysis of eleven years of deformation measured by GPS in the Corinth Rift Laboratory area, *Compt. Rendus Geosci.*, **336**, 301–311.
- Bagh, S., Chiaraluce, L., De Gori, P., Moretti, M., Govon, A., Chiarabba, C., Di Bartolomeo, P. and Romanelli M. (2007). Background seismicity in the central Apennines of Italy: the Abruzzo region case study, *Tectonophysics*, **444**, 80-92.
- Bakun, W.H. and Wentworth, C.M. (1997). Estimating earthquake location and magnitude from seismic intensity data, *Bull. Seism. Soc. Am.*, **87**, 1502–1521.
- Beckers, A., Hubert-Ferrari, A., Beck, C., Bodeux, S., Tripsanas, E., Sakellariou, D. and De Batist, M. (2015). Active faulting at the western tip of the Gulf of Corinth, Greece, from high-resolution seismic data, *Mar. Geol.* **360**, 55–69.
- Bell, R.E., McNeill, L.C., Bull, J.M. and Henstock, T.J. (2008). Evolution of the offshore western Gulf of Corinth. *Bull. Geol. Soc. Am.*, **120**, 156–178.
- Bell, R.E., McNeill, L.C., Bull, J.M., Henstock, T.J., Collier, R.E.L. and Leeder, M.R. (2009). Fault architecture, basin structure and evolution of the Gulf of Corinth Rift, central Greece, *Basin Research*, **21**, 824– 855.
- Benedetti, L., Finkel, R., King, G., Armijo, R., Papanastassiou, D., Ryerson, F.J., Flerit, F., Farber, D. and Stavrakakis, G. (2003). Motion on the Kaparelli fault (Greece) prior to the 1981 earthquake sequence determined from ³⁶Cl cosmogenic dating, *Terra Nova*, **15**, 118–124, <https://doi.org/10.1046/j.1365-3121.2003.00474.x>.
- Benioff, V.H. (1951). Global strain accumulation and release as revealed by great earthquakes, *Bull. Geol. Soc. Am.* **62**, 331-338.

- Ben-Zion, Y. and Sammis, C.G. (2003). Characterization of Fault Zones, *Pure Appl. Geophys.*, **160**, 677-715.
- Ben-Zion, Y. (2008). Collective behavior of earthquakes and faults: Continuum-discrete transitions, progressive evolutionary changes, and different dynamic regimes, *Reviews of Geophysics*, **46**, doi:10.1029/2008rg000260.
- Bernard, B., Briole, P., Meyer, B., Lyon-Caen, H., Gomez, J.-M., Tiberi, C., Berge, C., Cattin, R., Hatzfeld, D., Lachet, C., Lebrun, B., Deschamps, A., Courboux, F., Larroque, C., Rigo, A., Massonnet, D., Papadimitriou, P., Kassaras, J., Diagourtas, D., Makropoulos, K., Veis, G., Papazisi, E., Mitsakaki, C., Karakostas, V., Papadimitriou, E., Papanastassiou, D., Chouliaras, M. and Stavrakakis, G. (1997). The Ms=6.2, June 15, 1995 Aigion earthquake Greece): evidence for low angle normal faulting in the Corinth rift, *J. Seism*, **1**, 131-150.
- Bernard, P., Lyon-Caen, H., Briole, P., Deschamps, A., Boudin, F., Makropoulos, K., Papadimitriou, P., Lemeille, F., Patau, G., Billiris, H., Paradissis, D., Papazissi, K., Castarède, H., Charade, O., Necessian, A., Avallone, A., Pacchiani, F., Zahradnik, J., Sacks, S. and Linde A. (2006). Seismicity, deformation and seismic hazard in the western rift of Corinth: New insights from the Corinth Rift Laboratory (CRL), *Tectonophysics*, **426**, 7–30.
- Boiselet A., (2014). *Cycle sismique et aléa sismique d'un réseau de failles actives : le cas du rift de Corinthe (Grèce)*, Ecole doctorale des Sciences de la Terre, p. 252.
- Bonnet, E., O. Bour, N. E. Odling, P. Davy, I. Main, P. Cowie, and B. Berkowitz (2001). Scaling of fracture systems in geological media, *Rev. Geophys.*, **39**(3), 347– 383.
- Braunmiller, J., and J. Nabelek (1996). Geometry of continental normal faults: seismological constraints, *J. Geophys. Res.*, **10**, 3045-3052.
- Briole, P., Rigo, A. Lyon-Caen, H., Ruegg, J.C., Papazissi, K., Mitsakaki, C., Balodimou, A., Veis, G., Hatzfeld, D. and Deschamps, A. (2000). Active deformation of the Corinth rift, Greece: Results from repeated Global Positioning System surveys between 1990 and 1995, *J. Geophys. Res.*, **105**, 605-625.
- Brooks, M. and Ferentinos, G. (1984). Tectonics and sedimentation in the Gulf of Corinth and the Zakynthos and Kefallina Channels, Western Greece. *Tectonophysics*, **101**, 25-54.
- Burton, P.W., Xu, Y., Qin, C., Tselentis, G. and Sokos E., (2004). A catalogue of seismicity in Greece and the adjacent areas for the twentieth century. *Tectonophysics*, **390**, 117–127.
- Byerlee, J.D. (1978). Friction of rocks, *Pure appl. Geophys.*, **116**, 615–626.
- Caputo, R., Chatzipetros, A., Pavlides, S. and Sboras S. (2012). The Greek Database of Seismogenic Sources (GreDaSS): state-of-the-art for northern Greece, *Annals of Geophysics*, **55**, 5, doi: 10.4401/ag-5168.
- Carver, D. and G. A. Bollinger (1981). Aftershocks of the June 20, 1978, Greece earthquake: a multimode faulting sequence, *Tectonophysics*, **73**, 343 – 363.
- Castellaro, S. and Bormann, P. (2007). Performance of different regression procedures on the magnitude conversion problem, *Bull. Seismol. Soc. Am.*, **97**, 1167-1175.
- Castellaro, S., F. Mulargia and Y. Y. Kagan (2006). Regression problems for magnitudes, *Geophys. J. Int.*, **165**, 913–930.
- Cattin, R., Chamot-Rooke, N., Pubellier, M., Rabaute, A., Delescluse, M., Vigny, C., Fleitout, L. and Dubernet, P., (2009). Stress change and effective friction coefficient along the Sumatra–Andaman–Sagaing fault system after the 26 December 2004 ($M_w = 9.2$) and the 28 March 2005 ($M_w = 8.7$) earthquakes, *Geochem. Geophys. Geosyst.*, **10**, doi:10.1029/2008GC002167.
- Chatelain J. (1978). *Etude fine de la sismicité en zone de collision continentale à l'aide d'un réseau de stations portables: la région Hindu-Kush–Pamir*, PhD. Thesis, Univ. Paul Sabatier, Toulouse.
- Chatzipetros, A. (1998). *Paleoseismological - morphotectonic study and mechanical behavior of the active fault systems at Mygdonia basin, eastern Chalkidiki and Kozani-Grevena*, PhD Thesis, Department of Geology, A.U.Th.
- Chen, C., Lee, Y., and Chang, Y. (2008). A relationship between Hurst exponents of slip and waiting time data of earthquakes: *Physica A: Statistical Mechanics and its Applications*, **387**, 18, 4643-4648.
- Chouliaras, G., Kassaras, I., Kapetanidis, V., Petrou, P and Drakatos, G. (2015). Seismotectonic Analysis of the 2013 seismic sequence at the western Corinth Rift, *J. Geodynamics*, **90**, 42-57.
- Cisternas, A., Polat, O. and Rivera, L. (2004). The Marmara Sea region: Seismic behavior in time and the likelihood of another large earthquake near Istanbul (Turkey), *J Seism.*, **8**, 427–437.
- Cladouhos, T. T., and R. A. Marrett (1996). Are fault growth and linkage models consistent with power-law distributions of lengths?, *J. Struct. Geol.*, **18**, 281–293.

- Clarke, P. J., Davies R. R., England P. C., Prsons, B., Biliris, H., Paradissis, D., Veis, G., Cross, P. A., Denys, P. H., Ashkenazi, V., Bingley, R., Kahle H. G., Muller, M. V. and Briole, P. (1998). Crustal strain in central Greece from repeated GPS measurements in the interval 1989-1997, *Geophys. J. Int.*, **135**, 195-214
- Cocard M., Kahle H.-G., Peter Y., Geiger A., Veis G., Felekis S., Billiris H. and Paradissis D. (1999). New constraints on the rapid crustal motion of the Aegean region: recent results inferred from GPS measurements (1993-1998) acrosss the West Hellenic Arc, Greece. *Earth Planet. Sc. Lett.*, **172**, 39-47.
- Cocco, M., S. Hainzl, F. Catalli, B. Enescu, A. M. Lombardi, and J. Wossner (2010). Sensitivity study of forecasted aftershock seismicity based on coulomb stress calculation and rate- and state-dependent frictional response, *J. Geophys. Res.*, **115**, B05307, doi:10.1029/2009JB006838.
- Collier, R., Pantosti, D., D'Addezio, G., De Martini, P., Masana, E. and Sakellariou, D. (1998). Paleoseismicity of the 1981 Corinth earthquake fault: seismic contribution to extensional strain in centralGreece and implications for seismic hazard. *J. Geophys. Res.*, **103**, 30001-30019.
- Console, R., and F. Catalli (2006). A rate-state model for aftershocks triggered by dislocation on a rectangular fault: A review and new insights, *Ann. Geophys.*, **49**, 1259–1273, doi:https://doi.org/10.4401/ag-3095.
- Console, R., Murru, M. and Catalli, F. (2006). Physical and stochastic models of earthquake clustering, *Tectonophysics*, **417**, 141-153, doi:10.1016/j.tecto.2005.05.052.
- Console, R., Murru, M., Falcone, G. and Catalli F. (2008). Stress interaction effect on the occurrence probability of characteristic earthquakes in Central Apennines, *J. Geophys. Res.*, **113**, B08313, doi:10.1029/2007JB005418.
- Console, R., Falcone, G., Karakostas, V., Murru, M., Papadimitriou, E. and Rhoades, D. (2013). Renewal models and coseismic stress transfer in the Corinth Gulf, Greece, fault system. *J Geophys Res*, **118**, 3655–3673, doi:10.1002/jgrb.50277.
- Console, R., R. Carluccio, E. Papadimitriou, and V. Karakostas (2015). Synthetic earthquake catalogs simulating seismic activity in the Corinth Gulf, Greece, fault system, *J. Geophys. Res. Solid Earth*, **120**, 326–343, doi:10.1002/2014JB011765.
- Copley, A., Grützner, C., Howell, A., Jackson, J., Penney, C. and Wimpenny, S. (2018). Unexpected earthquake hazard revealed by Holocene rupture on the Kenchreai Fault (central Greece): Implications for weak sub-fault shear zones, *Earth Planet. Sc. Lett.*, **486**, 141-154, https://doi.org/10.1016/j.epsl.2018.01.014.
- Correig, A.M., Urquizu, M., Vila, J. and Marti, J. (1997). Analysis of temporal occurrence of seismicity at Deception Island (Antarctica): a nonlinear approach, *Pure Appl Geophys*, **149**, 553–574.
- Cowie, P.A., Vanneste, C. and Sornette, D. (1993). Statistical physics model for the spatiotemporal evolution of faults, *J. Geoph. Res*, **98**, B12, 21809-21.821.
- Cowie, P.A. and Roberts, G.P. (2001). Constraining slip rates and spacings for active normal faults. *Journal of Structural Geology* **23**, 1901–1915.
- Cowie, P.A. Scholz, C.H. Roberts, G., Faure Walker, G.P. and Steer, P. (2013). Viscous roots of active seismogenic faults revealed by geologic slip rate variations, *Nature Geoscience* **6**, 1036–1040, doi:10.1038/ngeo1991.
- Crider, J.G. and Pollard, D.D. (1998). Fault linkage: Three-dimensional mechanical interaction between echelon normal faults. *J. Geophys. Res.*, **103**, 24373–24391.
- Das, S. and Scholz, C.H. (1981). Theory of time-dependent rupture in the earth. *J. Geophys. Res.*, **86**, doi: 10.1029/JB086iB07p06039.
- Davies, R., England, P., Parson, B., Billiris, H., Paradissis, D. and Veis, G. (1997). Geodetic strain of Greece in the interval 1892–1992, *J. Geophys. Res.*, **102**, 24 571–24 588.
- Delibasis, N. and Carydis, P. (1977). Recent earthquake activity in Trichonis region and its tectonic significance. *Ann. Geofis.* **30**, 19–81.
- Deng, J. and Sykes, L. (1997). Evolution of the stress field in southern California and triggering of moderate–size earthquakes: A 200–year perspective. *J. Geophys. Res.*, **102**: 9859–9886.
- Deniz, A., and M. S. Yüçemen (2010). Magnitude conversion problem for the Turkish earthquake data, *Nat Hazards*, **55**, 333-352.
- Dimitriu, P. P. and Papadimitriou, E.E. (1990). A fractal analysis of the shallow seismicity of the Aegean and surrounding area, Proc. XXII Gen. Assembly ESC, Barcelona, 661–667.
- Dimitriu, P., Scordilis, M. and Karakostas V. (2000). Multifractal Analysis of the Arnea, Greece Seismicity with Potential Implications for Earthquake Prediction, *Natural Hazards*, **21**, 277–295.

- Doglioni, C., Carminati, E., Petricca, P. and Riguzzi, F. (2015). Normal fault earthquakes or graviquakes, *Scientific reports*, 5:12110 | DOI: 10.1038/srep12110.
- Doutsos, T., Kontopoulos, N. and Populimenos, G. (1988). The Corinth-Patras rift as the initial stage of the continental fragmentation behind an active island arc [Greece], *Basin Res.*, **1**, 177-190.
- Doutsos, T. and Piper, D. (1990). Listric faulting sedimentation and morphological evolution of the Quaternary eastern Corinth rift, Greece: first stage of continental rifting, *Geol. Soc. Am. Bull.*, **102**, 812-829.
- Duverger C., Godano, M., Bernard, P., Lyon-Caen, H. and Lambotte, S. (2015). The 2003–2004 seismic swarm in the western Corinth rift: Evidence for a multiscale pore pressure diffusion process along a permeable fault system, *Geophys. Res.*, **42**, 7374-7382.
- Ekstrom, G. and P. England (1989). Seismic strain rates in regions of distributed continental deformation, *J. Geophys. Res.*, **94**, 10,231-10,257.
- El-Isa, Z.H. and Eaton, D.W. (2014). Spatiotemporal variations in the b -value of earthquake magnitude–frequency distributions: classification and causes, *Tectonophysics*, **615**, 1–11, doi: 10.1016/j.tecto.2013.12.001 .
- Engdahl, E. R., R. D. van der Hilst, and R. P. Buland (1998). Global teleseismic earthquake relocation with improved travel time and procedures for depth determination, *Bull. Seismol. Soc. Am.* **88**, 722–743.
- Erikson, L. (1986). User's manual for DIS3D: A three-dimensional dislocation program with applications to faulting in the Earth. Masters Thesis, Stanford Univ., Stanford, Calif, 167.
- Feng, L., Newman, A.V., Farmer, G.T., Psimoulis, P. and Stiros, S.T. (2010). Energetic rupture, coseismic and post-seismic response of the 2008 MW 6.4 Achaia-Elia Earthquake in northwestern Peloponnese, Greece: an indicator of an immature transform fault zone, *Geophys. J. Int.*, **183**, 103–110.
- Flotté, N., Sorel, D., Müller, C. and Tensi, J. (2005). Along strike changes in the structural evolution over a brittle detachment fault: Example of the Pleistocene Corinth–Patras rift (Greece). *Tectonophysics*, **403**, 77-94.
- Ford, M., Rohais, S., Williams, E.A., Bourlange, S., Joussetin, D., Backert, N. and Malartre, F. (2013). Tectono-sedimentary evolution of the western Corinth rift (Central Greece), *Basin Res.*, **25**, 3–25, doi: 10.1111/j.1365-2117.2012.00550.x.
- Galanopoulos, A. G. (1953). Katalog der Erdbeben in Griechenland zur die Zeit von 1879 bis 1892, *Ann. Geol. Pays Hellen.*, **5**, 115–229.
- Gallovic, F., Zahradnik, J., Krizova, D., Plicka, V., Sokos, E., Serpetsidaki, A. and Tselentis G-A. (2009). From earthquake centroid to spatial-temporal rupture evolution: Mw 6.3 Movri Mountain earthquake, June 8, 2008, Greece, *Geoph. Res.Let.*, **36**, L21310, doi:10.1029/2009GL040283.
- Ganas A., G. Drakatos, J. Bosy, L. Petro, B. Kontny, M. Stercz, N. Melis, S. Cacon, M. Papanikolaou, A. Pirentis, and Kiratzi, A. (2007). Monitoring of the Kaparelli fault 2003-2006 (COST Action 625 Results). *Bulletin of the Geological Society of Greece* **40**, 287-296.
- Ganas, A., E. Serpelloni, G. Drakatos, M. Kolligri, I. Adamis, C. Tsimi, and E. Batsi (2009). The Mw 6.4 SW-Achaia (western Greece) earthquake of 8 June 2008: Seismological, field, GPS observations and stress modeling, *J. Earthquake Eng.*, **13**, 1101– 1124, doi: 10.1080/13632460902933899.
- Ganas, A., Chousianitis, K., Batsi, E., Kolligri, M., Agalos, A., Chouliaras, G. and Makropoulos, K., (2012). The January 2010 Efpalion earthquakes (Gulf of Corinth, Central Greece): earthquake interactions and blind normal faulting, *J. Seismol.*, **17**, 465–484, doi: 10.1007/s10950-012-9331-6.
- Gautier, P., Brun, J., Moriceau, R., Sokoutis, D., Martinod, J. and Jolivet, L. (1999). Timing, kinematics and cause of Aegean extension: a scenario based on a comparison with simple analogue experiments, *Tectonophysics*, **315**, 31–72.
- Gautier, S., Latorre, D., Virieux, J., Deschamps, A., Skarpeles, C., Sotiriou, A., Serpetsidaki, A. and Tselentis, A. (2006). A new passive tomography of the Aigion area (gulf of Corinth Greece) from the 2002 data set. *Pure Appl. Geophys.*, **163**, 431-453.
- Gkarlaouni, C., Papadimitriou, E., Kiliyas, A., Falalakis, G. and Gemitzi, A. (2007). The evolution of the stress field in eastern Macedonian and Thrace, *Bulletin of the Geological Society of Greece*, XXXVII, *Proceedings of the 11th International Congress*, Athens, May, 2007, **1**, 321–332.
- Global Positioning System measurements of present-day crustal movements in the Arabia-Africa-Eurasia plate collision zone, *J. Geophys. Res.*, **102**, 9983–9999.

- Godano M., Deschamps A., Lambotte S., Lyon-Caen H., Bernard P., and Pacchiani F. (2014). Focal mechanisms of earthquake multiplets in the western part of the Corinth rift (Greece): influence of the velocity model and constraints on the geometry of the active faults, *J. Int.*, **197**, 1660–1680, doi:10.1093/gji/ggu059.
- Goldsworthy, M. and Jackson, J. (2000). Active normal fault evolution in Greece revealed by geomorphology and drainage patterns, *Journal of the Geological Society of London*, **157**, 967–981.
- Goldsworthy, M. and Jackson, J. (2001.) Migration of activity within normal fault systems: examples from the Quaternary of mainland Greece, *Journal of Structural Geology*, **23**, 489–506.
- Goldsworthy, M., Jackson, J. and Haines, J. (2002). The continuity of active fault systems in Greece. *Geophys. J. Int.*, **148**, 596–618.
- Gutenberg B., and Richter C.F. (1944). Frequency of earthquakes in California, *Bull. Seismol. Soc. Am.* **34**: 185–188.
- Hanks, T.C. and Kanamori, H., (1979). A moment magnitude scale, *J. Geophys. Res. B Solid Earth*, **84**, 2348–2350, doi: 10.1029/JB084iB05p02348.
- Hardacre, K. M., and Cowie P. A. (2003) Controls on strain localization in a two-dimensional elastoplastic layer: Insights into size-frequency scaling of extensional fault populations, *J. Geophys. Res.*, **108**, 2529, doi:10.1029/2001JB001712.
- Harris, R. and Simpson, R. (1998) Suppression of Large Earthquakes by Stress Shadows: A Comparison of Coulomb and Rate – and – State Failure, *Journal of Geophysical Research*, **103**, 24439–24451.
- Harris, R.A. (1998). Introduction to special section: stress triggers, stress shadows, and implications for seismic hazard, *J. Geophys. Res.*, **103**, 24 347–24 358.
- Haslinger, F., Kissling, E., Ansoerge, J., Hatzfeld, D., Papadimitriou, E., Karakostas, V., Makropoulos, K., Hatzfeld, D, Karakostas V, Ziazia M, Kassaras I, Papadimitriou E, Makropoulos K, Voulgaris N. and Papaioannou, Ch. (2000). Microseismicity and faulting geometry in the Gulf of Corinth, *Geophys. J. Intern.*, **141**: 438–456.
- Hatzfeld, D., Christodoulou, A., Scordilis, E., Panagiotopoulos, D. and Hatzidimitriou, M. (1986/87). A microearthquake study of the Mygdonian graben (northern Greece). *Earth Planet. Sc. Lett.*, **81**, 379–396.
- Hatzfeld, D., Pedotti, G., Hatzidimitriou, P. and Makropoulos, K. (1990). The strain pattern in the western Hellenic arc deduced from a microearthquake survey, *Geophys. J. Int.*, **101**, 181–202.
- Hatzfeld, D., Kementzetzidou, D., Karakostas, V., Ziazia, M., Nothard, S., Diagourtas, D., Deschamps, A., Karakaisis, G., Papadimitriou, P., Scordilis, M., Smith, R., Voulgaris, N., Kiratzi, S., Makropoulos, K., Bouin, M.P. and Bernard, P. (1996). The Galaxidi earthquake of 18 November 1992: A possible asperity within the normal fault system of the Gulf of Corinth (Greece), *Bull. Seismol. Soc. Am.*, **86**, 1987–1991.
- Hatzidimitriou, P.M., Hatzfeld, D., Scordilis, E.M., Papadimitriou, E.E. and Christodoulou, A.A., (1991). Seismotectonic evidence of an active normal fault beneath Thessaloniki (Greece). *Terra Motae* **3**, 648–654.
- Hickman, S., R. H. Sibson, and R. Bruhn (1995). Introduction to special section: mechanical involvement of fluids in faulting, *J. Geophys. Res.*, **100**, 12,831–12,840.
- Holliday, J.R., Turcotte, D.L. and Rundle, J.B. (2008). A Review of Earthquake Statistics: Fault and Seismicity-Based Models, ETAS and BASS, *Pure and Applied Geophysics* **165**:1003–1024 doi:10.1007/s00024-008-0344-6.
- Hurst, H.E. (1951). "Long-term storage of reservoirs: an experimental study," *Transactions of the American Society of Civil Engineers*, **116**, 770–799.
- Hutton, L. and Boore, D. (1987). The M scale in southern California. *Bull. Seismol. Soc. Am.*, **77**, 2074–2094.
- Imoto, M. (1991). Changes in the magnitude frequency b-value prior to large ($M \geq 6.0$) earthquakes in Japan, *Tectonophysics*, **193**, 311–25, doi: 10.1016/0040-1951(91)90340-X.
- Ishibe, T., Shimazaki, K., Tsuruoka, H., Yamanaka, Y., and Satake K. (2011). Correlation between Coulomb stress changes imparted by large historical strike-slip earthquakes and current seismicity in Japan. *Earth Planet Sp*, **63**, 12, <https://doi.org/10.5047/eps.2011.01.008>.
- Jackson, J. A. and McKenzie, D.P. (1988). The relationship between plate motions and seismic tensors and the rate of active deformation in the Mediterranean and Middle East., *Geophys. J. Intern.*, **93**, 45–73.

- Jackson, J. A., J. Cagnepain, G. Houseman, G. C. P. King, P. Papadimitriou, C. Soufleris, and J. Virieux (1982). Seismicity, normal faulting and the geomorphological development of the Gulf of Corinth (Greece): The Corinth earthquakes of February and March 1981, *Earth Planet. Sci. Lett.*, **57**, 377–397.
- Jackson, J.A. and McKenzie, D.P. (1983). The geometrical evolution of normal fault systems, *J. Struct. Geol.*, **5**, 471–482
- Jackson, J.A. and White, N.J. (1989). Normal faulting in the upper continental crust: observations from regions of active extension, *J. Struct. Geol.*, **11**, 15–36.
- Janský J., Plicka V. and Novotný O. (2007). Determining a 1-D velocity model of the uppermost crust from P and S arrival times using the neighbourhood algorithm: synthetic test, *Acta Geodyn. Geomater.*, **4**, 5-12.
- Jaumé, S.C., (1994). Earthquakes in an evolving stress/strain field. PhD thesis, Columbia University, New York.
- Jolivet, L., Faccenna, C., Huet, B., Labrousse, L., Le Pourhiet, L., Lacombe, O., Lecomte, E., Burov, E., Denèle, Y., Brun, J.-P., Philippon, M., Paul, A., Salaün, G., Karabulut, H., Piromallo, C., Monié, P., Gueydan, F., Okay, A.I., Oberhänsli, R., Pourteau, A., Augier, R., Gadenne, L. and Driussi, O. (2013). Aegean tectonics: Strain localisation, slab tearing and trench retreat, *Tectonophysics*, 597-598, 1–33.
- Jonsdottir, K., Lindman, M., Roberts, R., Lund, B. and Bödvarsson, R. (2006). Modeling fundamental waiting time distributions for earthquake sequences, *Tectonophysics*, **424**, 195–208.
- Julia, J., Nyblade, A.A., Durrheim, R.J., Linzer, L.M., Gok, R., Walter, W., Spottiswoode, S.M., and Dirks, P.H.G.M. (2009) A Wadati filter for mine-induced seismicity, *South African Journal of Geology*, **112**, 371-380.
- Kafka, A. L., and S. Z. Levin (2000). Does the spatial distribution of smaller earthquakes delineate areas where larger earthquakes are likely to occur?, *Bull. Seismol. Soc. Am.* **90**, no. 3, 724–738.
- Kagan, Y.Y. and Jackson D.D. (1991a). Long-term earthquake clustering, *Geophys. J. Int.*, **104**, 117-133.
- Kagan, Y.Y. and Jackson D.D. (1991b). Seismic gap hypothesis: Ten years after, *J. Geophys. Res.*, **96**, 21,419-21,431.
- Kagan, Y.Y. and Jackson, D.D. (1998). Spatial aftershock distribution: Effect of normal stress, *J. Geophys. Res.*, **103**, 24.453-24.467.
- Kamberis E., Sotiropoulos S., Aximniotou O., Tsaila-Monopoli S. and Ioakim C. (2000). Late Cenozoic deformation of Gavrovo and Ionian zone in NW Peloponnesus (western Greece), *Annali di Geofisica*, **43**, 905-19.
- Kanamori H. and Anderson D. (1975). Theoretical basis of some empirical relations in seismology.
- Kapetanidis, V., Deschamps, A., Papadimitriou, P., Matrullo, E., Karakonstantis, A., Bozionelos, G., Kaviris, G., Serpetsidaki, A., Lyon-Caen, H., Voulgaris, N., Bernard, P., Sokos, E. and Makropoulos, K. (2015). The 2013 earthquake swarm in Helike, Greece: seismic activity at the root of old normal faults, *Geophys. J. Int.*, **202**, 2044–2073, doi: 10.1093/gji/ggv249.
- Kapetanidis, V. (2017). *Spatiotemporal patterns of microseismicity for the identification of active fault structures using seismic waveform cross-correlation and double-difference relocation*, PhD Thesis, National and Kapodistrian University of Athens, 365.
- Karakaisis, G.F. and Mikumo, T., (1993). Dynamic fault rupture process during the 1978 Thessaloniki earthquake, northern Greece. In: G. Ranalli (Editor), Heat Flow, Rock Mechanics, and Seismicity. *Tectonophysics*. **217**, 65-71.
- Karakostas, B. G., Papadimitriou, E. E., Hatzfeld, D., Makaris, D. I., Makropoulos, K. C., Diagourtas, D., et al. (1994). The aftershock sequence and focal properties of the July 14, 1993 (Ms = 5.4) Patras earthquake. *Bulletin of the Geological Society of Greece*, XXX/5, 167–174.
- Karakostas, V, Karagianni, E. and Paradisopoulou, P. (2012). Space–time analysis, faulting and triggering of the 2010 earthquake doublet in western Corinth Gulf. *Nat Hazards*, **63**, 1181–1202.
- Karakostas, V. G., Papadimitriou, E. E. and Gospodinov, D. (2013). Modeling the 2013 North Aegean (Greece) seismic sequence: geometrical and frictional constraints, and aftershock probabilities. *Geophysical Journal International*.
- Karakostas, V., E. Papadimitriou, and D. Gospodinov (2014). Modelling the 2013 North Aegean (Greece) seismic sequence: geometrical and frictional constraints, and aftershock probabilities, *Geophys. J. Int.* **197**, 1, 525-541, DOI: 10.1093/gji/ggt523.

- Karakostas, V. G., Papadimitriou, E. E. and Mesimeri M. (2015). A homogeneous M_w equivalent earthquake catalog for Greece 1990-2015. Proceedings of the International Conference, ScinTE 2015.
- Karakostas, V., Papadimitriou, E., Mesimeri, M., Gkarlaouni, C. and Paradisopoulou, P. (2015). The 2014 Kefalonia Doublet (M_w 6.1 and M_w 6.0), Central Ionian Islands, Greece: Seismotectonic Implications along the Kefalonia Transform Fault Zone, *Acta Geophys.*, **63**, 1–16, doi: 10.2478/s11600-014-0227-4.
- Karakostas, V., Mirek, K., Mesimeri, M., Papadimitriou, E. and Mirek, J. (2017). The Aftershock Sequence of the 2008 Achaia, Greece, Earthquake: Joint Analysis of Seismicity Relocation and Persistent Scatterers Interferometry, *Pure Appl. Geophys.* **174**, 151-176.
- Karamanos, Ch. K., Karakostas, V., Seeber, L., Papadimitriou, E. E. and Kiliyas, A. A. (2010). Recent seismic activity in central Greece revealing local seismotectonic properties. *Bull. Geol. Soc. Greece*, **XLIII**, 2075–2083.
- Karamanos, Ch., Karakostas V. and Papadimitriou, E. E. (2007). Present 2005–2006 strong seismic activity in Greece under the aspect of seismicity parameters temporal variation analysis. *Bull. Geol. Soc. Greece*, **XXXX**, 1055–1062.
- Kijko, A. (1993). Some recent developments in mining induced seismicity. Lecture notes. Second Workshop on non-linear dynamics and earthquake prediction, 22 November-10 December 1993. International Centre of Theoretical Physics, Trieste, Italy, 35.
- King, G.C.P., Ouyang, Z.X., Papadimitriou P., Deschamps, A., Gagnepain, J., Houseman, G., Jackson, J.A., Soufleris, C. and Virieux, J. (1985). The evolution of the Gulf of Corinth (Greece): an aftershock study of the 1981 earthquakes, *Geophys. J. R. Astr. Soc.*, **80**, 677-683.
- King, G. C. P., Stein, R. S. and J. Lin (1994). Static stress changes and the triggering of earthquakes, *Bull. Seismol. Soc. Am.*, **84**, 935-953.
- King, G. C. P. and Cocco, M. (2001). Fault interaction by elastic stress changes: New clues from earthquake sequences, *Adv. Geophys.*, **44**, 1-38.
- Kiratzi, A. and Louvari, E. (2003). Focal mechanisms of shallow earthquakes in the Aegean Sea and the surrounding lands determined by waveform modeling: a new database. *J. Geodyn.*, **36**, 251–274.
- Kiratzi, A. et al., (2008). The April 2007 earthquake swarm near Lake Trichonis and implications for active tectonics in western Greece, *Tectonophysics*, **452**, 51–65, doi:10.1016/j.tecto.2008.02.009.
- Kissel, C. and Laj, C. (1988). The Tertiary geodynamical evolution of the Aegean Arc: A paleomagnetic reconstruction, *Tectonophysics*, **146**, 183-201
- Kissel, C., Laj, C. and Muller, C. (1985). Tertiary geodynamical evolution of northwestern Greece: paleomagnetic results. *Earth and Planetary Science Letters*, **72**, 190–204.
- Klein F. (2000). User's Guide to HYPOINVERSE–2000, a Fortran program to solve earthquake locations and magnitudes. U.S. Geol. Surv. Open File Report 02–171 Version 1.0.
- Kokkalas, S., Pavlides, S., Koukouvelas, I., Ganas, A. and Stamatopoulos, L. (2007). Paleoseismicity of the Kaparelli fault (Eastern Corinth Gulf): evidence for earthquake recurrence and fault behavior, *Boll. Soc. Geol. Ital.*, **126**, 387-395.
- Konstantinou, K. I., Evangelidis C. P. and N. S. Melis (2011). The 8 June 2008 M_w 6.4 earthquake in northwest Peloponnese, western Greece: A case of fault reactivation in an overpressured lower crust?, *Bull. Seism. Soc. Am.* **101** (1), 438 – 445.
- Konstantinou, K. I., Melis N. S., Lee S.-J., Evangelidis C. P., and Boukouras K. (2009). Rupture process and aftershocks relocation of the 8 June 2008 M_w 6.4 earthquake in Northwest Peloponnese, Western Greece, *Bull. Seism. Soc. Am.* 99(6), 3374 – 3389, doi: 10.1785/0120080301.
- Kostrov, V. (1974). Seismic moment and energy of earthquakes, and seismic flow of rock *Izv. Acad. Sci. USSR Phys. Solid Earth*, **1**, 23-24.
- Kotti, E. and Tsaklidis, G. (2012). Statistical analysis of fractal point processes: an application to Northern Aegean (Greece) seismicity', 2nd Stochastic Modeling Techniques and Data Analysis International Conference (SMTDA).
- Kotzev V., Nakov R., Georgiev T., Burchfiel B. and King R. (2001). *Crustal motion and strain accumulation in western Bulgaria*. *Tectonophysics*, **413**, 189 – 200.
- Kotzev, V., Nakov, R., Georgiev, Tz., Burchfiel, B.C. and King, R.W. (2006). Crustal motion and strain accumulation in western Bulgaria, *Tectonophysics*, **413**, 127-145.
- Koukouvelas, I.K., Kokkalas, S. and Xypolias, P. (2009). Surface deformation during the M_w 6.4 (8 June 2008) Movri Mountain earthquake in the Peloponnese, and its implications for the



- seismotectonics of western Greece. *Int. Geol. Rev.*, **52**, 249–268, doi: 10.1080/00206810802674329.
- Koukouvelas, I.K., Zygouri, V., Papadopoulos, G.A. and Verroios, S., (2017). Holocene record of slip-predictable earthquakes on the Kenchreai Fault, Gulf of Corinth, Greece, *J. Struct. Geol.* doi: 10.1016/j.jsg.2016.12.001.
- Lambotte, S., Lyon-Caen, H., Bernard, P., Deschamps, A., Patau, G., Nercessian, A., Pacchiani, F., Bourouis, S., Drilleau, M. and Adamova, P. (2014). Reassessment of the rifting process in the Western Corinth Rift from relocated seismicity. *Geophys. J. Int.*, **197**, 1822–1844, doi: 10.1093/gji/ggu096.
- Latorre, D., Virieux, J., Monfret, T., Monteiller, V., Vanorio, T., Got, J.-L., Lyon- Caen, H. (2004). A new seismic tomography of Aigion area (Gulf of Corinth, Greece) from the 1991 data set, *Geophys. J. Int.*, **159**, 1013–1031, doi: 10.1111/j.1365-246X.2004.02412.x.
- Le Pichon, X. and Angelier, J. (1979). The Hellenic arc and trench system: A key to the neotectonic evolution of the eastern Mediterranean area. *Tectonophysics*, **60**, 1–42. doi:10.1016/0040-1951(79)90131-8.
- Le Pichon, X., Chamot-Rooke, N., Lallemand, S., Noomen, R. and Veis, G. (1995). Geodetic determination of the kinematics of central Greece with respect to Europe, *J. Geophys. Res.*, **100**, 12,675– 12,690.
- Lee, Y.T., Chen, C.C., Hasumi, T. and Hsu, H.L. (2009). Precursory phenomena associated with large avalanches in the long-range connective sand pile model II: an implication to the relation between the b-value and the Hurst exponent in seismicity, *Geophys. Res. Lett.*, **36**, L02308. doi: 10.1029/2008GL03654 .
- Lee, Y.T., Telesca, L. and Chen, C.C. (2012). Negative correlation between frequency–magnitude power–law exponent and Hurst coefficient in the long–range connective sandpile model for earthquakes and for real seismicity, *Europhys. Lett.*, **99**: 5pp.
- Leeder, M., Seger, M.J. and Stark, C.P. (1991). Sedimentation and tectonic geomorphology adjacent to major active and inactive normal faults, Southern Greece. *J. Geol. Soc. Lond.*, **148**, 331–343.
- Leeder M. R. and J. A. Jackson, J.A., (1993). The interaction between normal faulting and drainage in active extensional basins, with examples from the western United States and central Greece, *Basin Res.*, **5**, 79–102.
- Leeder, M.R., Portman, C., Andrews, J.E., Collier, R.E.L., Finch, E., Gawthorpe, R.L., McNeill, L.C., Perez-Arlucea, M. and Rowe, P. (2005). Normal faulting and crustal deformation, Alkyonides Gulf and Perachora Peninsula, Eastern Gulf of Corinth rift, Greece. *J. Geol. Soc.*, **162**, 549–561.
- Leptokaropoulos, K.M., Papadimitriou, E.E., Orlecka–Sikora, B. and Karakostas, V.G (2012.) Seismicity rate changes in association with evolution of the stress transfer in the Northern Aegean Sea, Greece, *Geophys. J. Int.*, **188**, 1322– 1338, doi:10.1111/j.1365–246X.2011.05337.x.
- Leptokaropoulos, K. Karakostas, V. Papadimitriou, E. Adamaki, A. Tan, O. and Inan, S. (2013). A homogeneous earthquake catalogue compilation for western Turkey and magnitude completeness determination, *Bull. Seismol. Soc. Am.*, **103**, 2739–2751.
- Leptokaropoulos, K.M. (2014). *Study of the influence of time dependent stress changes on seismicity rates with contribution in probabilistic seismic hazard assessment in Greece*, Aristotle University of Thessaloniki, Greece, p. 320.
- Leptokaropoulos, K.M., Papadimitriou, E.E., Orlecka–Sikora, B. and Karakostas, V.G. (2015). An Evaluation of Coulomb Stress Changes from Earthquake Productivity Variations in the Western Gulf of Corinth, Greece, *Pure Appl. Geophys.*, doi: 10.1007/s00024-015-1057-2
- Leptokaropoulos K. M., Papadimitriou E., Orlecka–Sikora B, and Karakostas V. (2016). An Evaluation of Coulomb Stress Changes from Earthquake Productivity Variations in the Western Gulf of Corinth, Greece, *Pure Appl. Geophys.*, doi: 10.1007/s00024-015-1057-2.
- Leptokaropoulos, K. and Gkarlaouni, C. (2016). A magnitude independent space – time earthquake clustering algorithm (MISTIC). *Bull. Geol. Soc. Greece, Proceedings of the 14th International Congress of the Geological Society of Greece*, L, 1359–1368.
- Lin, J., and Stein, R. S., (2004). Stress triggering in thrust and subduction earthquakes, and stress interaction between the southern San Andreas and nearby thrust and strike slip faults, *J. Geophys. Res.*, **109**, B02303, doi:10.1029/2003JB002607.
- Liotier, Y. (1989). *Modelisation des ondes de volume des seismes de l'arc egeen*, PhD Thesis, DEA de l' Universite Joseph Fourier, Grenoble, France.
- Lo, A.W. (1991). Long-term memory in stock market prices, *Econometrica* **59**, 1279–1313.
- Lomnitz, C. (1994). *Fundamentals of earthquake prediction*. John Wiley and Sons, New York, 165–171.

- Lyon-Caen, H., Papadimitriou, P., Deschamps, A., Bernard, P., Makropoulos, K., Pacchiani, F. and Patau, G. (2004). First results of the CRLN seismic network in the western Corinth Rift: evidence for old-fault reactivation, *Comptes Rendus Geosciences*, **336**, 343–351.
- Lyros, E., Kostelecky, J., Plicka, V., Vratislav, F., Sokos, E. and Nikolakopoulos, K. (2019). The Aitolio-Akarnania (Western Greece) GNSS network PPGNet – first results, *4th Joint International Symposium on Deformation Monitoring (JISDM)*, 15-17 May 2019, Athens, Greece.
- Ma, K.F., Chan, C.H. and Stein, R.S. (2005). Response of seismicity to Coulomb stress triggers and shadows of the 1999 Mw = 7.6 Chi-Chi, Taiwan, earthquake, *J. Geophys. Res.*, **110**, B05S19, <https://doi.org/10.1029/2004JB003389>.
- Maggi, C., Frepoli, A., Cimini, G., Console, R. and Chiappini, M. (2009). Recent seismicity and crustal stress field in the Lucanian Apennines and surroundings areas (Southern Italy): seismotectonic implications, *Tectonophysics*, **463**, 130-144.
- Mandelbrot, B. and Wallis, J. (1969). Robustness of the rescaled range R/S in the measurement of noncyclic long run statistical dependence, *Water Res*, **5**, 967–988.
- Mangira, O., Vasiliadis, G., Papadimitriou, E. (2017). Application of a linked stress release model in Corinth Gulf and Central Ionian Islands (Greece), *Acta Geophysica, De Gruyter Open*, **65**, 517 - 531. [ff10.1007/s11600-017-0031-zff](https://doi.org/10.1007/s11600-017-0031-zff). [ffhal-01676809f](https://doi.org/10.1007/s11600-017-0031-zff)
- Margaris, B. et al. (2010). The 8 June 2008 Mw 6.5 Achaia-Elia, Greece earthquake: source characteristics, ground motions and ground failure, *Earthq. Spectra*, **26**, 399–424, [doi:10.1193/1.3353626](https://doi.org/10.1193/1.3353626).
- Margaris, B. N. and Hadtzidimitriou, M. (1997). Source Parameters of the Arnea Earthquake, Ms=5.8, Based on Stochastic Simulation Method, 3rd Hellenic Conference on Geotechnical Engineering, Patra, 22-23 March, vol.2.
- Marone, C. and Scholz, C. (1988). The depth of seismic faulting and the upper transition from stable to unstable slip regimes, *Geophys. Res. Letters*, **15** (6), 621-624.
- Martinod, J., Hatzfeld, D., Savvaidis, P. and Katsambalos, K. (1997). Rapid N-S extension in the Mygdonian graben (Northern Greece) deduced from repeated geodetic surveys, *Geophys. Res. Letters*, **24**, 3293-3296.
- Matsumura, S. (1984). A one parameter expression of seismicity patterns in space and time, *Bull. Seism. Soc. Am.*, **74**, 2529 – 2576.
- McClusky, S., S. Balassania, A. Barka, C. Demir, S. Ergintav, I. Georgiev, O. Gurkan, M. Hamburger, K. Hurst, H. Kahle, L. Kastens, G. Kekelidze, R. W. King, V. Kotzev, O. Lenk, S. Mahmoud, A. Mishin, M. Nadariya, A. Ouzounis, D. Paradissis, Y. Peter, M. Prilepin, R. Reilinger, I. Sanli, H. Seeger, A. Taeleb, M. N. Toksoz, and G. Veis, (2000). GPS constraints on plate motions and deformation in the Eastern Mediterranean: Implications for plate dynamics, *J. Geophys. Res.*, **105**, 5695–5719, [doi:10.1029/1999JB900351](https://doi.org/10.1029/1999JB900351).
- McKenzie, D. (1972). Active tectonics of the Mediterranean region, *Geophys. J. R. Astron. Soc.*, **30**, 109–185.
- McKenzie, D. (1978). Active tectonics of the Alpine-Himalayan belt: the Aegean Sea and surrounding regions, *Geophys. J.R. Astron. Soc.*, **55**, 217-254.
- McNeill, L.C., Cotterill, C.J., Henstock, T.J., Bull, J.M., Stefatos, A., Collier, R.E.L., Papatheoderou, G., Ferentinos, G. and Hicks, S.E. (2005). Active faulting within the offshore western gulf of Corinth, Greece: implications for models of continental rift deformation, *Geology*, **33**, 241-244.
- Melis, N., and Tselentis, G. (1998). 3-D P-wave velocity structure in western Greece determined from tomography using earthquake data recorded at the University of Patras seismic network (PATNET), *Pure Appl. Geophys.*, **152**, 329 -348.
- Melis, N., Brooks, M. and Pearce, R.G. (1989). A microearthquake study in the Gulf of Patras region, western Greece, and its seismotectonic interpretation. *Geophysical Journal*, **98**, 515-524.
- Mercier J., Carey-Gailhardis E., Mouyaris N., Simeakis K., Roundoyannis T. and Anghelidhis C. (1983). Structural analysis of recent and active faults and regional state of stress in the epicentral area of the 1978 Thessaloniki earthquakes (northern Greece), *Tectonics*, **2**, 577-600.
- Mercier, J.L. and Carey-Gailhardis, E. (1989). Regional state of stress and characteristic fault kinematic instabilities shown by aftershock sequences: the 1978 Thessaloniki (Greece) and 1980 Campania-Lucania (Italy) earthquakes as examples, *Earth Planet. Sci. Lett.*, **92**, 247-264.
- Mercier, J.L., Sorel, D., Vergely, P. and Simeakis, K. (1989). Extensional tectonic regimes in the Aegean basins during the Cenozoic, *Basin Res.*, **2**, 49-71.



- Mesimeri, M., Karakostas, V., Papadimitriou, E., Schaff, D. and Tsaklidis, G. (2015). Spatio-temporal properties and evolution of the 2013 Aigion earthquake swarm (Corinth Gulf, Greece), *J. Seismol.*, **20**, 595–614, doi: 10.1007/s10950-015-9546-4.
- Mesimeri, M., Karakostas, V., Papadimitriou, E., Tsaklidis, G. and Tsapanos, T. (2017). Detailed microseismicity study in the area of Florina (Greece): Evidence for fluid driven seismicity, *Tectonophysics*, **694**, 424–435.
- Mesimeri, M. (2018). *Contribution to the study of earthquake swarms*, PhD Thesis, Aristotle University of Thessaloniki (in Greek).
- Messini, A., Papadimitriou, E., Karakostas, V. and Baskoutas, I. (2007). Stress interaction between thrust faults along the SW Hellenic arc (Greece), *Bull. Geol. Soc. Greece*, XXXVII, Proceedings of the 11th International Congress, Athens, May, 2007, 1, 386 - 398.
- Michailos, K. (2015). Seismicity and seismotectonic properties of southern Aegean, Master Thesis, Aristotle University of Thessaloniki, p. 116. (in Greek).
- Michas, G., Sammonds, P. and Vallianatos, F. (2015). Dynamic Multifractality in Earthquake Time Series: Insights from the Corinth Rift, Greece, *Pure Appl. Geophys.* **172**, 1909-1921. doi:10.1007/s00024-014-0875-y.
- Mignan, A. and Woessner, J. (2010). Completeness magnitude in earthquake catalogs, *Community Online Resource for Statistical Seismicity Analysis*, doi:10.5078/corssa-00180805.
- Mildon, Z.K., Roberts, G.P., Faure Walker, J.P. et al. (2019). Coulomb pre-stress and fault bends are ignored yet vital factors for earthquake triggering and hazard. *Nat Commun*, **10**, 2744 <https://doi.org/10.1038/s41467-019-10520-6>.
- Moretti, I., Sakellariou, D., Lykousis, V. and Micarelli, L. (2003). The Gulf of Corinth: an active half graben? *J. Geodynamics*, **36**, 323-340.
- Morewood, N.C. and Roberts, G.P. (1999). Lateral propagation of the surface trace of the South Alkyonides normal fault segment, central Greece: its impact on models of fault growth and displacement–length relationships, *J. Struct. Geol.* **21**, 635–652.
- Morewood, N.C. and Roberts, G.P. (2001). Comparison of surface slip and focal mechanism slip data along normal faults: an example from the eastern gulf of Corinth, Greece. *J. Struct. Geol.*, **23**, 473-487.
- Mountrakis, D., Psilovikos, A. and Papazachos, B. C. (1983). The geotectonic regime of the Thessaloniki earthquakes, In: The Thessaloniki, Northern Greece, Earthquake of June 20, 1978 and its Seismic Sequence (ed: Papazachos, B. C. and Carydis, P. G.), Tech. Chamb. Of Greece: 11-27.
- Mountrakis D., Syrides G., Polymenakos L. and Pavlides S. (1993). The neotectonic structure of the eastern margin of the Axios-Thermaikos depression at the area of western Halkidiki (central Macedonia), *Bull. Geol. Soc. Greece*, **28**, 379-395.
- Mountrakis D., Kiliyas A., Pavlides S., Sotiriadis L., Psilovikos A., Astaras Th., Vavliakis E., Koufos G., Dimopoulos G., Soulios G., Christaras V., Skordilis M., Tranos M., Spyropoulos N., Patras D., Syrides G., Lambrinos N. and Laggalis T. (1996a). Neotectonic map of Greece, Langadhas sheet. Earthquake Planning and Protection Organisation and European Centre on Prevention and Forecasting of Earthquakes, scale 1:100,000.
- Mountrakis D., Kiliyas A., Pavlides S., Sotiriadis L., Psilovikos A., Astaras Th., Vavliakis E., Koufos G., Christaras V., Skordilis M., Tranos M., Spyropoulos N., Patras D., Syrides G., Lambrinos N. and Laggalis T. (1996b). Neotectonic map of Greece, Thessaloniki sheet (scale 1:100,000). Earthquake Planning and Protection Organisation and European Centre on Prevention and Forecasting of Earthquakes.
- Mountrakis D., Tranos M., Papazachos C., Thomaidou E., Karagianni E. and Vamvakaris D. (2006). Neotectonic and seismological data concerning major active faults and the stress regimes of Northern Greece, *Geol. Soc. Special Publication*, **260**, 649-670.
- Mouratidis, A. (2010). *Contribution of -GPS and GIS-assisted spaceborne remote sensing in the morphotectonic research of Central Macedonia (N. Greece)*, PhD thesis, Aristotle University of Thessaloniki.
- Nalbant, S., Hubert, A. and King, G. (1998). Stress coupling between earthquakes in northwest Turkey and the north Aegean Sea, *J. Geoph. Res.*, **103**, 469 - 486.
- Nalbant, S. S., J. McCloskey, S. Steacy, and A. Barka, (2002). Stress accumulation and increased seismic risk in Eastern Turkey, *Earth Planet. Sci. Lett.*, **195**, 291 – 298.
- Nixon, C. W., et al. (2016). Rapid spatiotemporal variations in rift structure during development of the Corinth Rift, central Greece, *Tectonics*, **35**, doi:10.1002/2015TC004026.

- Novotny, O., Jansky, J., Plicka, V., Lyon-Caen, H. (2008). A layered model of the upper crust in the Aigio region of Greece, inferred from arrival times of the 2001 earthquake sequence. *Stud Geophys Geod.*, **52**, 123–131.
- Olszewska, D., Lasocki, S. and Leptokaropoulos, K. (2017). Non-stationarity and internal correlations of the occurrence process of mining-induced seismic events, *Acta Geophys.*, DOI 10.1007/s11600-017-0024-y.
- Pacchiani, F. and Lyon-Caen, H. (2010). Geometry and spatio-temporal evolution of the 2001 Agios Ioannis earthquake swarm (Corinth Rift, Greece), *Geophys. J. Int.*, **180**, 59–72.
- Palyvos, N., S. Pucci, F. Lemeille, and S. Pavlides (2004). Paleoseismological investigations across the Aigion fault (Gulf of Corinth, Greece), *C. R. Geosci.*, **336**, 335 – 342.
- Panagiotopoulos, D. and Papazachos, B. (1985). Travel times of Pn waves in the Aegean and surrounding area, *Geophys J R Astron. Soc.*, **80**, 165-176.
- Pantosti, D., De Martini, P.M., Koukouvelas, I.K., Stamatopoulos, L., Palyvos, N., Pucci, S., Lemeille, F. and Pavlides, S. (2004). Palaeoseismological investigations of the Aigion Fault (Gulf of Corinth, Greece), *C. R. Geoscience*, **336**, 335–342.
- Pantosti, D., Martini, P.D., Koukouvelas, I. Stamatopoulos, L., Palyvos, N., Pucci, S., Lemeille, F. and Pavlides S. (2004). Palaeoseismological investigations of the Aigion Fault (Gulf of Corinth, Greece), *Compt Rendus Geosci.*, **336**, 335–342, <https://doi.org/10.1016/j.crte.2003.12.005>.
- Papadimitriou, E.E. and Sykes, L.R. (2001). Evolution of the stress field in the northern Aegean Sea (Greece), *Geophys. J. Intern.*, **146**, 747–759.
- Papadimitriou, E.E. (2002). Mode of strong earthquake recurrence in central Ionian Islands (Greece). Possible triggering due to Coulomb stress changes generated by the occurrence of previous strong shocks, *Bull. Seism. Soc. Am.*, **92**, 3293–3308.
- Papadimitriou, E.E., and Karakostas, V.G. (2003). Episodic occurrence of strong (Mw≥6.2) earthquakes in Thessalia area (central Greece), *Earth Plant. Sci. Lett.*, **215**, 395-409.
- Papadimitriou, E., Sourlas, G. and Karakostas, V. (2005). Seismicity Variations in the Southern Aegean, Greece, Before and After the Large (M7.7) 1956 Amorgos Earthquake Due to Evolving Stress. *Pure appl. Geophys.* **162**, 783–804.
- Papadimitriou, E. E., Evison, F. F., Rhoades, D.A., Karakostas, V. G., Console, R. and Muru, M. R. (2006). Long-term seismogenesis in Greece: Comparison of the evolving stress field and precursory scale increase approaches, *Journal of Geophys. Res.*, **111**, B05318, doi: 10.1029/2005JB003805.
- Papadopoulos, G. A., Karastathis V., Kontoes Ch., Charalampakis M., Fokaefs A. and Papoutsis I. (2010). Crustal deformation associated with east Mediterranean strike-slip earthquakes: The 8 June 2008 Movri (NW Peloponnese), Greece, earthquake (Mw6.4), *Tectonophysics* **492**, 201 – 212.
- Papazachos, B.C. and Comninakis, P.E. (1971). Geophysical and tectonic features of the Aegean arc, *J. Geophys. Res.*, **76**, 8517–8533.
- Papazachos, B.C. (1975) Seismic activity along the Saronikos-Corinth-Patras gulfs. In: *Bulletin of the National Observatory of Athens*.
- Papazachos B., Mountrakis D., Psilovikos A. and Leventakis G. (1979). Surface fault traces and fault plane solutions of the May-June 1978 major shocks in the Thessaloniki area, Greece, *Tectonophysics*, **53**, 171-183.
- Papazachos B., Mountrakis D., Psilovikos A. and Leventakis G. (1980). Focal properties of the 1978 earthquakes in the Thessaloniki area, *Bulg. Geophys. J.*, **6**, 72-80.
- Papazachos BC, Comninakis PE, Hatzidimitriou PM, Kiriakidis EC, Kiratzi AA, Panagiotopoulos DG, Papadimitriou EE, Papaioannou CA, Pavlides SB, Tzanis E (1982). Atlas of Isoleismal Maps for Earthquakes in Greece 1902–1981. *Geophys Lab Univ Thessaloniki Publ 4*:126.
- Papazachos, B.C., Comninakis, P.E., Papadimitriou, E.E. and Scordilis, E.M. (1984). Properties of the February-March 1981 seismic sequence in the Alkionides gulf of Central Greece, *Annales Geophysicae*, **2**, 537-544.
- Papazachos BC, Papaioannou CA, Papazachos CB, Savvaidis AA. (1997). Atlas of isoseismal maps for strong earthquakes in Greece and surrounding area (426 B.C.–1995). *Geophys Lab Univ Thessaloniki Publ 4*, pp 126.
- Papazachos C., Soupios P., Savvaidis A. and Roumelioti Z. (2000). Identification of small-scale active faults near metropolitan areas: an example from the Asvestochori fault near Thessaloniki. Proc. Of the XXXII ESC General assembly, Lisbon, Portugal, 15-20 September 2000, 221-225.
- Papazachos, B. (1975). *Seismic activity along the Saronikos–Corinth–Patras gulfs*. *National Observatory of Athens*, Geodynamic Institute. Monthly Bulletin April 1975, 9.

- Papazachos, B.C., Kiratzi, A.A., and Karakostas, B.G. (1997). Towards a homogeneous moment magnitude determination for earthquakes in Greece and the surrounding area. *Bull Seismol Soc Am* **87**, 474–483.
- Papazachos, B.C., Papadimitriou, E.E., Kiratzi, A.A., Papazachos, C.B. and Louvari, E.K. (1998). Fault plane solutions in the Aegean Sea and the surrounding area and their tectonic implication, *Bol. di Geof. Teor. ed Applic.*, **39**, 199-218.
- Papazachos, C. B. (1999). Seismological and GPS evidence for the Aegean-Anatolia interaction, *Geophys. Res. Lett.*, **26**, 17, 2653-2656.
- Papazachos, B.C., Mountrakis, D.M., Papazachos, C.B., Tranos, M.D., Karakaisis, G.F. and Savvaidis, A.S. (2001). The faults that caused the known strong earthquakes in Greece and surrounding areas during 5th century B. C. up to present, *2nd Conf. Earthq. Engng. and Engin. Seism.*, 28–30 September 2001, Thessaloniki, **1**, 17–26.
- Papazachos, B., Karakostas, V., Kiratzi, A., Mergaris, B., Papazachos, C. and Scordilis, M. (2002). *Journal of Seismology*, **6**: 557-570. doi:10.1023/A:1021214126748.
- Papazachos, B. C. and Papazachou, C. B. (2003). The earthquakes of Greece (in Greek), Ziti Publ., Thessaloniki, 356, 1989.
- Papazachos, B.C., Scordilis, E.M., Panagiotopoulos, D.G. , Papazachos, C. B. and Karakaisis, G. F. (2004), Global relations between seismic fault parameters and moment magnitude of earthquakes, *Bull. Geol. Soc. Greece*, **36**, 1482–1489.
- Papazachos, B.C., Comninakis, P.E., Karakaisis, G.F., Karakostas, B.G., Papaioannou, Ch. A., Papazachos, C.B. and Scordilis, E.M. (2004a). A catalog of earthquakes in Greece and surrounding area for the period 550 BC-2004, Publ. Geophys. Lab. Univ. Thessaloniki, **1**, 338.
- Papazachos, B. C., Comninakis, P.E., Karakaisis, G.F., Karakostas, B.G., Papaioannou, Ch. A., Papazachos, C.B. and Scordilis, E.M. (2008). A catalogue of earthquakes in Greece and surrounding area for the period 550BC–2008, Geophysics Departm., Thessaloniki University Publ.
- Paradisopoulou, P.M., Karakostas, V.G., Papadimitriou, E.E., Tranos, M.T., Papazachos, C.B. and Karakaisis, G.F. (2004) Microearthquake study of the broader Thessaloniki area, *5th Intern. Symp. East. Mediter. Geol.*, 14–20 April 2004 Thessaloniki, Greece **2**, 623–626.
- Paradisopoulou, P.M., Karakostas, V.G., Papadimitriou, E.E., Tranos, M.T., Papazachos, C.B. and Karakaisis, G.F. (2006). Microearthquake study of the broader Thessaloniki area (Northern Greece), *Ann Geophys*, **49**, 1081–1093.
- Paradisopoulou P.M. (2009). Contribution to seismicity study of Greek region in association with Coulomb Stress Changes. PhD Thesis, Aristotle University of Thessaloniki, p. 291.
- Paradisopoulou, P.M., Papadimitriou E.E., Karakostas, V.G., Lasocki, S., Mirek, J. and Kiliyas, A. (2010a). Influence of stress transfer in probability estimates of $M \geq 6.5$ earthquakes in Greece and surrounding areas, *Bull. Geol. Soc. Greece*, Proceedings of the 12th International Congress, Patras, May, 2010.
- Paradisopoulou, P.M., Papadimitriou E.E., Karakostas, V.G., Taymaz, T., Kiliyas, A. and Yolsal, S. (2010b). Seismic Hazard Evaluation in Western Turkey as Revealed by Stress Transfer and Time-dependent Probability Calculations, *Pure Appl. Geophys.*, **167**, 1013–1048 DOI 10.1007/s00024-010-0085-1.
- Paradisopoulou, P., Papadimitriou, E. and Mirek, J. (2016). Significant earthquakes near the city of Thessaloniki (Northern Greece) and probability distribution on faults. *Bull. Geol. Soc. Greece*, **50**, 1389-1398.
- Parcharidis, I., Kourkouli, P., Karymbalis, E., Foumelis, M., Karathanassi V. (2013). Time Series Synthetic Aperture Radar Interferometry for Ground Deformation Monitoring over a Small Scale Tectonically Active Deltaic Environment Mornos, Central Greece, *Journal of Coastal Research*, **29**, 325 – 338, doi: 10.2112/JCOASTRES-D-11-00106.1.
- Parsons, T., R. S. Stein, R. W. Simpson, and P. A. Reasenber (1999). Stress sensitivity of fault seismicity: A comparison between limited-offset oblique and major strike slip faults, *J. Geophys. Res.*, **104**, 20,183-20,202.
- Parsons, T. (2002). Global Omori law decay of triggered earthquakes: Large aftershocks outside the classical aftershock zone, *J. Geophys. Res.*, **107**, doi:10.1029/2001JB0000646.
- Parsons, T. (2005). Significance of stress transfer in time-dependent earthquake probability calculations, *J. Geophys Res.*, **110**, doi: 10.1029/2004JB003190.
- Pavlidis, S. and Kiliyas, A. (1987). Neotectonic and active faults along the Serbomacedonian zone (SE Chalkidiki, northern Greece), *Ann.Tectonicae*, **1**, 97-104.

- Pavlidis, S., Kondopoulou, D., Kiliias, A. and Westphal M. (1988). Complex rotational deformations in the Serbo-Macedonian massif (north Greece): structural and paleomagnetic evidence, *Tectonophysics*, **145**, 3-4, 329-335.
- Pavlidis, S., Mountrakis, D., Kiliias, A. and Tranos, M. (1990). The role of strike slip movements in the extensional area of Northern Aegean (Greece), *Annales Tectonicae*, **IV**, 196–211.
- Pavlidis, S. B., and Tranos, M.D. (1991). Structural characteristics of two strong earthquakes in the North Aegean: Ierissos (1932) and Agios Efstratios (1968), *J. Struct. Geol.*, **13**, 2, 205-214.
- Pavlidis, S.B and Caputo, R. (2004). Magnitude versus faults' surface parameters: quantitative relationships from the Aegean Region, *Tectonophysics*, **380**, 159-188.
- Peacock, D.C.P., Knipe, R.J. and Sanderson D.J. (2000). Glossary of normal faults, *J. Struct. Geol.*, **22**, 291-305.
- Piccardi, L. (2000). Active faulting at Delphi, Greece: Seismotectonic remarks and a hypothesis for the geologic environment of a myth, *Geology*, **28**, 651–654, [https://doi.org/10.1130/0091-7613\(2000\)28<651:AFADGS>2.0.CO;2](https://doi.org/10.1130/0091-7613(2000)28<651:AFADGS>2.0.CO;2).
- Piccardi, L., Monti, C., Vaselli, O., Tassi, F., Gaki-Papanastassiou, K., Papanastassiou, D. (2008). Scent of a myth: tectonics, geochemistry and geomorphology at Delphi (Greece), *Journal of the Geological Society, London*, **165**, 5–18.
- Piccinini, D., Piana Agostinetti, N., Roselli, P., Ibs-von Seht, M. and Braun, T. (2009). Analysis of small magnitude seismic sequences along the Northern Apennines (Italy), *Tectonophysics*, 136-144.
- Pondrelli, S. (1999). Pattern of seismic deformation in the Western Mediterranean, *Annali di Geofisica*, **42**, 57-70.
- Pondrelli, S., A. Morelli and E. Boschi (1995). Seismic deformation in the Mediterranean area estimated by moment tensor summation, *Geophys. J. Int.*, **122**, 938-952.
- Ponomarev, A.V., Zavyalov, A.D., Smirnov, V.B. and Lockner, D.A. (1997). Physical modeling of the formation and evolution of seismically active fault zones, *Tectonophysics*, **277**, 57–81, doi: 10.1016/S0 040-1951(97)0 0 078-4
- Potanina, M. G.; Smirnov, V. B.; Bernard, P. (2011). Patterns of seismic swarm activity in the Corinth Rift in 2000-2005, *Physics of the Solid Earth*, **47**, 610-622.
- Psilovikos, A and Sotiriadis, L. (1983). The neotectonic graben complex of the Sevomacedonian massif at the area of Promygdonia basin, in northern Greece, *Clausthaler Geologische Abhandlungen*, **44**, 21-53.
- Reasenber, P. (1985). Second-order moment of central California seismicity, 1969– 1982, *J. Geophys. Res.*, **90**, 5479– 5495.
- Reasenber, P. A., and R. W. Simpson (1992). Response of regional seismicity to the static stress change produced by the Loma Prieta earthquake, *Science*, **255**, 1687-1690.
- Reid, H.F. (1910). *The California Earthquake of April 18, 1906. Volume II. The Mechanics of the Earthquake*. Washington DC: Carnegie Institution of Washington, Publication No. 87.
- Reilinger, R.E., McClusky, S.C., Oral, M.B., King, R.W., Toksoz, M.N., Barka, A.A., Kinik, I., Lenk, O. and Sanli, I. (1997). Global positioning system measurements of present-day crustal movements in the Arabia–Africa–Eurasia collision zone, *J. Geophys. Res.*, **102**, 9983–9999.
- Reilinger, R., McClusky, S., Vernant, P., Lawrence, S., Ergintav, S., Cakmak, R., Ozener, H., Kadirov, F., Guliev, I., Stepanyan, R., Nadariya, M., Hahubia, G., Mahmoud, S., Sakr, K., ArRajehi, A., Paradissis, D., Al-Aydrus, A., Prilepin, M., Guseva, T., Evren, E., Dmitrotsa, A., Filikov, S. V., Gomez, F., Al-Ghazzi R. and Karam, G. (2006). GPS constraints on continental deformation in the Africa–Arabia–Eurasia continental collision zone and implications for the dynamics of plate interactions, *J. Geophys. Res.*, **111**, doi: 10.1029/2005JB004051.
- Rice, J. and Cleary, M., (1976). Some basic stress diffusion solutions for fluid saturated elastic porous media with compressible constituents, *Rev. Geophys.*, **14**, 227–241.
- Rietbrock, A., Tiberi, C., Scherbaum, F. and Lyon-Caen, H. (1996). Seismic slip on a low angle normal fault in the Gulf of Corinth: evidence from high-resolution cluster analysis of microearthquakes *Geophys. Res. Lett.*, **23**, 1817–1820.
- Rigo, A., Lyon–Caen, H., Armijo, R., Deschamps, A., Hatzfeld, D., Makropoulos, K., Papadimitriou, P. and Kassaras, I. (1996). Microseismicity study in the western part of the Gulf of Corinth (Greece): Implications for large–scale normal faulting mechanisms. *Geophys. J. Int.*, **126**, 663–688.
- Rikitake, T. (1976). Earthquake prediction, Amsterdam, *Elsevier*.
- Roberts, G. (2006). Multi-seismic cycle velocity and strain fields for an active normal fault system, central Italy. *Earth and Plan. Sc. Lett.* **251**, 44-51.

- Roberts, G.P. and Koukouvelas, I.K. (1996). Structural and seismological segmentation of the Gulf of Corinth fault system: implication for models of fault growth, *Annali di Geophysica*, 39, 619–646.
- Roberts, S. and Jackson, J. A. (1991). Active normal faulting in central Greece: An overview, in *The Geometry of Normal Faults*, Spec. Publ. Geol. SOC. Lond., vol. 56, 125-142, eds Roberts, A. M., Yielding, G. and Freeman, B., Blackwell Scientific Publications, Oxford
- Robinson, R. and McGinty, P.J. (2000). The enigma of Arthur's Pass, New Zealand, earthquake 2. The aftershock distribution and its relation to regional and induced stress fields, *J. Geophys. Res.*, **105**, 139–16 150.
- Rolandone, F., Burgmann, R. and Nadeau, R. M. (2004). The evolution of the seismic-aseismic transition during the earthquake cycle: Constraints from the time-dependent depth distribution of aftershocks, *Geophys. Res. Lett.*, **31**, L23610, doi:10.1029/2004GL021379.
- Roumelioti, Z., Theodulidis, N. and A. Kiratzi (2006). The 20 June 1978 Thessaloniki (northern Greece) earthquake revisited: slip distribution and forward modeling of geodetic and seismological observations. Proceedings of the 4th International Conf. on Earthquake Geotechnical Engineering, paper ID: 1594.
- Roumelioti Z., Theodoulidis N., and Bouchon M. (2013). Constraints on the location of the 2008, Mw6.4 Achaia –Ilia earthquake fault from strong motion data. *Bull. of the Geol.Soc of Greece*.
- Rudzinski, L. and Debski, W. (2008). Relocation of mining induced seismic events in the upper Silesian coal basin Poland by a double-difference method, *Acta Geodyn Geomater* **5**, 97–104.
- Sakellariou, D., Lykousis, V., Alexandri, S., Kaberi, H., Rousakis, G., Nomikou, P., Georgiou, P. and Ballas, D. (2007). Faulting, seismic-stratigraphic architecture and Late Quaternary evolution of the Gulf of Alkyonides Basin–East Gulf of Corinth, Central Greece, *Basin Res.*, **19**, 273–295.
- Scholz, C.H. (1982). Scaling laws for large earthquakes: consequences for physical models, *Bull. Seism. Soc. Am.*, **72**, 1-14.
- Scholz, C.H. and Cowie, P.A. (1990). Determination of total strain from faulting using slip measurements, *Nature*, **346**, 837-839.
- Scholz, C. (2002). *The mechanics of earthquakes and faulting*, Cambridge University Press, Cambridge, 439.
- Scholz C. (2010). Large earthquake triggering, clustering, and the synchronization of faults. *Bull. Seismol. Soc. Am.*, 100:901–909.
- Schultz, R., Soliva, R., Okubo, C., and Mège, D. (2009). Fault populations. In T. Watters and R. Schultz (Eds.), *Planetary Tectonics* (Cambridge Planetary Science, pp. 457-510). Cambridge: Cambridge University Press.
- Scordilis, E.M. (1985). *Microseismic study of the Serbomacedonian zone and the surrounding area*, PhD Thesis, Univ. of Thessaloniki, p. 250.
- Scordilis, E.M., Karakaisis, G.F., Karakostas, B.G., Panagiotopoulos, D.G., Comminakis, P.E. and Papazachos, B.C. (1985). Evidence for transform faulting in the Ionian Sea: The Cephalonia island earthquake sequence of 1983, *Pure Appl. Geophys*, **123**, 388-397.
- Scordilis, E., Karakaisis, G., Papadimitriou, E., Margaris, B. (1989). Microseismicity study of the Servomacedonian zone and the surrounding area, *Geologica Rhodopica*, **1**, 79 – 83.
- Segou, M., Ellsworth, W. L. and Parsons, T. (2014). Stress Transfer by the 2008 Mw 6.4 Achaia Earthquake to the Western Corinth Gulf and Its Relation with the 2010 Efpalio Sequence, Central Greece, *Bull. Seism. Soc. Am.*, **104**, 1723–1734.
- Serpetsidaki, A., Elias, P., Ilieva, M., Bernard, P., Briole, P., Deschamps, A., Lambotte, S., Lyon-Caen, H., Sokos, E. and Tselentis, G.A. (2014). New constraints from seismology and geodesy on the Mw = 6.4 2008 Movri (Greece) earthquake: Evidence for a growing strike-slip fault system, *Geophys. J. Int.*, **198**, 1373–1386, doi: 10.1093/gji/ggu212.
- Sgroi, T., Nardis, R. and Lavecchia, G. (2012). Crustal structure and seismotectonics of central Sicily (southern Italy): new constraints from instrumental seismicity, *Geophys. J. Int.*, **189**, 1237–1252.
- Shadkhoo, S., Ghanbarnejad, F., Jafari, G.R., and Tabar, M.R.R. (2009). Scaling behavior of earthquakes' inter-events time series, *Central European Journal of Physics*, **7** (3), 620-623.
- Sokos, E., Zahradnik, J., Kiratzi, A., Jansky, J., Gallovič, F., Novotny, O., Kostelecky, J., Serpetsidaki, A. and Tselentis, G.A. (2012). The January 2010 Efpalio earthquake sequence in the western Corinth Gulf (Greece), *Tectonophysics*, 1–11.
- Soliva, R. and Schultz, R.A. (2008). Distributed and localized faulting in extensional settings: Insight from the North Ethiopian Rift-Afar transition area, *Tectonics*, **27**:n/a-n/a doi:10.1029/2007tc002148.

- Sornette, A., Davy P. and Sornette, D. (1990). Growth of fractal fault patterns, *Phys. Rev. Lett.*, **65**, 2266–2269.
- Sotiropoulos, S., Kamberis, E., Triantafyllou, M. and Doutsos T. (2003). Thrust sequences in the central part of the External Hellenides, *Geol. Mag.* **140** (6), 661–668.
- Soufleris, C. and Steward, G. (1981). A source study of the Thessaloniki (northern Greece) 1978 earthquake sequence, *Geophys. J. R. Astron. Soc.*, **67**, 343–358.
- Soufleris, C., Jackson, J., King, G., Spencer, C. and Scholz, C. (1982). The 1978 earthquake sequence near Thessaloniki (northern Greece), *Geophys. J. R. Astron. Soc.*, **68**, 429–458.
- Spyropoulos, C., Griffith, W., Scholz, C. and Shaw, B. (1999). Experimental evidence for different strain regimes of crack populations in a clay model, *Geoph. Res. Lett.*, **26**, 1081 – 1084.
- Stefatos, A., Papatheodorou, G., Ferentinos, G., Leeder, M. and Collier, R. (2002). Seismic reflection imaging of active offshore faults in the Gulf of Corinth: their seismotectonic significance, *Basin Res.*, **14**, 487–502, doi: 10.1046/j.1365-2117.2002.00176.x.
- Stein, R. S., G. C. P. King, and J. Lin, (1994). Stress triggering of the 1994 M = 6.7 Northridge, California, earthquake by its predecessors, *Science*, **265**, 1432–1435.
- Stein, R. S., A. A. Barka, and J. H. Dieterich, (1997). Progressive failure on the North Anatolian fault since 1939 by earthquake stress triggering, *Geophys. J. Int.*, **128**, 594–604.
- Stein, R. S. (1999). The role of stress transfer in earthquake occurrence, *Nature*, **402**, 594–604.
- Stein, S., Liu, M., Calais, E. and Li, Q. (2009). Mid-continent earthquakes as a complex system, *Seismol. Res. Lett.*, **80**, 551–553.
- Stekete, J. (1958). On Volterra's dislocations in a semi-infinite elastic medium, *Can. J. Phys.*, **36**, 192–205.
- Stewart, I., and C. Vita-Finzi (1996). Coastal uplift on active normal faults: The Eliki Fault, Greece, *Geophys. Res. Lett.*, **23**, 1853 – 1856.
- Stiros, S., Moschas, F., Feng, L. and Newman, A. (2013). Long-term versus short-term deformation of the meizoseismal area of the 2008 Achaia–Elia (M_w 6.4) earthquake in NW Peloponnese, Greece: Evidence from historical triangulation and morphotectonic data, *Tectonophysics*, **592**, 150–158, doi: 10.1016/j.tecto.2013.02.016.
- Tan, O., Papadimitriou, E.E., Pabucçu, Z., Karakostas, V., Yoruk, A. and Leptokaropoulos, K. (2014). A detailed analysis of microseismicity in Samos and Kusadasi (Eastern Aegean Sea) areas, *Acta Geophys.*, **62**, 1283–1309, <https://doi.org/10.2478/s11600-013-0194-1>.
- Taymaz, T., (1996). S-P-wave traveltimes residuals from earthquakes and lateral inhomogeneity in the upper mantle beneath the Aegean and the Hellenic Trench near Crete, *Geoph. J. Int.*, **127**, 545–558.
- Taymaz, T., Jackson, J. A. and McKenzie, D. P. (1991). Active tectonics of the North and Central Aegean Sea, *Geophys. J. Int.*, **106**, 433–490.
- Thompson, G. A., and Parsons T. (2016). Vertical deformation associated with normal fault systems evolved over coseismic, postseismic, and multi seismic periods, *J. Geophys. Res. Solid Earth*, **121**, 2153–2173, doi:10.1002/2015JB012240.
- Toda, S., Stein, R.S., Reasenber, P.A. and Dieterich, J.H. (1998). Stress transferred by the 1995 Mw = 6.9 Kobe, Japan, shock: Effect on aftershocks and future earthquake probabilities. *J. Geophys. Res.*, **103**, 24,543–24,565.
- Tranos, M. (2011). Strymon and Strymonikos Gulf basins (Northern Greece): Implications on their formation and evolution from faulting, *J. Geodyn.*, **51**, 285–305.
- Tranos, M., Kiliyas, A. and Mountrakis, D. (1999). Geometry and kinematics of the Tertiary post-metamorphic Circum Rhodope Belt Thrust System (CRBTS), Northern Greece, *Bulletin of Geological Society of Greece*, **33**, 5–16.
- Tranos, M., Papadimitriou, E. and Kiliyas, A. (2003). Thessaloniki-Gerakarou fault zone (TGFZ): the western extension of the 1978 Thessaloniki earthquake fault (northern Greece) and seismic hazard assessment, *J. Struct. Geol.*, **25**, 2109–2123.
- Tsodoulos, I., Koukouvelas, I., Pavlides, S. (2008). Tectonic geomorphology of the easternmost extension of the Gulf of Corinth (Beotia, Central Greece), *Tectonophysics*, **453**, 211–232.
- Utsu, T. (1966). A statistical significance test of the difference in b-value between two earthquake groups, *J. Phys. Earth*, **14**, 34–40.
- Valkaniotis, S. (2009). *Correlation of Neotectonic structures and seismicity in the broader area of Corinth Gulf (Central Greece)*, PhD thesis, Thessaloniki Aristotle University.

- Vamvakaris, D., Papazachos, C., Karagianni, E., Scordilis, E. and Hatzidimitriou P. (2006). Small-scale spatial variation of the stress field in the back-arc Aegean area: Results from the seismotectonic study of the broader area of Mygdonia basin (N. Greece), *Tectonophysics*, **417**, 249-267.
- van Hinsbergen, D.J.J. and Schmid S.M (2012). Map view restoration of Aegean–West Anatolian accretion and extension since the Eocene, *Tectonics*, **31**, TC5005 doi:10.1029/2012TC003132.
- Vere-Jones, D., Ben-Zion, Y. and Zúñiga, R. (2005). Statistical Seismology, *Pure Appl. Geophys.*, **162**, 6-7, 1023-1026.
- Wadati, K. (1933). On the travel time of earthquake waves, Part II. *Geophysical Magazine*, **7**, 101–111.
- Waldhauser, F. (2001). HypoDD - a program to compute double-difference hypocenter locations, US Geological Survey Open File Report, 01-113.
- Waldhauser, F. and Ellsworth, W.L. (2000). A double-difference earthquake location algorithm: method and application to the Northern Hayward Fault, California, *Bull. Seismol. Soc., Am.* **90**, 1353-1368.
- Ward, S. (1998). On the consistency of earthquake moment release and space geodetic strain rates, *Europe Geophysical Journal International*, **135**, 1011 – 1018.
- Wason, H. R., R. Das and M. L. Sharma (2012). Magnitude conversion problem using general orthogonal regression, *Geophys. J. Int.*, **190**, 1091-1096.
- Węglarczyk, S. and Lasocki, S. (2009). Studies of short and long memory in mining-induced seismic processes, *Acta Geophysica*, **57**, 696-715, doi:10.2478/s11600-009-0021-x.
- Wells, D. L. and Coppersmith K. L. (1994). New empirical relationships among magnitude, rupture width, rupture area, and surface displacement, *Bull. Seism. Soc. Am.*, **84**, 974-1002.
- Wessel, P. and Smith, W.H.F. (1995). New version of the Generic Mapping Tools released. *Eos* **76**, 329.
- Westaway, R. (1996). Quaternary elevation change in the Gulf of Corinth of central Greece. *Philos. Trans. R. Soc. London, Ser. A* **354**, 1125 – 1164.
- Westaway, R. (2002). The Quaternary evolution of the Gulf of Corinth, central Greece: coupling between surface processes and flow in the lower continental crust, *Tectonophysics*, **348**, 269–318.
- Wiemer, S., and Wyss, M. (1994). Seismic quiescence before the Landers (M=7.5) and Big Bear (M=6.5) 1992 earthquakes, *Bull. Seism. Soc. Am.*, **84**, 900-916.
- Wiemer, S. and Wyss, M. (2000). Minimum magnitude of completeness in earthquake catalogs: examples from Alaska, the Western United States, and Japan, *Bull. Seismol. Soc. Am.*, **90**, 859–869.
- Woessner, J., Hardebeck, J.L. and Hauksson E. (2010). What is an instrumental seismicity catalog, *Community Online Resource for Statistical Seismicity Analysis*, doi:10.5078/corssa-38784307.
- Xu, Y. and Burton, P.W. (1999). Spatial fractal evolution and hierarchies for microearthquakes in central Greece, *Pure Appl. Geophys.*, **154**, 73–99.
- Xu, Y. and Burton, P.W. (2001). Rescaled range analysis of the frequency of occurrence of moderate–strong earthquakes in the Mediterranean area. In: Novak, M.M. (Ed.), *Emergent Nature: Patterns, Growth and Scaling in the Sciences*, World Scientific, New Jersey, 305–314.
- Xu, Y. and Burton, P.W. (2006). Time varying seismicity in Greece: Hurst's analysis and Monte Carlo simulation applied to a new earthquake catalogue for Greece, *Tectonophysics*, **423**, 125–136.
- Zervopoulou, A.S. (2010). *Neotectonic faults of the broader area of Thessaloniki and foundation on them*, PhD Thesis, Aristotle University of Thessaloniki, 300.
- Zhuang J., Ogata Y. and Vere-Jones D. (2004). Analyzing earthquake clustering features by using stochastic reconstruction, *J. Geophys. Res.*, **109**, No. B5, B05301.
- Zhuang, J., Harte, D., Werner, M.J., Hainzl, S. and Zhou, S. (2012). Basic models of seismicity: temporal models, *Community Online Resource for Statistical Seismicity Analysis*, doi:10.5078/corssa-79905851.